# Palaeoenvironmental analysis of the Georgina River catchment and the wet and dry cycles of late Quaternary Australia.

Thesis submitted by

Russell Edward Singleton

November 2024

For the Degree of Doctor of Philosophy
James Cook University

In the College of Science and Engineering
within the
School of Earth and Environmental Science

## Statement of Access

I, the undersigned author of this thesis, understand that James Cook University will make this thesis available for use within the university library and allow access in other approved libraries after its submission. All users consulting this thesis will have to sign the following statement:

*In consulting this thesis, I agree not to copy or closely paraphrase it in whole or in part without the written consent of the author; and to make proper public written acknowledgement for any assistance which I have obtained from it.*

Beyond this, I do not wish to place any restrictions on access to this thesis.

Russell E. Singleton
November 2024

# Declaration

I declare that this thesis is my own work and has not been submitted in any form for another degree or diploma at any university or other institute or tertiary education. Information derived from the published or unpublished work of others has been acknowledged in the text and a list of references is given.

Russell E. Singleton
November 2024

# Acknowledgements

First, I would like to thank my partner, Dr. Theresa Orr for bringing our two boys Jett and Ocean into this world while completing her own thesis and helping me complete mine. Her help with sedimentological and palaeopedological analysis, late night geochemistry discussions, and her unwavering support has made this all possible. I cannot thank you enough.

Thank you to my primary supervisor Dr. Michael Bird for his guidance, mentoring and giving me the freedom to explore this research topic and grow as an academic. Additionally, the guidance and inspiration of my co-supervisors, Dr. Jonathan Nott and Dr. Robert Wasson has been immeasurable. I have also benefitted from the guidance and mentoring of Dr. Justine Kemp. I greatly appreciate the input and suggestions of Dr. Zenobia Jacobs, Dr. Christopher Wurster, Dr. Jen Whan, Dr. Nathan Jankowski, Dr. Eric Roberts and Mr. Rainy Comley. Thank you Mr. Michael brand for assistance with fieldwork and planning. Thanks, are also extended to the Mithaka Aboriginal Corporation, in particular Mr Max Goringe for meeting me out in Mithaka country.

I would also like to thank my mother Jill who always supported me with long phone conversations inquiring about me and what stage I was up to in my research. To my father Graham who is a scientist, thank you for always believing in me as well as enthusiastically assisting me with some microscope work, data recording, and exploding samples with peroxide. Thank you Cushla for looking after your grandsons giving me the research and writing time I needed to complete work. And finally, to Dawn and Heather, my two sisters who I’m so grateful to have in my life for inspiring me to be the best I can be.

Funding for this project was provided by the Australian Research Council (ARC), James Cook University, Geological Society of Australia, and Australian Government Research Training Program (RTP) Scholarship for tuition support.

# Statement of contribution of others

The following table provides a statement on the general contribution of others in relation to this thesis. Subsequent tables detail the specific contributions provided by my supervisors, colleagues, and collaborators in relation to each chapter, and any relevant publications.

| Nature of assistance | Contribution | Names and affiliations of co-contributors |
|---|---|---|
| Intellectual support | Proposal writing | Dr. Michael I. Bird, James Cook University |
| | Data analysis | Dr. Michael I. Bird, James Cook University<br>Dr. Robert J. Wasson, James Cook University<br>Dr. Jonathan Nott, James Cook University |
| | Editorial assistance | Dr. Michael I. Bird, James Cook University<br>Dr. Robert J. Wasson, James Cook University<br>Dr. Jonathan Nott, James Cook University<br>Dr. Justine Kemp, Griffith University |
| Financial support | Research funding | Australian Research Council (MIB)<br>James Cook University<br>Geological Society of Australia |
| | Stipend | Australian Government |
| Data collection | In-field assistance | Dr. Michael I. Bird, James Cook University<br>Dr Jonathan Nott, James Cook University<br>Dr Justine Kemp, Griffith University<br>Mr Michael Brand<br>Mr Max Goringe, Mithaka Aboriginal Corporation |
| | Research assistance | Dr. Michael I. Bird, James Cook University<br>Dr. Zenobia Jacobs, University of Wollongong<br>Dr. Christopher M. Wurster, James Cook University<br>Dr. Jen Whan, James Cook University<br>Dr. Theresa J. Orr, James Cook University<br>Dr. Nathan Jankowski, University of Wollongong<br>Dr. Eric M. Roberts, James Cook University<br>Mr Rainy Comley, James Cook University |

## Statement of contribution – Dr. Michael I. Bird

| Chapter | Publication | Nature and extent of contribution |
|---|---|---|
| 1 | Russell. E. Singleton, Michael I. Bird, Jonathan Nott, Robert J. Wasson. | Dr. Michael I. Bird provided editorial assistance. |
| 2 | Russell. E. Singleton, Michael I. Bird, Theresa J. Orr, Zenobia Jacobs, Jonathan Nott, Justine Kemp, Robert J. Wasson. (In preparation for submission to Journal of Quaternary Science) | Dr. Michael I. Bird contributed to concept development, sample collection and provided editorial assistance. |
| 3 | Russell. E. Singleton, Theresa J. Orr, Michael I. Bird, Zenobia Jacobs, Jonathan Nott, Robert J. Wasson. (In preparation for submission to Quaternary International) | Dr. Michael I. Bird contributed to concept development, sample collection and provided editorial assistance. |
| 4 | Russell. E. Singleton, Michael I. Bird, Jonathan Nott, Zenobia Jacobs, Justine Kemp, Robert J. Wasson. (In preparation for submission to Australian Journal of Earth Sciences) | Dr. Michael I. Bird contributed to concept development, sample collection and provided editorial assistance. |

## Statement of contribution – Dr. Robert J. Wasson

| Chapter | Publication | Nature and extent of contribution |
|---|---|---|
| 1 | Russell. E. Singleton, Michael I. Bird, Jonathan Nott, Robert J. Wasson. | Dr. Robert J. Wasson contributed to concept development and provided editorial assistance. |
| 2 | Russell. E. Singleton, Michael I. Bird, Theresa J. Orr, Zenobia Jacobs, Jonathan Nott, Justine Kemp, Robert J. Wasson. (In preparation for submission to Journal of Quaternary Science) | Dr. Robert J. Wasson contributed to concept development and provided editorial assistance. |
| 3 | Russell. E. Singleton, Theresa J. Orr, Michael I. Bird, Zenobia Jacobs, Jonathan Nott, Robert J. Wasson. (In preparation for submission to Quaternary International) | Dr. Robert J. Wasson contributed to concept development and provided editorial assistance. |
| 4 | Russell. E. Singleton, Michael I. Bird, Jonathan Nott, Zenobia Jacobs, Justine Kemp, Robert J. Wasson. (In preparation for submission to Australian Journal of Earth Sciences) | Dr. Robert J. Wasson contributed to concept development and provided editorial assistance. |

**Statement of contribution – Dr. Jonathan Nott**

| Chapter | Publication | Nature and extent of contribution |
|---|---|---|
| 1 | Russell. E. Singleton, Michael I. Bird, Jonathan Nott, Robert J. Wasson. | Dr. Jonathan Nott provided editorial assistance. |
| 2 | Russell. E. Singleton, Michael I. Bird, Theresa J. Orr, Zenobia Jacobs, Jonathan Nott, Justine Kemp, Robert J. Wasson. (In preparation for submission to Journal of Quaternary Science) | Dr. Jonathan Nott provided editorial assistance. |
| 3 | Russell. E. Singleton, Theresa J. Orr, Michael I. Bird, Zenobia Jacobs, Jonathan Nott, Robert J. Wasson. (In preparation for submission to Quaternary International) | Dr. Jonathan Nott provided editorial assistance. |
| 4 | Russell. E. Singleton, Michael I. Bird, Jonathan Nott, Zenobia Jacobs, Justine Kemp, Robert J. Wasson. (In preparation for submission to Australian Journal of Earth Sciences) | Dr. Jonathan Nott provided editorial assistance. |

**Statement of contribution – Dr. Justine Kemp**

| Chapter | Publication | Nature and extent of contribution |
|---|---|---|
| 1 | Russell. E. Singleton, Michael I. Bird, Jonathan Nott, Robert J. Wasson. | Dr. Justine Kemp provided editorial assistance. |
| 2 | Russell. E. Singleton, Michael I. Bird, Theresa J. Orr, Zenobia Jacobs, Jonathan Nott, Justine Kemp, Robert J. Wasson. (In preparation for submission to Journal of Quaternary Science) | Dr. Justine Kemp provided editorial assistance. |
| 3 | Russell. E. Singleton, Theresa J. Orr, Michael I. Bird, Zenobia Jacobs, Jonathan Nott, Robert J. Wasson. (In preparation for submission to Quaternary International) | Dr. Justine Kemp provided editorial assistance. |
| 4 | Russell. E. Singleton, Michael I. Bird, Jonathan Nott, Zenobia Jacobs, Justine Kemp, Robert J. Wasson. (In preparation for submission to Australian Journal of Earth Sciences) | Dr. Justine Kemp provided editorial assistance. |

## Statement of contribution – Dr. Zenobia Jacobs

| Chapter | Publication | Nature and extent of contribution |
|---|---|---|
| 2 | Russell. E. Singleton, Michael I. Bird, Theresa J. Orr, Zenobia Jacobs, Jonathan Nott, Justine Kemp, Robert J. Wasson. (In preparation for submission to Journal of Quaternary Science) | Dr Zenobia Jacobs conducted the optically stimulated luminescence (OSL) analyses and completed the associated data reduction. |
| 3 | Russell. E. Singleton, Theresa J. Orr, Michael I. Bird, Zenobia Jacobs, Jonathan Nott, Robert J. Wasson. (In preparation for submission to Quaternary International) | Dr Zenobia Jacobs conducted the optically stimulated luminescence (OSL) analyses and completed the associated data reduction. |
| 4 | Russell. E. Singleton, Michael I. Bird, Jonathan Nott, Zenobia Jacobs, Justine Kemp, Robert J. Wasson. (In preparation for submission to Australian Journal of Earth Sciences) | Dr Zenobia Jacobs conducted the optically stimulated luminescence (OSL) analyses and completed the associated data reduction. |

## Statement of contribution – Dr. Theresa J Orr

| Chapter | Publication | Nature and extent of contribution |
|---|---|---|
| 2 | Russell. E. Singleton, Michael I. Bird, Theresa J. Orr, Zenobia Jacobs, Jonathan Nott, Justine Kemp, Robert J. Wasson. (In preparation for submission to Journal of Quaternary Science) | Dr. Theresa J. Orr contributed facies and stratigraphy characterisation and provided editorial assistance. |
| 3 | Russell. E. Singleton, Theresa J. Orr, Michael I. Bird, Zenobia Jacobs, Jonathan Nott, Robert J. Wasson. (In preparation for submission to Quaternary International) | Dr. Theresa J. Orr conducted the palaeopedological analyses and completed the associated data reduction, analysis, and results description. |

## Statement of contribution – Dr. Christopher M. Wurster

| Chapter | Publication | Nature and extent of contribution |
|---|---|---|
| 2 | Russell. E. Singleton, Michael I. Bird, Theresa J. Orr, Zenobia Jacobs, Jonathan Nott, Justine Kemp, Robert J. Wasson. (In preparation for submission to Journal of Quaternary Science) | Dr. Christopher M. Wurster provided laboratory assistance |

**Statement of contribution – Mr Michael Brand**

| Chapter | Publication | Nature and extent of contribution |
|---|---|---|
| 2 | Russell. E. Singleton, Michael I. Bird, Theresa J. Orr, Zenobia Jacobs, Jonathan Nott, Justine Kemp, Robert J. Wasson. (In preparation for submission to Journal of Quaternary Science) | Mr Michael Brand contributed to fieldwork. |
| 3 | Russell. E. Singleton, Theresa J. Orr, Michael I. Bird, Zenobia Jacobs, Jonathan Nott, Robert J. Wasson. (In preparation for submission to Quaternary International) | Mr Michael Brand contributed to fieldwork. |
| 4 | Russell. E. Singleton, Michael I. Bird, Jonathan Nott, Zenobia Jacobs, Justine Kemp, Robert J. Wasson. (In preparation for submission to Australian Journal of Earth Sciences) | Mr Michael Brand contributed to fieldwork. |

# Thesis Abstract

The late Quaternary climatic history of central Australia remains largely unknown. Indeed, the history of the Lake Eyre Basin (LEB), one of the world's largest endorheic drainage basins, is mostly derived from records in the south and east, such as Kati-Thanda Lake Eyre, Lake Frome and Cooper Creek. However, the Georgina catchment, the LEB's most northern catchment, contains aeolian, fluvial and lacustrine sediments that document dramatic palaeoclimatic and palaeohydrological variations during the late Quaternary. This thesis investigates the late Quaternary climatic and hydrological evolution of the Georgina catchment. The study clarifies the spatial and temporal extent of climate forcing mechanisms and associated moisture source(s), as well as their impact on the arid interior of Australia including significant lake filling episodes. Using sedimentological, spatial, geochronological, and geochemical methods, this research identifies key wet and dry phases over the last ~500,000 years. The results are also compared with the published progression toward increased aridity in Australia during the late Pleistocene.

The key findings highlight that the Georgina catchment experienced major wet phases during MIS 7 and 5, contributing to lake fillings in both the southern reaches of the Georgina catchment and potentially Kati-Thanda Lake Eyre. The sedimentological records of Lakes Machattie and Koolivoo in the southern Georgina catchment reveal that during these times northern Australia was significantly wetter than today. A transition toward drier conditions began in MIS 4, with intensified drying in MIS 3, reflected in the loss of permanent water bodies. Further evidence from a dune-palaeosol sequence shows that pedogenesis in a humid climate ceased around ~50 ka, corresponding to a reduction in monsoonal rainfall and increased seasonality. This research also documents evidence of major flooding in the Lake Machattie shoreline deposits, including significant historical floods around 1784 and 1830 CE. Eleven modern flood events were also found to be responsible for lake highstands, with those in 1974, 1997, and 2001 creating substantial barrier overwash deposits. These flood events indicate the potential for the Georgina catchment to contribute to broader lake fillings in Kati-Thanda Lake Eyre during both modern and ancient times. This thesis provides the first palaeoenvironmental record of the Georgina catchment, offering novel insights into the northern LEB's natural history and the contribution of the catchment to central Australia's hydrological evolution.

# Table of Contents

# List of Figures

# List of Tables

## Introduction and Thesis Structure

The Lake Eyre Basin (LEB), one of the world's largest internally draining basins, is a critical archive for understanding long-term hydroclimatic variability in Australia's arid interior. The preservation of sedimentary sequences within its dunes, lakes and major tributaries provides key insights into Quaternary climate change, including the timing and magnitude of wet and dry phases. Indeed, palaeohydrological records from Kati-Thanda Lake Eyre (KT-LE), the termini of the LEB, and Lake Frome demonstrate links to late Quaternary climate oscillations on a range of timescales (e.g., Zuraida et al., 2009, Denniston et al., 2013b, Fu et al., 2017, De Deckker et al., 2019). These sites record a history of wet-dry cycles with a superimposed drying trend since at least marine isotope stage (MIS) 7 (Fu et al., 2017). Palaeoshorelines at KT-LE and in neighbouring Lake Frome show that mega-lake fillings in MIS 5, one of the wettest periods in central Australia over the last glacial period, reached depths of ≥24 m and 15m (respectively) (Nanson et al., 2008). These fillings were capable of connecting the two lakes via the 25-km-long Warrawoocara channel (Nanson et al., 2008) to form a vast mega-lake not seen since. In comparison under the wettest modern hydrological conditions (observed in 1974), the simultaneous flooding of all major LEB watercourses only filled these playa lakes to ~6m deep (-9.1m AHD) (Habeck-Fardy and Nanson, 2014). While minor low-level lake filling episodes continued in the late Pleistocene–Holocene at KT-LE and Lake Frome, a catastrophic drying phase began at ~48 ka (Cohen et al., 2011; 2015) that coincided with the ongoing mass extinction of a diverse range of Megafauna on mainland Australia (e.g., Roberts et al., 2001, Price et al., 2011, Miller et al., 2016a, Saltré et al., 2019), which peaked at ~42 ka (Saltré et al., 2016). Overall, these sedimentary records offer insights into past climate variability; however, their interpretation is influenced by the discontinuous nature of sediment deposition and the complexities of geochemical and geomorphic proxies (Fitzsimmons et al., 2013).

Existing knowledge of the LEB's hydroclimate has primarily been derived from sedimentary records in KT-LE and Lake Frome (e.g., Magee et al., 1995, Croke et al., 1996, Cohen et al., 2018), supplemented by aeolian and fluvial archives from Cooper Creek and the Diamantina River (e.g., Nanson et al., 1992b; 2008, Maroulis et al., 2007). These studies used a combination of sediment stratigraphy, luminescence dating and geochemical proxies to reconstruct past climate variability. For example, Cohen et al. (2015) used the $\delta^{13}C$ values of *Dromaius novaehollandiae* (emu) and *Genyornis newtoni* (large extinct bird) eggshells (see Miller et al., 1999; 2005), OSL dating and satellite imagery to determine the timing of hydrological transformations in central Australia, including a major hydrological change at ~48 ka. Magee et al. (2004) provided a continuous 150,000-year monsoon proxy record from KT-LE and identified a Northern Hemisphere insolation influence on monsoonal strength, using luminescence, radiocarbon, and thermal-ionisation mass spectrometry (TIMS) derived dates. Palaeoshoreline studies, such as those by Cohen et al. (2018), have documented past high lake levels and their correspondence with enhanced La Niña years and negative Interdecadal Pacific Oscillation (IPO) phases. Similarly, Fu et al. (2017) extended the lacustrine record beyond the last interglacial for KT-LE, demonstrating that it responded to millennial-scale climate change rather than orbital forcing, with major lake-filling events correlating with cold periods in the North Atlantic. However, these records are largely concentrated in the southern LEB, leaving the hydrological history of its northern catchments poorly constrained.

The hydroclimate of the LEB is influenced by a combination of tropical and extratropical climate mechanisms operating on multiple timescales. The northern LEB is strongly affected by monsoonal incursions, while the mid-latitude westerlies regulate rainfall variability in the south (Habeck-Fardy and Nanson, 2014). ENSO and the IPO cycles introduce interannual and decadal variability in rainfall, with La Niña conditions typically associated with increased regional precipitation (Denniston et al., 2013b). At longer timescales, orbital forcing (e.g., Milankovitch cycles) is generally considered a weak driver of wet and dry phases, as demonstrated in records from KT-LE and Lake Frome (Cohen et al., 2012; 2022). Additionally, high-latitude climate variability, including North Atlantic Heinrich events and glacial-interglacial cycles, has played a role in shaping moisture availability across Australia (e.g., De Deckker et al. 2019). While previous studies have identified these broad climate trends, questions remain about the spatial heterogeneity of hydrological responses and the relative influence of these mechanisms in different catchments. Addressing these gaps requires additional records from underrepresented regions such as the Georgina Catchment, which this study aims to provide.

The LEB extends through three latitudinal zones, from the Georgina catchment in the monsoon tropics at 19°S to the temperate Flinders Ranges at 32°S. Seven drainage catchments comprise the LEB, the largest of which are the Cooper (300,000 $km^2$), Georgina (205,000 $km^2$) and Diamantina (160,000 $km^2$) River basins (Habeck-Fardy and Nanson, 2014). Today, these three catchments are monsoon fed with headwaters in northern Australia (Donders et al., 2008) and generate significant flows to KT-LE and Lake Frome (Habeck-Fardy and Nanson, 2014), albeit infrequently under modern hydrological conditions. Considerable progress has been made in establishing a palaeohydrological chronology from aeolian and fluvial systems in Cooper Creek, the LEB's most eastern catchment (e.g., Maroulis et al., 2007, Nanson et al., 2008, Cohen et al., 2010). At least four millennial-scale episodes of enhanced river flows have been identified in the Cooper since MIS 7 and suggest progressive drying of the catchment occurred over the last 130 kyr. Palaeohydrological records for the Diamantina are scant; however, alluvial sand deposits suggest fluvial activity across the northern LEB probably peaked around 110 ka (Nanson et al., 1992b, Kershaw and Nanson, 1993) coincident with highstands in KT-LE at ~108 ka (Cohen et al., 2015) and Lake Frome at ~110 ka (Cohen et al., 2011). To date, the Georgina catchment remains curiously ill-researched; indeed, no palaeohydrological records exist for the LEB's most northern and second largest drainage network.

Understanding the complex interplay of regional and global climate drivers behind extreme pluvials in the largest catchment in Australia, therefore, remains an important challenge to Quaternary palaeoclimatic reconstructions. Indeed, the lack of high-resolution terrestrial climate records from central Australia has been identified as a knowledge gap (Reeves et al., 2013, Neukom et al., 2014) with southwest Queensland flagged not only as an area of poor data, but as an area for which no data worthy of investigation exists (Reeves et al., 2013). The Georgina catchment is the second largest drainage basin in the LEB and remains one of the least studied systems despite its key role in documenting northern Australia's natural history. By collecting monsoonal rainfall in the north and transporting both water and sediments southward, the Georgina River contributes to major lake-filling events at KT-LE, while also preserving important hydroclimate records. The Georgina River's path extends through two climate zones from northwest of the semi-arid Mt Isa region at ~19°S to the arid Diamantina River confluence, Goyder lagoon, at ~27°S. In the lower reaches, ~ 200 km northeast of Goyder lagoon, the

Georgina River feeds three lakes: Koolivoo, Machattie, and Mipia. Together, these lakes and surrounding floodplains, termed the Lake Machattie Area represent the last major depocenter of the Georgina River before the river travels west, as Eyre Creek, then south through Simpson Desert interdunes before joining the Diamantina River, eventually reaching KT-LE.

The overall aim of this thesis is to develop a comprehensive palaeoclimate and palaeoenvironmental history of the Georgina catchment using geochronology and sedimentology, and to investigate how the history of the Georgina catchment relates to the chronology of lake fillings in KT-LE. By reconstructing the hydrological history of the Georgina catchment, this study will also contribute to a broader understanding of Quaternary palaeoclimates globally. This research will also provide insights into long-term shifts in Australia's hydroclimatic balance. More specifically, this research will clarify the spatial and temporal extent of moisture source incursions over the northern LEB and improve the resolution of the timing and cause of precipitation and runoff variations in central Australia during the late Quaternary. The thesis focuses on three distinct sedimentary environments to best capture variation in the wet and dry history of the Georgina catchment: 1) lacustrine, 2) aeolian and 3) shoreline.

**1) Lacustrine**

Palaeolake records, such as those in the Georgina catchment, offer crucial long-term environmental insights into Australia's hydrological history (e.g., Chen and Barton, 1991, Bowler et al., 1998; 2001, English et al., 2001). Especially the playa lakes that are found across the LEB (e.g., Bourne and Twidale, 2010, Mann and Amos, 2022). Indeed, in arid and semi-arid environments, playa lake sediments often provide the most continuous archive of past hydrological conditions, as they accumulate over repeated wet-dry cycles (Rosen, 1994, Valero-Garces et al., 2000). Changes in geochemistry, mineralogy and salinity in response to large fluctuations in water levels, particularly in groundwater-fed discharge playas, make them sensitive environmental indicators (Rosen, 1994, Valero-Garces et al., 2000, Pourali et al., 2020). Although, deflation and erosion during dry periods can result in discontinuous records, and post-depositional alteration may obscure palaeoenvironmental signals (Magee et al., 2004, Fitzsimmons et al., 2013).

Studies exploring the central and northern lakes of Australia have reported a near stepwise reduction in late Quaternary lake fillings amidst progressive aridification that likely began in the Miocene (Martin, 2006), but accelerated in the Pleistocene (Chen et al., 1990, English et al., 2001, Cohen et al., 2011; 2012b; 2015; 2022, Fu et al., 2017). This shift to drier conditions was dramatic enough to disconnect lake systems (e.g., Bowler et al., 2001) and ultimately see the end of mega-lake phases across the Australian interior, including mega-Lakes Amadeus, Frome, and KT-LE (Chen et al., 1990, Fujioka and Chappell, 2010, Cohen et al., 2011; 2012b; 2015; 2022, Fu et al., 2017). While major palaeolakes such as KT-LE and Frome have been extensively studied, the Georgina catchment remains largely unexamined, despite its role as a key contributor to KT-LE inflows. This thesis investigates the lake floor sedimentology of the ephemerally flooded Lakes Koolivoo and Machattie and the alluvial/fluvial deposits of the western drainage channel Eyre Creek, to develop the Quaternary palaeodepositional evolution of the Lake Machattie Area. Multiple palaeoclimate proxies are used to develop the hydroclimatic history to explore whether palaeo-wet periods were established across the monsoon-fed LEB catchments at the same time and to what extent the Georgina catchment contributed to palaeofillings of KT-LE.

**2) Aeolian**

Sand dunes, such as those that border the Georgina River are one of the most common landforms in Australia and represent a major source of palaeoenvironmental information. Dune fields in arid Australia consist of several types of dunes, including longitudinal (linear), transverse, parabolic, reticulate and source-bordering dunes, each of which forms under distinct wind regimes and sediment supply conditions (Bowler, 1973, Wasson, 1983a, Wasson and Hyde, 1983, Wasson et al., 1988, Hesse, 2011, Fitzsimmons et al., 2013). Longitudinal dunes, which dominate the Simpson Desert and indeed most Australian deserts, form parallel to prevailing winds (Wasson et al., 1988; Hesse, 2010), whereas transverse dunes develop perpendicular to dominant wind directions and are commonly found in areas with abundant sediment supply (e.g., Wasson et al., 1988). Parabolic dunes form downwind of an often-abundant sediment supply, developing their characteristic U-shape in response to vegetation stabilising the limbs (Wasson et al., 1988). In contrast, source-bordering dunes are so named because of their depositional setting; adjacent to the lakes, playas or river systems that provide their sediment (Hesse, 2011). These dunes are unique in that they record both aeolian deposition and localised alluvial activity, providing crucial insights into past periods of enhanced aeolian and fluvial activity (e.g., Nanson et al., 1995; 2008, Fitzsimmons et al., 2007). Many source-bordering dunes in Australia also develop a transverse (e.g., Hesse, 2011) or linear morphology in response to the prevailing winds (e.g., Cohen et al., 2010, Hesse, 2016, Maroulis et al., 2007).

Aeolian sediments by themselves provide limited information, but when combined with palaeosols preserved within the dunes, they can qualitatively and quantitatively reconstruct past climates and environments (Fitzsimmons et al., 2009). Palaeosols within dunes act as valuable environmental archives, preserving evidence of past landscape stability, vegetation cover, and moisture availability (Fitzsimmons et al., 2009, Hollands et al., 2006). The presence of buried palaeosols suggests periods of reduced dune activity and increased soil formation, reflecting climate fluctuations (Bowler, 1998). Geochemical and mineralogical analyses of these palaeosols can reveal past precipitation levels, soil development processes, and dust influx from surrounding arid landscapes (Retallack, 2008).

In the LEB, sandy dunefields stretch across the Simpson, Strzelecki and Tirari Deserts (Pell et al., 2000) documenting a range of climatic and environmental changes through the late Quaternary. Yet, most work on Australian dunes has focused on inferring palaeoclimates through dune building chronologies and aeolian sediment characteristics (e.g., Nanson et al., 1992a; 1995, Twidale et al., 2001, Lomax et al., 2003, Hollands et al., 2006, Fitzsimmons et al., 2007b, Fujioka et al., 2009) perhaps unintentionally discounting the value held within palaeosol horizons. Indeed, in Australia, quantitative palaeosol climate reconstructions are limited to Precambrian–Neogene sediments (Driese et al., 1995, Retallack, 1999; 2008; 2021a; 2021b, Metzger and Retallack, 2010, Retallack et al., 2015, Zhou et al., 2015, Mao and Retallack, 2019), with no records for palaeosols during the Quaternary. This thesis explores the age architecture and sedimentology of a palaeosol-bearing, source-bordering dune along the northeast margin of the Simpson Desert in the northern LEB, to constrain the palaeoclimate and palaeoenvironment during deposition and pedogenic intervals. The resulting data will be examined in the context of available dune records to investigate whether established arid and/or pluvial phases of the Quaternary were documented within the sediments, in addition to providing the first palaeoprecipitation record from the Georgina catchment.

### 3) Shoreline

Shoreline deposits bordering ephemeral lakes, such as those in the Georgina catchment, can record extreme rainfall events, flood frequency and magnitude (Kotwicki, 1986), phases of transgression, still stand or regression (Magee and Miller, 1998, Cohen et al., 2022) including previous lake levels (Magee et al., 1995, Magee, 1997, Magee and Miller, 1998, Nanson et al., 1998), and in the case of the LEB's large drainage catchments such as the Georgina, spatial and temporal variations in climate patterns. Indeed, investigation into the shoreline deposits of KT-LE identified at least 5 (possibly 7) major lake fillings since the 1600s that were comparable to the modern maximum lake fillings in 1974 and 1949/1950 (Cohen et al., 2018). Provenance studies by Cohen et al. (2022) suggests most of the sediment came from the Cooper Creek and the Diamantina River, yet despite the Georgina and Diamantina inputs flowing into KT-LE via the same drainage it is not known whether the Georgina was also fluvially active or contributed to these palaeo fillings. Sedimentary sequences exposed along the dryland lake margins in the Georgina catchment likely contain lacustrine and shoreline deposits that archived a record of modern-palaeo flooding events in the northern LEB. Combining aerial and satellite images with direct sedimentological investigations can provide an exceptionally detailed history of modern hydrological events (Cassiani et al., 2020) helping us to better understand palaeofloods. This thesis examines the shoreline features of Lake Machattie using sedimentology and spatial analysis of satellite and aerial imagery to determine lake-level boundary variation and develop a record of historical fillings. The potential climate patterns associated with these high stands are also investigated.

**Research questions**

This study addresses the following key research questions:

- What were the major hydroclimatic and environmental changes in the LMA over the past ~500,000 years?
- How do the lake phases and depositional environments recorded in the LMA compare to those in other central Australian lake systems, including those in the broader LEB?
- What role did cyclic climate forcing mechanisms have in driving hydroclimatic and environmental changes in the Georgina catchment?
- How did changes in regional vegetation and landscape stability correspond with shifts in lake hydrology and climate?
- What is the significance of the Georgina catchment's hydrological contributions to the LEB over different climatic periods, particularly during major lake-filling events?

**Thesis Structure**

This thesis is arranged into five chapters, designed to address the overarching research questions by progressively examining the Georgina catchment's palaeohydrology and its broader implications for central Australian climate variability. The structure follows a chronological progression, from the late Pleistocene to modern climatic and environmental reconstructions, allowing for an integrated understanding of hydroclimatic variability over different timescales.

Chapter 1 presents a chronological summary of north Atlantic Heinrich(-like) events and how they relate to expansive lake filling episodes in KT-LE and Lake Frome from MIS 7 to MIS 4. Northern high-latitude cool periods are widely hypothesised to have played a major role in triggering pluvial phases in central Australia (e.g., De Deckker et al., 2019). This chapter focuses on the last two glacial cycles, beginning with MIS 7, the first known lake-filling episode at KT-LE, and extending to MIS 4, just before anthropogenic influences and the disconnection of the mega-lakes during early MIS 3. This provides a framework for understanding how a large-scale climatic mechanism may have influenced hydrological variability in the LEB, setting the context for the subsequent chapters. The following three chapters present sedimentological studies conducted in the Georgina catchment, arranged in chronological order from oldest to youngest, to reconstruct its palaeohydrological evolution.

Chapter 2 details the first sedimentologically-derived palaeoclimate and palaeoenvironment reconstruction of the Georgina catchment over the last ~470 ka, addressing the question of major hydroclimatic and environmental changes in the LMA over this period. This chapter establishes the long-term context for past wet and dry phases and assesses how lake phases and depositional environments in the LMA compare to those recorded elsewhere in central Australia. Chapter 3 shifts focus to MIS 3, examining the age architecture of a source-bordering longitudinal dune at the northeastern margin of the Simpson Desert. This chapter uses sedimentological, and palaeopedological methods to reconstruct environmental conditions and investigate evidence of aeolian and fluvial activity. MIS 3 represents a key interval in Australia's climatic history, as it marks a transition to increasingly arid conditions and significant landscape modification. This chapter contributes to the broader question of how regional vegetation and landscape stability responded to hydroclimatic variability.

Chapter 4 examines the shoreline features of Lake Machattie in the southern Georgina catchment, providing a modern-to-palaeo-hydrological record of flooding in the northern LEB. By integrating sedimentological and remote sensing analyses, this chapter reconstructs lake-level variations and investigates their potential climatic drivers. The findings address the significance of the Georgina catchment's hydrological contributions to the LEB, particularly during major lake-filling events, and provides insights into shorter-term hydroclimatic fluctuations.

Chapter 5 provides a summary of the thesis and discusses possible future directions for research into the sedimentology of the Georgina catchment. Chapter's two to four are in preparation for publication, as such there is some inevitable repetition between chapters, such as the regional setting. Together, the three individual studies of this thesis present, for the first time, a detailed palaeoenvironmental record of the Georgina catchment from the late Quaternary to Recent, providing new insights into the natural history of not only the LEB, but of Australia's renowned arid interior.

# Chapter 1

# Testing linkages between Heinrich events and late Quaternary hydrological conditions in Australian Mega-Lakes Kati-Thanda Eyre and Frome

Singleton, R.E[a,b*]

[a]College of Science and Engineering, James Cook University, Cairns, QLD 4870, Australia

[b]ARC Centre of Excellence for Australian Biodiversity and Heritage, James Cook University, Cairns, QLD 4870, Australia

**Author contributions:**

Russell Singleton collected and interpreted the data, developed the research question and wrote the manuscript. Michael Bird, Jonathan Nott and Robert Wasson provided editorial assistance.

**Abstract**

This review summarises the current state of knowledge of Late Quaternary north Atlantic Heinrich(-like) events and how they relate to expansive lake filling episodes in the Australian Lake Eyre Basin (LEB), one of the world's largest endorheic drainage basins. This review focuses on Kati-Thanda Lake Eyre (KT-LE) and Lake Frome, by presenting an integrated chronological summary of the palaeohydrological records from the LEB and its surrounding regions. Due to the spatial heterogeneity and discontinuous nature of records across the LEB, basin-wide synthesis remains challenging. However, hydrological responses recorded in the terminal lakes suggest links to large-scale climate drivers, including Northern Hemisphere cooling events. This review provides a summary of major lake filling episodes and what effect northern high latitude cooling, specifically Heinrich(-like) events, had on changing precipitation patterns in the LEB since Marine Isotope Stage (MIS) 7, highlighting the changes from the beginning of the penultimate glacial period through to MIS 4. This review is divided into three parts: **Part 1.1** provides an introduction and overview of the palaeoclimatic interpretations. **Part 1.2** presents evidence of major wetting phases in the LEB from MIS 7 to the end of MIS 4 and discusses the timing of millennial-scale Heinrich(-like) events and what effect positional changes of the intertropical convergence zone (ITCZ) had on precipitation patterns over the LEB. MIS age boundaries, and MIS 5 sub-stages, correspond to designations after Lisiecki and Raymo (2005). **Part 1.3** concludes with a summary.

**Abbreviations**

| | |
|---|---|
| AMOC | Atlantic Meridional Overturning Circulation |
| AM | Asian Monsoon |
| CIS | Chinese interstadial |
| HS | Hudson Straight Heinrich Events |
| IASM | Indo-Australian summer monsoon |
| IPWP | Indo Pacific Warm Pool |
| IRD | Ice-rafted debris |
| ITCZ | Intertropical convergence zone |
| KT-LE | Kati-Thanda Lake Eyre |
| LGM | Last Glacial Maximum |
| LEB | Lake Eyre Basin |
| MIS | Marine Isotope Stage |
| NHSI | Northern hemisphere summer insolation |
| OSL | Optically Stimulated Luminescence |
| PIRIR | Post-infrared infrared stimulated luminescence |
| PPET | Point-potential evapotranspiration |
| TT-OSL | Thermally Transferred OSL |
| TL | Thermoluminescence |
| WPWP | Western Pacific warm pool |

## 1.1 Part 1. Introduction and palaeoclimate overview

### 1.1.1 Introduction

The LEB is the largest drainage catchment in Australia (Figure 1.1). It extends through three latitudinal zones, from the Georgina River in the monsoon tropics at 19°S to the temperate Flinders Ranges at 32°S. Seven drainage catchments comprise the LEB, the largest of which include the Cooper (300,000 $km^2$), Georgina (205,000 $km^2$) and Diamantina (160,000 $km^2$) river basins (Habeck-Fardy and Nanson, 2014) (Figure 1.2). Today, these three catchments are monsoon fed, with moisture laden incursions enhanced during strengthened La Niña phases of the modern El Niño Southern Oscillation, believed to have intensified ~5 ka (Donders et al., 2008). The major rivers of these catchments can generate significant flows to KT-LE and Lake Frome, albeit infrequently under modern hydrological conditions. KT-LE and Lake Frome in the southwestern LEB in south Australia, are today, dry playa lakes at 15.6 m and ~2 m below sea level, respectively (Leon and Cohen, 2012).

Palaeohydrological records from KT-LE and Lake Frome demonstrate links to late Quaternary northern and southern hemisphere high latitude climate oscillations. Indeed, northern hemisphere high latitude cooling events had a profound effect on palaeo-monsoon patterns across Africa (Collins et al., 2011, Schefuß et al., 2011, Stager et al., 2011), Eastern Asia (Wang et al., 2001, Cheng et al., 2006) Western Asia (Bar-Matthews et al., 1999, Fleitmann et al., 2003), North America (Asmerom et al., 2010) and South America (Cruz et al., 2005, Wang et al., 2007, Kanner et al., 2012), as well as Australia (e.g. Zuraida et al., 2009, Ayliffe et al., 2013, Denniston et al., 2013b, Bayon et al., 2017, Fu et al., 2017, De Deckker et al., 2019). Northern high latitude cool periods are typically associated with millennial-scale Heinrich(-like) events that are widely hypothesised to have played a major role in expansive lake filling episodes in southern central Australia. KT-LE, Australia's largest lake ($1.14 \times 10^6$ $km^2$), and neighbouring South Australian Lakes, Callabonna, Blanche and Frome (Figure 1.2), represent the termini of the LEB (Habeck-Fardy and Nanson, 2014, Cohen et al., 2015) and record a history of extreme lake fillings over the last two glacial periods. These records, along with supplementary palaeolacustrine, palaeofluvial and various other climate proxies (e.g. speleothems), provide evidence for enhanced precipitation over inland Australia, including the LEB, possibly as a result of Heinrich-correlated southern displacement of Indo-Australian summer monsoon (IASM) precipitation.

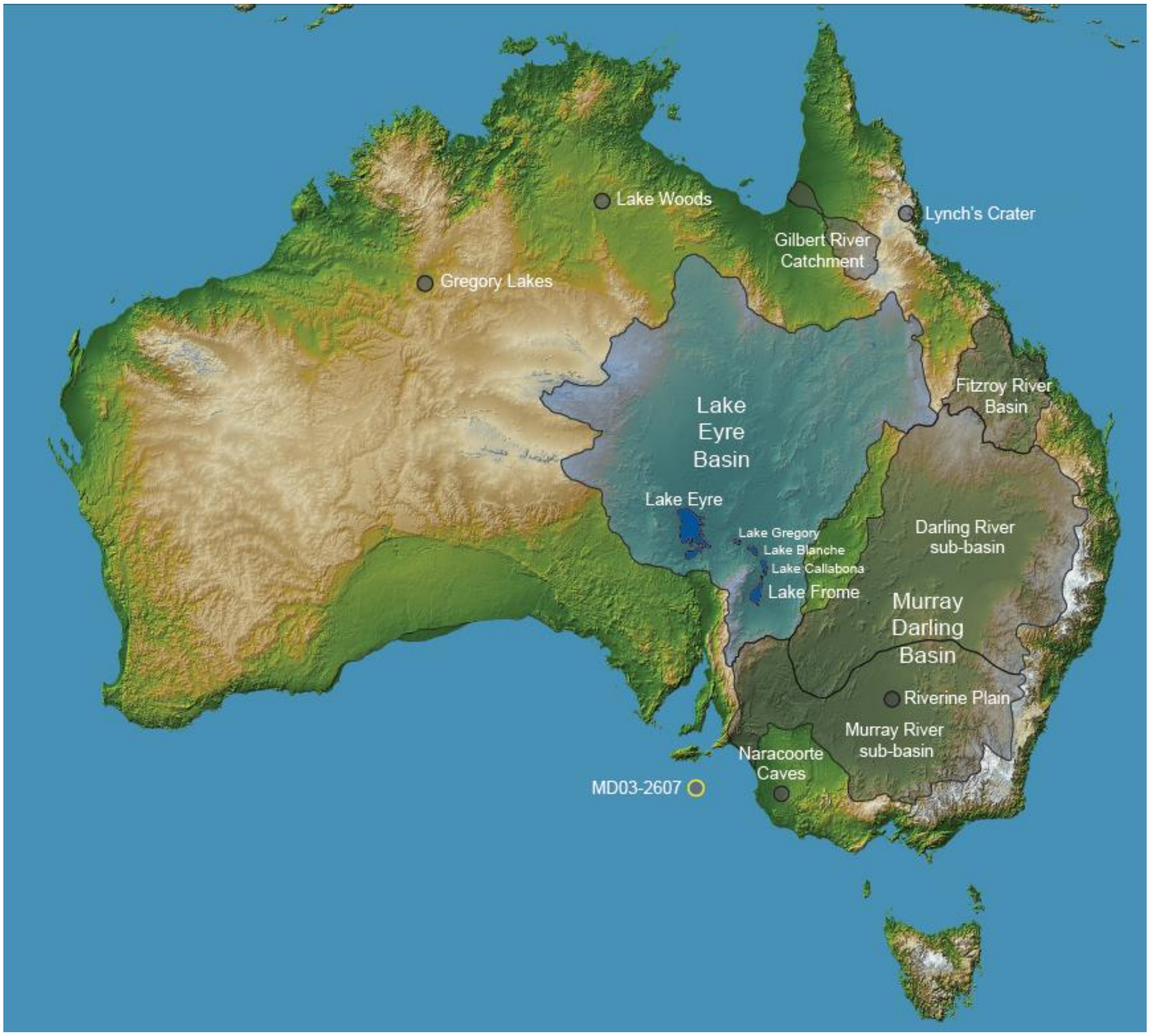


**Figure 1.1.** Map of Australia showing the Lake Eyre Basin (light blue shading) including generalised location of its terminal lakes (dark blue shading), other catchments (grey shading), terrestrial palaeorecords (grey shaded circles) and a marine sediment core (yellow circle) discussed in text. Note, the Murray Darlin Basin comprises the Darling River (northern) and Murray River (southern) sub-basins. Digital elevation model of Australia modified from the NASA Shuttle Radar Topography Mission Collection.

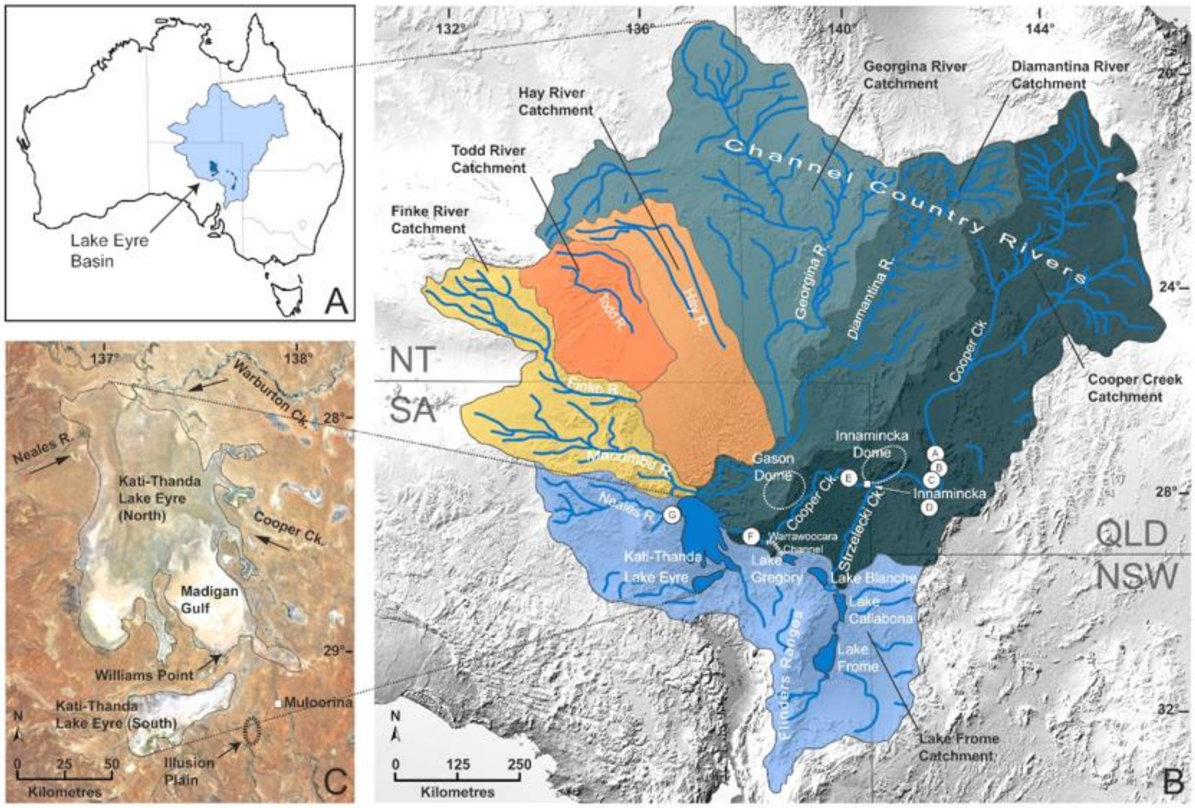


**Figure 1.2. Map A**: Map of Australia showing the Lake Eyre Basin (LEB; light blue shading) and location of its terminal lakes (dark blue shading). **Map B**: The seven drainage catchments of the LEB showing its generalised drainage network (dark blue lines and polygons) and major Rivers / Creeks. White circles show locations within the LEB referred to in text: A - Durham source-bordering dunes (Maroulis et al., 2007); B - Shire Road (Nanson et al., 2008); C - western Cooper Creek floodplain, Chookoo sandhill complex (Maroulis et al., 2007); D - Tooley Wooley waterhole (Maroulis et al., 2007); E - Gidgealpa floodplain and dune (Cohen et al., 2010); F - Lower Cooper Creek including the south Tilla Tilla and Pirranna Waterholes (Nanson et al., 2008); G - Lower Neales River, Ghost Yard Beds (Croke et al., 1999). Digital elevation model of Australia modified from the NASA Shuttle Radar Topography Mission Collection. **Map C**: Satellite image (Google Earth) of Kati-Thanda Lake Eyre (North and South) showing locations described in text, and inflows from major rivers and creeks. Note, Warburton Creek (sometimes called River) is the downstream confluence of the Georgina and Diamantina Rivers.

### 1.1.2 Heinrich events

Heinrich events were massive deglaciation events where "armadas of icebergs" (Broecker et al., 1992), sea ice and meltwater discharged from Northern Hemisphere ice sheets into the North Atlantic. Entrained ice-rafted debris (IRD) dropped from the melting ice as it drifted eastward with the North Atlantic Gulf stream, and are preserved as abundant layers of detrital carbonate and oxygen isotopic depletions in marine sediment cores between ~40 and ~55 °N, termed the North Atlantic IRD belt (Heinrich, 1988, Bond et al., 1992, Broecker et al., 1992, Rashid et al., 2003, Naafs et al., 2013). The cause of these events is still debated. Marine sediment core IRD characterisation and quantification varies between authors, lending disagreement to IRD provenance as well as the relative strength and timing of each event. Heinrich (1988) recognised a total of eleven Heinrich layers over the last glacial period, six of which contained high IRD percentages between 70 and 10 ka. An in-depth review of the occurrence and dynamics of Heinrich Events by Hemming (2004) defined Heinrich layers 5, 4, 2, and 1, as Hudson Straight Heinrich Events (HS) as they share many characteristics consistent with Hudson Straight provenance not seen in Heinrich IRD layers 6 and 3, which may have originated from Europe and/or Greenland (Snoeckx et al., 1999, Hodell et al., 2008).

For the purposes of this review, the reassessed timing of Heinrich events 1–6 by Hemming (2004) are used, with the exception of H5. The end of H5 is placed at 48 ka from correlation to the Hulu (China) speleothem record (Wang et al., 2001) to better represent the regional sensitivity between the Asian and Indo-Australian monsoon. However, the end of H5 can be equally assigned to ~45 ka (Wang et al., 2001) based on correlation methods described by Bond et al. (1993) with the Greenland Ice Sheet Project 2 (GISP2) (Meese et al., 1997) and North Atlantic SST records, the Greenland Ice Sheet Project (GISP) Summit (Dansgaard et al., 1993), and speleothem records from Sorel Cave (Israel) (Bar-Matthews et al., 1999). Rashid et al. (2003) identified an additional Heinrich(-like) event (H5a: 52–53 ka) from eight marine sediment cores in the Labrador Sea, immediately south of the Hudson Straight, and in the northwest Atlantic. The H5a event was also identified in the Irminger and Icelandic seas by Van Kreveld et al. (2000), who termed the Heinrich(-like) event H5.2. In the period between 126 and

70 ka, seven minor ice-rafting events, C26 to C19, are recognised in the IRD belt by Chapman and Shackleton (1999), although event C26 reflects a 2–3°C sea-surface temperature reduction at the NEAP18K core site rather than high abundance in IRD. Rasmussen et al. (2003) identified Heinrich layer 11 (H11) at ~135–130 ka, glacial termination II, as prominent increases in IRD and detrital carbonate from thick sequences in two sediment cores from the southeast Labrador Sea. Reports of Heinrich(-like) events during MIS 6 and MIS 7 in literature are rare. Some authors suggest no ice-rafts made it to the eastern North Atlantic during MIS 6 due to dramatically different surface water circulation patterns (e.g. Hodell et al., 2008). However, van Kreveld et al. (1996) identified six Heinrich(-like) layers in MIS 6 (h7–h12) and one in MIS 7 (h13); these layers from the Northeast Atlantic deep-sea core T88-9P contained high IRD but low detrital carbonate percentages, with the exception of h13 that had practically no detrital carbonate. In the Ocean Drilling Program core 980 (McManus et al., 1999), one prominent IRD event occurred at the MIS 6/5 transition interpreted as H11 and a smaller IRD event around 148 ka correlates with h9 in core T88-9P (van Kreveld et al., 1996), although no prominent IRD events are recorded during MIS 7. Henceforth, the term Heinrich event/layer will be used for all Heinrich(-like) events, despite true Heinrich layers pertaining only to those identified by Heinrich (1988). Heinrich events used in this review are summarised in Table 1.1 and illustrated in Figures 1.4 and 1.5.

Global climatic and thermohaline anomalies are tied to Heinrich events. In the Northern Hemisphere, Heinrich events are associated with increased ice and freshwater input (Broecker et al., 1992, Dahl et al., 2005, Broccoli et al., 2006), cold North Atlantic sea surface temperatures (Bond et al., 1992, Broecker et al., 1992), weakening of the Atlantic Meridional Overturning Circulation (AMOC; Figure 1.3) (Boyle, 2000, Knutti et al., 2004) and an associated reduction in northward surface-ocean heat transport (Broecker et al., 1992, McManus et al., 2004), resulting in major cooling at northern mid-latitudes. An intrahemispheric temperature gradient is created, which is balanced through the atmospheric transfer of heat energy from the warmer southern hemisphere to the cooler northern hemisphere, although the mechanism of transfer is debated (Broccoli et al., 2006, Kang et al., 2008, Cvijanovic and Chiang, 2013). The prevailing view is based on climate modelling studies (Dahl et al., 2005, Broccoli et al., 2006, Kang et al., 2008, Cvijanovic and Chiang, 2013, Donohoe et al., 2013, Singarayer et al., 2017) indicating the ITCZ, the primary source of tropical rainfall, shifts southward (Figure 1.3) to scavenge heat from the southern extratropics via the asymmetrical expansion and strengthening of the northern Hadley cell with its ascending branch shifting south of the equator. Conversely, model simulations and other studies have demonstrated forcing by the meridional temperature gradient may cause symmetrical widening of the Hadley cells across the equator and, by extension, the ITCZ rainbelt (Frierson et al., 2007, Collins et al., 2011, Stager et al., 2011). Either way, ITCZ forcing by Heinrich events is typically recorded as increased (reduced) monsoon precipitation in southern (northern) tropical sites (Wang et al., 2001, Muller et al., 2008, McGee et al., 2014). Indeed, the southward displacement of the ITCZ during Heinrich events has been associated with increased precipitation over central Australia, including the LEB (Bayon et al., 2017). Although non-uniform latitudinal shifts of the global ITCZ rainbelt has been suggested (e.g. Collins et al., 2011).

Modelled reconstructions in global ITCZ latitudinal positions over the last 25 kyr (including Heinrich Event 1) has seen some success using past tropical sea surface temperature (SST) gradients. McGee et al. (2014) suggests for larger ITCZ displacements (≥5° latitude) to occur over a zonally heterogenous region no greater than 70° longitude (i.e. nearly double the longitudinal width of Australia), ITCZ displacements will be at or near zero at all other latitudes across the globe. Therefore, it is conceivable that significant wet periods in Australia may be indicative of larger ITCZ displacements.

Analogues to Heinrich-correlated IASM displacements are commonly determined from stalagmite $\delta^{18}O$ records because of their high temporal resolution. In China, high-resolution absolute-dated speleothem $\delta^{18}O$ records extend over the last two glacial periods and show strong links to northern hemisphere warming during Dansgaard-Oeschger events (Wang et al., 2001), and successive cooling during Heinrich events as weakened Asian Monsoon (AM) rainfall (Wang et al., 2001, Cheng et al., 2006, Cheng et al., 2009). Chinese speleothem records provide a high-resolution proxy for Asian monsoon variability, which is dynamically linked to hydroclimate variability over northern Australia via shifts in the ITCZ during Heinrich events (Mohtadi et al., 2011, Denniston et al., 2013). So far, speleothem $\delta^{18}O$ records of the IASM are limited to the last 40 kyr (Partin et al., 2007, Griffiths et al., 2009, Lewis et al., 2011, Ayliffe et al., 2013, Denniston et al., 2013a; 2013b; 2015; 2017). Other terrestrial records from Australia showing proxy evidence of Heinrich-correlated IASM precipitation variability are few (Muller et al., 2008) and limited to the last 50 kyr. Marine sediment core records are also used to identify changes in terrigenous sedimentation and foraminiferal isotopic chemistry interpreted as IASM rainfall variability during Heinrich events. Many of these records only cover the last 25 kyr (Mohtadi et al., 2011, Muller et al., 2012) to 42 kyr (Ardi et al., 2022). Thus, little is currently known about what effect Heinrich events had on precipitation patterns over Australia beyond H5, around 50 ka (Muller et al., 2008), and the latitudinal extent of any possible earlier IASM incursions.

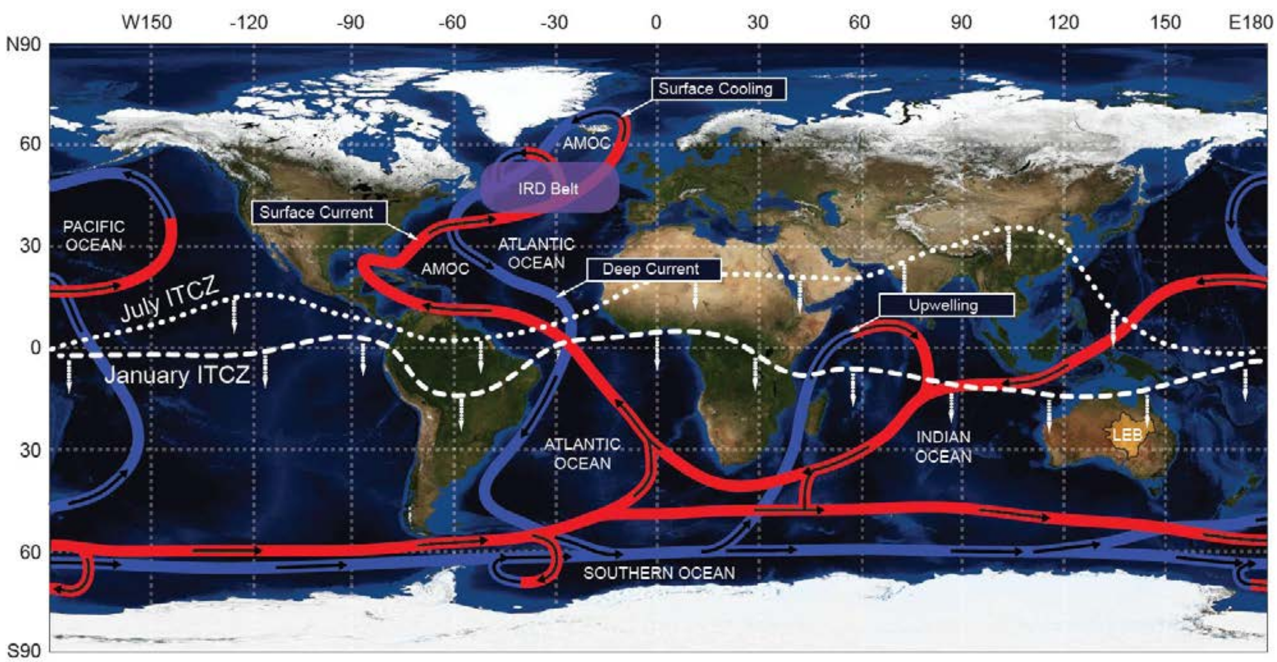


**Figure 1.3.** Map of ITCZ location. Dashed lines show the modern position of the ITCZ in July and January (after Cheng et al., 2012), with dashed white arrows depicting southward displacements caused by Heinrich events (note, the exact latitude of the ITCZ following displacement is unknown). Red and blue lines are a simplified depiction of the global thermohaline surface (warm) and deep (cool) water currents, respectively. IRD belt (purple) in the north Atlantic Ocean shown in relation to the AMOC. Lake Eyre Basin in central Australia shown in orange. World map with topography and bathymetry from the NASA Blue Marble Image Collection.

### 1.1.3 Chronological limitations and impacts on palaeoclimate interpretations

The identification of Heinrich events in MIS 7–4 presents a significant challenge due to the limitations of current chronological techniques. Heinrich events are millennial-scale events, typically lasting between 500 and 2,000 years (Hemming, 2004). However, the dating uncertainties in most records covering MIS 7–4 exceed this timescale, making it difficult to resolve individual events with confidence. Chronological precision decreases substantially in older sediments, particularly beyond the range of radiocarbon dating (~50 ka) (Reimer et al., 2020). In marine archives, age models for MIS 7–4 are often based on orbital tuning, isotope stratigraphy, and correlation to ice core records, all of which carry inherent uncertainties of several thousand years (e.g., Lisiecki and Raymo, 2005, Stern and Lisiecki, 2014). These uncertainties are particularly problematic when attempting to attribute individual climatic shifts in Australian hydroclimate records to specific Heinrich events.

Terrestrial records face similar limitations. While optically stimulated luminescence (OSL) dating provides an alternative method for dating quartz grains in aeolian and fluvial sediments, its precision is often insufficient for distinguishing millennial-scale events (Roberts et al., 2015). Uranium-series dating of speleothems offers greater accuracy but is limited by hiatuses in deposition and the availability of suitable material (Drysdale et al., 2009). The compounding effects of these uncertainties mean that while climatic fluctuations during MIS 7–4 may be consistent with the expected impacts of Heinrich events, confidently identifying them as direct responses to specific Heinrich events remains difficult. Future improvements in chronological resolutions, particularly through age modelling advances, may help to resolve these events in older stratigraphic sequences.

It is also important to note that correlation does not imply causation. While some late Quaternary lake-filling episodes align with Heinrich events, the exact mechanisms linking these climate shifts to Australian hydrology remain uncertain. The apparent scarcity of correlations between Heinrich events and hydroclimate oscillations in Australia before 50 ka may reflect several factors: (1) a lack of high-resolution proxy records or chronological uncertainties in older datasets (e.g., Cadd et al., 2021, De Deckker et al., 2019), (2) shifts in other climate drivers such as the IASM, western Pacific warm pool (WPWP) or ENSO, which may have had a stronger influence (Denniston et al., 2013b), and (3) potential differences in ITCZ behaviour over longer glacial-interglacial cycles (e.g., Wang et al., 2008). Given these uncertainties, further investigation is needed to determine whether Heinrich event-induced ITCZ displacement was a consistent driver of precipitation variability in the LEB or if alternative mechanisms played a more dominant role before 50 ka.

### 1.1.4 Palaeoclimate

KT-LE and mega-Lake Frome, the ancient coalescence of Lakes Gregory, Callabonna, Blanche and Frome, have been demonstrated to archive hydroclimate oscillations over the last two glacial periods. Lake level variability and proxy records that indicate patterns of enhanced precipitation over the LEB may reflect multiple influences, including changed position and strength of the southern hemisphere westerlies, WPWP, and variations in amount and/or penetration of IASM rainfall.

High intensity frontal rain can penetrate parts of the central and southern LEB. Southern hemisphere high latitude cooling or a weakened Leeuwin current have been linked with palaeo-latitudinal (northward) shifts in the sub polar front and south westerlies resulting in enhanced rainfall over western and southern parts of Australia (e.g. Shulmeister et al., 2004; 2016, Cohen et al., 2011, Marx et al., 2011, De Deckker et al., 2012, May et al., 2015). These equatorward shifts in the south westerlies are spatially and temporarily poorly constrained, especially beyond the Last Glacial Maximum (LGM; defined as 22–18 ka; Reeves et al., 2013), although attempts have been made (Shulmeister et al., 2004). Ultimately, northward shifts in the south westerlies generally occur during cold glacial climates (Toggweiler et al., 2006) and southward shifts during episodic southward displacements of the ITCZ (Denniston et al., 2013a).

**Table 1.1.** Ages of Heinrich Layers

| Heinrich Layer* | Calendar Age (Ka) | MIS Boundary (Ka)** | Reference | Authors nomenclature |
|---|---|---|---|---|
| | | 1/2 (11) | | |
| H1 | 16.8 | | Hemming (2004) | HS1 |
| H2 | 24 | | Hemming (2004) | HS2 |
| | | 2/3 (29) | | |
| H3 | 31 ± 1 | | Hemming (2004) | H3 |
| H4 | 38 | | Hemming (2004) | HS4 |
| H5 | 48[a] | | Wang et al., (2001) | H5 |
| H5a | 53-52 | | Rashid et al., (2003) | H5a |
| | | | Van Kreveld et al., (2000) | H5.2 |
| | | 3/4 (57) | | |
| H6 | 60 ± 5 | | Hemming (2004) | H6 |
| C19 | ~70–68.5 (peak 69) | | Chapman and Shackleton (1999) | C19 |
| | | 4/5 (71) | | |
| C20 | ~76–73.5 (peak 76) | | Chapman and Shackleton (1999) | C20 |
| | | 5a peak (82) | | |
| C21 | ~87–83 (peak 85.6) | 5b peak (87) | Chapman and Shackleton (1999) | C21 |
| C22 | ~90.5 | | Chapman and Shackleton (1999) | C22 |
| | | 5c peak (96) | | |
| C23 | ~102–101 (peak 102) | | Chapman and Shackleton (1999) | C23 |
| C24 | ~107–105 (peak 107) | | Chapman and Shackleton (1999) | C24 |
| C25 | ~109 | 5d peak (109) | Chapman and Shackleton (1999) | C25 |
| | | 5e peak (123) | | |
| H11 | ~135–130 | 5/6 (130) | Rasmussen et al., (2003; McManus et al., (1999) | H11 |
| | 131–128 | | van Kreveld et al., (1996) | h7 |
| H12 | 142 | | van Kreveld et al., (1996) | h8 |
| H13 | 149–146 | | van Kreveld et al., (1996); McManus et al., (1999) | h9 |
| H14 | 167–164 | | van Kreveld et al., (1996) | h10 |
| H15 | 183–182 | | van Kreveld et al., (1996) | h11 |
| H16 | 189 | | van Kreveld et al., (1996) | h12 |
| | | 6/7 (191) | | |
| H17 | 201 | | van Kreveld et al., (1996) | h13 |
| | | 7/8 (243) | | |

**Heinrich layer nomenclature in first column will be used for the purposes of this review.*
***MIS boundaries marked by "/" with bracketed ( ) numbers denoting age (ka: kilo annum thousand years ago), excluding MIS 5 sub-stages that only show peak global benthic $\delta^{18}O$ age determinations in brackets (i.e. not sub-stage boundaries).*
[a]*The 48 ka age represents the end of H5 derived from correlation to the Hulu (China) speleothem record (*Wang et al., 2001*) to better represent the regional sensitivity between the Asian and Indo-Australian monsoon.*

Another proposal is that semi-permanent ‘La Niña’ like conditions may have persisted from trapping of a WPWP close to the east Australian coast, particularly during global oceanic low stands facilitating a southward migration of warmer waters. Periods of enhanced precipitation in southeastern Australia (e.g. Singh et al., 1981, Page et al., 1996, Bayon et al., 2017), in the Cooper Creek catchment (e.g. Nanson et al., 2008, Cohen et al., 2010), and northern Queensland (Kershaw, 1991) coeval with mega-Lake fillings may support this interpretation.

The exact moisture source(s) responsible for mega-lake fillings has not been determined, although they are primarily associated with periods of enhanced monsoonal activity feeding major catchments in the northern and eastern LEB. Importantly, Magee et al. (2004) and Miller et al. (2005b) demonstrated that Quaternary wet phases in Australia do not correspond with southern hemisphere summer insolation maxima, but rather occur during northern hemisphere winter insolation minima. Indeed, Fu et al. (2017) reported a poor association between their sedimentological chronology of KT-LE peak wet phases and the Australian summer insolation maxima. This assumes northern hemisphere forcing is a major driver of the strength and position of the IASM and precipitation patterns over Australia. Many palaeolacustrine, palaeofluvial and other proxy records from the LEB and surrounding regions show evidence of enhanced precipitation corresponding to extratropical forcing during northern hemisphere deglaciation. A chronology of these records is provided in section 1.2, starting with MIS 7.

There is little doubt the last 50 kyr represents an important period in the palaeoclimatic history of Quaternary Australia. Early human colonisation in northern Australia had already occurred in MIS 4 ~65 ka (Roberts et al., 1990; 1994, Roberts and Jones, 1994, Clarkson et al., 2015; 2017) with complete continent-wide colonisation by 50–45 ka (Turney et al., 2001, Bowler et al., 2003, O'Connell and Allen, 2004, Rasmussen et al., 2011, Allen and O’Connell, 2014, Veth et al., 2014; 2017, O'Connell and Allen, 2015, Hamm et al., 2016, Hughes et al., 2017, Tobler et al., 2017, O'Connell et al., 2018). The 50–40 ka period is closely associated with a catastrophic drying phase beginning in KT-LE at 48 ±2 ka and Lake Frome at 48 ±3 ka (Cohen et al., 2011; 2015), the mass extinction of a diverse range of Megafauna between 50 and 46 ka on mainland Australia (Roberts et al., 2001, Miller et al., 2016a) and by 41 ka in Tasmania (Turney et al., 2008, McIntosh et al., 2009), and well documented vegetation changes (e.g. Kershaw, 1991, Kershaw et al., 2007). Debates surrounding the primacy of causal drivers including anthropogenic forcing (Johnson et al., 1999, Miller et al., 2005a; 2005b, Pitman and Hesse, 2007, Bird et al., 2013), natural climate variability (reduced precipitation) (Cohen et al., 2015), or a combination of both, have remained unresolved for more than 40 years. For this reason, this review focuses on the last two glacial cycles leading up to and including MIS 4, prior to any anthropogenic influences and the disconnection and demise of the mega-Lakes, KT-Eyre and Frome, during early MIS 3. For detailed reviews on the palaeohydrology of Australia from MIS 3 to the present the reader is directed to Kemp et al. (2019), and for more specific interpretations on the Cooper Creek palaeoriver system the reader is directed to Nanson et al. (2008). The intention here is to provide a comprehensive hydrological history since MIS 7 as it relates to lake fillings in mega-Lakes, KT-Eyre and Frome, whilst also attempting to clarify the spatial and temporal extent of moisture source incursions over the LEB during Heinrich events.

This review aims to identify any influence northern hemisphere high-latitude cool periods, recorded in north Atlantic marine cores as Heinrich events, had on the timing of late-Quaternary lake fillings in mega-lakes, KT-Eyre and Frome. More broadly, this study concludes by demonstrating how the lack of records from monsoon-influenced regions of inland Australia, and specifically within the LEB, continues to feed uncertainty in determining which climate pattern(s) governed major mega-lake fillings over the last two glacial periods.

## 1.2 Part 2. Lake Eyre Basin Palaeohydrology (MIS 7–4) and Heinrich-correlated ITCZ displacement interpretations

### 1.2.1 MIS 7 [243–191 ka]

#### *1.2.1.1 Palaeohydrology*

Glacial termination III marked the start of MIS 7, an interglacial, at which time KT-LE was dry (Fu et al., 2017, Cohen et al., 2022). Progressive drying in Australia had occurred since the Miocene (Chen and Barton, 1991, Fujioka and Chappell, 2010, Mao and Retallack, 2019, Stuut et al., 2019), especially since MIS 10 (~350 ka) (Nanson et al., 1988; 2008, Hesse, 1994, Bowler et al., 2001, Kershaw et al., 2003, Hocknull et al., 2007). By MIS 7, a landscape of deflationary aridity had excavated pre-existing lake-floor sediments in KT-LE to the basal Miocene Etadunna Formation, previously thought to have occurred during an ~30 kyr dry period in MIS 6 (Magee, 1997). Overlying the Etadunna Formation facies at Williams Point in the Madigan Gulf (Figure 1.2C), the main depocenter in KT-LE, are <10 m of Quaternary sediments (Magee et al., 1995), more recently dated to MIS 7 (Fu et al., 2017, Cohen et al., 2022). Here, remains one of the few palaeo-lacustrine-fluvial archives of the LEB and, more broadly, of hydroclimate variability across Australia.

Sedimentological evidence at Williams Point shows lake-floor deflation transitioned to shallow-water deposition and accretion of poorly laminated transgressive clayey sand between 221 ±19 ka and 201 ±10 ka (Fu et al., 2017). A shift to wetter conditions was also recorded in the eastern LEB. Cooper Creek, upstream of the Innamincka Dome (Figure 1.2B), shows enhanced fluvial activity between 250 and 230 ka, with bankfull discharges 5–7 times larger than today (Nanson et al., 2008) and complete reworking of the previously alluviated sandy alluvium (Katipiri Formation; Tedford and Wells, 1990, Callen and Nanson, 1992). Alluvium deposits were also found at the South Tilla Tilla Waterhole in the lower reaches of Cooper creek (TL dated at 220 ±27 ka; Nanson et al., 2008), downstream of the Gason Dome and immediately east of KT-LE (Figure 1.2B). No further records exist within the LEB supporting enhanced rainfall during this period. At the end of MIS 7, at 191 ±9 ka, KT-LE transitioned from a shallow-water depositional environment to a deep-water lacustrine phase (Fu et al., 2017). Although Bayesian modelling by Cohen et al. (2022) revised this deep-water deposition to 206 ±13 ka.

### *1.2.1.2 Interpretation*

Heinrich-induced southward displacement of IASM precipitation during MIS 7 cannot be established owing to the paucity of Heinrich events recorded in the north Atlantic, and a near absence of corresponding high-resolution palaeohydrological records from Australia. However, around the timing of the only north Atlantic MIS 7 Heinrich Event (H17 at 201 ka; van Kreveld et al., 1996), there was an appearance of an AM lag in $\delta^{18}O$ speleothem records from central China. The $\delta^{18}O$ values from Sanbao and Hulu Caves follow an ~23 kyr sinusoidal pattern of precession-dominated Northern Hemisphere summer insolation (NHSI) (Wang et al., 2008). Thus, monsoon lead or lag relative to NHSI can be interpreted as possible perturbations resulting from the occurrence of Heinrich events and, by extension, weak AM intervals and potential ITCZ southerly displacement. The Sanbao stalagmite (SB11) AM lag occurred immediately after Chinese interstadial (CIS) B22 (Wang et al., 2008) around 200 ka (Figure 1.4) (see Cheng et al. (2006) for definition and correlation of CIS with Dansgaard-Oeschger warming events). Lakes of northern Australia record significant expansions that may correlate to this event, including Gregory Lakes (in Western Australia) and Lake Woods (in Northern Territory) at 200 ka (Bowler et al., 2001) and 180 ±20 ka (Bowler et al., 1998), respectively (Figure 1.1). Importantly, evidence of these lake fillings come from dating of high palaeoshorelines, which can be indicative of a punctuating short-lived fluvial input and still-stand of the lake regression (Magee et al., 1995), as could be expected under Heinrich-induced ITCZ displacement. KT-LE's coeval transition to a deep-water lake at ~206 ka (Cohen et al., 2022) may have benefited from an H17-ITCZ rainfall displacement. However, another possible explanation for the KT-LE filling is enhanced precipitation over southern parts of Australia. Ayliffe et al. (1998) showed a period of high speleothem deposition between 220 and 155 ka at Naracoorte caves in south Australia (Figure 1.1), which suggests rainfall via the southern hemisphere south westerlies. Importantly, peak speleothem deposition during this period corresponds with stadials and cool interstadials, indicating the Naracoorte speleothem record is sensitive to temperature variations requiring a net water deficit for precipitation to occur. Thus, linking KT-LE fillings with the Naracoorte caves record may only be applicable within specific temperature ranges. Although there is evidence of a MIS 7 pluvial in northern Australia (e.g. Bowler et al., 1998; 2001), consistent with KT-LE filling and the Naracoorte precipitation record, the lack of accurate hydroclimate chronologies from the northern LEB hinders precise comparisons between records. Thus, links with H17-correlated precipitation is tenuous at best.

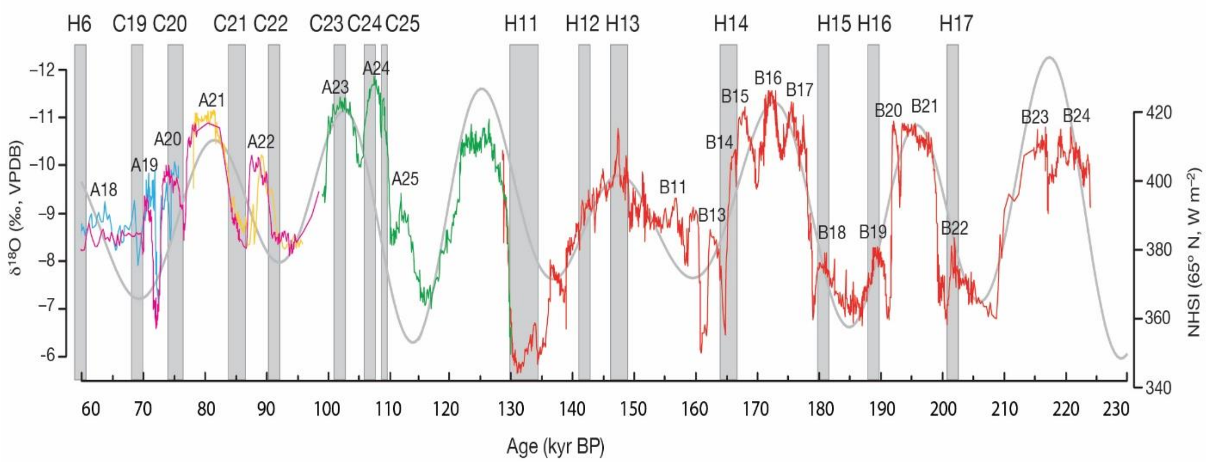


**Figure 1.4.** Time versus Chinese $\delta^{18}O$ speleothem records with NHSI (grey sinusoidal line, 65°N, 21 July) and Heinrich events (numbered grey bars). Sanbao $\delta^{18}O$ records (red, stalagmite SB11; green, SB23; yellow, SB25-1; pink, SB22) and Hulu cave (blue). Numbers over $\delta^{18}O$ speleothem records indicate Chinese Interstadials (CIS). Modified from Wang et al. (2008).

### 1.2.2 MIS 6 [191–130 ka]

#### *1.2.2.1 Palaeohydrology*

The MIS 7 deep-water lacustrine phase in KT-LE lasted for at least 10 millennia into early MIS 6, ending around 188–181 ka (Fu et al., 2017, Cohen et al., 2022). A thick sequence of finely laminated dark grey to grey clays suggests the existence of a perennial lake deep enough for salinity stratification to occur (Fu et al., 2017, Cohen et al., 2022). Mid MIS 6 saw the demise of perennial wet conditions in KT-LE at ~153 ±11 ka (Cohen et al., 2022), with ensuing playa conditions and effective aridity up until the end of the penultimate glacial (Magee et al., 1995; 2004, Fu et al., 2017). In the eastern LEB, twelve alluvial (Maroulis et al., 2007, Nanson et al., 2008) and two aeolian (Cohen et al., 2010) TL-dated sequences provide evidence of enhanced fluvial activity and sediment accumulation during MIS 6.

### *1.2.2.2 Interpretation*

MIS 6 Heinrich events H16, H15 and H14 correlate well with the timing of abrupt $\delta^{18}O$ positive shifts in the Chinese Sanbao cave stalagmite record (Wang et al., 2008) and during NHSI minima (Figure 1.4). These weakened AM intervals succeed CIS B19, B18 and B14 (respectively), supporting links between Dansgaard-Oeschger warming cycles preceding Heinrich events (Van Kreveld et al., 2000). Enhanced precipitation over northern Queensland during H16 and H15 is inferred from palynological evidence at Lynch's Crater (Figure 1.1) between 190 and 179 ka (Kershaw, 1991), and the formation of aeolian and alluvial sequences along the Cooper Creek near the Innamincka Dome (Nanson et al., 2008, Cohen et al., 2010). Furthermore, the onset KT-LE's deep-water phase around H16 and ending shortly after H15 provides compelling evidence supporting Heinrich-induced precipitation changes in the LEB. There are no dated palaeoshorelines that support the existence of this deep-water lake or any short-lived punctuating Heinrich Events. However, Nanson et al. (1988) reported two (undated) shorelines at ~25 and ~35 m-AHD near Muloorina (Figure 1.2C) in KT-LE that may correlate with at least one of these Heinrich events. H14-correlated precipitation in the LEB is less clear. The H14 Heinrich event terminated in the North Atlantic around 164 ka (van Kreveld et al., 1996) whereas playa-like conditions in KT-LE ensued from ~153 ka (Cohen et al., 2022). Some coherency may exist between H14 and two alluvial sequences in Cooper Creek, TL-dated at 169 ka (2 ka before H14 onset) and 164 ka (Nanson et al., 2008). However, both samples are reported with very large TL errors (83 and 25 ka, respectively) making it difficult to attribute any doubt to any correspondence with the H14 event. More likely are changed precipitation patterns over parts of inland Australia including Cooper Creek as a result of strengthened south westerlies. Bestland and Rennie (2006) reported a speleothem growth phase in Naracoorte caves between 179–162 ka, occurring shortly after H15 and through H14. Stalagmite colour banding and lateral isotopic variations in growth bands indicates it was a slower growth phase compared to MIS 5 (~114–96 ka), interpreted by Bestland and Rennie (2006) as $CO_2$ degassing and $\delta^{18}O$ fractionation at the time of precipitation. Nonetheless a change from the ITCZ dominated precipitation occurred during H16 and H15. H13 and H12 occurred concurrently when KT-LE was reportedly dry (Magee et al., 1995, Magee et al., 2004, Fu et al., 2017), despite continued fluvial activity in Cooper Creek (Nanson et al., 2008). Neither event is evident in Chinese speleothem records as weakened AM. Thus, ITCZ southern displacement and subsequent LEB rainfall coeval with H13 or H12 is unlikely.

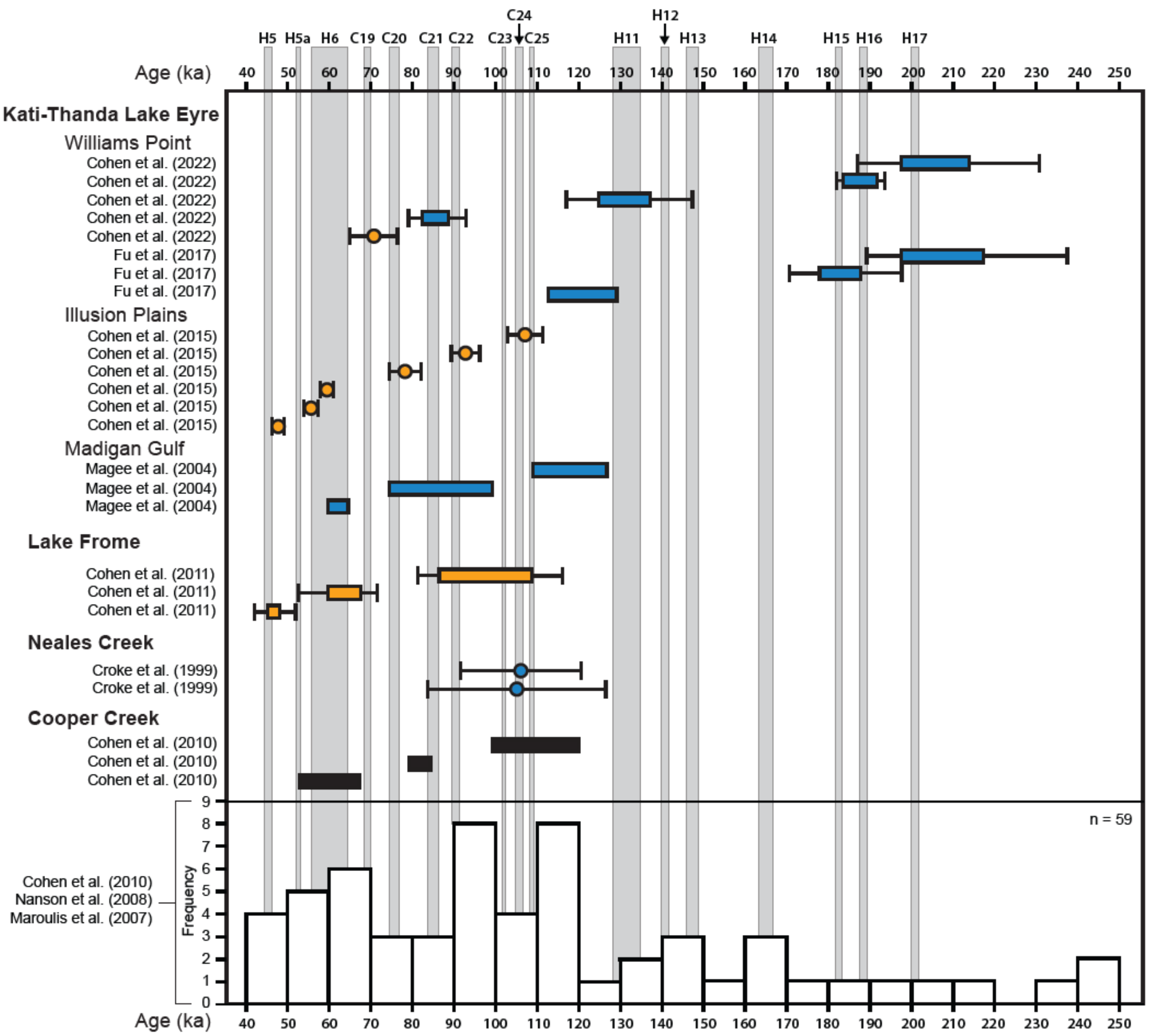


**Figure 1.5.** Chronology of palaeohydrological records from MIS 7 to the end of MIS 4 (~186 kyr) as recorded in the LEB, and relative position of Heinrich events (grey bars), recorded in various marine sediment cores from the North Atlantic Ocean (see Table 1.1 for details). Blue boxes: lake sediment records. Orange boxes or dots: palaeoshoreline records. Black boxes: main wet period specified by author. Age histogram illustrating frequency of fluvial and alluvial samples in Cooper Creek (Maroulis et al., 2007; Nanson et al., 2008; Cohen et al., 2010), representing a total of 59 samples collected from mechanical drill holes, auger holes and excavation pits.

Certainly, a prolonged weak monsoon interval is evident in Chinese Sanbao (Wang et al., 2008), Hulu (Wang et al., 2001, Cheng et al., 2006) and Dongee (Kelly et al., 2006) cave records as a significant AM lag relative to NHSI that lasted from 135.5 ±1.0 ka to 129.0 ±1.0 ka. Cheng et al. (2006) and Wang et al. (2008) attributed this weak AM interval to Heinrich event H11. There is some corresponding evidence of fluvial activity in Cooper Creek at 133 ±15 ka (Shire Road) and 132 ±23 ka (Pirranna Waterhole: Lower Cooper Creek; Nanson et al., 2008) (Figure 1.2B), highlighting eastern LEB runoff still occurred during this period of glacial temperature and sea level minima. Under these conditions, rainfall over the eastern LEB may have occurred from the formation of a trapped WPWP, although the glacial temperature extreme makes this unlikely. Alternatively, some of the Cooper Creek deposits reported by Nanson et al. (2008) were normally graded sandy alluvium with mud intraclasts and balls, which suggests rapid deposition or event-based flow reduction with flows powerful enough for lateral reworking of bank muds and overbank fines. This may imply intense fluvial activity akin to monsoon input not seen today.

### 1.2.3 MIS 5 [130–71 ka]

#### *1.2.3.1 Palaeohydrology*

MIS 5, comprising sub-stages 5e–a (Lisiecki and Raymo, 2005), represented one of the wettest periods in central Australia over the last glacial period. A complete sedimentary chronology of KT-LE at Williams Point Madigan Gulf was presented by Magee et al. (1995), and later refined in Magee et al. (2004), identifying two major deep-water lacustral phases at 128–110 ka (MIS 5e–d) and 100–75 ka (MIS 5c–a), separated by at least one, albeit brief, interpluvial around MIS 5c. According to Magee et al. (2004), early MIS 5e saw the onset of the wettest period of the last glacial period, describing sedimentary units that formed in a deep perennial lake subject to continuous and regular flooding. However, re-examination of the Williams Point deposits older than 100 ka by Fu et al. (2017), using Bayesian modelled results from K-feldspar PIRIR and quartz TT-OSL dating techniques, characterised KT-LE in MIS 5e as shallow-water lacustrine. Cohen et al. (2022) later confirmed the deposition of shallow water lacustrine facies at 131 ±9 ka. Certainly, no palaeoshoreline records have been found for MIS 5e.

A later MIS 5 pluvial period(s) is supported by shoreline deposition. Three high palaeoshorelines at 9, 10 and 11 m-AHD at Illusion Plains (Figure 1.2C), show KT-LE filled to ≥24 m depths between MIS 5d–a (at 108.0 ±4.6 ka, 93.5 ±3.8 ka and 78.8 ±4.2 ka, respectively; Cohen et al., 2015) (Figure 1.5). Indeed, a palaeoshoreline in neighbouring Lake Frome shows a 15 m deep lake (OSL/TL dated between 109.9 ±7.5 ka to 87.3 ±5.8 ka: 3 samples pooled mean at 96 ±7 ka; Cohen et al., 2011; 2012b) that was capable of connecting with KT-LE via the 25-km-long Warrawoocara channel (Figure 1.2B) (Nanson et al., 1998).

Palaeofluvial records from the downstream (southern) reaches of Cooper Creek, near the Innamincka Dome, show significant alluvial aggradations during MIS 5. Nanson et al. (2008) described a period of pronounced fluvial activity and sand transport between 120 and 80 ka, and Cohen et al. (2010) identified two phases of enhanced river flow and sand supply to source-bordering dunes at ~120–100 ka and ~85–80 ka. Despite there being a clear fluvial re-working of alluvial sediments during MIS 5, Nanson et al. (2008) estimated only one third of the sediments were re-worked compared to the complete reworking during the larger MIS 7-6 discharges. Indeed, reworking of almost the entire western Cooper Creek floodplain (at Chookoo sandhill complex (Figure 1.2B) has been previously suggested (Maroulis et al., 2007). In the western LEB, Croke et al. (1996) identified flood-reworked sands in the lower Neales River immediately west of KT-LE (Figure 1.2B), TL-dated at 107 ±15 ka and 106 ±22 ka. The underlying green-grey clays of Ghost Yard Beds are undated; However, deposition is believed to have occurred during an expanded and deep-water phase of KT-LE (Croke et al., 1999), presumably during a regressive phase of earlier MIS 5 high lake levels.

#### *1.2.3.2 Interpretation*

No Heinrich events occurred during MIS 5e. MIS 5e, glacial termination II, represents the sea level (e.g. Stirling et al., 1995; 1998, Thompson and Goldstein, 2005, Rabineau et al., 2006) and temperature maxima of the last interglacial, with peak global benthic $\delta^{18}O$ occurring at ~123 ka (Lisiecki and Raymo, 2005, Hansen et al., 2013). Pluvial phases in Australia were previously thought to occur during interglacials (Nanson et al., 1992b). However, an absence of records indicating elevated monsoon rainfall in northern Australia or the LEB during MIS 5e, and recent investigations determining KT-LE as a shallow-water lacustrine environment (Fu et al., 2017, Cohen et al., 2022), indicate no pluvial interglacial as previously suggested (e.g. Magee et al., 1995, Magee and Miller, 1998). Nanson et al. (2008) and Cohen et al. (2010) have convincingly demonstrated Cooper Creek was fluvially active in MIS 5e from ~120 ka and was capable of significant sediment reworking, albeit less powerful than during MIS 7. Similarly, high precipitation over northern Queensland is inferred from the existence of complex mesophyll vine forests based on palynological evidence from Lynch's Crater (Kershaw, 1991), a maximum wet phase between 126 and 115 ka equivalent to modern day precipitation. Despite these records of enhanced precipitation occurring over north-eastern Australia in late MIS 5e, there is no evidence KT-LE or Lake Frome significantly benefited from this input.

Palaeolacustrine and palaeofluvial evidence clearly indicates that inland Australia was wet from at least MIS 5d onwards. The influence of a strong IASM providing perennial/persistent precipitation over sub(tropical) Australia beginning around MIS 5d is directly inferred from lake fillings and proxy records (e.g. speleothems). High palaeoshorelines from KT-LE and Lake Frome correlate well with MIS 5 Heinrich events (Figure 1.5). Heinrich event C25 occurred at ~109 ka, coeval with the MIS 5d global benthic $\delta^{18}O$ peak (Lisiecki and Raymo, 2005) and was the first mid-latitude North Atlantic cooling and ice-rafting event after the last interglacial (Chapman and Shackleton, 1999). A correlating wet phase was recorded in Australia as peak fluvial activity in the Channel country (Figure 1.2B) around 109 ka (Nanson et al., 1992b), with highstands in KT-LE at 108.0 ka (Cohen et al., 2015) and Lake Frome at 109.9 ka (oldest optical age; sample LFP1_245; Cohen et al., 2011). Indeed, enhanced fluvial activity was also recorded in the Fitzroy River Basin in northeastern Australia (Figure 1.1) from ~105 ka (Croke et al., 2011). Heinrich event C24 is reported as one of the more intense MIS 5 ice-rafting episodes at ~107 ka, followed closely by C23 at ~102 ka; both events are considered by Chapman and Shackleton (1999) to represent a two-stage ice-sheet deglaciation. Unsurprisingly, both C25 and C24 events are recorded as abrupt positive shifts in the Sanbao cave stalagmite (SB23) record in central China (Wang et al., 2008), occurring shortly after CIS A25 ($\delta^{18}O$ peak at 111.8 ka) and A24 ($\delta^{18}O$ peak at 107.5 ka) during a period of AM lead relative to NHSI. In the lower Neales River, deposition of sandy alluvium over the Ghost Yard

Beds at 107 ±15 ka and 106 ±22 ka (Croke et al., 1996) attests to higher velocity in-flows and western LEB rainfall coeval with the C24 event; however, the catchment can receive rainfall via the south westerlies or from tropical depressions. Evidence of C23-correlated precipitation at ~102 ka is also clear. Concurrently, NHSI was near maximum, although a sharp reduction in AM was recorded around 100 ka (Wang et al., 2008). According to Magee et al. (2004), a major deep-water phase in KT-LE started around 100 ka. High palaeoshorelines are also evident in monsoon-fed Gregory Lakes and Lake Woods, respectively at 100 ka (Bowler et al., 2001) and 96 ka (Bowler et al., 1998), and one of three reported optical ages from the Lake Frome 15 m high palaeoshoreline (sample LFP1_300) is dated at 97.5 ±9.8 ka (Cohen et al., 2011). Collectively, these records support a mid-late MIS 5 IASM enhancement during a period of relative AM strength that could well be tied to these Heinrich events.

Heinrich event C22, recorded at ~90.5 ka (Chapman and Shackleton, 1999), coincides with major lake full stages in KT-LE (Magee et al., 2004) and mega-Lake Frome (Cohen et al., 2011), but aligns poorly with the 10 m-AHD palaeoshoreline in KT-LE at 93.5 ±3.8 ka (Cohen et al., 2015) (although still within lower bounds of optical stimulated luminescence error). The KT-LE filling during this period is however more synchronous with NHSI minimum (at 65°N), denoting weaker AM and by extension, possible strengthened IASM precipitation in Australia. However, speleothem records in central China do not record the C22 event as a punctuating positive shift in $\delta^{18}O$ relative to the governing NHSI trend, which is typical of other Heinrich events. There is also a lack of alluvial or aeolian sequences in Cooper Creek coincident with the C22 event, although Maroulis et al. (2007) reported the deposition of a fine fluvial sand unit at 92.1 ±10.6 ka. Thus, the relative strength of the C22 event and influence on the Australian hydroclimate is questionable. Indeed, in the north Atlantic the C22 event was only recorded as a minor IRD peak in the NEAP18K core site by Chapman and Shackleton (1999), and coeval IRD evidence was lacking in other north Atlantic Deep Sea Drilling Project sites (e.g. McManus et al., 1994). Despite the C22 event aligning with lake full episodes in the LEB, there is no direct evidence in Australia of Heinrich-induced ITCZ displacement.

Wet periods recorded in eastern parts of Australia may align with Heinrich extra tropical forcing around MIS 5b. Two palaeochannels in the Murrumbidgee sector of the Riverine Plain, Murray River sub-basin (Figure 1.1), show enhanced fluvial activity occurred between MIS 5c-a (100.0 ±9.0 ka to 83.0 ±4.5 ka; Page et al., 1996). Enhanced precipitation over this region via the south westerlies during MIS 5c is supported by high rates of speleothem depositions at Naracoorte Caves between 100 and 90 ka (Ayliffe et al., 1998), but this does not explain the younger fluvial enhancement. Interestingly, Page et al. (1996) noted prominent source-bordering dunes in the upstream reaches of the younger dated Murrumbidgee River palaeochannel infill (Yamma Arm: TL ages from 86.8 ±7.5 ka to 83.0 ±4.5 ka). Source-bordering dunes are a known indicator of a seasonal/periodic supply of bedload, typical of monsoon precipitation. During enhanced flows abundant sandy alluvium is deposited as bedload, something not seen in the LEB today, with seasonal drying facilitating the aeolian supply of sand to the transverse source-bordering dunes. Some coherency may be suggested between the ice-rafting event C21, the most pronounced North Atlantic excursion of ice-berg-laden polar waters during MIS 5 (~87 to 83 ka; Chapman and Shackleton, 1999), and the southern displacement of the ITCZ, inferred from $\delta^{18}O$ AM lag relative to NHSI after CIS A22 in the Sanbao Cave records (Wang et al., 2008). However, rainfall over the southern Murray Darling Basin, the Murray River sub-basin, typically occurs via the south westerlies (Bayon et al., 2017) and Heinrich-induced southern ITCZ excursions influencing rainfall this far south may be difficult to convincingly demonstrate.

The C21 event aligns well with enhanced fluvial activity in the Cooper Creek between ~87–80 ka. This is shown by sandy alluvium deposited in the Gidgealpa floodplain at ~85 ka (Cohen et al., 2010), around the IRD peak of C21 (at 85.6 ka), and coeval sediment accumulation on the Gidgeapla dune (Figure 1.2B) at 86.3 ±9 ka. Further, Maroulis et al. (2007) identified sediment accumulation on the source-bordering dunes Durham and Chookoo (Figure 1.2B), OSL dated between 86.7 ±8.2 and 83.9 ±6.7 ka, respectively. Testament to this activity in the eastern LEB is the 15 m high lake level recorded in mega-Lake Frome at 87.3 ±5.8 ka (Cohen et al., 2011) that likely benefited from inputs via Strzelecki Creek and/or KT-LE overflows. Indeed, Cohen et al. (2022) identified a fluvio-lacustrine sequence at Williams Point in KT-LE that was OSL dated to 86 ±4 ka. Further north, in the monsoon tropics in the eastern Gulf of Carpentaria, Nanson et al. (2005) TL-dated alluvial sands from the base of the Gilbert River (Figure 1.1) at

~85 ka, suggesting this as evidence of a major fluvial episode at that time. Precipitation enhancement did occur in the eastern parts of Australia and LEB during Heinrich event C21. Whether a governing monsoonal influence or semi-permanent La-Nina (like) conditions, caused by a WPWP, or a combination of the two led to the enhanced fluvial activity in Cooper Creek and filling of mega-Lake Frome during this period is yet to be determined.

Very importantly, it appears the greatest lake filling in KT-LE over the last two glacial periods may not have been monsoon driven. KT-LE reached its greatest depth of 26 m (11 m-AHD) at 78.8 ka ±4.2 ka (Cohen et al., 2015). This coincides with the NHSI maxima and CIS A21; a strong AM phase linked with weakened IASM. In the period between Heinrich events C21 and C20 (~83–76 ka), Cohen et al. (2010) found no evidence of sediment accumulation on source-bordering dunes in Cooper Creek west or east of the Innamincka Dome or in the Lower Cooper Creek until at least 70 ka. This may indicate precipitation in Cooper catchment between C21 and C20 was unlikely to be seasonal, as expected under monsoon conditions, and that bedload sands probably did not dry out sufficiently for aeolian transport to source-bordering dunes to occur. However, Maroulis et al. (2007) obtained one sample from a source-bordering dune near the Tooley Wooley Waterhole (Figure 1.2B) (TL-dated at 81.7 ±18 ka) that does not support this. The C20 Heinrich event is recorded as an abrupt $\delta^{18}O$ positive shift in the Sanbao cave stalagmite record (Wang et al., 2008) in central China, but also corresponds with an end to the deep-water lacustral phase in KT-LE at ~75 ka (Magee et al., 2004). High rates of speleothem deposition at Naracoorte caves occurred between 85–70 ka (Ayliffe et al., 1998), which might suggest rainfall delivery via southerly moisture sources rather than monsoonal, although this is not reflected as coeval fillings in mega-Lake Frome. Given, Nanson et al. (2008), Cohen et al. (2010) and Maroulis et al. (2007) clearly identified that fluvial activity in the Cooper Creek continued throughout the NHSI maxima and between Heinrich events C21 and C20 and also the lack of coeval mega-Lake Frome fillings with southern speleothem depositions, the formation of mega-KT-LE at this time is presumed to have resulted largely from an active WPWP close to the Australian coast.

### 1.2.4 MIS 4 [71–57 ka]

#### *1.2.4.1 Palaeohydrology*

Sedimentary records for MIS 4 from KT-LE or mega-Lake Frome are rare. Palaeosols at Williams Point, KT-LE, that developed in late MIS 5 were subsequently truncated by deflation (Magee et al., 1995) before a brief return to weak lacustrine conditions that formed a coquina palaeoshoreline at -3.1m AHD around 70 ka. However, Magee et al. (2004) later refined this return to lacustrine conditions to 65–60 ka, characterised as oscillating deep- and shallow-water lacustrine or fluvio-deltaic, which Cohen et al. (2022) further revised to 79–63 ka (95% credible interval). A 5 m-AHD high palaeoshoreline at Illusion Plains (OSL dated at 59.8 ±1.9 ka; Cohen et al., 2015) supports a mid-late MIS 4 lake filling (20 m lake depth), although a 15 m deep lake filling episode in neighbouring Lake Frome appears to span the entire MIS 4 period (OSL dated between 68.2 ±4.2 ka to 60.1 ±7.6 ka; Cohen et al., 2011). Collectively, these results indicate mega-Lake fillings during MIS 4 were substantial, although shallower and probably of shorter duration compared to those of MIS 5.

#### *1.2.4.2 Interpretation*

MIS 4 began at the end of the strong pluvial episodes of MIS 5. According to De Deckker et al. (2019), MIS 4 represents a major glacial period in Australia, rivalling the LGM. Little published information exists to definitively separate hydroclimate forcing by Heinrich event C19, at 70–68.5 ka (peak 69 ka), and the onset of this glacial. There are two tid-bits of evidence pertaining to the C19 event. (1) In Lake Frome, Cohen et al. (2011) discovered a coarse-grained shoreline formed at 68.2 ±4.2 ka (16.2 m-AHD) over an MIS 5d near-shore lacustrine unit. Their stratigraphical depiction (in Pit 1) shows gravel and pebble basal sediments transitioning to cross-bedded sand containing both intact and crushed shells, suggested here as indicating deposition under a fleeting high-energy fluvial episode with limited reworking. (2) Cohen et al. (2010) interpreted the oldest MIS 4 age from the Gidgealpa dune (67.8 ±3.0 ka) in Cooper Creek as the start of the next period of source-bordering dune formation after 70 ka. However, the sample represents the basal age of hole 2, and an older TL age from hole 4 (69.4 ±3.5 ka) exists in stratigraphic association ~7 km farther north. Both are within OSL age range of the C19 event but cannot be definitively tied to ITCZ displacement, as the undated underlying sediments within the same unit could push an earlier onset of fluvial activity in Cooper Creek to around Heinrich event C20.

In the subtropical climate zone, the northern and southern sub-basins of the Murray Darling Basin in southeastern Australia (Figure 1.1) were fluvially active. Today, the inland northern Darling River sub-basin (~25–32°S) is weakly governed by ITCZ-driven summer monsoon rainfall, whereas the southern Murray River sub-basin (~32–37°S) receives winter precipitation via the south westerlies (Bayon et al., 2017). Proxy river discharge εNd isotope signatures from deep-sea core MD03-2607, taken opposite the mouth of the River Murray (Figure 1.1), show greater sediment contributions from the Darling sub-basin during Heinrich events H6, H5 and H4 compared to the Murray sub-basin (See figure 3(d) in Bayon et al., 2017). Further analysis on the MD03-2607 core by (De Deckker et al., 2019) confirmed sediment provenance from the Darling sub-basin around H6, with the lowest εNd values (stronger Darling signature) occurring during the 65–63.2 ka interval. Together, these findings clearly indicate Heinrich-induced southern ITCZ excursions likely influenced rainfall in inland southeast Australia up to ~32°S, the southern latitudinal extent of the Darling sub-basin and, coincidently, the LEB.

Palaeoshoreline ages from KT-LE (Magee et al., 1995, Cohen et al., 2015) and mega-Lake Frome (Cohen et al., 2011) also support peak lake fillings around H6. Indeed, eggshell-derived point-potential evapotranspiration (PPET) values from KT-LE show the wettest conditions over the last glacial period occurred at ~65 ka (Miller et al., 2016a), supporting H6-correlated precipitation in central Australia around the peak of MIS 4. Both mega-Lakes, KT-Eyre and Frome, likely received input from the eastern LEB. Cohen et al. (2010) suggested pronounced fluvial activity occurred between 68 and 53 ka, spanning the H6 event (Figure 1.5), as evidenced by the seasonal supply of bedload sands to source-bordering dunes in Cooper Creek. However, mega-Lake Frome appears to have become wet earlier and remained full for longer. This is likely a result of mega-lake Frome being the main beneficiary of Cooper Creek flows, which remained active throughout MIS 4. Mega-Lake Frome could receive surface water input from Strzelecki Creek, a Cooper Creek distributary starting at Innamincka Dome, and possible discharge overflow from KT-LE via the Warrawoocara channel, when above 15 m-

AHD. Due to low sea levels weakening the Leeuwin Current, additional precipitation from the south westerlies may have reached mega-Lake Frome via tributaries in the local Flinders Ranges. However, the lack of increased speleothem deposition at Naracoorte Caves in south Australia (Ayliffe et al., 1998) does not support this.

An in-depth review of the occurrence and dynamics of Heinrich Events by Hemming (2004) showed the age of H6, in the North Atlantic marine sediment core records and Greenland ice core $\delta^{18}O$ values, is very poorly constrained to 60 ka, ±5 kyr. Thus, the exact timing and extratropical forcing during H6 on the Australian hydroclimate is also poorly constrained. Taken together, the Darling sub-basin εNd signature, eggshell-derived PPET values, an early MIS 4 onset of wet conditions in KT-LE and Lake Frome, and heightened fluvial activity in Cooper Creek, points to earlier rather than later extratropical climate forcing by H6-ITCZ displacement, probably around 65 ka.

It is not known whether the Diamantina or Georgina catchments were as fluvially active as Cooper Creek during MIS 4 or whether monsoon rainfall was even received this far inland during the H6-ITCZ displacement. Miller et al. (2016a) argued the very wet conditions in KT-LE was derived from monsoon runoff in the LEB's northern catchments. However, by mid-MIS 4, global sea levels were close to 100 m below what they are today (Grant et al., 2012), and the Indonesian throughflow was in a sustained weakened episode (Zuraida et al., 2009, Holbourn et al., 2011) indicative of a contracted and weakened Indo Pacific Warm Pool (IPWP) (De Deckker, 2016). In this scenario, the Australian landmass would be significantly larger, particularly in its northern regions with exposure of the Sahul Shelf, and advection of additional heat and moisture from the IPWP (De Deckker et al., 2003, De Deckker and Yokoyama, 2009) reduced across northern Australia. Therefore, rainfall into the Diamantina or Georgina catchments would require deeper incursions of the Australian northern monsoon and associated northwesterlies from the Indian Ocean and southern Asian ocean waters, a stronger monsoon unlike anything in the northern LEB today. Comparatively, control by WPWP and associated semi-permanent La Niña (like) conditions may have supported moisture-laden trade winds delivering rainfall over the northern LEB. The data sets of Bayon et al. (2017) and De Deckker et al. (2019) support a strong southerly H6-ITCZ displacement, although determining the longitudinal extent of these moisture incursions from Australia's east coast into the northern LEB is yet to be determined.

### 1.3 Conclusion

The complex interplay of regional and global climate drivers is evident in attributing a primary source of enhanced precipitation in the LEB during the late Quaternary. While periods of fluvial activity or quiescence are useful in interpreting the relative spatial and temporal runoff variations within and between catchments, their relationship to moisture source(s), or, ultimately, Heinrich-induced precipitation may be limited due to the complex nature of the global hydrologic system. However, some coherency can be observed between lake-full episodes in the LEB and northern hemisphere cooling periods. Most lake filling episodes in KT-LE and mega-Lake Frome correspond with Heinrich events, excluding the sedimentologically evidenced MIS 5e wet period in KT-LE. However, the strength of this relationship varies, with some events showing clearer evidence of influence than others. There is strong evidence Heinrich events H16, H15, H11, C25, C24, C23, C21, and H6 influenced late-Quaternary Lake fillings in mega-Lakes, KT-Eyre and Frome. This is less clear during Heinrich events H17, H14, H13, H12, C22, C20 and C19. It is also unlikely the C22 event had any direct influence Australian hydroclimate, despite aligning with lake full episodes in the LEB.

It is apparent that the vast majority of late Quaternary research on the LEB is conducted in the east and southeast of the continent. This is at odds with assertions in the literature that lake-filling episodes are the result of enhanced monsoonal activity feeding into the major catchments of the northern and eastern LEB, when little data exists for the northern catchments. While the Cooper Creek has been relatively well studied, research on the Diamantina and Georgina catchments are notably absent. These catchments are clearly capable of delivering immense flows to the LEB, and KT-LE in particular, and the paucity of the data for these catchments suggests that the true moisture sources and primary drivers of rainfall into the LEB over the last 240 kyr remains unclear.

# Chapter 2

# Late Quaternary climate change from lacustrine, fluvial and alluvial records in the Georgina catchment, Queensland

Singleton, R.E[a,b*], Orr, T.J[a,b], Wasson, R.J[a,b]., Jacobs, Z[c,d]., Nott, J[a]., and Bird, M.I[a,b]

[a]College of Science and Engineering, James Cook University, Cairns, QLD 4870, Australia

[b]ARC Centre of Excellence for Australian Biodiversity and Heritage, James Cook University, Cairns, QLD 4870, Australia

[c]ARC Centre of Excellence for Australian Biodiversity and Heritage, University of Wollongong, Wollongong, NSW, Australia

[d]Centre for Archaeological Science, School of Earth and Environmental Sciences, University of Wollongong, Wollongong, NSW, Australia

**In preparation for submission**

**Author contributions:**

Russell Singleton collected, sampled and processed the cores, analysed and interpreted the data, developed the research question and wrote the manuscript. Theresa Orr contributed to facies characterisation. Michael Bird, Jonathon Nott and Robert Wasson contributed to concept development prior to fieldwork. Michael Bird provided funding for the project through the ARC grant. Zenobia Jacobs completed the OSL analyses and completed the associated data reduction. Michael Brand provided field assistance. All authors provided editorial assistance.

## 2.1 Introduction

The late Quaternary climatic history of northern Australia remains largely unknown. This period saw significant environmental change, including megafaunal extinctions, human expansion across the continent, and a transition toward modern arid landscapes (e.g., Roberts et al., 2001, Fitzsimmons et al., 2013, Saltré et al., 2019). Understanding the late Quaternary is critical for reconstructing past hydroclimatic variability, particularly monsoonal shifts, which influenced water availability across the arid interior. Changes in rainfall penetration from the north shaped the hydrological connectivity of lake systems and impacted landscape evolution and sediment transport, preserving evidence of many of these environmental transitions in sedimentary archives. Palaeolake records offer crucial long-term environmental insights into Australia's hydrological history, with many providing evidence of permanent water bodies intermittently through the late Pleistocene (e.g., Chen and Barton, 1991, Bowler et al., 1998, Bowler et al., 2001, English et al., 2001). Importantly, the central and northern lakes archive a near stepwise reduction in lake fillings amidst progressive aridification that accelerated around ~50 ka, documenting the disconnection of lake systems and ultimately the demise of Australia's mega-lakes (Cohen et al., 2011, Cohen et al., 2012b, Cohen et al., 2015, Fu et al., 2017, Cohen et al., 2022).

To place the environmental history of northern Australia into context, it is essential to examine existing palaeolake records, which document long-term hydroclimatic changes across the region. An ancient foreshore dune in the Gregory Lakes system in northwestern Australia provides one of the earliest terrestrial records of a significantly wetter climate than today. Bowler et al. (2001) documented that around 300 ka (MIS 9), the Gregory Lakes system formed a 'mega-lake' covering ~6,500 $km^2$, nearly seventeen times the area of the current lake (387 $km^2$). While this expansive lake filling ended at some time before ~250 ka, the time of onset of this wet phase in the Gregory Lakes system and across other parts of northern Australia is still unknown. Smaller expansions in the Gregory Lakes occurred around 200 ka and 100 ka, covering 4,600 $km^2$ and 1,500–2,000 $km^2$ (Bowler et al., 2001), respectively, indicating a progressive shift to drier conditions over at least the past three glacial-interglacial cycles. Further to the east, Lake

Woods in the Northern Territory records its earliest known mega-lake phase around 180 ka, covering over 5,000 km$^2$ (Bowler et al., 1998), coincident with the MIS 7 mega-lake phase in Lake Gregory (Figure 2.1).

Expansive lake fillings also occurred in the main depocenters of the Lake Eyre Basin (LEB). Around MIS 5a, Kati Thanda-Lake Eyre (KT-LE) and the mega-Lake Frome series – comprising Lakes Gregory, Callabonna, Blanche and Frome – all located in the southwestern LEB (Figure 2.1a), merged to form a single vast mega-lake covering an estimated 34,886 km$^2$ and KT-LE reached a depth of ~25 m (Leon and Cohen, 2012, Cohen et al., 2015). After ~48 ka, both KT-LE and Lake Frome continued to experience significant lake fillings but remained permanently disconnected from each other, with each subsequent filling being progressively lower (Cohen et al., 2015, Cohen et al., 2022).

There is little doubt the gradual demise of the late Pleistocene mega-lakes was likely linked to hydroclimate variations in the summer monsoon and ITCZ, affecting rainfall penetration into northern Australia, including the LEB. Driven by seasonal land-sea heating contrasts, the Australian summer monsoon brings intense rainfall and wind shifts that extend poleward to about 25° latitude (Geen et al., 2020), representing a localised, seasonal amplification of the broader insolation-driven dynamics of the ITCZ. In contrast, the position of the ITCZ, confined within 10° of the equator, is primarily controlled by insolation, with its position shifting with the thermal equator on orbital timescales. While insolation forcing probably had some level of control on perennial mega-lakes in central Australia, other factors likely played a role, such as variations in ice-sheet growth and decay (Miller et al., 2018), El Ninõ Southern Oscillation (ENSO) dynamics (Turney et al., 2004), sea surface temperatures and land-ocean heating contrasts (Wyrwoll and Valdes, 2003).

Cyclostratigraphic (frequency) analysis of palaeoclimate proxies offers a tool to investigate cyclic climatic responses at orbital- to sub-decadal timescales. The well-documented Milankovitch cycles include short and long eccentricity (~100 thousand years (kyr) and 405 kyr, respectively), obliquity (~41 kyr), and precession (~19 to 23 kyr), which represent climatic responses to external (orbital) forcings. These cycles are evident in various geological archives worldwide (Colman et al., 1995, Lückge et al., 2009, Gebregiorgis et al., 2018, Liu et al., 2018), including in the Australian region (Lückge et al., 2009, Tachikawa et al., 2011, Shiau et al., 2012). Amplitude modulation of primary Milankovitch cycles, or harmonics of Milankovitch or sub-Milankovitch periodicities, are also frequently expressed in late Quaternary palaeoclimate archives (Huang et al., 2021, Zhang et al., 2022) and modelled reconstructions (Scafetta, 2012). Sub-Milankovitch cycles, typically requiring higher resolution proxy records (Sinnesael et al., 2019), are generally driven by internal (climate) forcings. In the context of regional Australian palaeoclimate, sub-Milankovitch cycles have previously shown links to solar activity (Breitenmoser et al., 2012, Haig and Nott, 2016, Asten and McCracken, 2022), interhemispheric climate teleconnections (e.g., Bond cycles, Dansgaard-Oeschger events, Heinrich events; Turney et al., 2004, Skilbeck et al., 2005), and tropical pacific phenomena such as ENSO (Wang et al., 2000, Turney et al., 2004, Tachikawa et al., 2011) and the Interdecadal Pacific Oscillation (IPO) (McGowan et al., 2010).

So far, frequency analysis of late Quaternary terrestrial palaeoclimate records from Australia are limited to the last ~50 ka. Most are from marginal areas of the continent such as Lynch's Crater in northeast Queensland (Turney et al., 2004) or the Myall lakes in coastal southeastern Australia (Skilbeck et al., 2005). Inland areas such as the Snowy Mountains region of southeastern Australia (McGowan et al., 2010) also record Holocene climate cyclicities. Cohen et al. (2022) suggested orbital forcing may have partly driven KT-LE fillings over the last glacial cycle based on monsoon climate modelling by (Wyrwoll and Valdes, 2003). Magee et al. (2004) also showed similarities between northern hemisphere winter insolation minima and major wet periods in KT-LE during MIS 5 and the early Holocene, inferring deeper penetration of monsoon rainfall into the LEB caused by orbital forcing. Indeed, (Fu et al., 2017) highlighted the significant role of Northern Hemisphere climate dynamics in shaping the Indo-Australian monsoon and suggested that high lake levels in KT-LE appeared more influenced by millennial-scale North Atlantic cooling events and stadials than by Southern Hemisphere orbital forcing. While lacustrine sedimentary archives can be discontinuous due to episodic deposition and erosion, (Kramer et al., 2000, Cohen, 2003, Fitzsimmons et al., 2013), applying frequency analysis to these records can still help identify recurring depositional trends over orbital to millennial timescales (e.g., Fagel et al., 2008, Minyuk and Subbotnikova, 2021). However, frequency analysis has not yet been conducted on palaeoclimate proxies from the LEB, Australia's largest drainage basin (1,140,000 km$^2$). Consequently, the relative importance and timing of orbital-scale and sub-Milankovitch climate patterns potentially driving wet and dry periods archived in the LEB's sedimentary sequences, spanning the past two glacial-interglacial cycles (e.g., Magee et al., 1995, Magee et al., 2004, Cohen et al., 2015, Fu et al., 2017, Cohen et al., 2018, Cohen et al., 2022, Krapf et al., 2022), remains largely unknown.

Three major drainage basins comprise ~58% of the LEB, including the Cooper, Georgina and Diamantina, all of which have headwaters in northern Australia and modern ephemeral flows that rarely reach KT-LE in south Australia. Input to KT-LE only occurs during enhanced summer monsoonal activity. The largest historical filling occurred in 1974, when all three northern LEB catchments were active, causing KT-LE to reach a depth of ~6.1 m and cover an area of 8,000-10,000 km$^2$.

Presumably, late Pleistocene mega-lake stages in the southern LEB also required fluvial contributions from the three major northern catchments, and possibly from the western tributaries of the Neales and Macumba Rivers (Figure 2.1a), although the associated climate forcing mechanisms and allied moisture source(s) were likely dissimilar to those of today. Indeed, spatial and temporal variations in rainfall inputs across the three northern catchments are largely unknown. Interpreting the hydrological evolution of the LEB has relied heavily on sedimentary records from the Cooper (Maroulis et al., 2007, Nanson et al., 2008, Cohen et al., 2010) and Diamantina (Nanson et al., 1992b, Kershaw and Nanson, 1993), as well as from KT-LE and the Frome lake series (Magee et al., 1995, Croke et al., 1996, Magee et al., 2004, Cohen et al., 2015, Fu et al., 2017, Cohen et al., 2018, Krapf et al., 2022). To date, the sedimentological and palaeoclimate proxy records of the Georgina catchment, and it's lakes in particular, remain an unexplored palaeoarchive of the wet and dry history of central Australia.

This study examines lacustrine and fluvial/alluvial deposits from the Georgina catchment (the LEB's second largest and most northern sub-catchment). The Georgina River flows southwards into three Lakes (as Eyre Creek): Machattie, Koolivoo, and Mipia. Collectively, these lakes and the adjacent floodplains cover roughly 900 $km^2$, hereafter referred to as the Lake Machattie Area (LMA). The LMA, located ~110 km northeast of Birdsville (Figure 2.1a), serves as the final depocenter for the Georgina River before it flows westward as Eyre Creek. It then continues south through the interdune regions of the Simpson Desert, eventually merging with the Diamantina River and ultimately flowing into KT-LE.

The primary aims of this study are to (1) document the sedimentology and stratigraphy of the LMA, (2) identify depositional systems and palaeoenvironments, (3) reconstruct the hydroclimatic history of the Georgina, and (4) investigate palaeoclimate proxies to determine potential cyclic climate forcing mechanisms and long-term environmental climate changes. Element and isotope geochemistry, magnetic susceptibility, micromorphology, sedimentology, and spectral frequency analysis in three sediment cores are used to define spatial and temporal variations in water availability between Lake Machattie, Lake Koolivoo and Eyre Creek, within the LMA through the late Quaternary. Accelerator mass spectrometry (AMS) $^{14}C$ and Optical Stimulated Luminescence (OSL) dating provide the geochronological framework for these analyses.

## 2.2 Background

Australia's Georgina catchment, a large (~205,000 $km^2$) semi-arid to arid drainage basin in central northern Australia, drains the monsoon-fed north of the continent. Starting at ~19°S, the Georgina River (and later as Eyre Creek from about 23.4°S) flows southward, entering the LMA around 25°S. Low flow inputs to the LMA typically follow the ~35 m wide Eyre Creek channel, entering from the north and flowing into Lakes Koolivoo and then Lake Mipia before continuing westward. During large flood events, Lakes Machattie, Koolivoo and Mipia, and the surrounding flood plains including LMA outflows (northwest of Lake Mipia), become inundated almost simultaneously, forming one vast water body (Figure S1; Appendix A1). The lake boundaries referenced in this study are based on mapped extents from existing topographic and hydrological datasets, as well as satellite imagery (e.g., BOM, GeoAust 2024b). No new delineation of lake boundaries was conducted as part of this study, and the spatial extent of each lake is referenced according to its observed or documented hydrological footprint.

Inundation frequency data generated from satellite imagery from 1986 to 2024 reveals significant variations in water permanence across the LMA (GeoAust, 2024b). Lake Machattie, the largest of the three lakes at ~263 $km^2$, was dry for ~80% of this period, with inundation around the lake's margins occurring only during the most extreme flooding events (~<1% of the time). Comparatively, Lake Koolivoo (~19 $km^2$) and Lake Mipia (~24 $km^2$) are relatively permanent water bodies, remaining wet 80% of the time, allowing for potential sediment deposition during both low- and high-flow inputs. Westward outflows from the LMA (as Eyre Creek) are also rare, observed in less than 1% of the satellite data, mainly in response to flooding, when most or all the floodplain, waterholes and the westward-flowing, anabranching channels of Eyre Creek become submerged.

During significant historical flooding events, surface waters travel nearly 1,000 km from the top of the catchment to reach the Georgina-Diamantina confluence at Goyder's lagoon in south Australia (Figure 2.1a). This has only occurred 12 times in the last 46 years. Strengthened La Niña phases of ENSO in superposition with negative phases of the IPO are tied to most of the largest floods in the Georgina (Singleton - unpublished data; refer to Chapter 4, section 4.5.2.). Rainfall is dominated by summer monsoon rainfall (JFM), with the highest mean monthly rainfall falling in January across northern Australia (117.0 mm) and in the northern Georgina catchment (e.g., Camooweal: 99.8 mm) (BOM, 2024a) (Figure S2; Appendix A1). Mean annual rainfall in the Georgina ranges from ≤300 mm in the south, around the LMA, and up to 700 mm in the north. Mean temperatures range from 24 °C to 27 °C across the catchment, with maximum temperatures around the LMA reaching ~32 °C. The FAO aridity index (AI: annual rainfall/potential evapotranspiration; Spinoni et al., 2015) ranges from 0.22–0.41 (semi-arid) in the north to 0.07–0.14 (arid) in the south (BOM, 2024b).

Surface geology in the north of the catchment is dominated by the siliciclastic and carbonate rocks of the Cambrian Barkly and Narpa Groups, and Late Tertiary to Quaternary alluvium and colluvium (NTGS, 2006, QGlobe, 2024a). In the northeast there are some metavolcanics and granitoids of the Mt Isa region, including the Paleoproterozoic Haslingden Group and Sybella Suite, in addition to the siliciclastics and carbonates of the Ballara Quartzite and Corella Formation. However, most of the metamorphosed rocks of the Mt Isa Inlier lie outside the catchment. To the south, the Georgina catchment hosts Cretaceous mudstones, siltstones and sandstones of the Allaru, Mackunda, and Wallumbilla Formations. Several outcrops of the Late Cambrian to Early Ordovician Cockroach Group siliciclastics and carbonates, and Oligocene-Miocene conglomerates, sandstones and mudstones are also present. Immediately surrounding the LMA are Quaternary quartzose sands, and arenites and mudstones of the Cretaceous Winton Formation. The LMA itself comprises lacustrine and lagoonal deposits of clay, silt, and sand (QGlobe, 2024a).

## 2.3 Materials and Methods

### 2.3.1 Core acquisition

Three sediment cores were collected from the LMA (Figure 2.1c) using a mechanical hydraulic coring-rig. The first was taken at the northern margin of Lake Machattie (core LM; 2.79 m in length; 24.757164°S, 139.741844°E), today an area inundated only during extreme flooding. A core from Lake Koolivoo's southern margin (core LK; 6.44 m in length; 24.935806°S, 139.601549°E), roughly in the centre of the LMA, represents a lacustrine depositional environment capable of receiving sediment during low- and high-flow periods. A third core was taken ~20 km northwest of Lake Mipia near the left bank of the main Eyre Creek channel (core EC; 2.88 m in length; 24.818379°S, 139.295500°E), a flood plain depositional environment characterised by a network of westward flowing Eyre Creek anabranches. These sites were selected to capture spatial variability in depositional settings, providing a record of both lacustrine and fluvial influences within the LMA, while also being constrained by site accessibility, as more central lake locations were not feasible for coring. Satellite data shows that during major flooding in March 1997, the LM, LK and EC core locations were inundated by floodwaters to estimated depths of 1.2, 2.0 and 1.2 m, respectively. However, water levels in Lake Machattie during the 1974 flood were observed at ~1.6 m higher than in 1997 (Singleton - unpublished data, refer to Chapter 4, section 4.4.4) suggesting the potential for much deeper inundations across the LMA during historical wet periods, such as 1974–1977 and 1949/1950 (Rust, 1981, Kotwicki and Allan, 1998), and in the ancient past.

Efforts were made to maximise sediment recovery and preserve core integrity. All cores were acquired in continuous 1 m sections (46 mm diameter) using 2 mm thick black PVC tubes that were immediately capped at both ends and black plastic wrapped to ensure minimal disturbance during retrieval. An additional 1.0 m and 0.5 m of sediment was collected at Lake Machattie and Eyre Creek, below their respective maximum continuous core depths using an open coring barrel, with bulk samples collected in the field at 10 cm intervals. While the coring approach effectively captured stratigraphic transitions, compaction and minor sediment loss at depth remain potential limitations, particularly in more unconsolidated units. Elevation data for the core locations and surrounding topography was recorded using a Hemisphere S321+ receiver with the ATLAS H10 L-band Global Navigation Satellite System (GNSS), which has a reported horizontal positional error of 8 cm with 95% precision (4 cm RMS). Precision of elevation was on average 5 ±0.1 cm (Horizontal RMS) and 10 ±0.02 cm (Vertical RMS) across all sites.

#### *2.3.1.1 Core sampling*

Cores were split under dim red-light, clear plastic wrapped, and half of each 1 m section was black plastic wrapped for later OSL and accelerator mass spectrometry (AMS) $^{14}C$ sampling. OSL samples were collected from each core under dim red-light every ~1 m, with additional samples taken ≥10 cm on either side of major unit boundaries to account for ionising radiation from the adjoining sediment matrix (total n=19). Single-grain OSL analyses was conducted by the OSL dating laboratory, University of Wollongong, Australia. AMS $^{14}C$ samples were taken from the Eyre Creek core with sufficient spacing to improve the age-depth model resolution and sediment accumulation rates within the <50 ka BP (OSL-dated) period. AMS $^{14}C$ sample pretreatment was carried out at James Cook University following the standard ABA protocols of Hatté et al. (2001), followed by hydrogen pyrolysis (HyPy), an ABA/HyPy chemical pretreatment method recommended by Orr et al. (2021) to improve exogenous carbon decontamination and date accuracy of terrestrial sediment samples with low carbon content. AMS $^{14}C$ dating was conducted by the University of Waikato's radiocarbon dating laboratory (New Zealand). All light-exposed half core sections were sampled at ~10 cm intervals for particle size analysis, bulk density and isotopic and geochemical analyses ($\delta^{13}C$ of organic carbon, total organic and inorganic carbon, and other major elements). All cores were sampled for thin section preparation and micromorphology within each unit, across unit boundaries, and through evaporite crystallisation zones (total n=21). Additionally, 21 gypsum crystals were extracted from cores LK and LM for $\delta^{34}S$ measurement - core EC contained insufficient gypsum for analysis. Munsell (2009) colours were determined on moist core sediment profiles.

### 2.3.2 Sedimentology

Sediment composition and texture was investigated via macromorphological analysis and petrographic microscopy. Standard thin sections (30 μm) were prepared by a commercial laboratory (Vancouver Petrographics, Ltd.). Sedimentological analysis focussed on bioturbation features, clast morphology, colour, mineralogy, mineral accumulations, pedogenic features, secondary concretions and sedimentary structures (e.g., Gile et al., 1966, Klappa, 1980, Birkeland, 1984, Munsell, 2009, Mees et al., 2012, Miall, 2013, Stoops et al., 2018). Individual facies were identified based on lithology, biogenic features, and sedimentary structures and textures. Facies were then characterised into associations of depositional environments and processes. The characteristic evidence for alluvial, lacustrine, and playa sediments used in this study rely on previous studies (Miall, 1977, Turnbridge, 1981, Arakel et al., 1989, Rosen and Warren, 1990, Magee, 1991, Miall, 1992, Magee et al., 1995, Alonso-Zarza and Wright, 2010, Miall, 2013, Swan et al., 2018).

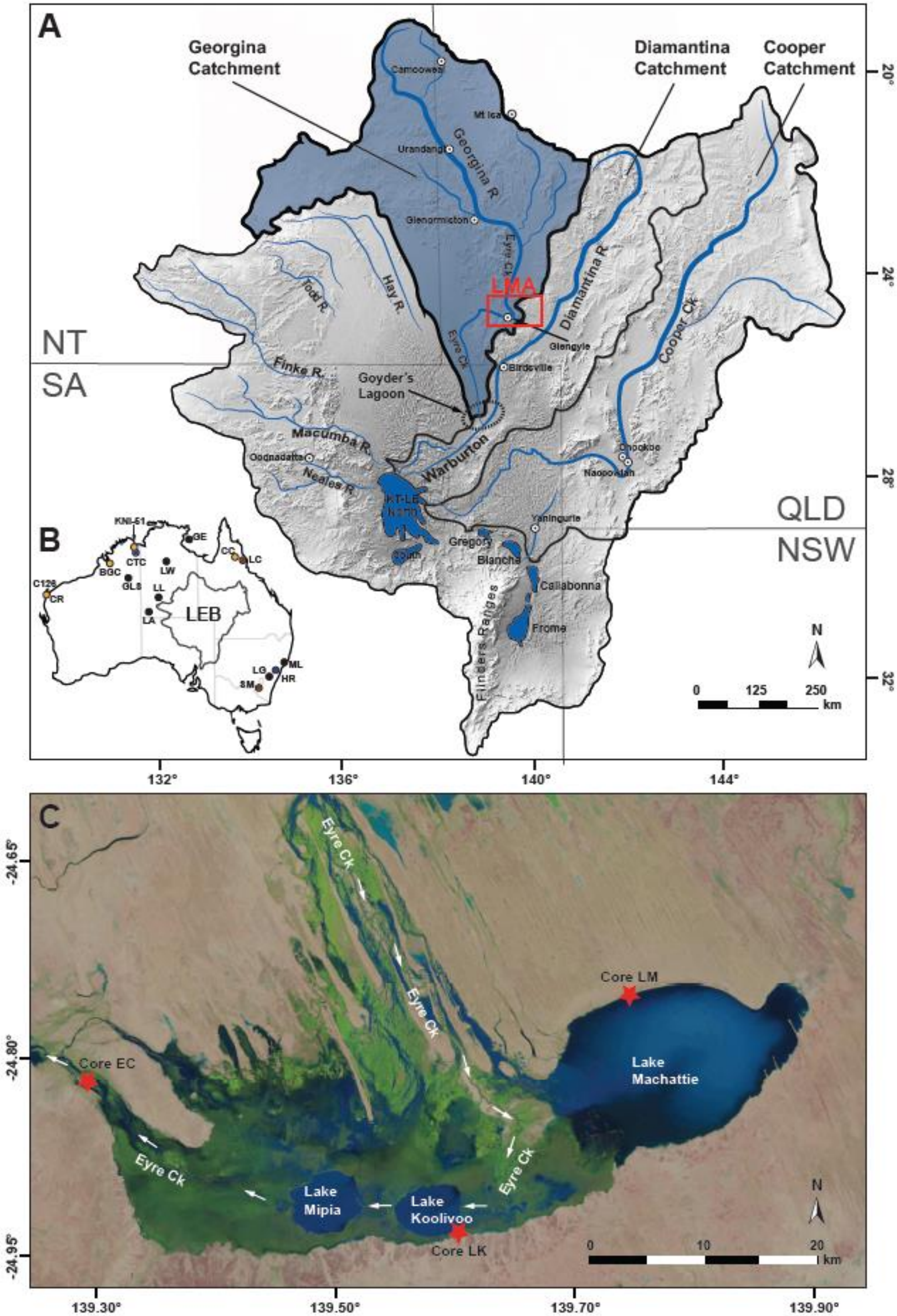

A
Georgina Catchment
Diamantina Catchment
Cooper Catchment
Camooweal
Mt Isa
Urandangi
Georgina R.
Glenormiston
Eyre Ck
LMA
Hay R.
Todd R.
Diamantina R.
Cooper Ck
Glengyle
Birdsville
NT
SA
Finke R.
Goyder's Lagoon
Macumba R.
Oodnadatta
Warburton
Neales R.
Innamincka
Nappa Merrie
QLD
NSW
Yaningurie
Gregory
Blanche
Callabonna
Frome
Flinders Ranges
B
KNI-51
GE
CTC
BGC
LW
CC
LC
C126
CR
GL8
LL
LA
LEB
ML
LG
HR
SM
N
0
125
250
km
20°
24°
28°
32°
132°
136°
140°
144°
C
Eyre Ck
Eyre Ck
Core LM
Lake Machattie
Core EC
Eyre Ck
Eyre Ck
Lake Mipia
Lake Koolivoo
Core LK
N
0
10
20
km
-24.65°
-24.80°
-24.95°
139.30°
139.50°
139.70°
139.90°

**Figure 2.1**. Locality: **(A)** Lake Eyre Basin (LEB), with sub-catchments, Georgina (blue shading), Diamantina and Cooper. Kati Thanda-Lake Eyre (KT-LE) and Frome Lake series (Lakes, Gregory, Blanche, Callabonna, and Frome) shown in dark blue. Lake Machattie Area (LMA) shown with red box and in map C. Locations referred to in text (white circles with black dot). **(B)** Map of Australia, with the LEB. Terrestrial sites referred to in text include **lakes** [black dots: Gregory Lakes system (GLS), Lake Woods (LW), Lake Lewis (LL), Lake Amadeus (LA), Four Mile Billabong at Groote Eylandt (GE), Myall Lakes (ML), Lake Gregory (LG)], **speleothems** [yellow dots: Cape Range peninsula (CR and C126), Ball Gown Cave (BGC), cave (KNI-51), Chillagoe cave (CC)], **peat cores** [brown dots: Lynch's Crater (LC), Snowy Mountains (SM)], and **fluvial records** [blue dots: Cabbage Tree Creek (CTC), Hawkesbury River (HR)]. Note, locations of marine sediment cores and speleothem records (outside of Australia) referred to in text are listed in Table S1 (Appendix A2). **(C)** Map of Lake Machattie Area including core locations (red stars) and main flow pathways (white arrows) in flood. Image: Landsat collection 2 reflective full resolution browse, a 3-band composite showing a "natural" looking (false colour) image.

### 2.3.3 Chronological control

The chronology for cores LM, LK and EC were defined by a total of 15 OSL dates and two AMS $^{14}C$ dates. All samples were measured using single grains of quartz and potassium-rich feldspar. Quartz grains were tested using the conventional single-aliquot regenerative-dose (SAR; Murray and Wintle, 2000) method, with the Ln/Tn method (Li et al., 2017) applied to samples that contained a large proportion of 'saturated' grains. The Ln/Tn method was also applied to K-feldspar (KF) grains, where present. Measurements of De were obtained for all samples, except for some saturated quartz grains at depths below 2 m in Eyre Creek, 1.5 m in Lake Machattie, and 5 m in Lake Koolivoo. Sample preparation and measurement followed the methodologies and instrumentation described in Jacobs et al. (2019) and Forbes et al. (2021). Quartz and feldspar grains with diameters of 180–212 μm were extracted and density separated using standard procedures (Jacobs et al., 2015). The resulting De data set was processed using the functions available in the numOSL (Peng et al., 2013) and Luminescence (Kreutzer et al.,

2012) R-packages. The environmental dose rate was determined based on external beta, gamma, and cosmic-ray dose rates, along with an internal alpha dose rate. A constant internal alpha dose rate of $0.03 \pm 0.01$ Gy kyr$^{-1}$ was applied to all samples. Beta dose rates were directly measured using a Risø GM-25-5 beta counter, following established protocols (Bøtter-Jensen and Mejdahl, 1988; Guérin et al., 2001, Jacobs and Roberts, 2015). Gamma dose rates were derived from the concentrations of U, Th and K, which were measured by inductively coupled plasma mass spectrometry (ICP-MS; for U and Th) and inductively coupled plasma optical emission spectroscopy (ICP-OES; for K). The internal content of feldspars was estimated at 12.5 ±0.5 % for K and 400 ±100 ppm for Rb (Huntley and Baril, 1997, Huntley and Hancock, 2001). Cosmic-ray dose rates were calculated using site-specific parameters, including latitude, longitude, altitude, sediment depth, and overburden density, with an assumed average sediment density of 1.8 g/cm$^3$. Water content measured in the lab was used to correct the dose rates.

The appropriate statistical age model for final OSL age model estimates was determined by visual assessment of radial plot equivalent dose ($D_e$) distributions. Bayesian age-depth modelling (Bacon; Blaauw and Christen, 2011) of OSL and AMS $^{14}C$ age determinations were generated using R (version 4.3.3). Interpretation of all data was constrained between the oldest absolute OSL dates and the youngest absolute OSL dates extrapolated to zero (at surface). For core LK, a 'hiatus' period of ~31,100 years was also included in the model at 1.52 m depth, allowing for ages and sediment accumulation rates not auto correlating across this unconformity. Unless stated otherwise, the Bayesian modelled median age is reported throughout the text. Sedimentation rates were calculated in R at 10 cm depth increments and these data were used in TOC-MAR calculations.

### 2.3.4 Laboratory

#### *2.3.4.1 Magnetic susceptibility*

Magnetic volume susceptibility (MS) was measured in SI units (dimensionless constant) on the un-split cores to help identify trends in magnetic sediment distribution with depth. High-resolution measurements were conducted at room temperature at 0.5 cm intervals for 2 seconds each at a frequency of 565 Hz using a Bartington MS3 susceptibility meter, MS2C loop core logging sensor and manual core track system. Sequential 1 m core lengths were abutted to avoid end-of-core measurement drift and to maintain optimal measurement accuracy.

#### *2.3.4.2 Particle Size Analysis*

Sample pre-treatment included suspension at room temperature in 30% $H_2O_2$ (three times for 12 hours) to remove organic matter and 2.0 M HCl for 12 hours to remove carbonates (Konert and Vandenberghe, 1997). Particle size analyses were performed using a set of stacked sieves at 1 phi (φ) intervals for >500 µm and a Malvern Mastersizer 2000 for <500 µm. Samples <500 µm were pre-treated with a 10% sodium hexametaphosphate dispersant solution before laser analysis. To account for this, samples were also examined under a microscope for visible aggregates. The use of sodium hexametaphosphate as a dispersant ensured full disaggregation of flocculated clay and likely broke down aggregated mud pellets, as described by Bowler (1973) and Rust and Nanson (1989). While this means that clay fractions represent total disaggregated material, rather than its potential original transport form, interpretations consider the likelihood of reworked aggregates when assessing depositional processes.

#### *2.3.4.3 Major Elements*

Major element geochemical analysis was conducted using a Bruker Tracer III-SD portable X-ray fluorescence spectrometer (pXRF). This instrument is an energy dispersive (ED)-XRF unit equipped with a rhodium target X-ray tube and Pelteir-cooled silicon PIN diode detector. Sample preparation included 2 mm sieving, lyophilisation, milling to <75 µm using a Rocklabs BenchTop Ring Mill Pulverisor, thorough homogenisation using a vortex mixer, and 10 mm deep loading into pXRF sample cups using 4 µm polypropylene X-ray film at the base of each cup. The pXRF gun was operated upside down in a benchtop stand, with sample cups positioned over the sensing window on a sample stage and then covered with a sample shield. Each sample was analysed at 3 different spots for 60 s at 15 KeV and 29 µA under <15 torr vacuum to quantify light elements (Mg, Al, Si, K, Ca, V and Mn), and at 40 KeV and 30 µA (no vacuum) including a 'yellow' filter (0.0254 mm Ti and 0.3048 mm Al) inserted in the X-Ray path to quantify heavy elements (Ti, Cr, Fe, Rb, Sr and Zr). Quality assurance and quality control (QA/QC) was achieved through replicate analysis of a metal check sample (Duplex 2205; T3S2795) to monitor instrument drift, and an $SiO_2$ blank to monitor for contamination of the spectrometer or probe window after every ~15 samples.

A pXRF cannot accurately quantify several low-Z elements, including Na and P, while analyses of other elements such as Ti, V and Cr are hampered by spectral overlapping (Hunt and Speakman, 2015). Ti, often present at higher concentrations (wt.%), can be quantified, whereas V and Cr, typically in lower ppm levels, are more prone to spectral interference and are only semi-quantitative (Hunt and Speakman, 2015). Grain size, mineralogy and sediment heterogeneity also influence the accuracy of pXRF analyses; however, these effects can be reduced by thorough sample homogenisation (Hunt and Speakman, 2015; Takahashi, 2015), as in this study

Calibration of the pXRF raw spectral data was completed using the CloudCal v3.0 application (Drake, 2018), employing the algorithm proposed by Lucas-Tooth and Price (1961). Raw spectral data was standardised to the Compton (or inelastic) peak of the rhodium X-ray backscatter at 19.0–22.0 KeV. The calibration was performed using four certified reference materials (CRMs) that covered the samples geochemical range of monitored elements and were a matrix-matched suite of sediment or soil compositions (Table 2.1). Each CRM was analysed four times on distinct spots for 60 s using the same method protocols as the samples.

Data robustness and reproducibility was assessed using criteria from the United States Environmental Protection Agency method 6200 (USEPA, 2007) (Table 2.2). The coefficient of determination ($r^2$), relative standard deviation percent (RSD%), and inferential statistics of both slope and intercept values were used to categorise the pXRF data quality produced for the four replicate measurements of the CRMs. Elements were only considered if data quality level between the pXRF measurements and the CRM reference values were definitive or quantitative. Three statistical criteria ($r^2$, RSD, Inferential Statistics) are required to meet the corresponding data quality level.

**Table 2.1.** Certified Reference Materials used in this study.

| CRM | Host lithology | Matrix | Certifying Agency[1] |
|---|---|---|---|
| OREAS 140 | Smectite Clay | Sediment | ORE |
| OREAS 45c | Ferruginous soil | Soil | ORE |
| OREAS 120 | Sandstone | Sediment | ORE |
| sdAR-M2 | Soil | Sediment (metal-rich) | IAG |

[1] ORE: Ore Research ad Exploration PTY LTD; IAG: International Association of Geoanalysts; MV Laboratories INC, a subsidiary of Seastar Chemicals INC. CRMs were provided by Portable Spectral Services, Perth, Western Australia.

A wide variety of geochemical indices have been developed for palaeohydrological and limnological studies. For the purposes of this study, element abundance and ratios were calculated for the following: Ti, Ti/Al, Fe/Mn, Si/Zr, Si/Ti, Al/Mg, K/Rb and K/Al.

**Table 2.2**. Criteria for characterising data quality adapted from (USEPA, 2007). $r^2$ is the coefficient of determination. RSD is the relative standard deviation percent between the replicate mean of measured pXRF data and the CRM reference value. Inferential statistics is a test for slope and intercept of the straight-line regression. To qualify for the definitive (DL) data quality level, the inferential statistic slope and intercept coefficients must not be significantly different from unity and zero, respectively (at $\alpha = 0.05$).

| Data Quality Level | Statistical Criteria | | | Description |
|---|---|---|---|---|
| | $r^2$ | RSD (%) | Inferential statistics | |
| Definitive (DL) | $\geq 0.85$ | $\leq 10$ | $y = x$ | Statistically similar |
| Quantitative (Quant) | $= 0.70 – 1.00$ | $< 20$ | $y = mx \pm b$ or $y = mx$ | Statistically different |
| Qualitative (Qual) | $< 0.70$ | $> 20$ | $y \neq x$ | Statistically different |

Titanium (Ti) was used as an indicator of detrital siliciclastic flux. Ti/Al ratio was used to indicate the degree of homogeneity of the sedimentary source (e.g., Rodrigo-Gámiz et al., 2014, De Deckker et al., 2019, Parth et al., 2021). Lake redox conditions were evaluated using Fe/Mn. A reducing environment can be caused by many factors such as rapid sedimentation, water depth changes and stratification, increased biological productivity and associated de-oxygenation from microbial decomposition of organic matter, temperature, rainfall, and wind (Davies et al., 2015). On reduction, the solubility of Fe and Mn increase and both diffuse out of sediments, but reduction of Mn occurs before Fe leading to higher Fe/Mn ratios. Conversely, oxidation and precipitation of Fe occurs before Mn and is reflected in lower Fe/Mn ratios (Boyle, 2001).

Silica (Si) in lake sediments is either detrital or biological in origin (Peinerud, 2000). Normalising Si to Ti, Al, or Zr can serve as indicators of biogenic silica mainly produced by diatoms, which are commonly found in the LEB (Costelloe et al., 2005), with possible contributions from chrysophycean cysts (Lengyel et al., 2023), sponge spicules (Conley and Schelske, 1993, Peinerud et al., 2001) or phytoliths (Morgan-Edel et al., 2015). Diatoms were identified in sediment samples from the LMA, supporting the use of Si-based indices to infer biogenic silica contributions. However, Al can be present in clay minerals and Al-oxyhydroxides, potentially skewing Si/Al ratios to underestimate biologically produced Si. Considering Zr and Ti are only found in resistant detrital material, mostly zircon and rutile (respectively), the Si/Zr and Si/Ti ratios were used as preferred indicators of biogenic silica (BSi) and therefore as a proxy for primary productivity. The Al/Mg ratio is applied as a lake freshening proxy on the basis that high relative values of Al represent mainly detrital input of clays that formed from catchment weathering during wetter climate conditions. Conversely, low Al/Mg ratios suggest Mg-enrichment of authigenic lake clays or were alteration products that typically form during drier climates in shallow, alkaline, oxidising lakes (e.g., Deocampo et al., 2017, Stanistreet et al., 2020). Ratios including K/Rb and K/Al are based on selective removal of the more mobile and water-soluble K during chemical weathering. Rb and Al are hosted by feldspars, micas and clay minerals and are more resistant to weathering than K, with Rb more mobile than Al during chemical weathering (Harriss, 1965, Bayon et al., 2022).

*2.3.4.4 Carbon*

Total carbon (TC), total organic carbon (TOC), and bulk sediment organic carbon isotope ($\delta^{13}C_{ORG}$) abundances were determined for samples using a Costech Elemental Analyser Isotope Ratio Mass spectrometry (EA-IRMS) at the Advanced Analytical Centre, James Cook University. Sample preparation included sieving to 2 mm, lyophilisation, and then milling to <75 µm (Rocklabs BenchTop Ring Mill Pulverisor) before being thoroughly homogenised. TC values were determined from raw samples, while TOC% and $\delta^{13}C_{ORG}$ values were determined for acid-treated samples employing the "capsule method" after Brodie et al. (2011). This method of carbonate removal was chosen over acidifying followed by water rinsing to avoid loss of soluble salts or soluble organic carbon during separation of the spent acid. Briefly, samples were loaded in open silver (Ag) capsules held in a microtiter Teflon plate, moistened with 10 µL distilled water, and then treated with step additions of 6 M HCL at 10, 20, 30, 50 and 100 µL while being slowly dried on a hotplate at ~50°C for ~1h. The Ag capsules were crimped, loaded into a tin (Sn) capsule, crimped again, and the Ag+Sn capsules loaded into the element analyser carousel.

$\delta^{13}C_{ORG}$ values (‰) are reported respective to Vienna Pee Dee Belemnite (VPDB). The analytical performance of the instrumentation, drift correction and linearity performance were calculated from the repetitive analysis of internal standards with known isotopic composition ($\delta^{13}C_{VPDB}$ ‰: LOC = -26.54, Taipan = -11.63, HOC = -27.87). Precision of these standards was ±0.2 ‰ ($\delta^{13}C_{ORG}$ values), and ±0.2% for carbon abundance values. The percentage of $C_4$ vegetation was estimated from $\delta^{13}C_{ORG}$ as $C_4$ (%) = $[(\delta^{13}C_{ORG} - \delta^{13}C_{C3}) / (\delta^{13}C_{C4} - \delta^{13}C_{C3})]$ (Boutton, 1996), where $\delta^{13}C_{C3}$ and $\delta^{13}C_{C4}$ are the global isotopic averages for $C_3$ (-28‰) and $C_4$ (-14‰) vegetation, respectively (Smith and Epstein, 1971, O'Leary, 1988). Sediment $\delta^{13}C_{ORG}$ values were used to estimate the fraction of woody cover ($f_{wc}$) through the palaeo-shade proxy equation by Cerling et al. (2011): $f_{wc} = (\sin[-1.06688 - 0.08538(\delta^{13}C_{ORG})])^2$. Vegetation types are categorised based on $f_{wc}$: grassland ($f_{wc}$ < 0.10), wooded grassland (0.10 < $f_{wc}$ < 0.40), wooded/bushland/thicket/shrubland (0.40 < $f_{wc}$ < 0.80), and forest ($f_{wc}$ > 0.80) (Cerling et al., 2011).

Total inorganic carbon (TIC) was obtained by subtracting TOC from TC. The total organic carbon mass accumulation rate (TOC-MAR) was calculated as TOC-MAR (mg $cm^{-2}yr^{-1}$) = [BD (mg $cm^{-3}$) x SR (cm $yr^{-1}$)] x TOC (%), where BD is the sediment dry bulk density and SR is the sedimentation rate (based on Bacon age-depth models).

#### *2.3.4.5 Gypsum $\delta^{34}S$*

Authigenic gypsum crystals were extracted from cores LK and LM for sulfur isotope analysis to provide information on long-term environmental and climatic changes through the determination of sulfur sources, which could include marine aerosol sulfate input, bedrock weathering, or biologically reduced sulfides. Crystal selection criteria included 1) morphology (prismatic, lenticular or tabular), 2) crystal size (sieved to >355 µm), and 3) degree of preservation (original formation maintained). Crystals were cleaned using deionised water under a light microscope before air drying in paper bags for 1 week. Samples were milled to <75 µm (Rocklabs BenchTop Ring Mill Pulverisor) and homogenised. Gypsum sulfur isotope ($\delta^{34}S_{gyp}$) abundances were determined at the central science laboratory, University of Tasmania, using infrared laser assisted combustion VG Sira Series II mass spectrometry. The $\delta^{34}S_{gyp}$ values (‰) are reported as deviations from the Canyon Diablo Troilite (CDT) reference standard. International reference standards with known isotopic composition ($\delta^{34}S_{CDT}$ ‰: IAEA-S2 = 22.66, IAEA-S3 = -32.3, IAEA-S4 = 16.9, IAEA-SO5 = 0.48, IAEA-SO6 = -34.1, NBS-123 = 17.44, and NBS-127 = 20.32) were measured after every 6$^{th}$ sample. Precision of these standards was ±0.2 ‰ for $\delta^{34}S$ abundance values.

### 2.3.5 Spectral frequency analysis

Spectral analysis was applied to identify potential periodicities in climate signals within the three LMA cores. Palaeoenvironmental studies at astronomical or climate driven frequencies require a high-resolution proxy record with high continuity to capture cyclic climate variations through the sedimentary succession (Sinnesael et al., 2019). For this reason, this study focussed on the fine-scale and uninterrupted magnetic susceptibility time-series available in each core, which together span the last ~470 ka.

Magnetic susceptibility cycles are typically used to indicate fluctuations in siliciclastic mineral input in both marine (Ellwood et al., 2000, Reuning et al., 2006, Boulila et al., 2010) and lake (Minyuk and Subbotnikova, 2021) environments resulting from climate change. MS in the LMA primarily reflects catchment erosion and clastic transport and is used here as a proxy for increased precipitation in the Georgina catchment. Spectral frequency analysis ideally assumes a relatively continuous and climatically driven sedimentary record (Martinez et al., 2016), though natural variability, episodic deposition, and minor hiatuses are inherent to all sediment archives (Sinnesael et al., 2019). While variability in sedimentation rates and potential hiatuses can affect spectral interpretations, the use of high-resolution MS time-series helps mitigate these uncertainties by providing a consistent proxy for hydroclimatic variability. Sedimentological evidence was also examined to identify potential hiatuses or abrupt facies shifts, helping to contextualise spectral results and assess the reliability of detected periodicities. The Multitaper method (MTM), which includes an f-test (Fischer-Snedecor test) for the significance of the amplitude spectra using the Astrochron R-statistical package (Meyers, 2014; https://cran.r-project.org/package=astrochron), was applied on the continuous core MS time-series for each core. To account for higher sedimentation rates in the upper sections of each core, spectral frequencies were compared for two distinct sections: Lake Machattie, 2.70 – 0.50 m and 0.50 – 0.00 m; Lake Koolivoo, 3.50 – 1.50 m and 1.50 – 0.00 m; Eyre Creek, 2.40 – 1.50 m and 1.50 – 0.00 m. Periodicities were only considered that have high relative total spectral power, and if the confidence level (CL) of both the MTM *F-test* and red noise were >0.90%. To further account for potential discontinuities, a spectral cycle was only considered significant at an *F-test* CL of 95% or higher.

### 2.3.6 Statistical treatment

Correlations were calculated as Pearson correlations through a 2-tailed test of significance set at 0.05 alpha (t-distribution). These analyses for core EC were only performed on samples above the underlying calcrete (0.0 m to 2.4 m depth). Additional analyses between our data and published works were completed by wiggle matching and correlations using the QAnalyseries program (Paillard et al., 1996). Correlation coefficient values were interpreted as very strong (± 0.7 – 1), strong (± 0.5 – 0.7), moderate (± 0.3 – 0.5), weak (± 0 – 0.3), and none (≈ 0).

## 2.4 Results

Sedimentological results including facies descriptions are detailed in section 2.4.1 and thin section micrographs are displayed in Figures 2.2 and 2.3. Bayesian age-depth models of the sediment cores are shown in Figure 2.4. The results of the main physical and chemical properties measured in cores LM, LK and EC are detailed below and displayed in Figures 2.5, 2.6 and 2.7, respectively. These include grain size, TC, TOC, TIC, BD, TOC-MAR, MS, SR, $\delta^{13}C$, $\delta^{34}S_{gyp}$, Ti, Ti/Al, Al/Mg, Fe/Mn, Si/Ti, Si/Zr, K/Rb and K/Al content. Comparison of pXRF data and reference values of certified materials are shown in Figure 2.8. Results of the spectral analysis for each core is presented in Figure 2.9 and section 2.4.10.

### 2.4.1 Sedimentology

A suite of 17 units were identified in the LM and LK cores, with a further 10 in EC. Repeated sedimentological features, including clast morphology, grain size distribution, mineralogy, structure, and external and internal geometries (e.g., boundaries, bed gradations) were used to determine nine facies (Table 2.3). The facies are silty sands (Facies 1A), silty clays (Facies 1B), interbedded gypsum and silty sand (Facies 2A), nodular gypsum (Facies 2B), rooted fines (Facies 3A), sandy silt (Facies 3B), calcrete (Facies 3C), planar cross-bedded sands (Facies

4A) and finely laminated silty sands (Facies 4B). Facies identified in cores LM, LK and EC are displayed in Figures 2.5, 2.6 and 2.7, respectively. These facies are categorised into four primary facies associations, comprising lacustrine sediment (FA1), playa lake deposits (FA2), alluvial plain and palaeosols (FA3), and fluvial channel deposits (FA4).

#### *2.4.1.1 Facies Association 1 – Lacustrine*

##### 2.4.1.1.1 Facies 1A: Silty sand

Facies 1A comprises the uppermost lake sediments in both lakes (LK: 1.52 – 0.00m; LM: 0.47 – 0.00 m), and an additional 20-cm thick bed (1.84 – 1.68 m) in Lake Machattie. Lower and upper contacts (where present) are gradational to diffuse, excluding the lower contact in Lake Koolivoo, which is abrupt and represents an unconformity. Silty sand is typically massive, very poorly sorted, and composed of subangular to angular fine sand grains. The sand grains are matrix supported by coarse to fine silt, with a minor clay component. The coarse fraction is composed principally of quartz (monocrystalline >90%, polycrystalline <5%, microcrystalline <5%), with minor alkali feldspar and trace detrital Fe-Ti oxides, and clastic reworked lenticular-tabular gypsum. Deposits of this facies are light grey (2.5Y 7/1), grey (2.5Y 6/1), light brownish grey (2.5Y 6/2) or greyish brown (2.5Y 5/2). The sediment contains biogenic opaline silica (diatoms), gyrogonites, micrite, oncoids, peloids and shell fragments (Figure 2.2a–g), though not in great abundance. The fine-grained, non-laminated nature of these deposits and the scarcity of complete shells suggests shallow lacustrine to near-shore sedimentation.

##### 2.4.1.1.2 Facies 1B: Silty clays

Facies 1B deposits are between 0.50 and 1.35 m thick and are found exclusively in Lake Koolivoo (6.44 – 5.93 m; 5.39 – 4.04 m; 3.50 – 2.74 m). Lower contacts are abrupt, whereas the upper contacts are typically clear to gradational. Silty clay is massive, well-sorted and almost entirely composed of equal parts silt and clay that is interbedded with thin laminations of lenticular gypsum. Facies 1B deposits are light grey (2.5Y 7/1 and 5Y 7/2) or white to pale brown (2.5Y 8/1 – 8/2). They contain biogenic opaline silica (diatoms), peloids, shells and thalli (algae) fragments (Figure 2.2h–i). The well preserved (sub)horizontal laminations of settled gypsum interbedded with fine-grained sediment, and the presence of shells and diatoms indicates deposition under low-energy conditions below the wave base. The lack of laminations within the mud fraction suggests sedimentation was likely not in the deep limnetic zone, although certainly in deeper water than facies 1A.

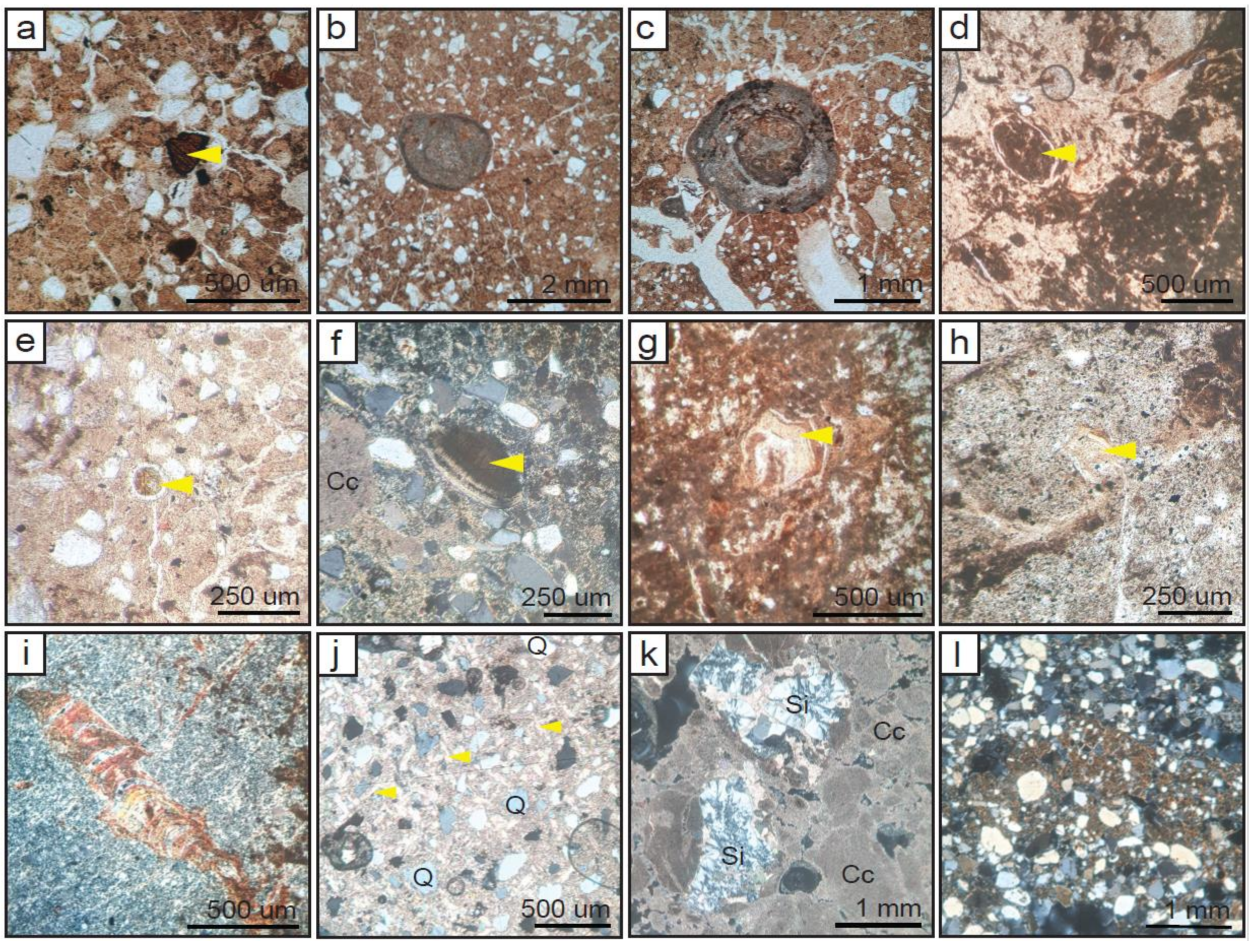

**Figure 2.2**. **Micrographs of calcitic, fluvial, and lacustrine sediments** (all images were taken under plane-polarised light, unless stated otherwise). **a)** Gyrogonite in silty sand (LK). **b-c)** Clotted cortex oncoids (LK and LM). **d)** Ostracod filled with micrite (LK). **e)** diatom (LK). **f)** Micromollusk and micrite (Cc) in silty sand in XPL (LM). **g–h)** Bivalve with inner lamellar calcite layers (LK). **i)** Algae thalli fragments in XPL (LK). **j)** Calcrete with coarse crystal laths (yellow arrow) in microspar groundmass with monocrystalline quartz grains in XPL (EC). **k)** Chalcedonic opaline silica in micritic calcrete in XPL (EC). **l)** Layers of clast-supported fine to medium sand and matrix-supported fine sand to coarse silt in XPL (EC).

*2.4.1.2 Facies Association 2 – Playa*

2.4.1.2.1 Facies 2A: Interbedded gypsum and silty sand

Facies 2A deposits are present in both Lakes Koolivoo (5.93 – 5.39 m; 2.74 – 1.52 m) and Machattie (1.68 – 0.98 m; 0.83 – 0.77 m) and are generally >0.50 m thick. Lower boundaries are clear to gradational, with upper boundaries abrupt to clear. Siliciclastic beds between 3 and 30 cm are composed of subrounded to subangular, very poorly sorted very fine sand grains in a clayey silt matrix, excluding a single bed at the base of Koolivoo that is almost entirely clayey silt. The coarse fraction is predominantly quartz (monocrystalline >80%, polycrystalline <2%, microcrystalline <2%) and reworked gypsum, with minor alkali feldspar (<10%) and plagioclase (<5%). Accessory detrital Fe-Ti oxides and opaque minerals (including pyrite) are also present. Gypsiferous beds that range from 8 to 64 cm in thickness interbed these siliciclastics. Two forms of gypsum are common within these beds: 1) large (>5 mm) tabular-prismatic anhydrite pseudomorph after gypsum crystals and 2) small (<1 mm) lenticular-tabular gypsum crystals (Figure 2.3a–b). Many of the anhydrite pseudomorph crystals are twinned and exhibit swallow-tail to complex terminations (Figure 2.3c–d), groundmass (clay) inclusions are also common. Gypsum is found as vertical (displacive) growths (Figure 2.3e) and as pore, root, and mud-crack infills (Figure 2.3f), whereas the anhydrite crystals are predominantly reworked and broken. Displacive gypsum has disrupted or destroyed any original depositional fabric or sedimentary structures. Deposits of this facies are light yellowish brown (2.5Y 6/4) or pale brown (2.5Y 7/3, 8/2 and 8/4) and contain pedogenic features including root traces and carbonate nodules. Root traces are often infilled with calcium carbonate or gypsum and have Fe-oxide (hematite) or Mn-oxide accumulations or rims. The matrix is also frequently stained reddish-brown with Fe-oxides, especially around root traces; however large areas are unaffected suggesting the accumulations are the product of alternating oxidising and reducing conditions.

Pyritised gypsum (Figure 2.3g) was also observed in a thin section from Lake Machattie (~1.50 m depth) confirming the presence of redoximorphic conditions (Shen et al., 2021) that was also microbially driven, such as by sulfur-reducing bacteria (e.g., Jaworska, 2012, Huang et al., 2022). Mottles are pervasive with areas of Fe-depletion exhibiting a light brown to white

(2.5Y 7/1 to 8/1) colour and Fe-accumulation a dark yellowish brown (10YR 3/6), which in some cases includes nodules of goethite. Alternations between gypsum and siliciclastic beds with mottled and oxidised fabric (Figure 2.3h), and abundant pedogenic features suggest deposition in a playa environment. Reworked and broken gypsum incorporated within the silty sands, (sub)vertical displacive gypsum growths and the predominantly brown colour of the sediment suggests a groundwater controlled proximal playa-margin that was mostly dry (e.g., Magee et al., 1995).

##### 2.4.1.2.2 Facies 2B: Nodular gypsum

Facies 2B deposits are found exclusively in the Lake Machattie core and are between 0.20 and 0.30 m thick (2.80 – 2.40 m; 2.13 – 1.84 m). Lower and upper boundaries are gradational. Deposits of this facies contain gypsum nodules (balls) that are between 2.5 and 5 cm in diameter within a silty sand matrix. More than 90% of the clastic grains are monocrystalline quartz, with only minor components of polycrystalline quartz (<5%) and alkaline feldspar and plagioclase (~5%). Gypsum (nodular and crystal) often constitutes more than 70% of the sediment; in these areas silt and clay surround the gypsum with sand grains rarely observed. Nodular accumulations are often surrounded by sub(vertical) displacive gypsum crystals that are tabular-lenticular and up to 2 cm in size; smaller (>7 mm) anhydrite pseudomorph after gypsum crystals with twinning are also present. Facies 2B deposits are pale yellow (5Y 8/3) to light yellowish brown (10YR 6/4). Mud cracks are common; however, pedogenic features such as roots, burrows, peds or pedogenic carbonates are absent. The co-occurrence of displacive gypsum crystals and nodular accumulations, mud-cracks, and silty sands that lack pedogenic development suggest shallow flooded playa conditions. Indeed, the nodular gypsum accumulations lack the features characteristic of a burial-diagenetic origin (Machel and Burton, 1991) and are considered playa nodules. The increase in gypsum crystal size and mud content relative to facies 2A, and the lack of pedogenic features indicates deposition was in the medial to distal (basin-ward) playa margin.

*2.4.1.3 Facies Association 3 – Alluvial plain and palaeosols*

2.4.1.3.1 Facies 3A – Rooted fines

Facies 3A is found in Eyre Creek (2.28 – 1.88 m; 0.88 m – 0.80 m; 0.55 – 0.39 m), and both Lakes Koolivoo (4.04 – 3.50 m) and Machattie (2.40 – 2.13 m; 0.98 – 0.83 m; 0.77 – 0.47 m) as deposits that are generally less than 0.50 m thick. Lower boundaries are mostly gradational, whereas upper boundaries are clear to abrupt. Rooted fines are developed on silty clays (Lake Koolivoo), or silty sand to slightly gravelly muddy sands (Eyre Creek and Lake Machattie) that are light yellowish brown (10YR 6/4), light brownish grey (2.5Y 6/2) or pale brown (2.5Y 8/3). The coarse grain fraction is dominated by monocrystalline quartz (>75%), with polycrystalline (~20%) and microcrystalline quartz (~5%) also observed. Accessory grains include alkali feldspar, rutile and large (~2–3 mm) lithic grains. The deposits are extensively bioturbated with root traces and burrows that have disturbed or destroyed any primary structures. Other pedogenic features include pedogenic carbonate nodules, slickensides, rare gypsum infill of mud cracks, and Fe-oxide nodules (Figure 2.3i), Fe-Mn dendritic nodules (Figure 2.3j), Mn-oxide traces along root channels and as rims (Figure 2.3k–l), and calcium carbonate infilled rhizoliths with Fe-oxide rims. Fe-oxide clay staining is also pervasive. Soil structure is mostly subangular blocky, with occasional angular blocky to wedge-shaped fabric also observed. Ped development ranges from (absent to) weak in Lake Koolivoo and at the base of Eyre Creek to strong in Lake Machattie and the upper units in Eyre Creek. Facies 3A, which is subdivided into two end members, represents palaeosols. One end member exhibits weak soil development with poor ped structure, and Fe-oxide nodule and Mn-oxide trace accumulations, and represent Protosols (Mack et al., 1993). The other end member are Calcisols that are characterised by Bk (subsurface carbonate) (Mack et al., 1993) and weak Bt (subsurface clay) horizons, with abundant calcium carbonate infilled rhizoliths with Fe-oxide rims, pedogenic carbonate nodules, sediment-infilled burrows and medium (~1.5 cm) to coarse (~2.5 cm) peds.

#### 2.4.1.3.2 Facies 3B – Sandy silt

Sandy silt forms a structureless ~0.55 m thick deposit in Eyre Creek (1.81 – 1.26 m) that normally grades from massive silty fine and medium sands to very fine sand and coarse silt. Facies 3B is grey (2.5Y 5/1) and comprises quartz (monocrystalline >80%, microcrystalline 10%, polycrystalline <5%), alkali feldspar (microcline <2%, orthoclase ~1%) and plagioclase (<2%). Trace medium to fine sand sized lithic grains are also present. Grains are subrounded and poorly sorted. This facies exhibits weak pedogenesis including rare root traces and small (<1 mm) carbonate nodules. Facies 3B is interpreted as an overbank deposit (Miall, 1977, Miall, 2013) that experienced ponding, subaerial exposure and weak soil development in poorly drained conditions.

#### 2.4.1.3.3 Facies 3C – Calcrete

Facies 3C is a thick massive bed of calcium carbonate that represents the basal 0.90 m of the Eyre Creek core (2.48+ m). The upper boundary shows a clear contact with the overlying fluvial channel fill. The calcrete is structureless and lacks any evidence of bioturbation or ped development. Alpha microfabrics are observed in thin section, including areas of coarse crystals within micrite or microspar (Figure 2.2j), crystalline groundmass and floating 'grains' that are solely silica (Alonso-Zarza and Wright, 2010). Chalcedonic or opaline silica (Figure 2.2k) appear to be late-stage void fills within the carbonate, similar to those reported by Arakel et al. (1989) in the Quaternary calcretes of Karinga Creek (Amadeus Basin, NT) and Lakes Way and Miranda (WA) palaeodrainages. The massive nature of the calcium carbonate, alpha-dominated microfabric and lack of pedogenic carbonate morphologies suggests Facies 3C is a groundwater (phreatic) calcrete that formed in a drainage channel (e.g., Alonso-Zarza and Wright, 2010).

#### *2.4.1.4 Facies Association 4 – Fluvial*

##### 2.4.1.4.1 Facies 4A – Planar cross-bedded sands

Facies 4A is found exclusively in the Eyre Creek core and represents more than 40% of the sediment (2.48 – 2.28 m; 1.88 – 1.81 m; 1.26 – 0.88 m; 0.39 – 0.00 m). Lower boundaries are clear, whereas the upper boundaries are abrupt to clear. Deposits of this facies are light grey (2.5Y 7/2), grey (2.5Y 5/1) or pale brown (2.5Y 7/3) and contain subrounded to subangular moderately to poorly sorted silty sand to slightly gravelly muddy sands. The coarse grain fraction is predominantly quartz (monocrystalline >80% polycrystalline >5%, microcrystalline <5%), with minor plagioclase (<5%), alkali feldspar (<2%), and accessory opaque minerals, rutile and reworked carbonate (calcrete?) and siliceous (silcrete?) clasts. Facies 4A exhibits normal grading, planar stratification and cross-bedding, with massive structure limited to two units (1.88 – 1.81 m and 1.26 – 0.88 m). Planar stratified units also exhibit an alternation of wavy layers of clast-supported coarser sediment (fine to medium sand) to matrix-supported fine sand (Figure 2.2l). Facies 4A units are interpreted as fluvial channel fill deposits based on the sedimentary characteristics (grain size, sorting, clast composition) and structures. Stratified deposits represent lower-flow regime deposition within the channel, whereas massive sands likely experienced rapid sedimentation under higher energy flood stage fluvial conditions (e.g., Miall, 1977).

##### 2.4.1.4.2 Facies 4B – Finely laminated silty sands

A single 0.25 m-thick deposit of Facies 4B is observed in the Eyre Creek core (0.80 – 0.55 m). The deposit exhibits a clear lower boundary above a palaeosol and a clear upper boundary that transitions into fluvial channel fill. Facies 4B is grey (2.5Y 5/1) and composed of subrounded to subangular poorly sorted silty sands. The coarse fraction is composed of predominantly quartz (monocrystalline >80% polycrystalline >5%, microcrystalline <5%), with minor alkali feldspar (<5%) and plagioclase (<5%), and lithics (<5%). The deposit alternates between massive to crudely laminated sands (lesser silt) and finely laminated silty sands. The silt is medium to coarse, whereas the sand is fine to very fine. Based on the horizontally laminated very fine to fine sand interlayered with medium to coarse silt, Facies 4B is interpreted to be the product of deposition in a splay (crevasse) environment. The repeated internal alternations in grain size (coarse to fine) are likely the results of flow velocity variations, with the finer grained sequences representing suspension fallout.

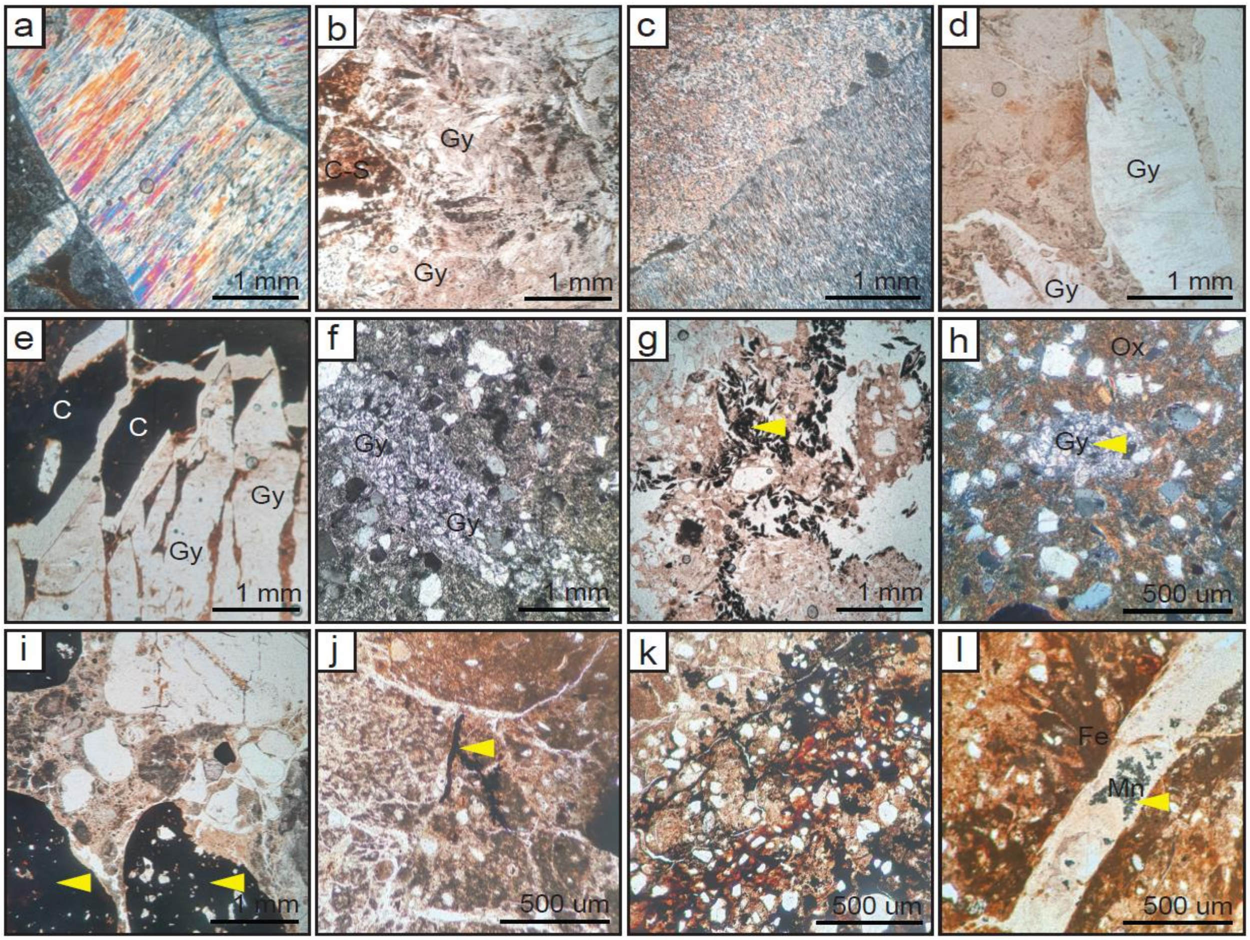


**Figure 2.3. Micrographs of gypsum, pedogenic features and playa sediments** (all images were taken under plane-polarised light, unless stated otherwise). **a)** Anhydrite pseudomorph after gypsum in XPL (LK). **b)** Lenticular-tabular gypsum in clayey silt (C-S) matrix (LK). **c)** Anhydrite after gypsum displaying twinning along the 101 axis in XPL (LM). **d)** Gypsum with complex terminations (LM). **e)** Vertically oriented displacive gypsum (Gy) in clay (C) (LK). **f)** Gypsum (Gy) infilling in XPL (LK). **g)** Pyritised gypsum (LM). **h)** Oxidised matrix (Ox) and gypsum (Gy) infilling in XPL (LK). **i)** Fe-accumulations (EC). **j)** Fe-Mn dendritic nodules (LK). **k)** Root trace with Fe-oxide core and Mn-oxide rim (EC). **l)** Root trace with Mn-dendrites (Mn) and Fe-oxide (Fe) rim (LK).

**Table 2.3.** Facies and facies associations in the Lake Koolivoo, Lake Machattie and Eyre Creek cores.

| Facies association | Facies code | Facies name | Texture | Structure and features | Colour | Interpretation |
|---|---|---|---|---|---|---|
| Lacustrine | 1A | Silty sand | Very poorly sorted, subangular to angular fine sand grains in a silt matrix, with minor clay | Massive, non-laminated; diatoms, gyrogonites, oncoids, peloids and shell fragments | Light grey to greyish brown (2.5Y 7/1, 6/1, 6/2 & 5/2) | Shallow lacustrine to near-shore sedimentation |
| | 1B | Silty clays | Well-sorted silty clay interbedded with thin lenticular gypsum laminations | Massive; horizontal laminations of gypsum; diatoms, peloids, shells and algae fragments | Light grey to pale brown (2.5Y 7/1, 8/1 & 8/2) | Low-energy conditions below wave base |
| Playa | 2A | Interbedded Gypsum & Silty Sand | Very poorly sorted very fine sand in a clayey silt matrix; alternating gypsiferous beds | Interbedding of massive siliciclastic silty sand and displacive lenticular-tabular gypsum; reworked anhydrite; root traces, carbonate nodules; Fe-oxide staining | Light yellowish brown to pale brown (2.5Y 6/4, 8/2 & 8/4) | Playa margin; periodic subaerial exposure |
| | 2B | Nodular gypsum | Silty sand with pebble-sized gypsum nodules (balls) | Mud cracks, displacive gypsum | Pale yellow to light yellowish brown (5Y 8/3 - 10YR 6/4) | Medial to distal playa margin |

| | | | | | | |
|---|---|---|---|---|---|---|
| Alluvial Plain & Palaeosols | 3A | Rooted fines | Silty clays (LK) or silty sands to slightly gravelly muddy sands (EC & LM) | Primary structures destroyed; sub-angular blocky to angular blocky peds; burrows, calcified root traces; carbonate nodules; Fe-oxide staining | Light yellowish brown (10YR 6/4), light brownish grey (2.5Y 6/2) or pale brown (2.5Y 8/3) | Palaeosols (Protosols & Calcisols) |
| | 3B | Sandy silt | Silty fine and medium sand to very fine sand and coarse silt | Massive; normally graded; rare root traces and carbonate nodules | Grey (2.5Y 5/1) | Overbank deposits |
| | 3C | Calcrete | Calcium carbonate | Structureless; alpha microfabrics, chalcedonic silica infill | White (2.5Y 9.5/1) | Phreatic calcrete formation in drainage channel |
| Fluvial | 4A | Planar Cross-Bedded Sands | Poorly sorted, subrounded to subangular silty sands to gravelly muddy sands | Planar stratification, cross-bedding, normal grading; reworked calcrete and silcrete | Light grey to pale brown (2.5Y 7/2, 5/1, 7/3) | Fluvial channel fill, unidirectional medium to high energy flow deposits |
| | 4B | Finely Laminated Silty Sands | Poorly sorted, subrounded to subangular silty sands | Alternations of massive to crudely laminated sandy beds and finely laminated silty sandy beds | Grey (2.5Y 5/1) | Splay (crevasse) deposits; suspension and sediment-gravity fallouts |

### 2.4.2 Geochronology

OSL and $^{14}C$ AMS ages obtained from the LMA range from ~501 to 0.44 ka and are respectively summarised in Table S2 and Table S3 (Appendix A2), with corresponding OSL radial plots displayed in Figure S3 (Appendix A1). All ages are in relative stratigraphic order, and Bayesian age-depth models are displayed in Figure 2.4. Sedimentological analysis identified an unconformity, marking an interval of non-deposition or erosion. This was incorporated into the Bayesian age-depth model, in addition to natural site-specific sedimentation variability, to refine chronostratigraphic interpretations.

Samples from the LM and EC cores show large scatter in $D_e$ or renormalised Ln/Tn distributions for K-feldspar, whereas most LK and EC samples show a major component in each of the $D_e$ distributions for Quartz, with some discrete outliers. Hence, OSL ages were estimated for most samples using the central age model (CAM; Galbraith et al., 1999) after identifying statistical outliers using the normalised median absolute deviation (nMAD) method (e.g., Clarkson et al., 2017, Jacobs et al., 2019). Quartz measurements using the SAR or Ln/Tn method were at dose saturation for deeper core samples (LMB155, LMC270, LKF530, LKG630, ECC270), but K-feldspar measurements using the Ln/Tn method obtained reliable $D_e$ values for samples LMB155, LMC270 and ECC270. No K-rich grains were obtained from the LK core, and no quartz grains were found in samples LKC230 or LKE400.

Ten samples record low to moderate overdispersion (OD) values consistent with adequate grain bleaching pre-burial, including all samples from the LM core (average OD = 24.8 ±8.1%) and most samples from the EC core (average OD = 26.5 ±6.3%, excluding sample ECB150 = 47%). These averaged overdispersion values are broadly comparable with the global average of 20 ±1% reported by Arnold and Roberts (2009) for well-bleached and unmixed single-grain $D_e$ datasets. Overdispersion is moderate to high in all core LK samples (average OD = 50.4 ±20.0%), excluding LKB140 that was low (21%), suggesting either partial bleaching of grains prior to burial or post-deposition mixing.

The finite mixture model (FMM; Roberts et al., 2000) was used for samples LMA50 and ECB150, which revealed discrete dose components. Sample LMA50 shows four discrete components with a large age range from 69.0 ±9.1 ka to 1.37 ±0.14 ka, of which the lowest two have approximately equal grain proportions (22%), indicating post-depositional sediment mixing possibly from bioturbation or wave action during high stands in Lake Machattie. This is supported by moderate OD (34%). Sample ECB150 displays two discrete components, although FMM-1 has the highest proportion of grains (84%) yielding 1.9 ±0.1 ka and was therefore used as the most reliable age estimation.

### 2.4.3 Magnetic susceptibility

Magnetic susceptibility (MS) values in core LM range between 0.81 and 3.25 SI. The lowest values are recorded around 1.16 m, coincident with the penultimate glacial maximum. Through MIS 5, MS values steadily increase to 2.95 SI and remain above 3.0 SI from ~70 ka to 12.8 ka before a decline around the mid-Holocene. Variations in MS coincide with stratigraphic changes in both cores LK and EC. From the base of core LK, MS values gradually increase from ~1.25 SI before reaching a peak of 2.57 SI around 5.25 m depth (which is cautiously placed around the start of MIS 5 based on extrapolation of the age-depth model). MS values progressively decline through MIS 5 and 4 and reach their lowest measured value of 0.63 SI around at 2.11 m (~53 ka). Low MS is recorded throughout early- to mid-MIS 3 (below the unconformity at ~1.5 m), whereas the highest MS values (>2.5 SI) are recorded in the Holocene sediments between ~8.0 ka to 2.0 ka (above the unconformity). Core EC MS values range from 2.22 to 4.39 SI, with the underlying calcrete recording much lower values (range = 0.25 – 0.87 SI).

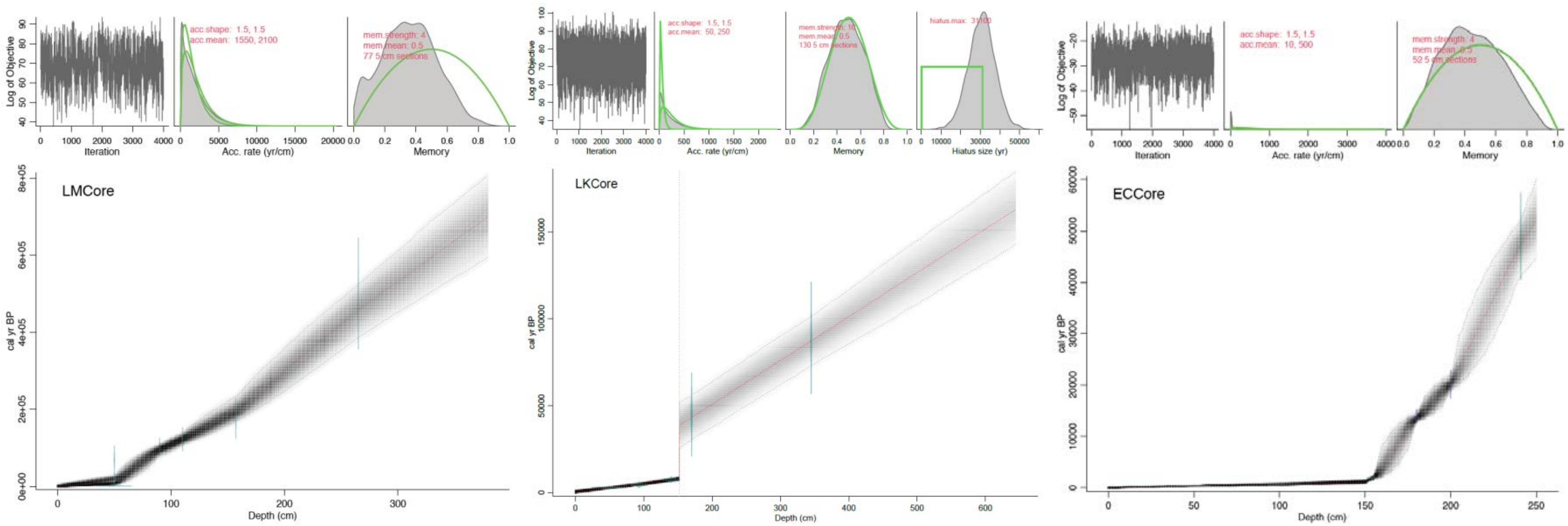


**Figure 2.4.** Bayesian age-depth models of sediment cores Lake Machattie (LM), Lake Koolivoo (LK) and Eyre Creek generated in R (version 4.3.3) (Bacon; Blaauw and Christen, 2011). The depositional 'hiatus' period of ~31,100 years added to the core LK age-depth model is based on liner interpolation from OSL age determinations above and below the unconformity observed at 1.52 m, allowing for ages and sediment accumulation rates not auto correlating across this unconformity.

### 2.4.4 Grain size

Core LM is comprised of 66.0 ±11.9% sand, with the highest sand content found at 0.3 m (~87%). There is little variation down core in the mean sand and silt (20.8 ±6.8%) fractions, but a strong negative correlation exists with mean clay content (1.89 ±1.1%; $r = -0.596$). Gravel increases with depth as a function of gypsum ($r = 0.737$), which is mainly found below ~0.9 m.

From the base of core LK to ~3.8 m depth, the dominant mean sizes are silt (52.3 ±5.5%, mainly fine to very fine silt) followed by clay (44.5 ±6.1%) and minor amounts of sand and gravel. Between ~3.0 m to 1.5 m, gypsum constitutes ~92.5% of the grains >500 µm. An unconformity at ~1.52 m is marked by a decrease in Munsell colour value of pale brown (2.5Y 8/4 to 7/4) and a sharp transition to coarser fractions of mainly sand (52.4 ±9.8%) that contain no observable gypsum, silt (40.4 ±8.2%) and some clay (7.11 ±1.6%). Throughout the core, gravels are almost exclusively gypsum crystals, and there is a strong positive (negative) correlation between depth and clay: $r = 0.860$ (sand: $r = -0.892$).

The base of core EC is mainly calcium carbonate accumulations (calcrete) that sit in the sand (36.9 ±17.8%), granule and pebble (together 38.2 ±21.1%) mean size fractions – boulders of calcrete were also observed at the equivalent core elevation within the nearby Eyre Creek channel. The transition from calcrete to mainly fluvial/alluvial sediments is between 2.5 m and 2.2 m, marked by a distinct colour change from very pale yellow (white page 2.5Y_/1) to pale brown (2.5Y 7/3), a decrease in mean granule size fractions (2.9 ±3.8%), and an increase in sand (71.4 ±6.0%) and silt (23.3 ±3.0%). Above 2.2 m, sand (71.3 ±7.2%) and silt (25.0 ±5.9%) remain the dominant mean size fractions along with some clay (3.41 ±1.5%), none of which show a strong correlation with depth. A small amount of gypsum (<15%) is found in the coarse sand fraction size between 2.0 m and 1.7 m.

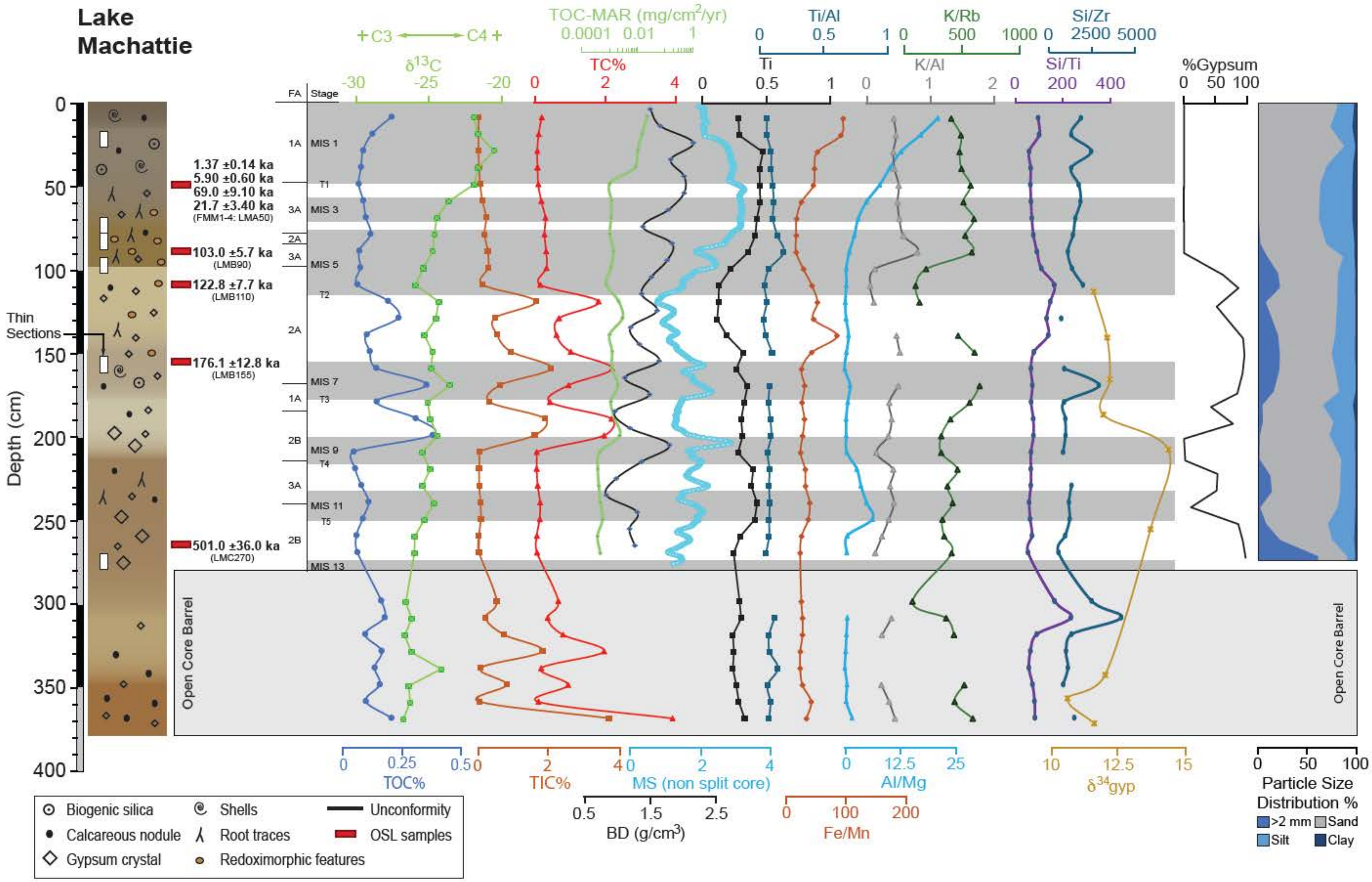

**Figure 2.5.** Lake Machattie physical and chemical properties. Facies (FA) described in section 2.4.1. Note, depiction of Marine Isotope Stages (horizontal grey bars) and glacial terminations (T #) is according to Bayesian age-depth modelling.

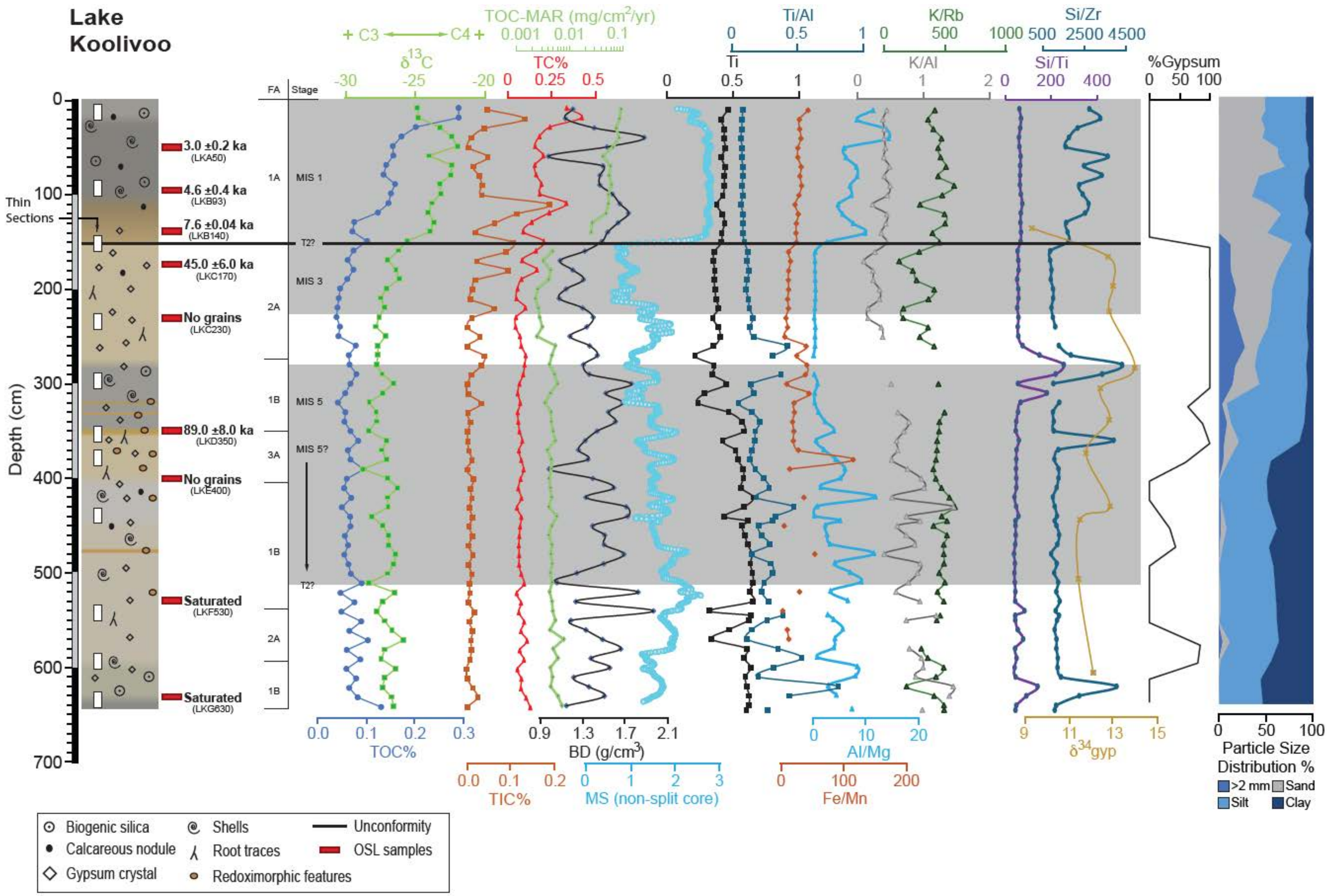


**Figure 2.6.** Lake Koolivoo physical and chemical properties. Facies (FA) described in section 2.4.1. Note, depiction of Marine Isotope Stages (horizontal grey bars) and glacial terminations (T #) is according to Bayesian age-depth modelling.

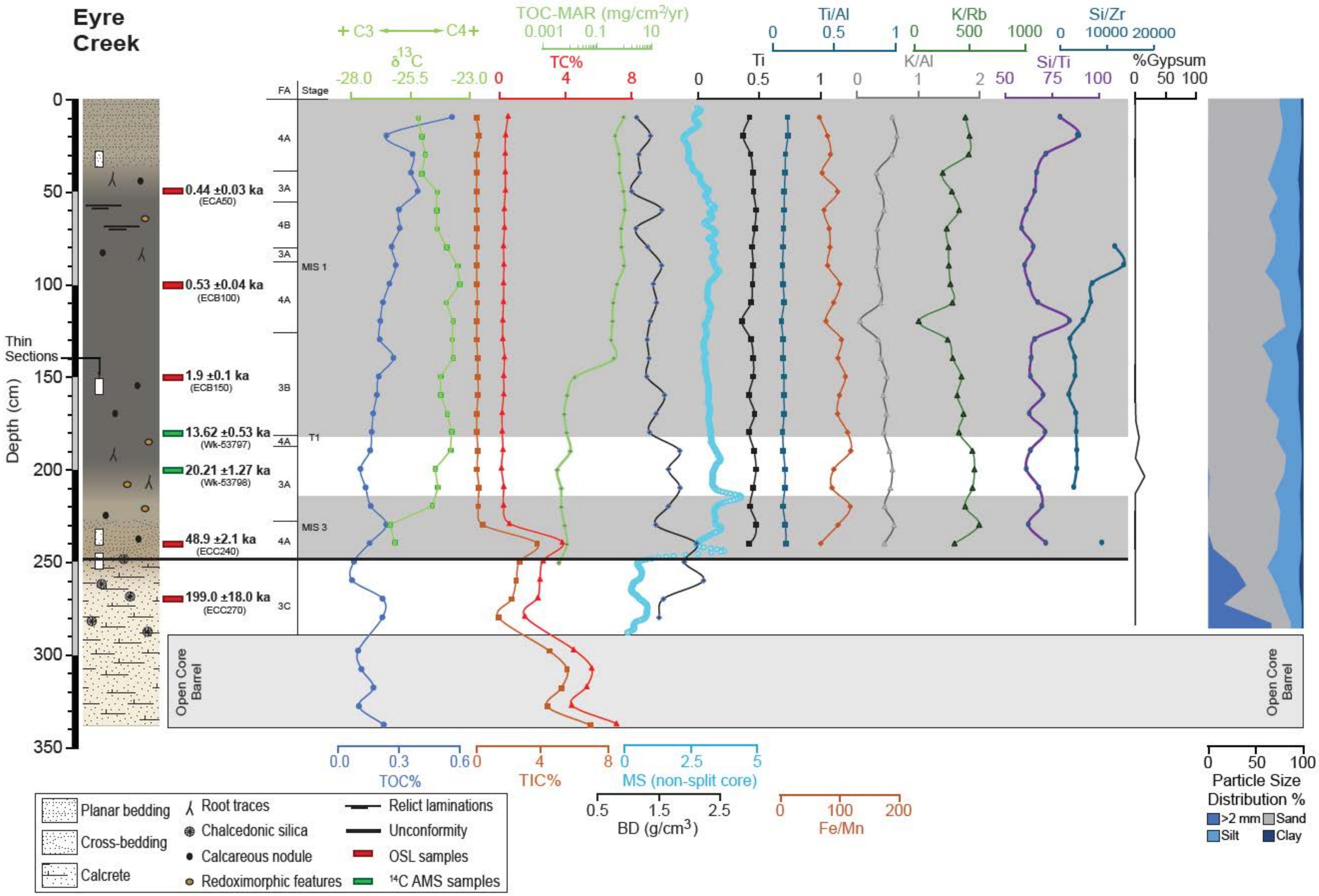


**Figure 2.7.** Eyre Creek physical and chemical properties. Facies (FA) described in section 2.4.1. Note, depiction of Marine Isotope Stages (horizontal grey bars) and glacial terminations (T #) is according to Bayesian age-depth modelling.

2.4.5 Major elements

The relationships between the pXRF measurements and CRM values are displayed in Figure 2.8. The RSD values and statistical outcomes of regression analysis to satisfy the criteria to categorise the data quality for each element are shown in Table 2.4. Ten elements returned $r^2$ values >0.7 and satisfied the y = x relationship model as the 95% confidence limits contained the target values of 1 and 0 for slope and intercept respectively. Four of these elements are categorised as definitive data quality (Al, Si, Mn and Rb) and five are considered quantitative data quality (Mg, Ti, Fe, Sr and Zn) due to some pXRF CRM analyses returning RSD values between 10 and 20%. Potassium (K) is classified as qualitative as one CRM analyses recorded <2% above the RSD criteria for quantitative data quality; however, priority was given for the high $r^2$ value (0.997) and that inferential statistics indicate the two datasets are statistically similar at the 5% level.

Low Ti values suggest there was minimal detrital siliciclastic input to Lake Machattie (Figure 2.5) from early MIS 6 to about the MIS 5d peak (~109 ka; Ti = 0.15 ±0.05 wt%), and to Lake Koolivoo (Figure 2.6) around the MIS 5a peak (~82 ka; Ti = 0.24 wt%) and in early MIS 4 (Ti = 0.22 wt%). In Lake Machattie, Ti increases abruptly around MIS 5d and maintains a high mean value of 0.40 ±0.08 wt% before a drop in mid MIS 1 to around 0.28 ±0.01. Lake Koolivoo records high, but steadily declining mean Ti values of 0.53 ±0.11 wt% in MIS 5, and lower Ti values and variability in early MIS 3 (0.37 ±0.02 wt%) and in MIS 1 (0.43 ±0.02 wt%). From MIS 3–1, Ti in core EC (Figure 2.7) shows similar values and low variability (0.44 ±0.03 wt%). Maximum Ti/Al values, steadily decrease from MIS 5 to 1 in both lakes, indicating an increase in sediment source homogeneity. High Ti/Al is observed in Lake Koolivoo from the start of MIS 4 through about mid-MIS 4 (2.9 – 2.5 m). In Eyre Creek, Ti/Al is almost constant throughout MIS 3 to MIS 1, with values between 0.07 and 0.12, which indicates relatively stable and homogenous sediment sources.

Groundwater can influence the salinity and geochemistry of lacustrine sediments, particularly in semi-arid and arid regions where evaporative concentration and fluctuating water tables drive ion migration (e.g., Bowen and Benison, 2009, Crosbie et al., 2012). The sediment cores indicate a groundwater-controlled playa lake environment at certain intervals, suggesting that groundwater fluctuations may have influenced salinity dynamics. However, no diagenetic alteration was observed. In this study, "freshening" refers to an increase in the Al/Mg ratio, indicative of greater detrital clay input relative to Mg-rich authigenic minerals. Higher Al/Mg values are interpreted as periods of enhanced surface water inflow and lower evaporative concentration, suggesting increased freshwater conditions in the LMA.

Freshening in Lake Machattie progressively increases through MIS 5 to MIS 1. In Lake Koolivoo, lake freshening also occurs in MIS 5, and Mg-enrichment, represented by lower Al/Mg values, intensifies around the MIS 5a peak (~82 ka) through to about mid-MIS 3 (~39 ka). The lowest value of 0.08 is recorded at the start of MIS 4. Although the LK core lacked sediment between ~39 ka and 8 ka, lake freshening conditions returned in MIS 1. Fe/Mn values in Lake Machattie decreased from about 42 to 16 during MIS 5 indicating a shift to greater oxidising conditions starting around MIS 5c that continued through MIS 4. Higher Fe/Mn values suggest reducing conditions started to return around mid-MIS 3 before reaching a peak of 94 in late MIS 1. A similar trend is observed in Lake Koolivoo, with Fe/Mn values indicating a higher potential for reducing conditions during MIS 5, oxidising conditions in MIS 4 and early MIS 3, and a progressive increase in reducing conditions during late-MIS 1. Based on extrapolation of the LK age-depth model, the two highest Fe/Mn values of 53.8 and 115.0 are estimated at around the peak of MIS 5e (~123 ka) and MIS 5c (~96 ka), respectively. Core EC records a relatively consistent range in Fe/Mn values between 13.1 and 23.6 from MIS 3 to 1.

Proxy biogenic silica production ratios record maximum values in MIS 5 with Si/Ti values of 165 and 255 in core LM and LK, respectively, and Si/Zr of 4336 in core LK. Consistently high mean Si/Zr values of 2411 ±637 are also recorded in core LK during MIS 1, and the lowest values of <1,000 are recorded during early MIS 3. Core LM shows little change in Si/Zr over the last glacial period, but an increase is seen in core EC around 0.5 ka.

The K/Rb and K/Al weathering ratios are well correlated in cores LM (r = 0.911), LK (r = 0.659), and EC (r = 0.960), which demonstrates the similar mobility of Rb and Al. Lake Machattie records minimal chemical weathering in early MIS 5 followed by a sharp increase around the MIS 5d peak (~108 ka). Weathering intensity generally declines after MIS 5c, with maximum K/Al and K/Rb values decreasing from 0.79 to 0.50 and 603 to 574 by mid-MIS 1, respectively. Based on tentative extrapolation of the LK age-depth model, estimated maximum values in Lake Koolivoo occur at 4.3 m depth (~108 ka) with a K/Rb ratio of 581 and a K/Al ratio of 1.46. The K/Rb record suggests less weathering in MIS 4 and 3 compared to MIS 5 and 1, with mean MIS 1 values (447 ±65) equivalent to that of MIS 5 (471 ±44). K/Al shows a similar decline in MIS 4 and in early MIS 3, but substantially lower mean values are recorded for MIS 1 (0.42 ±0.06) compared to MIS 5 (0.77 ±0.23). Core EC shows a generally consistent weathering regime from MIS 3 to 1, except for low values of K/Rb (40) and K/Al (0.05) recorded at 1.2 m depth (~0.87 ka).

### 2.4.6 TC, TOC and TIC

Organic carbon accounts for the highest proportion of total carbon content in core LM from ~2.7 m to 2.1 m (TOC% = 0.07 ±0.02; TIC% = 0.03 ±0.02) and from ~0.5 m to the surface (TOC% = 0.11 ±0.06; TIC% = 0.01 ±0.02), whereas TIC dominated between 2.0 m and 0.6 m (TOC% = 0.17 ±0.11; TIC% = 0.74 ±0.69). Comparatively, core LK and EC are dominantly organic carbon. Mean TOC% and TIC% in core LK are recorded at 0.09 ±0.05 and 0.02 ±0.04, respectively. In core EC, mean TOC% and TIC% are 0.25 ±0.10 and 0.21 ±0.74, respectively.

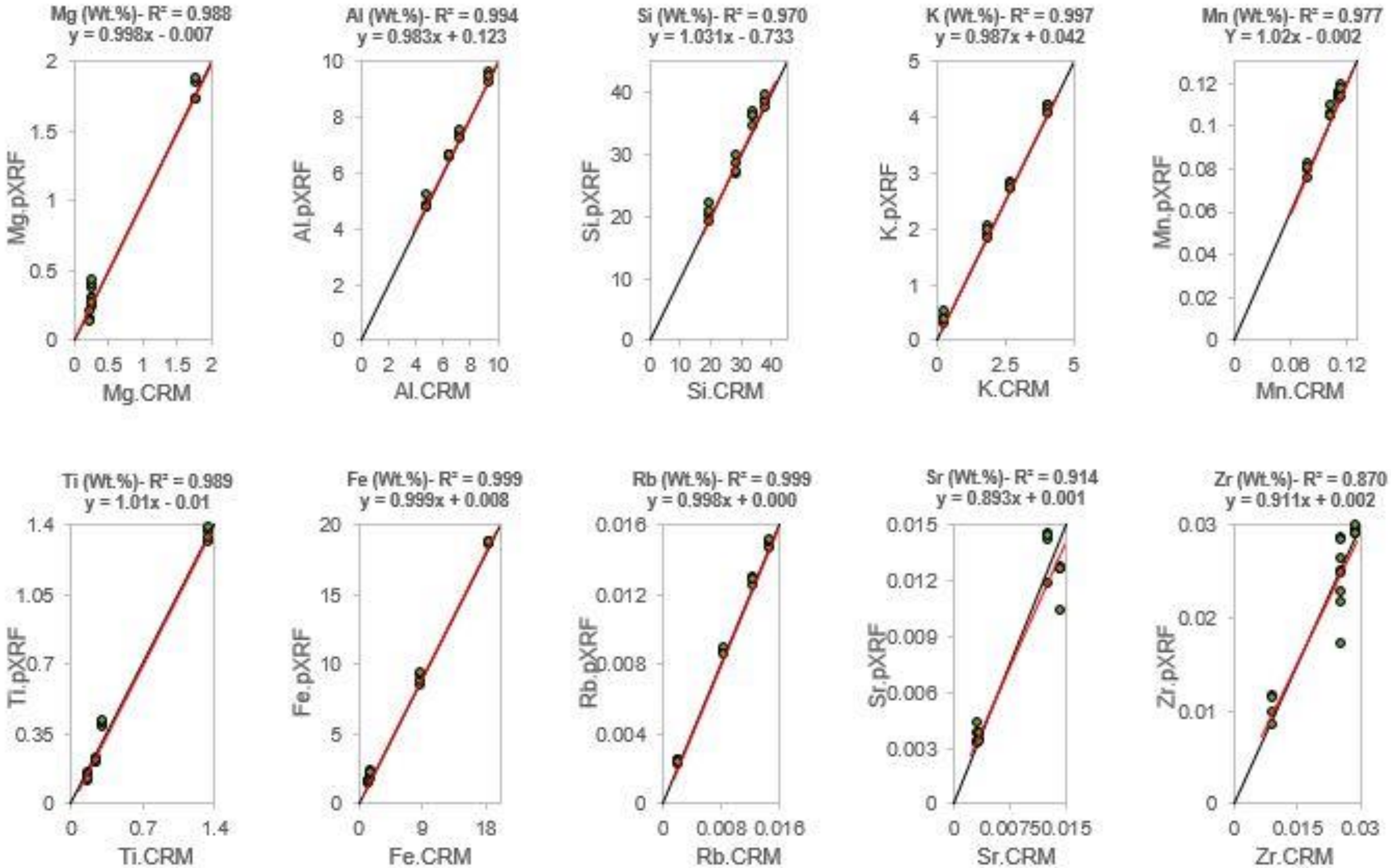


**Figure 2.8.** Comparison of pXRF data and reference values of 4 certified reference materials (CRMs) using a Bruker Tracer III-SD energy dispersive portable X-ray fluorescence. Solid line (black) bisecting each graph represents the 1:1 relationship. The red line represents the straight-line regression and depicts how well the pXRF data agrees with the CRM reference value. Units are in weight percent (Wt.%).

**Table 2.4**. Data quality results of pXRF measurements against CRM values (REF) displayed at 3 significant figures. CRM RSD values >20% are bold underlined and values between 10 and 20% are underlined.

| | Elements | Mg | Al | Si | K | Mn | Ti | Fe | Rb | Sr | Zr |
|---|---|---|---|---|---|---|---|---|---|---|---|
| | $r^2$ = | 0.988 | 0.994 | 0.970 | 0.997 | 0.977 | 0.989 | 0.999 | 0.999 | 0.914 | 0.870 |
| CRM | | Wt.% | | | | | | | | | |
| OREAS | Mean | 1.79 | 6.57 | 27.9 | 1.92 | 0.114 | 0.398 | 8.92 | 0.013 | 0.003 | 0.010 |
| 140 | REF | 1.80 | 6.56 | 28.7 | 1.92 | 0.114 | 0.328 | 9.00 | 0.013 | 0.003 | 0.009 |
| | RSD% | 3.78 | 0.398 | 4.11 | 4.32 | 1.46 | 2.06 | 3.72 | 1.18 | 18.6 | 12.1 |
| | %diff | -0.690 | 0.079 | -3.11 | 0.257 | -0.152 | 21.2 | -0.923 | 0.394 | 1.99 | 8.78 |
| OREAS | Mean | 0.278 | 7.33 | 20.4 | 0.390 | 0.116 | 1.35 | 18.6 | 0.002 | 0.004 | 0.029 |
| 045c | REF | 0.271 | 7.33 | 20.2 | 0.346 | 0.116 | 1.36 | 18.6 | 0.002 | 0.004 | 0.029 |
| | RSD% | 8.80 | 1.76 | 5.07 | **21.8** | 1.82 | 2.08 | 0.456 | 3.57 | 10.0 | 1.26 |
| | %diff | 2.53 | -0.033 | 1.12 | 12.7 | 0.108 | -0.831 | 0.104 | 1.09 | -0.412 | -0.255 |
| OREAS | Mean | 0.157 | 4.88 | 38.4 | 2.75 | 0.079 | 0.211 | 1.46 | 0.009 | 0.012 | 0.026 |
| 120 | REF | 0.247 | 4.84 | 38.3 | 2.75 | 0.080 | 0.256 | 1.59 | 0.009 | 0.013 | 0.026 |
| | RSD% | 18.2 | 3.37 | 1.87 | 1.83 | 3.10 | 3.09 | 4.64 | 1.82 | 16.4 | 8.92 |
| | %diff | -36.5 | 0.926 | 0.382 | 0.115 | -0.982 | -17.4 | -8.02 | 0.000 | -8.86 | 3.43 |
| sdAR | Mean | 0.360 | 9.41 | 35.7 | 4.14 | 0.106 | 0.130 | 2.03 | 0.015 | 0.013 | 0.022 |
| M2 | REF | 0.295 | 9.44 | 34.3 | 4.15 | 0.104 | 0.180 | 1.84 | 0.015 | 0.014 | 0.026 |
| | RSD% | 17.6 | 1.44 | 2.41 | 1.49 | 1.83 | 12.1 | 11.7 | 1.29 | 19.1 | 14.2 |
| | %diff | 21.8 | -0.370 | 4.02 | -0.201 | 1.71 | -27.6 | 10.2 | -0.168 | -10.1 | -14.6 |
| | | Inferential Statistics | | | | | | | | | |
| | Slope | 0.998 | 0.983 | 1.03 | 0.987 | 1.02 | 1.01 | 0.999 | 0.998 | 0.869 | 0.911 |
| | Slope 95% CI | (0.934, 1.06) | (0.940, 1.03) | (0.928, 1.14) | (0.957, 1.02) | (0.934, 1.11) | (0.947, 1.07) | (0.979, 1.02) | (0.980, 1.02) | (0.689, 1.05) | (0.709, 1.11) |
| | Intercept | -0.007 | 0.123 | -0.733 | 0.042 | -0.002 | -0.013 | 0.01 | 0.000 | 0.001 | 0.002 |
| | Intercept 95% CI | (-0.067, 0.053) | (-0.191, 0.437) | (-3.96, 2.49) | (-0.038, 0.122) | (-0.011, 0.007) | (-0.056, 0.031) | (-0.201, 0.217) | (-0.001, 0.001) | (-0.001, 0.002) | (-0.003, 0.006) |
| Data Quality | | Quant | DL | DL | Qual | DL | Quant | Quant | DL | Quant | Quant |

### 2.4.7 BD and TOC-MAR

Bulk density in all three cores range between 0.84 and 2.16 $g/cm^3$ (average = 1.45 $g/cm^3$). A significant relationship between bulk density and depth is observed in cores LM (r = -0.704) and EC (r = 0.735), although there were no obvious trends with gypsum content. TOC-MAR generally increases with depth in each core. Core EC records the highest average TOC-MAR (0.58 ±0.85 $mg.cm^2.yr^{-1}$), with the greatest values observed from ~1.0–0.6 m depth (2.15 ±0.15 $mg.cm^2.yr^{-1}$). Average TOC-MAR is much lower in cores LM (0.01 ±0.03 $mg.cm^2.yr^{-1}$) and LK (0.02 ±0.02 $mg.cm^2.yr^{-1}$), although core LK exhibits a ten-fold increase (from 0.006 ±0.001 to 0.05 ±0.02 $mg.cm^2.yr^{-1}$) above the unconformity at ~1.5 m.

### 2.4.8 Organic carbon $\delta^{13}C$

Stable carbon isotope values from all three cores exhibit a first order trend to increasing $\delta^{13}C$ values towards the surface, with values ranging between $\delta^{13}C$ -26.8 and -20.56 ‰ in LM, $\delta^{13}C$ -28.7 and -22.0 ‰ in LK, and $\delta^{13}C$ -26.4 and -23.4 ‰ in EC, indicative of a predominantly $C_3$ signature. The peak in the $C_4$ signature is recorded in core LM (53%), LK (43%) and EC (33%) at 0.3 m, 0.5 m and 1.0 m depths, respectively, but return to greater proportions of $C_3$ towards the surface. The $f_{wc}$ varies between forest ($f_{wc}$ > 0.80) and woodland/bushland/thicket/shrubland (0.40 < $f_{wc}$ < 0.80), with most estimates falling into the latter for core LM and EC. It is worth noting that the $f_{wc}$ recorded in core LM approached wooded grassland values around the mid-Holocene ($f_{wc}$ = 0.41). For core LK, the $f_{wc}$ coincides with the unconformity at 1.5 m depth, characterised as forest (below) and woodland/bushland/thicket/shrubland (above).

### 2.4.9 Gypsum $\delta^{34}S$

Gypsum $\delta^{34}S$ values from both Lakes, Machattie and Koolivoo, record a mean of $\delta^{34}S_{GYP}$ +12.2 ±1.12 ‰ (n = 21). One sample ($\delta^{34}S_{GYP}$ ~+9 ‰) from core LK falls outside the 2-σ uncertainty range, recovered at 1.35 m depth. Two samples from core LM ($\delta^{34}S_{GYP}$ +13.70 ‰ and +14.35 ‰) and one from core LK ($\delta^{34}S_{GYP}$ +13.95 ‰) fall outside the 1-σ uncertainty range, recovered at 2.55 m, 2.08 m, and 2.83 m, respectively.

### 2.4.10 Spectral frequencies

The spectral analysis using the Multitaper Method (MTM) revealed distinct frequencies in each core, identified at the 90% confidence level based on the MTM harmonic f-test and first-order autoregressive (AR1) red noise model (Figure 2.9). The high-resolution MS data from Lake Machattie between 2.7 and 0.5 m (~470 to 9 ka) exhibits frequency bands of 202.6, 40.5, 24.6, 13, 10.9, 9.8 and 8.4 kyr (average sedimentation rate = 0.0006 cm/yr), and between 0.5 and 0.0 m (~9 to 0 ka) cyclicity is in the 0.86 kyr band (average sedimentation rate = 0.0062 cm/yr). MS frequency bands recorded in Lake Koolivoo between 3.5 and 1.5 m (~88.5 to 39 ka) include 11.5, 3.6, 2.7, 1.9, 1.7, 1.5 and 1.3 kyr (average sedimentation rate = 0.0051 cm/yr), and between 1.5 and 0.0 m (~8 to 0 ka) include 0.45, 0.24 and 0.17 kyr (average sedimentation rate = 0.0256 cm/yr). No spectral peaks exceeding the >90% f-test CL were found in Eyre Creek between 2.4 and 1.5 m, but from 1.5 and 0.0 m (~2 to 0 ka), frequency bands at 0.07, 0.04 and 0.03 kyr were identified (average sedimentation rate = 0.17736 cm/yr).

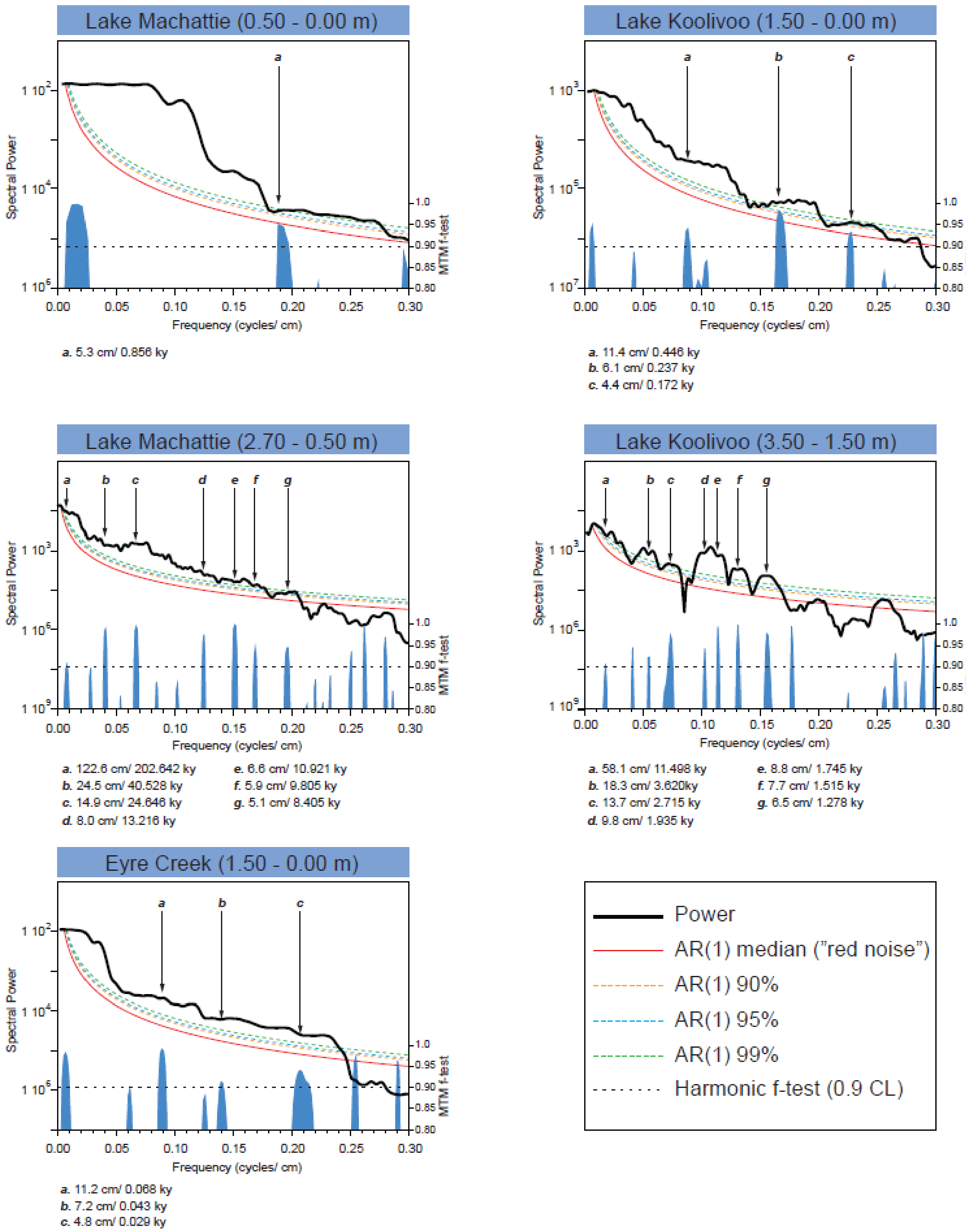


**Figure 2.9**. MTM spectrum of magnetic susceptibility in cores LM, LK and EC. The estimated red noise background and 90, 95 and 99% significance levels are shown as smooth coloured curves (solid red, dashed orange, blue, green, respectively). Blue peaks show MTM f-test significance (right y-axis), black dashed line is the >0.9 significance level. Letters denote spectra with both high amplitude and high f-test significance (>0.9) and are listed below each figure as

period (cm)/ periodicity (ky). MTM bandwidth parameters (cycles per cm) include LM: 2.7–0.5 m = 0.03, 0.5–0.0 m = 0.05; LK: 3.5–1.5 m = 0.02, 1.5–0.0 m = 0.05, EC: 1.5–0.0 m = 0.03. Note that two separate analyses were performed on each core based on different accumulation rates. No spectral peaks >90% CL were identified for Eyre Creek (2.4–1.5 m).

## 2.5 Discussion

The geochemistry, sedimentology and stratigraphy of the LMA cores reveal clear transitions between perennial lacustrine environments and ephemeral playa lakes, documenting significant environmental shifts from MIS 13 through the Holocene. Identification of depositional systems and palaeoenvironments enables reconstruction of the Georgina catchment's hydroclimatic history, showing its potential episodic contribution to major lake fillings in KT-LE, particularly during the pluvial phases of MIS 7 and 5. The spectral frequency analysis of palaeoclimate proxies identifies potential climate forcing mechanisms, including solar and orbital cycles, as well as influences from Northern Hemisphere cooling events and tropical Pacific phenomena such as ENSO, which together shaped the hydroclimatic evolution of central Australia.

### 2.5.1 Stable isotope geochemistry

#### *2.5.1.1 Organic matter $\delta^{13}C$ constrains northern LEB ecosystem change*

Sedimentary organic carbon $\delta^{13}C$ variations serve as lake productivity and palaeovegetation proxies reflecting changes in climate and ecosystems. In productive lakes, photoautotrophs preferentially incorporate $^{12}C$ during DIC ($CO_{2(aq)}$ and $HCO_3^-$) uptake (Leng and Marshall, 2004, Brenner et al., 2006, Leng and Melanie, 2006), leading to progressive $\delta^{13}C$ enrichment in the remaining DIC pool and sedimentary organic matter (Laws et al., 1995). Primary productivity is considered the dominant biogeochemical driver of $\delta^{13}C$ variations in organic matter within lake systems.

In anoxic conditions, biogenic methane is produced through the fermentation of organic carbon at the sediment–water interface. Methanotrophic bacteria, which oxidise this methane, produce biomass with very low $\delta^{13}C$ values, due to their consumption of $^{13}C$-depleted biogenic methane ($\delta^{13}C$ of -50 to -70‰; Whiticar, 1999) and fractionation during biosynthesis (-16‰ to -30‰; Summons et al., 1994). This process can lead to the formation of particulate organic matter with $\delta^{13}C$ values as low as -60‰, as observed in some lakes (e.g., Bernasconi and Hanselmann, 1995, Behrens et al., 2000, Lehmann et al., 2004, Teranes and Bernasconi, 2005).

In general, microbial biomass generation in anoxic waters can be indicated where a substantial decrease in the $^{13}C/^{12}C$ ratio is accompanied by an increase in Fe/Mn and the presence of redoximorphic features, e.g., pyrite. Where $\delta^{13}C$ values increase and there is an associated increase in organic matter accumulation and additional evidence of lake productivity (e.g., diatoms, algae fragments, increased Si/Zr values), water column primary productivity is considered the primary driver of the isotopic signal, rather than solely a shift in the $C_3/C_4$ ratio of the catchment's terrestrial vegetation.

The $C_3$ and $C_4$ photosynthetic pathways of carbon fixation yield global average $\delta^{13}C$ values of -28‰ and -14‰, respectively (Smith and Epstein, 1971, O'Leary, 1988). Australian trees, shrubs and forbs are mostly $C_3$ plants, and the photosynthetic pathway of native grasses is primarily determined by seasonal effective rainfall. Winter precipitation patterns derived from southern Australia favour the proliferation of $C_3$ grasses, whereas $C_4$ grasses become increasingly numerous in areas more affected by summer monsoonal rainfall (Hattersley, 1983, Murphy and Bowman, 2007). Indeed, the relative abundance of $C_4$ grasses, compared to $C_3$ grasses, was estimated from modern $\delta^{13}C$ values in Kangaroo bone collagen and is highest in the northern half of Australia including all of the Georgina catchment (Figure 2.10) (Murphy and Bowman, 2007).

For the LMA, Lake Machattie consistently shows higher $\delta^{13}C_{ORG}$ values compared to both Lake Koolivoo and Eyre Creek. For example, the Holocene interval in Lake Machattie is on average ~2.0 ‰ and 2.7 ‰ more enriched in $\delta^{13}C_{ORG}$ than those in Lake Koolivoo and Eyre Creek, respectively. Considering that floodwaters generated in the north can inundate the entire LMA delivering a broader catchment organic carbon $\delta^{13}C$ signature, the enriched $\delta^{13}C$ values recorded in core LM suggests that the local vegetation assemblages contributing to Lake Machattie's organic material differ from those at Lake Koolivoo and Eyre Creek. Under the current climate regime ~<60% woody vegetation cover is found around Lake Koolivoo, Lake Mipia and the surrounding flood plains, with up to 80% woody cover bordering waterholes and the (semi-)permanent ingress Eyre Creek channels (Figure 2.10d). Comparatively, there is little to no permanent woody cover surrounding Lake Machattie. This is likely because Lake Machattie quickly becomes a closed system after major flooding, drying within one or two years, providing little in the way of permanent water to support the vegetation. Whereas Lakes Koolivoo and Mipia remain wet for ~80% of the time based on nearly 40 years of satellite data (Figure 2.10c). While the enriched $\delta^{13}C$ values in core LM could have been caused by greater density of $C_4$ grasses, forbs or herbs, today there appears to be no major difference in the proportion of these ground covers across the LMA (Figure 2.10e).

Overall, the difference in $\delta^{13}C$ values between Lake Machattie and the other coring sites probably reflects a local signature of lower total woody vegetation at Lake Machattie over the ancient past - an environment not that dissimilar to today. Variations in $\delta^{13}C$ are further discussed in the context of lake primary productivity and palaeoenvironment interpretations from MIS 13 through to MIS 1 in section 2.5.2.

#### *2.5.1.2 Gypsum $\delta^{34}S$ as an indicator of sulfur sources*

The range in $\delta^{34}S$ values obtained from authigenic gypsum in both lakes, Machattie and Koolivoo (21 sample mean of $\delta^{34}S_{GYP}$ +12.2 ±1.12 ‰), indicate several possible sulfur sources. Weathering of igneous or metamorphic bedrock may be a significant sulfur source. $\delta^{34}S$ values of exposed granites and shales throughout the Georgina catchment are unknown, but the total sulfur in granites (e.g., Sybella Suite) should be far lower than in shales. The only known $\delta^{34}S$ values for shale-hosted sulfides, from Urquhart Shale near Mt Isa Mine (Figure 2.1a) ($\delta^{34}S$ -3.3 to +26.3 ‰; Painter et al., 1999), lie just outside the northeastern edge of the catchment. However, basement rocks from eastern sections of Mt Isa mine mineralisation zones, well within the Georgina catchment, have $\delta^{34}S$ values ranging from -8 to +9 ‰, with a likely mean near ~0 ‰ (Davidson and Dixon, 1992). Although this potential sulfur source lies more than 400 km from the LMA, suggesting it likely had little to no effect on the $\delta^{34}S_{GYP}$ values. Indeed, the primary sources of sulfur found in Australian inland lakes are largely of marine origin including sea-salt ($\delta^{34}S$ +21 ‰; Rees et al., 1978), and biogenic sulfur compounds, as the volatile metabolites from marine autotrophs: dimethylsulfide (DMS) and its precursor, dimethylsulfoniopropiohate (DMSP) ($\delta^{34}S$ +18.9 to +20.3 ‰; Amrani et al., 2013), and minor amounts of $H_2S$ (as low as $\delta^{34}S$ -40 ‰; Chivas et al., 1991). The relative combination of DMS, DMSP and $H_2S$ in marine aerosols yields mean $\delta^{34}S$ values closer to $\delta^{34}S \sim 0$ ‰ (Wakshal and Nielsen, 1982), making it difficult to distinguish between the non-sea-salt marine components and igneous or metamorphic rock-weathering within the Georgina catchment (mean $\delta^{34}S$ ~0 ‰; Davidson and Dixon, 1992).

All marine aerosols follow the prevailing southerly winds and are deposited inland via rainfall. Sea-salt sulfides decrease by ~55% 1,000 km inland, while biogenic sulfur compounds, though a relatively minor component, can travel further inland due to their abundance in higher level air masses. As such, $\delta^{34}S_{GYP}$ values decrease regionally from the south Australian coast, averaging ~+14.6 ‰ between 29°S (KT-LE north and Yaningurie waterhole) and 27°S (Oodnadatta) (Figure 2.1a) (Chivas et al., 1991). At a similar latitude, groundwater dissolved sulfate-$\delta^{34}S$ values range from +8.2 to +12.2 ‰ at Cooper Creek waterholes (Chookoo and Naccowlah; Figure 2.1a) (Cendón et al., 2010), which is equivalent to a hypothetical gypsum precipitation $\delta^{34}S$ value of +9.85 to +13.85 ‰ (including a brine-gypsum $\delta^{34}S$ fractionation factor of +1.65 ‰; Thode and Monster, 1965). This confirms increasing rainout of atmospheric sulfate with increasing distance from the southern coastline. Given lakes Machattie and Koolivoo are located farther north, at ~25°S, marine aerosol sulfates would continue to decline, and it may be anticipated that $\delta^{34}S$ values would fall closer to our recorded mean of $\delta^{34}S_{GYP}$ +12.2 ‰.

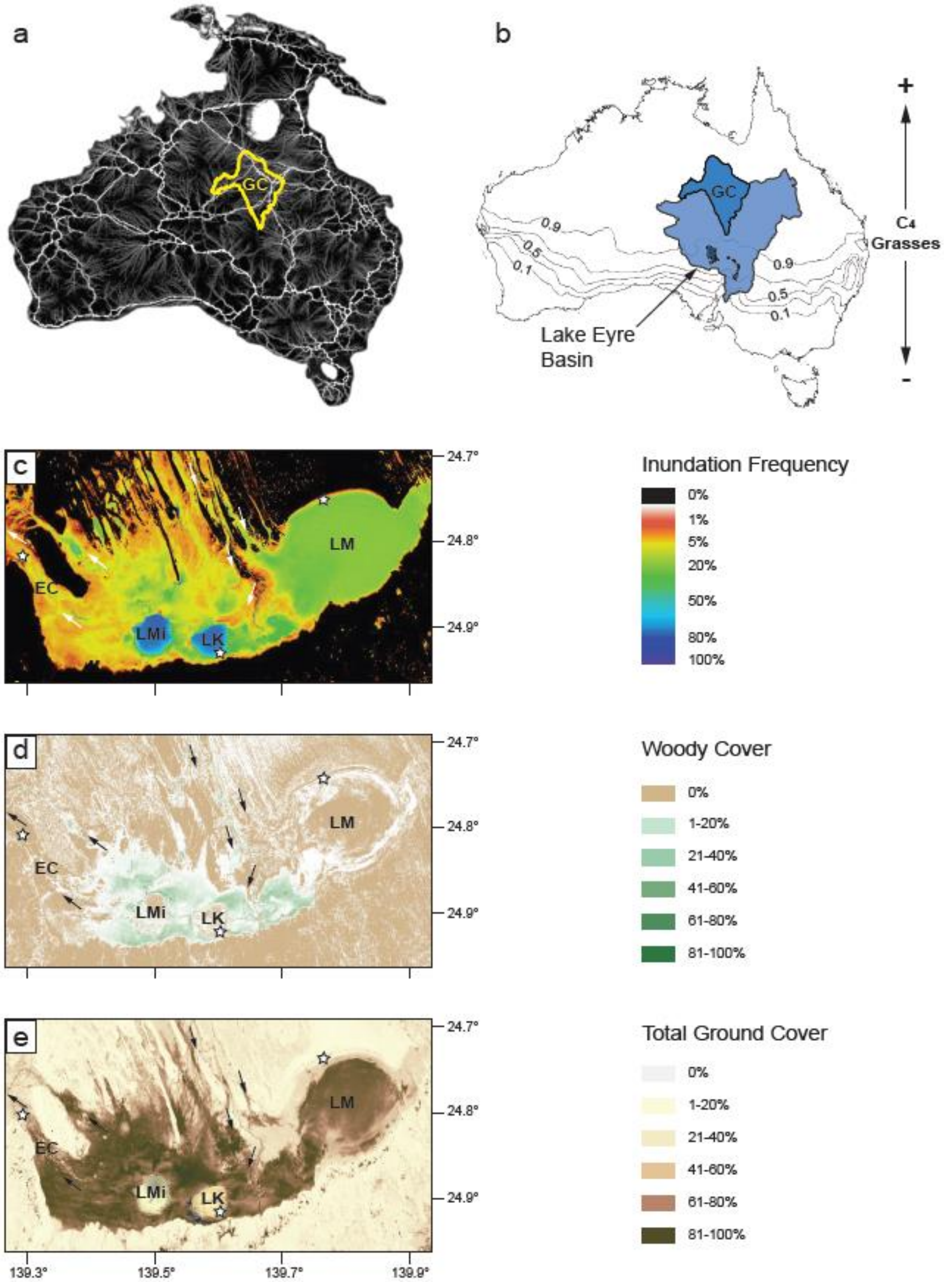


**Figure 2.10. a)** Sahul-Australian continent. Thick white lines are modelled main migration pathways during peopling of Sahul (Crabtree et al., 2021). Note the major pathways through the Georgina catchment (yellow polygon) indicating a possible inland route following the Georgina River. **b)** Relative abundance of $C_4$ grasses vs. $C_3$ grasses, showing $C_4$ grasses dominating the Georgina catchment and northern LEB (determined from $\delta^{13}C$ values in Kangaroo bone collagen; Murphy and Bowman, 2007). **c)** Inundation frequency map generated from the proportion of Landsat observations between 1986 and 2024 showing the presence of water in a particular area (GeoAust, 2024b). **d)** Woody cover (persistent over-story vegetation as trees and

shrubs) and, **e)** total ground cover (grasses, forbs and herbs – excludes over-story and mid-storey vegetation). These vegetation maps are a seasonal composite of Landsat images (spring 2011 was used as an example of vegetation prior to summer monsoon input) (Beutel et al., 2019). Abbreviations and map symbols: LM (Lake Machattie), LK (Lake Koolivoo), LMi (Lake Mipia), EC (Eyre Creek), GC (Georgina Catchment), star shapes (coring locations), white or black arrows (general flow pathways).

##### 2.5.1.2.1 Palaeoenvironmental implications and the lacustrine record

Relatively lower or higher gypsum $\delta^{34}S$ values in Lakes Machattie and Koolivoo in the past may indicate a change in wind strength or direction, or differing contributions from catchment sources. The most depleted $\delta^{34}S$ gypsum sample (+9.30 ‰) fell outside the 2-σ uncertainty range and was collected from young (Holocene) sediments in Lake Koolivoo. Post-LGM reorientation of linear dunes in the northwest Simpson Desert (Hollands et al., 2006) indicates a southward shift in the prevailing wind regime. However, there is no evidence of Holocene weakened wind speeds that might explain a reduced flux of enriched $\delta^{34}S$ salt spray to central Australia. The relatively depleted $\delta^{34}S_{GYP}$ could reflect early–middle Holocene IASM intensification (e.g., Nott and Price, 1994, Griffiths et al., 2009, Griffiths et al., 2013) and more southerly penetration of monsoon rainfall (Singh and Luly, 1991, Quigley et al., 2010), causing mobilisation of $\delta^{34}S$-depleted sulfates from weathered basalts and shales and/or the dissolution of evaporites in northern regions of the Georgina catchment.

Another possibility is the production of $H_2S$ by sulfate-reducing bacteria oxidising organic matter under anoxic lake sediment conditions; however, the Lake Koolivoo $\delta^{34}S_{GYP}$ +9.3 0‰ value is far from those of sulfate-reduction bacteria producing $H_2S$ with $\delta^{34}S$ values as low as -40 ‰. Biogenic $\delta^{34}S_{H2S}$ eventually forms pyrite following reaction with ferrous iron (Pasquier et al., 2017). Pyrite was not found in thin section in these Holocene sediments, indicating $H_2S$ was probably not fixed as sedimentary iron sulfide (pyrite) and that Lake Koolivoo has remained a relatively open system for $H_2S$, which could re-enter the water column and be re-oxidised. This is supported by variable Al/Mg values in Lake Koolivoo (Figure 2.6), indicative of frequent wetting and drying throughout the Holocene.

Positive shifts in $\delta^{34}S_{GYP}$ values (outside the 1-σ uncertainty range) are recorded in Lake Machattie at 436 ka ($\delta^{34}S_{GYP}$ +13.70 ‰) and 320 ka ($\delta^{34}S_{GYP}$ +14.35 ‰), and in Lake Koolivoo at 71 ka ($\delta^{34}S_{GYP}$ +13.95 ‰), that respectively coincide with glacial maximum 5, termination 4 (T4), and the start of MIS 4. While the $\delta^{34}S_{GYP}$ +14.35 ‰ value is tentatively placed around T4, we propose this is more likely associated with the glacial maximum 4 around ~345 ka (e.g., Raymo, 1997, Cheng et al., 2016) because of uncertainties in our age depth model, with rapid increases in other proxies (TOC, $\delta^{13}C_{ORG}$, MS and K/Al) at ~2.1 m depth indicative of T4 proper (Figure 2.5) supporting this assertion. MIS 4 represents a significant glacial period in Australia that, according to De Deckker et al. (2019), was comparable to the LGM.

The synchronicity of enriched $\delta^{34}S_{GYP}$ samples with these past glacial stages suggest input of $\delta^{34}S$-enriched marine sulfate aerosols to inland Australia was possibly caused by stronger southerly winds as a consequence of intensification and northward expansion of the mid-latitude westerlies (e.g., Falster et al., 2018, Fitzsimmons and Gromov, 2022). Indeed, the impact of stronger winds and aridity on the landscape, during glacial periods, is documented well by dates on aeolian dust flux from Australia in the Indian Ocean (Stuut et al., 2014) and Tasman Sea (Hesse, 1994). While variations in $\delta^{34}S$ values suggest multiple possible sulfur sources, the potential overlapping isotopic signatures of marine aerosols, weathered catchment material, and microbial processes make it difficult to isolate a definitive driver. Given these uncertainties, the current dataset does not allow for a fixed or unambiguous interpretation of sulfur cycling in the LMA, though it highlights the complexity of sulfate inputs and their potential climatic and hydrological controls. We acknowledge the low sampling resolution of our $\delta^{34}S_{GYP}$ record and note that, given the limitations of our age-depth model, $\delta^{34}S$-enriched values are not recorded during all glacial stages. However, based on our initial findings, we suggest lacustrine $\delta^{34}S_{GYP}$ may provide a useful continental record of northward shifting southern westerlies during glacial stages that warrants future investigation.

### 2.5.2 Late Quaternary palaeoenvironmental history for the Georgina catchment based on the LMA core records.

#### *2.5.2.1 MIS 13 – 8 (~524 – 243 ka)*

Sediments in the base of the Lake Machattie core represent the onset of groundwater-controlled playa lake conditions at ~490.4 ka, prior to the beginning of MIS 12 and glacial termination 5 (424 ka) (Figure 2.11). Deposition of nodular gypsum and silty sands during this time suggests fluctuating saturation states in the medial to distal playa-margin, with drier conditions resulting in gypsum precipitation. Higher Al/Mg, K/Al and Ti values suggest wetter conditions with some surface water inputs from ~421 ka until the start of MIS 11. $\delta^{13}C_{ORG}$ values indicate an environment with more than 80% woody cover was established around the playa until ~396 ka.

The playa lake eventually dried and became subaerially exposed, undergoing pedogenesis through MIS 11 and 10 (between ~396 and 330 ka), before a return to playa lake conditions. Soil development was dominated by the shrinking and swelling of clays with wetting and drying, and cracking around roots and burrows. The development of a Calcisol suggests arid to semi-arid conditions, with pedogenic carbonates typical of environments with rainfall less than 600 mm/yr (Mack et al., 1993). Indeed, $\delta^{13}C_{ORG}$ values show a shift to a more $C_3/C_4$ mixed vegetation environment with a woodland/bushland/shrubland present until ~323 ka, before an increase in woody cover. A return to sediment aggradation and gypsum precipitation in a medial to distal playa-margin at around 330 ka also suggests an increase in water availability not long after glacial termination 4 and the start of MIS 9 (337 ka). A gradual decline in Al/Mg, K/Al and Ti, and increase in TIC% and $C_4$ vegetation suggests the playa was mostly dry from ~298 ka. Although, a playa lake environment remained in Lake Machattie until ~260 ka when shallow lacustrine conditions become established, immediately prior to glacial termination 3 and the start of MIS 7 at 243 ka. It is worth noting that the monsoon-fed Gregory Lake System in Western Australia also recorded an increase in water availability in MIS 9–8, with an ancient foreshore dune documenting a mega-lake phase sometime between ~358 and 250 ka (Bowler et al., 2001).

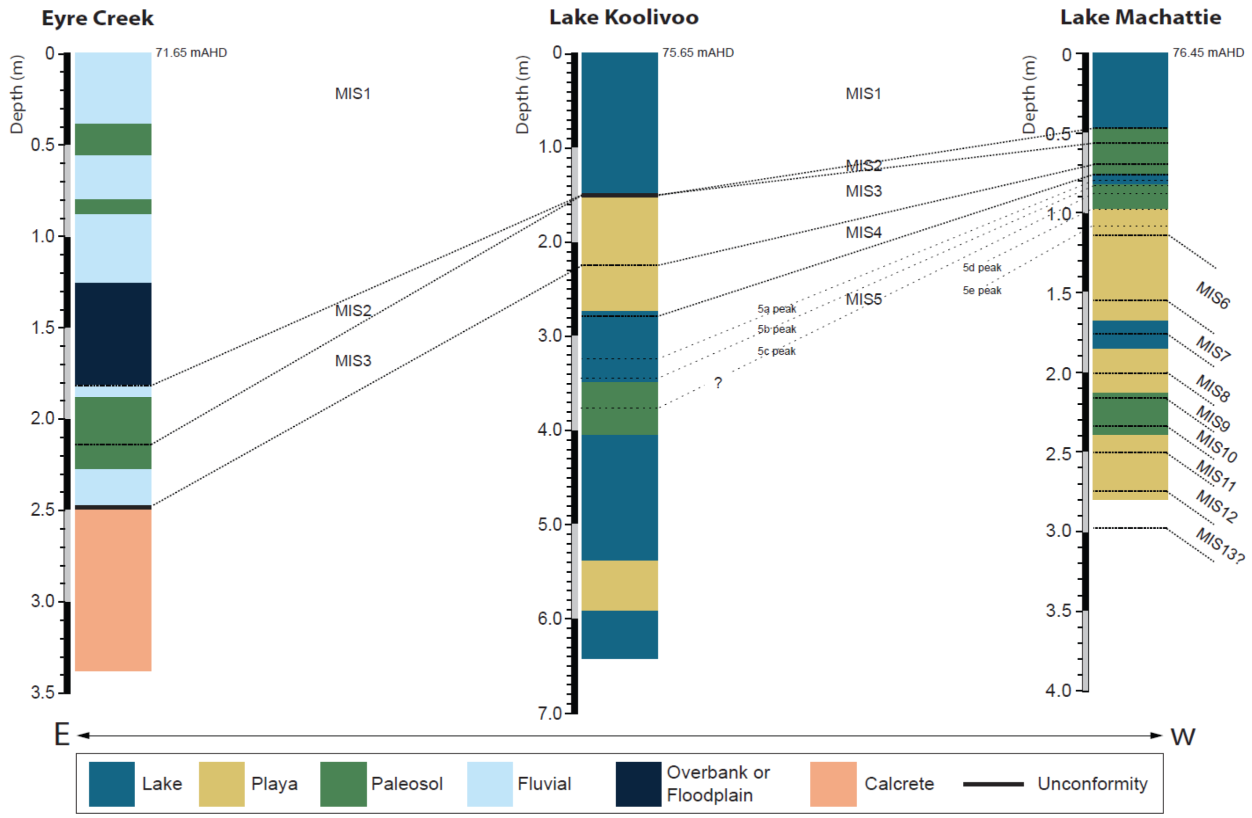


**Figure 2.11**. Depositional environment and processes of the Lake Machattie Area cores. Correlation of the LM, LK and EC cores relies on the Bayesian age-depth modelling. Marine Isotope Stages (including peak MIS 5 substages a–e) are provided for chronostratigraphic context.

#### *2.5.2.2 MIS 7 (243 – 191 ka)*

Shallow lacustrine conditions (likely perennial) were established in Lake Machattie throughout early MIS 7 until ~220 ka. An increase in primary productivity at 220 ka is evidenced by a spike in $\delta^{13}C_{ORG}$, TOC% and Si/Zr, accompanied by the presence of diatoms. Although only slight increases in Ti and K/Rb values and no notable change in the lake freshening proxy Al/Mg, indicate there was not a large increase in water availability. However, this mild pluvial shift is coincident with enhanced fluvial activity in the Cooper creek between 250 and 230 ka

(Nanson et al., 2008), and shallow-water deposition at KT-LE (Williams Point) that continued until 201 ka (Fu et al., 2017). While KT-LE then recorded a change to a deep-water lacustrine phase (Cohen et al., 2022) synchronous with lacustrine expansions in the Gregory Lakes system (~200 ka; Bowler et al., 2001), a return to drier conditions in Lake Machattie led to the development of an ephemerally flooded playa environment for the remainder of MIS 7. An increase in TIC% and decrease in Al/Mg, Si/Zr and Ti values also points to drier conditions from ~200 ka. Oxidised and pedogenically modified interbedded gypsum and silty sands indicates a proximal playa-margin that was mostly dry. Although sufficient moisture was present to support a woodland/bushland/shrubland with more than 65% woody cover.

#### *2.5.2.3 MIS 6 (191 – 130 ka)*

A mostly dry ephemerally flooded playa persisted in Lake Machattie through MIS 6, with pedogenically altered, interbedded gypsum and silty sands continuing to develop until ~107 ka. Alternations between silty sands and gypsum layers occur on average with a ~21 ka cyclicity, suggesting wet and dry successions in Lake Machattie during this time may have been governed, at least in some part, by orbital-forcing due to precession cycles. Lower Ti, Al/Mg, K/Al, and K/Rb values all indicate drier conditions through the period, with a substantial increase in Fe/Mn suggesting redoximorphic conditions peaked at ~168 ka. A woodland/bushland/shrubland environment remained around the playa until the end of MIS 6, with increased TOC% documented from ~168 ka onwards.

While the Lake Koolivoo core is not dated beyond ~89 ka, extrapolation of the age-depth model allows us to provide some chronostratigraphic context to the sediments beyond 3.50 m, albeit tentatively. Bayesian modelling suggests that lacustrine silty clays gave way to interbedded gypsum and silty sands to form a proximal playa-margin in Lake Koolivoo briefly in MIS 6. A shift to lower Al/Mg, K/Al and Ti values in the interbedded gypsum and silty sands also points to a period of drier conditions. Sedimentological evidence suggests KT-LE also saw the demise of perennial wet conditions around the same time, with the establishment of playa conditions sometime between 175 ka (Cohen et al., 2022) and 158 ka (Fu et al., 2017) until the end of MIS 6. Similarly, a high lake stand further to the north at Lake Woods around ~180 ka that led to the deposition of ostracod sands did not occur again for another 84,000 years (Bowler et al., 1998), providing further evidence of a drying central Australia in MIS 6.

#### *2.5.2.4 MIS 5 (130 – 71 ka)*

Lakes Machattie and Koolivoo documented somewhat wetter conditions during MIS 5e, with woody cover increasing beyond 80% across the LMA for the final time. Al/Mg values also moderately increased in both lake cores, providing further evidence of lake freshening in early MIS 5. An increase in water availability was also recorded elsewhere in the LEB, with KT-LE documenting a shallow-lacustrine phase (Fu et al., 2017) until ~113 ka (Cohen et al., 2022). This wet phase was insufficient for the establishment and preservation of a palaeoshoreline record in KT-LE, which are commonly associated with its deeper lacustrine phases. Although, Cooper Creek also recorded a period of enhanced fluvial flow between ~120–100 ka (Cohen et al., 2010) suggesting most of the northern LEB was wet during MIS 5e.

The Lake Machattie playa eventually dried near the peak of MIS 5d (~107 ka) and remained subaerially exposed and dry enough for pedogenesis to form a Protosol on the slightly gravelly muddy sands. Conditions dried sufficiently for a decrease in woody cover to see the end of forested vegetation around Lake Machattie. Moderate increases in K/Al and K/Rb values during this time are considered evidence of weathering of the subaerially exposed sediments. Lake Koolivoo also recorded a shift to drier conditions in MIS 5d, with a Protosol developing on its lacustrine sediments between ~102 and 88.5 ka. Although, $C_3$-dominated vegetation remained established around Lake Koolivoo despite the decrease in water availability. An increase in Fe/Mn suggests that there was sufficient water available for periods of waterlogging (or water held in a poorly drained soil) that likely sustained the vegetation. This period of pedogenesis in the LMA was relatively brief and ended by MIS 5b/a.

Indeed, shallow lacustrine conditions were established in Lake Machattie by ~82 ka, while a deeper-water lacustrine (probably perennial) phase began in Lake Koolivoo at ~88.5 ka that continued for the remainder of MIS 5 – conditions wetter than today. Increases in Al/Mg and TOC-MAR in both cores, as well as Si/Ti and Si/Zr in Lake Koolivoo confirms the resumption of wetter conditions. Lakes Frome and KT-LE recorded a return to wetter conditions earlier, with palaeoshorelines dated between ~93 and 96 ka (Cohen et al., 2011, Cohen et al., 2012b, Cohen et al., 2015) suggesting sufficient depths for the connection of the lakes via the Warrawoocara channel (Nanson et al., 2008). However, enhanced river flows were not recorded in the Cooper Creek until ~85–80 ka (Cohen et al., 2010), indicating the northern LEB was drier during MIS 5c and became wet in MIS 5b/a. This evidence suggests that the mega-lake filling of KT-LE-Frome during MIS 5c may have been influenced by more southern-sourced precipitation rather than solely by the monsoon-driven waters of the northern catchments (e.g., Cohen et al., 2022). Certainly, the Neales River documented extensive fluvial deposition from ~107 ka through MIS 5 (Croke et al., 1996) that would have contributed water to KT-LE.

#### *2.5.2.5 MIS 4 (71 – 57 ka)*

The entire LMA shifted from a perennial lacustrine environment to an ephemeral playa at the beginning of MIS 4 (~69 ka) that was drier than today. A gradual decrease in TOC% and woody cover (increased $C_4$) in both lakes also suggests a shift to drier conditions with seasonal rains. Conversely, higher Al/Mg values in the Lake Machattie sediments would normally suggest an increase in water availability; however, contemporaneous increases in Fe/Mn, extensive pedogenic alteration and the presence of redoximorphic features (e.g., goethite nodules) suggests otherwise. Soils that contain clay, are low in organic matter and subjected to repeated wet and dry cycles can see an increase in acid-forming cations and the formation of Fe-oxy(hydr)oxides such as goethite, accompanied by greater $Al^{3+}$ saturation because of hydrolysis (e.g., Zhao et al., 2023). As Al is preferentially adsorbed onto clays before Mg (Zhao et al., 2023), an increase in Al saturation could lead to an increase in sediment Al/Mg values that could falsely be attributed to lake freshening, rather than in response to redoximorphic conditions amidst alternating wet/dry cycles. This is supported by the absence of redoximorphic features and lack of increase in either Al/Mg or Fe/Mn ratios in Lake Koolivoo, which when combined with the increase in $\delta^{13}C_{ORG}$ values and TIC%, and sedimentological shifts in both lakes, points to overall drier conditions.

These drier conditions were likely accompanied by increased supply of airborne material to the core site. The Simpson Desert and Channel country regions are major sources of dust (McTainsh, 1998) that are transported to the margins of Australia and beyond (Bowler, 1976). In a marine sediment core off the south Australian coast (MD03-2607), De Deckker et al. (2019) recorded increased dust deposition, represented by increased Ti/Al, between 70.8 and 60.8 ka, with a peak at 65.2 ka. This matches an increase in Ti/Al in Lake Koolivoo recorded between ~74 and 63 ka, and the highest Ti/Al value during this period was recorded at 66 ka, which indicates a shift to an aeolian signature in the terrestrial sediment supply.

Although drier conditions were documented in the LMA from ~69 ka, a regressive shoreline was deposited at Williams Point in KT-LE between ~78 and ~63 ka (Cohen et al., 2022), with Lake Frome preserving a coarse-grained shoreline between ~68 and ~60 ka (Cohen et al., 2011). Source-bordering dune formation in the Cooper Creek at ~68 ka indicates it was fluvially active during this same period (Cohen et al., 2010). A fluvio-deltaic sequence has also been documented at Illusions Plains (KT-LE) at ~59 ka, indicating a 20-m-deep lake filling episode (Cohen et al., 2015) during late MIS 4. Nevertheless, drier conditions are documented in other monsoon-fed lake systems to the north and west, with Lake Woods subaerially exposed sediment undergoing soil formation until ~60 ka (Bowler et al., 1998) and both pedogenesis and longitudinal dune building marking the Gregory Lakes system around ~68 ka (Bowler et al., 2001).

#### *2.5.2.6 MIS 3 (57 – 29 ka)*

An ephemeral playa-lake environment persisted in Lake Koolivoo until ~39 ka, whereas the Lake Machattie sediments were subaerially exposed and undergoing pedogenic alteration throughout most of MIS 3. While the Lake Koolivoo playa sediments do not show signs of pedogenesis, soil development in Lake Machattie was sufficient to form a compound Calcisol. Deposition of normally graded silty sands that disrupted pedogenesis between ~54 and ~45 ka suggests a wetter period, before resumption of subaerial exposure and soil development. Slight increases in Al/Mg, K/Rb, and K/Al, and an accompanying decrease in $\delta^{13}C$ values also imply wetter conditions in Lake Koolivoo between ~53 ka and ~45 ka. Eyre Creek was also active, with fluvial channel fill deposited between ~51 and ~39 ka, directly overlying and cutting into an undated phreatic calcrete. Increases in K/Rb, K/Al and Ti in the Eyre Creek sediments imply an increase in weathering in the catchment during the same period.

Approximately 200 km north of the LMA, quantitative palaeoclimate reconstructions of a dune-buried palaeosol near Glenormiston within the Georgina catchment (Figure 2.1a), determined soil formation also occurred in a humid, mesic climate in early MIS 3 (OSL dated at 50.1 ±2.8 ka; Singleton – unpublished data, refer to Chapter 3, section 3.4.3). Bioturbation features and rhizoliths (root casts and rhizohaloes) observed in the Glenormiston palaeosol indicate a woodland or forest dominated landscape, supporting our sedimentary carbon isotopic records from the LMA of a dominant $C_3$ cover (core LK and EC) or woodland/bushland/thicket/shrubland (core LM) in early MIS 3. Indeed much of central and northern Australia was predominantly wet from ~50–45 ka (Kemp et al., 2019), with the Australian monsoon serving as an effective moisture source between 65 and 45 ka, as evidenced by other regional proxy records, including $\delta^{13}C$ values in fossil emu (*Dromaius novaehollandiae*) eggshells from KT-LE (Johnson et al., 1999), lake levels (Chen and Barton, 1991, Bowler et al., 1998, Fu et al., 2017), and fluvial activity in the east Kimberley (Wende et al., 1997).

A temporal hiatus and sedimentological unconformity in Lake Koolivoo coincide with a shift from fluvial channel fill deposition to subaerial exposure, weathering and weak pedogenesis in Eyre Creek in mid-MIS 3 (~39 ka). No such unconformity is observed in the LM core; however, soil development continued in Lake Machattie with bioturbation likely responsible for sediment mixing and the resultant four discrete age components and moderate overdispersion value observed in the OSL sample. The hiatus in Lake Koolivoo may represent a period of non-deposition or landscape stability, such as those recorded in the Eyre Creek and Lake Machattie palaeosols, or an unconformity formed by deflationary winds or water erosion. A shift in $f_{wc}$ from a $C_3$ dominated landscape to woodland/bushland/thicket/shrubland suggests an increase in moisture stress recorded in Eyre Creek between ~40.5 and 33.5 ka. The hiatus/erosional unconformity in core LK from ~39 ka to 8 ka precludes the possibility of identifying a similar pattern, although the $f_{wc}$ declined from ~61 ka to 39 ka indicative of progressive drying. The transition from a $C_3$ dominated landscape to woodland/bushland/thicket/shrubland occurred much earlier in LM, between the MIS 5e peak (123 ka) and MIS 5d peak (109 ka), with a continued decline in $f_{wc}$ until the mid-Holocene. These findings suggest a trend towards continental aridity possibly driven by a decline in monsoon precipitation and increase in precipitation seasonality.

Reduced precipitation from mid- to late-MIS 3 appears ubiquitously in palaeoclimate records from central and northern parts of Australia. In the Gregory Lakes region of NW Australia, Fitzsimmons et al. (2012) inferred the onset of aridity began around 47 ka amidst intermittent lake fillings, followed by lake drying and dune building around 37 ka. Cyclic evaporite precipitation, driven by high water tables and groundwater replenishment, along with aeolian redeposition onto shoreline dunes, ceased at Lake Amadeus around 45 ka (Chen et al., 1990, Chen and Barton, 1991). Similar deposition of aeolian gypsum and quartz dunes at Lake Lewis, caused by high groundwater discharge, ended around 33 ka, indicating drier conditions (Chen et al., 1995). Lake Woods also experienced drying of its previously expanded, shallow palaeolake after 30 ka (Bowler et al., 1998). In the LMA, this drying period is documented by landscape stability, subaerially exposed sediment, soil development and ever decreasing amounts of woody cover and a shift to more seasonal ($C_4$) vegetation.

#### *2.5.2.7 MIS 2 (29 – 11 ka)*

Landscape stability and pedogenesis continued in the LMA for much of MIS 2, with Eyre Creek not becoming fluvially active again until ~16 ka. Lake Machattie continued to document periods of sediment aggradation throughout the period, but these were insufficient enough to exceed rates of pedogenesis. Slight increases in K/Rb and K/Al in the Eyre Creek and Lake Machattie soil profiles provide evidence of weathering of the exposed sediment. It is worth noting that Lake Koolivoo did not preserve any sediments from MIS 2, with the temporal hiatus/unconformity extending into early MIS 1. A decrease in woody cover in both Eyre Creek and Lake Machattie, and a shift towards more $C_4$ vegetation highlights the decrease in overall water availability in the LMA during MIS 2, and a possible shift towards greater seasonality. Interestingly, enhanced flows were recorded between ~28 and ~18 ka in Cooper Creek (Cohen et al., 2010), although it is more likely to be influenced by east coastal rainfall patterns than the further inland Georgina catchment.

Organic carbon isotope data from a 9-m-thick sedimentary sequence in the Lake Gregory region records a vegetation change from mixed $C_3$/$C_4$ to >60% $C_4$ after ~29 ka (Pack et al., 2003), confirming changes in precipitation patterns. Summer monsoon rainfall favours $C_4$ grasses (Hattersley, 1983, Murphy and Bowman, 2007) and considering the latitudinal equivalence of the Georgina River headwaters to the Gregory Lakes system, it is inferred that the reduction in $f_{wc}$ in the LMA from mid- to late-MIS 3 was likely from decreased monsoon precipitation and increased seasonality in rainfall. However, replacement of $C_3$ trees and shrubs with dominantly $C_4$ grasses from increased burning frequency by early human colonisers is also a possibility.

A fluvial channel fill deposit in Eyre Creek extends from ~16 ka until 14 ka, documenting a return to wetter conditions that is not documented in either lake core. However, it is unclear whether the hiatus in Lake Koolivoo represents a depositional hiatus, or an erosional unconformity. Although, the massive nature of the fluvial deposit indicates rapid sedimentation under higher energy flood stage conditions that could be responsible for erosion of at least some of Lake Koolivoo's sediments. Sediment mixing in Lake Machattie over the same interval makes examination of this short pluvial period difficult, although a moderate increase in Al/Mg points to an increase in water availability. Lake Mega-Frome also experienced a return to wetter conditions, with a moderate refilling of almost 7 m deep between ~17.6 and ~15.8 ka, which

Cohen et al. (2011) attributed to southern derived lake waters (viz. Flinders ranges) rather than via the Cooper Creek. Despite evidence of a wet phase in these areas of the LEB, KT-LE remained dry with episodic deflation of the playa until ~14 ka (Magee et al., 2004), suggesting any waters from the Georgina Catchment were insufficient to have any great effect on lake levels.

#### *2.5.2.8 MIS 1 (11 ka onwards)*

Enhanced rainfall in the early Holocene is inferred by low $\delta^{13}C_{ORG}$ values recorded in core LM at 9.35 ka and in core LK at 7.9 ka. Sedimentology also indicates a return to deposition under lacustrine conditions at ~8.8 ka in Lake Machattie and ~8.0 ka in Lake Koolivoo. Sharp increases in Al/Mg and TOC-MAR from ~7.6 ka in both lakes suggests there was an associated increase in sediment delivery. Eyre Creek was also in a wet phase with preservation of an overbank deposit providing evidence of an active river system through most of MIS 1 (from ~14 until ~0.9 ka). This coincides with a period of IASM strengthening associated with sea level rise and associated increase in moisture and heat supply to Australia and the Indonesian archipelago, evidenced by declining speleothem $\delta^{18}O$ values in Ball Gown Cave and cave KNI-51, NW Australia (Denniston et al., 2013b, Denniston et al., 2013c) (Figure 2.1b), and Liang Luar cave, Flores (Griffiths et al., 2009). Enhanced fluvial activity is recorded in the east Kimberley between 12 ka and 5 ka (Wende et al., 1997). The northern hemisphere meltwater event between 8.4–8.2 ka (Barber et al., 1999, Yim et al., 2006) may have also increased precipitation over the northern LEB through the southward movement of the ITCZ (Rohling and Pälike, 2005), as previously identified by precipitation proxies from Lynch's Crater in northeast Queensland (Muller et al., 2008). The Indo Pacific Warm Pool (IPWP) was substantially warmer in the early to middle Holocene (Moffa-Sanchez et al., 2019), acting as a negative feedback on the dynamics driving El Niño/La Niña phases of the Southern Oscillation (Dang et al., 2020). In this context, wetter conditions recorded in the LMA during this period appear controlled by ocean-continent hydrological cycles within the Indo-Australian summer monsoon domain.

Between 6 ka and 5 ka, ENSO variability was strongly reduced (Donders et al., 2008). While this coincides with drier conditions in the LMA, as recorded by the highest $\delta^{13}C_{ORG}$ values in Lake Machattie at 5.9 ka and progressive decline in $f_{wc}$ in Lake Koolivoo, the upper ocean heat storage in the IPWP was also declining in tune with precession (Moffa-Sanchez et al., 2019, Gong et al., 2023). However, primary productivity was still high in Lake Machattie, indicated by higher Si/Zr values and TOC%, and the presence of diatoms. A slight sediment change, including an increase in weathering and TIC%, and decreases in Al/Mg, K/Al, K/Rb, and Ti by ~5.7 ka in Lake Koolivoo points to a shift in conditions. This suggests that the drier conditions in the LMA were probably due to the decline in IPWP heating rather than reduced ENSO activity, where precession-modulated variations and insolation forcing in the IPWP controlled moisture convergence and latent heat in the Australasian monsoon system.

Drying of central Australian regions may have occurred earlier than in coastal regions. Indeed, peak rainfall around the mid-west coast of Australia is documented at ~6 ka in pollen records from a marine core (Fr10/95-17) (Van der Kaars et al., 2006) and in stalagmite oxygen and carbon isotope data from cave C126 in Cape Range Peninsula (Denniston et al., 2013a). Strong IASM conditions also continued to be recorded in cave KNI-51 until ~4 ka (Denniston et al., 2013c). However, a shift to more arid conditions is seen not only in the LMA $\delta^{13}C_{ORG}$ records, but also in Lake Frome and the Gregory Lakes region. Cohen et al. (2011) reported a return to a playa-lake environment across Lake Mega-Frome from ~5 ka onwards, while Fitzsimmons et al. (2012) documented substantial sand mobilisation and dune construction in the Gregory Lakes region between 6 ka and 3 ka, with ~2.5 m of sediment deposited during a rapid mid-Holocene 'arid event'. This period coincides with widespread dune building and aridity across the Australian continent (Hesse et al., 2004).

Palaeoclimate records from the equatorial Pacific and maritime continent indicate ENSO strengthening around ~5 ka (Donders et al., 2008). Pollen records from Four Mile Billabong, a perennial lake on Groote Eylandt (Shulmeister, 1992), located ~600 km north of the Georgina catchment in the Gulf of Carpentaria, show an effective precipitation maximum between 5 ka and 4 ka, and a clear decline after 4 ka that has previously been interpreted as the onset of the present-day high-amplitude ENSO-dominated climate (Shulmeister and Lees, 1995). A brief record of slightly wetter conditions is documented in Lake Machattie at ~4.2 ka, with mild increases in Al/Mg, Si/Ti, K/Al, and K/Rb; however, this was short-lived. Indeed, the lowest $\delta^{13}C_{ORG}$ values in Lake Machattie are recorded at ~3ka, indicative of reduced rainfall. Pollen records from Groote Eylandt indicate a return to high effective precipitation after 2 ka (Shulmeister and Lees, 1995). Similarly, a return to wetter conditions is evident in Lake Koolivoo and Lake Machattie, with geochemical (greater Al/Mg) and sedimentological shifts (decreased weathering) at ~2.6 and ~1.9 ka respectively, and their respective $\delta^{13}C_{ORG}$ values comparable to those from the early Holocene.

Shallow lacustrine conditions remained in Lakes Koolivoo and Machattie throughout MIS 1 and continue today. Although wet/dry alternations in the Holocene are recorded as relatively small changes in the geochemical and isotopic record of the lakes, Eyre Creek documented a more notable series of environmental changes in its sediments over the last 1,000 yrs. Indeed, Eyre Creek provides the highest resolution of $\delta^{13}C$ data over the last millennium (n = 14) for the LMA.

Eyre Creek documented progressive drying through early MIS 1 until ~0.9 ka, with declining K/Al, K/Rb, and Ti values. Further to the south, Lake Mega-Frome also recorded dry conditions, aside from a short lake-filling phase at ~0.96 ka (Cohen et al., 2011). Fluvial channel fill and crevasse splay deposits in Eyre Creek preserved evidence of wetter periods between ~0.91 and ~0.60 ka, ~0.56 and ~0.44 ka, and ~0.32 ka onwards. The sedimentological shift to predominantly planar cross-bedded sands in these intervals are generally accompanied by increases in TOC%, K/Al, K/Rb and Ti, and decreases in $\delta^{13}C_{ORG}$ values. The intervening periods (~0.60 – 0.56 ka and ~0.43 – 0.32 ka) are characterised by subaerial exposure and pedogenesis. Soil development was fleeting, but sufficient for the development of medium to coarse angular blocky peds.

The wettest conditions are recorded as depleted $\delta^{13}C$ values during the last ~330 years (since 1686 CE). Sedimentology indicates a return to fluvial deposition started around 324 years ago. Two palaeoshoreline deposits from Lake Machattie record significant flood events at about 1784 CE and 1830 CE that were of similar magnitude to the largest lake filling events today (Singleton – unpublished data, refer to Chapter 4, section 4.5.2). A detailed investigation by Haig et al. (2014) shows the turn of the 18th century marked the start of a multi-centennial cycle of increased Tropical Cyclone (TC) activity, which is particularly evident in the speleothem $\delta^{18}O$ records from Chillagoe in northeast Queensland (Figure 2.1b). Haig et al. (2014) inferred that cyclone activity on the east coast (west coast: Cape Range) began declining after 1743 (1960). It is likely the Georgina catchment benefited from tropical low-pressure rainfall from inland-tracking tropical cyclones. Such input occurs regularly under modern hydrological conditions, such as in 2001 (TC Sam), 2011 (TC Yasi), 2019 (TC Trevor), and 2023 (TC Ellie), despite the Australian region experiencing the lowest levels of cyclone activity for the past 550–1,500 years (Haig et al., 2014). Cave KNI-51 speleothem $\delta^{18}O$ records show IASM rainfall strengthened at 1 ka (Denniston et al., 2013c), with peak rainfalls occurring in the last ~200 years that support our sedimentological and $\delta^{13}C$ record at Eyre Creek.

### 2.5.3 Magnetic susceptibility cyclicity on past precipitation in the Georgina catchment

#### *2.5.3.1 Milankovitch frequencies*

The 202.6 kyr signal in the Lake Machattie MS MTM is close to cycles ranging between ~200 to 160 kyr detected in various sedimentary palaeoclimate records as variations in MS (Boulila et al., 2010, Boulila et al., 2014, Charbonnier et al., 2018, Zhang et al., 2022), TOC (Liu et al., 2014, Kim et al., 2016, Huang et al., 2021), $\delta^{13}C_{ORG}$ (Laurin et al., 2015, Huang et al., 2021) and/or grain size (Liu et al., 2024). Such low frequency cycles are typically ascribed to the amplitude modulation (AM) of obliquity (~173 kyr per cycle) caused by gravitational interactions between Earth and Saturn (denoted as s3-s6 with reference to planet orders from the sun) (Beaufort, 1994, Westerhold et al., 2005, Boulila et al., 2018). Cycles near ~200 kyr are also explained as harmonics of the ~405 kyr cycle (long eccentricity) or as “double” ~100 kyr cycles resulting from nonlinear climate responses to eccentricity’s primary components (Hilgen et al., 2015, Liebrand et al., 2016). In such cases, however, a strong short eccentricity (~100 kyr) band should be evident, which is not the case from the LM MS record. Given the primary Milankovitch obliquity frequency (41 kyr) is clearly expressed in the LM MTM power spectrum centred at 40.5 kyr (98.97% CL) (Figure 2.12a), we hypothesise the s3-s6 AM obliquity cycle as the likely origin of the ~200 kyr cycle observed in our MS time series. Variations in Earth's orbital inclination could also theoretically cause the expression of a 200 kyr cycle. However, the maximum change in average total solar irradiance is ~0.003 $W/m^2$ over timescales of thousands of years, which is 500 times less than for eccentricity (Vieira et al., 2012), and would not be detected in palaeoclimate proxies such as those used in this research

Following application of a 173 kyr bandpass filter on MS, the s3-s6 AM obliquity cyclicity appears well tuned to the raw MS broader-scale minima and maxima (Figure 2.12c). This suggests that the long-term variations in the Lake Machattie MS record and, by extension, climate variability, may be tied to AM obliquity. However, this record is short (<500 kyr) and, as such, the expression of the s3-s6 AM obliquity cycle in the Lake Machattie MS time series may be coincidental and should be viewed with caution. The collection of a longer core that spans multiple wavelengths of the s3-s6 AM obliquity signal would be a worthy undertaking given how little is understood about what effect long orbital forcing had on the Australian monsoon climate system (e.g., Gong et al., 2023).

The significant 24.6 kyr cycle (99.6% CL) in the Lake Machattie MS record is ascribed to the primary Milankovitch frequency for precession. Bandpass filtered (18–24 kyr) MS data shows an antiphase relationship with precession ($r = -0.263$; QAnalyseries correlation), particularly between ~132 and 70 ka (Figure 2.13a). This antiphase pattern is less clear in the younger LM sediments and occurs intermittently prior to glacial termination 2 (T2) (442–430 ka, 379–355 ka, 331–317 ka, and 192–181 ka), suggesting that precipitation enhancement over the northern LEB was unlikely driven solely by southern summer insolation.

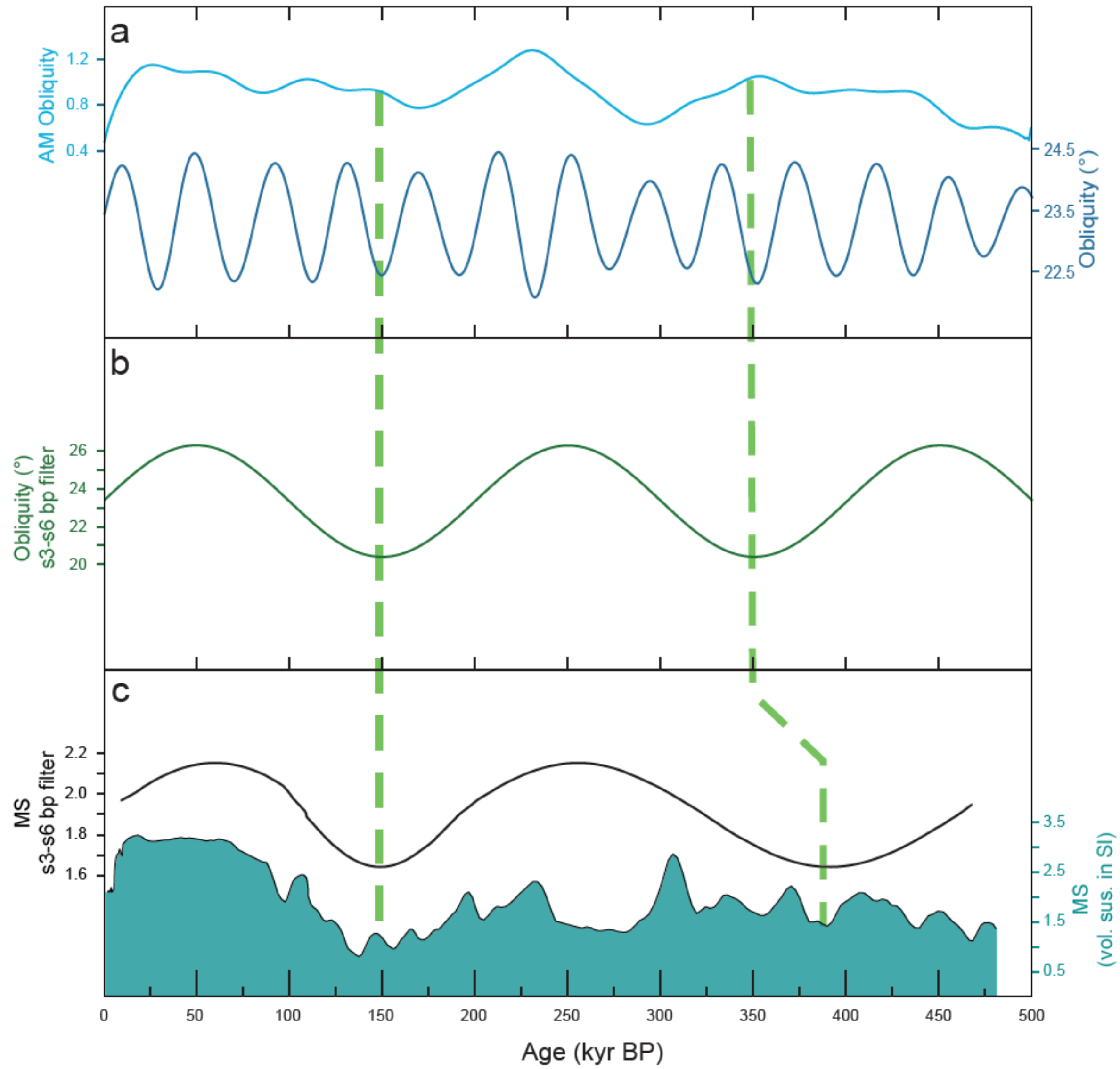


**Figure 2.12.** Obliquity correlations of the Lake Machattie magnetic susceptibility (MS) record. **a)** Amplitude modulation obtained by Hilbert transformation of obliquity (light blue line) in the Astrochron package in R (Meyers, 2014); obliquity (dark blue line). **b)** s3-s6 (~173 kyr) bandpass for obliquity (dark green line) obtained from obliquity AM curves with a bandpass of 0.00575 ±0.001 cycles/ka using Gaussian filters in the Astrochron package in R. **c)** s3-s6 bandpass for MS (black line) extracted from MS data (470 – 9 ka) with a bandpass filter of 0.009559 ±0.001 cycles/cm that covers cycles ranging between ~200 and 160 kyr; and MS (blue shading). Vertical light green dashed lines highlight correspondence between MS and the s3-s6 cycle minima for obliquity (~173 kyr).

To confirm this, we compared the timing and magnitude of the LM MS record for potential links with local summer insolation. Mean January insolation was chosen for analysis as it coincides with the peak precipitation month for northern Australia and the northern Georgina catchment under modern conditions (Figure S2; Appendix A1) and represents the midpoint of the standard three-month summer average used in climate modelling studies (e.g., Kutzbach et al., 2008). While precise correlation of some MS peaks is precluded by the limited dating resolution, there appears to be no direct in-phase response of the Australian summer monsoon to low latitude (21°S) summer insolation (Figure 2.13b), suggesting that other factors are important for generating the MS precession band. Our findings are consistent with other sedimentological chronologies from the LEB, including from KT-LE (e.g., Magee et al., 2004, Fu et al., 2017, Cohen et al., 2022), but are generally opposite to terrigenous palaeo precipitation records offshore Papua New Guinea (PNG) (Tachikawa et al., 2011, Shiau et al., 2012) and modelling experiments based on atmospheric circulation and ocean feedback mechanisms (Wyrwoll and Valdes, 2003, Wyrwoll et al., 2007).

Modelling by Wyrwoll et al. (2007) suggests monsoon activity over the Australian region should be substantially enhanced through the combined insolation effects from obliquity and precession maxima (+20 $W/m^2$). This combination could have caused stronger land-ocean heating contrasts and advection of additional heat and moisture feeding the monsoon system over northern Australia. While the direct effect of obliquity on tropical insolation is small compared to precession (Wu et al., 2016), some Lake Machattie MS peaks fit with the orbital forcing combination of coeval obliquity and precession maxima including at ~450 ka, 370 ka, 170 ka, and 48 ka (Figure 2.13c). Interestingly, global sea levels during these periods were between 60 and 100 m below what they are today (Grant et al., 2014), resulting in much larger distances for moisture laden air masses to traverse before reaching the Georgina catchment. Despite the larger Australian landmass, particularly with exposure of the Sahul Shelf over northern Australia, superposition of obliquity and precession maxima potentially facilitated deeper incursions of the summer monsoon.

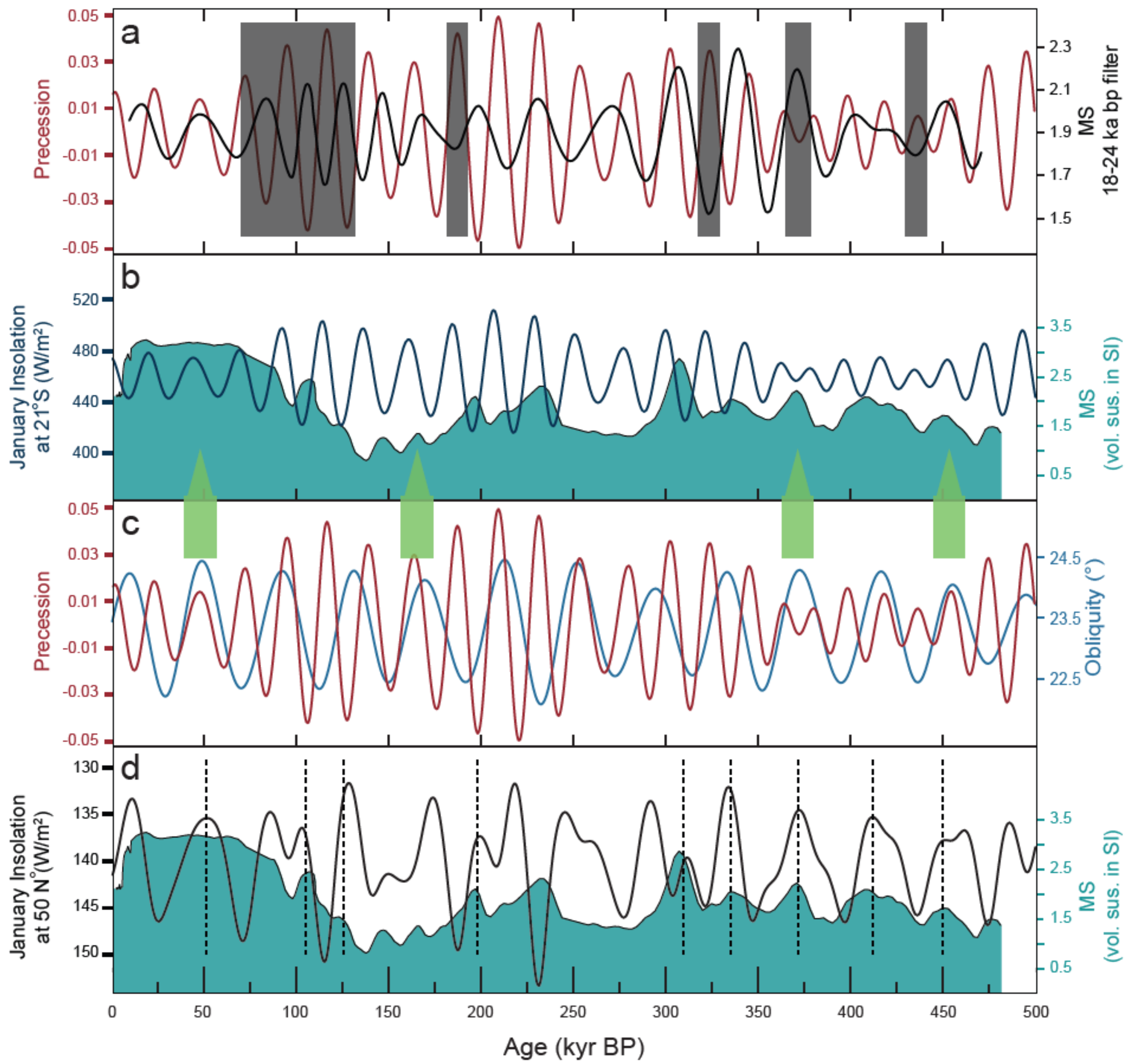


**Figure 2.13**. Precession, obliquity and insolation correlations with the Lake Machattie magnetic susceptibility (MS) record. **a)** Precession (red) and the 18-24 ka bandpass for MS (black line) obtained with a bandpass of 0.0789 ±0.023 cycles/cm. Grey bars indicate periods of antiphase relationship between MS and precession. **b)** MS compared with variations in January Insolation for 21°S. **c)** Precession and obliquity maxima that coincide with MS peaks (shows with green arrows to MS peaks into Figure 2.13b). **d)** MS compared with variations in January Insolation for 50°N (vertical dashed lines indicate periods where northern winter insolation maxima coincide with MS peaks).

Another possibility is northern insolation variations could have contributed to a stronger Australian monsoon in the precession frequency band. An in-phase response to southern insolation maxima is expected during intensification of northern hemisphere Asian winter monsoon based on monsoon winds crossing the equator to bring rain to Australia. Modern meteorological studies indicate strong East Asian winter monsoons can intensify the Australian summer monsoon by shifting the intertropical convergence zone southward, deepening the monsoon trough (Godfred-Spenning and Reason, 2002). Indeed, Magee et al. (2004) showed that some peak lake fillings in their 150 kyr KT-LE sedimentary record showed similarities with northern high latitude (50°N) winter insolation minima. However, modelling by Liu et al. (2003) shows an out-of-phase response is generated when SST changes along the western coastal region of Australia are insufficient, with the northerly winter monsoon winds instead delivering precipitation to the South Indian Ocean. While dating of the LM core is not resolved enough to be certain, LM MS maxima show some consistency with northern winter (50°N, January 21) insolation minima (Figure 2.13d) is suggestive that northern insolation and cross-hemispheric ITCZ migrations may have some level of control on monsoon variability over northern Australia between 470 and 9 ka.

#### *2.5.3.2 Sub-Milankovitch frequencies*

A significant (97.6% CL) 13.2 kyr band is present in the Lake Machattie MS record. Berger et al. (1991) reported that coupling of obliquity and precession could produce 13 and 15 kyr bands. Longer frequencies at 52 (Clemens and Prell, 1991), 54, 56–58 and 64 kyr (Berger, 1977, Daniau et al., 2023) have also been described as indicative of non-linear interactions within the climate system in response to the combination of obliquity and precession. The presence of the 13.2 kyr cycle, as well as 15.5 and 58 kyr periodicities in LM MS, albeit at the 76% CL (not shown), supports the interpretation of a non-linear climate response to insolation forcing from the coupling of obliquity and precession.

#### 2.5.3.2.1 Half precession frequencies

Half-precessional MS cycles are also evident in both Lakes, Machattie (10.9 and 9.8 kyr) and Koolivoo (11.5 kyr). These cycles could suggest that monsoon dynamics were influenced by harmonics of local insolation variations. At the equator, the solar zenith passage occurs twice a year, creating a double maximum in annual insolation. While this applies for the whole intertropical belt, prominent half-precession signals are generally observable in palaeoclimate records between 5°N and 5°S of the equator (e.g., Verschuren et al., 2009, Bolton et al., 2013) and diminish rapidly with increasing latitude (Berger and Loutre, 1997, Berger et al., 2006). While the headwaters of the Georgina River begin at ~19°S (i.e., well within the southern intertropical modern boundary of 23.5°), the half-precessional (11 ka) insolation component could reflect monsoon moisture responses to the double culmination of the Sun at zenith.

In the prevailing monsoon and ENSO controlled area of the Western Pacific Warm Pool (WPWP) in the southern hemisphere, half-precessional bands have been identified in several marine and terrestrial palaeoclimate archives. At Lynch's Crater in northeastern Australia (Figure 2.1b), variations in peat humification over the past 45 ka show a half-precessional precipitation cycle centred on ~11.9 kyr, which the authors attributed to ENSO type phenomena (Turney et al., 2004), although this has been debated (Leduc et al., 2009). Interestingly, half-precession frequencies were not found in the 250 kyr pollen and charcoal records from Ocean Drilling Program core site 820 (Moss and Kershaw, 2000; Leg 133, 16°S, Table S1; Appendix A2) that was recovered ~100 km northeast of Lynch's Crater, around 30 km from the modern shoreline.

ENSO variability was however suggested as a factor for half-precession cycles recorded in terrigenous Ti and elemental ratios (ln(Ti/K) and ln(Ti/Ca)) from river runoff by the Sepik and Ramu River system to the Bismarck Sea, north of New Guinea Island (core MD05-2920, 2.8°S, Table S1; Appendix A2) (Tachikawa et al., 2011). A half-precession (11 kyr) band was also found in coccolith assemblages in the Bismarck Sea, which Liang and Liu (2018) used to infer primary productivity and nutricline depth variations over the past 270 kyr (core KX12-1, 1.8°S, Table S1; Appendix A2) that were indicative of east-west thermocline slope changes akin to ENSO-type mechanisms. However, a 180 kyr terrestrial flux record from offshore southeastern PNG showed a poor coherency with the Nino 3 index at the half-precession (11 ka) band (Shiau et al. (2012); core MD052928, 11°S, Table S1; Appendix A2), which suggests that ENSO variability may not fully explain precipitation changes in this region.

Time-transgressive Heinrich events could account for half-precession sedimentary cycles ranging between ~10 and 12 kyr according to Berger et al. (2006). Indeed, Leduc et al. (2009) highlighted that wet periods in the Lynch's Crater peat deposits (Turney et al., 2004) coincide with Heinrich events and Dansgaard-Oeschger (D-O) stadials, and that ENSO variability may not be solely responsible for precipitation changes in the tropical Pacific on half-precession timescales. A reassessment of the Lynch's Crater precipitation response to Heinrich and D-O variability by Muller et al. (2008) involved the identification of sediment layers high in ash, Si/Al, and heavier $\delta^{15}N$ isotopes during Heinrich events, confirming increased rainfall during these periods. Additionally, their findings suggest past southward migrations of the ITCZ might not be exclusively linked to Heinrich events but could also be influenced by other dry/cold periods, such as Bond cycles.

#### 2.5.3.2.2 Other frequencies

The 8405-year and 3,620-year cycles that respectively appear in core LM (2.7–0.5 m) and LK (3.5–1.5 m) show potential links with northern hemisphere high latitude cooling and monsoon dynamics. The 8405-year cycle is similar to ≈8,000-year periods previously identified in the IMAGES core MD95-2043 from the Alboran Sea, western Mediterranean Sea (e.g., Cacho et al., 1999, Moreno et al., 2002, Sánchez Goñi et al., 2002) (Table S1; Appendix A2). An in-depth comparison by Moreno et al. (2005) of Greenland Ice Sheet Project 2 (GISP2) data with various proxy records in core MD95-2043 revealed the 8000-year cycle was associated with cold D-O events (stadials) and North Atlantic Heinrich events. The presence of this cycle in our MS record in the Georgina catchment may indicate interhemispheric teleconnections during these events.

A 3,700-year cycle was identified by Pestiaux et al. (1988) in southern Indian Ocean hydrography (core MD73025) and a similar 3,300-year cycle in REE by Sirocko et al. (1996) in the Arabian Sea, northern Indian Ocean (core 74KL) (Table S1; Appendix A2). Both show links to palaeo-monsoon dynamics potentially in response to solar or orbital forcing. In the Sulu Sea, northeast of Borneo, de Garidel-Thoron et al. (2001) reported a significant periodicity of 3,600-years in their primary productivity record between 30 and 60 ka (core MD972141, Table S1; Appendix A2). This cycle appears in our MS record at 3,620-years in core LK (3.5–1.5 m) from about mid-MIS 5 to mid-MIS 3. The recurring identification of this cycle in various palaeo-monsoon records, now including our lacustrine record from central northern Australia, implies its importance in the dynamics of the Asian-Australian monsoon system.

The significant 2,715-year period (97.3% CL) falls just outside the Hallstatt solar cycle (2,100–2,500 years), which is not unsurprising as it is typically found in Holocene palaeoclimate and cosmogenic radionuclide records (e.g., Steinhilber et al., 2012, Scafetta et al., 2016, Usoskin et al., 2016). Bray (1968) proposed a 2600-year climate cycle based on global glacier growth and retreat, including data from the southern Hemisphere in New Zealand and South America. This cycle is supported by observations of sunspots, auroras, and various geophysical, biological, and glaciological evidence. The 2600-year cycle is close to the 2,715-year periodicity found in the Lake Koolivoo MS record, suggesting a possible connection.

Bond et al. (1999) identified a persistent pattern of episodic cooling events in the North Atlantic over the last ~80,000 years, evidenced by increases in ice-rafted debris (IRD) within deep-sea sediments. Regular pacing of these cool events was demonstrated by averaging the time between IRD cycles over 12-kyr step intervals, which ranged between 1,328 and 1,795 years, yielding a consistent periodicity of 1,469 ±515-years (79-0 ka). Four of the LK MS cycles, 1,935, 1,745, 1,515 and 1,278-year, fall within this 1- to 2-kyr envelope identified by Bond et al. (1999), suggesting potential interhemispheric teleconnections with these cooling events.

Interestingly, the 1,935-year (94.2% CL) and significant 1,745-year (99.4% CL) cycles appear in the same spectral peak (Figure 2.9: LK 3.50–1.50 m letters d and e) suggesting they may be more closely related and part of the same underling signal. Averaging these periods yields an 1,840-year cycle, aligning closely with a strong ~1,800-year Ice-Rafted Debris (IRD) cycle identified by Bond et al. (1997) and Bond et al. (1999). Bond et al. (1997) also identified a 5,000-year modulation cycle affecting the strength of the 1,800-year cycle. It is worth noting that a 4,887-year cycle was also identified in core LK (3.50–1.50 m) with a 94.45% f-test CL (not shown), although the red noise signal was low at 76.85% CL suggesting the signal may not be distinguishable from background noise. However, this supports the likelihood that the averaged 1,840-year cycle in our LK MS record represents a potential climate response to northern Hemisphere forcing. Heinrich events, characterised by massive discharges of icebergs in the North Atlantic, fit into this framework as they are often preceded by IRD events by 500 to 1,000 years (Bond et al., 1992, Bond et al., 1999). This close link between Heinrich events and the 1,800-year IRD cycle suggest our 1,840-year averaged spectral peak could also be tied with Heinrich or Heinrich(-like) events. Palaeoclimate proxies, including magnetic susceptibility (MS), calcium carbonate ($CaCO_3$), and total organic carbon (TOC) from estuary water bodies in southeast Australia, reveal a recurring 1,800-year cycle (Skilbeck et al., 2005). The researchers suggest that this pattern may be linked to changes in solar insolation or disturbances in orbital cycles influenced by feedback mechanisms.

Turney et al. (2004) identified a 1,490-year drying cycle in Lynch's Crater corresponding with increases in Greenland temperatures throughout the past 45 kyr. The significant 1,515-year cycle (99.8% CL) in LK MS also closely aligns with the mean 1,470-year cyclicity of D-O warming events observed in the GISP2 $\delta^{18}O$ data (Bond et al., 1993, Bond et al., 1997, Schulz, 2002). Yet, unlike Turney et al. (2004), the D-O warming periods do not directly correspond with increased drying in Lake Koolivoo, as would be indicated by low MS. Instead, there is a moderate negative correlation between LK MS and GISP2 $\delta^{18}O$ from 89 and 39 ka ($r = -.372$;

QAnalyseries correlation), highlighting that Lake Koolivoo generally experienced wetter conditions during cooler periods in Greenland. However, the origin of this significant climate cyclicity remains elusive. A similar periodicity of 1,500 years was also reported by de Garidel-Thoron et al. (2001) in an East Asian winter monsoon record from the Sulu Sea, northeast of Borneo (Table S1; Appendix A2). The authors suggesting this frequency was not forced from high latitudes despite being pervasive during MIS stages 3 and 5.

#### *2.5.3.3 Holocene cycles*

Centennial and multi-decadal scale cycles characterise the Holocene sediments in each core. The longest cycle of 856 years, significant at >95% CL in Lake Machattie, could reflect various climate oscillations such as Bond events (Holocene pacing of 1,374 ±502 years; Bond et al., 1999) or the Eddy solar activity cycle (900–1050 years). These cycles are commonly identified in palaeoclimate records such as ice cores (Davis and Bohling, 2000, Bond et al., 2001) and $^{14}C$ of tree rings (Eddy, 1976), as well as modelled harmonics of solar cycles (e.g., Scafetta, 2012). Furthermore, the 856-year cycle is close to the 900 ±200-year oscillations in soil organic matter $\delta^{13}C$ in central North America as a result palaeo-ENSO cycles (Wang et al., 2000).

The 446-year periodicity identified in the Lake Koolivoo matches to the alignment of lunar nodal cycles and Earth’s axial wobble, both influenced by the moon's gravitational pull. These cycles impact sea surface temperatures and regional climate patterns. Similar 446-year cycles have been observed in Greenland's GISP2 temperature variations (Yndestad, 2022), reflecting solar-lunar interference effects on climate.

The 237-year and 172-year cycles potentially reflect the de Vries (Suess) cycle (230–180 years). This cycle is believed to be one of the most intense and dominant solar cycles during the Holocene (Raspopov et al., 2008) and has previously been identified in annually resolved tree ring climate proxies across the globe including from Tasmania (Breitenmoser et al., 2012).

Skilbeck et al. (2005) identified a 210-year cycle in their Australian coastal lake record, linked with variations in solar insolation or perturbations in orbital cycles brought about by feedback loops. Haig and Nott (2016) attributed a 128–256-year cycle in their cyclone activity index from Cape Range and Chillagoe (Figure 2.1b) to the De Vries solar cycle. Indeed, Antarctic productivity cycles of 200–300 years also point to solar-forcing (Leventer et al., 1996).

The 172-year cycle is also close to the basic cycle of solar motion of ~178.7 years (Jose, 1965) caused by the gravitational interactions between the Sun and the giant planets, primarily Jupiter and Saturn, affecting solar irradiance and Earth's climate patterns over centennial timescales (Charvátová, 2000). A slightly shorter 161-year dust deposition cycle was observed in a 1 m peat core collected from southeastern Australia (Snowy Mountains), that was attributed to solar forcing by McGowan et al. (2010).

The significant 68-year cycle (99% CL) in the EC MS record may relate to a multi-decadal IPO cycle and/or the Gleissberg cycle of solar irradiance (70–100 years). The Gleissberg cycle has been identified in extreme rainfall and flood records from Eastern New South Wales spanning the last 200 years (Asten and McCracken, 2022), and variations in palaeo-monsoon precipitation over India (Nigam et al., 1995) and eastern China (Shen et al., 2006), highlighting the significant impact of solar activity on regional hydrology. Cook et al. (2006) also identified a spectral cycle centred on 69 years in a 3,600-year tree ring record of temperature reconstruction from Tasmania that matches our EC MS 68-year cyclicity.

Solar activity affects climate primarily through variations in total solar irradiance and the interaction of solar radiation with the atmosphere. Higher solar activity increases total solar irradiance, altering atmospheric circulation and cloud formation (Gray et al., 2010). Solar activity also modulates ocean-atmosphere interactions, like ENSO, by influencing sea surface temperatures and circulation (Meehl and Arblaster, 2009). Increases in ultraviolet radiation during heightened solar activity also boosts stratospheric ozone production, warming it and altering the temperature gradient between the upper atmosphere and the ocean or land surface.

These changes can influence weather patterns, alter storm tracks and precipitation, and affect the positioning and strength of jet streams and subtropical highs (Gray et al., 2010). In regions with already warm sea surface temperatures, such as those surrounding northern Australia, solar-induced atmospheric warming results in a decrease in the intensity and frequency of weather events that depend on these energy differentials.

This relationship is exemplified in palaeorecords from the western Atlantic (Elsner and Jagger, 2008, Hodges and Elsner, 2012, Hodges et al., 2014) and in Australia (Haig and Nott, 2016) of decreased tropical cyclogenesis when sunspot activity is higher. As such, we might expect increased (decreased) fluvial activity in the Georgina catchment as a function of decreased (increased) solar activity. Indeed, there is a moderate negative correlation between EC MS and annually resolved solar activity proxy tree-ring $\delta^{14}C$ data (Usoskin et al., 2021) ($r = -0.420$; QAnalyseries correlation), suggesting Eyre Creek generally experienced wetter conditions during periods of low solar activity, at least over the last millennium.

The shorter cycles of 45 years and 29 years observed in core EC record a lower confidence level (91% and 94%, respectively), but likely correspond to the positive and negative phases of the IPO, which operates on a modern timescale of ~15 to 35 years (Power et al., 1999, Folland et al., 2002). Negative IPO phases, resembling La Niña conditions, strengthen Austral monsoon connections with ENSO, increasing summer monsoon rainfall variability (Power et al., 1999, Mantua and Hare, 2002, Verdon et al., 2004, Cai and Van Rensch, 2012, Heidemann et al., 2022, Heidemann et al., 2023). These conditions are also more conducive to La Niña development and cyclogenesis in the western Pacific and Coral Sea (Grant and Walsh, 2001, Mantua and Hare, 2002, Magee et al., 2017), increasing the probability of the Georgina catchment receiving rainfall from inland-tracking tropical cyclones. Palaeoclimate records from southeast Australia and around the Pacific basin show increased hydroclimate variability associated with IPO cycles (Mantua and Hare, 2002, McGowan et al., 2010). While spectral analyses suggest orbital-, centennial-, and sub-decadal-scale influences, we acknowledge that sedimentation discontinuities and variable accumulation rates may impact precision. The identified periodicities exceed the

90% confidence level, but further refinement with additional high-resolution records would improve confidence in these cyclicities.

### 2.5.4 Human arrival and landscape change

Beyond climate-driven variability, broader regional studies have examined the role of Indigenous land-use in shaping late Quaternary Australian ecosystems. While our dataset does not directly resolve these influences, the Georgina catchment can be considered within this wider discussion. There is little doubt that with early human dispersals to the Sahul-Australian continent, starting in the north around 65 ka (Roberts et al., 1990, Roberts and Jones, 1994, Roberts et al., 1994, Clarkson et al., 2017), or possibly as late as 50 ka (Williams et al., 2021), came an increased frequency of landscape burning that favoured the expansion of grass areas at the expense of trees and shrubs. Indeed, the Georgina River may have been a preferred southward migratory pathway, a 'superhighway' (Crabtree et al., 2021), based on visually prominent landscape features and potentially abundant freshwater resources transecting the arid interior (Figure 2.10a). As such, one would expect that by the time continent wide colonisation occurred ~50–45 ka (O'Connell and Allen, 2015, Hughes et al., 2017, Veth et al., 2017, O'Connell et al., 2018), a shift to greater $C_4$ grasses, particularly in the monsoon-fed northern LEB, should be evident in our lacustrine and fluvial records from the Georgina. While an expansion of grasslands in response to increased burning is often inferred from parallel increases in $C_4$ vegetation and charcoal, the LMA cores do not contain a well-resolved charcoal record indicative of significant fire-induced ecosystem change. However, as charcoal analysis was not a primary focus of this study, its absence may reflect both a true environmental signal and the limitations of preservation and detection within the sampled sequences.

Drying in Australia has been ongoing since the Miocene (Martin, 2006, Mao and Retallack, 2019), intensified after ~350 ka (Nanson and Price, 1998, Hesse et al., 2004, Nanson et al., 2008), and coincides with dramatic landscape and biota changes after ~50 ka (Roberts et al., 2001, Cohen et al., 2011, Cohen et al., 2015, Miller et al., 2016a). While humans occupied arid Australia by at least 50 ka (e.g., Bowler et al., 2003), archaeological evidence suggests repeated but variable habitation in the broader LEB by at least 25 ka (e.g., Robins, 2005). Occupation patterns fluctuated in response to climatic shifts, with evidence of human abandonment of the LEB's dunefields and plains during drier periods (e.g., Williams et al., 2015, Hughes et al., 2017). Despite these changes, our sedimentary organic carbon $\delta^{13}C$ record from the LMA is an ineffective differentiator of direct ecosystem changes caused by natural climate change, megafaunal extinction, or human-induced alterations in fire regimes during or after the peopling of Sahul-Australia.

## 2.6 Conclusions

Cycles observed in the high-resolution magnetic susceptibility records from the LMA suggest that precipitation over northern Australia over the past ~500,000 years was potentially influenced by a combination of solar, lunar, and orbital/insolation forcing, northern high-latitude climate variability, as well as tropical Pacific mechanisms such as palaeo ENSO-like phenomena and the IPO. Further investigations may benefit from additional spectral frequency analysis, such as wavelet or evolutive harmonic MTM analysis, to better constrain the identified periodicities and potential forcing mechanism through time. For example, many of the identified frequencies appear to align with solar cycles, but the sun is not the only driver of the climate system, and other climatic drivers such as greenhouse gases and volcanic or dust aerosols can obscure temporally such solar fingerprints. Furthermore, the Milankovitch and sub-Milankovitch cycles identified in the MS time series remain unexplored in the other proxies from the LMA cores; however, higher sampling resolution of correlative proxies would be required, particularly for identification of the sub-Milankovitch frequencies.

The sedimentology of the Lake Machattie area documents major climatic and environmental changes during the late Quaternary. The sediments and geochemical markers document transitions from perennial lacustrine environments during wet periods to groundwater-controlled ephemeral playa lakes in drier times, interspersed with phases of soil development.

During MIS 13 to 8, the LMA was a groundwater-controlled playa lake that supported a forested landscape with over 80% woody cover, which gradually transitioned to a mixed $C_3/C_4$ vegetation environment as arid to semi-arid conditions developed around MIS 10. In late MIS 8 to 7, shallow lacustrine conditions were established, with the landscape continuing to be dominated by woodland/bushland/shrubland vegetation, reflecting a relatively dry climate. By MIS 6, dry playa conditions dominated, persisting until a significant shift to wetter conditions in MIS 5. While MIS 5 brought a pronounced increase in water availability, allowing for widespread woody cover and a return to lacustrine conditions, the extent and timing of wet phases within MIS 5 remain challenging to resolve precisely. Although, our sedimentary record suggests a return to drier conditions around MIS 5d contributing to the gradual decline of forested environments, before a brief return to wetter conditions in MIS 5b that were wetter than today. Progressively drier conditions followed, with increasing $C_4$ vegetation surrounding the ephemeral playa in MIS 4 and 3, signalling a trend towards greater aridity and seasonality. In the Holocene, although shallow lacustrine conditions and fluvial activity returned, the vegetation remained dominated by woodland/bushland/shrubland, indicating that while the climate was wetter than during MIS 3, it was substantially drier compared to the particularly wet phases of MIS 5. Indeed, a shift from deep water lacustrine facies to shallow water deposition during lake phases and the ultimate demise of forest vegetation in the LMA from MIS 5 onwards indicates successively less effective wet phases in the Georgina catchment.

Major lake phases in the LMA during the late Quaternary broadly correspond with those recorded in the ephemeral lake systems that dot central Australia. In particular, with the Gregory Lake System in MIS 8, KT-LE in early MIS 7 and KT-LE-Frome in MIS 5b/a. While this study did not identify lake phases during MIS 9–10 or late MIS 7, such as the mega-lake phases of the Gregory Lake System or Lake Woods (respectively), undated lacustrine units older than 100 ka in Lake Koolivoo may hold an answer for future examination. Drier periods of landscape stability and pedogenesis, such as those in MIS 4, appear to correspond better with the northern monsoon-fed Gregory Lakes system and Lake Woods than with KT-LE and Lake Frome to the south.

Therefore, the Georgina Catchment appears to have a nuanced influence on the hydrological balance of the greater LEB. While not consistently a primary contributor, the catchment may have played an important role during certain periods, particularly during wetter phases, such as those documented in MIS 5. During these times, the Georgina Catchment likely delivered increased water volumes to KT-LE via the Georgina-Diamantina-Warburton River and contributed to lake fillings. However, the influence of the Georgina Catchment is largely episodic, and its pluvial periods often align better with other northern monsoon-fed lakes than with the wet phases preserved in the southern LEB. Mega-lake fillings in KT-LE-Frome may have required the activation of all its northern catchments, including the Georgina. Though it is more likely contributions from both northern and southern rainfall sources, such as the Neales River and Flinders Ranges, were necessary to sustain these large-scale hydrological events, in particular the mega-lake fillings of MIS 5.

The key findings of this study are threefold. Firstly, that the Georgina catchment experienced enhanced pluvial periods during MIS 7 and 5, broadly aligning with those documented in other central Australian lakes. Secondly, that major wet phases in the LMA do not always correspond with those in KT-LE, despite its role as one of the three northern catchments, highlighting the spatial variability of hydrological responses within the LEB. Lastly, that progressive drying from MIS 4 onwards is recorded with a notable increase in moisture stress from ~69 ka, excluding a pluvial phase between ~53 and ~39 ka. While these findings contribute to the broader understanding of late Quaternary aridification in central Australia, they should be interpreted in the context of the inherent uncertainties associated with single-core records, discontinuous nature of deposition, chronological constraints and sediment preservation biases. These results represent the first sedimentologically-derived palaeoclimate reconstruction of the Lake Machattie Area that highlights the importance of the Georgina catchment as a record of central Australia's natural history.

# Chapter 3

# An early MIS 3 perennial wet and cool phase in central northern Lake Eyre Basin: Evidence from a dune-palaeosol sequence in the northeastern Simpson Desert.

Singleton, R.E[a,b*]., Orr, T.J[a,b]., Wasson, R.J[a,b]., Jacobs, Z[c,d]., Nott, J[a]., and Bird, M.I[a,b]

[a]College of Science and Engineering, James Cook University, Cairns, QLD 4870, Australia

[b]ARC Centre of Excellence for Australian Biodiversity and Heritage, James Cook University, Cairns, QLD 4870, Australia

[c]ARC Centre of Excellence for Australian Biodiversity and Heritage, University of Wollongong, Wollongong, NSW, Australia

[d]Centre for Archaeological Science, School of Earth and Environmental Sciences, University of Wollongong, Wollongong, NSW, Australia

**Author contributions:**

Russell Singleton collected and processed the samples, analysed and interpreted the data, developed the research question and wrote the manuscript. Michael Bird provided funding for the project through the ARC grant. Theresa Orr completed the palaeopedological analyses and the associated data reduction, analysis and results description. Zenobia Jacobs completed the OSL analyses and the associated data reduction. Michael Brand provided field assistance. All authors provided editorial assistance.

## 3.1 Introduction

Dunes are one of the most common landforms in Australia. In the arid central parts of Australia, dune deposits have attracted increasing attention because of their potential for preserving information of Quaternary climate change, in a region where such archives are particularly scarce. In the Lake Eyre Basin (LEB), covering nearly 15% of the Australian continent, sandy dunefields including the Strzelecki, Tirari and Simpson appear to have largely been built from aeolian mobilisation of the underlying relict sedimentary basins (Pell et al., 2000, Hollands et al., 2006). Deflation of material onto the dunes is also thought to have been sourced from active alluvial aggradation in flood plains and lakes, as well as from ancient salt lakes and claypans cut off from modern streams (Wasson, 1983b). Today, these dominantly linear (longitudinal) dunes are meta-stable, generally well-vegetated with a cyanobacterial crust (Hesse and Simpson, 2006). The lack of any preserved sinuosity suggests evolution from a seif dune morphology is unlikely and hyper-aridity has not previously occurred (Hesse, 2016). While debates surround the various modes of longitudinal dune construction, including vertical accretion (Pell et al., 2000, Hollands et al., 2006, Craddock et al., 2015), lateral migration (Nanson et al., 1992a) and linear extension (Telfer, 2011, Telfer et al., 2020), vertical accumulation on Australian dunes is generally slow (<10 cm/kyr; Hesse, 2016), although ground penetrating radar surveys of the Simpson and Strzelecki Deserts show linear (dune-front) accumulations may be more rapid (~300 m/kyr; Bristow et al., 2007). Overall, Australian longitudinal dunes have remained relatively stable despite experiencing a range of climates in the late Quaternary.

Previous work on Australian dunes primarily focussed on inferring palaeoclimates based on dune building chronologies and sediment characteristics. Thermoluminescence (TL) and Optically Stimulated Luminescence (OSL) dating of sand, and $^{14}C$ dating of charcoal and pedogenic carbonates from the LEB, record dune activity over the last two periods of glaciation (Wasson, 1983b, Gardner et al., 1987, Nanson et al., 1992a, Nanson et al., 1995, Twidale et al., 2001, Lomax et al., 2003, Hollands et al., 2006, Bristow et al., 2007, Fitzsimmons et al., 2007b, Fujioka et al., 2009). While cosmogenic nuclide burial dating places the onset of formation of the

Simpson dunefield at ~1 Ma (Fujioka et al., 2009), the oldest luminescence dune age within the LEB comes from an aeolian source-bordering dune flanking the Diamantina River, ~200 km east of the Simpson Desert. Here, Nanson et al. (1988) recorded three alternating units of clayey sand and sand, with the lowest clayey sand unit TL-dated at 274 ±22 ka.

Syntheses of TL and OSL dune ages indicate peak aridity and dune activity occurred during the last glacial maximum (Wasson, 1986, Nanson et al., 1992b, Fitzsimmons et al., 2013, Hesse, 2016), although source-bordering longitudinal dunes in the Strzelecki appear to cluster at 15–10 ka rather than the LGM (Hesse, 2016). This suggests fluvial activity around the Pleistocene–Holocene transition influenced the material supply on nearby dunes. This is similar to the findings of Hollands et al. (2006) for changes in Late Quaternary longitudinal dune orientations at Camel Flat basin (northwest Simpson Desert) caused by a post-LGM fluvial supply reduction and south-eastward shift in prevailing winds. In addition, Fitzsimmons et al. (2013) examined luminescence ages for the period 40–0 ka and identified Holocene, post-LGM-Holocene transition (14–10.7 ka), and marine isotope stage (MIS) 3 (40–29 ka) peaks in dune activity throughout Australia, by a reduced $\chi^2$ test. Holocene easterly accretion of pre-existing longitudinal dunes is recorded in the Simpson and Strzelecki Deserts (e.g., Bristow et al., 2007), but many other dunes record low or no Holocene accumulation. In regional source-bordering dunefields in the western and eastern Simpson Desert, Holocene dune migrations of ~100 m from the underlying Pleistocene dune cores have been reported (Nanson et al., 1992a, Nanson et al., 1995). The monsoon-influenced Gregory Lakes in Western Australia also preserve evidence of rapid mid-Holocene dune accumulations (Fitzsimmons et al., 2012).

Pedogenic features are found in many late Quaternary sandy dunes in central Australia (e.g., Nanson et al., 1992a, Lomax et al., 2003, Bristow et al., 2007, Fitzsimmons, 2007, Fitzsimmons et al., 2007a; 2009, Fujioka et al., 2009) and are often used as qualitative indicators of periods of relative environmental stability: enhanced humidity, hiatuses in aeolian activity, and denser vegetation cover. Indeed, Fitzsimmons et al. (2009) conducted detailed sedimentological investigations of 28 different dunes in the Strzelecki and Tirari Deserts and concluded palaeosols represent the most unambiguous marker of past environmental stability in dunes. However, both qualitative and quantitative palaeoclimate reconstructions are possible. Globally, palaeosols have been used to interpret the palaeoclimate associated with aeolian deposits from the Cretaceous and Miocene in Brazil (Fernandes and Basilici, 2009, Dal'Bó et al., 2010, Mescolotti et al., 2019), Argentina and Chile (Rech et al., 2019, Lizzoli et al., 2021), and the Pleistocene–Holocene in the USA (Forman et al., 1995, Reheis et al., 2005) and China (Gallet et al., 1996, Jia et al., 2015, Ding et al., 2021). In Australia, quantitative palaeosol climate reconstructions are limited to Precambrian–Neogene sediments (Driese et al., 1995, Retallack, 1999; 2008; 2021a; 2021b, Metzger and Retallack, 2010, Retallack et al., 2015, Zhou et al., 2015, Mao and Retallack, 2019). These studies primarily used natural exposures, such as outcrops in river channels, road cuttings, and quarry sites, as well as existing drill cores housed at state-run facilities (e.g., the Northern Territory Geological Survey core facility; Retallack, 2021a). However, palaeosols preserved in dune sediments present additional challenges as they are often spatially discontinuous and difficult to access. This has likely contributed to the lack of Quaternary palaeoclimate reconstructions from Australian dune palaeosols. Only six studies (Retallack, 2008; 2021a; 2021b, Metzger and Retallack, 2010, Retallack et al., 2015, Mao and Retallack, 2019) quantitatively reconstruct the palaeoprecipitation and palaeotemperature of these valuable terrestrial records, using a combination of major element geochemistry (e.g., weathering indices such as the salinisation ratio) and morphology-based climofunctions (e.g., depth-to-carbonate and mean annual precipitation relationship). While these methods have revealed insights into older palaeoenvironments, they have yet to be applied to Quaternary Australian dune palaeosols. Their use in arid Australia could extend existing palaeoclimate and palaeoenvironmental records into the late Quaternary.

Many authors highlight the importance of understanding the climatic and environmental history of central Australia, and of the LEB, in particular (e.g., Fitzsimmons et al., 2013, Fu et al., 2017, Cohen et al., 2022). Progressive aridification during the last two glacial cycles played a significant role in shaping Australia's inland landscape and biota though other factors, such as ecological changes and human activity, likely contributed to these transformations. Evidence used to infer the nature of Quaternary environments includes vegetation changes and megafaunal extinctions, though interpretations of their causes remain complex and multifaceted (Roberts et al., 2001, Wroe and Field, 2006, Rule et al., 2012, Saltré et al., 2019), the demise of perennial mega-lakes, lower lake fillings and shift to playa-dominated conditions toward the present reflects long-term hydrological variability rather than a simple, unidirectional drying trend (Magee et al., 1995, Croke et al., 1996, Magee and Miller, 1998, Fu et al., 2017, Cohen et al., 2018; 2022). Similarly, dune building over, or bordering, lacustrine/fluvial sediments may not be solely attributed to increased aridity but could also reflect periods of enhanced sediment availability (Bowler et al., 1998, Magee and Miller, 1998, Bowler et al., 2001, Magee et al., 2004, Fitzsimmons et al., 2012, Cohen et al., 2022), including sand transported as bedload during wetter intervals. Studies have shown that dunes may continue to accrete even when rivers are actively flowing, provided wind conditions are favourable for sediment transport (e.g., Gunn et al., 2022). Records of enhanced palaeoprecipitation over the LEB span the last two glacial periods and include palaeofluvial (Maroulis et al., 2007, Nanson et al., 2008, Cohen et al., 2010), palaeolacustrine (Magee et al., 1995, Magee, 1997, Croke et al., 1998; 1999, Magee et al., 2004, Cohen et al., 2011; 2015; 2018; 2022, Fu et al., 2017) and proxy rainfall reconstructions such as egg shell-derived point-potential evapotranspiration from Kati-Thanda Lake Eyre (KT-LE) and Lake Frome (Miller et al., 2016a). Each of these provide evidence of LEB-wide or major-catchment inputs but do not specifically record how far precipitation penetrated inland. To date there are no direct palaeorecords of regional rainfall falling within any of the LEB's major catchments.

This study explores the age architecture of a source-bordering longitudinal dune, that has been fluvially cut by waters draining a small catchment bordering the northeast margin of the Simpson Desert, to constrain the palaeoenvironment during deposition. Source-bordering dunes are unique in that their sediments offer crucial insights into past periods of enhanced regional aeolian and fluvial activity (e.g., Nanson et al., 1995; Fitzsimmons et al., 2007; Nanson et al., 2008). Longitudinal dunes, which dominate the Simpson Desert, developed in response to prevailing winds (e.g., Wasson et al., 1988, Cohen et al., 2010; Hesse, 2016), with many also located adjacent to the lakes, playas or river systems that act as a sediment source (Hesse, 2011). We combine techniques of field sampling, OSL dating, and particle size analysis of dune sediments to reconstruct the palaeoenvironment. In addition, macromorphology and geochemistry of a palaeosol are used to reconstruct the mean annual precipitation and temperature during soil formation.

## 3.2. Regional Setting

The Georgina catchment, located in central Australia, is the second largest and most northerly sub-catchment of the LEB. Its main river channel, the Georgina River, has headwaters in the monsoon tropics that, under modern hydrological conditions, lead to ephemeral flows southward, eventually reaching Goyder's lagoon (as Eyre Creek), the Georgina-Diamantina River confluence.

In the central Georgina catchment, approximately 23 km SW of the Glenormiston homestead (and rainfall gauging station), exists a relict dunefield (hereafter the Glenormiston dunefield) that confines fluvial flows from a relatively small (420 $km^2$) sub-catchment through a single dune breach (Figure 3.1a and c–e). Historical aerial imagery clearly depicts the breach was already open in 1978 (Figure S1; Appendix B1) (GeoAust, 2024a) and its well-vegetated margins suggest incision probably occurred prior to the largest modern flooding event on record, 1974, and maximum rainfall recorded at Glenormiston (677 mm; BOM, 2024a). Heavy rainfall at Glenormiston in 1950 (650 mm) may have initiated the dune breach, although it also could have formed in the distant past. The dunefield covers a ~57 $km^2$ area and is located on the northeastern margin of the Simpson Desert. Its location is far from any of the rainfall and wind amplifiers associated with the humid margins of Australia, such as tropical cyclones, southern hemisphere westerlies and cold fronts, and coastal onshore winds. Today, lacking strong deflationary/formative winds (Ash and Wasson, 1983), the dune acts as a relatively stable recorder of the Australian palaeoclimate.

The central position of the breach in the dunefield is important, as the longitudinal dune has likely been maintained through vertical, lateral and downwind accumulations. Aeolian sediment transport pathways may, however, be interrupted or limited given there is a network of connected interdune fluvial channels and ponds that cross the entire dunefield — a hydrologically open system. Aeolian-derived material that ends up in the local flood plains or fluvial courses can be flushed downstream out of the dunefield (Al-Masrahy and Mountney, 2015), potentially reaching the Georgina River. Evidence of ancient fluvial erosion on the dunes can be seen in the presence of aligned dunes on both sides of the floodplain and multiple wide dune breaches located to the west of the study site (Figure 3.1d). The western flank of the drainage catchment shares a headwater divide with Twenty Mile Creek, which is a tributary of the Mulligan River. Fringing the northeastern Simpson Desert, the Mulligan River is the most westerly major drainage line in the Georgina catchment which ephemerally flows southwest, eventually joining the Georgina River (as Eyre Creek) around 25°S.

Except for the narrow 35 m wide breach, the 10 km long longitudinal dune shares a similar morphology with the surrounding regional dunefield and that of the Simpson Desert. The dunes are narrow crested, generally low (~6 m; swale to crest) with a close mean spacing of 407 m (n=16). The closely spaced dunes at Glenormiston compare well with dunes across the Simpson Desert (<600 m spacing; Wasson et al., 1988) and likely reflects a fine-grained sandy alluvium substrate, similar to the closely spaced clayey linear dunes found in the Mallee in southeastern Australia (Wasson, 1986). The dunes are northwest trending in tune with the anticlockwise whorl of longitudinal dunes around the continental centre, believed to be wind-aligned by the dominant subtropical high-pressure system over continental Australia (Brookfield, 1970, Wasson et al., 1988). Some dunes have y-junctions opening to the southeasterly upwind direction, with most having their upwind ends on either floodplain alluvium, lithic sandstones, limestones or dolarenite.

The regional climate is dominated by the monsoon. On average, 65% of the annual rainfall is received at Glenormiston during Austral summer (December–March, DJFM), with an annual mean rainfall of 215 mm. Climate data are available from the closest weather station, Boulia, ~100 km east of Glenormiston, with over a century of continuous temperature, wind speed and wind direction data. Mean annual temperature maxima and minima is 32 °C and 17 °C (135 data years), respectively, 9 am wind direction is from the southeast and south (131 data years), and 3 pm wind speed is 12.1 km/h (112 data years) (BOM, 2024a).

The dominant surface geology of the drainage catchment feeding into the Glenormiston dunefield (Figure 3.1c) is Georgina Limestone (middle–late Cambrian flaggy calcilutite and sandy calcilutite with chert, sandstone), Ninmaroo Formation (late Cambrian – Early Ordovician calcarenite and dolarenite, oolitic and algal limestone and calcilutite), mudrock of the Wallumbilla Formation (Early Cretaceous deeply weathered mudstone and siltstone with calcareous concretions), and Longsight Sandstone (Middle Jurassic – Early Cretaceous sandstone, ferruginous sandstone, conglomerate, some siltstone). The floodplain contains late Tertiary – Quaternary alluvium and colluvium (clay, silt, sand, gravel, and soil) (QGlobe, 2024a).

Sand provenances are unlikely from sources requiring long distance transport (Wasson, 1983a), but rather from local sub-catchment sources including fluvial and lacustrine sediments, weathered rocks, and the dunefield itself. Sediments of the dunefield and sandplains are Quaternary fine-medium grained quartz sand, with interdune claypans (QGlobe, 2024a). The main modern sources of aeolian dust are the Simpson Desert and Channel Country regions (McTainsh, 1998), with the dust being transported to the humid margins of Australia and beyond via two main trajectories: southeast and northwest (Bowler, 1976) (Figure 3.1b). The Glenormiston dunefield lies within the latter dust trajectory. Consistent with these regional dust transport patterns, wind data from Boulia Airport (1888–2010) indicate a dominant southeasterly near-surface wind regime, with the highest frequency of winds originating from the SE quadrant, typically at an average annual speed of 12.2 km/h (BOM, 2025).

## 3.3 Material and Methods

### 3.3.1 Field Sampling

One of the difficulties with sampling of aeolian dunes is not being able to view the dune's internal stratigraphy, particularly in the lowermost dune sections that potentially contain the oldest sediment. Most samples at depth are collected by vertical augering (e.g., Nanson et al., 1992a; 1995; 2006, Hollands et al., 2006, Fitzsimmons et al., 2007b), which poorly preserves internal dune structures and permits only limited observations of stratigraphic subdivisions (e.g, Fitzsimmons et al., 2009). Natural dune exposures such as occur in gullies are uncommon (e.g., Gardner et al., 1987, Fitzsimmons et al., 2009), and man-made exposures (e.g., road cuttings, drill holes, borrow pits, drainage cuts, or excavation pits on dune crests or flanks) do not always permit access to dune core stratigraphy, although there are some exceptions (Twidale et al., 2001). The dune site in this study was selected because of a distinctive fluvial breach located approximately midway along its otherwise unbroken length, and its potential to preserve evidence of multiple depositional processes, including aeolian, alluvial, and fluvial influences, as well as pedogenic alteration. The breach is important as it provides a natural cross section to enable easy investigation of the dune's core and is the only fluvial pathway out of the drainage catchment.

Three pits were dug in the middle of the vegetated dune's upwind snout on the northwestern side of the breach. Each pit was 6 m apart, up to 150 cm deep, and dug at stepped elevations in alignment with the dune's northwest trending long axis (i.e., the surface of pit 1 was located ~0.9 m and ~1.7 m higher than the surface of pit 2 and 3, respectively) (Figure 3.2a). Elevation data for pit stratigraphy and dune topography was recorded using a Hemisphere S321+ receiver with the ATLAS L-band Global Navigation Satellite System (GNSS), which has a reported RMS positional error down to 2 cm. Dune stratigraphy was described, and bulk samples were collected from each pit in 10 cm increments down profile for particle size analyses. A palaeosol exposed at the base of pit 3 was described and sampled every 10 cm ($n = 10$) for major element geochemical analyses and bulk clay mineralogy. Palaeosol descriptive characteristics were compiled for each sample, including colour, lithology, abundance and morphology of peds, vertic features, mottles and mineral accumulations, referencing various methodologies (e.g., Klappa, 1980, Birkeland, 1984, Mack et al., 1993, Marriott and Wright, 1993). Classification of the palaeosol followed the criteria established by Mack et al. (1993).

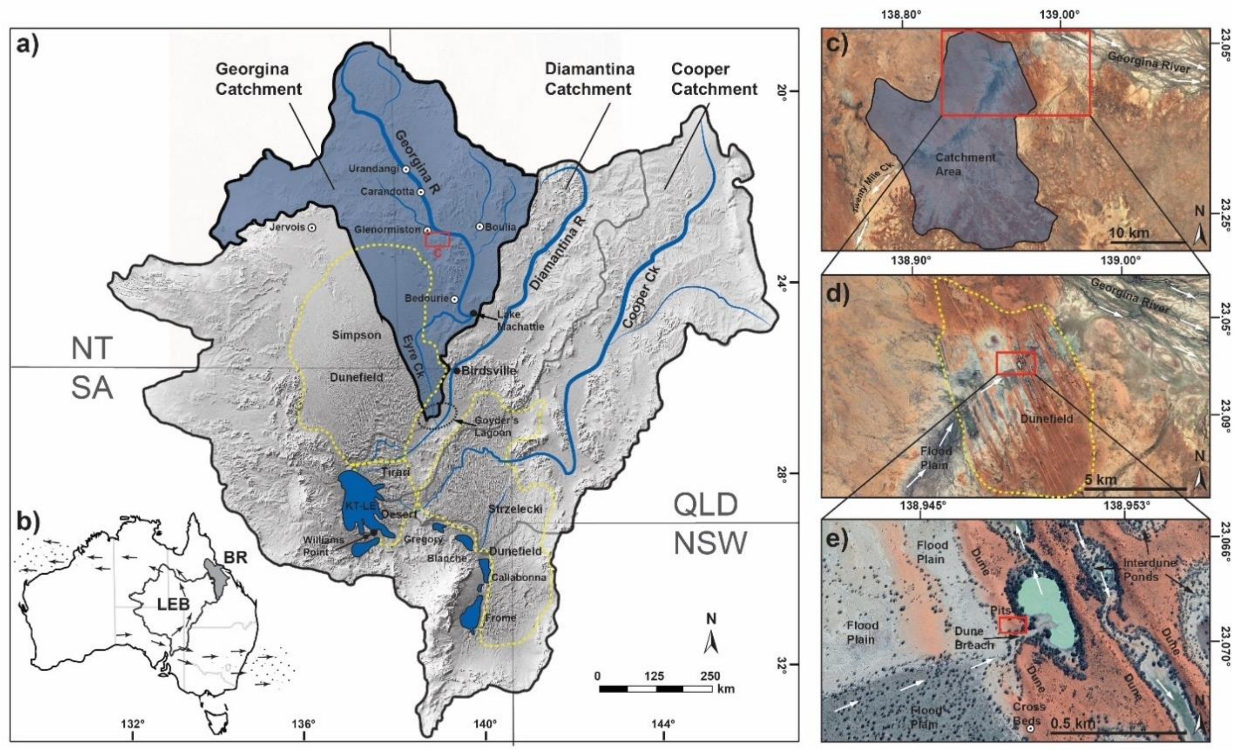


**Figure 3.1.** Locality: **a)** Lake Eyre Basin (LEB) including major sub-catchments, the Georgina (blue shading), Diamantina and Cooper, dunefields (yellow dotted polygons), and Kati Thanda-Lake Eyre (KT-LE) and the Lake Frome-Callabonna-Blanche-Gregory system (dark blue shading). White circles with black dot show the location of Glenormiston, Carandotta, Bedourie, Boulia, Jervois and Urandangi Stations referred to in text. **b)** LEB and Burdekin River (BR) catchments. Australian dust paths (arrows and dots) after Bowler (1976). **c)** Drainage catchment that feeds into the Glenormiston dunefield, adjoining flood plains, interdune ponds, eventually reaching the Georgina River (top right). **d)** Dunefield marked with yellow dotted line. White arrows show the direction of water flow. **e)** Dune breach and location of excavation pits (red box), adjoining flood plains, longitudinal dunes, interdune ponds, water flow direction (white arrows), and dune cross bedding pit (white circle with black dot). Note: Red box in map a, c and d is the location of map c, d and e, respectively.

OSL analysis was used to obtain depositional ages of sediments. Six sediment samples were collected in PVC tubes, 30 cm long by 5 cm diameter, hammered horizontally into fresh pit exposures that were subsequently removed at night under dim red light, capped and black plastic wrapped. Five OSL samples were collected from pit 2 and one sample was collected each from pits 1 and 3. The sample from Pit 1 was not dated. Single-grain OSL analyses were conducted at the OSL dating laboratory, University of Wollongong, Australia, with measurements of De obtained for all samples. Sample preparation and measurement followed the methodologies and instrumentation described in Jacobs et al. (2019) and Forbes et al. (2021). Quartz grains with diameters of 180–212 µm were analysed using the single-aliquot regenerative (SAR) dose procedure (Galbraith et al., 1999; Murray and Wintle, 2000). The resulting De data set was processed using the functions available in the numOSL R-package (Peng et al., 2013). The environmental dose rate was determined based on external beta, gamma, and cosmic-ray dose rates, along with an internal alpha dose rate. A constant internal alpha dose rate of $0.03 \pm 0.01$ Gy $kyr^{-1}$ was applied to all samples. Beta dose rates were directly measured using a Risø GM-25-5 beta counter, following established protocols (Bøtter-Jensen and Mejdahl, 1988; Guérin et al., 2001; Jacobs and Roberts, 2015). Gamma dose rates were derived from uranium, thorium, and potassium concentrations obtained via inductively coupled plasma mass spectrometry (ICP-MS) and inductively coupled plasma optical emission spectroscopy (ICP-OES). Cosmic-ray dose rates were calculated using site-specific parameters, including latitude, longitude, altitude, sediment depth, and overburden density, with an assumed average sediment density of 1.8 $g/cm^3$. Water content measured in the lab was used to correct the dose rates.

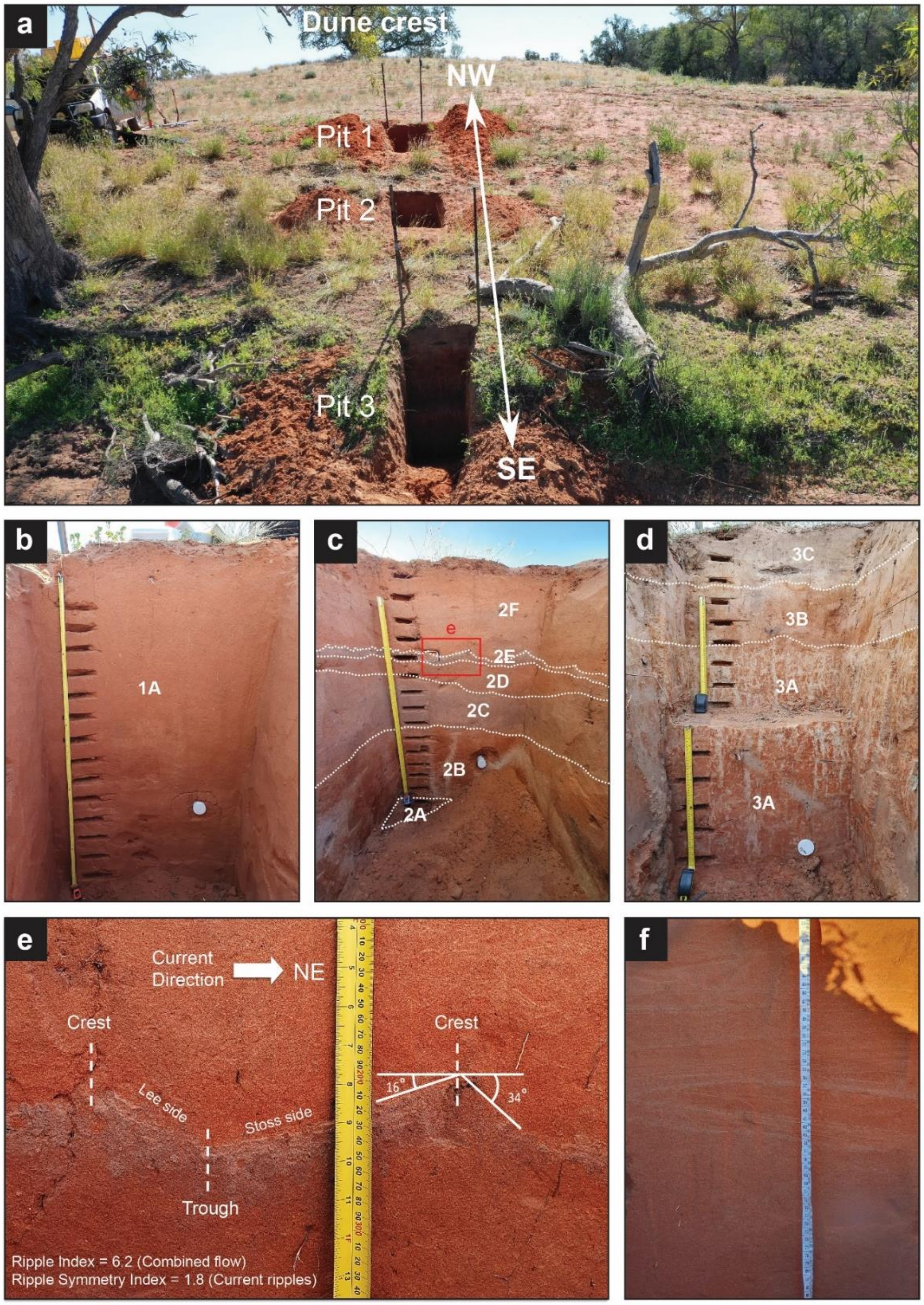


**Figure 3.2. a)** Glenormiston dune pits aligned with the dune's northwest trending long axis. **b)** Pit 1. **c)** Pit 2. Red box is location of figure 3.2e. **d)** Pit 3. Note that a stepped pit was dug as shown with the placement of 2 measurement tapes. **e)** Zoomed in on current ripple in pit 2 (unit 2E). **f)** Cross bedding in the same linear dune but on the southeast side of the breach, ~400 m

from pits 1, 2 and 3 (location shown in Figure 3.1e). Note, vertical sample holes on left side of figures 3.2b–d are 10 cm apart, otherwise measurement tapes can be used for scale.

### 3.3.2 Laboratory

#### *3.3.2.1 Particle Size Analysis*

Samples were dry sieved to <2000 µm and then treated with 2.0 M HCl and with 30% $H_2O_2$ (three times) to remove carbonates and organic matter, respectively. Samples were pre-treated with a 10% sodium hexametaphosphate dispersant solution before the grain size distribution was determined using a laser particle-size analyser (Mastersizer 3000, Malvern) at the Queensland University of Technology (QUT), Central Analytical Research Facility. Statistical parameters for particle-size analyses including mean, sorting, skewness, and kurtosis were analysed using the particle size distribution and statistics package, GRADISTAT (Blott and Pye, 2001). Particle size descriptive terminology follows Folk and Ward (1957).

#### *3.3.2.2 Major Elements*

Major element composition of each sample from the palaeosol were determined using X-ray fluorescence spectrometry (XRF; Bruker S8 Tiger Series II) by the Central Analytical Research Facility at QUT. Sample preparation included gravimetric determination of loss on ignition (LOI) of an aliquot of the dried sample (ca. 0.1 g) in a high-alumina sintered silica crucible at 1050 °C. A separate aliquot of the dried sample (ca. 0.5 g) was fused into a glass disk using lithium metaborate/lithium tetraborate flux (50:50 LiT:LiM, 0.5 wt% LiBr) in a platinum crucible using an electric fusion furnace (The Ox, Claisse). Samples were analysed under vacuum using a 4 KW Rh X-ray tube. Calibration of the spectrometer used Geo-Quant Advanced calibration set with a *quasi*-Lachance matrix correction. Oxide data were normalised to their respective molecular weights.

### *3.3.2.3 Clay Mineralogy*

Bulk phase analysis of the clay mineralogy of the palaeosol was determined by X-ray diffraction (XRD) at the QUT, Central Analytical Research Facility, using a Bruker D8 Advance powder diffractometer with cobalt Kα radiation operating in Bragg-Brentano geometry. Corundum ($AL_2O_3$), an internal standard, was combined at 20 wt% with each sample. A McCrone mill with zirconia beads and ethanol were used to form a homogeneous micronised powder before being dried overnight at 40 °C. Powders were pressed into sample holders and step-scanned XRD patterns were collected for one hour per sample. To aid in clay identification, a small portion of the micronised powder was also dispersed in water, sonicated (5 min) and allowed to settle (5 min) before the suspended fine fraction (nominally < 5 µm) was pipetted onto a low background plate and then air dried. Glycol atmosphere (60 °C) was used to treat the air-dried slides for several hours before immediate re-examination. Data was analysed using JADE (V2010, Materials Data Inc.), EVA (V5, Bruker) and X'Pert Highscore Plus (V4, PANalytical) with various reference databases (PDF4+, AMCSD, COD) for phase identification. Rietveld refinement was completed using TOPAS (V6, Bruker).

### *3.3.2.4 Weathering Indices and Climofunctions*

Dominant pedogenic processes were evaluated using the molecular weathering ratios 1) $CaO + MgO)/Al_2O_3$ for the degree of calcification (CAL), 2) $Al_2O_3/(CaO + MgO + K_2O + Na_2O)$ as a measure of hydrolysis, 3) total $Fe/Al_2O_3$ of oxidation (OX), 4) $(K_2O + Na_2O)/Al_2O_3$ of salinisation (SAL) and 5) MgO/CaO as a proxy for palaeoaridity (Retallack, 2001; 2003, Sheldon and Tabor, 2009). Calcareous soils are indicated by CAL values >2, salinised soils by SAL >2 and oxic soils usually have Ox >1.2 (Retallack, 2001). The chemical index of alteration ($CIA = 100*(Al_2O_3/ Al_2O_3 + CaO + Na_2O + K_2O)$ was used to indicate the overall weathering and pedogenesis of the palaeosol, where CIA values of 50–60, 60–80 and 80–100 indicate incipient, moderate and intense weathering and pedogenesis, respectively (Nesbitt and Young, 1982, McLennan, 1993). CIA values <50 represent unweathered rocks (McLennan, 1993).

Mean annual precipitation (MAP) was estimated using the CIA-K and ΣBases/Al climofunctions (Sheldon et al., 2002), which were applied to the uppermost B horizon (Bt). The CIA-K function is CIA-K = $100*[Al_2O_3/ (Al_2O_3 + CaO + Na_2O)]$, with MAP derived from MAP = $221.12e^{0.0197(CIA\text{-}K)}$ (Nesbitt and Young, 1982, Maynard, 1992). The CIA-K–MAP relationship is based on the preferential removal of alkali and alkaline earth elements and retention of the refractory element Al with increased weathering and can be used over a range of 200–1600 mm/yr (SE ±182 mm; Sheldon et al., 2002). The ΣBases/Al–MAP relationship (MAP = -259.34ln(ΣBases/Al) + 759.05) has a similar basis but includes Mg as one of the primary alkaline earth elements affected by weathering (ΣBases = Ca + Mg + Na + K), and is useful over the same 200–1600 mm/yr range (SE ±235 mm/yr; Sheldon et al., 2002). These relationships can be applied to most soils, excluding aeolian, hillslope, or waterlogged profiles.

While the Glenormiston palaeosol developed on aeolian parent materials, the soil itself did not form under desert-like conditions and is not considered an aeolian soil. Indeed, the profile lacks pedogenic carbonate or gypsum accumulations (wt% of both CaO and NaO are less than 1%), and the morphology is characterised by argillic features, including an apparent Bt-horizon and clay cutans. However, it is possible there is some inherited weathering signal within the aeolian sediments, and these relationships are applied here with caution. It is worth noting that the CIA-K climofunction has been used successfully to estimate MAP values on aeolian sediments previously (e.g., Dal'Bó et al., 2010, Lizzoli et al., 2021). Mean annual temperature (MAT) was calculated by applying the salinisation climofunction to the Bt horizon. The SAL-MAT relationship is useful over 2–20 °C (SE ±4.4 °C) for any soil that is not aeolian, frigid, hilly, or swampy (Sheldon et al., 2002); the Glenormiston palaeosol is not precluded by soil type. All oxides were normalised to their molecular weights before application of the MAP and MAT climofunctions. MAP is discussed in zones of arid (< 250 mm), semiarid (250–500 mm), subhumid (500–1,000 mm), and humid (1,000– 2,000 mm), and MAT in zones of frigid (0–8 °C), mesic (8–15 °C), thermic (15–22 °C), and hyperthermic (>22 °C) (Bull, 1991).

## 3.4 Results

### 3.4.1 Sedimentology

A summary of the dune sedimentology sampled in this study is provided in Table 3.1. Pit stratigraphy is shown in Figure 3.3, and the results of grain size analyses are shown in Figure 3.4. Palaeosol XRF and XRD results are shown in Table S1 (Appendix B2) and Figure S2 (Appendix B1), respectively.

Grain shape in all pits is dominantly sub-angular to well-rounded, with less variability observed in pit 3, particularly in the palaeosol. Sphericity is generally lower in pit 3, at least below 20 cm (low to medium), compared to pits 1 and 2 (low to high). Relict grain cutans, primarily haematic (red coloured; 10R 4/6) clays remaining in the concave areas of clean grains, were ubiquitous in all pits and indicates aeolian reworking and abrasion of grain cutans prior to deposition (Bullard et al., 2004, Bullard and White, 2005). Intact grain cutans, primarily white coloured clays (7.5YR 8/1), were only observed in the palaeosol at the base of pit 3.

The size distribution of the Glenormiston sediments is dominantly unimodal, with seven and nine of the 40 samples exhibiting bimodality and trimodality, respectively (Figure 3.4). The unimodal distributions are fine sands. Unimodality is ubiquitous in pit 1. Bimodal distributions vary between pits 2 and 3, where the dominant and secondary modal peaks are typically in the silt and clay size fraction in pit 2, respectively, and are in the fine sand and silt size fractions in the palaeosol in pit 3, respectively. The surface sediment in pit 2 also has a bimodal distribution of dominantly fine sand and a smaller peak in silt. Seven of the nine trimodal distributions were observed in pit 2, with dominant peaks ranging from silt to fine sand, secondary peaks between silt and very fine sand, and tertiary peaks within the clay to very fine sand ranges. Pit 3 trimodality is dominantly in the fine sand size fraction, with smaller modal peaks in silt.

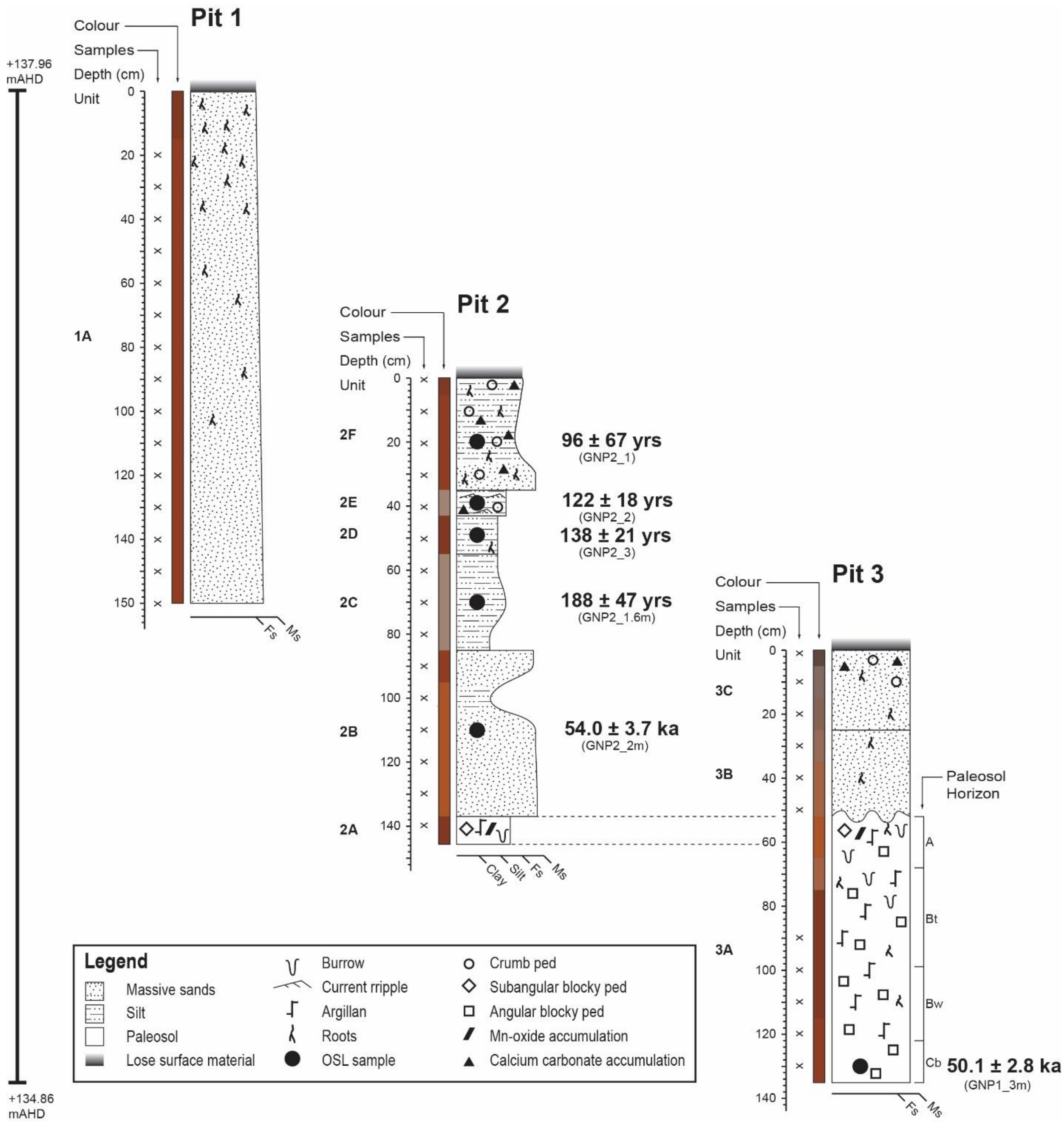


**Figure 3.3.** Detailed measured pit sections of the Glenormiston longitudinal dune. Matrix and Munsell colours (Munsell, 2009), as determined in the field. Pit stratigraphy is vertically aligned as measured in the field.

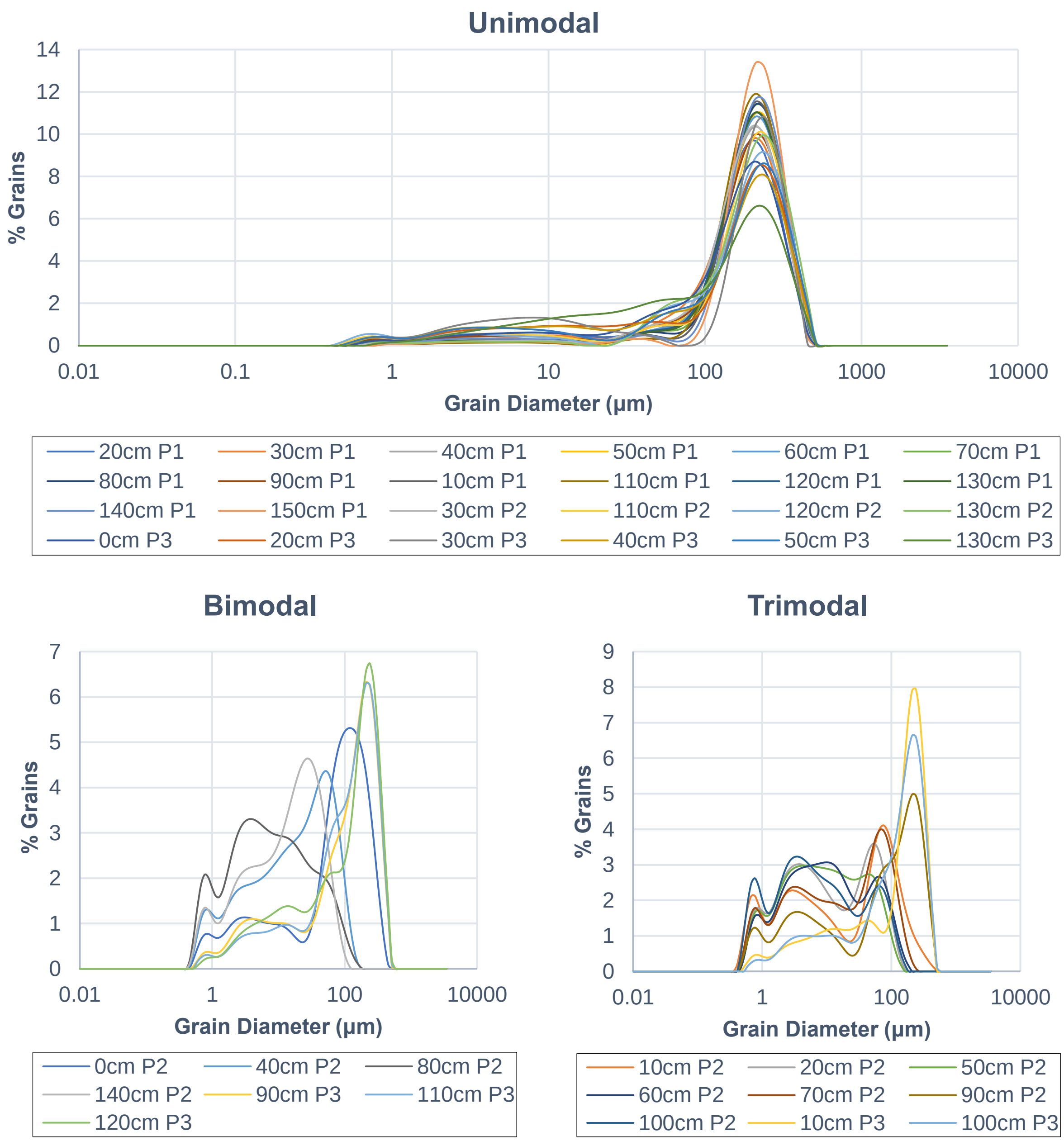


**Figure 3.4.** Particle size distributions separated as unimodal, bimodal and trimodal for all samples in pits 1 (P1), 2 (P2) and 3 (P3) in Glenormiston dune, northeast of the Simpson Desert.

**Table 3.1.** Summary of Glenormiston dune sedimentology. Depth is cumulative depth downprofile. Abbreviations: Sedimentology (GA, GS, MA = grain angularity (SA, SR, R, WR = subangular, subrounded, rounded, well rounded), grain sphericity (H, M, L = high, medium, low), mud accumulation); Mineralogy (Q, F, G, L = quartz, feldspar, gypsum, lithics); Cutans [I, R, C = intact (pedogenic), relict (non-pedogenic), clean grains]; Presence (X) or absence (-). Note, mineralogy of palaeosol sample #s GNP3_20 to GNP3_100, determined by XRD (see Figures 3.6 and S1).

| Pit # | Sample # | Depth (cm) | Colour | Sedimentology | | | Mineralogy | | | | Pedogenic Indicators | | |
|---|---|---|---|---|---|---|---|---|---|---|---|---|---|
| | | | | GA | GS | MA | Q | F | G | L | Peds | $CaCO_3$ | Cutans |
| 1 | GNP1_10 | 20 | 2.5YR 4/6 Red | SA-WR | H-M | - | X | - | - | X | - | - | R, C |
| | GNP1_20 | 30 | 2.5YR 4/8 Red | SA-WR | H-M | - | X | - | - | X | - | - | R, C |
| | GNP1_30 | 40 | 2.5YR 4/8 Red | SA-WR | H-L | - | X | X | - | X | - | - | R, C |
| | GNP1_40 | 50 | 2.5YR 4/8 Red | SA-WR | H-L | - | X | - | - | X | - | - | R, C |
| | GNP1_50 | 60 | 2.5YR 4/8 Red | SA-WR | H-L | - | X | X | - | X | - | - | R, C |
| | GNP1_60 | 70 | 2.5YR 4/8 Red | SA-WR | H-L | - | X | - | X | X | - | - | R, C |
| | GNP1_70 | 80 | 2.5YR 4/8 Red | SA-WR | H-L | - | X | - | - | X | - | - | R, C |
| | GNP1_80 | 90 | 2.5YR 4/8 Red | SA-WR | H-L | - | X | - | - | X | - | - | R, C |
| | GNP1_90 | 100 | 2.5YR 4/8 Red | SA-WR | H-L | - | X | - | - | X | - | - | R, C |
| | GNP1_100 | 110 | 2.5YR 4/8 Red | SA-WR | H-L | - | X | - | - | X | - | - | R, C |
| | GNP1_110 | 120 | 2.5YR 4/8 Red | SA-WR | H-L | - | X | - | - | X | - | - | R, C |
| | GNP1_120 | 130 | 2.5YR 4/8 Red | SA-WR | H-L | - | X | X | - | - | - | - | R, C |
| | GNP1_130 | 140 | 2.5YR 4/8 Red | SA-WR | H-L | - | X | - | - | X | - | - | R, C |
| | GNP1_140 | 150 | 2.5YR 4/8 Red | SA-WR | H-L | - | X | - | - | X | - | - | R, C |
| 2 | GNP2_10b | 0 | 2.5YR 4/6 Red | SA-WR | H-L | - | X | - | - | X | X | X | R, C |
| | GNP2_0 | 10 | 2.5YR 4/8 Red | SA-WR | H-L | - | X | - | - | X | X | X | R, C |
| | GNP2_10 | 20 | 2.5YR 4/8 Red | SA-WR | H-L | - | X | X | - | X | X | X | R, C |
| | GNP2_20 | 30 | 2.5YR 4/8 Red | SA-WR | H-L | - | X | - | - | X | X | X | R, C |
| | GNP2_30 | 40 | 5YR 6/3 light reddish brown | SA-WR | H-L | x | X | - | - | X | X | X | R, C |
| | GNP2_40 | 50 | 2.5YR 4/6 Red | SA-WR | H-L | x | X | - | - | X | - | - | R, C |

| | | | | | | | | | | | | | |
|---|---|---|---|---|---|---|---|---|---|---|---|---|---|
| | GNP2_50 | 60 | 5YR 6/3 light reddish brown | SA-WR | H-L | x | X | - | - | X | - | - | R, C |
| | GNP2_60 | 70 | 5YR 6/3 light reddish brown | SR-WR | H-L | x | X | X | - | X | - | - | R, C |
| | GNP2_70 | 80 | 5YR 6/3 light reddish brown | SA-WR | H-L | x | X | X | - | X | - | - | R, C |
| | GNP2_80 | 90 | 2.5YR 4/8 Red | SR-WR | H-L | - | X | - | - | X | - | - | R, C |
| | GNP2_90 | 100 | 2.5YR 4/8 Red | SA-WR | H-L | - | X | - | - | X | - | - | R, C |
| | GNP2_100 | 110 | 2.5YR 4/8 Red | SA-WR | H-L | - | X | - | X | X | - | - | R, C |
| | GNP2_110 | 120 | 2.5YR 5/8 Red | SA-WR | H-L | - | X | - | - | X | - | - | R, C |
| | GNP2_120 | 130 | 2.5YR 5/8 Red | SA-WR | H-L | - | X | - | - | X | - | - | R, C |
| | GNP2_130 | 140 | 2.5YR 4/6 Red | SA-WR | H-L | - | X | - | - | X | X | - | I, R, C |
| 3 | GNP3_30b | 0 | 5YR 4/2 Dark reddish grey | SA-R | H-L | X | X | - | - | X | X | - | R, C |
| | GNP3_20b | 10 | 5YR 5/2 Reddish grey | SA-WR | H-L | X | X | - | - | X | - | - | R, C |
| | GNP3_10b | 20 | 5YR 5/3 Reddish brown | SA-WR | M-L | - | X | - | - | X | - | - | R, C |
| | GNP3_0 | 30 | 2.5YR 5/4 Reddish brown | SA-R | M-L | - | X | - | - | X | - | - | R, C |
| | GNP3_10 | 40 | 2.5YR 5/6 Red | SA-R | M-L | - | X | - | - | X | - | - | R, C |
| | GNP3_20 | 50 | 2.5YR 5/6 Red | SA-WR | M-L | - | X | X | - | X | X | - | R, C |
| | GNP3_30 | 60 | 2.5YR 5/8 Red | SA-R | M-L | - | X | X | - | X | X | - | I, R, C |
| | GNP3_40 | 70 | 2.5YR 5/6 Red | SA-R | M-L | - | X | X | - | X | X | - | I, R, C |
| | GNP3_50 | 80 | 2.5YR 4/6 Red | SR-R | M-L | - | X | X | - | X | X | - | I, R, C |
| | GNP3_60 | 90 | 2.5YR 4/6 Red | SA-R | M-L | - | X | X | - | X | X | - | I, R, C |
| | GNP3_70 | 100 | 2.5YR 4/6 Red | SR-R | M-L | - | X | X | - | X | X | - | I, R, C |
| | GNP3_80 | 110 | 2.5YR 5/8 Red | SR-WR | M-L | - | X | X | - | X | X | - | I, R, C |
| | GNP3_90 | 120 | 2.5YR 4/8 Red | SR-R | M-L | - | X | X | - | X | X | - | I, C |
| | GNP3_100 | 130 | 2.5YR 4/8 Red | SR-WR | M-L | - | X | X | - | X | X | - | R, C |

### *3.4.1.1 Pit 3*

Pit 3 comprises 3 units (units 3A-C). Grain size analysis of the 60–80 cm samples could not be completed due to insufficient sample amounts. Sediment colour ranges from 5YR 4/2 to 2.5YR 5/8 and there is a general upward trend of increasing colour value and decreasing chroma, with the 5YR hue limited to the top 25 cm of the profile. Pit 3 grains are dominantly very poorly sorted silty, fine to medium sand (mean range = 70.28–125.6 μm) with a very fine skewed distribution. Modern fine roots are present down to ~55 cm depth, with some 2–5 cm thick tree roots extending throughout the pit.

A palaeosol was documented at the base of pit 3 that extends from ~135 cm to 52 cm depth (unit 3A). The single, simple profile is classified as an Argillisol because of its prominent argillic horizon and abundant illuvial clay features. The profile exhibits an A-Bt-Bw-Cb succession in a red (2.5YR 4/6 - 5/8), very fine sandy matrix (Figure 3.5a). Ped development is fine to medium in size (1–3 cm), mostly angular blocky, becoming sub-angular blocky in the top 8 cm of the preserved A horizon, where bioturbation is also greatest. Distinct pinkish grey (5YR 7/2) rhizohaloes are the dominant morphological features (Figure 3.5a). Rhizoliths (rhizohaloes and root casts) are between 1.0 cm and 2.5 cm in diameter, display first order branching, and extend vertically and sub-vertically 50 cm down the unit profile, through the A and Bt horizons. Some modern overprinting by thin, fibrous roots is also present down to 110 cm depth. Moderately sized burrows (≤1.5 cm diameter; ≤12 cm long) that are predominantly vertical to sub-vertical, and homogenously passively filled with sand from the current or a previously deposited overlying unit were observed in the A-horizon and uppermost 14 cm of the Bt horizon (Figure 3.5b–d). Morphologies include i) unlined, nonbranching, sub-vertical J-shaped burrows, and 2) unlined, branching, horizontal to vertical burrows, tunnels and an apparent relict chamber. Argillic features (void, ped and grain argillans) are in all horizons, excluding the Cb-horizon. Void argillans were limited to the lower 6 cm of the A-horizon, whereas grain argillans (cutans) were found in all horizons, excluding the Cb horizon, and ped argillans were observed within the Bt and Bw horizons. Sub-mm, filamentous Mn-oxides are rare, and limited to the upper 10 cm of the A-horizon (Figure 3.5d). Calcium carbonate accumulations were notably absent. A 2–5 cm clear wavy transition (Retallack et al., 1988, NCoSA, 2009) exists between the palaeosol and the overlying sediments (unit 3B).

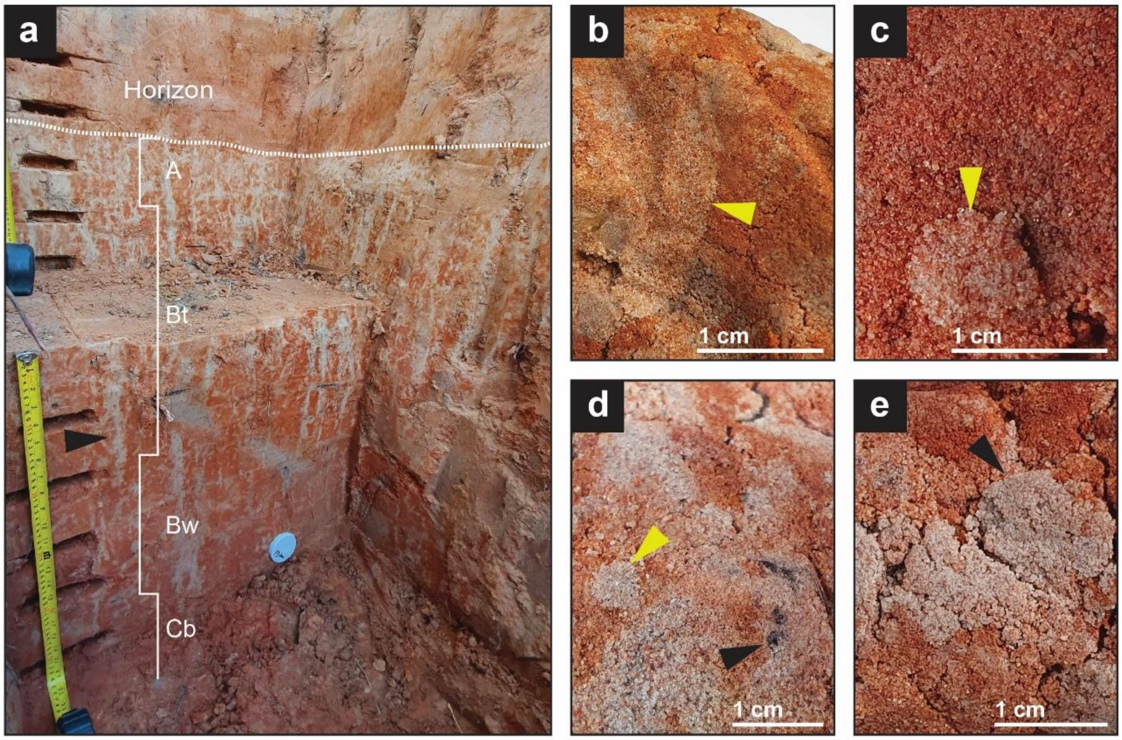


**Figure 3.5.** Palaeosol. Yellow arrows show examples of borrows in vertical (b) and horizontal (c and d) cross section. Black arrows show examples of rhizohaloes (a), mottles (e), and Mn-oxides (d). Note, sample holes on left side of (a) are 10 cm apart for scale.

Although unit 3B and 3C share a similar grain size distribution, there are some notable differences. Unit 3B extends from ~52–25 cm depth and there is an upward gradational sediment colour transition from 2.5YR 5/6 to 5/4. Unit 3C is characterised by modern pedogenic processes including ped development in the top 10 cm of the ~25 cm unit, which is lacking in unit 3B. The peds in unit 3C are coarse (0.5–1.0 cm) crumb, colour in dark reddish grey (5YR 4/2).

#### *3.4.1.2 Pit 2*

Pit 2 comprises six units (units 2A–F). Sediment colour ranges from 5YR 4/2 to 2.5YR 5/8, with 5YR hues limited to units 2C and 2E. Modern millimetre-scale (≤2 mm) roots were very rare down to ~50 cm depth.

A palaeosol at the base of the pit 2 (unit 2A: ~140 cm depth) is comprised of poorly sorted sandy, coarse to very coarse silt (mean = ~12 μm) with a fine skewed distribution. The unit contains multiple pedogenic features, including fine sub-angular blocky peds, void and grain argillans (cutans), and rare filamentous Mn-oxide accumulations on ped planes. Bioturbation is apparent in the form of unfilled sub-mm to 1 mm diameter burrow cavities, pinkish-grey (5YR 7/2) rhizohaloes (2–4 cm in diameter) and rhizocasts (≤1.5 cm diameter) infilled with rounded white to grey quartzose fine to medium sand. The palaeosol has the greatest mud (silt and clay) content (94.3%) compared to all other samples from pit 2. This unit is interpreted as a possible A-horizon, based on bioturbation evidence and fine ped development. Further classification is beyond our scope given only a 10 cm interval of the palaeosol was observed, with the remainder, if present, buried.

A clear transition (2–5 cm; Retallack et al., 1988, NCoSA, 2009) exists between the palaeosol and the overlying 52 cm thick sediments (unit 2B). Unit 2B is predominantly poorly to very poorly sorted silty, fine to medium sand with a very fine skewed distribution, although at 100 cm depth there is an increase (decrease) in the silt (sand) component that exhibits a coarse skewed distribution (mean range = 7.8–183.5 μm). Rhizohaloes span unit 2B as semi-vertical to vertical large-diameter (~3–5 cm) tree root mineral depletions distinguished as pinkish-grey colour (5YR 6/2) variations from the surrounding red sediment matrix (2.5YR 4/8 and 5/8) (Figure 3.5a).

Unit 2B and 2C are separated by an erosional surface and obvious colour change to light reddish brown (5YR 6/3). Unit 2C is ~30 cm thick, laterally continuous, and comprised of very poorly sorted sandy, fine to very coarse silt (mean range = 7.8–14.1 μm). Grain size distributions are symmetrical towards the top and bottom of the unit and fine skewed in the centre (70 cm depth).

Unit 2D is ~12 cm thick. The red sediment colour of 2.5YR 4/6 distinguishes unit 2D from that of the underlying and overlying units (5YR 6/3 light reddish brown). Due to samples being collected at exactly 10 cm increments, grain size data of the red coloured sediment is unavailable. The grain size analysis of the light reddish brown (5YR 6/3) coloured sample taken closest to this unit at 50 cm depth is very poorly sorted sandy, fine to medium silt (mean = 9.5 μm) with a symmetrical skewed distribution. It is considered representative of the top of unit 2C rather than 2D. Field observation of the red coloured sediment of unit 2D showed it is fine to medium grained sand.

Unit 2D is truncated by ~8 cm thick current ripples (unit 2E) that exhibit a combined flow regime (ripple index (RI) = 6.2; ripple symmetry index (RSI) = 1.8) in a northeast direction through the dune breach. These wave ripples are laterally continuous on all sides of the vertical pit profile and were traceable deeper into the dune upon further excavation, although they were not found as far back as pit 1. Unit 2E comprises very poorly sorted sandy, coarse to very coarse silt (mean = 15.3 μm) and has a fine skewed distribution.

Unit 2F extends from ~35 cm depth to the pit surface and has some pedogenic features (peds and calcium carbonate accumulations) that are also found in the underlying wave ripples (unit 2E). Peds in units 2E and 2F are medium to coarse (0.5–2.0 cm) crumb, colour in yellowish red (5YR 4/6). Filamentous calcium carbonate accumulations were confirmed by reaction with 10% HCl. Grain size in unit 2F is dominantly very poorly sorted sandy, very fine to very coarse silt (mean range = 10.1–46.9 μm), except for the very base of the unit that is poorly sorted fine to medium sand (mean = 178.8 μm). Skewness ranges from very fine to symmetrical.

*3.4.1.3 Pit 1*

Pit 1 comprises a single aeolian unit (unit 1A) dominated by poorly-moderately sorted fine sands that exhibit very fine to fine skewed distributions throughout the 150 cm profile. Mean grain size increased slightly down profile (mean range = 147.5 µm to 219.8 µm); however, deviating from this trend, a relatively low mean of 158.7 µm is recorded at 90 cm depth. Average sand and mud compositions are 90.2% and 9.8% throughout the pit, respectively, with more mud recorded in the top 40 cm (11.7% to 16.2%) and at 90 cm (15.3%), and the least mud recorded at 110 cm (5.1%) and 150 cm (5.4%) depths. Sediment colour is somewhat homogenous throughout (2.5YR 4/8 Red), although there was lower chroma at the surface (2.5YR 4/6 Red). Some modern millimetre-scale roots are present down to ~40 cm depth and very rare between 40 cm and 110 cm depth.

3.4.2 Palaeosol Geochemistry and Mineralogy

The palaeosol is composed primarily of quartz (>83%), with minor amounts of clay minerals (<7%), feldspar (<2.4%), and an amorphous component (<6.5%). Trace amounts of plagioclase are also present, excluding the Cb horizon. The clay and amorphous mineral components notably increase in the Bt horizon (Figure 3.6), attributable to illuviation, whereas the quartz component decreases. There is little variation in the K-feldspar and plagioclase mineral content down profile. Clay mineralogy is dominated by kaolinite and illite, with a trace component of smectite (Table 3.2). See Figure S2 for XRD spectra.

Mean elemental composition is dominated by $SiO_2$ (92%), with minor components of $Al_2O_3$ (3.5%) and $Fe_2O_3$ (1.5%). Trace amounts of $K_2O$ (0.5%), MgO (0.3%), $TiO_2$ (0.2%) and CaO (0.1%) are present, with MnO and $Na_2O$ less than 0.1% (Table S1; Appendix B2). $Al_2O_3$, $Fe_2O_3$, $K_2O$ and MgO were greatest in the A and Bt horizons, whereas $SiO_2$ content was highest in the Bw and Cb horizons. The overlying dune material has less $Al_2O_3$, $K_2O$, MgO, $TiO_2$, CaO and $Na_2O$, and more $SiO_2$ relative to the palaeosol. The palaeosol is characterised by high hydrolysis (>2.2) and Mg/Ca (>2.5) values (Figure 3.6). Hydrolysis is greatest in the Bt horizon before decreasing down profile, indicating surface weathering of minerals (e.g., feldspars) to clays and an associated accumulation of Al (Sheldon and Tabor, 2009). CIA values also indicate intense weathering conditions (>80), and a similar pattern to hydrolysis values, with the greatest values observed in the Bt horizon and a decrease down profile. However, this variation is minimal (<1%). The high CIA values also indicate sufficiently wet conditions that would simultaneously lead to the removal of mobile alkalis and alkaline earth elements and prevent the accumulation of calcium carbonate or soluble salts in the profile (e.g., Retallack, 2003; Sheldon and Tabor, 2009; Dal'Bó et al., 2010). Indeed, there was little evidence of calcification (<1.0), salinisation (<0.2), or oxidation (<0.4) down profile (Figure 3.6). Although, oxidation does decrease down profile suggesting what little effect reduction processes had was limited to the uppermost horizons (Dal'Bó et al., 2010).

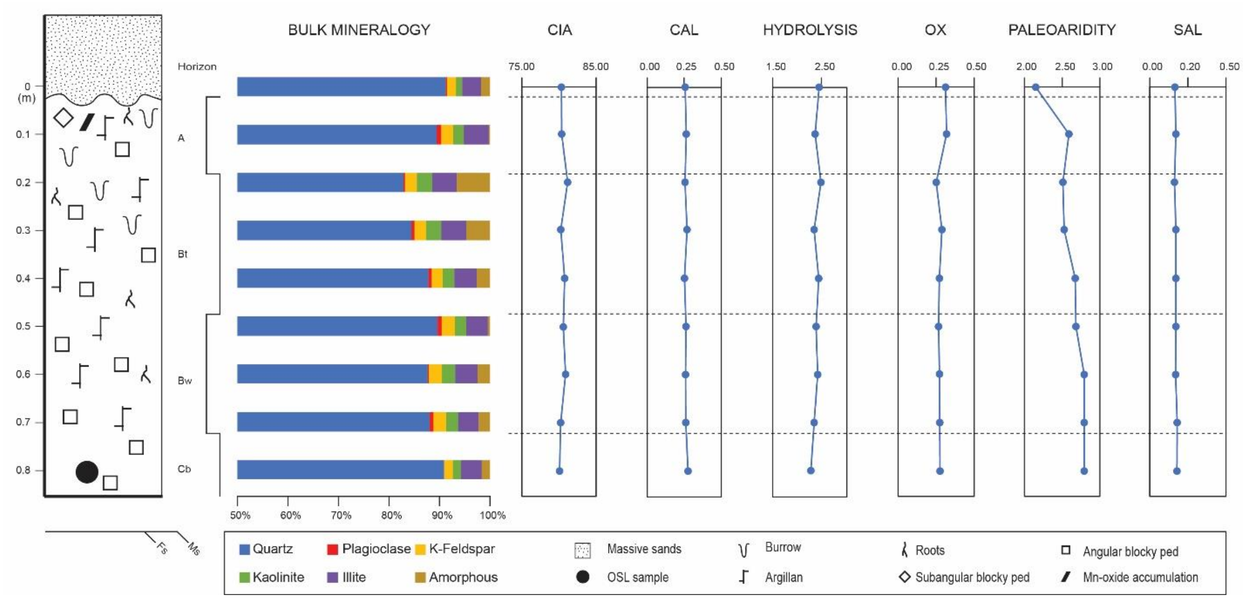


**Figure 3.6.** Detailed measured section, pedogenic features, bulk mineralogy and selected geochemical weathering ratios for the Glenormiston palaeosol. CIA - $[Al_2O_3/(Al_2O_3 + CaO + Na_2O + K_2O)]*100$; Calcification - $(CaO + MgO)/Al_2O_3$; Hydrolysis - $Al_2O_3/ (CaO + MgO + K_2O + Na_2O)$; Oxidation - $Fe_2O_3/Al_2O_3$; Palaeoaridity – $MgO/CaO$; Salinisation - $(K_2O + Na_2O)/Al_2O_3$. Note, bulk mineralogy stacked bar graph x-axis starts at 50% so minor components are easily visible.

**Table 3.2**: Mineral composition of the clay fraction of the Glenormiston palaeosol.

| | | Non-smectites | | |
|---|---|---|---|---|
| Horizon | Depth | Kaolinite | Illite | Smectite |
| Overlying sediment | 0 cm | ++ | ++ | + |
| A | 10 cm | ++ | ++ | + |
| Bt | 20 cm | ++ | ++ | + |
| Bt | 30 cm | ++ | ++ | + |
| Bt | 40 cm | ++ | ++ | + |
| Bw | 50 cm | ++ | ++ | + |
| Bw | 60 cm | ++ | ++ | + |
| Bw | 70 cm | ++ | ++ | + |
| Cb | 80 cm | ++ | ++ | + |

**Note**: Depth of sample is palaeosol profile depth; relative abundances: +++ abundant, ++ major phase, + minor phase, – absent.

### 3.4.3 Single-grain OSL Chronology

The results from six single-grain OSL samples from Glenormiston dune, including equivalent dose, overdispersion and final OSL age determinations, are summarised in Table 3.3 and the corresponding radial plots are displayed in Figure 3.7. Two distinct populations are evident from the OSL samples, including an older group that fall between 54.0 ±3.7 ka and 50.1 ±2.8 ka (n=2) and a very young to modern age group that lies between 188 ±47 years and 96 ±67 years (n=4).

**Table 3.3**. Results of single-grain OSL analysis for Glenormiston pits 2 and 3.

| Sample | Water content (%)[a] | Dose rate (Gy/ka)[b] Beta | Gamma | Cosmic | Total | Grains[c] | $D_e$ (Gy)[d] | Method[e] | Age Model | OD (%)[f] | Age |
|---|---|---|---|---|---|---|---|---|---|---|---|
| GNP2_1 | 5 ± 1 (2) | 0.34 ± 0.01 | 0.22 ± 0.01 | 0.188 | 0.78 ± 0.03 | 66 | 0.08 ± 0.05 | SAR (Q) | CAMul | 120 ± 31 | 96 ± 67 years |
| GNP2_2 | 5 ± 1 (2) | 0.25 ± 0.01 | 0.17 ± 0.01 | 0.186 | 0.64 ± 0.03 | 80 | 0.08 ± 0.01 | SAR (Q) | CAMul | 45 ± 19 | 122 ± 18 years |
| GNP2_3 | 5 ± 1 (2) | 0.28 ± 0.01 | 0.20 ± 0.01 | 0.185 | 0.70 ± 0.03 | 99 | 0.10 ± 0.01 | SAR (Q) | CAMul | 80 ± 18 | 138 ± 21 years |
| GNP2_1.6m | 5 ± 1 (2) | 0.22 ± 0.01 | 0.15 ± 0.01 | 0.183 | 0.59 ± 0.03 | 69 | 0.11 ± 0.03 | SAR (Q) | CAMul | 146 ± 41 | 188 ± 47 years |
| GNP2_2m | 5 ± 1 (2) | 0.22 ± 0.01 | 0.15 ± 0.01 | 0.179 | 0.58 ± 0.03 | 61 | 31.2 ± 1.2 | SAR (Q) | nMAD CAM | 32 ± 4 (23) | 54.0 ± 3.7 ka |
| GNP1_3m | 12 ± 3 (12) | 0.34 ± 0.02 | 0.23 ± 0.01 | 0.156 | 0.76 ± 0.03 | 112 | 38.0 ± 1.2 | SAR (Q) | nMAD CAM | 94 ± 7 (23) | 50.1 ± 2.8 ka |

[a] Water content calculated as the % mass of water per unit of dried sediment measured in the laboratory. Dried dose rates were corrected to the weighted mean (±1σ) water content for age determination.

[b] Measured and calculated dose rates (±1σ). Cosmic-ray dose rate based on longitude, latitude and altitude of site as well as depth and density of current sediment overburden, sediment densities estimated at 1.8 g/cm$^3$.

[c] Number of grains accepted for $D_e$ determinations.

**[d]** Mean ± total (1σ) uncertainty. $D_e$ values were calculated using the un-logged version of the central age model ($CAM_{UL}$) because of negative $D_e$ values in each sample (consistent with zero) (Arnold et al., 2009). nMAD was used to identify statistical outliers (shown as open triangles in the radial plots). The rest (shown as filled circles in the radial plots) are then combined using the weighted mean (CAM).

**[e]** Single aliquot regenerative (SAR) dose for quartz (Q). Note: Grain size was 180–212 µm diameter for all samples.

**[f]** Overdispersion (OD) in $D_e$ values.

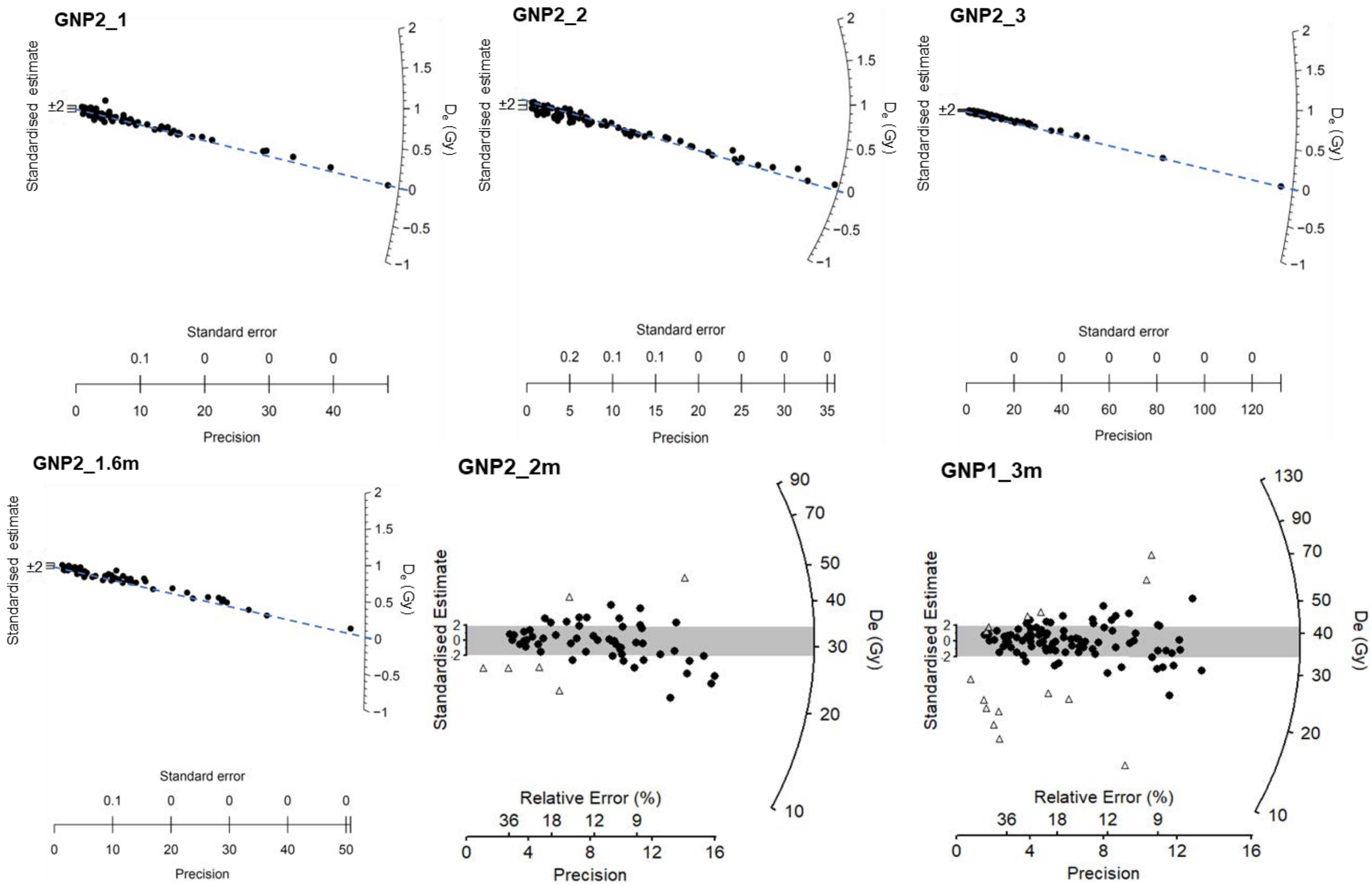


**Figure 3.7.** Radial plots of single-grain $D_e$ distributions for the Glenormiston dune. OSL ages were estimated using the unlogged central age model ($CAM_{UL}$) for samples GNP2_1, GNP2_2, GNP2_3, and GNP2_1.6m. For samples close to zero and that include negative De values (consistent with zero) the radial plots are shown on a linear scale and the blue line is centred on zero. For samples GNP2_2m and GNP1_3m, OSL ages were estimated using the central age model (CAM) after identifying statistical outliers (shown as open triangles in the radial plots) using the normalised median absolute deviation (nMAD) method. The grey bands are centred on the CAM weighted mean De values for each dose population.

For the older single-grain OSL samples, GNP1_3m and GNP2_2m, the normalised median absolute deviation (nMAD) method was used to improve depositional age estimates by identifying and subsequently removing statistical outliers before application of the central age model (CAM). The nMAD-identified outliers comprise 13.4% (GNP1_3m) to 9.8% (GNP2_2m) of the total number of the standardised growth curve (SGC) $D_e$ values. Following the removal of modern or light-exposed grains (e.g., Douka et al., 2014), overdispersion was low (23%) in both samples compared the global average value of 20 ±1% reported for 'ideal' well-bleached and unmixed samples (Arnold and Roberts, 2009).

The four very young to modern age OSL samples have $D_e$ characteristics indicating grains were well bleached before burial with little to no post-depositional sedimentary mixing. Each single-grain OSL sample exhibits minimal scatter around the mean central $D_e$ value (Figure 3.7), and $D_e$ estimates display negative, zero or near-zero values at $\pm 1\sigma$ (range: 0.08 ±0.05 to 0.11 ±0.03 Gy). Application of the unlogged central age model ($CAM_{UL}$) is therefore considered the most suitable method for deriving accurate burial dose estimates for these very young to modern age samples (Arnold et al., 2009). OSL ages are in relative stratigraphic order.

## 3.5 Discussion

### 3.5.1 Sediment characteristics as indicators of past sediment sources and environmental conditions at the time of deposition

Comparing the grain size data from this study with previous results from Australian dunefields, most sediments from the Glenormiston dune are generally less well sorted, more finely skewed, and have higher positive kurtosis values than central Australian dune crests and swales (Figure 3.8a and b). Only five samples fall entirely within the size-sorting envelopes for dune crests (Folk, 1971, Breed and Breed, 1979, Wasson, 1983a, Buckley, 1989), and eleven samples fall within that reported for dune swales (Folk, 1971, Breed and Breed, 1979, Buckley, 1989). Nineteen of the samples analysed in this study are within the mean grain size range reported by (Wasson, 1983a), which covers a broad range of variation, but most samples exhibit poorer sorting. In pit 1, sorting ($\sigma_1$) values decreased with depth (i.e., sorting improved) and shows a significant relationship with decreasing mud (clay and silt) content at the 95% confidence level ($p$ = <0.05; $r^2$ = 0.94); however, this relationship was poor in pits 2 ($r^2$ = 0.3) and 3 ($r^2$ = 0.2).

The high proportion of mud-sized grains in Glenormiston dune may reflect numerous sediment sources, modes of transport and environmental conditions. Across the Gibson and Simpson Deserts, Buckley (1989) found mud-sized grains typically decreased upslope from longitudinal dune swales to crests (4% to <0.5%). The proportion of fines in mid-flank sediments also varied across the Simpson Desert, with less (more) fines found in the south-eastern (north-western) Simpson (maximum = 0.3% and 4.1%, respectively). Dune crests and flanks in the Strzelecki and Tirari Deserts are reported to have up to 10% clay- to silt-sized grains (Fitzsimmons et al., 2009). While we did not measure grain size from the dune swales or crest, the proportion of mud averaged across all pits in the Glenormiston dune is comparatively high at 34 ±29%. Pit 1, located roughly halfway up the dune snout, has the lowest average mud content of 9.8 ±3.1%, dominantly silt (8.6 ±2.8%), which is still over three times greater than in dune flanks (3%) reported by Buckley (1989) and at the upper range reported by Fitzsimmons et al. (2009). This suggests that a high proportion of fines are being deposited on the dune via alluvial or aeolian processes, and/or formed *in situ*.

The biggest variation in the mud fraction is in pit 2, recording between 10.3% and 94.3%. All pit 2 samples with relatively low mud contents (~14 ±4%) exhibit unimodal distributions in the sand-sized fraction that are comparable to the unimodal distributions of the aeolian material in pit 1 and most samples above the palaeosol in pit 3 (Figure 3.4). In comparison, samples from pit 2 with high mud contents (>60%) have trimodal (n=6) or bimodal (n=3) distributions with dominant modal peaks in the silt to very fine sand size fractions. Trimodality has previously been observed in the Strzelecki and Tirari Deserts where the dunes overlie alluvial sediments (Fitzsimmons et al., 2009). This implies that the high mud content and trimodal grain size distributions observed in the Glenormiston dune, particularly in pit 2, likely corresponds with the presence of alluvial fines that occur locally. Alluvial sedimentation on the Glenormiston dune is shown by the presence of wave ripples in pit 2 (unit 2E) (Figure 3.2e). Unit 2C shares similar characteristics with unit 2E including high mud content (84 ±7%), colour (5YR 6/3 light reddish brown), platykurtic distribution, symmetrical- to fine-skewness, very poor sorting, and the presence of sand-sized mud accumulations, indicating unit 2C is also an alluvial deposit.

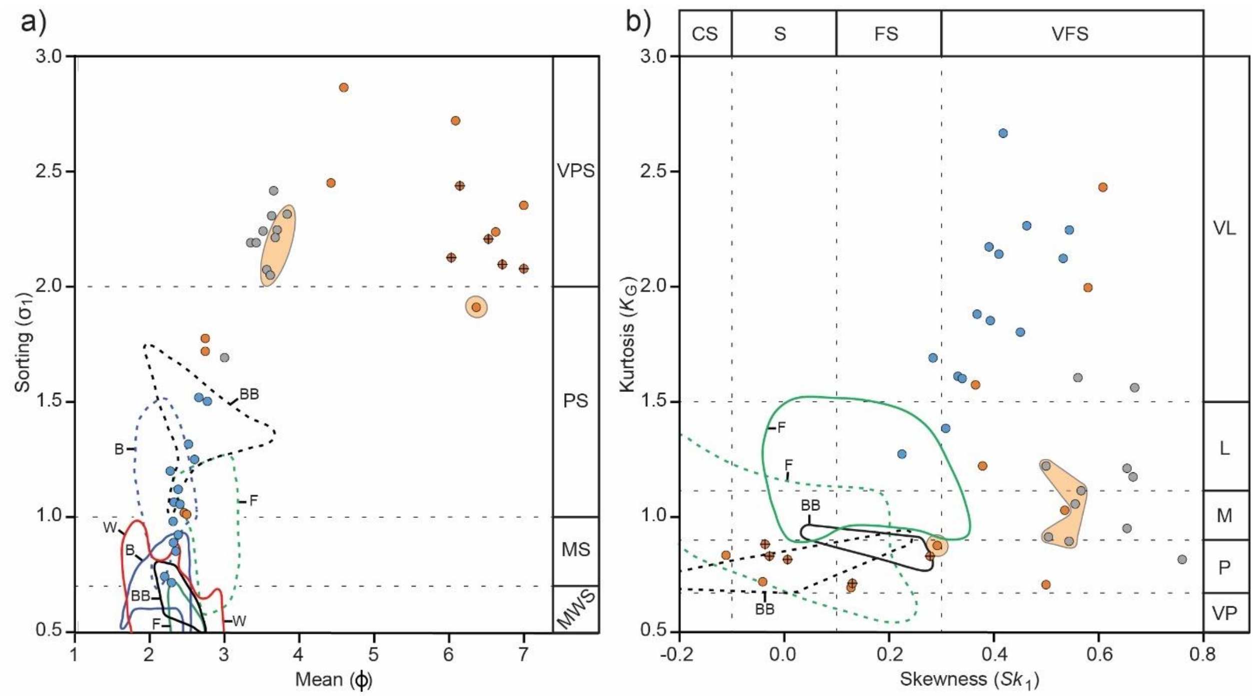


**Figure 3.8.** Bivariant plots of grain size results from Glenormiston dune. Coloured dots correspond to pits 1 (blue), 2 (orange) and 3 (grey). Palaeosol samples are identified within orange polygons. Alluvial deposits are dots with crosses. **a)** Mean grain size ($\phi$) vs. sorting ($\sigma_1$). Sorting y-axis abbreviations: VPS – very poorly sorted; PS – poorly sorted; MS – moderately sorted; MWS – moderately well sorted. Size-sorting envelopes for Australian longitudinal dune-crests (solid lines) and swales (dotted lines): B – Gibson and Simpson Deserts (Buckley, 1989); BB – Strzelecki and Simpson Deserts (Breed and Breed, 1979); F – Simpson Desert (Folk, 1971); W - Strzelecki and Simpson Deserts (Wasson, 1983a). **b)** Skewness ($Sk_1$) vs. Kurtosis ($K_G$). Skewness x-axis abbreviations: CS - coarse skewed; S – symmetrical; FS – fine skewed; VFS – very fine skewed. Kurtosis y-axis abbreviations: VL – very leptokurtic; L – leptokurtic; M – mesokurtic; P – platykurtic; VP – very platykurtic. Skewness-kurtosis envelopes for Australian longitudinal dune-crests (solid lines) and swales (dotted lines): BB – Strzelecki and Simpson Deserts (Breed and Breed, 1979); F – Simpson Desert (Folk, 1971); Note: data from Buckley (1989) is outside our data range, and kurtosis data from Wasson (1983a) is not available.

Mud aggregates were ubiquitous on the adjacent flood plain, and their presence in units 2E and 2C could indicate they were likely transported as stream bedload (e.g., Maroulis and Nanson, 1996, Gibling et al., 1998, Ainsworth et al., 2012) before flow deceleration in an expanded interdune pond and subsequent deposition on the dune snout. The highest clay content of 21% was recorded at 100 cm depth in pit 2, which is below these alluvial deposits (average clay content = 14.7 ±2.1%) and probably reflects an illuviation zone within the underlying dune material, although no intact cutans were found at this depth. The alluvial deposits fall almost entirely within the kurtosis-skewness envelopes for swale sediments analysed by (Folk, 1971) and (Breed and Breed, 1979) (Figure 3.8). The wave ripple sediments (unit 2E) are slightly more positively skewed, falling within the kurtosis-skewness envelope for dune crest sands analysed by Breed and Breed (1979). This can probably be explained by partial mixing with the overlying very-fine skewed aeolian sediments during sampling. Despite this mixing, all the alluvial deposit samples presented in this study fall well outside of the size-sorting envelopes for dune crests and swales for Australian dunefields (Folk, 1971, Breed and Breed, 1979, Wasson, 1983a, Buckley, 1989) (Figure 3.8).

The adjoining clay and silt alluvium flood plains and interdune claypans are ideal environments for the formation of mud aggregates through the variously proposed mechanisms including pedogenesis, vertisol pedogenesis (Butler, 1974, Rust and Nanson, 1989), shrink and swelling of clays (Nanson et al., 1988, Rust and Nanson, 1989), biogenesis (e.g., faecal pellets) (Rust and Nanson, 1986), flocculation (Wasson, 1983a), and the efflorescence of salts in the clay-rich sediments (Bowler, 1973). Pedogenesis on the floodplain is certainly possible considering argillaceous rocks are common in the headwaters of the catchment and that wooded vegetation and grasses are capable of modern soil establishment, particularly on the floodplain margins; however, vertic pedogenic features such as desiccation cracks or slickensides were not found. Indeed, less than 5% of illite and kaolinite were identified in the palaeosol, which supports the likelihood the surrounding alluvium clays also have a low shrink-swell capacity and are poor flocculants. Biogenic formation of mud aggregates is unlikely in this arid zone environment (e.g., Rust and Nanson, 1989). Intrasedimentary gypsum precipitates from the floodplain alluvium starting at ~50 cm depth, indicating a brine concentration in the near-surface water table, and could suggest efflorescence of the clay-rich sediments contributed to the formation of mud aggregates during wetting and drying cycles.

The scarcity of gypsum in the clay-rich Glenormiston dune (Table 3.1), and shorelines of the floodplain, indicates that evaporative gypsum probably does not form in large quantities on the alluvium floodplain surface following inundation and was not subsequently deflated onto the dune. This also reflects that deflationary aridity was probably not so extreme as to cause excavation of the pre-existing floodplain clays down to the underlying intra-sedimentary gypsum. However, recognised late Quaternary arid dune building periods (e.g., Fitzsimmons et al., 2013, Hesse, 2016) were notably absent in the Glenormiston dune's upwind snout, and perhaps gypseous dune deposition occurred but any record of such has since been deflated. It is worth noting that individual dunes may record active growth while others remain stable, and sediment reworking can lead to incomplete records (Hesse, 2016). Although, the presence of palaeosol(s) indicate that this dune has not been completely reworked or deflated (Fitzsimmons et al., 2009). To overcome potential site-specific bias, sampling multiple dunes within the dunefield would enable stratigraphic correlation between profiles and improve the resolution of our palaeoclimatic and palaeoenvironmental reconstructions.

Aeolian deposition of fines was not definitively observed in pits 1-3; however, lee-side excavation of the same linear dune ~400 m to the southeast (Figure 3.1e) revealed isolated low-angle cross bedding features (total thickness = 25 cm) with distinctive whitish coloured (5YR 8/1 white) lamina (Figure 3.2f) comprising sand-sized mud aggregates. Aeolian transportation of silt and clay aggregates is only possible over short-distances (Bowler, 1973) and their accumulation in the dune is therefore considered indicative of a local source (e.g., Maroulis et al., 2007) such as from the floodplain or interdune claypans. Dust raising occurs in LEB due to high climatic variability, aridity, strong winds, and a renewed supply of fines within the endorheic drainage catchment (Bullard and McTainsh, 2003, Hesse and McTainsh, 2003). Glenormiston is located within an active dust entrainment region, the Channel country in southwest Queensland, and is also a beneficiary of the northwest dust pathway. Eluviation of these fines, along with locally sourced mud aggregates that have since disaggregated, could have led to the high mud content in the Glenormiston dune. However, eluviated fines do not appear to uniformly increase towards the base of each pit.

Post-depositional addition of fines could have also formed *in situ* from weathering of feldspars, or surficial deposition of biogenic silica. Feldspars constitute <1% of grains observed in hand samples, and palaeosol XRD results show feldspar concentrations are no greater than 2.6% (average = 2.29 ±0.31%). These feldspar proportions are comparable with previous results from the Strzelecki dunefields that can range from 0.7 to 18% (Wasson, 1983a, Fitzsimmons et al., 2009), which are typically lower (1–7%; Fitzsimmons et al., 2009) when distant from feldspar-rich sources such as the Flinders Ranges or large playa lakes such as Lake Frome. The drainage catchment feeding the Glenormiston dune flood plain comprises feldspar-poor lithologies, except for a small exposure of the feldspathic Sylvester Sandstone located to the southeast, and possible feldspar-bearing dolarenite and limestone at the upwind end of some dunes. Given the arid environment, surficial deposition of biogenic silica likely only contributed trace amounts of clay. Hence, while the *in-situ* weathering of feldspars and surficial deposition of biogenic silica could potentially add to the total clay content, the amount is probably minor compared to input from aeolian dust or locally sourced mud aggregates.

Stratigraphically, the top of the palaeosol in pit 2 (unit 2A, Ab horizon) is equal in elevation to that of the palaeosol in pit 3 (unit 3A, A horizon) (Figure 3.3). An accurate comparison of palaeosol grain size data between pits is difficult as only the bottom 40 cm of the palaeosol in pit 3 could be analysed. The most notable difference in the pit 2 palaeosol sample, however, is the very high mud content (94.3 %), dominantly silt, compared to the palaeosol samples in pit 3 (30.3 ±2.6%). Intact clay cutans were ubiquitous in all palaeosol samples, excluding the Cb horizon, providing strong evidence of clay illuviation, pedogenesis and, by extension, dune stability (Fitzsimmons et al., 2009). Compared to the palaeosol samples from pit 3, the pit 2 palaeosol has the greatest clay content (11.5%) – a possible illuviation zone. Another possibility is the lack of fine to medium sand in the pit 2 palaeosol, a feature we primarily observed in the alluvial sediments higher up in the profile, which could suggest a mud cap was deposited when the flood plain/interdune pond was full and was subsequently subjected to pedogenic processes. Several pedogenic features between pits 2 and 3 are similar including fine, sub-angular blocky peds, sub-mm burrows, root traces as both pinkish rhizohaloes and rhizocasts infilled with grey to clear quartzose sand, void and grain argillans (cutans), and filamentous Mn-oxide accumulations.

### 3.5.2 Palaeosol-based palaeoclimate and palaeoenvironment interpretations

Palaeoprecipitation and palaeotemperature values estimate a subhumid to humid, mesic climate during the late Pleistocene. The MAP values range from 981 ±235 mm/yr to 1344 ±182 mm/yr, based on the ΣBases/Al and CIA-K climofunctions respectively, and a MAT of 14.1 ±4.4 °C was calculated using the salinisation relationship. The MAP values for the Glenormiston palaeosol fall within the 2-σ uncertainty range and are not statistically different. Given the possibility of some inherited weathering signal from the recycled sediment parent material, these values are considered maximum palaeoprecipitation estimates. Nonetheless, the thick Bt horizon, abundant argillic phases and complete lack of calcium carbonate accumulations support a positive moisture balance. Pedogenic carbonates are not found in soils with MAP>1000 mm (Nordt et al., 2006), rather they are typical of soils with MAP<600 mm (Mack et al., 1993); such as the filamentous carbonate accumulations observed in the dune's modern soil that developed under an ~arid climate regime. The increase in illite and kaolinite in the Bt and Bw horizons relative to the Cb horizon and overlying dune material provides further evidence of humidity during formation. While much of the clay is undoubtably detrital and accumulated in these horizons through illuviation, the increase in these minerals also reflects weathering of feldspar minerals within the soil (Sheldon and Tabor, 2009). High hydrolysis values indicate there was ample water available for a relatively high reaction rate of feldspar to illite, with complete K removal resulting in the formation of kaolinite within the profile (Sheldon and Tabor, 2009). The high Mg/Ca value and low K and Na content of the Glenormiston palaeosol also indicate a humid climate (Song, 2005, Krauß et al., 2018, Zou et al., 2021). A lack of vertic features suggests that there was little seasonality during formation (Mack et al., 1993).

The simple profile formed on aeolian sands, representing a period of environment stability (Marriott and Wright, 1993, Kraus, 1999) and increased water availability relative to previous dune building conditions (Bowler, 1976, Fitzsimmons et al., 2009). The very fine–fine quartzose sand parent material contains little mud and likely represents an aeolian desert dune palaeoenvironment. Indeed, the mineralogy of the Cb horizon is almost indistinguishable from that of the overlying dune material (Figure 3.6), which both supports an aeolian dune interpretation and implies an unchanged (probably local) sediment source. Soil formation ceased when sediment accumulation rates exceeded the rate of soil profile development (Marriott and Wright, 1993). Pedogenesis was dominated by clay illuviation, hydrolysis, and cracking around burrows and roots, which formed angular and sub-angular blocky peds (Birkeland, 1984, Retallack et al., 1988). Dark red argillans (cutans) and pink-grey mottled rhizohaloes that lack Fe-oxide accumulation along the boundaries of the Fe depletion suggest it was a well-drained soil environment (e.g., McCarthy and Guy Plint, 1998, Kraus and Hasiotis, 2006, Tabor and Myers, 2015). The deeply penetrating tap roots are also indicative of well-drained conditions (Sarjeant, 1975) and a soil of little strength, which is typical of a porous soil (Whalley et al., 1995), such as one formed on desert sands.

Bioturbation features suggest a woodland or forest dominated the landscape at the time of soil formation. The diameter and depth of the root casts and rhizohaloes, and general lack of fine root traces, are typical of wooded vegetation (Gocke et al., 2014). This is notably different from the modern soil at the dune crest, which formed under more arid conditions and supports a vegetation community dominated by tussocky grasses and open shrubland to woodland (QGlobe, 2024). The modern soil also lacks the deep root penetration and rhizohaloes observed in the palaeosol, supporting that past soil formation occurred under conditions of greater moisture availability and higher biomass productivity. Hydrolysis values >2 (Retallack, 2003) and low LOI values (Cleveland et al., 2008) suggest soil fertility was low, which is unsurprising given the nutrient poor aeolian parent material (Herr et al., 2009). Although, the low LOI values may also reflect a lack of organic preservation because of oxidising conditions in the well-drained soil (Cleveland et al., 2008). Horizontal and vertical branching burrow networks, and chambers in the palaeosol likely represent termites (e.g., Hembree and Hasiotis, 2007, Genise and Genise, 2017) that preferred warm and humid conditions (Genise and Genise, 2017). Today, many subterranean termites found in Queensland forests prefer dead wood for foraging, e.g., *Schedorhinotermes actuosus* and *Heterotermes paradoxus* (Houston et al., 2015), moderate temperatures and high humidity (Evans and Gleeson, 2001). The isolated J-shaped burrows may be the traces of myriapods (such as centipedes) (e.g., Hembree and Bowen, 2017), and although common from deserts to rainforest, most prefer moist settings (Hembree, 2019) such as those found in a humid woodland or forest.

### 3.5.3 Palaeoclimatic and palaeoenvironmental implications – late Pleistocene

The palaeosol OSL age (50.1 ±2.8 ka) is within error of the aeolian material overlying the palaeosol in pit 2 (unit 2B; 54.0 ± 3.7 ka), suggesting dune building still occurred at a time when humid conditions prevailed around late MIS 4 or early MIS 3. The age of the palaeosol at pit 2 is unknown although it is certainly older than the burial age of unit 2B (~54 ka). We assume adequate grain bleaching of unit 2B occurred pre-burial given the sediment is aeolian. To minimise the net effect of pedogenesis and bioturbation introducing younger grains, the palaeosol OSL sample in pit 3 was collected from the least weathered horizon (Cb), in which no macro-traces of bioturbation were observed. The palaeosol OSL sample therefore provides a maximum age constraint on soil formation, and not of sediment deposition (e.g., Fujioka and Chappell, 2010, Ahr et al., 2013). It is not a reliable minimum age indicator as soils form over tens of thousands (or even millions) of years (Retallack, 1983). This also indicates pedogenesis of the palaeosol sediments at pit 3 continued during and/or after aeolian deposition of unit 2B.

Burial of the palaeosol at pit 2 occurred by renewed dune building in late MIS 4 to early MIS 3 (~58–50 ka) that is tied to records of dune activity across central and northern Australia. In the monsoon-influenced Gregory Lakes system in Western Australia, longitudinal dune building over a late-Pleistocene transverse lunette base started around 51 ±9 ka (TL dated) at Kurdu Kudu (Bowler et al., 2001), coeval with our findings of dune building over the palaeosol. Longitudinal dune accumulations are also recorded in Camel Flat basin in the western Simpson Desert at 54.8 ±2.8 ka (TL age; Hollands et al., 2006) and 54 ±4 ka (OSL age; Fujioka et al., 2009). To the west of the LEB, gypseous dune building on the margins of a shallow Lake Amadeus occurred from 60–45 ka (TL age; Chen et al., 1990), although this also reflects an abundance of gypsum deposited in near-shore groundwater seepage zones that was subsequently deflated in dry seasons. Hesse (2016) noted that late Quaternary dunefield activity does not necessarily translate to heightened or widespread aridity and that his compilation of luminescence dune ages suggest Australia experienced spatially variable climates during the last glacial cycle.

A recent analysis of 40 MIS 3 hydroclimate records by Kemp et al. (2019) revealed Australia experienced spatially variable climates from ~57 ka to 49 ka, was predominantly wet from ~49 to 40 ka (~50–45 ka in central and northern Australia), and continental aridity increased for the remainder of MIS 3. Indeed, (Johnson et al., 1999) found that the Australian monsoon was most effective between 65 and 45 ka based on $\delta^{13}C$ values in fossil emu (*Dromaius novaehollandiae*) eggshells from KT-LE in South Australia including modern samples from Glenormiston and Marion Downs in the Georgina catchment. Importantly, evidence of progressive drying in monsoon-influenced regions appears around ~48 ka (Kemp et al., 2019). This corresponds with the last time KT-LE was connected with the Lake Frome-Callabonna-Blanche-Gregory system via the Warrawoocara channel (Cohen et al., 2011; 2015), indicating less (likely perennial) rainfall was received in the LEB's monsoon-fed catchments. The shift to drier conditions after 48 ka corresponds with the end of Heinrich event 5, documented in the Hulu (China) speleothem record (Wang et al., 2001), and reduced monsoon rainfall over Australia caused by the northward retreat of the Intertropical convergence zone. It is therefore possible that the 50.1 ±2.8 ka maximum formation age of the palaeosol described here represents the early MIS 3 wet period that ended in central and northern Australia around ~45 ka in tune with reduced monsoon input in the northern LEB beginning at ~48 ka.

The morphological features, mineralogy and reconstructed MAP and MAT values of the Glenormiston palaeosol show that it developed under substantially wetter and cooler conditions than today. Six possible analogs were identified for comparison of our estimated MAP and MAT values with modern climate data from the IAEA global database (Rozanski et al., 1993). In the northern hemisphere, Hatteras (USA), Pohang (South Korea), Ponta Delgada (Portugal) and Tokyo (Japan) recorded similar climatic conditions (MAP = 1106–1378 mm/yr; MAT = 13.2–16.6 °C; Rozanski et al. (1993). While in the southern hemisphere Huan Fernandez Island (Chile) and Kaitaia (New Zealand) also report a mesic and humid climate (MAP = 1062–1382 mm/yr; MAT = 15.1—15.4 °C; Rozanski et al. (1993). It is interesting to note that each of these locations is latitudinally situated between 33 and 36° (N and S), suggesting that the climate in central Australia during early MIS 3 was much cooler than today. Indeed, our estimated MAT of 14.1 °C is 9.9 °C cooler than the current average annual temperature (24.0 °C). To quantify this change, we calculated the average annual temperature for the four nearest climate stations to the study site at Glenormiston. Urandangi, Boulia, Bedourie and Jervois, located to the north, east, south and west of Glenormiston, recorded long-term average annual temperatures of 24.3 °C, 24.2 °C, 24.3 °C and 22.9 °C (BOM, 2024a), respectively. Importantly, our 9.9 ±4.4 °C temperature reduction during the late Pleistocene is in line with the findings of Miller et al. (1997), in which an average 9 °C depression from at least 45 ka (to ~16 ka) was calculated from amino-acid racemization rate changes in emu eggshells collected from the Australian interior.

The simple profile of the Glenormiston palaeosol suggests it is a well-developed soil that formed during a period of low sediment input that represents many thousands of years (Kraus, 1999). Classification as an Argillisol, or its modern equivalent Ultisol, is also indicative of a mature soil that formed over millennia (Retallack, 1983). The palaeosol climate data therefore represents the average conditions over the life of the soil, which continued after ~50 ka. A change in at least environmental stability (and most likely climate) ultimately resulted in the cessation of pedogenesis, either because of the sediment aggradation or erosion rate exceeding that of soil formation (Marriott and Wright, 1993, Kraus, 1999). An analog of the Glenormiston dune-palaeosol sequence can be found in many Quaternary loess-palaeosol sequences, in which low sediment accumulation rates during palaeosol formation are attributed to humid conditions, and sediment aggradation rates sufficient to overwhelm pedogenesis to form loess deposits are the result of drier climates (Pécsi, 1995, Kraus, 1999).

Our record of a humid, mesic climate quantitatively demonstrates for the first time that monsoon rainfall deeply penetrated northern inland Australia immediately before an inferred reduction in summer-rainfall-dependent $C_4$ grasses across the semi-arid interior (50–45 ka; Miller et al., 2005a; 2016a), and continent-wide megafaunal extinctions (51.2–39.8 ka; Roberts et al., 2001), including *Genyornis newtoni*, an ostrich-sized flightless bird (47.5 ka; Miller et al., 2016b). A major hydrological change also saw the end of the mega-lake KT-LE-Frome-Callabonna-Blanche-Gregory system at around ~48 ka (Cohen et al., 2015; 2022). Cohen et al. (2015) suggests large perennial inflows were needed to maintain this mega-lake status, with KT-LE receiving most of its moisture from its northern catchments, including the Georgina. Several other large lakes in the monsoon north of inland Australia experienced perennial conditions in early MIS 3 including Lake Amadeus Chen et al. (1993), Lake Woods (Bowler et al., 1998) and at Wolfe Creek Crater (Miller et al., 2018). There is a complete lack of seasonality-associated pedogenic features (e.g., vertic features, calcium carbonate accumulations) in the profile of the Glenormiston palaeosol, suggesting that the rainfall was indeed relatively aseasonal and not limited to summer monsoon-driven falls.

### 3.5.4 Palaeoclimatic and palaeoenvironmental implications – historic period

Aeolian deposition of unit 2D at 1881 ±21 Common Era (CE) and unit 2F at 1923 ±67 CE encompasses several dry periods that potentially drove increased aeolian activity and deposition at Glenormiston. Historical droughts during these periods include the Goyder Line Drought (1861–1866), Federation Drought (1895–1902), 1914–1915 drought, World War II Drought (1935–1945), and the 1965–1968 and 1982–1983 droughts (Helman, 2009, Freund et al., 2017, BOM, 2024c) (Figure 3.9). Modelled rainfall reconstructions (Freund et al., 2017) shows the Goyder Line Drought and Federation Drought brought average rainfall to the Monsoonal North and Rangeland natural resource management regions of Australia, defined by CSIRO and Meteorology (2015). In the Georgina catchment, however, rainfall deciles were very much below average, extending to some of the lowest on record during the Federation drought (at least in 1900 and 1902), and the 1914–1915, 1965–1968 and 1982–1983 droughts (BOM, 2024d), the latter being one of Australia's most severe droughts in the 20$^{th}$ century (BOM, 2024c). The World

War II Drought caused dust storm activity between 1944 and 1945 in south Australia (Cattle, 2016), northern Victoria and southern New South Wales, but intermittent wet years in the Georgina catchment (1936, 1939, 1940, 1941 and 1944; BOM, 2024d) resulted in average rainfall deciles over this 10-year period. Overall, the central OSL ages of aeolian deposition at 1881±21 CE and 1923 ±67 CE do not fall precisely within recorded drought periods, but given the 1σ uncertainty range, deposition may have occurred closer to one or more drought phases. Interestingly, Fitzsimmons et al. (2013) identified dune activity at 0.1 ka in a small (non-significant) proportion of desert dunes throughout Australia using a finite mixture model (Roberts et al., 2000) and highlighted historical dune building may be influenced by natural climate change or land use practices.

Dune building around 1923 CE roughly coincides with dunes near Bedourie extending downwind (northwest) some 70–90 m in the decade prior to 1936/37 (Ratcliffe, 1937). Wopfner and Twidale (2001) associated this rapid dune advancement with the height of the Australian rabbit plagues in the 1920's and 1930's. While the denudation effect of rabbits (and livestock) causing localised dune building is unknown in this area, high rates of vertical sediment accumulation were recorded on the dune (0.36 cm/year) coincident with the arrival of cattle since the establishment of the Glenormiston station in 1877 (Pearson and Lennon, 2010). For comparison, most longitudinal dunes in Australia accumulate vertically at 1–10 cm/kyr over $10^3$–$10^4$ yrs, although can be more rapid at >1 m/kyr over $10^3$ yrs (Hesse, 2016). However, Ratcliffe (1937) highlighted that drought, rather than grazing pressure or rabbits, is the governing cause of reducing dune vegetation. Therefore, it may be possible to constrain the onset of this dune building phase closer to the underlying alluvial deposit (unit 2E). Given the wave ripples (unit 2E) are well preserved, it is inferred that aeolian burial was probably rapid. The OSL age of 1897 ±18 CE suggests deposition likely occurred in the late 19th century, with the 1σ uncertainty range (1879–1915 CE) overlapping with the Federation drought (1895–1902) and the 1914–1915 drought. Perhaps, prolonged drought coupled with intense European-induced pressures (such as grazing and pests) decreased vegetation cover and increased the size and distribution of localised bare patches causing the observed rapid dune building at Glenormiston, and in other dunes across Australia (Fitzsimmons et al., 2013).

Another possibility is dune building at Glenormiston in the historical period (last 200 years) may reflect aeolian reworking of locally sourced sands independent of drought or land use influences. Vegetation acts to stabilise dunes, interdune flats and floodplains, which can limit erosion of these substrates and the availability of sediment for subsequent aeolian dune building (Al-Masrahy and Mountney, 2015). Under the current climate regime, vegetation cover on the Glenormiston dune is ~30%, which would reduce the sand transport rate by up to 99.3% based on the experimental quantification by (Buckley, 1987) of plant cover on dune sand transport when winds reach 10 m/s. However, desert vegetation cover has a tendency to be distributed among bare patches (Kéfi et al., 2007, Scanlon et al., 2007), and localised dune activity can still occur despite a vegetated landscape. Using an empirical equation for the threshold of dune mobilisation ($M$), outlined by Ash and Wasson (1983), the ratio between actual and potential evapotranspiration ($E_a$ / $E_p$; a vegetation cover proxy) at Glenormiston (0.2) is nearly triple that of the Simpson Desert (0.07; Ash and Wasson, 1983), and days with sand moving winds ($P$) only occur 8.6% of the time (Figure 3.10). This shows the Glenormiston dunes are currently not close to the threshold for reactivation, and long-distance transport and delivery of sand to the Glenormiston dunefield, even during drought, is unlikely given the low windiness and high ratio of $E_a$ / $E_p$ (or precipitation / evaporation) in the region. Sand supplied from the upwind dunes, alluvial floodplain, swales, or natural bare patches (e.g., Yizhaq et al., 2009) is considered more likely, although Ash and Wasson (1983) noted considerably higher values in their mobility index is probably required for the saltation of sands sourced from swales than on dunes.

Alluvial deposition on the Glenormiston dune at 1831 ±47 CE corresponds with palaeoflooding in the Georgina catchment and reconstructed rainfall. In the southern Geogina catchment lies a series of three ephemeral lakes including Lake Machattie, Lake Koolivoo and Lake Mipia, with the largest lake, Lake Machattie, filling infrequently and only during large monsoonal inputs mainly in the northern parts of the catchment. A landward dipping overwash deposit in Lake Machattie dated at 1830 ±28 CE (Singleton, 2023 – unpublished data) indicates lake full conditions and highlights that significant rainfall was received in the Georgina catchment around 1830/31. These findings are supported by peak rainfalls reconstructed for the Monsoonal North and Rangland NRM regions (Freund et al., 2017) (Figure 3.9).

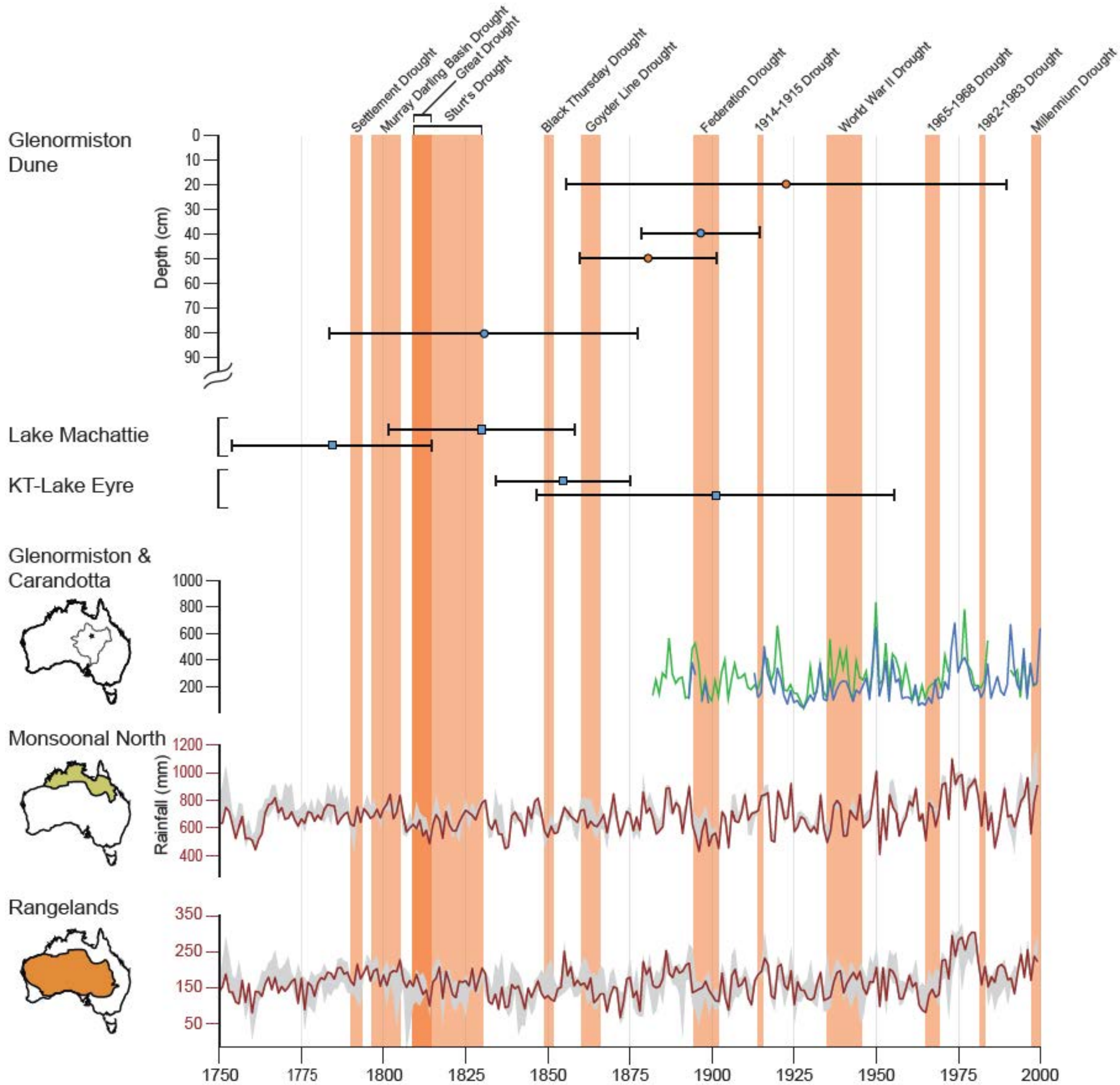


**Figure 3.9.** Glenormiston dune sedimentation (1750–2000 CE) compared to LEB palaeoflood records, modern and reconstructed rainfall, and droughts. Figure descriptions from top to bottom: Orange vertical bars are historical drought records, and the darker orange bar is where droughts overlap. Glenormiston dune OSL dates for the very young to modern periods of dune building (orange dots) and alluvial sedimentation (blue dots). LEB palaeoflood records (blue squares) from Lake Machattie in the Georgina catchment (Singleton, 2024 – unpublished data) and Williams Point in KT-LE (Cohen et al., 2018). The black error bars represent the ±1σ uncertainty range. Given these uncertainties, deposition events cannot be assigned to specific years but

instead indicate approximate time windows that overlap with multiple recorded drought and flood periods. Modern rainfall records sourced from the Australian Bureau of Meteorology (http://www.bom.gov.au/) for Glenormiston Station (blue line, station ID: 38010) and Carandotta Station (green line, station ID: 037011), with the star within LEB on inset image showing their approximate location. Modelled rainfall reconstructions by Freund et al. (2017) for warm seasons (October–March; red lines) in the Monsoonal North and Rangelands natural resource management regions (inset images bottom left), defined by CSIRO and Meteorology (2015), with grey shading indicating uncertainty estimates for the data spread.

Connections between rainfall in the Burdekin catchment, located in northeast Queensland (Figure 3.1b), coeval with rainfall received in central Queensland has been previously demonstrated by Lough (1991). Reconstructed proxy rainfall data for the Burdekin River (Lough et al., 2015) indicates there was a 30-year period of minimal river flows that ended with a large Burdekin discharge in 1831. The 1831 ±47 CE alluvial deposit in the Glenormiston dune is also within error of a pluvial record in KT-LE at 1854 ±21 CE (Cohen et al., 2018), although these authors suggested this KT-LE filling was probably tied to 1870, based on the large Burdekin River discharge reconstructed by Lough et al. (2015). A Burdekin River flow in 1801, that was larger than 1831 but smaller than in 1870, also falls within error of the 1831 ±47 CE deposit at Glenormiston. However, reconstructed rainfall for the Monsoonal North NRM region was lower in 1801 compared to both 1831 and 1870, and 1831 saw higher rainfalls in the Rangelands NRM region (Figure 3.9). Based on the evidence presented here, we interpret alluvial deposition of unit 2C on the Glenormiston dune to be in 1830/31.

In 1897, below average rainfall (86 mm) was recorded at Glenormiston suggesting deposition of the wave ripples (unit 2E) at the OSL central age of 1897 CE is unlikely. Rainfall data is available from the Australian Bureau of Meteorology (http://www.bom.gov.au/) for Glenormiston from 1893–1901 and again from 1913 onwards, and Carandotta station (Figure 3.1a), located ~100 km farther north in the Georgina catchment, provides a long-term record starting in 1882. Several heavy rainfall events were recorded within the OSL age range (1879–1915), including 1885, 1887, and 1894/95. In February 1885, the Brisbane Courier Newspaper reported anecdotally that the Georgina and Diamantina Rivers were in flood, with between 305 and 432 mm of rain falling at Glenormiston station (Brisbane Courier, 1885); although there is no official rainfall data available. However, only 298 mm was recorded at Carandotta in 1885, nearly half that in 1887, during which 563 mm of rain fell, with large (~12.5 $km^3$) inflows to KT-LE also modelled by Kotwicki and Isdale (1991). Unfortunately, rainfall data at Glenormiston is not available for corroboration of this event. At both Glenormiston and Carandotta stations, heavy rainfalls in 1894 (374 and 483 mm, respectively) and 1895 (287 and 524 mm, respectively) far exceeded that of 1897, and we interpret the wave ripples dated to 1897 ±18 CE were most likely deposited in 1894/95. Modelled annual inflows to KT-LE (Kotwicki and Isdale, 1991) also show a large input in 1894 (~14 $km^3$), which shows rainfall in the Georgina catchment potentially contributed to the Diamantina River flow and this KT-LE filling event. Another possibility is deposition in 1906/07 in tune with modelled high inflows at KT-LE (~10 $km^3$; Kotwicki and Isdale, 1991) and a beach facies shoreline deposit at Williams Point that Cohen et al. (2018) dated at 1901 ±55 CE, but interpreted deposition likely occurred in 1906/1907. It is unknown if waters from the Georgina River reached the Diamantina River or KT-LE during this filling event; however, it is less likely the wave ripples were deposited on the Glenormiston dune in 1906/1907 as rainfalls recorded at Carandotta were lower than in 1894/95 (Figure 3.9). While several large rainfall events were recorded within the OSL age range, unit 2E was likely deposited during 1894/95 when flooding was occurring in an already saturated catchment and represents the largest rainfall event closest to the central OSL age. Deposition in 1894/95 is coincident with large flood plumes in the Great Barrier Reef from the Burdekin River, which shares a headwater divide with the Cooper catchment, suggesting that it was wet from central Australia to the East coast and that all three northern catchments of the LEB were likely active.

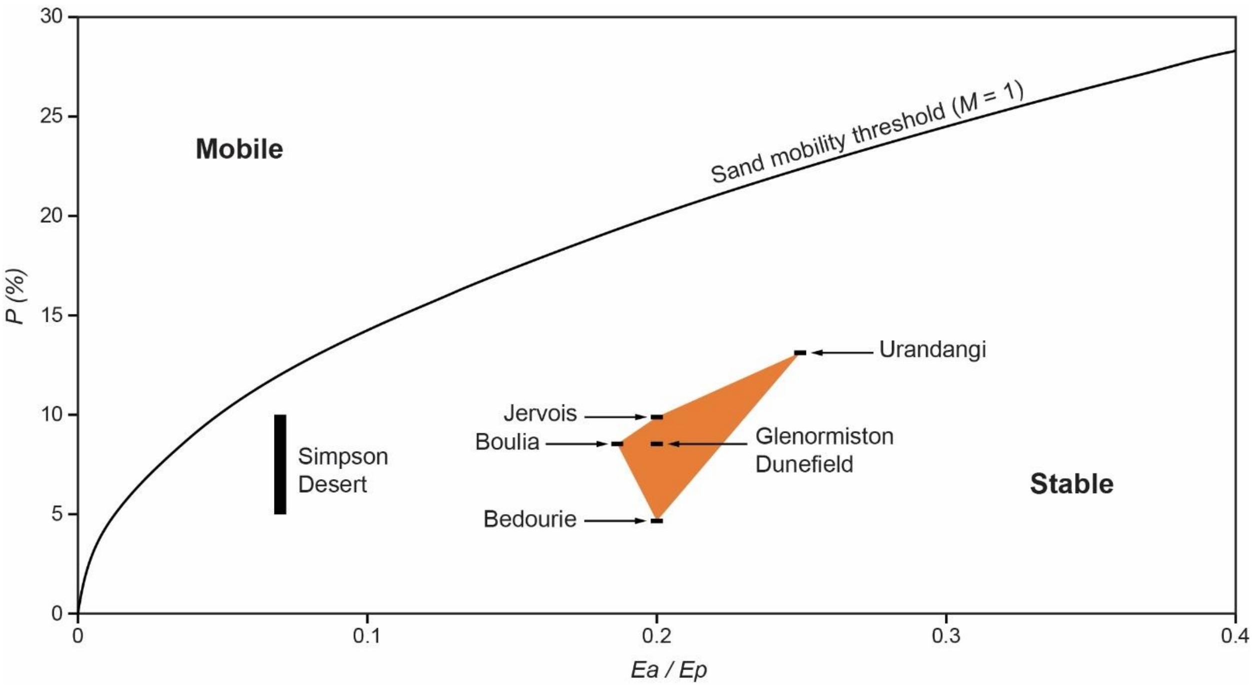


**Figure 3.10.** Sand mobility threshold (after Ash and Wasson, 1983) index ($M$) is defined as $M$ = 5X10-4$(P)^2$ / ($E_a$ / $E_p$), where $P$ is the percentage of days per year sufficient for sand movement (>8 m/s) calculated as $P$ = 0.76Xmean wind speed at surface, and $E_a$ and $E_p$ denote the actual and potential evapotranspiration, respectively. Sand mobility occurs when M >1. The ratio $E_a$ / $E_p$ for Glenormiston and surrounding weather stations (Bedourie, Boulia, Jervois and Urandangi; Figure 3.1a) are based on the standard 30-year averages from 1961 to 1990 (BOM, 2024b) and long-term 3pm wind speed data from each station (excluding Glenormiston as wind is not recorded), and for the Simpson Desert (0.07) sourced from Ash and Wasson (1983). Note, the calculated $P$ for Boulia (8.6%) was used for Glenormiston given its proximity (~100 km apart) and availability of long-term wind speed data (112 years).

### 3.6 Conclusions

Aeolian, fluvial and lacustrine sediment studies over the last fifty years have provided a more detailed understanding of the palaeoclimate and palaeoenvironment in central Australia during the late Quaternary. However, many records are from the southeast of the arid zone and are used to infer climatic changes in the monsoon-watered northern catchments of the LEB. To address this issue, we constructed a chronostratigraphic and palaeoenvironmental record from a longitudinal dune along the northeastern margin of the Simpson Desert, in the Georgina catchment. The dune sediments preserve evidence of environmental stability and enhanced water availability during the late Pleistocene (~50 ka). An unconformity separates the Pleistocene sediments from overlying strata that extends the last ~200 years. In the context of central Australian palaeoclimate data, this study not only supports the concept of a wet early MIS 3, but also provides quantitative evidence for the first time that this monsoon-dominated catchment was experiencing a humid, mesic climate at the same time KT-LE was last in a mega-lake phase. This late Pleistocene palaeosol record is noteworthy not only for its record of a wet phase immediately prior to a period of known megafauna extinctions and hydrologic change, but also because it documented a uniformly wet climate, likely the result of both inland penetration of the summer-monsoon, and aseasonality.

Sediments from the historic period documented aeolian dune accumulation punctuated by two alluvial/fluvial events, which allowed comparison with the limited available modern flood and rainfall data, and direct interpretation of the palaeoenvironment during a period of active dune building. Importantly, the flood record of 1831 preserved in the dune sediment corresponds with a high lake stand at Lake Machattie, in the southern Georgina catchment, and a reconstructed large inflow into KT-LE, indicating that monsoon rainfall penetrated to at least 23 °S and that the entire catchment was active and feeding water south into KT-LE. This record predates modern rainfall data and emphasises the value of sedimentary records as sources of palaeoenvironmental information. In particular, the palaeosols preserved in the desert dunes of inland Australia remain a relatively untapped source of late Quaternary terrestrial palaeoclimate data that could improve our understanding of climate variability through a critical period of megafaunal extinctions, ecosystem change and early human occupation.

# Chapter 4

# Sedimentology and evolution of a modern barrier spit, Lake Machattie, central Australia

Singleton, R.E[a,b*]., Wasson, R.J[a,b]., Jacobs, Z[c,d]., Nott, J[a]., and Bird, M.I[a,b]

[a]College of Science and Engineering, James Cook University, Cairns, QLD 4870, Australia

[b]ARC Centre of Excellence for Australian Biodiversity and Heritage, James Cook University, Cairns, QLD 4870, Australia

[c]ARC Centre of Excellence for Australian Biodiversity and Heritage, University of Wollongong, Wollongong, NSW, Australia

[d]Centre for Archaeological Science, School of Earth and Environmental Sciences, University of Wollongong, Wollongong, NSW, Australia

**In preparation for submission**

**Author contributions**

Russell Singleton collected and processed the samples, analysed and interpreted the sedimentological and spatial data, and imagery, developed the research question and wrote the manuscript. Michael Bird provided funding for the project through the ARC grant. Zenobia Jacobs completed the OSL analyses and the associated data reduction. Michael Brand provided field assistance. All authors provided editorial assistance.

## 4.1 Introduction

Rainfall in the northern regions of Australia's Lake Eyre Basin (LEB) varies between dry states and extreme pluvials, although whether palaeo-wet periods were established across all the monsoon-fed LEB catchments at the same time is less clear. Interpreting the hydroclimate evolution of the LEB has relied heavily upon late Quaternary palaeoenvironmental records from Kati Thanda-Lake Eyre (KT-LE) and the Lake Frome series (Lakes Gregory, Callabonna, Blanche and Frome) (Magee et al., 1995, Magee et al., 2004, Cohen et al., 2015; 2018, Fu et al., 2017, Krapf et al., 2022) and the rivers from the northeast that terminate in these lakes, the Diamantina River (Nanson et al., 1992b, Kershaw and Nanson, 1993) and, in particular, Cooper Creek (Maroulis et al., 2007, Nanson et al., 2008, Cohen et al., 2010). To date, no palaeohydrological records exist for the Georgina catchment, the LEB's most northern and second largest river catchment.

Few multi-century palaeoprecipitation reconstructions exist from within the LEB (Cohen et al., 2018) because of a lack of terrestrial records that can unambiguously be related to precipitation and/or fluvial activity. Indeed, most palaeorainfall records for recent centuries are derived from proxies located outside the LEB nearer to the continental margin, such as dendroclimatological precipitation models (Palmer et al., 2015, Cook et al., 2016, Freund et al., 2017), speleothem records (Denniston et al., 2015, Denniston et al., 2016) and coral luminescence rainfall reconstructions (Lough, 1991, Lough et al., 2015). Shoreline deposits in dryland playa (ephemeral) lakes reflect extreme rainfall in terrestrial settings, previous lake levels (Magee et al., 1995, Magee, 1997, Magee and Miller, 1998, Nanson et al., 1998), sediment flux (Mann and Amos, 2022), flood frequency and magnitude (Kotwicki, 1986), phases of transgression, still stand or regression (Magee and Miller, 1998, Cohen et al., 2022) and, in the case of large drainage catchments that comprise the LEB, spatial and temporal variations in climate patterns (Cohen et al., 2012a; 2012b; 2022). Sedimentary sequences exposed along dryland lake margins in the Georgina catchment likely contain lacustrine and shoreline deposits that record key palaeoenvironmental shifts within the LEB in the recent past.

Recent work by Cohen et al. (2022) using trace element provenance studies of sediments from a shoreline deposit at Williams Point in KT-LE, confirmed the main sources of sediment (and water) that reached KT-LE since the penultimate glaciation derived from Cooper Creek and the Diamantina River (in particular). However, the Cohen et al. (2022) study only used two sample locations from the lowest reaches of the Georgina River catchment, northwest of Birdsville, and trace element provenance was not differentiated between the Diamantina and Georgina catchments given KT-LE input occurs via the same drainage system, the Georgina-Diamantina-Warburton River. While the headwaters of Cooper Creek and the Diamantina River share similar latitudes in the LEB's northeast near the western Pacific (Coral Sea), the Georgina River drains the central northern LEB with headwaters closer to the Gulf of Carpentaria (Figure 4.1a). Palaeoshoreline research (Cohen et al., 2018) suggests there were at least 5 (possibly 7) major KT-LE fillings since the 1600's that were comparable to the modern maximum lake fillings in 1974 and 1949/1950. There is some evidence that these fillings corresponded with enhanced fluvial activity in the Burdekin River, which shares a headwater divide with Cooper Creek but drains eastward to the Great Barrier Reef (Figure 4.1b). This suggests input to KT-LE likely occurred via the Cooper and Diamantina (Cohen et al., 2018), but it is not known whether the Georgina was also fluvially active or contributed to these palaeo fillings. Thus, it is not clear as to what role the Georgina River directly played in KT-LE fillings over recent centennial or millennial time scales.

The temporal and spatial variability of modern precipitation patterns across the LEB may not be comparable with palaeo-precipitation or climate patterns on centennial time scales. In recent decades, northern regions of Australia have received increased summer rainfall. From the mid- to late-20$^{th}$ century, Freund et al. (2017) identified a marked upward trend in summer (October–March) rainfall across the entire monsoonal north and wet tropics regions compared to previous centuries, based on 185 individual palaeoclimate records dating back to 1200 Common Era (CE). Indeed, increased rainfall variability in northern Australia led to some of the more extreme Burdekin flows since the 1950's. Freund et al. (2017) and other studies (Cai et al., 2001, Hendy et al., 2003) primarily attributed this trend to monsoon strengthening associated with El Niño Southern Oscillation (ENSO) conditions in the western Pacific, although a combination of other climate drivers likely played a role (Wardle and Smith, 2004, Taschetto and England, 2009, Feng et al., 2013). This marked shift in climate conditions highlights the importance of sedimentary deposits in the northern LEB as crucial archives of long-term palaeoclimatic and palaeoenvironment transformation.

Understanding the complex interplay of regional and global climate drivers behind extreme pluvials in the largest drainage catchment in Australia, therefore, remains an important challenge to Quaternary palaeoclimatic reconstructions. Indeed, the paucity of high-resolution terrestrial climate records from central Australia has been identified as a knowledge gap (Reeves et al., 2013, Neukom et al., 2014) that impedes our understanding of past moisture regimes, with southwest Queensland flagged not only as an area of poor data, but as an area of non-existent data worthy of investigation (Reeves et al., 2013).

This study examines the shoreline features of Lake Machattie, a dryland playa lake located in the southern reaches of the Georgina River, to reconstruct the palaeoenvironment of the northern LEB at the time of their deposition. Lake Machattie receives infrequent ephemeral floodwaters during the Austral summer months and exhibits large-scale littoral sedimentary features in the form of shore-parallel barrier spits. Inundation of the lacustrine barriers occurs infrequently and only during the largest lake fillings. As such, they represent a key stratigraphic location within the Georgina catchment, providing an important modern-palaeo-hydrological archive of flooding in the most northern LEB and, more broadly, of hydroclimate variability across northern Australia. Sedimentology is combined with spatial analysis of satellite and aerial imagery to determine lake-level boundary variation and develop a record of historical fillings at Lake Machattie. The findings are also used to clarify the spatial and temporal variation in late Quaternary climate and flood patterns in the region.

## 4.2 Background

The Georgina River catchment extends through two climate zones from northwest of the semi-arid Mt Isa region at ~19°S to the arid Diamantina River confluence, Goyder's lagoon, at ~27°S. The Georgina River feeds Eyre Creek, starting around Marion Downs, and continues southward via a network of anastomosing channels and anabranches that feed into the Pallico Channel and King Creek. From the confluence of Eyre Creek and King Creek (Figure 4.1c), southward flows occur via Eyre Creek that feeds three lakes: Lake Machattie, Lake Koolivoo, and Lake Mipia. Together, these lakes and surrounding floodplains (~900 $km^2$), represent the last major depocenter of the Georgina River before travelling west, as Eyre Creek, then south through Simpson Desert interdunes to join the Diamantina River, eventually reaching KT-LE (Figure 4.1c).

In Lake Machattie, two conspicuous sedimentary features are located along the nearly 23 km long northern (downwind) shoreline. In the northeast, a ~5 km long and ~40 m wide barrier spit emerges in a northwest direction from a dune-covered headland. To the northwest, an ~4.8 km long barrier spit emerges about halfway along the northern crescent-shaped lake margin exhibiting westward progradation with a characteristic narrowing from the spit apex (~40 m wide) and neck to the gently hooked terminus (~30 m wide) located further west. Together, these shore-parallel barriers show longshore drift is from east to west at lake high stands in tune with modern prevailing south to southwest winds. During flooding or input from large regional rainfall, the northeast barrier spit typically holds two to three back lagoons between 0.25 and 1.8 km long and 0.06 and 0.23 km wide, while the northwest barrier spit contains one large lagoon ~4.5 km long and 0.25 km wide. The focus of this study is on the northwest barrier spit (Figure 4.1d).

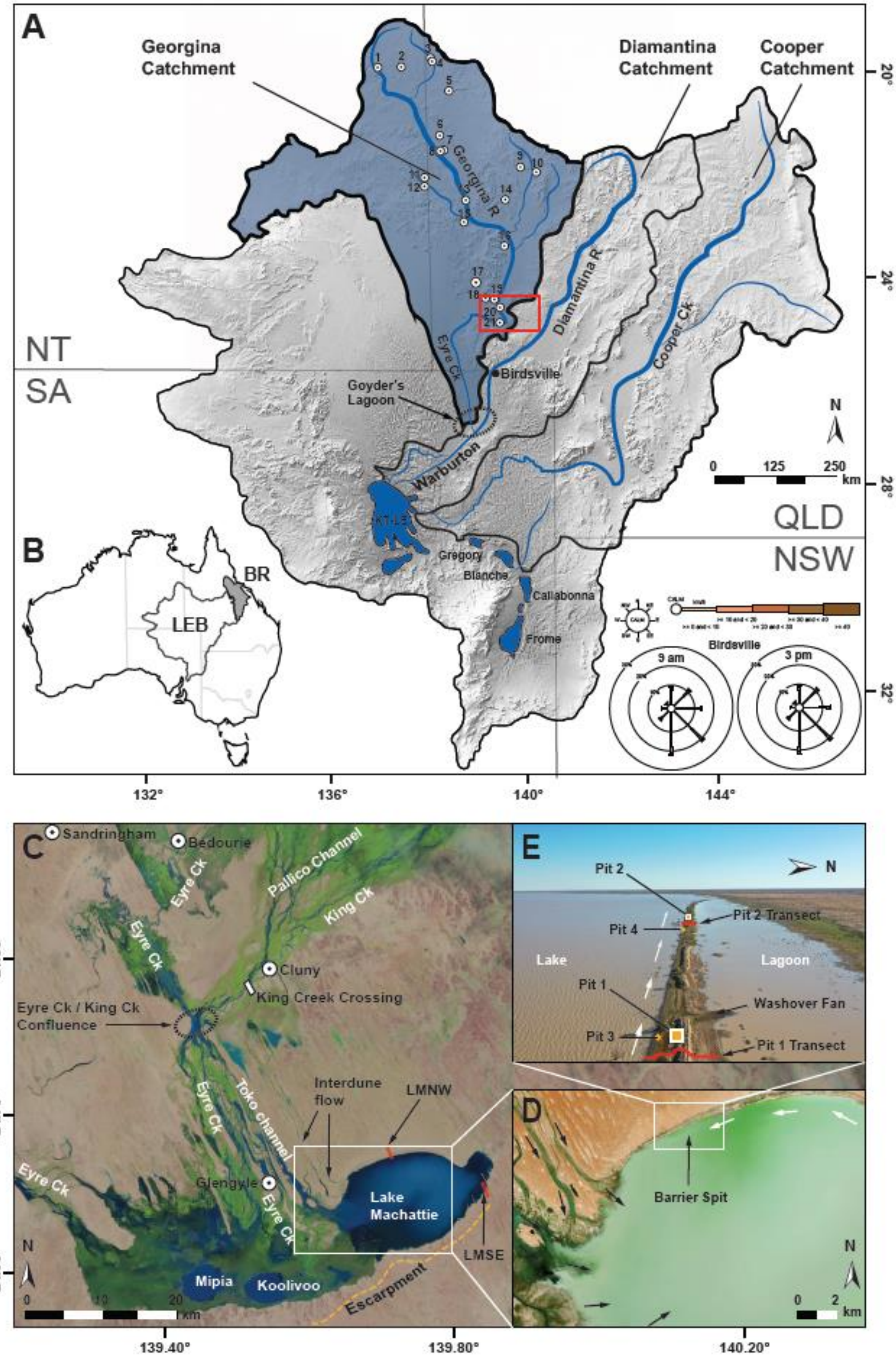

A
Georgina Catchment
Diamantina Catchment
Cooper Catchment
Georgina R
Diamantina R
Cooper Ck
Eyre Ck
Birdsville
Goyder's Lagoon
Warburton
KT-LE
Gregory
Blanche
Callabonna
Frome
NT
SA
QLD
NSW
N
0 125 250 km
Birdsville
9 am
3 pm
20°
24°
28°
32°
132°
136°
140°
144°
B
BR
LEB
C
Sandringham
Bedourie
Eyre Ck
Pallico Channel
King Ck
Cluny
King Creek Crossing
Eyre Ck / King Ck Confluence
Toko channel
Interdune flow
LMNW
Glengyle
Lake Machattie
LMSE
Mipia
Koolivoo
Escarpment
N
0 10 20 km
-24.50°
-24.70°
-24.90°
139.40°
139.80°
140.20°
E
Pit 2
N
Pit 2 Transect
Pit 4
Lake
Lagoon
Pit 1
Washover Fan
Pit 3
Pit 1 Transect
D
Barrier Spit
N
0 2 km

**Figure 4.1.** Locality: **A** Lake Eyre Basin (LEB), with sub-catchments including the Georgina (blue shading), Diamantina and Cooper, and Kati Thanda-Lake Eyre (KT-LE) and the Frome Lake series (Lakes, Gregory, Blanche, Callabonna, and Frome). Georgina and Diamantina confluence at Goyder's lagoon shown in centre of LEB. Red box in Georgina catchment is location of map C. Location of gauging stations referred to in text (numbered circles) and are listed in Table S1 (Appendix C1). Wind roses for Birdsville (038002) shown at 9am and 3pm, annual. **B** Map of Australia, with the endorheic draining LEB. The exorheic draining Burdekin River (BR) catchment shown at headwaters of the Cooper catchment. **C** Map of Lake Machattie Area including flow pathways, Lakes Koolivoo and Mipia and surrounding flood plains. Image: Landsat collection 2 reflective full resolution browse, a 3-band composite showing a "natural" looking (false colour) image. Note the westward flow of Eyre Creek, which eventually reaches Goyder's lagoon and KT-LE. **D** Lake Machattie in flood (Sentinel-2 L2A image, 13/06/2023), with multiple inflow pathways (black arrows) and east to west longshore sediment transport direction (white arrows). **E** Drone image of northwest barrier spit (facing SW), with location of pits 1–4, barrier transects and recent washover fan. White arrows indicate longshore sediment transport direction. Note the calmer lagoon waters compared to the lake.

### 4.2.1 Flood pathways

During smaller floods, input to Lake Machattie occurs from the southwest as Eyre Creek overbank flows and from the west via the Toko channel, an Eyre Creek distributary starting near the confluence of King and Eyre Creek (Figure 4.1c) that terminates at Lake Machattie via a lobate delta. Larger flood discharges form a flood front up to 30 km wide that is carried across the Georgina River microchannel, defined in Croke et al. (2016) and Croke et al. (2017), east of Bedourie causing most or all the floodplain, waterholes and smaller channels including Eyre Creek, the Pallico Channel and King Creek to become submerged. These flood waters reach Lake Machattie from variable pathways. Floodplains and interdunes around Eyre Creek and the Toko channel remain the main flood pathways entering the lake. When flood levels in the Georgina macrochannel are high enough, interdune flows also extend ~28 km southeast from King Creek Crossing near Cluny station (Figure 4.1c) to a lobate or lobate-cuspate delta in the west and northwest of Lake Machattie, respectively. Regional input occurs over an ~980 $km^2$ area (Stein et al., 2011), including the lake surface (263 $km^2$; QGlobe, 2024b), via interdune flows in the north and southeast, and numerous 1–2 km-long ephemeral channels on a ~15 m-high escarpment, located on Lake Machattie's southern margin (Figure 4.1c), marked by small alluvial fans and slope-wash features. As floodwaters recede and low flows are again confined to the Eyre Creek channel that normally flows west into Lakes Koolivoo and Mipia, Lake Machattie becomes a closed system. Lake Machattie fills to reach the shoreline barriers every four years on average and takes around one to two years to become dry.

### 4.2.2 Surface Geology

The surface geology of the Georgina River is dominated by Quaternary and Holocene alluvium (QGlobe, 2024a). The Lake Machattie area floodplains are Quaternary alluvium, while Lakes Machattie, Koolivoo and Mipia are lacustrine and lagoonal deposits of clay, silt, and minor sand. While both Lakes Machattie and Koolivoo, are bordered by Quaternary sandy deposits, only Lake Machattie has formed sandy barriers on its northern margin. Fine to medium quartz dominates the sandplains and claypans of the adjacent dune field north of Lake Machattie. On the lake's southern margin, alluvial fans and slope-wash deposits at the escarpment toe are composed of late Tertiary to Quaternary clayey to sandy gravels, sand and clays. On the upper slopes of the escarpment are channelised labile sandstones, siltstones, and mudstones of the Late Cretaceous Winton Formation. In Lake Machattie's east, Late Tertiary to Quaternary clay, silt, sand, gravel, and colluvium are regularly inundated during moderate to high lake stands.

### 4.2.3 Climate and climatic patterns

The climate in the Georgina catchment is semi-arid; a summer rainfall regime dominates, with the highest average rainfalls up to 700 mm/year occurring in the north and lowest average rainfalls ≤300 mm/year occurring in the south around Lake Machattie. The FAO aridity index (AI: annual rainfall/potential evapotranspiration; Spinoni et al., 2015) was calculated between

0.22 – 0.41 (semi-arid) in the north and 0.07 – 0.14 (arid) in the south (BOM, 2024b). The mean annual temperature is 24–27°C across the catchment, and the mean annual maximum temperature near Lake Machattie is 32°C (Bedourie). Prevailing winds at Lake Machattie are from the south and southeast; the closest weather stations are Bedourie (~50 km northwest; ID: #038000) and Birdsville (~125 km southwest; ID #038002) (Figure 4.1c and a, respectively). Dominant mean annual wind speeds and average Austral wet season (Nov–Apr) wind speeds at Bedourie reach ~9 km/h, with higher monthly averages generally exceeding 11 km/h in spring (BOM, 2024a).

Rainfall in the Georgina catchment is primarily under the control of equatorial climate patterns. Modern precipitation is variable, with wetter years primarily tied to La Niña (positive) phases of the ENSO and associated deeper incursions of enhanced monsoon activity and increased variability in the catchment during the Austral summer (Lough, 1991, Hendy et al., 2003, Freund et al., 2017). Other large scale climate processes can modulate summer rainfall-ENSO teleconnections or increase rainfall totals and variability over northern and eastern parts of Australia, including negative phases of the Interdecadal Pacific Oscillation (IPO) (Power et al., 1999, Vance et al., 2022) and Indian Ocean Dipole (IOD) (Risbey et al., 2009, Ummenhofer et al., 2009) and the eastward propagation of the Madden-Julian Oscillation (MJO) (Cowan et al., 2023). Flood waters that reach Lake Machattie are mainly generated in the north by synoptic-scale tropical cyclones, monsoon depressions, troughs, and onshore circulations (Kotwicki and Allan, 1998, Wheeler et al., 2009).

#### *4.2.3.1 IPO*

The IPO, the Pacific-wide sea surface temperature anomaly, is characterised by positive and negative phases operating on low-frequency timescales (~15–35 years) (Power et al., 1999, Folland et al., 2002). Positive IPO phases include 1924–1944 and 1977–1998 following Henley et al. (2015), which engender El Niño-like Pacific Ocean conditions through warm Western tropical Pacific SSTs and associated eastward shift of maximum convection, leading to weakened ENSO-rainfall teleconnections over northern and eastern parts of Australia (Power et al., 1999). Negative IPO phases co-vary with the "cool" phases of the northern Pacific Decadal Oscillation (PDO) (Mantua and Hare, 2002), with the associated cool SSTs in the eastern equatorial Pacific strengthening the Pacific Walker Circulation with the major ascending branch of convection shifting westward towards Australia. Under negative IPO, the La Niña-like Pacific Ocean sea surface temperature anomalies (Vance et al., 2015) engender stronger Austral monsoon teleconnections with ENSO (Cai and Van Rensch, 2012, Heidemann et al., 2022, Heidemann et al., 2023), increased summer monsoon rainfall variability (Power et al., 1999, Mantua and Hare, 2002, Heidemann et al., 2023), particularly over eastern Australia (e.g. Verdon et al., 2004, Cai and Van Rensch, 2012), and conditions more conducive for La Niña development (Mantua and Hare, 2002) as well as western Pacific and Coral Sea cyclogenesis (Grant and Walsh, 2001, Magee et al., 2017). Negative IPO phases include 1945–1976, and more recently from 1999–2014 based on the filtered IPO Tripole Index (TPI) by Henley et al. (2015). The current state of the IPO is unclear, although recent data suggests a likely continuation or return of the negative IPO (Lim et al., 2021).

#### *4.2.3.2 MJO*

The MJO is a sub-seasonal (30–60 day), convective pulse of rain and cloud that propagates eastward through equatorial tropic regions of the globe. Wheeler et al. (2009) found that in the December–February (DJF) and March–May (MAM) seasons, active MJO passage through the Real-Time Multivariate MJO (RMM) zones 4, 5 and 6 displayed the greatest statistically significant positive correlations with enhanced rainfall over the Georgina River catchment area. Cowan et al. (2019) and Tsai et al. (2021) showed MJO passage in RMM zone 7 can also influence the monsoon trough and cause increased rainfall in Queensland.

During Austral summer (December to March, DJFM), active phases of the MJO mainly affects rainfall variability in the monsoonal north (Cowan et al., 2023) and directly relates to MJO tropical convective anomalies (Wheeler et al., 2009). In contrast, extratropical and inland regions of Australia, such as the central and southern regions of Queensland, are mainly affected by active MJO-influenced moisture laden low-level northerly winds from tropical regions and from weak low-level cyclonic winds anomalies (Wheeler et al., 2009). Thus, active MJO-convection mainly influences rainfall in the most northern regions of the Georgina catchment, while MJO-influenced low-level (850 hPa) wind anomalies increase the probability of heavy rain in the central and southern regions of the Georgina catchment. Active MJO periods have also been shown to enhance cyclogenesis in the Australian region (e.g. Hall et al., 2001, Leroy and Wheeler, 2008, Wheeler et al., 2009), with the Georgina catchment potentially benefiting from tropical low pressure rainfall inputs derived from tropical cyclones as they track inland and quickly dissipate.

#### *4.2.3.3 IOD*

Australian rainfall variability is influenced by SST anomalies in the Indian Ocean. A coupled ocean-atmosphere mode of variability, the IOD has a biennial tendency and typically reaches peak amplitude around September–November (Li et al., 2003, McKenna et al., 2020). Negative, <-0.4°C, (positive, >0.4°C) IOD phases present as sustained warmer than average SSTs in the tropical south-eastern (western) Indian Ocean and are typically associated with increased (decreased) average winter-spring rainfall in south-eastern and western Australia. Being seasonally phase-locked (Saji et al., 1999), the IOD decays with the onset of the Austral monsoon (Yoo et al., Jourdain et al., 2013), although seasonally dependent thermodynamic air-sea feedbacks counter some of the negative monsoon-IOD interactions (Li et al., 2003). The IOD has a weak impact on Australian monsoon rainfall totals, although negative IOD phases slightly increase the likelihood of an early monsoon onset (Lisonbee and Ribbe, 2021); positive IOD phases delay monsoon onset. The Australian monsoon onset typically occurs in late December in Darwin, defined by the Australian Bureau of Meteorology (http://www.bom.gov.au/) as the reversal of prevailing winds from the southeast to the northwest.

IOD-ENSO modulation occurs primarily through the Walker circulation that connects the Indian and Pacific Oceans, such that negative (positive) IOD phases typically occur with La Niña (El Niño) (Meyers et al., 2007). Previous work by Iskandar et al. (2018) and Lim and Hendon (2017) showed negative IOD conditions can also strengthen La Niña phases of ENSO. Risbey et al. (2009) obtained statistically significant partial IOD-rain correlations in the Georgina catchment area during ENSO and negative IOD interaction, using the Meyers et al. (2007) IOD index, but found no relationship when the effects of ENSO were removed.

## 4.3 Materials and methods

### 4.3.1 Historical Aerial Imagery

Aerial imagery provided the baseline for mapping changes to shoreline sedimentary features including the northwest barrier spit along the northern margin of Lake Machattie. Aerial images were downloaded from Geoscience Australia (GeoAust, 2024a) (Film CABG9; Frame 5054; Run 12; Flight date: 11/10/1957) and from the Queensland Government (QImagery, 2023) (Film CAB7057; Frame 244; Run 7; Flight date: 01/09/1970), which were georeferenced in ArcGIS 10.7.1 with an RMSE of 1.65 m and 2.17 m, respectively. Both images depicted Lake Machattie as dry (Figure S1a and b; Appendix C2). The spatial extent of the barrier spit in 1957 and 1970 were then mapped in ArcGIS and any changes were compared to Landsat satellite imagery over the following 51-year study period.

### 4.3.2 Landsat Imagery

Landsat images were used to evaluate lake water levels capable of interacting with the northwest barrier spit in Lake Machattie between 1972 and 2023. A total of 1307 images of Landsat Collection 2, Tier 1 and Tier 2 surface reflectance data were visually inspected. All images used in this study were generated with Level 1 Precision Terrain Correction (L1TP) before downloading from the United States Geological Survey Global Visualization Viewer (GloVis, 2023). L1TP Tier-1 images are reported as being orthorectified to approximately 12-m, or <1-pixel positional root mean squared error (RMSE), and L1TP Tier-1 and Tier-2 products are comparable as they generally align to <1-pixel for any sensor combination.

From 1972 to 1987, 68 Landsat 1–3 (path/row: p105r077, p104r077; resampled resolution: 60 m) and 93 Landsat 4-5 (path/row: p098r077; resampled resolution: 60 m) Tier 2 Multispectral Scanner (MSS) images were inspected. Peak flood levels and the duration of water-barrier spit interactions and inundations could not be accurately determined from Landsat 1–5 MSS products prior to 1980 due to low numbers of consecutive images and large data gaps in image collections. Notably, no Landsat images of the entire lake area were captured between 1974 and 1977, which coincided with a period of substantial flooding in Channel Country rivers (Rust, 1981, Kotwicki and Allan, 1998) and the largest modern filling of KT-LE in 1974 (Kotwicki, 1986). A small portion of Lake Machattie's southeast was, however, captured by Landsat 1 on February 7, 1974 (via path/row: p104r077), that was used to estimate the lake height at the time the image was taken. The 1974 satellite image is considered the maximum flood height reached at Lake Machattie as the peak discharge at Glengyle station, located 10 km to the west, was recorded just four days earlier on February 3.

From 1987 to 2023, a total of 1146 Tier 1 Landsat 5-9 TM, Enhanced Thematic Mapper Plus (ETM+) and Operational Land Imager (OLI) images with consistent 30 m resolution were visually inspected to precisely monitor peak flood heights, barrier spit interaction and inundation periods. The first TM image of the study area generated with L1TP was captured from Landsat 5 in May 1987. To avoid the effect of Landsat 7's scan-line corrector failure on the extraction of lake boundaries, Landsat 5 images were used after 31st May 2003. The number of Landsat images and the acquisition path/row for each year from 1972 to 2023 are displayed in Figure S2 (Appendix C2).

#### *4.3.2.1 Extraction of lake boundaries from Landsat data*

Lake boundaries were classified based on the Modification of the Normalised Difference Water Index (MNDWI) (Xu, 2006), for Landsat TM, ETM+ and OLI images (1987 to 2013), or the Normalised Difference Water Index (NDWI) (McFeeters, 1996) for Landsat MSS images (1972 to 1986). Both water indices delineate land and water boundaries using the band combination of green with either the mid-infrared (MIR) band, for MNDWI, or near infrared

(NIR), for NDWI. MNDWI is widely used in lake mapping studies (e.g. Hui et al., 2008, Leon and Cohen, 2012) and has been shown to extract water bodies from shadowed areas with greater accuracy than NDWI (e.g. Li et al., 2013, Du et al., 2014, Singh et al.) with the benefit of reducing noise from vegetation and soil while enhancing open-water features.

However, NDWI is still an effective method of extracting water bodies, particularly in non-urban built-up areas, and was used for Landsat MSS images as these products only contain the NIR band. MNDWI and NDWI are calculated using the following equations:

$$MNDWI = [\rho_{GREEN} - \rho_{MIR}]/[\rho_{GREEN} + \rho_{MIR}]$$

$$NDWI = [\rho_{GREEN} - \rho_{NIR}]/[\rho_{GREEN} + \rho_{NIR}]$$

Where $\rho_{GREEN}$, $\rho_{MIR}$, and $\rho_{NIR}$ are the reflectance values of the visible green (GREEN) band, mid-infrared (MIR) band (e.g., Landsat ETM+ band 5), and near infrared (NIR) band (e.g., Landsat MSS band 4), respectively. MNDWI and NDWI images were generated from Landsat products using ArcGIS 10.7.1 for peak lake levels during floods, and for the start and end of water-barrier spit interaction periods over flood transgression-regression cycles. Images were reclassified using a binary raster format in ArcGIS based on Otsu's image thresholding algorithm (Otsu, 1979) using Fiji/ImageJ software (version 2.13.1). These binary maps were then converted to lake boundaries with line shapefile format that were subsequently used to interpolate lake water levels relative to in-field measurements of shoreline topographies taken in 2019.

#### *4.3.2.2 Extraction of nearshore bars from Landsat data*

The general size and postion of nearshore bars were identified using the same methods as the flood lake boundaries to evaluate the potential for these bars as sediment sources to the coastal system. Calculated bar areas could not be established given subaerial exposure area varied depending on lake height at the time of each Landsat observation.

### 4.3.3 Estimation of barrier spit interactions

Lake water interactions with the barrier spit were evaluated for the 1986 to 2023 period using two different approaches. Firstly, the duration between the first and last barrier spit interactions were estimated by observing successive Landsat images over each flood transgression-regression cycle. Interaction was defined using a 1-pixel (30 m) buffer between the barrier spit and the transgressive/regressive wet boundaries (i.e., if the MNDWI-determined wet lake boundary was within a 1-pixel distance of the barrier spit the water was considered interactive). Lake filling occurred rapidly during floods, and first interactions were often missed within Landsat 16-day observation frequencies or within the 8-day offset between different satellites (e.g., between Landsat 5 and 7). Comparatively, regression was slow, and the last water-barrier spit interactions could be estimated more accurately. Hence, temporal errors were applied to interaction and inundation cycles including ±15 days for singular satellite orbits (16-day return frequency = 15 non-observable days) and ±7 days for multi-satellite orbits (8-day offset return frequency= 7 non-observable days).

Secondly, spatial variations of water-barrier spit interactions were assessed using spectral indices extracted from a multi-year frequency inundation map sourced from Geoscience Australia GeoAust (2024b). The frequency inundation data is a composite of each Landsat observation between 1986 to near present (2023) that depicts the presence or absence of water at 30 m intervals (Mueller et al., 2016). Data was extracted in ArcGIS 10.7.1 utilising three shore-parallel transects including at “lakeward”, “central” and “landward” positions on the barrier spit. It is worth noting that while the landward transect captures the presence of water during high lake stands, regional input also fills the lagoon and may cause an overrepresentation in the landward data. In contrast, the lakeward and central transects only identified the presence of water during lake full episodes.

### 4.3.4 Shoreline topography and lake level variations

Elevation data were collected in July 2019 for the reconstruction of modern- and palaeo-flood heights. Elevations were recorded using a Hemisphere S321+ receiver with the L-band

ATLAS Global Navigation Satellite System (GNSS), which has a global sub-decimetre-scale accuracy with a reported twice distance (2D) RMS positional error of 16 cm. Two 30- to 40 m-long transects were taken perpendicular from the lake shore across the barrier pit at pits 1 and 2 (Figure 4.1d). Shoreline to backshore elevation transects were also acquired in Lake Machattie's northwest (LMNW: ~800 m long), adjacent to pit 1, and southeast (LMSE: ~2,000 m long) (Figure 4.1c). Elevations of unit boundaries in pits 1–4 and shoreline features such as the beach ridge, swales and regression berm debris heights were also measured.

A 1-sec Digital Elevation Model (DEM) (Gallant et al., 2011) corresponded poorly with in-field elevation measurements taken across the LMNW transect ($r^2 = 0.26$) and LMSE transect ($r^2 = 0.83$) (Figure S3a and b; Appendix C2), which limited the reliability of interpolating flood heights using DEM contours of the lake. To evaluate the accuracy of interpolating lake water levels from Landsat data, in-field measurements of the water line were taken at LMNW on the same day as a Landsat 8 observation, and at LMSE five days later. These ground truth water levels were then visually compared to the MNDWI-determined lake boundary of the analogous Landsat 8 image. Elevation differences between LMSE and LMNW were also compared for each MNDWI-determined lake boundary using regression analysis, with a p-value $<0.05$ indicating a significant relationship. To evaluate the accuracy of comparing lake elevations between NDWI- and MNDWI-determined lake boundaries, lake boundaries were visually compared using both water indices.

### 4.3.5 Barrier spit investigation

Four pit sites at the northwest margin of Lake Machattie were selected to examine sedimentary units deposited during high lake stands. Two pits were dug at high points on the barrier spit. Pits 1 and 2 were located 1.7 and 2.5 km west of the barrier spit's modern apex. Pits 3 and 4 were excavated into the mantled beach ridge located on the lakeward facing erosion slope near pits 1 and 2, respectively. Bulk samples were taken at pit 1 for grain size analysis including from each stratigraphic unit (excluding unit E) and 7 sub-samples were taken from the largest foreset (unit A). For pits 2, 3 and 4, grain size was evaluated in-field.

### 4.3.6 Geochronology

The chronologies for the Lake Machattie barrier spit are defined by a total of six (6) Optical Stimulated Luminescence (OSL) dates. Five samples were collected from pit 1 and one sample was collected from the underlying Lake Machattie lacustrine sediments. OSL samples were collected at night under dim red-light using 30 cm lengths of 5 cm diameter PVC pipe (n=5) or a black plastic-wrapped bag (n=1). Units in pits 2, 3 and 4 were not dated. OSL dating was conducted by Dr. Zenobia Jacobs at the University of Wollongong, Australia, OSL dating laboratory. Single-grain optically stimulated luminescence measurements of De were collected for all samples. Samples were prepared and measured using methods and equipment outlined in Jacobs et al. (2019) and Forbes et al. (2021). Single quartz grains with diameters of 180–212 µm were measured using the single-aliquot regenerative (SAR) dose procedure (Gailbraith et al., 1999; Murray And Wintle, 2000). Analysis of the resulting De data set was conducted using the functions implemented in the numOSL R-package (Peng et al., 2013). The environmental dose rate consists of the external beta, gamma and cosmic ray dose rates and an internal alpha dose rate. An internal alpha dose rate of $0.03 \pm 0.01$ Gy $kyr^{-1}$ was assumed for all samples. Beta dose rates were measured directly using a Risø GM-25-5 beta-counter following procedures outlined in Bøtter-Jensen, L. and Mejdahl (1988), Guérin et al. (2001) and Jacobs and Roberts, (2015). Gamma dose rates for all samples were calculated using estimates of U, Th and K from inductively coupled plasma mass spectroscopy (ICP-MS) and inductively coupled plasma optical emission spectroscopy (ICP-OES). Cosmic-ray dose rate was based on the longitude, latitude and altitude of the study site as well as the depth and density of current sediment overburden. An average sediment density of 1.8 g/$cm^3$ was used. The dose rates were corrected for water content measured in the lab.

### 4.3.7 Particle size analysis

Samples were treated with 2.0 M HCl to remove carbonates then 30 % $H_2O_2$ (three times) to remove organic matter (Konert and Vandenberghe, 1997). Particle size analysis was performed using a set of stacked sieves at 1 phi intervals for >2000 µm and a Malvern

Mastersizer 3000 for <2000 μm. Samples <2000 μm were pre-treated with a 10 % sodium hexametaphosphate solution before laser analysis conducted at the University of Queensland, Central Analytical Research Facility. Statistical particle-size parameters including mean and sorting were analysed using the particle size distribution and statistics package, GRADISTAT (Blott and Pye, 2001). Additionally, the $10^{th}$ (D10), $50^{th}$ (D50), and $90^{th}$ (D90) percentile particle size data were extracted and used to calculate the dimensionless sorting index (SPAN), defined as [D90-D10]/D50] by Foster et al. (2008).

### 4.3.8 Flow depth on overwash fan estimation

Shaw et al. (2015) demonstrated the elevation of the topset-foreset-break (TFB) in a storm surge deposit, formed from Hurricane Ike (2008) on the Matagorda peninsula in Texas (USA), could be used to estimate the minimum and maximum flow depth on the barrier. This led to an expression for the storm surge (water) elevation landward of the barrier ($\xi$) outlined below.

$$\xi = \eta + H$$

Where $\eta$ is the elevation of the TFB, and $H$ is the depth of flow during sedimentation. Applying this method to the upper topset-foreset beds (unit C) in pit 1, the TFB elevation ($\eta$) was measured at different points on the upper surface of unit C (average $\eta = 0.22$ m). The lower flow depth ($H_L$) was estimated from the nominal diameter of the largest clast, represented by the A-axis of an elongate pebble (assuming saltation) found near the centre of the foreset bed, yielding $H_L \geq 0.04$ m. The upper flow depth ($H_U$) was estimated starting with the settling velocity ($W_s$) of the smallest bedload grains >2mm using the formula in Zhiyao et al. (2008) for natural sediment particles:

$$W_s = \frac{v}{d} d_*^3 \left[38.1 + 0.93 d_*^{12/7}\right]^{-7/8}$$

where $v$ is the kinematic viscosity (1.0034 mm$^2$/s), $d$ is the particle diameter (2 mm), and $d_*$ is the dimensionless particle diameter described by Camenen (2007):

$$d_* = d\left[\frac{\Delta g}{v^2}\right]^{1/3}$$

This incorporated gravitational acceleration ($g$ = 9.8 m/s/s), and the difference between the density of fluid (1.00 g/mm$^3$) and the density of the particles, which was represented by quartz at 0.00265 g/mm$^3$ as the dominating grain type.

Finally, resolving $W_s$ at 14.1 cm$^2$/s, $H_U$ was estimated at ≤ 0.48 m from the rearrangement of the depth-slope product equation as:

$$H_U = \frac{u_*^2}{gS}$$

where $u_*$ is the velocity of flow that was substituted for the value of $W_s$ (i.e. $u_* = W_s$) as an upper estimate, and $S$ is the measured angle between the topset bed surface and the horizontal (1.5° = 0.0042%). Results from this analysis were used to constrain the minimum and maximum water depth to form the upper foreset beds (unit C) in pit 1 and are discussed in relation to estimated flood heights.

### 4.3.9 Climate patterns

Climate patterns were evaluated for modern Lake Machattie high stands between 1973 and 2023. Climate data including rainfall, river discharge, the state of the MJO, historical Mean Sea Level Pressure, and synoptic patterns (available from 1999 onwards) and tropical cyclone track maps were sourced from the Australian Bureau of Meteorology (http://www.bom.gov.au/), unless specified otherwise. Precipitable water content followed (Kalnay et al., 1996) using NCEP/NCAR Reanalysis 1 of 4x daily individual observations where the atmosphere is considered as a single layer. Air parcels arriving at the Georgina catchment at 1500 m above ground level (mAGL) were calculated using the Hybrid Single-Particle Lagrangian Integrated Trajectory model (HYPLIT) (Draxler and Rolph, 2010) with NCEP/NCAR Global Reanalysis Data (1948 onwards).

## 4.4 Results

### 4.4.1 Characterisation of Lake Machattie sedimentology

#### *4.4.1.1 Pit 1*

***Basal transgressive foreset unit (Unit A):*** Overlying the Lake Machattie sediments at +76.48 m AHD is 48 cm of high-angle (>20°) planar crossbedding representing avalanche foresets. These avalanche foresets characteristically abut sharply with the underlying lake sediments at a discordant angle. The unit is dominated by moderately well sorted (SPAN 1.00–1.36) slightly to very fine gravelly coarse sand, with a mean and D90 coarsening trend downprofile (Figure 4.2). Each thin to medium foreset (3 – 12 cm; 5.8 cm average) generally exhibits a basal concentration of coarser grains (coarse-grained sand and some granules) that are normally graded in the palaeoflow direction. The avalanche slopes show an average dip of ~24° with a uniform northwest direction indicating landward progradation. Some coarse-grained massive sediment avalanches are evident within individual foresets. A few clastic pebbles (mainly quartz) are found throughout the unit. Occasional mollusc shell fragments (at ~124 cm) are in the finer sands that delineate individual foresets.

***Sandy clay bed (Unit B):*** A thin bed (3 – 10 cm) of poorly sorted (SPAN 2.36) very fine silty medium sand that sharply truncates the underlying avalanche foresets. The lower bed surface has discrete sections with a shallow parabolic form (5 – 10 cm bed thickness) or near horizontal form (3 cm bed thickness). Scouring of the upper bed surface is infilled with the overlying unit. Bioturbation is lacking.

***Upper transgressive foreset-topset unit (Unit C):*** The upper foreset unit is 22 cm thick with rollover points, also termed the topset-foreset-break (TFB) (Shaw et al., 2015) and is clearly visible through the major slipface and accretionary topsets. Bottomsets are lacking and foresets abut sharply with unit B. The high angle foreset unit consists of basal granules to poorly sorted (SPAN 1.84) very fine gravelly coarse sand that grade upwards. Individual very thin foresets (1.8 cm on average) normally grade from coarse- or very-coarse sand to fine-medium sand. Landward palaeoflow direction is the same as unit A shown by northwest-dipping foreset slopes with a conspicuously consistent angle of 22° across the 2.5 m cross section. The gently inclined (2-5°) accretionary topset beds have coarse- and fine-grained couplets disrupted by planar thin beds of sandy gravels. There is no evidence of any disconformity evident at the upper boundary between the foresets and these topset plane-bed sandy gravels. However, an elevation rise of the TFB occurs approximately halfway along the cross section which is maintained in the direction of progradation. There is some overprinting in topsets by millimetre- to centimetre-scale roots structures. Clastic pebbles (mainly quartz) are found throughout the unit (largest pebble (silcrete) axis: A = 40 mm; B = 11 mm; C = 9 mm).

***Convolute bedding (Unit D):*** The 21 cm unit is characterised by sets of very thin (1.0 – 2.5 cm) sub-horizontal to convolute moderately well sorted (SPAN 1.29) medium sandy beds. Individual beds are normally graded. Convolute bedding is variably developed, with some examples showing weak structures that collapsed during excavation revealing underlying medium- to fine-grained massive aeolian sands, identified as such by relict haematic grain cutans in the concave areas of abraded clean grains. A dark-coloured thin lamina of what appears to be organic material is also noted in both the upper parallel and convolute beds. Remnant foreset bedding is also observed, which sharply abuts the underlying topset bed of unit C and displays landward (northerly) progradation. Substantial overprinting by millimetre- to centimetre-scale roots structures.

***Sub-horizontal planar bedding (unit E):*** a 47 cm unit of sub-horizontal planar bedding. Grain sizes range from course- to fine-grained sands and are poorly sorted. Large broken tree branches are occasionally observed in this unit with some overprinting by millimetre- to centimetre-scale modern root structures. Overlying unit E are massive medium- to fine-grain aeolian sands found in discrete decimetre thick sections.

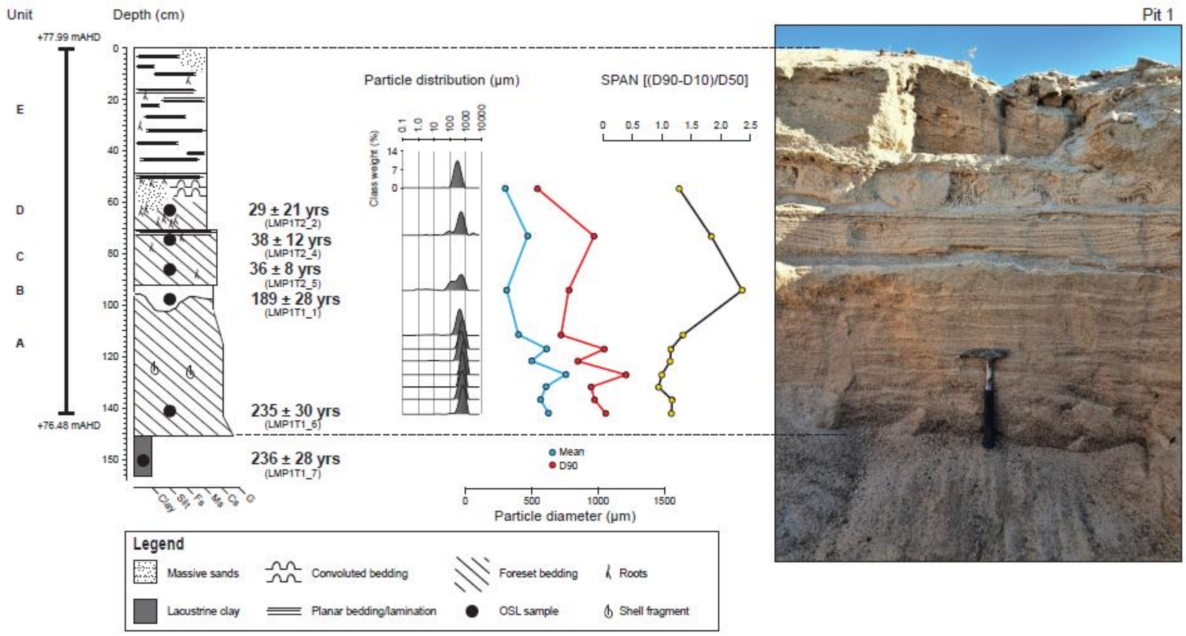

**Figure 4.2.** Pit 1 stratigraphy, together with unit nomenclature (letters A-E, left column, referred to in the text), elevation, grain size (particle distribution graphs, mean and D90) and sorting variations (SPAN index). Pit photograph shown facing north (lake behind). See Table 4.1 for OSL sample details.

*4.4.1.2 Pit 2*

Stratigraphy and profiles of pits 2, 3 and 4 are shown in Figure 4.3.

***Basal transgressive foreset unit (Unit A2):*** This 52 cm thick unit overlying the Lake Machattie sediments at +76.45 m AHD is characterised by high-angle avalanche foresets of course-grain sand and some granules. The unit lacks bottomsets and is sharply truncated by overlying sandy clays (unit B2). Fine sand delineates individual thin bed foresets (3 – 5 cm: 4.5

cm average). There is no obvious upward fining of the unit or grading within the individual foresets. Foreset angles dip between 20° and 22° northward indicating landward progradation. Overprinting by millimetre- to centimetre-scale roots is also present.

***Current ripple sandy clay bed (Unit B2):*** A very thin (1 – 3 cm) sandy-clay bed with asymmetric ripple marks. Averaged ripple index and ripple symmetry index values with regard to four measurable ripple marks are 7.76 and 2.71, respectively, indicating combined current and wave flow Tanner (1967). Ripple asymmetry suggests a lakeward current flow direction (Figure 4.4). Bioturbation is lacking.

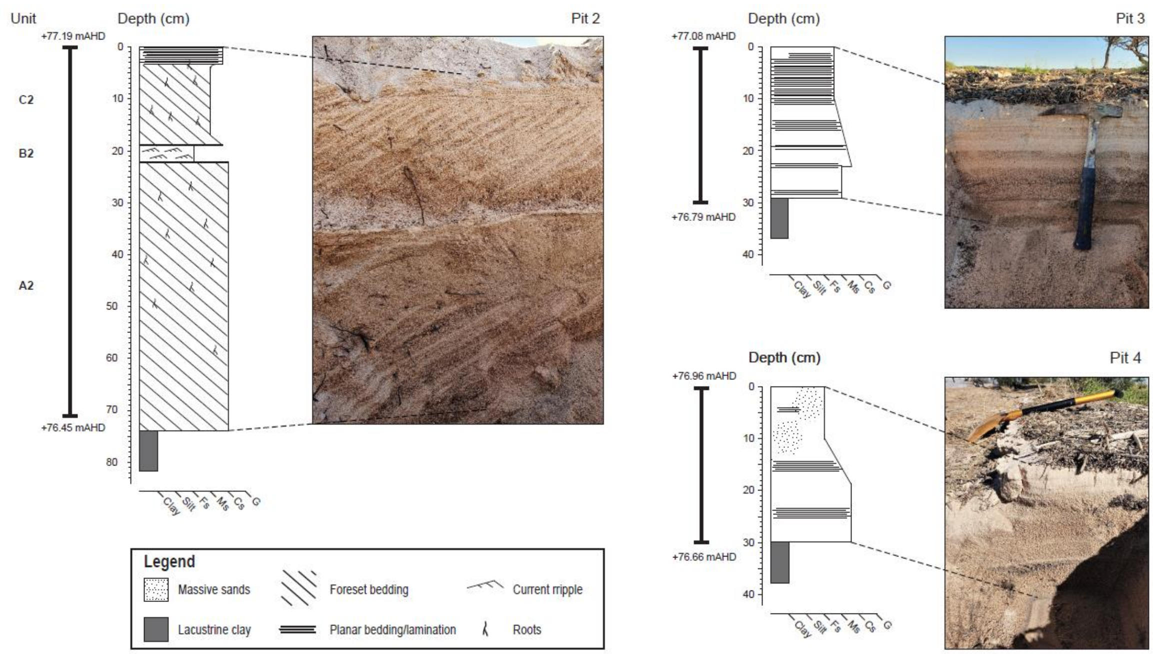


**Figure 4.3.** Pits 2, 3 and 4 stratigraphy, together with unit nomenclature for pit 2 (A2–C2, left column, referred to in the text) and elevations. Pit photograph directions: pit 2 facing east (lake on right); pit 3 facing north (lake behind); pit 4 facing west (lake on left).

***Upper transgressive foreset-topset unit (Unit C2):*** A 19 cm thick unit of high-angle avalanche foresets including well-defined TFB and topset. Foresets sharply abut the underlying sandy clay bed with well-defined infilling of current/wave ripple swales (where visible). A basal concentration of coarse to medium sand and some granules is clearly visible throughout the unit, which fined upward to medium sands at ~16 cm depth. Fine sand delineates the individual very thin bed foresets (1 – 1.5 cm: 1.25 cm average). Palaeoflow direction is landward as shown by a uniform northerly foreset dip angle of 23°. The topset medium to coarse grain sands are a gently inclined (2-5°) planar thin bed (4 – 5 cm thick). Millimetre to centimetre scale roots is present. Overlying unit C2 are medium to fine aeolian sands ~20 cm thick.

#### *4.4.1.3 Pit 3*

Pit 3 is 29 cm deep and dominated by medium to coarse sand. The coarsest sediment overlays a dark coloured lamina at 23 cm depth and fines upward to medium to fine sands at around 10 cm depth. Below 23 cm, medium sand dominates. Pit 3 beds are normally graded, gently sloping parallel to the lake sediments, and discontinuous down the regressive foreshore slope.

#### *4.4.1.4 Pit 4*

Pit 4 is 30 cm deep and dominated by coarse to medium sand. A very thin bed of fine sand at ~25 cm depth overlays a thin layer of organic-rich material in some sections. Sediments in the upper 14 cm of pit 4 are a mixture of massive fine sands and loose organic debris. Throughout the unit, plane beds are normally graded, deposited parallel to the lake sediments, and are discontinuous lakeward.

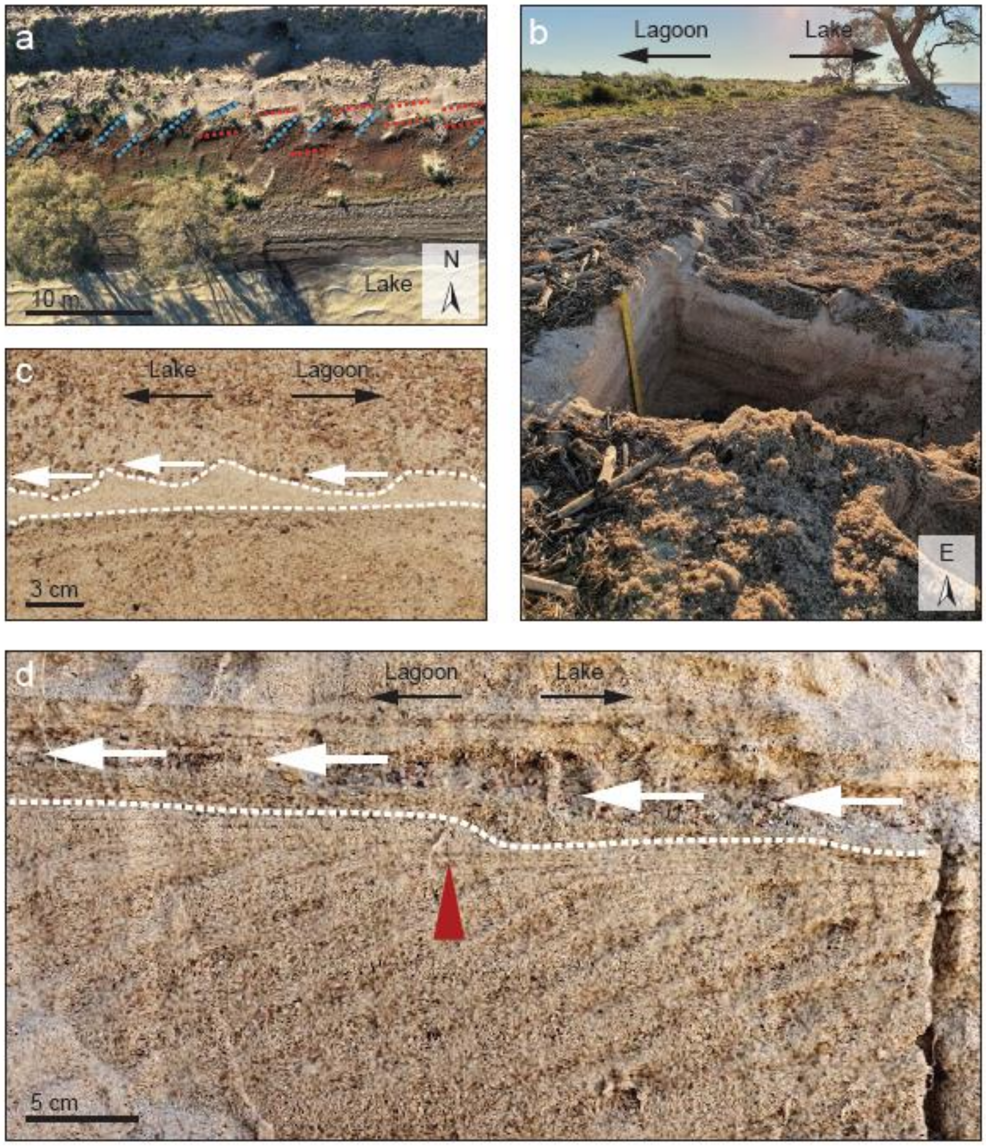


**Figure 4.4**. Photos taken in 2019. **a:** debris lines and sediment deposits on the beach ridge (~ at tree line) and swale (immediately behind tree line) showing wave-directed movement north (dotted red lines) and northwest (dotted blue lines); **b:** mantled beach ridge at pit 3 facing east; **c:** pit 2 unit B2, sandy-clay bed with asymmetric ripple marks (white arrows indicate current flow direction); **d:** pit 1, unit c elevation rise lakeward in topset-foreset-break (red triangle shows step up in topset accretion, white arrows indicate flow direction).

### 4.4.2 Single-grain OSL chronology

The results of single-grain OSL analyses from pit 1 (n = 6) are listed in Table 4.1 and corresponding radial plots are displayed in Figure 4.5. The OSL ages of the barrier spit range between 235 ±30 years to 29 ±21 years and form two different age clusters. The older population ranges between 235 ±30 years and 189 ±28 years. The pit 1 basal foreset (Unit A; LMP1T1_6) recorded an OSL age of 235±30 years, which is consistent with the Lake Machattie lacustrine sediments collected 10 cm below the surface with an OSL age of 236 ±28 years (sample LMP1T1_7). The younger population ranges between 38 ±12 years and 29 ±21 years and are equivalent within error. However, the presence of fine-grained massive aeolian sands and landward oriented prograding foresets in unit D suggests deposition probably occurred during a more recent lake filling event. As such, two samples from unit C (LMP1T2_4 and LMP1T2_5) gave a pooled mean age of 37.0 ±10.2 years, while the overlying convolute bedding (unit D) was dated at 29 ±21 (sample LMP1T2_2). Unit E was not dated.

All samples have $D_e$ distributions with grains indicative of being well-bleached before burial and were undisturbed. Mean true $D_e$ values range between 0.03 and 0.26 Gy and have small standard errors (i.e. precise $D_e$ values) and many of the measured grains in each sample have $D_e$ values consistent with 0 Gy at $\pm 1\sigma$ suggesting they have been fully bleached prior to deposition (Arnold et al., 2009). Accordingly, the unlogged central age model is considered appropriate in providing accurate burial ages for these very young to modern-age fluvial samples (Ballarini et al., 2007, Arnold et al., 2009). Radial plots show a minimal spread of $D_e$ values around the central $D_e$ value, which further supports the contention that grains were well-bleached before burial with little to no post-depositional disturbance. Overdispersion values ranged from 0.035 ± 0.006 to 0.25 ± 0.028 Gy.

**Table 4.1.** Results of the single-grain OSL dating for pits 1 and 4 at Lake Machattie.

| Sample code | Mean ± 1σ water content (%)[a] | External dose rate (Gy/ka)[b] | | | Total dose rate (Gy/ka) | Number of grains (N)[c] | $D_e$ (Gy)[d] | Method[e] | Age Model | OD (Gy)[f] | Age (yrs) |
|---|---|---|---|---|---|---|---|---|---|---|---|
| | | Beta | Gamma | Cosmic | | | | | | | |
| **LMP1T2_2** | 3 ± 1 (0.3) | 0.51 ± 0.02 | 0.28 ± 0.01 | 0.218 | 1.04 ± 0.04 | 25 | 0.03 ± 0.02 | SAR (Q) | $CAM_{UL}$ | 0.041 ± 0.026 | 29 ± 21 |
| **LMP1T2_4** | 3 ± 1 (0.4) | 0.43 ± 0.02 | 0.25 ± 0.01 | 0.212 | 0.92 ± 0.04 | 106 | 0.04 ± 0.01 | SAR (Q) | $CAM_{UL}$ | 0.073 ± 0.010 | 38 ± 12 |
| **LMP1T2_5** | 3 ± 1 (0.3) | 0.33 ± 0.01 | 0.25 ± 0.01 | 0.205 | 0.82 ± 0.04 | 109 | 0.03 ± 0.01 | SAR (Q) | $CAM_{UL}$ | 0.035 ± 0.006 | 36 ± 8 |
| **LMP1T1_1** | 3 ± 1 (1.8) | 0.64 ± 0.02 | 0.31 ± 0.01 | 0.181 | 1.22 ± 0.04 | 117 | 0.23 ± 0.03 | SAR (Q) | $CAM_{UL}$ | 0.25 ± 0.028 | 189 ± 28 |
| **LMP1T1_6** | 3 ± 1 (0.8) | 0.37 ± 0.01 | 0.28 ± 0.01 | 0.171 | 0.85 ± 0.03 | 89 | 0.20 ± 0.02 | SAR (Q) | $CAM_{UL}$ | 0.17 ± 0.02 | 235 ± 30 |
| **LMP1T1_7** | 8 ± 2 (7.7) | 0.57 ± 0.02 | 0.35 ± 0.02 | 0.157 | 1.10 ± 0.04 | 62 | 0.26 ± 0.03 | SAR (Q) | $CAM_{UL}$ | 0.15 ± 0.026 | 236 ± 28 |

[a] *Water content calculated as the % mass of water per unit of dried sediment measured in the laboratory. Dried dose rates were corrected to the weighted mean (±1σ) water content for age determination.*

[b] *Measured and calculated dose rates (±1σ). Cosmic-ray dose rate based on longitude, latitude and altitude of site as well as depth and density of current sediment overburden, sediment densities estimated at 1.8 g/cm$^3$.*

[c] *Number of grains accepted for $D_e$ determinations.*

[d] *Mean ± total (1σ) uncertainty. $D_e$ values were calculated using the un-logged version of the central age model ($CAM_{UL}$) because of negative $D_e$ values in each sample (consistent with zero) (*Arnold et al., 2009*).*

[e] *Single aliquot regenerative (SAR) dose for quartz (Q). Note: Grain size was 180–212 µm diameter for all samples.*

[f] *Overdispersion (OD) in $D_e$ values.*

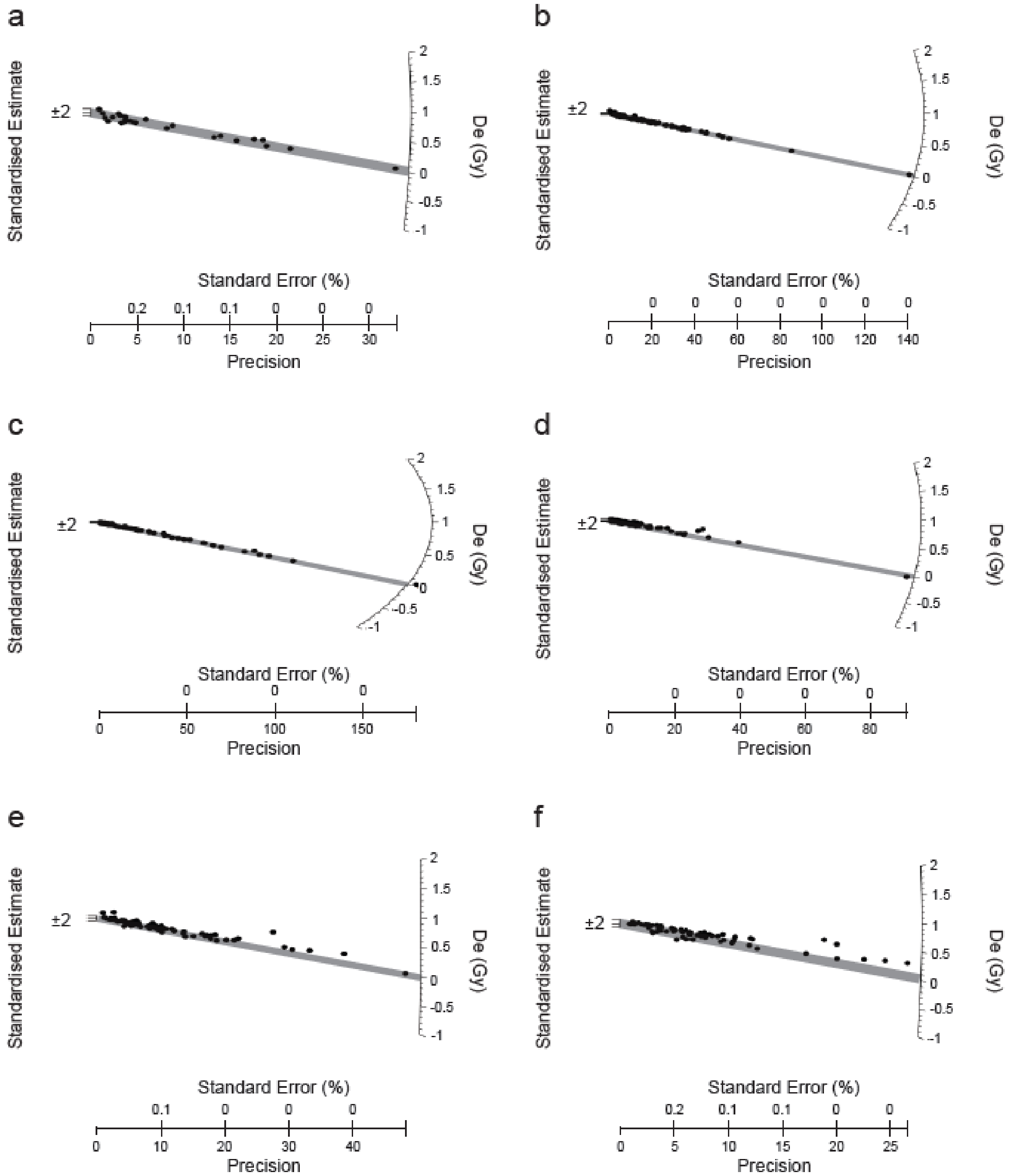


**Figure 4.5**. Radial plots of single-grain $D_e$ distributions (plotted on an unlogged scale) for samples collected from Lake Machattie. The unlogged central age model ($CAM_{UL}$) was used to estimate OSL ages. The grey bands in each plot are centred on zero for each dose population.

### 4.4.3 Validation of shoreline topography and lake water level estimations

The Landsat 8 MNDWI-determined lake boundary is estimated at ≤8 m (<½ a pixel) horizontal distance from the analogous in-field measurements of the water line taken at both LMNW and LMSE in July 2019. This equates to an average vertical error of ±0.02 m AHD. The elevation of the beach ridge and debris lines on the lakeward side of the barrier suggests wave run-up and overtopping reached ~0.4–0.5 m above the estimated peak flood height in 2019. However, average elevation measurements of the high-water debris line on the landward side of the lagoon (76.55 ±0.01 m AHD) are equivalent to the 2019 MNDWI-determined lake boundary (76.47 m AHD). Therefore, all MNDWI-determined lake boundaries at LMNW were estimated from in-field measurements taken on the landward side of the lagoon where there is likely substantial wave diminution, rather than on the lakeward facing erosion slope of the barrier which is subject to greater wave action and morphological change over time.

Elevations of MNDWI-determined peak flood lake boundaries at LMSE and LMNW show a significant relationship ($p = <0.05$; $r^2 = 0.98$; Figure 4.6), with the 2007 flood exhibiting the greatest difference in lake level (0.2 m) between the two locations. There is no discernible visual difference between the extents of the NDWI- and MNDWI-determined lake boundaries. Thus, interpolation of in-field elevation data across the lake are considered reliable for the approximation of flood levels from lake boundaries observed in pit stratigraphy, and the flooded lake boundaries derived from satellite imagery using the water indices, NDWI and MNDWI.

### 4.4.4 Water-barrier spit interactions and inundations

From 1980 to 2023, lake water interactions with the barrier spit occurred over nine flood transgression-regression cycles for a total 6.46 ±0.07 years (or 15.02 ±0.17% of the time). During this period, the two largest lake fillings were in 1997 and 2001 reaching peak elevations at 77.61 m AHD and 77.55 m AHD, respectively (Figure 4.7). Total inundation of the barrier spit in 1997 and 2001 lasted for a total of 48 ±16.5 days, representing 0.31 ±0.11% of the total time between 1980 and 2023.

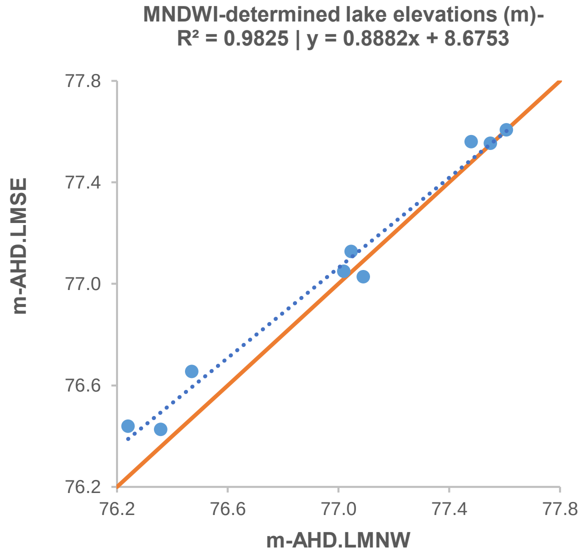


**Figure 4.6.** Comparison between MNDWI-determined lake boundary elevations at Lake Machattie northwest (LMNW) and Lake Machattie southeast (LMSE), with the dotted blue line representing the straight-line regression of the elevation data. Regression analysis shows a significant relationship between the data ($p = <0.05$; $r^2 = 0.98$). Solid line (orange) bisecting each graph represents 1:1 relationship. Units are in meters Australian Height Datum (m-AHD).

As previously mentioned, peak flood levels and duration of water-barrier spit interactions could not be accurately determined for years prior to 1980. However, the 1973 and 1974 floods interacted with the barrier spit.

Prior to the start of April 1973, minimal river discharge was recorded at Glengyle, located 10 km west of Lake Machattie. The peak discharge at Glengyle (1328 $m^3/s$) was on April 8, and the first available satellite image shows flood waters reached an elevation of 76.41 m AHD and interacted with the barrier spit on May 15. Although lake water levels likely dropped during this ~5-week period, the lake water elevation on May 15 is considered near maximum as other flood years show minimal regression over similar time frames. The 1973 flood height reached in Lake Machattie was comparable to 2010 and 2019 (Figure 4.7).

The single Landsat 1 image of the 1974 flood captured over LMSE shows water levels reached at least 79.20 m AHD in early February and exceeded the 1997 flood by 1.59 m (Figure 4.7). Based on the highest modern elevation point measured on the barrier spit in 2019, the 1974 lake filling would have inundated the entire barrier by at least 0.60 m depth.

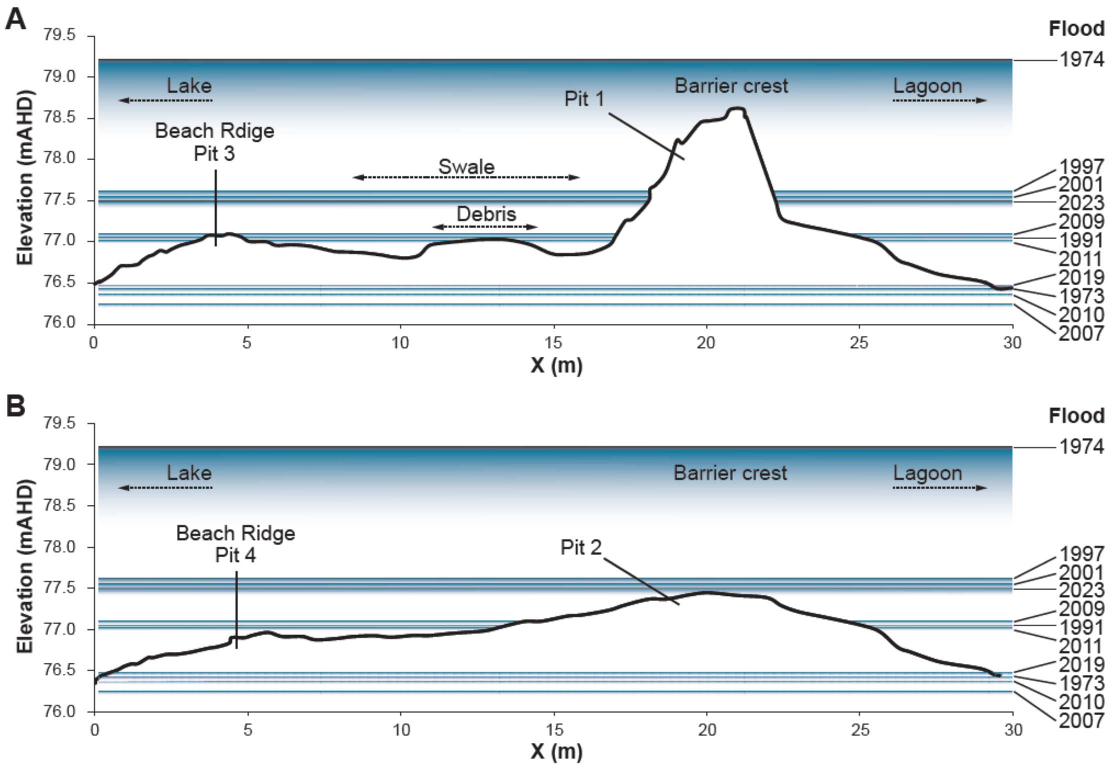


**Figure 4.7.** Maximum flood heights reached in Lake Machattie between 1972 and 2023 relative to topographic profile of barrier spit in 2019 at **A**: pits 1 and 3, and **B**: pits 2 and 4.

Between 1980 and 1986, satellite observations show no floods interacted with the barrier spit. Data extracted from a multi-year (1986-2023) frequency inundation map shows flood waters inundated the western side of the barrier spit more often than the eastern side (Figure 4.8). Inundation of the barrier spit (central transect) at pit 2 was more frequent than at pit 1. Inundation of the barrier spit and lagoon (landward transect) from ~0 m to 1500 m (east to west) was low and relatively similar. Although lagoon inundations appear higher than in the lagoon between ~3700 m and 4800 m, this is due to regional input filling the lagoon more often.

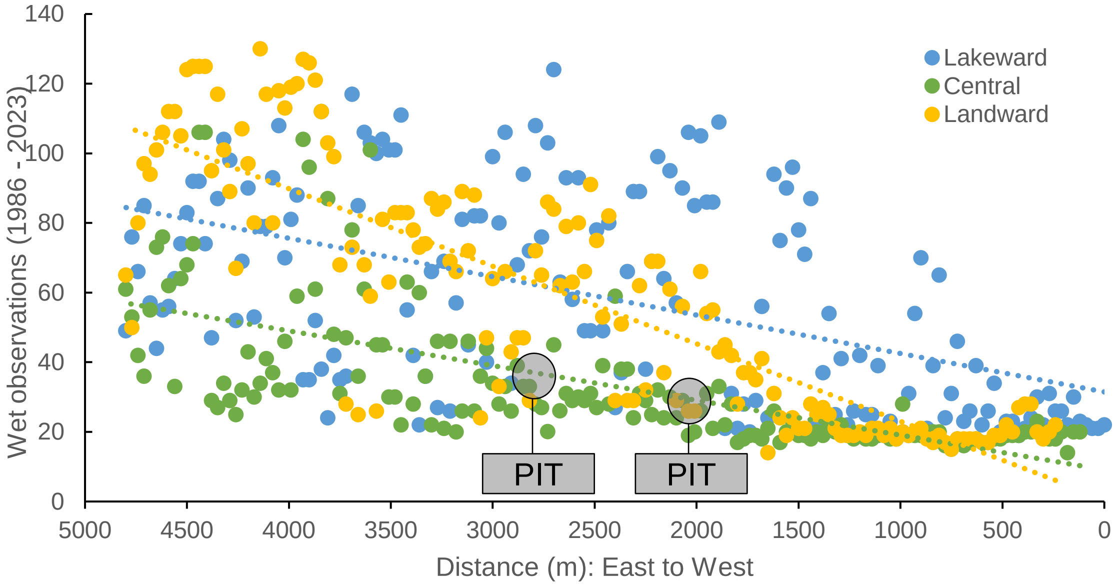


**Figure 4.8**. Spatial variations of water-barrier spit frequency inundations. Wet observations are the number of Landsat observations showing the presence of water in a particular location between 1986 and 2023 along three shore-parallel transects (each 30 m apart): lakeward, central, and landward. Data extracted from a multi-year (Landsat) frequency inundation map (GeoAust, 2024b) using ArcGIS 10.7.1. The locations of pits 1 and 2 are displayed along the central transect tend line (follows approximate position of barrier crest). Trend lines are colour coded the same as per each transect.

#### 4.4.5 Identification and characterisation of nearshore bars

Nearshore bar sizes range from ~0.1 km up to 2.0 km, increasing in size alongshore from east to west. The largest and most proximal bar is located ~0.8 km, 1.5 km and 2.3 km from the spit apex, pit 1 and pit 2, respectively. Bar positions were roughly shore-parallel, with the largest bar aligning to the southwest for ~2 km near the spit apex. Little to no offshore or onshore changes in bar positions were observed between 1987 and 2023.

#### 4.4.6 Flow depth on overwash fan estimation

Formation of the upper foreset and topset beds (unit C) in pit 1 required a minimum and maximum flow depth of 0.26 m and 0.70 m, respectively. This shows water levels in the lagoon (ξ) were between 77.49 m AHD, based on $\eta + H_L$, and 77.93 m AHD, based on $\eta + H_U$. Standing lagoon water level is considered equivalent to the standing lake water level given inundation of the spit terminus occurs at or above ~76.24 m AHD, based on the 2007 flood height and prior to a barrier breach in 2011.

### 4.4.7 Climate patterns associated with high stands

A summary of the climate patterns during Lake Machattie high stands between 1973 and 2023 are listed in Table 4.2 and are discussed in depth in section 5.2. Watercourse discharge data for gauging stations on the Georgina River (at Camooweal and Roxborough Downs) and Eyre Creek (at Glengyle) is often discontinuous or missing, but available peak discharges are listed in Table 4.2 and daily discharges are displayed in Figure S15 (Appendix C2). No river discharge data is available during the 1991, 1997 and 2001 high stands. River discharge data is only available for Glengyle during the 1973 and 1974 high stands and for Camooweal during the 1974 high stands. Precipitation in the Georgina catchment that led to these lake fillings is largely derived from air masses travelling from warm waters in the Coral Sea, Gulf of Carpentaria, Arafura Sea, Tasman Sea, and the Indian Ocean and are discussed in relation to precipitable water contents, the MJO and cyclone activity in section 5.2 and are displayed in Figures S4–14 and 10 (Appendix C2).

**Table 4.2**. Summary of major Lake Machattie fillings (and rank), with the associated climate patterns, preexisting lake conditions and available peak river discharges.

| Year | Rank | ENSO | IPO[a] | IOD[b] | Cyclone | Relatively full after inputs from year prior (Y/N) | Peak River Discharge ($m^3/s$)[c] |
|---|---|---|---|---|---|---|---|
| **1973** | 9 | Neutral | nIPO | Positive | Bella | Y | **RD**: 1336<br>**G**: 1328 |
| **1974** | 1 | La Niña | nIPO | Neutral | | Y | **CW**: 1228<br>**RD**: 3498<br>**G**: 4770 |
| **1991** | 6 | Neutral | pIPO | Neutral | | N | NA |
| **1997** | 2 | Neutral | pIPO | Negative | | N | NA |
| **2001** | 3 | La Niña | nIPO | Neutral | Sam | Y | NA |
| **2007** | 11 | El Niño | nIPO | Neutral | | Y | **RD:** 1667 |
| **2009** | 5 | La Niña | nIPO | Neutral | | N | **RD**: 2443 |
| **2010** | 10 | El Niño | nIPO | Neutral | Yasi | Y | **RD:** 560 |
| **2011** | 7 | La Niña | nIPO | Negative | | Y | **RD:** 1658 |
| **2019** | 8 | Neutral | nIPO | Positive | Trevor | N | **RD:** 1633 |
| **2023** | 4 | La Niña | nIPO | Negative | | Y | **RD:** 3117 |

[a] *IPO: negative IPO (nIPO); positive IPO (pIPO).*

[b] *IOD is for the year preceding (i.e., during the Austral winter).*

[c] *Peak Georgina River discharge at Camooweal (**CW**; station #001204A; data availability 02/10/1968 – 29/09/1988; missing data = 0.03%), Roxborough Downs (**RD**; station #001203A; data availability 01/10/1967 – 18/07/2023; missing data = 29.90%) and Glengyle (**G**; station* #001101A; data availability 11/12/1966 – 21/05/1990; missing data = 17.66%).

## 4.5 Discussion

### 4.5.1 Interpretation of depositional processes

#### *4.5.1.1 Pits 1 and 2*

The predominant internal structure of the barrier spit observed at pits 1 and 2 are transgressive avalanche foresets that provide an important palaeo- to modern-hydrologic record of shoreline processes relative to high stands. Units in pit 2, including the sandy-clay bed, share a similar stratigraphical sequence, thickness and internal architecture with units A, B and C of pit 1. For each unit in pits 1 and 2, the general consistency of foreset dip angles and oblique clinoform surface from topset to foreset indicates deposition under relatively steady flow conditions in a low-energy lagoon environment (e.g., Bray Jr and Carter, 1992). Basal units in both pits were deposited directly on the existing Lake Machattie sediments at a consistent mean height of 76.46 ±0.02 m AHD, which highlights that the greater modern inundation frequency at pit 2 compared to pit 1 (Figure 4.8) relates to the preexisting barrier height rather than underlying topography. The timing of landward progradation at pit 1 is well constrained at 235±30 years given the equivalent burial age of the underlying Lake Machattie sediments, suggesting little to no erosion of the Lake Machattie sediments occurred prior to, or during, burial as the sediments were well-bleached and lacked scouring.

The basal foresets in pit 1 (unit A) are thicker and steeper than all other foreset beds in either pit 1 or pit 2, which indicates the washover terrace was steeper and/or the standing water level in the lagoon was higher during deposition (Bray Jr and Carter, 1992). The pit 1 basal foresets (unit A; sample LMP1T1_6; OSL age 235 ±30 years) and sandy clay bed (unit B: sample LMP1T1_1; OSL age 189 ±28 years) have overlapping OSL age errors. However, deposition of unit B occurred during a separate lake filling episode given their mean 46-year OSL age difference, both have well-bleached grains, and unit B sharply but irregularly truncates unit A. The parabolic lower surface of the sand-clay bed in discrete thicker sections is interpreted as pre-deposition erosion of the underlying sandy foresets (unit A), probably from barrier overwash. Erosion of unit A during syn-deposition of the sandy-clays is unlikely for two reasons, (i) muddy overwash deposits were not found, and (ii) all foreset slopes in pit 1 and 2 were high-angled and lacked bottomsets suggesting barrier overwash typically occurred without mud that would cause destabilising turbidity currents on the foreset slipface and toe (Kostic et al., 2002, Kostic and Parker, 2003). The near horizontal upper surface of the sandy clay bed indicates lagoon deposition, probably during transgression, as the low-energy environment limited reworking by waves or successive overwash (e.g., Bray Jr and Carter, 1992).

Foresets in both pits 1 and 2 have high dip angles ranging between 20 and 24°, which suggests subaqueous sediment progradation in wave-protected lagoon waters deep enough for rapid deceleration to occur (e.g., Schwartz, 1982, Murakoshi and Masuda, 1991, Neal et al., 2003, Horwitz and Wang, 2005). As previously mentioned, the standing lagoon water level is considered equivalent to the standing lake water level at or above ~76.24 m AHD. Therefore, the elevation of the well preserved topset-foreset break in unit C, pit 1, demonstrates water levels in Lake Machattie reached a minimum (maximum) elevation of ~77.49 m AHD (~77.93 m AHD) between 1972 and 1992 (pooled mean OSL age = 1982). Three observable floods occurred during this period: 1973, 1974 and 1991.

The 1973 lake filling (76.41 m AHD) was too low to form the deposit. It is possible an overwash regime could have been produced during the 1991 filling where wave run-up height plus the estimated peak high stand (77.05 m AHD) reached the minimum foreset deposition height of 77.49 m AHD. However, the foresets were high-angle (22°) and lacked bottom sets, which is indicative of subaqueous lagoonal deposition as a Gilbert-style microdelta rather than wetted-subaerial overwash deposition that typically exhibits clinoform morphologies of low-angle (~5–15°) dipping planar beds and bottomset strata (e.g. Schwartz, 1982, Blair, 1999, Shaw et al., 2015).

The 1974 flood reached an elevation of 79.20 m AHD in Lake Machattie and is the only flood between 1972 and 1992 large enough to have produced standing lagoonal waters deep enough for subaqueous deposition of unit C. The noted elevation rise in the TFB in unit C suggests deposition occurred during water level rise rather than at a constant level (Shaw et al., 2015). This implies deposition occurred during flood transgression and, given the 1974 high stand was ~1.3 m greater than the maximum flow depth required to form unit C, the foreset had finished building before the flood peaked in Lake Machattie.

Other possibilities include major flooding in 1976 or 1977. Satellite images were unavailable during this period and, therefore, flood levels in Lake Machattie could not be estimated. However, the peak river discharge at Glengyle in 1976 (1331 $m^3/s$) was comparable to 1973 (ranked ninth highest on the list) suggesting water levels in Lake Machattie were probably too low. River discharge recorded at Glengyle in 1977 (4031 $m^3/s$) was second only to 1974 (4770 $m^3/s$). Indeed, river discharge recorded at Camooweal, in the northern catchment, and Roxborough Downs, in the central catchment, was greater in 1977 than in 1974. Given this flood occurred on an already wetted catchment and Lake Machattie likely still held water from the 1976 input, it is certainly possible deposition of unit C could have been in 1977 rather than 1974.

The upper parallel and convolute beds in pit 1 (unit D) show water levels reached a minimum height of 77.52 m AHD between 1969 and 2011 (mean OSL age = 1990). As previously discussed, the 1974 (or 1977) flood likely formed unit C, providing a lower age bound for deposition of unit D. While it was difficult to measure the slope angle of the foresets in unit D, they dipped steeply landward and abutted sharply with the underlying sediments indicating subaqueous deposition in standing lagoon waters ~0.5 m deeper than the 1991 high stand. Both the 1997 and 2001 high stands (77.61 and 77.55 m AHD, respectively) were equivalent in height with the top of unit D and could have formed these structures by turbulence produced by high-energy flow or wave action during the barrier overwash regime or through channels into the lagoon (e.g., Tankard and Hobday, 1977). Hudock et al. (2014) suggests subaqueous overwash deposits within a lagoon are better preserved if transgression is rapid due to limited opportunity for reworking. Satellite imagery shows that in 1997 the onset of water-barrier spit interaction was coeval with the lake high stand (±7-day satellite observational error), whereas in 2001 transgression took longer (~16 ±7 days). This could suggest deposition and subsequent deformation of unit D occurred in 2001 because of reworking during slower transgression.

Convolute bedding structures are often mentioned in studies of washover stratigraphy (e.g., Tankard and Hobday, 1977, Bray Jr and Carter, 1992, Murakoshi and Masuda, 1992, Baucom and Rigsby, 1999, Flemming, 2011) but are generally not a significant portion of the deposit. Several mechanisms can produce convolute deformation in shoreline environments associated with rapid sedimentation and current flow, especially liquefaction, dewatering and loading of sediment following recent deposition (Murakoshi and Masuda, 1992, Reineck and Singh, 2012). Wave action and turbidity currents over the rapidly deposited loose sand, typical of overwash deposits, are particularly common (Murakoshi and Masuda, 1992). The convolute beds in pit 1 appear to have no internal discordances (individual beds are parallel and traceable round several folds) indicating deformation was post-depositional (Allen, 1977).

The sub-horizontal planar bedding in pit 1 (unit E) likely resulted from wave run-up overtopping the barrier subaerially. Such deposits are also described for coastal barriers (e.g., Horwitz and Wang, 2005). Formation of unit E would require wave run-ups capable of reaching at least 77.99 m AHD. Wave run-ups during the 1997 or 2001 events, the only events capable of forming unit D, would have to be in the range of 0.38 m to 0.44 m above their respective MNDWI-determined high stands to form unit E. Comparatively, lake fillings between 2007 and 2019 would have to produce run-ups in the range of 0.90 m to 1.75 m to form unit E. The maximum fetch at Lake Machattie (~13 km) follows a northwest trajectory and the combination of daily wind variability (see section 4.5.1.3) and moderate wind strengths during the Austral wet season (9 km/h) limits significant wave height on the lake. At the time of our sampling in 2019, fair weather waves were observed at maximum heights of ~0.3 m, and wave run-up during the peak high stand in 2019 was estimated at ~0.4–0.5 m. Considering Dulhunty (1989) recorded an ~90 cm fair weather run-up at the Madigan Gulf in KT-LE (1974–1977 filling), which has a fetch nearly four times that of Lake Machattie, it is not unreasonable to assume that unit E was formed by run-up in 1997 or 2001. This may also suggest deformation of the underlying sediments in unit D could have been caused by deposition of unit E soon after unit D in either 1997 or 2001, possibly during lake regression.

#### *4.5.1.2 Pits 3 and 4*

Construction of the beach ridge is assumed to have probably occurred during the 2019 filling. Although beach ridges in lacustrine environments can build during transgression, they are principally built from still stands during regression (Magee and Miller, 1998). The previous flood in 2011 was ~0.55 m higher than the modern beach ridge and any preexisting beach ridge or berm would have been rapidly inundated and likely reworked and modified into the barrier or alongshore. However, the distinct change to coarser grain sizes compared to the underlying sediments at ~23 cm depth in pit 3 may indicate these lower deposits were formed during the 2011 lake regression or still stand. The lack of additional beach ridges or mantling down the regression foreshore slope and discontinuation of the beach sands lakeward indicates regression in 2019 was continuous and somewhat rapid (Magee and Miller, 1998).

#### *4.5.1.3 Wind and waves*

According to the lake classification by Nutz et al. (2018), Lake Machattie is a wind driven water body ($I_{WWB}$ index of 9.29) and the distribution of shoreline sedimentary features should be largely driven by wind-driven lake-scale water circulation processes, as confirmed in this study. Obvious surface expressions of such features include the two barrier spits, barrier washover fans, northward curvature of the northwest barrier spit terminus, lobate-cuspate delta, and nearshore bars (Houser and Greenwood, 2005).

Foreset progradation directions in pits 1 and 2 are in tune with the prevailing winds. It is worth noting that during 2019 field investigations, debris lines and sediment deposits on the beach ridge and swale near pit 1 were oriented perpendicular to winds blowing from the south and southeast (Figure 4a), which suggests wave-directed movement was in sympathy with prevailing wind directions. Southerly winds dominate in the afternoon, but south to southeasterly winds are recorded more frequently in the mornings at Bedourie (BOM, 2024a). Thus, the direction of foreset progradation may be an artefact of overwash flows directed by changes in daily wind patterns. Daily cycles have not been previously reported in washover deposits but are theoretically possible considering a coastal wind-wave regime only requires prolonged wind blowing over a fetch for ~12 h (Boccotti, 2000). What is more likely, however, is the observed north westerly and northerly foreset dip directions are a product of lateral fan-shaped distributions across the washover microdelta during subaqueous deposition (e.g. Schwartz, 1982). Although the original morphology and size of the overwash deposits are unknown, the internal foreset geometries confirm landward progradation and supports the classification of Lake Machattie as a wind driven water body (Nutz et al., 2018).

*4.5.1.4 Sediment supply and barrier degradation*

Longshore drift occurs on Lake Machattie's northern shoreline from east to west, evidenced by the two barriers with easterly emergent points, and the attenuating hooked terminus on the western end of the northwest barrier spit. Longshore currents are illustrated from satellite imagery as littoral transport of light-coloured sediment during high stands (e.g., Figure 4.9). Baseline aerial imagery taken in 1957 shows that over six decades the size and position of the barrier spit is unchanged, with the spit lengthening just 300 m between 1957 and 1970 (~23 m per year). A series of degraded or eroded sedimentary features beyond the modern spit terminus (Figure 4.9a) resembles a remnant westward-prograding spit of ~2 km that likely existed some time prior to the first aerial image captured over Lake Machattie in 1957. Degradation of the barrier suggests a changed wind regime, decreased or changed sediment supply, or increased removal of material.

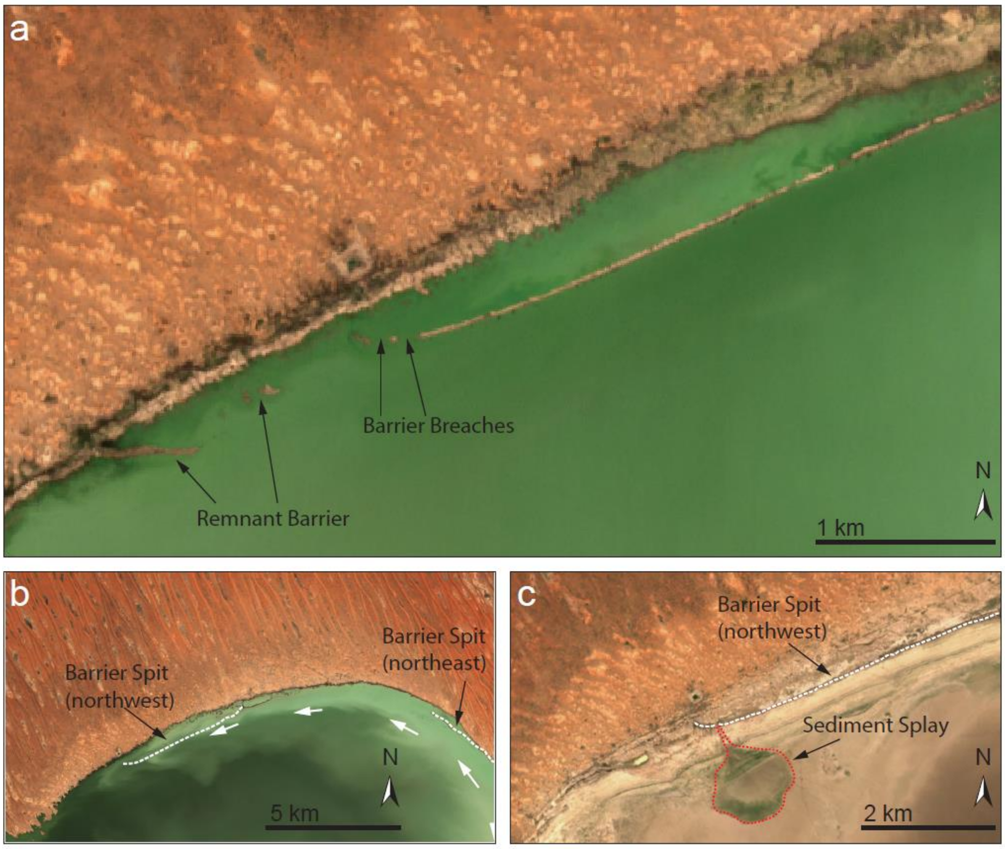


**Figure 4.9.** Lake Machattie satellite images: **a)** Northwest barrier spit depicting remnant barriers and barrier breaches (opened in 2011) (Senitnel-2 L2A image, 13/06/2023); **b)** Northwest and northeast barrier spits (dotted white lines), with east to west longshore

sediment transport of light-coloured sediment (white arrows show direction) (Sentinel-2 L2A image, 24/04/2023); **c)** Wetted sediment splay (red dotted line) from regional rainfall lagoon filling travelling lakeward through barrier breach in northwest barrier spit (dotted line) (Sentinel-2 L2A image, 18/02/2022).

There is no evidence that barrier degradation was caused by a change in prevailing wind direction or strength. Long-term wind rose data from Birdsville and Bedourie show a consistent wind regime dating back to 1957 and 1998, respectively (BOM, 2024a). There was no change in the lobate-cuspate delta ridge convergence angle or cusp apex position to suggest wave action or wind direction on the delta had significantly changed (e.g., Pranzini, 2001) since 1957. The northwest trending longitudinal dunes adjacent to Lake Machattie attests to a relatively consistent south to southeast wind regime despite likely being reworked during the Holocene, similar to the analogous oriented and thermoluminescence-dated dunes at Birdsville (Nanson et al., 1992a).

The long-term sediment flux to Lake Machattie has not been quantified. Rivers appear as the major sediment source for longshore drift and subsequent progradation of the sandy spit, and deposition on the sandy beach ridge and barrier during transgression, still stands or regression. Sand is abundant in the Channel Country although it is mainly flood-entrained from uncommon sandy bedload deposits and sandy bench accretions (e.g. Gibling et al., 1998) and aeolian dunes bordering flood pathways. Auger samples collected by Veevers and Rundle (1979) near Marion Downs (~1 m depth) and Bedourie (~2 m depth) confirms an abundance of sand in the Georgina River, although typically under a thick (~1 m) veneer of cohesive mud. Sand and mud that feed into Lake Machattie and the barrier spit comes through flood-excavation of floodplain surface muds and entrainment of the underlying sands, the fine to medium quartz sand in adjacent dune fields (QGlobe, 2024a), aeolian lake material, and from dust storms that are frequent across the Channel Country (Bullard and McTainsh, 2003). Gravel clastics may have also gradually travelled longshore, likely sourced from the Late Cretaceous to Quaternary outcrops and deposits on the southern escarpment at Lake Machattie's southern margin.

Lough (1991) showed summer rainfall in Queensland was above the long-term mean in the 30-year period between 1949 and 1978. Sediment supply was likely lower between 1919 and 1949 as summer rainfall in Queensland was less variable and below the long-term mean likely due to a weak Southern Oscillation (Lough, 1991), whereas it was higher between 1891 and 1920 for much of central Queensland based on a strong December to January SOI rainfall relationship. However, there were no obvious changes in delta front accretion or erosion up to 2023 that would suggest river sediment supply to Lake Machattie significantly changed since the 1957 aerial image baseline.

Nearshore bars are common in low-angle, storm-wave dominated littoral zones in lacustrine environments (Houser and Greenwood, 2005). Kilometre-scale nearshore bars were identified adjacent to the highest constructed barrier crest near the spit apex, which may indicate the barrier spit is morphologically coupled to the alongshore variability in sediment sourced from the nearshore bars (e.g., Aagaard et al., 2004). Subaerial exposure of nearshore bars during regression shows their position in satellite imagery remained largely unchanged between 1987 and 2023. Their generally shore-parallel orientation shifts southwest near the spit apex and pit 1 consistent with longshore currents following a smaller lake boundary. Nearshore bathymetric changes have been shown to alter sediment transport pathways and, by extension, shoreline morphodynamics on century-scale timeframes (Cooper and Navas, 2004). This might suggest that under consistently lower lake fillings, with infrequent-rare high stands, the spit neck and terminus may be temporarily starved of sediment sourced from eroded nearshore bars, assuming river sediment supply was unchanged, thus resulting in barrier degradation and the suggested eastward retreat.

Barrier breaches opened ~200 m and ~300 m from the spit terminus in 2011 (Figure 4.9a). This provided more direct pathways for exchange of flood water into the lagoon and regional rainfall lagoon fillings to flow lakeward, the latter clearly seen in recent satellite imagery, including an associated sediment splay (e.g., Figure 4.9c). The connected barrier limb migrated ~40 m landward, beginning in 2019, and breaches have not re-welded despite fluvial interaction and associated littoral drift during the 2019 and 2023 floods, which suggests the spit may still be in starved retreat and could return to a similar 1957 morphology. However, degradation of the spit followed three consecutive yearly floods with water-barrier spit interactions totalling 2.3 ±0.03 years. None of these floods were exceptionally large (maximum high stand in 2009 = 77.09 m AHD). Therefore, breaches may be a product of prolonged wave attack on the barrier's lakeward surface and ridge crest rather than reduced longshore sediment supply.

Another possibility is the effect of increased flooding frequency on aeolian sediment supply and barrier spit morphodynamics. Aeolian deposits such as foredunes are commonly described features in coastal and lacustrine settings that initiate and develop seaward/lakeward of barriers (e.g., Psuty, 1992, Houser and Greenwood, 2005, Houser et al., 2008, Reimann et al., 2011). Such deposits are either partially eroded by swash and minor run-ups during lower water levels or are destroyed by wave collision, overwash or inundation during storms or higher water levels (Sallenger Jr, 2000). Aeolian accumulations were observed in pit stratigraphy (pit 1, unit D) and as surficial deposits on the barrier at pits 1 and 2 but did not constitute a significant portion of the barrier's architecture in 2019. However, during drier periods, aeolian material was probably deposited on preexisting beach ridge(s), the backshore and barrier crest. If present, aeolian accumulations could have provided some level of barrier protection from wave attack and acted as a significant sediment source for littoral transport, welding barrier breaches and transgressive barrier rollover. However, elevated summer rainfall and variability over northern Australia since about the 1950's has been variously identified by many researchers (Suppiah and Hennessy, 1998, Wardle and Smith, 2004, Taschetto and England, 2009, Feng et al., 2013, Freund et al., 2017). As a result, increased flooding and water-barrier spit interactions were likely more frequent from about the mid-20$^{th}$ century and potentially a morphodynamic stage of limited aeolian accumulation, increased barrier degradation and the observed landward retreat.

### 4.5.2 Comparison with flood events and climate patterns

The eleven barrier-spit interactions identified by satellite imagery correspond to documented flood events from 1973 and 2023. Comparison of flood events and climate patterns are discussed in chronological order.

#### *4.5.2.1 1973*

The 1973 lake filling ranks as the third lowest modern filling at Lake Machattie. Following the strong 1972 El Niño that ended around November, ENSO remained neutral until after the 1973 Lake Machattie filling. The 1972 El Niño occurred during an extreme positive phase of the IOD (Saji et al., 1999). The IPO was near the end of a prolonged negative phase.

Satellite imagery from early 1973 shows Lake Machattie was still relatively full after inputs in 1972. It is unknown if the 1972 flood interacted with the barrier spit. A single L1TP image of Lake Machattie's southeast captured the 1972 flood (via path/row: p104r077), albeit at the end of July when lake waters are typically in regression, and the NDWI-determined lake boundary showed water levels at that time were too low to be interactive. Considering the 1972 peak river discharge recorded at Glengyle on March 20 (990 $m^3/s$) was lower than in 1973 (1328 $m^3/s$) and that the 1973 high stand (76.41 m AHD) was comparable with other low fillings (2010 and 2019), it is possible that the 1972 flood was non-interactive.

The first available satellite image of the 1973 high stand was on May 15. As previously mentioned, this high stand is considered equivalent to the maximum flood height reached in Lake Machattie despite an estimated 5-week period of regression since the April 8 peak river discharge recorded at Glengyle and the May 15 satellite image.

In 1973, the highest rainfalls were received in the Georgina catchment from March 25-28 in association with Ex-Tropical Cyclone Bella. After March 25, Ex-Tropical Cyclone Bella travelled in a southerly direction as a tropical low from the southwest Gulf of Carpentaria across the Northern Territory (Figure S4d; Appendix C2) and heavy rains ensued from about March 25-28. The highest March rainfall totals were recorded in the north at Avon Downs (178 mm) and Camooweal (130 mm), and in the central Georgina at Tobermorey (187 mm), Glenormiston (142 mm) and Chatsworth (162 mm). Little to no rain was received around Lake Machattie during this period. 48-h air parcel back trajectory frequencies indicate the Gulf of Carpentaria, Arafura Sea and Coral Sea were the dominant sources of moisture arriving around these northern (e.g., Figure S4c; Appendix C2) and central (e.g., Figure 4.4e) areas of the Georgina catchment. However, from March 25-28, the Gulf of Carpentaria had a higher precipitable water content compared to the Coral Sea (Figure S4b; Appendix C2).

#### *4.5.2.2 1974*

The 1974 event ranks as the largest modern filling at Lake Machattie and is therefore evaluated in detail. A combination of climate mechanisms resulted in widespread flooding across the Georgina catchment from January to the end of February 1974. The position of the MJO during the January-February flooding in 1974 is unknown as satellite data is limited to June 1974 onwards. From June 1973 to 1976, a strong La Niña event contributed to persistent above average rainfall over most of the country, with 1974 being Australia's wettest year on record. For the Georgina River catchment, January rainfall deciles were the highest on record, and the highest monthly rainfall totals, up to 400 mm, were recorded in the northern and central catchment areas (Figure S5; Appendix C2). Georgina River discharges peaked in the north (Camooweal) on January 22, in the central catchment (Roxborough Downs) on January 29 and in the south (Glengyle) on February 3, indicating an approximate two-week lag between rain falling in the headwaters and arriving in Lake Machattie during extreme flooding. As previously mentioned, the only satellite image of the 1974 flood at Lake Machattie was captured on February 7, but the two-week discharge lag confirms the estimated maximum flood elevation at Lake Machattie (79.20 m AHD) was primarily from rain falling in January.

Up until 1976, the IPO had been in a negative phase for nearly three decades (Henley et al., 2015, Vance et al., 2015). This abnormally long negative IPO was the only complete negative phase in the 20$^{th}$ century and did not return until 1999 (Parker et al., 2007, Henley et al., 2015, Vance et al., 2022). The associated westward position of warm sea surface temperature anomalies in the Pacific Ocean likely enhanced Australian rainfall variability and ENSO-monsoon teleconnections that led to the major 1974 Lake Machattie high stand.

In the preceding year, 1973, satellite imagery from September 17 (via path/row: p104r077) shows the lake had remained full since the April/May filling. The monsoon also arrived early (November 1973), which increased the level of catchment saturation antecedent to the 1974 January flooding. This relatively early monsoon was likely caused by the strong La Niña (Lisonbee and Ribbe, 2021) rather than the IOD, which was in a neutral phase. A negative IOD developed in 1974 with the La Niña, which may have gained in strength as a result (e.g., Lim and Hendon, 2017, Iskandar et al., 2018).

Strong north westerly monsoonal winds developed in late December 1973 and persisted throughout January 1974. Warmer than average seas surface temperatures in the eastern tropical Indian Ocean likely served as a significant moisture source for the already monsoon-saturated catchment. This is supported by air parcel backward trajectory frequencies over the extreme January–February 1974 flood period (Figure 4.10).

In January, anomalously high precipitable water over the warm waters of the Indian Ocean (Figure 4.10a) provided the dominant moisture source for air parcels, and associated heavy rainfalls, arriving in the north (near Camooweal) and central (near Roxborough Downs) areas of the Georgina catchment (Figure 4.10b). For the northern Georgina catchment, air parcel trajectories began shifting from the Indian Ocean to the Pacific Ocean (Coral Sea) on January 29. These findings are similar to those of Treble et al. (2017), who identified air parcel trajectories arriving at Mairs Cave in south Australia shifted from the Indian Ocean to Pacific Ocean on February 1, 1974. Peak discharges at Camooweal and Roxborough Downs on January 23 and January 29 (Figure 4.10c), respectively, supports the conclusion that a large proportion of the January rainfall originated from the Indian Ocean.

In February, reduced availability of precipitable water (Figure 4.10a), coupled with a shift in air parcels originating mainly from the Western Pacific Ocean (Coral Sea) and Southern Ocean (Figure 4.10b), reduced the amount of rainfall received in the central and southern areas of the Georgina catchment. The February inputs produced a shallow falling limb on the Roxborough Downs and Glengyle hydrographs (Figure 4.10c).

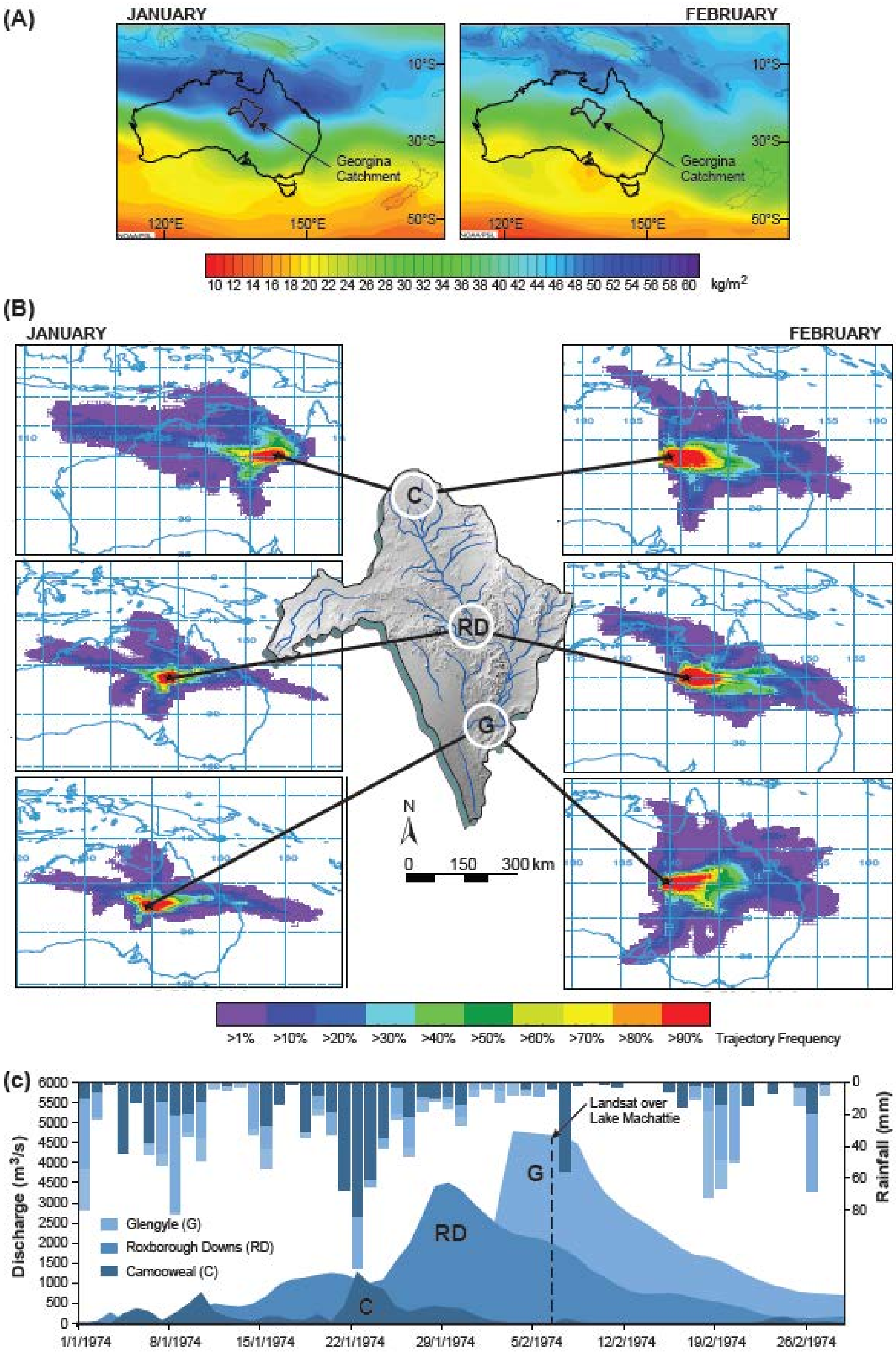


**Figure 4.10.** January–February 1974, flooding in the Georgina catchment, Australia. **(A)** Precipitable water content (kg/m$^2$) used NCEP/NCAR Reanalysis 1 (Kalnay et al., 1996) of 4x daily individual observations where the atmosphere is considered as a single layer. **(B)** Air parcel (moisture-source) back trajectory frequencies are 31-days (January: left column) and 28-days (February: right column) long, ending at Camooweal (C), Roxborough Downs (RD) or Glengyle (G) and 1500 mAGL in the Georgina catchment (inset centre image). The coloured 48-h back trajectory frequencies were calculated using the Hybrid Single-Particle

Lagrangian Integrated Trajectory model (HYPLIT) (Draxler and Rolph, 2010) and NCEP/NCAR Global Reanalysis Data (1948 onwards). **(C)** Daily discharge of the Georgina River (Eyre Creek at Glengyle) and rainfall (stacked bar graph) recorded at Camooweal (C), Roxborough Downs (RD) and Glengyle (G) during January and February 1974. Note, rainfall is the average of all gauging stations within the Georgina catchment boundary and 100 km of C (n=4), RD (n=2), or G (n=3). Rainfall is colour coded the same as for discharge. Dashed line is February 7 when Landsat 1 captured Lake Machattie during the 1974 flood.

#### *4.5.2.3 1991*

1991 was the sixth largest Lake Machattie filling and occurred under neutral phases of ENSO and the IOD. January and February were the wettest months, with the highest rainfalls occurring in February in the central Georgina catchment at Glenormiston (381 mm), Marion Downs (303 mm) and Alderley Station (235 mm). Almost all the February rainfall totals were received over a one-week period from February 5–12 (Figure S6b; Appendix C2). Over this period, 48-h air parcel back trajectory and atmospheric precipitable water content, Figures S6c–d (Appendix C2) (respectively), indicate the Gulf of Carpentaria, Arafura Sea, Timor Sea and Indian Ocean were the dominant sources of moisture arriving in the central catchment area.

Satellite imagery shows water entering Lake Machattie by February 9 via Eyre Creek and the Toko Channel, and the first water-barrier spit interaction and peak high stand occurring by February 25. The MJO gained in strength from February 15 to 25 during eastward passage through RMM phase 5 and 6 (Maritime Continent to Western Pacific, Figure S6a; Appendix C2), although it did not appear to significantly increase rainfall in the catchment. El Niño conditions developed in March; no further input was received, although flood waters continued to interact with the barrier spit for a total of 257±15 days.

#### *4.5.2.4 1997*

The March 1997 Lake Machattie filling was the second largest after 1974. In the previous year, 1996, ENSO was neutral and the IOD was in a negative phase (Saji et al., 1999), which suggests the negative IOD was not a factor in antecedent catchment saturation as a result of ENSO-IOD interactions (e.g. Risbey et al., 2009); a very strong El Niño event began in April 1997. After the Lake Machattie high stand, a positive IOD developed in 1997 at the start of the austral winter. In the north of the catchment, the 1997 January and February rainfall totals were up to 200 mm and the highest daily rainfalls were recorded on January 29 at Camooweal, Barkly Downs, Avon Downs, and Soudan (141, 58, 44 and 108 mm, respectively).

By mid-February a strengthening MJO tracked eastward through the Maritime continent (zone 4) (Figure S7a; Appendix C2). In late February, the MJO moved from the Maritime Continent (zone 5) into the Western Pacific (zone 6), and satellite imagery shows flood waters had started entering Lake Machattie. In early March, some of the largest daily rainfalls up to 200 mm occurred in the eastern central catchment area (Figure S7b; Appendix C2) (e.g., near Headingly station: 21.3225 °S, 138.2906 °E) in tune with a strong MJO phase in zone 6 of the Western Pacific. Indeed, 1997 had the strongest March zone 6 MJO of all the modern floods that interacted with the barrier spit in Lake Machattie. The 7-day air parcel back trajectory frequency and precipitable water content (Figure S7c–d; Appendix C2) shows the Coral Sea was the dominant moisture source reaching the catchment around Headingly Station between March 1–7. As the MJO reduced in strength after March 12 and continued its eastward propagation through RMM zone 7, the heavy rainfalls in the Georgina catchment ceased and Lake Machattie reached its peak around March 30.

##### *4.5.2.5 2001*

Starting in May 1998 and ending in March 2001, a La Niña event led to yearly heavy rainfalls in the Georgina River catchment and moderate to high lake fillings in Lake Machattie. From March 2000, pluvial lake conditions persisted until September 2002. During this three-year La Niña event, 2001 was the only flood year that water interacted with the barrier spit, starting around January 12. The shift to a negative IPO in 1999 potentially increased summer monsoon rainfall variability and the strength of ENSO teleconnections (e.g., Power et al., 1999, Mantua and Hare, 2002, Cai and Van Rensch, 2012, Heidemann et al., 2022, Heidemann et al., 2023).

Influence from the MJO from late December 2000 through to the end of January 2001 was unlikely given its position in the Western Hemisphere and Africa and in the Indian Ocean (Figure S8c–d; Appendix C2). However, in late November 2000, the active MJO in zone 4 coincided with the development of a broad area of low pressure in the Gulf of Carpentaria around November 28, eventually forming Tropical Cyclone Sam off the north Kimberly coast on December 5. After December 10, Ex-Tropical Cyclone Sam travelled as a tropical low in an easterly direction across the Great Sandy Desert in northwest western Australia (Figure S8a; Appendix C2), reaching just shy (~100 km) of the northern Georgina catchment on December 14.

The monsoon trough was located over northern Australia for most of December 2000. Southward perturbations of the monsoon, and associated low-pressure systems and troughs, were generally associated with higher daily rainfalls in the Georgina catchment. From December 7–29, continuous heavy rainfalls were recorded mainly in the northern (~300 mm) and central (~200 mm) regions of the catchment. Air parcels reaching the northern catchment during this period originated from areas with high precipitable water content (Figure S8f–g; Appendix C2) in the Arafura Sea (Gulf of Carpentaria) and Coral Sea.

Rainfall in January 2001 was substantially lower (<100 mm), partly because air parcels arriving in the northern Georgina came from the drier southeast (Figure S8e; Appendix C2) rather than from the moisture filled north as in December 2000 (Figure S8b; Appendix C2). Overall, the ephemeral saturation of the catchment caused by the prolonged La Niña, the active monsoon trough and low-pressure systems, coupled with a final input from the MJO-forced Ex-Tropical Cyclone Sam led to the third largest high stand in Lake Machattie in late January 2001.

#### *4.5.2.6 2007*

2007 is the lowest ranked flood that interacted with the barrier spit in Lake Machattie and occurred during an El Niño and the negative IPO phase. Most of the rain fell in January resulting from the development of a low-pressure trough across eastern Northern Territory and southwest Queensland (January 7–25), and an active monsoon trough (January 15–21) and a tropical depression (January 21–25) that tracked slowly eastward over the catchment. MJO passage through zone 5 of the maritime continent and zone 6 of the Western Pacific from January 2–15 (Figure S9a; Appendix C2) may have enhanced these monsoon-related low-pressure systems.

While continuous heavy rainfalls were received in the north and central areas of Georgina catchment from January 15–27, the heaviest rainfalls were near Lake Machattie fed mainly by moisture filled air parcels arriving from the Coral Sea from January 20–21 (Figure S9b–c; Appendix C2). Within 100 km of Lake Machattie, the heaviest daily rainfalls were recorded at Sandringham, Bedourie, Kamaran Downs, Cluny and Glengyle (175, 169, 169, 133 and 127 mm, respectively). Despite these large inputs in the south, satellite imagery from January 28–29 shows the entire Georgina River was in flood, which suggest the flood waters were probably generated in further north. On January 29, flood waters started entering Lake Machattie that was previously dry. The high stand occurred around February 22 and water-barrier spit interaction lasted for a total of 224 days (±7 days).

#### *4.5.2.7 2009*

The January 26, 2009, high stand was the fifth largest filling that interacted with the barrier spit for a total of 272±7 days. A weak La Niña between August 2008 and April 2009 was superimposed on the negative IPO. From December 30, 2008, through to January 7, 2009, an active monsoon trough and embedded low-pressure trough were located over central Northern Territory and western Queensland delivering the bulk total rainfalls for January.

Consistent high daily rainfalls in the north and south of the catchment were received in the first week of January from moisture laden air parcels coming from the Timor Sea and Arafura Sea (Figure S10b–d; Appendix C2). Satellite imagery from January 10 shows Lake Machattie did not receive fluvial input from the southern rainfall; however, a large flood front was located ~50 km upstream of Bedourie in the Georgina River microchannel, which suggests most of the flood waters were generated further north. From January 3–10, there was a brief passage of the active, albeit relatively weak, MJO in RMM zone 6 (Figure S10a;

Appendix C2) that may have enhanced tropical convective anomalies and increased rainfall deliveries in the northern Georgina catchment during this period.

Camooweal, in the north, and Marion Downs, in the lower central region of the Georgina catchment, both recorded their highest daily rainfalls on January 7 (113 mm and 192 mm, respectively). In the central catchment area, the highest daily rainfalls received at Roxborough Downs, Glenormiston and Urandangi were from January 19-20 (49, 48 and 62 mm, respectively). From 2009 onwards, pluvial lake conditions persisted in lake Machattie until December 2012, with the rise and fall of water levels interacting with the barrier spit each year.

#### *4.5.2.8 2010*

The 2010 lake filling occurred at the end of an 11-month long weak El Niño (ending in March). It ranks as the second lowest high stand after 2007, which also occurred during El Niño. The IOD was neutral in 2009 but emerged as a strong negative phase in 2010, albeit after Lake Machattie was already full. Negative IPO conditions persisted. There were two main wet periods in the lead up to this high stand.

The first event occurred within a 2-week period starting in late December 2009 where heavy rainfalls were mainly received in the northern and central regions of the Georgina catchment. A low-pressure trough was situated across the Northern Territory and central and southern Queensland (December 29 to January 4), and an active monsoon trough tracked southward across the Northern Territory (December 30 to January 7) with a low-pressure trough extending from the monsoon trough across into central Queensland (January 6–7).

The highest daily rainfalls were recorded in the north at Camooweal (63 mm, December 31) and at Avon Downs and Soudan (125 mm and 122 mm, January 8 and 9, respectively). Roxborough Downs in the central Georgina catchment recorded 115 mm (January 6), and Glengyle in the south recorded 43 mm (January 8). 48-h air parcel back trajectories show the Gulf of Carpentaria as the main source of moisture (Figure S11c;

Appendix C2) arriving in the northern and central Georgina catchment from December 29, 2009, to January 10, 2010 (Figures S11d–e; Appendix C2, respectively). Although substantial flooding occurred across the northern and central areas of the Georgina catchment and Lake Machattie eventually received input from this wet period around February 6, it did not cause an observable lake level rise. This first flood did however saturate the catchment prior to the second, and more intense, flooding event that started in late February.

Between February 22 to March 1, high rainfall was received across the catchment from a low-pressure system within an active monsoon trough that remained over the Northern Territory until February 28 before tracking eastward into southwest Queensland on March 1. Some of the heaviest daily rainfalls occurred on March 1 over central areas of the catchment including at Glenormiston and Roxborough Downs (both 115 mm), and in the south at Glengyle and Cluny (163 and 160 mm, respectively). Across the catchment, 48-h back trajectories show the Coral Sea, Gulf of Carpentaria, Arafura Sea and Tasman Sea were the main sources of moisture arriving between February 22 and March 1 (Figures S11g–i; Appendix C2). However, the Gulf of Carpentaria had higher precipitable water content during this period compared to other sources (Figure S11f; Appendix C2). The first major input to Lake Machattie, and interaction with the barrier spit, was around March 10 and the peak high stand was observed on April 3. Passage of the active MJO through zones 4–6 (March 26 to April 7: Figures S11a–b; Appendix C2) was not associated with increased rainfall during this wet period. Indeed, after March 3, little to no rain was received in the catchment.

Overall, the 2010 flooding occurred in an already saturated catchment and Lake Machattie was still relatively full because of the 2009 filling. Only 4.5 months had passed since flood waters stopped interacting with the barrier spit in 2009 before Lake Machattie started receiving input in 2010. The input from 2010 continued to interact with the barrier spit until early January 2011.

*4.5.2.9 2011*

The 2011 Lake Machattie high stand was the seventh largest in our record. In August 2010, a strong La Niña developed that was potentially strengthened by the co-developing strong negative IOD (e.g., Lim and Hendon, 2017, Iskandar et al., 2018). The negative IOD may have also contributed to the early (November) arrival of the monsoon in Australia. However, Lisonbee and Ribbe (2021) showed a strong La Niña had the greatest impact on expediting the monsoon onset. The IPO was negative.

2010 was the highest recorded monthly southern oscillation index (SOI) (+27.1) for December for the entire period of study. Above average SSTs across northern Australia were estimated to have contributed ~25% of the total December rainfall received across Queensland, mainly falling in the southeast (Evans and Boyer-Souchet, 2012). In the Georgina catchment, December rainfall totals were <100 mm and mainly confined to the north. An active, albeit relatively weak, MJO may have caused deep convection and enhanced rainfall in the northern Georgina during passage through RMM zones 4–6 from December 4–14 (Figure S12a; Appendix C2). Although these flood waters did not reach Lake Machattie, they saturated the catchment prior to the February-March floods.

The SOI in January (+19.9) was the third highest January on record, and the February and the March SOI values were the highest on record for these months (+22.3 and +21.4, respectively). The MJO may have played a role in enhancing rainfall deliveries in early January due to its position in RMM zone 6 (Figure S12b; Appendix C2) but had little to no effect on the February and March rainfall totals. Ex-Tropical cyclone Yasi (Figure S12c; Appendix C2) reached the Georgina catchment as a tropical low around February 4 and was associated with an active monsoon trough that delivered a brief but intense rainfall event to the north. Lake Machattie did not receive fluvial input from this event.

Persistent rainfall was received across the catchment from January to March 2011 mainly related to the active monsoon and low-pressure systems and troughs. The highest January-March rainfall totals ranged from 257 to 322 mm in the north at Rocklands and Avon Downs, and from 150 to 165 mm in the central Georgina at Urandangi and Glenormiston, respectively. However, the largest monthly falls occurred within 100 km of Lake Machattie in March including at Kamaran Downs (573 mm), Bedourie (474 mm), Glengyle (438 mm) and Cluny (432 mm). Most of the rain fell in early March and had ceased by March 20. 72-h air parcel back trajectories indicate the Coral Sea and Gulf of Carpentaria were the main source of moisture arriving near Lake Machattie from March 1–20 (Figure S12e; Appendix C2). However, higher precipitable water contents were available in the Gulf of Carpentaria (Arafura Sea) compared to the Coral Sea during this period (Figure S12d; Appendix C2).

The highest daily rainfalls were on March 6. The active monsoon tough was positioned over the southern Georgina catchment and the stations within 100 km of Lake Machattie received daily rainfall totals >180 mm. Kamaran Downs received its highest daily rainfall on record on March 6, which accounted for 63% of its March total. Satellite imagery shows the first interaction with the Barrier spit was on March 21 and the peak high stand was on April 22.

#### *4.5.2.10 2019*

The 2019 high stand occurred around April 28 and was the eighth highest filling. Following the end of La Niña conditions in March 2018, ENSO remained neutral until September 2020. However, ENSO conditions bordered on El Niño from the 2018 austral winter until well after the Lake Machattie filling. Positive IOD conditions in 2018 may have contributed to the late arrival of the monsoon between January 18–23 (in Darwin). A negative IPO phase was likely based on recent TPI data (unfiltered). Two relatively short rainfall events in the Georgina catchment led to the 2019 lake filling.

At the start of February 2019, rainfall from an MJO-influenced monsoon trough (Cowan et al., 2019, Tsai et al., 2021) and embedded tropical low contributed to a partial filling of Lake Machattie in early March. The quasi-stationary monsoon depression was located over northwest Queensland (February 1–5) before slowly travelling east towards the Queensland coast (February 6–8). During this period, the MJO was in RMM zones 6 and 7 (Figure S13a; Appendix C2), and the heaviest daily rainfalls were <100 mm in the north and central Georgina catchment. The Coral Sea was a source of high precipitable water (Figure

S13b; Appendix C2) and the origin of air parcels arriving in the northern Georgina between February 1–8 (Figure S13c; Appendix C2).

In late March, Ex-Tropical Cyclone Trevor travelled through the northern Georgina catchment up to 21°S as a tropical low delivering substantial rainfall over a one-week period (Figure S13f; Appendix C2). The heaviest daily rainfalls were in the north at Soudan (85 mm), in the central Georgina at Urandangi Aerodrome (135 mm), Manners Creek (160 mm) and Glenormiston (77 mm), and in parts of the central eastern catchment such as Phosphate Hill (163 mm). Air parcels reaching these areas between March 24-31 originated from the Coral Sea and Tasman Sea, although comparatively lower precipitable water was available from the Tasman Sea (Figure S13d–e; Appendix C2). Flood waters reached Lake Machattie in early April and started to interact with the barrier spit around April 20.

#### *4.5.2.11 2023*

The 2023 Lake Machattie filling was the fourth highest lake filling and occurred at the end of a three-year La Niña event. This was the first three-year La Niña since 1998–2001 (Fang et al., 2023), which also ended with flood waters interacting with the spit. Lake Machattie filled during the 2022 Austral wet season, but was non-interactive with the barrier spit, and surface waters dried before the years end. The IOD was negative until October 2022 and remained neutral up to at least the end of April 2023. The long La Niña ended in March 2023. Recent (unfiltered) TPI data indicates the IPO was likely in a negative phase.

In 2022, monsoon bursts coupled with the development of Tropical Cyclone Ellie northwest of Darwin in the Timor Sea coincided with enhanced convection from the active MJO in RMM zone 4 from December 20–21 (Figure S14a; Appendix C2). From December 22–27, Ex-tropical cyclone Ellie travelled as a tropical low in a southeast direction across the Northern Territory towards the Georgina catchment (Figure S14e; Appendix C2). Almost all the December rainfall totals in the north and central areas of the catchment related to this event including at Rocklands (200 mm), Camooweal (162 mm), Tobermorey (143 mm), Glenormiston (102 mm) and Roxborough Downs (149 mm); little to no rain was received in the southern catchment. Between December 22–27, 2022, the atmosphere over the Gulf of

Carpentaria, Tasman Sea and Arafura Sea was high in precipitable water content (Figure S14c; Appendix C2) and 72-h back trajectories show these regions were the main moisture sources for air parcels arriving in the north and central areas of the Georgina catchment (Figure S14d and f; Appendix C2, respectively). Moisture from the Coral Sea also reached areas in the central catchment. January and February rainfall totals were <100 mm, with the heaviest falls recorded in the north. Satellite imagery shows water started entering Lake Machattie in late January.

A second heavy rainfall event occurred in early March. A low-pressure system and trough moved in an easterly direction across the Northern territory (March 1–4) into the Gulf of Carpentaria for three days (March 5–7) before it travelled south into northwest Queensland (March 8–10). The monsoon trough also developed with these low-pressure systems during March 1 and from March 5–8, which was potentially influenced by the MJO as it entered zones 6 and 7 between February 28 and March 7 (Figure S14b; Appendix C2). Record breaking March rainfalls occurred in the north at Camooweal (423 mm) and Rocklands (429 mm) - records previously held since 1903 and 2011, respectively. The bulk of these rains occurred before March 11 in sympathy with the passage of the low-pressure systems through the Northern Territory and Queensland. 72-h back trajectories indicate the Coral Sea and Arafura Sea as the main moisture sources for air parcels reaching the northern catchment between March 1–11 (Figure S14g–h; Appendix C2). Flood waters started interacting with the barrier spit in late February and the high stand occurred around April 23.

*4.5.2.12 Summary: Implications for climate*

Most of the lake fillings were during La Niña events at times of a negative IPO, and four out of the five largest high stands occurred during this climate superposition. Verdon et al. (2004) showed IPO-La Niña modulations had the greatest impact on rainfall and streamflow variability in coastal areas of Queensland and New South Wales, and inland areas of Victoria, related to the southward migration of the South Pacific Convergence Zone in summer months. However, only two gauging stations within the Georgina catchment were used in the Verdon et al. (2004) study, both of which showed rainfall during periods of superposition of La Niña and negative IPO was not significantly higher than during La Niña alone.

Although nine out of the eleven modern high stands in Lake Machattie were during a negative IPO, palaeo-IPO records from trans-Pacific tree rings (Buckley et al., 2019) show deposition of unit A (1784 CE) and B (1830 CE) were during neutral-slightly positive IPO conditions. Drought indices, based on the Palmer Drought Severity Index, shows reconstructed summer rainfall for Western Queensland was also average during these periods (Cook et al., 2016). However, Haig et al. (2014) showed there was elevated cyclone activity in the north of the continent during the late 1700's and early 1800's, relative to present, which suggests cyclone-generated flooding could have led to deposition of these units in Lake Machattie. Expansion of the Indo-Pacific tropical rain belt towards the end of the Little Ice Age (LIA; AD 1400–1850) (Denniston et al., 2016) could have also been a contributing factor.

Two of the modern high lake stands correspond with El Niño events, which were the lowest ranked fillings and occurred where the lake level remained high from flooding in the preceding year. It is interesting to note that 1991 and 1997 were the only two fillings to occur during neutral ENSO conditions, a positive IPO phase and where the lake was dry from the year prior. Paradoxically, 1997 was the time of the second largest high stand in Lake Machattie.

The four most recent Lake Machattie high stands (2023, 2019, 2011 and 2010) occurred in April, and the three most recent events were in late April. Except for the 1973 filling that also peaked somewhere between early-April and mid-May, all other high stands were in January-March. A delay in the monsoon onset could have potentially caused these later lake fillings. While positive IOD phases can delay the monsoon (Lisonbee and Ribbe, 2021), this only applied to the 1973 and 2019 April lake fillings and indicates the IOD was probably not a forcing factor. Similarly, Lisonbee and Ribbe (2021) also showed the El Niño increases the probability of a delayed monsoon onset by 60%, but out of these later fillings, only the 2010 flood occurred during an El Niño.

### 4.5.3. Comparison with Burdekin River flows

The Burdekin River catchment is Queensland's second largest exorheic drainage basin. River flood plumes on the Great Barrier Reef (GBR) have been effectively reconstructed using coral luminescence (or fluorescence) lines observed under ultra-violet light in annually banded massive *Porites* spp. skeletons (Isdale, 1984). Lough (1991) demonstrated Burdekin River flow-derived coral fluorescence, from Pandora Reef (~150 km from the river mouth), were strongly correlated with the instrumental summer rainfall record (1923–1984) for central northern Queensland including most of the Georgina catchment and concluded flood plume coral fluorescence is a reliable palaeo-rainfall proxy for central Queensland. Very large freshwater plumes from the Burdekin River reached Britomart Reef, ~180 km northwest of the river mouth (Lough et al., 2015), coinciding with the 1974, 1991, 2009, and 2011 Lake Machattie fillings. Indeed, Lough et al. (2015) ranked the 1974, 1991, and 2011 Burdekin River flows as the most extreme in their 364-year reconstruction (1648–2011). The Lake Machattie high stands including 2001, 2007, 2009, 2010 and 2011 also correspond to one of the four wettest 10-year periods in the Lough et al. (2015) Burdekin River flow reconstruction.

Not all large Burdekin River flows correspond with modern high stands in Lake Machattie. Burdekin River runoff was high in 1981 (17.98 $km^3$) and was also recorded in coral fluorescence signatures at Britomart (Lough et al., 2015) and Kurrimine (Hendy et al., 2003) reefs, with the latter also receiving freshwater contributions from the Herbert River. However, fluvial input to Lake Machattie in 1981 was only moderate and did not interact with the barrier spit. 1972 and 2008 were also large Burdekin flow years >$90^{th}$ percentile (18.91 $km^3$ and 27.97 $km^3$, respectively, Figure 4.11), but it is unclear whether the 1972 flood interacted with the barrier spit, as previously mentioned, and no input to Lake Machattie was observed in 2008. Interestingly, despite the 1997 Lake Machattie filling being the second largest in our record, the corresponding Burdekin River flow was only slightly above median (Figure 4.11), which shows that wet periods in the Georgina catchment do not always translate to east coastal areas.

Deposition of the basal avalanche foresets (unit A) at 1784 CE (range: 1754–1814) and the sandy clay bed (unit B) at 1830 CE (range: 1802–1858), pit 1, correspond with extended dry periods in coral luminescence records. Hendy et al. (2003), who created a master Burdekin River flow chronology from eight coral cores dating back to 1615 CE, identified the mid-1760's to mid-1780's and the 1790's as stand out dry periods, and suggested weak ENSO teleconnections with north-east Queensland rainfall persisted from the 1800's to 1870's. An extended dry period between the 1760's and 1850's was identified by Lough (2011) in their 20-coral core river flow record, and Lough et al. (2015) later identified 30-year periods of minimum Burdekin River flows in 1771–1800 and 1802–1831. These reconstructions of Burdekin River flow show low rainfall variability in northeast Queensland (Hendy et al., 2003) persisted at the time when the basal foresets and sand-clay bed in pit 1 were deposited. The largest Burdekin flow within error of 1830 ±28 CE was in 1831 based on the reconstruction of Lough et al. (2015), indicating deposition of the sandy clay bed was probably in 1831. Although the dry periods in the mid- to late-18$^{th}$ century and early 19$^{th}$ century were identified in the coral record, our sedimentological record of the 1784 CE and 1830 CE high stands shows Lake Machattie still received significant input equivalent to modern magnitudes.

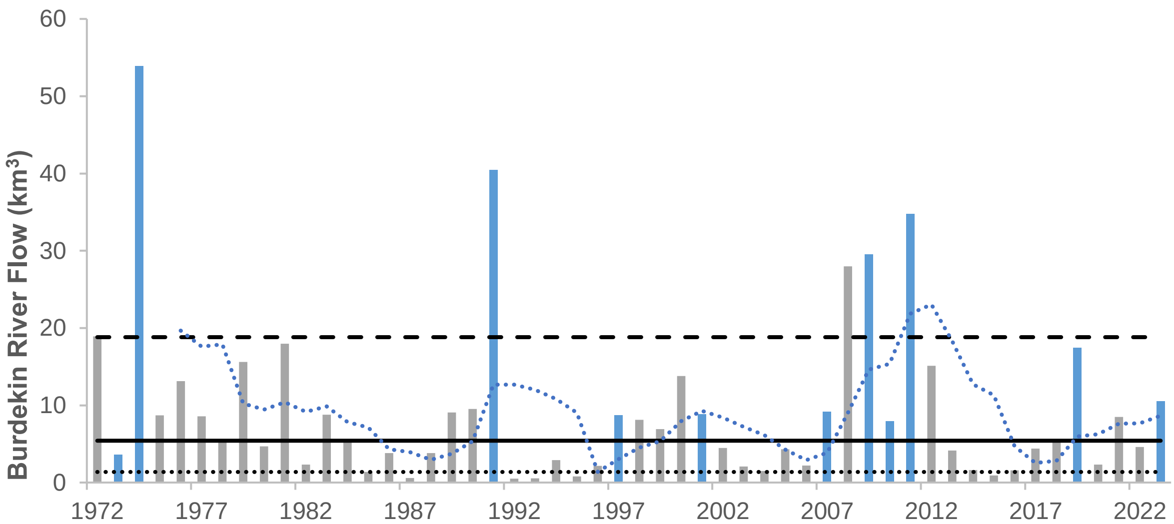


**Figure 4.11.** Yearly Burdekin River flow (km$^3$) volumes for Burdekin River gauging stations (Clare: ID120006A and 120006B) for 1972 to 2023 were obtained from the Queensland Government (https://water-monitoring.information.qld.gov.au). The annual total river flow data is the "water year" defined as July 1 to June 30 by the Australian Bureau of Meteorology. Median (solid black line); 90$^{th}$ percentile (dashed black line); 10$^{th}$ percentile (dotted black line); 3-year moving average (dotted blue line). Blue coloured bars are Lake Machattie high stands discussed in text.

### 4.5.4 Implications for LEB

KT-LE is the ultimate beneficiary, and depocenter, of flood waters from the Georgina River catchment. However, the amount of water from the Georgina River that reaches the Diamantina River at Goyder's lagoon and, eventually, KT-LE is unknown. There are no river gauging stations in the Georgina downstream of Glengyle (as Eyre Creek). Satellite imagery shows that, except for a small input in 1995, flood waters only reached Goyder's lagoon in the years that water interacted with the barrier spit in Lake Machattie. It is unknown if the 1973 or 1974 flood waters reached Goyder's lagoon due to excessive cloud cover and a limited number of satellite images over that area. However, it is assumed the 1974 flood waters reached the Diamantina given it was the largest modern flood on record. This highlights that while the three major river catchments of the LEB including the Cooper, Diamantina and Georgina can generate significant flows to KT-LE, input from the Georgina only occurs during large floods or when the lower reaches of the catchment are already saturated (e.g., during 2010). This suggests that our record of Georgina River palaeoflooding in 1784 ±30 CE and 1830 ±28 CE likely contributed to the Diamantina River flow and possibly reached KT-LE. Some consistency can be observed between these two events and a beach facies shoreline deposit at Williams Point in KT-LE, OSL-dated at 1854 ±21 CE (Cohen et al., 2018). Ultimately, the modern- and palaeo-high stands observed in satellite imagery and recorded in the shoreline deposits at Lake Machattie provide a useful proxy for flood levels large enough to potentially reach KT-LE.

## 4.6 Conclusion

This research presented here shows the barrier spit in northwest Lake Machattie holds sedimentological evidence of major flooding in the Georgina dating back to the late 18$^{th}$ century. The overall internal stratigraphic architecture of the Lake Machattie barrier spit is dominated by a series of landward-prograding overwash deposits generated during extreme lake fillings. Modern flood events were identified from these sedimentary units within the barrier including 1974 (or 1977) and 1997 and/or 2001, which were coincidently the largest lake fillings between 1972 and 2023 based on available Landsat spectral data. The sandy beach ridge was most likely formed during the 2019 filling that was followed by a relatively rapid and continuous regression. All modern floods that interacted with the barrier spit reached the Diamantina River and highlighting the fact that waters from the Georgina River can contribute to modern- and palaeo-KT-LE fillings. Hence, the Lake Machattie shoreline deposits are considered an accurate palaeo-archive of extreme flooding events in the LEB's most northern catchment. We identified two palaeoflooding events from the barrier's sedimentary units at 1784 ±30 CE and 1830 ±28 CE. The latter that may well be tied to pluvial conditions in KT-LE around 1854 ±21 CE.

The climate patterns associated with the generation of pluvial conditions in the Georgina catchment is less clear. Our analysis showed modern Lake Machattie high stands are generally tied to La Niña events combined with negative phases of the IPO, suggesting precipitation over the northern LEB could be strengthened by IPO-La Niña modulations. However, the second largest filling in 1997 and Queensland rainfall correlations (Verdon et al., 2004) indicate that the superposition of La Niña and negative IPO conditions is not necessary. Indeed, positive IPO conditions were also likely present during the identified Georgina River palaeoflooding events in the late 1700's and early 1800's. Burdekin River flows were similarly quiescent during this period, which could indicate flooding in the Georgina may have been partly caused by elevated cyclone activity over northern Australia (Haig et al., 2014) and an expanded tropical rain belt in the Indo-Pacific (Denniston et al., 2016). Comparatively, our modern record of high stands in Lake Machattie generally supports the existence of a positive relationship between rainfall in the Burdekin River catchment and the Georgina catchment, but not always. Further investigations of the shoreline deposits around Lake Machattie, and possibly nearby playas such Lake Torquinie and Mumbleberry Lake in the Georgina catchment, are required to elucidate the frequency and variability of fluvial activity in the Georgina River particularly as it relates to KT-LE fillings over past centuries.

# Chapter 5

# Summary and future work

Singleton, R.E

## 5.1 Main Findings

The significance of the Georgina River catchment, and its potential contributions to Kati-Thanda Lake Eyre (KT-LE) filling, have been discussed for more than 70 years (e.g., Bonython and Mason, 1953, Gunn and Fleming, 1984, Kotwicki and Isdale, 1991, Habeck-Fardy and Nanson, 2014, Cohen et al., 2022). Yet despite this apparent significance, no detailed sub-surface sedimentological studies have (until now) been carried out on either dunefields or lakes in the catchment. This thesis set out to fill this knowledge gap. Given the limited data and the unknown age of the sediments, this thesis investigated three distinct sedimentary environments — aeolian, lacustrine, and shoreline — to capture the maximum spatial and temporal details for the natural history of the Georgina catchment. The discovery of past major wet and dry phases that include significant lake expansions in the wetland areas of the Georgina catchment during MIS 7 and 5 highlight the importance of the Georgina catchment to understanding the palaeohydrological history of the Lake Eyre Basin. Evidence of a cool and wet early MIS 3 before a period of known aridification and megafauna extinctions further cement the Georgina catchment's place as an important and integral part of the late Quaternary climatic history of central Australia.

The primary aim of this thesis was to develop a comprehensive palaeoclimate and palaeoenvironmental history of the Georgina catchment, and to investigate how these relates to the palaeo-lake fillings observed in KT-LE. This overarching aim was achieved through the realisation of three additional aims. The first aim was to investigate the sub-surface sedimentology of the ephemerally flooded Lakes Koolivoo and Machattie, and Eyre Creek, to develop an understanding of the palaeodepositional evolution of the Lake Koolivoo and Machattie area. The second aim was to constrain the depositional and pedogenic palaeoclimate and palaeoenvironment of a palaeosol-bearing, source-bordering dune along the northeast margin of the Simpson Desert. The third aim was to examine the shoreline sedimentary features of Lake Machattie to determine lake-level variation and develop a record of historical fillings and relate these to coeval climate phenomena. These three aims formed the foundation for the research presented in chapters 2 to 4, which is summarised here, with additional discussion of the limitations and potential for future work.

The first aim was achieved using a multi-proxy approach that included macro- and micro-morphology, major element and isotope geochemistry, optically stimulated luminescence (OSL) and radiocarbon dating, and spectral frequency analysis. Each of these techniques were applied to the sediment cores extracted from Eyre Creek, and Lakes Koolivoo and Machattie. Collectively, the data revealed that over the last 500,000 years Lakes Koolivoo and Machattie have oscillated between perennial lacustrine environments during wet periods and groundwater-controlled ephemeral playas punctuated by phases of soil development in drier times. Spectral frequency analysis suggests cycles of enhanced precipitation were influenced by a combination of lunar, orbital/insolation, and solar forcing, northern high-latitude cooling/warming events, as well as tropical Pacific mechanisms. As expected, the timing of several important wet phases in the Georgina catchment correspond with those in other central Australian lakes, for example early MIS 7 and late MIS 5. So too, the discovery that the Lake Machattie Area documented progressive drying from MIS 4 onwards was unsurprising given the extensive body of evidence for continental aridification of Australia during the late Quaternary (e.g., Miller et al., 2005a, Miller et al., 2016a). However, it provides evidence that major wet and dry phases in the Lake Machattie Area do not always parallel with those in KT-LE. That was not anticipated and is a key finding of this thesis.

The second aim of constraining the palaeoclimate and palaeoenvironment of a palaeosol-bearing, source-bordering dune, was achieved using palaeosol geochemistry and mineralogy, sedimentology and OSL geochronology. Using these techniques in a dune pit, rather than on a drill core, enabled the discovery of multiple sediment beds from two distinct time periods – the late Pleistocene and the Historic Period – separated by an unconformity. By focusing equally on both the palaeosol and non-pedogenically altered sediments a detailed reconstruction of palaeoclimate and palaeoenvironment was possible. Indeed, our record of a humid, mesic climate around ~50 ka demonstrated that monsoon rainfall deeply penetrated northern inland Australia at the same time KT-LE was last in a mega-lake phase. While aeolian sediments documented dune building over the last 200 years that period was interrupted by two alluvial/fluvial events, one in 1831 and the other most likely in 1894/95. The flood record of 1831 corresponds with a high lake stand at Lake Machattie and a reconstructed large inflow into KT-LE, implying monsoon rainfall penetrated to at least 23°S and that the entire Georgina catchment was active and feeding water into KT-LE. IN contrast, flooding in 1894/95 was coincident with flooding in the Burdekin River, which shares a headwater divide with the Cooper catchment, suggesting that it was wet from central Australia to the East coast and that all three northern catchments of the LEB were likely active. Importantly, this thesis delivers the first palaeoprecipitation record for one of the Lake Eyre Basin's major northern catchments, and the first quantitative palaeosol climate reconstruction for the Quaternary in Australia.

The third aim of determining historical lake-level variations in Lake Machattie, was achieved using OSL geochronology, sedimentology and spatial analysis of aerial and satellite imagery. By combining remote sensing data with direct sedimentological investigations of the barrier spits at Lake Machattie this thesis was able to provide a detailed record of historical fillings and lake-level variations, manifest as shoreline positions. In fact, the Lake Machattie barrier spit is dominated by a series of landward-prograding overwash deposits that were generated during extreme lake fillings dating back to the late 18$^{th}$ century. Two palaeoflood deposits from ~1784 and ~1830 are overlain by sediments that represent eleven separate modern flood events that have occurred since 1974. These modern Lake Machattie high stands are generally tied to La Niña events combined with negative phases of the IPO, although not always (e.g., 1997). A generally positive relationship between rainfall in the Burdekin River catchment and the Georgina catchment is also suggested. There is also little doubt that periods of elevated cyclone activity over northern Australia (e.g., Haig et al., 2014) or an expanded tropical rain belt in the Indo-Pacific (e.g., Denniston et al., 2016) led to increased rainfall, influencing the hydrology of the Georgina catchment.

## 5.2 Limitations

Whilst sedimentologic and stratigraphic analyses of the sequences in the Georgina catchment successfully determined the palaeoclimate and palaeoenvironment during the late Quaternary, it would be remiss to not discuss the limitations associated with this research. The depth and frequency of samples collected for geochronological analysis were carefully selected. Unfortunately, budgetary constraints limited the total number of OSL and radiocarbon analyses. In addition to several OSL samples not returning a date (i.e., no grains or saturated). While chronologic data is in stratigraphic order within each section, the relatively small number of dates limits the temporal accuracy of the palaeoenvironmental interpretations. Palaeoenvironmental results of the Lake Machattie Area cores are also limited by relatively low sampling resolutions in some proxies. For example, major element data were only collected every 10 cm, whereas magnetic susceptibility was possible every 0.5 cm. This sample resolution discrepancy also prevented reliable identification of sub-Milankovitch frequencies that may have influenced precipitation over the Georgina catchment. In addition, analysis of the dune sediments along the northeast margin of the Simpson Desert would have benefited from the examination of multiple dunes, although this was not possible given time and financial confines.

Though this thesis set out to determine when the Georgina catchment was feeding water south to KT-LE, the lack of continuous gauging data in the lower reaches of the Georgina catchment prevents the determination of how much stream flow reaches the Georgina-Diamantina confluence under modern hydrologic conditions. This limits our ability to quantify the Georgina Catchment's inputs to KT-LE in modern times and inhibits a clearer understanding of its palaeo contributions.

**5.3 Future Work**

The research presented in this thesis is noteworthy because it provides valuable new insights into the palaeodepositional environments and palaeoclimate of the Georgina catchment, filling known knowledge gaps for several key periods in central Australia’s late Quaternary history. Whilst the results in this study are novel and an important contribution to the previously untold natural history of the Georgina catchment, they are far from exhaustive. Indeed, the catchment stretches across 205,000 $km^2$ that encompasses vast dunefields, floodplains, lakes, and river channels that remain unexplored.

Several key areas are of interest to the candidate. The candidate would like to explore other lakes and shoreline deposits in the Georgina catchment, such as Lake Torquinie and Mumbleberry Lake, to better understand the frequency and variability of fluvial activity in the Georgina River, particularly as it relates to KT-LE fillings. Investigating multiple dunes across multiple dunefields in the LEB to reconstruct the depositional and pedogenic palaeoclimate and palaeoenvironment through the late Quaternary is also of interest. Future work would focus on palaeosol-bearing dunes that contain mature profiles with a minimum of two preserved horizons (one of which is a B horizon), to enable further development of quantitative palaeotemperature and palaeoprecipitation records that could help identify the timing of aridification in the late Pleistocene. There is no doubt that the playa lakes and palaeosols preserved in the desert dunes of inland Australia remain a relatively untapped resource of late Quaternary terrestrial palaeoclimate data that could improve our understanding of climate variability through a critical period of early human occupation and megafaunal extinctions.

# References


Aagaard, T., Davidson-Arnott, R., Greenwood, B., & Nielsen, J. (2004). Sediment supply from shoreface to dunes: linking sediment transport measurements and long-term morphological evolution. Geomorphology, 60(1–2), 205–224.

Ahr, S. W., Nordt, L. C., & Forman, S. L. (2013). Soil genesis, optical dating, and geoarchaeological evaluation of two upland Alfisol pedons within the Tertiary Gulf Coastal Plain. Geoderma, 192, 211–226.

Ainsworth, R. B., Hasiotis, S. T., Amos, K. J., Krapf, C. B., Payenberg, T. H., Sandstrom, M. L.,…Lang, S. C. (2012). Tidal signatures in an intracratonic playa lake. Geology, 40(7), 607–610.

Al-Masrahy, M. A., & Mountney, N. P. (2015). A classification scheme for fluvial–aeolian system interaction in desert-margin settings. Aeolian Research, 17, 67–88.

Allen, J. R. (1977). The possible mechanics of convolute lamination in graded sand beds. Journal of the Geological Society, 134(1), 19–31.

Allen, J., & O'Connell, J. (2014). Both half right: updating the evidence for dating first human arrivals in Sahul. Australian Archaeology, 79(1), 86–108.

Alonso-Zarza, A. M., & Wright, V. P. (2010). Calcretes. Developments in Sedimentology, 61, 225–267.

Amrani, A., Said-Ahmad, W., Shaked, Y., & Kiene, R. P. (2013). Sulfur isotope homogeneity of oceanic DMSP and DMS. Proceedings of the National Academy of Sciences, 110(46), 18413–18418.

Arakel, A., Jacobson, G., Salehi, M., & Hill, C. (1989). Silicification of calcrete in palaeodrainage basins of the Australian arid zone. Journal of the Geological Society of Australia, 36(1), 73–89.

Ardi, R., Maryunani, K., Yulianto, E., Putra, P., & Nugroho, S. (2022). Australian–Indonesian monsoon rainfall responses to the northern hemisphere climatic changes prior to the Last Glacial Maximum: an early indication. IOP Conference Series: Earth and Environmental Science, 1047(1), 012031.

Arnold, L. J., & Roberts, R. G. (2009). Stochastic modelling of multi-grain equivalent dose (De) distributions: Implications for OSL dating of sediment mixtures. Quaternary Geochronology, 4(3), 204–230.

Arnold, L. J., Roberts, R. G., Galbraith, R. F., & DeLong, S. (2009). A revised burial dose estimation procedure for optical dating of young and modern-age sediments. Quaternary Geochronology, 4(4), 306–325.

Ash, J., & Wasson, R. (1983). Vegetation and sand mobility in the Australian desert dunefield. Zeitschrift fur Geomorphologie, 45 (Supp.), 7–25.

Asten, M., & McCracken, K. (2022). Time-series analysis of extreme rainfall and flood events in two water catchments of Eastern New South Wales shows an indicative link to Gleissberg 87 yr cycles. Authorea Preprints.

Asmerom, Y., Polyak, V. J., & Burns, S. J. (2010). Variable winter moisture in the southwestern United States linked to rapid glacial climate shifts. Nature Geoscience, 3(2), 114–117.

Ayliffe, L. K., Gagan, M. K., Zhao, J. X., Drysdale, R. N., Hellstrom, J. C., Hantoro, W. S.,…Suwargadi, B. W. (2013). Rapid interhemispheric climate links via the Australasian monsoon during the last deglaciation. Nature Communications, 4, 2908.

Ayliffe, L. K., Marianelli, P. C., Moriarty, K. C., Wells, R. T., McCulloch, M. T., Mortimer, G. E., & Hellstrom, J. C. (1998). 500 ka precipitation record from southeastern Australia: evidence for interglacial relative aridity. Geology, 26(2), 147–150.

Ballarini, M., Wallinga, J., Wintle, A., & Bos, A. (2007). Analysis of equivalent-dose distributions for single grains of quartz from modern deposits. Quaternary Geochronology, 2(1–4), 77-82.

Barber, D. C., Dyke, A., Hillaire-Marcel, C., Jennings, A. E., Andrews, J. T., Kerwin, M. W.,…Morehead, M. D. (1999). Forcing of the cold event of 8,200 years ago by catastrophic drainage of Laurentide lakes. Nature, 400(6742), 344–348.

Bar-Matthews, M., Ayalon, A., Kaufman, A., & Wasserburg, G. J. (1999). The Eastern Mediterranean paleoclimate as a reflection of regional events: Soreq cave, Israel. Earth and Planetary Science Letters, 166(1–2), 85–95.

Baucom, P. C., & Rigsby, C. A. (1999). Climate and lake-level history of the northern Altiplano, Bolivia, as recorded in Holocene sediments of the Rio Desaguadero. Journal of Sedimentary Research, 69(3), 597–611.

Bayon, G., Bindeman, I. N., Trinquier, A., Retallack, G. J., & Bekker, A. (2022). Long-term evolution of terrestrial weathering and its link to Earth's oxygenation. Earth and Planetary Science Letters, 584, 117490.

Bayon, G., De Deckker, P., Magee, J. W., Germain, Y., Bermell, S., Tachikawa, K., & Norman, M. D. (2017). Extensive wet episodes in Late Glacial Australia resulting from high-latitude forcings. Scientific reports, 7(1), 1–7.

Beaufort, L. (1994). Climatic importance of the modulation of the 100 kyr cycle inferred from 16 my long Miocene records. Paleoceanography, 9(6), 821–834.

Behrens, A., Schaeffer, P., Bernasconi, S., & Albrecht, P. (2000). Mono-and bicyclic squalene derivatives as potential proxies for anaerobic photosynthesis in lacustrine sulfur-rich sediments. Geochimica Et Cosmochimica Acta, 64(19), 3327–3336.

Berger, A. (1977). Support for the astronomical theory of climatic change. Nature, 269(5623), 44–45.

Berger, A., & Loutre, M.-F. (1997). Intertropical latitudes and precessional and half-precessional cycles. Science, 278(5342), 1476–1478.

Berger, A., Loutre, M.-F., & Mélice, J. (2006). Equatorial insolation: from precession harmonics to eccentricity frequencies. Climate of the Past, 2(2), 131–136.

Berger, A., Melice, J., & Hinnov, L. (1991). A strategy for frequency spectra of Quaternary climate records. Climate Dynamics, 5, 227–240.

Bernasconi, S., & Hanselmann, K. (1995). The influence of bacterial activity at the chemocline on particulate organic matter fluxes and nutrient cycling in meromictic Lake Cadagno. Organic geochemistry: developments and applications to energy, climate, environment and human history. AIGOA, San Sebastián, 1169–1171.

Bestland, E. A., & Rennie, J. (2006). Stable isotope record (δ18O and δ13C) of a Naracoorte Caves speleothem from before and after the Last Interglacial. Alcheringa: An Australasian Journal of Palaeontology, 30(S1), 19–29.

Beutel, T. S., Trevithick, R., Scarth, P., & Tindall, D. (2019). VegMachine. net. online land cover analysis for the Australian rangelands. The Rangeland Journal, 41(4), 355–362.

Bird, M. I., Hutley, L. B., Lawes, M. J., Lloyd, J., Luly, J. G., Ridd, P. V.,…Wurster, C. M. (2013). Humans, megafauna and environmental change in tropical Australia. Journal of Quaternary Science, 28(5), 439–452.

Birkeland, P. W. (1984). Soils and geomorphology. Oxford university press.

Blaauw, M., & Christen, J. A. (2011). Flexible paleoclimate age-depth models using an autoregressive gamma process. Bayesian Analysis, 6, 457–474.

Blair, T. C. (1999). Sedimentology of gravelly Lake Lahontan highstand shoreline deposits, Churchill Butte, Nevada, USA. Sedimentary Geology, 123(3–4), 199–218.

Blott, S. J., & Pye, K. (2001). GRADISTAT: a grain size distribution and statistics package for the analysis of unconsolidated sediments. Earth Surface Processes and Landforms, 26(11), 1237–1248.

Boccotti, P. (2000). Wave mechanics for ocean engineering. Elsevier: Amsterdam, The Netherlands.

Bolton, C. T., Chang, L., Clemens, S. C., Kodama, K., Ikehara, M., Medina-Elizalde, M.,…Yamamoto, Y. (2013). A 500,000 year record of Indian summer monsoon dynamics recorded by eastern equatorial Indian Ocean upper water-column structure. Quaternary Science Reviews, 77, 167–180.

BOM. (2024a). Historical Weather Observations and Statistics. http://www.bom.gov.au/climate/data-services/station-data.shtml

BOM. (2024b). Maps of average conditions. http://www.bom.gov.au/climate/maps/averages/

BOM. (2024c). Historical droughts. http://www.bom.gov.au/climate/drought/knowledge-centre/previous-droughts.shtml

BOM. (2024d). Recent and historical rainfall maps. http://www.bom.gov.au/climate/maps/rainfall

BOM. (2025). Wind roses. http://www.bom.gov.au/climate/_averages/wind

Bond, G., Broecker, W., Johnsen, S., McManus, J., Labeyrie, L., Jouzel, J., & Bonani, G. (1993). Correlations between climate records from North Atlantic sediments and Greenland ice. Nature, 365(6442), 143–147.

Bond, G., Heinrich, H., Broecker, W., Labeyrie, L., McManus, J., Andrews, J.,…Simet, C. (1992). Evidence for massive discharges of icebergs into the North Atlantic ocean during the last glacial period. Nature, 360(6401), 245.

Bond, G., Kromer, B., Beer, J., Muscheler, R., Evans, M. N., Showers, W.,…Bonani, G. (2001). Persistent solar influence on North Atlantic climate during the Holocene. Science, 294(5549), 2130–2136.

Bond, G., Showers, W., Cheseby, M., Lotti, R., Almasi, P., DeMenocal, P.,…Bonani, G. (1997). A pervasive millennial-scale cycle in North Atlantic Holocene and glacial climates. Science, 278(5341), 1257–1266.

Bond, G. C., Showers, W., Elliot, M., Evans, M., Lotti, R., Hajdas, I.,…Johnson, S. (1999). The North Atlantic's 1–2 kyr climate rhythm: relation to Heinrich events, Dansgaard/Oeschger cycles and the Little Ice Age. Geophysical Monograph-American Geophysical Union, 112, 35–58.

Bonython, C. W., & Mason, B. (1953). The filling and drying of Lake Eyre. The Geographical Journal, 119(3), 321–330.

Boulila, S., Galbrun, B., Hinnov, L. A., Collin, P. Y., Ogg, J. G., Fortwengler, D., & Marchand, D. (2010). Milankovitch and sub-Milankovitch forcing of the Oxfordian (Late Jurassic) Terres Noires formation (SE France) and global implications. Basin Research, 22(5), 717–732.

Boulila, S., Galbrun, B., Huret, E., Hinnov, L. A., Rouget, I., Gardin, S., & Bartolini, A. (2014). Astronomical calibration of the Toarcian Stage: implications for sequence stratigraphy and duration of the early Toarcian OAE. Earth and Planetary Science Letters, 386, 98–111.

Boulila, S., Vahlenkamp, M., De Vleeschouwer, D., Laskar, J., Yamamoto, Y., Pälike, H.,…Röhl, U. (2018). Towards a robust and consistent middle Eocene astronomical timescale. Earth and Planetary Science Letters, 486, 94–107.

Bourne, J. A., & Twidale, C. R. (2010). Playas of inland Australia. *Coruña,* 35, 71–98.

Boutton, T. W. (1996). Stable carbon isotope ratios of soil organic matter and their use as indicators of vegetation and climate change. In: T.W. Boutton & S. Yamasaki (Eds), Mass spectrometry of soils. New York, NY, USA: Marcel Dekker Inc., 47–82.

Bowen, B. B., & Benison, K. C. (2009). Geochemical characteristics of naturally acid and alkaline saline lakes in southern Western Australia. *Applied Geochemistry*, 24(2), 268-284.

Bowler, J. M. (1973). Clay dunes: their occurrence, formation and environmental significance. Earth-Science Reviews, 9(4), 315–338.

Bowler, J. M. (1976). Aridity in Australia: age, origins and expression in aeolian landforms and sediments. Earth-Science Reviews, 12(2–3), 279–310.

Bowler, J. M., Duller, G., Perret, N., Prescott, J. R., & Wyrwoll, K. (1998). Hydrologic changes in monsoonal climates of the last glacial cycle: stratigraphy and luminescence dating of Lake Woods, NT Australia. Palaeoclimates, 3(1–3), 179–207.

Bowler, J. M., Johnston, H., Olley, J. M., Prescott, J. R., Roberts, R. G., Shawcross, W., & Spooner, N. A. (2003). New ages for human occupation and climatic change at Lake Mungo, Australia. Nature, 421(6925), 837–840.

Bowler, J. M., Wyrwoll, K.-H., & Lu, Y. (2001). Variations of the northwest Australian summer monsoon over the last 300,000 years: the paleohydrological record of the Gregory (Mulan) Lakes System. Quaternary International, 83, 63–80.

Boyle, E. A. (2000). Is ocean thermohaline circulation linked to abrupt stadial/interstadial transitions? Quaternary Science Reviews, 19(1–5), 255–272.

Boyle, J. (2001). Inorganic geochemical methods in palaeolimnology. In W.M. Last & J.P. Smol (Eds.), Tracking environmental change using lake sediments. Volume 2: physical and geochemical methods. Dordrecht: Kluwer Academic Publishers, 83–141.

Bray, J. R. (1968). Glaciation and solar activity since the Fifth Century BC and the solar cycle. Nature, 220(5168).

Bray Jr, T. F., & Carter, C. H. (1992). Physical processes and sedimentary record of a modern, transgressive, lacustrine barrier island. Marine Geology, 105(1–4), 155–168.

Breed, C. S., & Breed, W. (1979). Dunes and other windforms of central Australia (and a comparison with linear dunes on the Moenkopi Plateau, Arizona). Apollo-Soyuz test project summary science report, 2, 319–358.

Breitenmoser, P., Beer, J., Brönnimann, S., Frank, D., Steinhilber, F., & Wanner, H. (2012). Solar and volcanic fingerprints in tree-ring chronologies over the past 2000 years. Palaeogeography, Palaeoclimatology, Palaeoecology, 313, 127–139.

Brenner, M., Hodell, D. A., Leyden, B. W., Curtis, J. H., Kenney, W. F., Gu, B., & Newman, J. M. (2006). Mechanisms for organic matter and phosphorus burial in sediments of a shallow, subtropical, macrophyte-dominated lake. Journal of Paleolimnology, 35, 129–148.

Brisbane Courier. (1885, 18 February 1885). Queensland News. Brisbane Courier (Qld. : 1864 – 1933), 5. http://nla.gov.au/nla.news-article3439248.

Bristow, C., Jones, B. G., Nanson, G., Hollands, C., Coleman, M., & Price, D. (2007). GPR surveys of vegetated linear dune stratigraphy in central Australia: Evidence for linear dune extension with vertical and lateral accretion. Geological Society America Bulletin Special Paper 432, 19–33.

Broccoli, A. J., Dahl, K. A., & Stouffer, R. J. (2006). Response of the ITCZ to Northern Hemisphere cooling. Geophysical Research Letters, 33(1).

Brodie, C. R., Leng, M. J., Casford, J. S., Kendrick, C. P., Lloyd, J. M., Yongqiang, Z., & Bird, M. I. (2011). Evidence for bias in C and N concentrations and δ13C composition of terrestrial and aquatic organic materials due to pre-analysis acid preparation methods. Chemical Geology, 282(3–4), 67–83.

Broecker, W., Bond, G., Klas, M., Clark, E., & McManus, J. (1992). Origin of the northern Atlantic's Heinrich events. Climate Dynamics, 6(3–4), 265–273.

Brookfield, M. (1970). Dune trends and wind regime in central Australia. Zeitschrift für Geomorphologie Supplementband, 10, 121–153.

Buckley, R. (1987). The effect of sparse vegetation on the transport of dune sand by wind. Nature, 325(6103), 426–428.

Buckley, R. (1989). Grain-size characteristics of linear dunes in central Australia. Journal of Arid Environments, 16(1), 23–28.

Buckley, B. M., Ummenhofer, C. C., D’Arrigo, R. D., Hansen, K., Truong, L., Le, C., & Stahle, D. (2019). Interdecadal Pacific Oscillation reconstructed from trans-Pacific tree rings: 1350–2004 CE. Climate Dynamics, 53, 3181–3196.

Bull, W. B. (1991). Geomorphic responses to climatic change. Oxford University Press, Oxford.

Bullard, J. E., & McTainsh, G. H. (2003). Aeolian-fluvial interactions in dryland environments: examples, concepts and Australia case study. Progress in Physical Geography, 27(4), 471–501.

Bullard, J. E., McTainsh, G. H., & Pudmenzky, C. (2004). Aeolian abrasion and modes of fine particle production from natural red dune sands: an experimental study. Sedimentology, 51(5), 1103–1125.

Bullard, J. E., & White, K. (2005). Dust production and the release of iron oxides resulting from the aeolian abrasion of natural dune sands. Earth Surface Processes and Landforms: The Journal of the British Geomorphological Research Group, 30(1), 95–106.

Butler, B. (1974). Contribution towards the better specification of parna and some other aeolian clays in Australia. Zeitschrift für Geomorphologie Supplementband, 20, 106–116.

Cacho, I., Grimalt, J. O., Pelejero, C., Canals, M., Sierro, F. J., Flores, J. A., & Shackleton, N. (1999). Dansgaard-Oeschger and Heinrich event imprints in Alboran Sea paleotemperatures. Paleoceanography, 14(6), 698–705.

Cadd, H., Petherick, L., Tyler, J., Herbert, A., Cohen, T. J., Sniderman, K., ... & Harris, M. R. (2021). A continental perspective on the timing of environmental change during the last glacial stage in Australia. Quaternary Research, 102, 5–23.

Cai, W., Purich, A., Cowan, T., van Rensch, P., & Weller, E. (2014). Did climate change–induced rainfall trends contribute to the Australian Millennium Drought? Journal of Climate, 27(9), 3145–3168.

Cai, W., & Van Rensch, P. (2012). The 2011 southeast Queensland extreme summer rainfall: a confirmation of a negative Pacific Decadal Oscillation phase? Geophysical Research Letters, 39(8).

Cai, W., Whetton, P., & Pittock, A. (2001). Fluctuations of the relationship between ENSO and northeast Australian rainfall. Climate Dynamics, 17(5–6), 421.

Callen, R., & Nanson, G. (1992). Formation and age of dunes in the Lake Eyre Depocentres. Geologische Rundschau, 81(2), 589–593.

Camenen, B. (2007). Simple and general formula for the settling velocity of particles. Journal of Hydraulic Engineering, 133(2), 229–233.

Cassiani, G., Bellizia, E., Fontana, A., Boaga, J., D'Alpaos, A., & Ghinassi, M. (2020). Geophysical and sedimentological investigations integrate remote-sensing data to depict geometry of fluvial sedimentary bodies: an example from Holocene point-bar deposits of the Venetian plain (Italy). Remote Sensing, 12(16), 2568.

Cattle, S. R. (2016). The case for a southeastern Australian Dust Bowl, 1895–1945. Aeolian Research, 21, 1–20.

Cendón, D. I., Larsen, J. R., Jones, B. G., Nanson, G. C., Rickleman, D., Hankin, S. I.,…Maroulis, J. (2010). Freshwater recharge into a shallow saline groundwater system, Cooper Creek floodplain, Queensland, Australia. Journal of Hydrology, 392(3–4), 150–163.

Cerling, T. E., Wynn, J. G., Andanje, S. A., Bird, M. I., Korir, D. K., Levin, N. E.,…Remien, C. H. (2011). Woody cover and hominin environments in the past 6 million years. Nature, 476(7358), 51–56.

Chapman, M. R., & Shackleton, N. J. (1999). Global ice-volume fluctuations, North Atlantic ice-rafting events, and deep-ocean circulation changes between 130 and 70 ka. Geology, 27(9), 795–798.

Charbonnier, G., Boulila, S., Spangenberg, J. E., Adatte, T., Föllmi, K. B., & Laskar, J. (2018). Obliquity pacing of the hydrological cycle during the Oceanic Anoxic Event 2. Earth and Planetary Science Letters, 499, 266–277.

Charvátová, I. (2000). Can origin of the 2400-year cycle of solar activity be caused by solar inertial motion? Annales Geophysicae, 18(4), 399–405.

Chen, X., & Barton, C. (1991). Onset of aridity and dune-building in central Australia: sedimentological and magnetostratigraphic evidence from Lake Amadeus. Palaeogeography, Palaeoclimatology, Palaeoecology, 84(1–4), 55–73.

Chen, X., Bowler, J., & Magee, J. (1993). Late Cenozoic stratigraphy and hydrologic history of Lake Amadeus, a central Australian playa. Australian Journal of Earth Sciences, 40(1), 1–14.

Chen, X., Chappell, J., & Murray, A. (1995). High (ground) water levels and dune development in central Australia: TL dates from gypsum and quartz dunes around Lake Lewis (Napperby), Northern Territory. Geomorphology, 11(4), 311–322.

Chen, X., Prescott, J., & Hutton, J. (1990). Thermoluminescence dating on gypseous dunes of Lake Amadeus, central Australia. Australian Journal of Earth Sciences, 37(1), 93–101.

Cheng, H., Edwards, R. L., Broecker, W. S., Denton, G. H., Kong, X., Wang, Y.,…Wang, X. (2009). Ice age terminations. Science, 326(5950), 248–252.

Cheng, H., Edwards, R. L., Wang, Y., Kong, X., Ming, Y., Kelly, M. J.,…Liu, W. (2006). A penultimate glacial monsoon record from Hulu Cave and two-phase glacial terminations. Geology, 34(3), 217–220.

Cheng, H., Edwards, R. L., Sinha, A., Spötl, C., Yi, L., Chen, S.,…Li, X. (2016). The Asian monsoon over the past 640,000 years and ice age terminations. Nature, 534(7609), 640–646.

Chivas, A., Andrews, A., Lyons, W., Bird, M., & Donnelly, T. (1991). Isotopic constraints on the origin of salts in Australian playas. 1. Sulphur. Palaeogeography, Palaeoclimatology, Palaeoecology, 84(1–4), 309–332.

Clarkson, C., Jacobs, Z., Marwick, B., Fullagar, R., Wallis, L., Smith, M.,…Carah, X. (2017). Human occupation of northern Australia by 65,000 years ago. Nature, 547(7663), 306–310.

Clarkson, C., Smith, M., Marwick, B., Fullagar, R., Wallis, L. A., Faulkner, P.,…Jacobs, Z. (2015). The archaeology, chronology and stratigraphy of Madjedbebe (Malakunanja II): A site in northern Australia with early occupation. Journal of Human Evolution, 83, 46–64.

Clemens, S. C., & Prell, W. L. (1991). One million year record of summer monsoon winds and continental aridity from the owen ridge (site 722), northwest arabian sea. In: Prell, W.N.N., et al. (Eds.), Proceedings of the Ocean Drilling Program, Scientific Results. Ocean Drilling Program: College Station, TX, 365–388.

Cleveland, D. M., Nordt, L. C., & Atchley, S. C. (2008). Paleosols, trace fossils, and precipitation estimates of the uppermost Triassic strata in northern New Mexico. Palaeogeography, Palaeoclimatology, Palaeoecology, 257(4), 421–444.

Cohen, A. S. (2003). *Paleolimnology: the history and evolution of lake systems*. Oxford university press.

Cohen, T. J., Arnold, L. J., Gázquez, F., May, J.-H., Marx, S. K., Jankowski, N. R.,…Parker, A. G. (2022). Late quaternary climate change in Australia's arid interior: Evidence from Kati Thanda–Lake Eyre. Quaternary Science Reviews, 292, 107635.

Cohen, T. J., Jansen, J. D., Gliganic, L. A., Larsen, J. R., Nanson, G. C., May, J.-H.,…Price, D. M. (2015). Hydrological transformation coincided with megafaunal extinction in central Australia. Geology, 43(3), 195–198.

Cohen, T. J., Meyer, M. C., & May, J.-H. (2018). Identifying extreme pluvials in the last millennia using optical dating of single grains of quartz from shorelines on Australia's largest lake. The Holocene, 28(1), 150–165.

Cohen, T. J., Nanson, G. C., Jansen, J. D., Jones, B. G., Jacobs, Z., Treble, P.,…Hellstrom, J. C. (2011). Continental aridification and the vanishing of Australia's megalakes. Geology, 39(2), 167–170.

Cohen, T. J., Nanson, G. C, Jansen, J. D., Gliganic, L., May, J.-H., Larsen, J.,…Price, D. (2012a). A pluvial episode identified in arid Australia during the Medieval Climatic Anomaly. Quaternary Science Reviews, 56, 167–171.

Cohen, T., Nanson, G., Jansen, J. D., Jones, B., Jacobs, Z., Larsen, J.,…Smith, A. (2012b). Late Quaternary mega-lakes fed by the northern and southern river systems of central Australia: varying moisture sources and increased continental aridity. Palaeogeography, Palaeoclimatology, Palaeoecology, 356, 89–108.

Cohen, T. J., Nanson, G. C., Larsen, J. R., Jones, B., Price, D. M., Coleman, M., & Pietsch, T. (2010). Late Quaternary aeolian and fluvial interactions on the Cooper Creek Fan and the association between linear and source-bordering dunes, Strzelecki Desert, Australia. Quaternary Science Reviews, 29(3–4), 455–471.

Collins, J. A., Schefuß, E., Heslop, D., Mulitza, S., Prange, M., Zabel, M.,…Mackensen, A. (2011). Interhemispheric symmetry of the tropical African rainbelt over the past 23,000 years. Nature Geoscience, 4(1), 42–45.

Colman, S. M., Peck, J., Karabanov, E., Carter, S. J., Bradbury, J., King, J., & Williams, D. (1995). Continental climate response to orbital forcing from biogenic silica records in Lake Baikal. Nature, 378(6559), 769–771.

Conley, D. J., & Schelske, C. L. (1993). Potential role of sponge spicules in influencing the silicon biogeochemistry of Florida lakes. Canadian Journal of Fisheries and Aquatic Sciences, 50(2), 296–302.

Cook, B. I., Palmer, J. G., Cook, E. R., Turney, C. S., Allen, K., Fenwick, P.,…Ho, M. (2016). The paleoclimate context and future trajectory of extreme summer hydroclimate in eastern Australia. Journal of Geophysical Research: Atmospheres, 121(21), 12–820.

Cook, E. R., Buckley, B. M., Palmer, J. G., Fenwick, P., Peterson, M. J., Boswijk, G., & Fowler, A. (2006). Millennia-long tree-ring records from Tasmania and New Zealand: A basis for modelling climate variability and forcing, past, present and future. Journal of Quaternary Science: Published for the Quaternary Research Association, 21(7), 689–699.

Cooper, J., & Navas, F. (2004). Natural bathymetric change as a control on century-scale shoreline behavior. Geology, 32(6), 513–516.

Costelloe, J. F., Powling, J., Reid, J. R., Shiel, R. J., & Hudson, P. (2005). Algal diversity and assemblages in arid zone rivers of the Lake Eyre Basin, Australia. River Research and Applications, 21(2–3), 337–349.

Cowan, T., Wheeler, M., Alves, O., Narsey, S., de Burgh-Day, C., Griffiths, M.,…Hawcroft, M. (2019). Forecasting the extreme rainfall, low temperatures, and strong winds associated with the northern Queensland floods of February 2019. Weather and Climate Extremes, 26, 100232.

Cowan, T., Wheeler, M. C., & Marshall, A. G. (2023). The combined influence of the Madden–Julian oscillation and El Niño–Southern Oscillation on Australian rainfall. Journal of Climate, 36(2), 313–334.

Crabtree, S. A., White, D. A., Bradshaw, C. J., Saltré, F., Williams, A. N., Beaman, R. J.,…Ulm, S. (2021). Landscape rules predict optimal superhighways for the first peopling of Sahul. Nature Human Behaviour, 5(10), 1303–1313.

Craddock, R. A., Tooth, S., Zimbelman, J. R., Wilson, S. A., Maxwell, T. A., & Kling, C. (2015). Temporal observations of a linear sand dune in the Simpson Desert, central Australia: Testing models for dune formation on planetary surfaces. Journal of Geophysical Research-Planets, 120(10), 1736–1750.

Croke, J., Fryirs, K., & Thompson, C. (2016). Defining the floodplain in hydrologically-variable settings: implications for flood risk management. Earth Surface Processes and Landforms, 41(14), 2153–2164.

Croke, J., Jansen, J. D., Amos, K., & Pietsch, T. J. (2011). A 100 ka record of fluvial activity in the Fitzroy River Basin, tropical northeastern Australia. Quaternary Science Reviews, 30(13–14), 1681–1695.

Croke, J., Magee, J., & Price, D. (1996). Major episodes of Quaternary activity in the lower Neales River, northwest of Lake Eyre, central Australia. Palaeogeography, Palaeoclimatology, Palaeoecology, 124(1–2), 1–15.

Croke, J., Magee, J., & Price, D. (1998). Stratigraphy and sedimentology of the lower Neales River, west Lake Eyre, central Australia: from Palaeocene to Holocene. Palaeogeography, Palaeoclimatology, Palaeoecology, 144(3–4), 331–350.

Croke, J., Magee, J., & Wallensky, E. (1999). The role of the Australian Monsoon in the western catchment of Lake Eyre, central Australia, during the Last Interglacial. Quaternary International, 57, 71–80.

Croke, J., Thompson, C., & Fryirs, K. (2017). Prioritising the placement of riparian vegetation to reduce flood risk and end-of-catchment sediment yields: Important considerations in hydrologically-variable regions. Journal of Environmental Management, 190, 9–19.

Crosbie, R. S., McCallum, J. L., Walker, G. R., & Chiew, F. H. (2012). Episodic recharge and climate change in the Murray-Darling Basin, Australia. Hydrogeology Journal, 20(2), 245.

Cruz, F. W., Burns, S. J., Karmann, I., Sharp, W. D., Vuille, M., Cardoso, A. O.,…Viana, O. (2005). Insolation-driven changes in atmospheric circulation over the past 116,000 years in subtropical Brazil. Nature, 434(7029), 63–66.

CSIRO, & BoM (2015). Climate change in Australia information for Australia's natural resource management regions: technical report. Canberra, AUS.

Cvijanovic, I., & Chiang, J. C. (2013). Global energy budget changes to high latitude North Atlantic cooling and the tropical ITCZ response. Climate Dynamics, 40(5), 1435–1452.

Dahl, K. A., Broccoli, A. J., & Stouffer, R. J. (2005). Assessing the role of North Atlantic freshwater forcing in millennial scale climate variability: A tropical Atlantic perspective. Climate Dynamics, 24(4), 325–346.

Dal'Bó, P. F. F., Basilici, G., & Angélica, R. S. (2010). Factors of paleosol formation in a Late Cretaceous eolian sand sheet paleoenvironment, Marília Formation, Southeastern Brazil. Palaeogeography, Palaeoclimatology, Palaeoecology, 292(1–2), 349–365.

Dang, H., Jian, Z., Wang, Y., Mohtadi, M., Rosenthal, Y., Ye, L.,…Kuhnt, W. (2020). Pacific warm pool subsurface heat sequestration modulated Walker circulation and ENSO activity during the Holocene. Science Advances, 6(42), eabc0402.

Daniau, A.-L., Loutre, M.-F., Swingedouw, D., Laepple, T., Bassinot, F., Malaizé, B.,…Carfantan, H. (2023). Precession and obliquity forcing of the South African monsoon revealed by sub-tropical fires. Quaternary Science Reviews, 310, 108128.

Dansgaard, W., Johnsen, S. J., Clausen, H. B., Dahl-Jensen, D., Gundestrup, N., Hammer, C.,…Jouzel, J. (1993). Evidence for general instability of past climate from a 250-kyr ice-core record. Nature, 364(6434), 218–220.

Davidson, G., & Dixon, G. (1992). Two sulphur isotope provinces deduced from ores in the Mount Isa Eastern Succession, Australia. Mineralium Deposita, 27, 30–41.

Davies, S. J., Lamb, H. F., & Roberts, S. J. (2015). Micro-XRF core scanning in palaeolimnology: recent developments. In Micro-XRF studies of sediment cores. Springer, 189–226.

Davis, J. C., & Bohling, G. C. (2000). The search for patterns in ice core temperature curves. Environmental Geosciences, 7(4), 213–214.

De Deckker, P. (2016). The Indo-Pacific Warm Pool: critical to world oceanography and world climate. Geoscience Letters, 3(1), 1–12.

De Deckker, P., & Yokoyama, Y. (2009). Micropalaeontological evidence for Late Quaternary sea-level changes in Bonaparte Gulf, Australia. Global and Planetary Change, 66(1–2), 85–92.

De Deckker, P., Arnold, L. J., van der Kaars, S., Bayon, G., Stuut, J.-B. W., Perner, K.,…Demuro, M. (2019). Marine Isotope Stage 4 in Australasia: A full glacial culminating 65,000 years ago–Global connections and implications for human dispersal. Quaternary Science Reviews, 204, 187–207.

De Deckker, P., Moros, M., Perner, K., & Jansen, E. (2012). Influence of the tropics and southern westerlies on glacial interhemispheric asymmetry. Nature Geoscience, 5(4), 266–269.

De Deckker, P., Tapper, N. J., & van der Kaars, S. (2003). The status of the Indo-Pacific Warm Pool and adjacent land at the Last Glacial Maximum. Global and Planetary Change, 35(1–2), 25–35.

de Garidel-Thoron, T., Beaufort, L., Linsley, B. K., & Dannenmann, S. (2001). Millennial-scale dynamics of the East Asian winter monsoon during the last 200,000 years. Paleoceanography, 16(5), 491–502.

Denniston, R., Asmerom, Y., Polyak, V., Wanamaker Jr, A., Ummenhofer, C., Humphreys, W.,…Lucker, S. (2017). Decoupling of monsoon activity across the northern and southern Indo-Pacific during the Late Glacial. Quaternary Science Reviews, 176, 101–105.

Denniston, R. F., Asmerom, Y., Lachniet, M., Polyak, V. J., Hope, P., An, N.,…Humphreys, W. F. (2013a). A Last Glacial Maximum through middle Holocene stalagmite record of coastal Western Australia climate. Quaternary Science Reviews, 77, 101–112.

Denniston, R. F., Ummenhofer, C. C., Wanamaker, A. D., Lachniet, M. S., Villarini, G., Asmerom, Y.,…Woods, D. (2016). Expansion and contraction of the Indo-Pacific tropical rain belt over the last three millennia. Scientific reports, 6, 34485.

Denniston, R. F., Villarini, G., Gonzales, A. N., Wyrwoll, K.-H., Polyak, V. J., Ummenhofer, C. C.,…Woods, D. (2015). Extreme rainfall activity in the Australian tropics reflects changes in the El Niño/Southern Oscillation over the last two millennia. Proceedings of the National Academy of Sciences, 112(15), 4576–4581.

Denniston, R. F., Wyrwoll, K.-H., Asmerom, Y., Polyak, V. J., Humphreys, W. F., Cugley, J.,…Greaves, E. (2013b). North Atlantic forcing of millennial-scale Indo-Australian monsoon dynamics during the Last Glacial period. Quaternary Science Reviews, 72, 159–168.

Denniston, R. F., Wyrwoll, K.-H., Polyak, V. J., Brown, J. R., Asmerom, Y., Wanamaker Jr, A. D.,…Cleary, D. (2013c). A Stalagmite record of Holocene Indonesian–Australian summer monsoon variability from the Australian tropics. Quaternary Science Reviews, 78, 155–168.

Deocampo, D., Berry, P., Beverly, E., Ashley, G., & Jarrett, R. (2017). Whole-rock geochemistry tracks precessional control of Pleistocene lake salinity at Olduvai Gorge, Tanzania: A record of authigenic clays. Geology, 45(8), 683–686.

Ding, Z., Lu, R., Wang, L., Yu, L., Liu, X., Liu, Y.,…Wang, S. (2021). Early-Mid Holocene climatic changes inferred from colors of eolian deposits in the Mu Us Desert. Geoderma, 401, 115172.

Donders, T. H., Wagner-Cremer, F., & Visscher, H. (2008). Integration of proxy data and model scenarios for the mid-Holocene onset of modern ENSO variability. Quaternary Science Reviews, 27(5–6), 571–579.

Donohoe, A., Marshall, J., Ferreira, D., & Mcgee, D. (2013). The relationship between ITCZ location and cross-equatorial atmospheric heat transport: From the seasonal cycle to the Last Glacial Maximum. Journal of Climate, 26(11), 3597–3618.

Douka, K., Jacobs, Z., Lane, C., Grün, R., Farr, L., Hunt, C.,…Aubert, M. (2014). The chronostratigraphy of the Haua Fteah cave (Cyrenaica, northeast Libya). Journal of Human Evolution, 66, 39–63.

Drake, B. L. (2018). CloudCal v3.0. GitHub. https://github.com/leedrake5/CloudCal.

Draxler, R., & Rolph, G. (2010). HYSPLIT (HYbrid Single-Particle Lagrangian Integrated Trajectory) model access via NOAA ARL READY website (http://ready.arl.noaa.gov/HYSPLIT.php), NOAA Air Resources Laboratory. Silver Spring, MD, 25.

Driese, S. G., Simpson, E. L., & Eriksson, K. A. (1995). Redoximorphic paleosols in alluvial and lacustrine deposits, 1.8 Ga Lochness Formation, Mount Isa, Australia; pedogenic processes and implications for paleoclimate. Journal of Sedimentary Research, 65(4a), 675–689.

Drysdale, R. N., Hellstrom, J. C., Zanchetta, G., Fallick, A. E., Sánchez Goñi, M. F., Couchoud, I., ... & Isola, I. (2009). Evidence for obliquity forcing of glacial termination II. Science, 325(5947), 1527-1531.

Du, Z., Li, W., Zhou, D., Tian, L., Ling, F., Wang, H.,…Sun, B. (2014). Analysis of Landsat-8 OLI imagery for land surface water mapping. Remote sensing letters, 5(7), 672–681.

Dulhunty, J. (1989). Some significant features of the 1974 filling. In C. W. Bonython & A. S. Fraser (Eds.), The great filling of Lake Eyre in 1974. Royal Geographical Society of Australasia, 44–51.

Eddy, J. A. (1976). The Maunder Minimum: The reign of Louis XIV appears to have been a time of real anomaly in the behavior of the sun. Science, 192(4245), 1189–1202.

Ellwood, B. B., Crick, R. E., Hassani, A. E., Benoist, S. L., & Young, R. H. (2000). Magnetosusceptibility event and cyclostratigraphy method applied to marine rocks: detrital input versus carbonate productivity. Geology, 28(12), 1135–1138.

Elsner, J. B., & Jagger, T. (2008). United States and Caribbean tropical cyclone activity related to the solar cycle. Geophysical Research Letters, 35(18).

English, P., Spooner, N., Chappell, J., Questiaux, D., & Hill, N. (2001). Lake Lewis basin, central Australia: environmental evolution and OSL chronology. Quaternary International, 83, 81–101.

Evans, J. P., & Boyer-Souchet, I. (2012). Local sea surface temperatures add to extreme precipitation in northeast Australia during La Niña. Geophysical Research Letters, 39(10).

Evans, T. A., & Gleeson, P. V. (2001). Seasonal and daily activity patterns of subterranean, wood-eating termite foragers. Australian Journal of Zoology, 49(3), 311–321.

Fagel, N., Boës, X., & Loutre, M. F. (2008). Climate oscillations evidenced by spectral analysis of Southern Chilean lacustrine sediments: the assessment of ENSO over the last 600 years. Journal of Paleolimnology, 39(2), 253–266.

Falster, G., Tyler, J., Grant, K., Tibby, J., Turney, C., Lohr, S.,…Kershaw, A. P. (2018). Millennial-scale variability in south-east Australian hydroclimate between 30,000 and 10,000 years ago. Quaternary Science Reviews, 192, 106–122.

Fang, X., Zheng, F., Li, K., Hu, Z.-Z., Ren, H., Wu, J.,…Feng, L. (2023). Will the historic southeasterly wind over the equatorial Pacific in March 2022 trigger a third-year La Niña event? Advances in Atmospheric Science, 40, 6–13.

Feng, J., Li, J., & Xu, H. (2013). Increased summer rainfall in northwest Australia linked to southern Indian Ocean climate variability. Journal of Geophysical Research: Atmospheres, 118(2), 467–480.

Fernandes, L. A., & Basilici, G. (2009). Transition of ephemeral palustrine to aeolian deposits in a continental arid–semi-arid environment (Upper Cretaceous Bauru Basin, Brazil). Cretaceous Research, 30(3), 605–614.

Fitzsimmons, K. E. (2007). Morphological variability in the linear dunefields of the Strzelecki and Tirari Deserts, Australia. Geomorphology, 91(1–2), 146–160.

Fitzsimmons, K. E., & Gromov, S. S. (2022). Northward expansion of the westerlies over glacial southeastern Australia: evidence from semi-arid lunette dunes, temperate basalt plains, and wind modelling. Frontiers in Earth Science, 10, 921264.

Fitzsimmons, K. E., Bowler, J. M., Rhodes, E. J., & Magee, J. M. (2007a). Relationships between desert dunes during the late Quaternary in the Lake Frome region, Strzelecki Desert, Australia. Journal of Quaternary Science: Published for the Quaternary Research Association, 22(5), 549–558.

Fitzsimmons, K. E., Cohen, T. J., Hesse, P. P., Jansen, J., Nanson, G. C., May, J.-H.,…Kelly, T. (2013). Late Quaternary palaeoenvironmental change in the Australian drylands. Quaternary Science Reviews, 74, 78–96.

Fitzsimmons, K. E., Magee, J. W., & Amos, K. J. (2009). Characterisation of aeolian sediments from the Strzelecki and Tirari Deserts, Australia: implications for reconstructing palaeoenvironmental conditions. Sedimentary Geology, 218(1–4), 61–73.

Fitzsimmons, K. E., Miller, G. H., Spooner, N., & Magee, J. (2012). Aridity in the monsoon zone as indicated by desert dune formation in the Gregory Lakes basin, northwestern Australia. Australian Journal of Earth Sciences, 59(4), 469–478.

Fitzsimmons, K. E., Rhodes, E. J., Magee, J. W., & Barrows, T. T. (2007b). The timing of linear dune activity in the Strzelecki and Tirari Deserts, Australia. Quaternary Science Reviews, 26(19–21), 2598–2616.

Fleitmann, D., Burns, S. J., Mudelsee, M., Neff, U., Kramers, J., Mangini, A., & Matter, A. (2003). Holocene forcing of the Indian monsoon recorded in a stalagmite from southern Oman. Science, 300(5626), 1737–1739.

Flemming, B. W. (2011). Siliciclastic back-barrier tidal flats. In Principles of tidal sedimentology. Dordrecht: Springer Netherlands, 231–267.

Folk, R. L. (1971). Longitudinal dunes of the northwestern edge of the Simpson Desert, Northern Territory, Australia, 1. Geomorphology and grain size relationships. Sedimentology, 16(1–2), 5–54.

Folk, R. L., & Ward, W. C. (1957). Brazos River bar [Texas]; a study in the significance of grain size parameters. Journal of Sedimentary Research, 27(1), 3–26.

Folland, C., Renwick, J., Salinger, M., & Mullan, A. (2002). Relative influences of the interdecadal Pacific oscillation and ENSO on the South Pacific convergence zone. Geophysical Research Letters, 29(13), 21–24.

Forbes, M., Cohen, T., Jacobs, Z., Marx, S., Barber, E., Dodson, J., ... & Woodward, C. (2021). Comparing interglacials in eastern Australia: A multi-proxy investigation of a new sedimentary record. Quaternary Science Reviews, 252, 106750.

Forman, S. L., Oglesby, R., Markgraf, V., & Stafford, T. (1995). Paleoclimatic significance of late Quaternary eolian deposition on the Piedmont and High Plains, central United States. Global and Planetary Change, 11(1–2), 35–55.

Foster, I. D., Oldfield, F., Flower, R. J., & Keatings, K. (2008). Mineral magnetic signatures in a long core from Lake Qarun, Middle Egypt. Journal of Paleolimnology, 40(3), 835–849.

Freund, M., Henley, B. J., Karoly, D. J., Allen, K. J., & Baker, P. J. (2017). Multi-century cool-and warm-season rainfall reconstructions for Australia's major climatic regions. Climate of the Past, 13(12), 1751–1770.

Frierson, D. M., Lu, J., & Chen, G. (2007). Width of the Hadley cell in simple and comprehensive general circulation models. Geophysical Research Letters, 34(18), L18804.

Fu, X., Cohen, T. J., & Arnold, L. J. (2017). Extending the record of lacustrine phases beyond the last interglacial for Lake Eyre in central Australia using luminescence dating. Quaternary Science Reviews, 162, 88–110.

Fujioka, T., & Chappell, J. (2010). History of Australian aridity: chronology in the evolution of arid landscapes. Geological Society, London, Special Publications, 346(1), 121–139.

Fujioka, T., Chappell, J., Fifield, L. K., & Rhodes, E. J. (2009). Australian desert dune fields initiated with Pliocene–Pleistocene global climatic shift. Geology, 37(1), 51–54.

Galbraith, R. F., Roberts, R. G., Laslett, G. M., Yoshida, H., & Olley, J. M. (1999). Optical dating of single and multiple grains of quartz from Jinmium rock shelter, northern Australia: Part I, experimental design and statistical models. Archaeometry, 41(2), 339–364.

Gallant, J., Wilson, N., Dowling, T., Read, A., & Inskeep, C. (2011). SRTM-derived 1 Second Digital Elevation Models Version 1.0. Record 1. Geoscience Australia, Canberra. http://pid.geoscience.gov.au/dataset/ga/72759

Gallet, S., Jahn, B.-m., & Torii, M. (1996). Geochemical characterization of the Luochuan loess-paleosol sequence, China, and paleoclimatic implications. Chemical Geology, 133(1–4), 67–88.

Gardner, G. J., Mortlock, A. J., Price, D. M., Readhead, M. L., & Wasson, R. J. (1987). Thermo-Luminescence and Radiocarbon Dating of Australian Desert Dunes. Australian Journal of Earth Sciences, 34(3), 343–357.

Gebregiorgis, D., Hathorne, E. C., Giosan, L., Clemens, S., Nürnberg, D., & Frank, M. (2018). Southern Hemisphere forcing of South Asian monsoon precipitation over the past ~1 million years. Nature Communications, 9(1), 1–8.

Geen, R., Bordoni, S., Battisti, D. S., & Hui, K. (2020). Monsoons, ITCZs, and the concept of the global monsoon. Reviews of Geophysics, 58(4), e2020RG000700.

Genise, J. F. (2017). Paleosol ichnofacies. Ichnoentomology: Insect Traces in Soils and Paleosols, 559–577.

GeoAust. (2024a). Geoscience Australia, Historical Aerial Photography - Foundation Spatial Data. www.aerialphotography-geoscience-au.hub.arcgis.com/

GeoAust. (2024b). Geoscience Australia Water Observations, Digital Earth Australia Multi Year (Landsat) Frequency Statistics, 1986 to near present. https://maps.dea.ga.gov.au/

Gibling, M. R., Nanson, G. C., & Maroulis, J. C. (1998). Anastomosing river sedimentation in the Channel Country of central Australia. Sedimentology, 45(3), 595–619.

Gile, L. H., Peterson, F. F., & Grossman, R. B. (1966). Morphological and genetic sequences of carbonate accumulation in desert soils. Soil Science, 101(5), 347–360.

GloVis. (2023). Global Visualization (GloVis) Viewer. [Reston, Va.] :U.S. Dept. of the Interior, U.S. Geological Survey, 2023. Retrieved 31/02/2023 from https://glovis.usgs.gov/

Gocke, M., Hambach, U., Eckmeier, E., Schwark, L., Zöller, L., Fuchs, M.,…Wiesenberg, G. L. (2014). Introducing an improved multi-proxy approach for paleoenvironmental reconstruction of loess–paleosol archives applied on the Late Pleistocene Nussloch sequence (SW Germany). Palaeogeography, Palaeoclimatology, Palaeoecology, 410, 300–315.

Godfred-Spenning, C. R., & Reason, C. J. (2002). Interannual variability of lower-tropospheric moisture transport during the Australian monsoon. International Journal of Climatology: A Journal of the Royal Meteorological Society, 22(5), 509–532.

Gong, L., Holbourn, A., Kuhnt, W., Opdyke, B., Zhang, Y., Ravelo, A. C.,…Aiello, I. (2023). Middle Pleistocene re-organization of Australian Monsoon. Nature Communications, 14(1), 2002.

Grant, A. P., & Walsh, K. J. (2001). Interdecadal variability in north-east Australian tropical cyclone formation. Atmospheric Science Letters, 2(1–4), 9–17.

Grant, K., Rohling, E., Bar-Matthews, M., Ayalon, A., Medina-Elizalde, M., Ramsey, C. B.,…Roberts, A. (2012). Rapid coupling between ice volume and polar temperature over the past 150,000 years. Nature, 491(7426), 744–747.

Grant, K., Rohling, E., Ramsey, C., Cheng, H., Edwards, R., Florindo, F.,…Tamisiea, M. (2014). Sea-level variability over five glacial cycles. Nature Communications, 5(1), 5076.

Gray, L. J., Beer, J., Geller, M., Haigh, J. D., Lockwood, M., Matthes, K.,…Hood, L. (2010). Solar influences on climate. Reviews of Geophysics, 48(4), RG4001.

Griffiths, M. L., Drysdale, R. N., Gagan, M., Zhao, J.-x., Ayliffe, L., Hellstrom, J. C.,…Cartwright, I. (2009). Increasing Australian–Indonesian monsoon rainfall linked to early Holocene sea-level rise. Nature Geoscience, 2(9), 636.

Griffiths, M. L., Drysdale, R. N., Gagan, M. K., Zhao, J.-x., Hellstrom, J. C., Ayliffe, L. K., & Hantoro, W. S. (2013). Abrupt increase in east Indonesian rainfall from flooding of the Sunda Shelf ~9500 years ago. Quaternary Science Reviews, 74, 273–279.

Guérin, G., Mercier, N. & Adamiec, G. (2011) Dose-rate conversion factors: update. Ancient TL, 29, 5–9.

Gunn, A., Casasanta, G., Di Liberto, L., Falcini, F., Lancaster, N., & Jerolmack, D. J. (2022). What sets aeolian dune height?. Nature communications, 13(1), 2401.

Gunn, R. H., & Fleming, P. M. (1984). The estimated store of soluble salts in the Lake Eyre catchment in Queensland and their possible transport in streamflow to the lake. Soil Research, 22(2), 119–134.

Habeck-Fardy, A., & Nanson, G. C. (2014). Environmental character and history of the Lake Eyre Basin, one seventh of the Australian continent. Earth-Science Reviews, 132, 39–66.

Haig, J., Nott, J., & Reichart, G.-J. (2014). Australian tropical cyclone activity lower than at any time over the past 550–1,500 years. Nature, 505(7485), 667–671.

Haig, J. E. A., & Nott, J. (2016). Solar forcing over the last 1500 years and Australian tropical cyclone activity. Geophysical Research Letters, 43(6), 2843–2850.

Hall, J. D., Matthews, A. J., & Karoly, D. J. (2001). The modulation of tropical cyclone activity in the Australian region by the Madden–Julian oscillation. Monthly Weather Review, 129(12), 2970–2982.

Hamm, G., Mitchell, P., Arnold, L. J., Prideaux, G. J., Questiaux, D., Spooner, N. A.,…Stephenson, B. (2016). Cultural innovation and megafauna interaction in the early settlement of arid Australia. Nature, 539(7628), 280–283.

Hansen, J., Sato, M., Russell, G., & Kharecha, P. (2013). Climate sensitivity, sea level and atmospheric carbon dioxide. Philosophical Transactions of the Royal Society A: Mathematical, Physical and Engineering Sciences, 371(2001), 20120294.

Harriss, R. C. (1965). Geochemical and mineralogical studies on the weathering of granitic rocks. American Journal of Science, 264, 146–173.

Hattersley, P. (1983). The distribution of C 3 and C 4 grasses in Australia in relation to climate. Oecologia, 57(1–2), 113–128.

Hatté, C., Morvan, J., Noury, C., & Paterne, M. (2001). Is classical acid-alkali-acid treatment responsible for contamination? An alternative proposition. Radiocarbon, 43(2A), 177–182.

Heidemann, H., Cowan, T., Henley, B. J., Ribbe, J., Freund, M., & Power, S. (2023). Variability and long-term change in Australian monsoon rainfall: A review. Wiley Interdisciplinary Reviews: Climate Change, e823.

Heidemann, H., Ribbe, J., Cowan, T., Henley, B. J., Pudmenzky, C., Stone, R., & Cobon, D. H. (2022). The influence of interannual and decadal Indo-Pacific sea surface temperature variability on Australian monsoon rainfall. Journal of Climate, 35(1), 425–444.

Heinrich, H. (1988). Origin and consequences of cyclic ice rafting in the northeast Atlantic Ocean during the past 130,000 years. Quaternary Research, 29(2), 142–152.

Helman, P. (2009). Droughts in the Murray Darling Basin since European Settlement, Griffith Centre for Coastal Management, Research Report No 100. Griffith University, Brisbane.

Hembree, D. I. (2019). Burrows and ichnofabric produced by centipedes: modern and ancient examples. Palaios, 34(10), 468–489.

Hembree, D. I., & Bowen, J. J. (2017). Paleosols and ichnofossils of the Upper Pennsylvanian–Lower Permian Monongahela and Dunkard groups (Ohio, USA): a multi-proxy approach to unraveling complex variability in ancient terrestrial landscapes. Palaios, 32(5), 295–320.

Hembree, D. I., & Hasiotis, S. T. (2007). Paleosols and ichnofossils of the White River Formation of Colorado: Insight into soil ecosystems of the North American Midcontinent during the Eocene-Oligocene transition. Palaios, 22(2), 123–142.

Hemming, S. R. (2004). Heinrich events: Massive late Pleistocene detritus layers of the North Atlantic and their global climate imprint. Reviews of Geophysics, 42(1), RG1005.

Hendy, E., Gagan, M., & Lough, J. (2003). Chronological control of coral records using luminescent lines and evidence for non-stationary ENSO teleconnections in northeast Australia. The Holocene, 13(2), 187–199.

Henley, B. J., Gergis, J., Karoly, D. J., Power, S., Kennedy, J., & Folland, C. K. (2015). A Tripole Index for the Interdecadal Pacific Oscillation. Climate Dynamics, 45(11–12), 3077–3090.

Herr, A., Smith, T., & Brake, L. (2009). Regional profile of the Lake Eyre Basin catchments. In DKCRC Research Report 45. Desert Knowledge Cooperative Research Centre: Alice Springs, 41–88.

Hesse, P. P. (1994). The record of continental dust from Australia in Tasman Sea sediments. Quaternary Science Reviews, 13(3), 257–272.

Hesse, P. P. (2016). How do longitudinal dunes respond to climate forcing? Insights from 25 years of luminescence dating of the Australian desert dunefields. Quaternary International, 410, 11–29.

Hesse, P. P., & McTainsh, G. H. (2003). Australian dust deposits: modern processes and the Quaternary record. Quaternary Science Reviews, 22(18–19), 2007–2035.

Hesse, P. P., & Simpson, R. L. (2006). Variable vegetation cover and episodic sand movement on longitudinal desert sand dunes. Geomorphology, 81(3–4), 27–6291.

Hesse, P. P., Magee, J. W., & van der Kaars, S. (2004). Late Quaternary climates of the Australian arid zone: a review. Quaternary International, 118, 87–102.

Hilgen, F. J., Abels, H. A., Kuiper, K. F., Lourens, L. J., & Wolthers, M. (2015). Towards a stable astronomical time scale for the Paleocene: Aligning Shatsky Rise with the Zumaia–Walvis Ridge ODP Site 1262 composite. Newsletters on Stratigraphy, 48(1), 91–110.

Hocknull, S. A., Zhao, J.-x., Feng, Y.-x., & Webb, G. E. (2007). Responses of Quaternary rainforest vertebrates to climate change in Australia. Earth and Planetary Science Letters, 264(1–2), 317–331.

Hodell, D. A., Channell, J. E., Curtis, J. H., Romero, O. E., & Röhl, U. (2008). Onset of "Hudson Strait" Heinrich events in the eastern North Atlantic at the end of the middle Pleistocene transition (~640 ka)? Paleoceanography, 23(4), PA4128.

Hodges, R. E., & Elsner, J. B. (2012). The Spatial Pattern of the Sun-Hurricane Connection across the North Atlantic. International Scholarly Research Notices, 2012(1), 517962.

Hodges, R. E., Jagger, T. H., & Elsner, J. B. (2014). The sun-hurricane connection: Diagnosing the solar impacts on hurricane frequency over the North Atlantic basin using a space–time model. Natural hazards, 73, 1063–1084.

Holbourn, A., Kuhnt, W., & Xu, J. (2011). Indonesian Throughflow variability during the last 140 ka: The Timor Sea outflow. Geological Society, London, Special Publications, 355(1), 283–303.

Hollands, C. B., Nanson, G. C., Jones, B. G., Bristow, C. S., Price, D. M., & Pietsch, T. J. (2006). Aeolian–fluvial interaction: evidence for Late Quaternary channel change and wind-rift linear dune formation in the northwestern Simpson Desert, Australia. Quaternary Science Reviews, 25(1–2), 142–162.

Horwitz, M., & Wang, P. (2005). Sedimentological characteristics and internal architecture of two overwash fans from hurricanes Ivan and Jeanne. Gulf Coast Association of Geological Societies Transactions, 55, 342–352.

Houser, C., & Greenwood, B. (2005). Profile response of a lacustrine multiple barred nearshore to a sequence of storm events. Geomorphology, 69(1–4), 118–137.

Houser, C., Hapke, C., & Hamilton, S. (2008). Controls on coastal dune morphology, shoreline erosion and barrier island response to extreme storms. Geomorphology, 100(3–4), 223–240.

Houston, W. A., Wormington, K. R., & Black, R. L. (2015). Termite (Isoptera) diversity of riparian forests, adjacent woodlands and cleared pastures in tropical eastern Australia. Austral Entomology, 54(2), 221–230.

Huang, H., Gao, Y., Ma, C., Jones, M. M., Zeeden, C., Ibarra, D. E.,…Wang, C. (2021). Organic carbon burial is paced by a ~173-ka obliquity cycle in the middle to high latitudes. Science Advances, 7(28), eabf9489.

Huang, J., Han, M., Yang, J., Kappler, A., & Jiang, H. (2022). Salinity impact on composition and activity of nitrate-reducing Fe (II)-oxidizing microorganisms in saline lakes. Applied and environmental microbiology, 88(10), e00132–00122.

Hudock, J. W., Flaig, P. P., & Wood, L. J. (2014). Washover fans: A modern geomorphologic analysis and proposed classification scheme to improve reservoir models washover fans: A modern geomorphologic analysis and classification. Journal of Sedimentary Research, 84(10), 854–865.

Hughes, P. J., Sullivan, M. E., & Hiscock, P. (2017). Palaeoclimate and human occupation in southeastern arid Australia. Quaternary Science Reviews, 163, 72–83.

Hui, F., Xu, B., Huang, H., Yu, Q., & Gong, P. (2008). Modelling spatial-temporal change of Poyang Lake using multitemporal Landsat imagery. International journal of remote sensing, 29(20), 5767–5784.

Hunt, A. M., & Speakman, R. J. (2015). Portable XRF analysis of archaeological sediments and ceramics. Journal of Archaeological Science, 53, 626–638.

Huntley, D. J., & Baril, M. R. (1997). The K content of the K-feldspars being measured in optical dating or in thermoluminescence dating. Ancient TL, 15(1), 11–13.

Huntley, D. J., Hancock, R. G. V., & Ancient, T. L. (2001). The Rb contents of the K-feldspar grains being measured in optical dating. Ancient TL, 19(2), 43–46.

Isdale, P. (1984). Fluorescent bands in massive corals record centuries of coastal rainfall. Nature, 310, 578–579.

Iskandar, I., Lestari, D., Utari, P., Khakim, M., Poerwono, P., & Setiabudidaya, D. (2018). Evolution and impact of the 2016 negative Indian Ocean Dipole. Journal of Physics: Conference Series, 985(1), 012017.

Jacobs, Z. & Roberts, R. G. (2015). An improved single grain OSL chronology for the sedimentary deposits from Diepkloof Rockshelter, Western Cape, South Africa. Journal of Archaeological Science, 63, 175–192.

Jacobs, Z., Li, B., Jankowski, N., & Soressi, M. (2015). Testing of a single grain OSL chronology across the Middle to Upper Palaeolithic transition at Les Cottés (France). Journal of Archaeological Science, 54, 110–122.

Jacobs, Z., Li, B., Shunkov, M. V., Kozlikin, M. B., Bolikhovskaya, N. S., Agadjanian, A. K.,…Derevianko, A. P. (2019). Timing of archaic hominin occupation of Denisova Cave in southern Siberia. Nature, 565(7741), 594–599.

Jaworska, J. (2012). Crystallization, alternation and recrystallization of sulphates. Advances in crystallization processes, 1, 465–490.

Jia, F., Lu, R., Gao, S., Li, J., & Liu, X. (2015). Holocene aeolian activities in the southeastern Mu Us Desert, China. Aeolian Research, 19, 267–274.

Johnson, B., Miller, G. H., Fogel, M. L., Magee, J., Gagan, M., & Chivas, A. (1999). 65,000 years of vegetation change in central Australia and the Australian summer monsoon. Science, 284(5417), 1150–1152.

Jose, P. D. (1965). Sun's motion and sunspots. Astronomical Journal, 70(3), 193–200.

Jourdain, N. C., Gupta, A. S., Taschetto, A. S., Ummenhofer, C. C., Moise, A. F., & Ashok, K. (2013). The Indo-Australian monsoon and its relationship to ENSO and IOD in reanalysis data and the CMIP3/CMIP5 simulations. Climate Dynamics, 41, 3073–3102.

Kalnay, E., Kanamitsu, M., Kistler, R., Collins, W., Deaven, D., Gandin, L.,…Woollen, J. (1996). The NCEP/NCAR 40-year reanalysis project. Bulletin of the American Meteorological Society, 77(3), pp. 437–472.

Kang, S. M., Held, I. M., Frierson, D. M., & Zhao, M. (2008). The response of the ITCZ to extratropical thermal forcing: Idealized slab-ocean experiments with a GCM. Journal of Climate, 21(14), 3521–3532.

Kanner, L. C., Burns, S. J., Cheng, H., & Edwards, R. L. (2012). High-latitude forcing of the South American summer monsoon during the last glacial. Science, 335(6068), 570–573.

Kéfi, S., Rietkerk, M., Alados, C. L., Pueyo, Y., Papanastasis, V. P., ElAich, A., & De Ruiter, P. C. (2007). Spatial vegetation patterns and imminent desertification in Mediterranean arid ecosystems. Nature, 449(7159), 213–217.

Kelly, M. J., Edwards, R. L., Cheng, H., Yuan, D., Cai, Y., Zhang, M.,…An, Z. (2006). High resolution characterization of the Asian Monsoon between 146,000 and 99,000 years BP from Dongge Cave, China and global correlation of events surrounding Termination II. Palaeogeography, Palaeoclimatology, Palaeoecology, 236(1–2), 20–38.

Kemp, C., Tibby, J., Arnold, L., & Barr, C. (2019). Australian hydroclimate during Marine Isotope Stage 3: A synthesis and review. Quaternary Science Reviews, 204, 94–104.

Kershaw, A. (1991). A comparison of long Quaternary pollen records from the Atherton and Western Plains volcanic provinces, Australia. The Cainozoic in Australia: A Re-appraisal of the Evidence. Special Publication Geological Society of Australia, (18), 288–301.

Kershaw, A. P., & Nanson, G. (1993). The last full glacial cycle in the Australian region. Global and Planetary Change, 7(1–3), 1–9.

Kershaw, A. P., Bretherton, S. C., & van der Kaars, S. (2007). A complete pollen record of the last 230 ka from Lynch's Crater, north-eastern Australia. Palaeogeography, Palaeoclimatology, Palaeoecology, 251(1), 23–45.

Kershaw, A. P., van der Kaars, S., & Moss, P. T. (2003). Late Quaternary Milankovitch-scale climatic change and variability and its impact on monsoonal Australasia. Marine Geology, 201(1–3), 81–95.

Kim, S., Khim, B.-K., & Takahashi, K. (2016). Late Pliocene to early Pleistocene (2.4–1.25 Ma) paleoproductivity changes in the Bering Sea: IODP expedition 323 Hole U1343E. Deep Sea Research Part II: Topical Studies in Oceanography, 125, 155–162.

Klappa, C. F. (1980). Rhizoliths in terrestrial carbonates: classification, recognition, genesis and significance. Sedimentology, 27(6), 613–629.

Konert, M., & Vandenberghe, J. (1997). Comparison of laser grain size analysis with pipette and sieve analysis: a solution for the underestimation of the clay fraction. Sedimentology, 44(3), 523–535.

Kotwicki, V., & Allan, R. (1998). La Nina de Australia—contemporary and palaeo-hydrology of Lake Eyre. Palaeogeography, Palaeoclimatology, Palaeoecology, 144(3–4), 265–280.

Knutti, R., Flückiger, J., Stocker, T., & Timmermann, A. (2004). Strong hemispheric coupling of glacial climate through freshwater discharge and ocean circulation. Nature, 430(7002), 851–856.

Konert, M., & Vandenberghe, J. (1997). Comparison of laser grain size analysis with pipette and sieve analysis: a solution for the underestimation of the clay fraction. Sedimentology, 44(3), 523–535.

Kostic, S., & Parker, G. (2003). Progradational sand-mud deltas in lakes and reservoirs. Part 1. Theory and numerical modeling. Journal of Hydraulic Research, 41(2), 127–140.

Kostic, S., Parker, G., & Marr, J. G. (2002). Role of turbidity currents in setting the foreset slope of clinoforms prograding into standing fresh water. Journal of Sedimentary Research, 72(3), 353–362.

Kotwicki, V. (1986). Floods of Lake Eyre. Engineering and Water Supply Department, South Australia.

Kotwicki, V., & Allan, R. (1998). La Nina de Australia—contemporary and palaeo-hydrology of Lake Eyre. Palaeogeography, Palaeoclimatology, Palaeoecology, 144(3–4), 265–280.

Kotwicki, V., & Isdale, P. (1991). Hydrology of Lake Eyre, Australia - El-Nino Link. Palaeogeography Palaeoclimatology Palaeoecology, 84(1–4), 87–98.

Krapf, C. B., Lang, S. C., & Werner, M. (2022). The interplay of fluvial, lacustrine and aeolian deposition and erosion along the Neales Cliffs and its relevance to the evolution of Kati Thanda-Lake Eyre, central Australia, during the Quaternary. Transactions of the Royal Society of South Australia, 146(1), 7–30.

Kraus, M. J. (1999). Paleosols in clastic sedimentary rocks: their geologic applications. Earth-Science Reviews, 47(1–2), 41–70.

Kraus, M. J., & Hasiotis, S. T. (2006). Significance of different modes of rhizolith preservation to interpreting paleoenvironmental and paleohydrologic settings: examples from Paleogene paleosols, Bighorn Basin, Wyoming, USA. Journal of Sedimentary Research, 76(4), 633–646.

Krauß, L., Kappenberg, A., Zens, J., Kehl, M., Schulte, P., Zeeden, C.,…Lehmkuhl, F. (2018). Reconstruction of Late Pleistocene paleoenvironments in southern Germany using two high-resolution loess-paleosol records. Palaeogeography, Palaeoclimatology, Palaeoecology, 509, 58–76.

Kreutzer, S., Schmidt, C., Fuchs, M. C., Dietze, M., Fischer, M., & Fuchs, M. (2012). Introducing an R package for luminescence dating analysis. Ancient TL, 30(1), 1–8.

Kutzbach, J., Liu, X., Liu, Z., & Chen, G. (2008). Simulation of the evolutionary response of global summer monsoons to orbital forcing over the past 280,000 years. Climate Dynamics, 30, 567–579.

Laurin, J., Meyers, S. R., Uličný, D., Jarvis, I., & Sageman, B. B. (2015). Axial obliquity control on the greenhouse carbon budget through middle-to high-latitude reservoirs. Paleoceanography, 30(2), 133–149.

Laws, E. A., Popp, B. N., Bidigare, R. R., Kennicutt, M. C., & Macko, S. A. (1995). Dependence of phytoplankton carbon isotopic composition on growth rate and [$CO_2$]aq: Theoretical considerations and experimental results. Geochimica Et Cosmochimica Acta, 59(6), 1131–1138.

Leduc, G., Vidal, L., Tachikawa, K., & Bard, E. (2009). ITCZ rather than ENSO signature for abrupt climate changes across the tropical Pacific? Quaternary Research, 72(1), 123–131.

Lehmann, M. F., Bernasconi, S. M., Barbieri, A., Simona, M., & McKenzie, J. A. (2004). Interannual variation of the isotopic composition of sedimenting organic carbon and nitrogen in Lake Lugano: A long-term sediment trap study. Limnology and Oceanography, 49(3), 839–849.

Leng, M. J., & Marshall, J. D. (2004). Palaeoclimate interpretation of stable isotope data from lake sediment archives. Quaternary Science Reviews, 23(7–8), 811–831.

Leng, M. J., & Melanie, J. (2006). Isotopes in palaeoenvironmental research (Vol. 10). Dordrecht: Springer.

Lengyel, E., Barreto, S., Padisák, J., Stenger-Kovács, C., Lázár, D., & Buczkó, K. (2023). Contribution of silica-scaled chrysophytes to ecosystems services: a review. Hydrobiologia, 850(12), 2735–2756.

Leon, J. X., & Cohen, T. (2012). An improved bathymetric model for the modern and palaeo Lake Eyre. Geomorphology, 173, 69–79.

Leroy, A., & Wheeler, M. C. (2008). Statistical prediction of weekly tropical cyclone activity in the Southern Hemisphere. Monthly Weather Review, 136(10), 3637–3654.

Leventer, A., Domack, E. W., Ishman, S. E., Brachfeld, S., McClennen, C. E., & Manley, P. (1996). Productivity cycles of 200–300 years in the Antarctic Peninsula region: understanding linkages among the sun, atmosphere, oceans, sea ice, and biota. Geological Society of America Bulletin, 108(12), 1626–1644.

Lewis, S. C., Gagan, M. K., Ayliffe, L. K., Zhao, J.-x., Hantoro, W. S., Treble, P. C.,…Schmidt, G. A. (2011). High-resolution stalagmite reconstructions of Australian–Indonesian

monsoon rainfall variability during Heinrich stadial 3 and Greenland interstadial 4. Earth and Planetary Science Letters, 303(1–2), 133–142.

Li, B., Jacobs, Z., Roberts, R. G., Galbraith, R., & Peng, J. (2017). Variability in quartz OSL signals caused by measurement uncertainties: Problems and solutions. Quaternary Geochronology, 41, 11–25.

Li, T., Wang, B., Chang, C., & Zhang, Y. (2003). A theory for the Indian Ocean dipole–zonal mode. Journal of the Atmospheric Sciences, 60(17), 2119–2135.

Li, W., Du, Z., Ling, F., Zhou, D., Wang, H., Gui, Y.,…Zhang, X. (2013). A comparison of land surface water mapping using the normalized difference water index from TM, ETM+ and ALI. Remote Sensing, 5(11), 5530–5549.

Liang, D., & Liu, C. (2018). Coccolith assemblages and primary productivity variations in the central Western Pacific Warm Pool over the last 380 kyr. Journal of Ocean University of China, 17, 563–570.

Liebrand, D., Beddow, H. M., Lourens, L. J., Pälike, H., Raffi, I., Bohaty, S. M.,…Van Dijk, A. E. (2016). Cyclostratigraphy and eccentricity tuning of the early Oligocene through early Miocene (30.1–17.1 Ma): Cibicides mundulus stable oxygen and carbon isotope records from Walvis Ridge Site 1264. Earth and Planetary Science Letters, 450, 392–405.

Lim, E.-P., & Hendon, H. H. (2017). Causes and predictability of the negative Indian Ocean Dipole and its impact on La Niña during 2016. Scientific reports, 7(1), 1–11.

Lim, E.-P., Hudson, D., Wheeler, M. C., Marshall, A. G., King, A., Zhu, H.,…Griffiths, M. (2021). Why Australia was not wet during spring 2020 despite La Niña. Scientific reports, 11(1), 1–15.

Lisiecki, L. E., & Raymo, M. E. (2005). A Pliocene-Pleistocene stack of 57 globally distributed benthic δ18O records. Paleoceanography, 20(1), PA1003.

Lisonbee, J., & Ribbe, J. (2021). Seasonal climate influences on the timing of the Australian monsoon onset. Weather and Climate Dynamics, 2(2), 489–506.

Liu, W., Liu, Z., An, Z., Sun, J., Chang, H., Wang, N.,…Wang, H. (2014). Late Miocene episodic lakes in the arid Tarim Basin, western China. Proceedings of the National Academy of Sciences, 111(46), 16292–16296.

Liu, X., Nie, J., Zhou, B., & Zhang, Z. (2024). East Asian summer monsoon variations across the Miocene–Pliocene boundary recorded by sediments from the Guide Basin, northeastern Tibetan Plateau. Bulletin, 136(3–4), 1541–1552.

Liu, Z., Huang, C., Algeo, T. J., Liu, H., Hao, Y., Du, X.,…Peng, L. (2018). High-resolution astrochronological record for the Paleocene-Oligocene (66–23 Ma) from the rapidly subsiding Bohai Bay Basin, northeastern China. Palaeogeography, Palaeoclimatology, Palaeoecology, 510, 78–92.

Liu, Z., Otto-Bliesner, B., Kutzbach, J., Li, L., & Shields, C. (2003). Coupled climate simulation of the evolution of global monsoons in the Holocene. Journal of Climate, 16(15), 2472–2490.

Lizzoli, S., Raigemborn, M. S., & Varela, A. N. (2021). Controls of pedogenesis in a fluvial-eolian succession of Cenomanian age in northern Patagonia. Palaeogeography, Palaeoclimatology, Palaeoecology, 577, 110549.

Lomax, J., Hilgers, A., Wopfner, H., Grün, R., Twidale, C., & Radtke, U. (2003). The onset of dune formation in the Strzelecki Desert, South Australia. Quaternary Science Reviews, 22(10-13), 1067–1076.

Lough, J. M. (1991). Rainfall variations in Queensland, Australia: 1891–1986. International Journal of Climatology, 11(7), 745–768.

Lough, J. M. (2011). Great Barrier Reef coral luminescence reveals rainfall variability over northeastern Australia since the 17th century. Paleoceanography, 26(2), PA2201.

Lough, J. M., Lewis, S., & Cantin, N. (2015). Freshwater impacts in the central Great Barrier Reef: 1648–2011. Coral Reefs, 34(3), 739–751.

Lucas-Tooth, H., & Price, B. (1961). A mathematical method for the investigation of interelement effects in X-Ray fluorescence analysis. Metallurgia, 64(2), 149–152.

Lückge, A., Mohtadi, M., Rühlemann, C., Scheeder, G., Vink, A., Reinhardt, L., & Wiedicke, M. (2009). Monsoon versus ocean circulation controls on paleoenvironmental conditions off southern Sumatra during the past 300,000 years. Paleoceanography, 24(1), PA1208.

Machel, H. G., & Burton, E. A. (1991). Burial-diagenetic sabkha-like gypsum and anhydrite nodules. Journal of Sedimentary Research, 61(3), 394–405.

Mack, G. H., James, W. C., & Monger, H. C. (1993). Classification of paleosols. Geological Society of America Bulletin, 105(2), 129–136.

Magee, J. (1991). Late Quaternary lacustrine, groundwater, aeolian and pedogenic gypsum in the Prungle Lakes, southeastern Australia. Palaeogeography, Palaeoclimatology, Palaeoecology, 84(1–4), 3–42.

Magee, J. W. (1997). Late Quaternary environments and palaeohydrology of Lake Eyre, arid central Australia. Unpublished Ph.D. Thesis, Australian National University, Canberra.

Magee, J. W., Bowler, J. M., Miller, G. H., & Williams, D. (1995). Stratigraphy, sedimentology, chronology and palaeohydrology of Quaternary lacustrine deposits at Madigan Gulf, Lake Eyre, South Australia. Palaeogeography, Palaeoclimatology, Palaeoecology, 113(1), 3–42.

Magee, J. W., & Miller, G. H. (1998). Lake Eyre palaeohydrology from 60 ka to the present: beach ridges and glacial maximum aridity. Palaeogeography, Palaeoclimatology, Palaeoecology, 144(3–4), 307–329.

Magee, J. W., Miller, G. H., Spooner, N. A., & Questiaux, D. (2004). Continuous 150 ky monsoon record from Lake Eyre, Australia: insolation-forcing implications and unexpected Holocene failure. Geology, 32(10), 885–888.

Magee, A. D., Verdon-Kidd, D. C., Diamond, H. J., & Kiem, A. S. (2017). Influence of ENSO, ENSO Modoki, and the IPO on tropical cyclogenesis: a spatial analysis of the southwest Pacific region. International Journal of Climatology, 37, 1118–1137.

Mann, S. J., & Amos, K. J. (2022). Sedimentology and geomorphology of Lake Yamma Yamma-A long-lived structurally controlled playa lake of the Lake Eyre Basin, Australia. Transactions of the Royal Society of South Australia, 146(1), 31–58.

Mantua, N. J., & Hare, S. R. (2002). The Pacific decadal oscillation. Journal of oceanography, 58, 35–44.

Mao, X., & Retallack, G. (2019). Late Miocene drying of central Australia. Palaeogeography, Palaeoclimatology, Palaeoecology, 514, 292–304.

Maroulis, J., & Nanson, G. (1996). Bedload transport of aggregated muddy alluvium from Cooper Creek, central Australia: a flume study. Sedimentology, 43(5), 771–790.

Maroulis, J. C., Nanson, G. C., Price, D. M., & Pietsch, T. (2007). Aeolian–fluvial interaction and climate change: source-bordering dune development over the past ~100 ka on Cooper Creek, central Australia. Quaternary Science Reviews, 26(3–4), 386–404.

Marriott, S., & Wright, V. (1993). Palaeosols as indicators of geomorphic stability in two Old Red Sandstone alluvial suites, South Wales. Journal of the Geological Society, 150(6), 1109–1120.

Martin, H. (2006). Cenozoic climatic change and the development of the arid vegetation in Australia. Journal of Arid Environments, 66(3), 533–563.

Martinez, M., Kotov, S., De Vleeschouwer, D., Pas, D., & Pälike, H. (2016). Testing the impact of stratigraphic uncertainty on spectral analyses of sedimentary series. Climate of the Past Discussions, 2016, 1–22.

Marx, S. K., Kamber, B. S., McGowan, H. A., & Denholm, J. (2011). Holocene dust deposition rates in Australia's Murray-Darling Basin record the interplay between aridity and the position of the mid-latitude westerlies. Quaternary Science Reviews, 30(23–24), 3290–3305.

May, J.-H., Wells, S. G., Cohen, T. J., Marx, S. K., Nanson, G. C., & Baker, S. E. (2015). A soil chronosequence on Lake Mega-Frome beach ridges and its implications for late Quaternary pedogenesis and paleoenvironmental conditions in the drylands of southern Australia. Quaternary Research, 83(1), 150–165.

Maynard, J. (1992). Chemistry of modern soils as a guide to interpreting Precambrian paleosols. The Journal of Geology, 100(3), 279–289.

McCarthy, P. J., & Guy Plint, A. (1998). Recognition of interfluve sequence boundaries: integrating paleopedology and sequence stratigraphy. Geology, 26(5), 387–390.

McFeeters, S. K. (1996). The use of the Normalized Difference Water Index (NDWI) in the delineation of open water features. International journal of remote sensing, 17(7), 1425–1432.

McGee, D., Donohoe, A., Marshall, J., & Ferreira, D. (2014). Changes in ITCZ location and cross-equatorial heat transport at the Last Glacial Maximum, Heinrich Stadial 1, and the mid-Holocene [Article]. Earth and Planetary Science Letters, 390, 69–79.

McGowan, H. A., Marx, S. K., Soderholm, J., & Denholm, J. (2010). Evidence of solar and tropical-ocean forcing of hydroclimate cycles in southeastern Australia for the past 6500 years. Geophysical Research Letters, 37(10), L10705.

McIntosh, P., Price, D., Eberhard, R., & Slee, A. (2009). Late Quaternary erosion events in lowland and mid-altitude Tasmania in relation to climate change and first human arrival. Quaternary Science Reviews, 28(9–10), 850–872.

McKenna, S., Santoso, A., Gupta, A. S., Taschetto, A. S., & Cai, W. (2020). Indian Ocean Dipole in CMIP5 and CMIP6: characteristics, biases, and links to ENSO. Scientific reports, 10(1), 1–13.

McLennan, S. M. (1993). Weathering and global denudation. The Journal of Geology, 101(2), 295–303.

McManus, J. F., Bond, G. C., Broecker, W. S., Johnsen, S., Labeyrie, L., & Higgins, S. (1994). High-resolution climate records from the North Atlantic during the last interglacial. Nature, 371(6495), 326–329.

McManus, J. F., Francois, R., Gherardi, J.-M., Keigwin, L. D., & Brown-Leger, S. (2004). Collapse and rapid resumption of Atlantic meridional circulation linked to deglacial climate changes. Nature, 428(6985), 834–837.

McManus, J. F., Oppo, D. W., & Cullen, J. L. (1999). A 0.5-million-year record of millennial-scale climate variability in the North Atlantic. Science, 283(5404), 971–975.

McTainsh, G. (1998). Dust storm index. In Sustainable agriculture: assessing Australia's recent performance, a Report of the National Collaborative Project on Indicators for Sustainable Agriculture. SCARM Technical Report 70, 65–72.

Meehl, G. A., & Arblaster, J. M. (2009). A lagged warm event–like response to peaks in solar forcing in the Pacific region. Journal of Climate, 22(13), 3647–3660.

Mees, F., Casteñeda, C., Herrero, J., & Van Ranst, E. (2012). The nature and significance of variations in gypsum crystal morphology in dry lake basins. Journal of Sedimentary Research, 82(1), 37–52.

Meese, D., Gow, A., Alley, R., Zielinski, G., Grootes, P., Ram, M.,…Bolzan, J. (1997). The Greenland Ice Sheet Project 2 depth-age scale: methods and results. Journal of Geophysical Research: Oceans, 102(C12), 26411–26423.

Mescolotti, P. C., Varejão, F. G., Warren, L. V., Ladeira, F. S. B., Giannini, P. C. F., & Assine, M. L. (2019). The sedimentary record of wet and dry eolian systems in the Cretaceous of Southeast Brazil: stratigraphic and paleogeographic significance. Brazilian Journal of Geology, 49, e20190057.

Metzger, C., & Retallack, G. (2010). Paleosol record of Neogene climate change in the Australian outback. Australian Journal of Earth Sciences, 57(7), 871–885.

Meyers, G., McIntosh, P., Pigot, L., & Pook, M. (2007). The years of El Niño, La Niña, and interactions with the tropical Indian Ocean. Journal of Climate, 20(13), 2872–2880.

Meyers, S. (2014). Astrochron: An R package for astrochronology. https://cran.r-project.org/package=astrochron.

Miall, A. D. (1977). A review of the braided-river depositional environment. Earth-Science Reviews, 13(1), 1–62.

Miall, A. D. (1992). Alluvial deposits. In R.G. Walker & N.P. James (Eds.), Facies models: response to sea level change. Geological Association of Canada: St Johns, 119–142.

Miall, A. D. (2013). The geology of fluvial deposits: sedimentary facies, basin analysis, and petroleum geology. Springer.

Miller, G. H., Fogel, M. L., Magee, J. W., & Gagan, M. K. (2016a). Disentangling the impacts of climate and human colonization on the flora and fauna of the Australian arid zone over the past 100 ka using stable isotopes in avian eggshell. Quaternary Science Reviews, 151, 27–57.

Miller, G. H., Fogel, M. L., Magee, J. W., Gagan, M. K., Clarke, S. J., & Johnson, B. J. (2005a). Ecosystem collapse in Pleistocene Australia and a human role in megafaunal extinction. Science, 309(5732), 287–290.

Miller, G. H., Magee, J. W., Fogel, M. L., Wooller, M. J., Hesse, P. P., Spooner, N. A.,…Wallis, L. (2018). Wolfe Creek Crater: A continuous sediment fill in the Australian Arid Zone records changes in monsoon strength through the Late Quaternary. Quaternary Science Reviews, 199, 108–125.

Miller, G., H., Magee, J. W., Smith, M., Spooner, N., Baynes, A., Lehman, S.,…Clark, P. (2016b). Human predation contributed to the extinction of the Australian megafaunal bird Genyornis newtoni ~47 ka. Nature Communications, 7(1), 10496.

Miller, G. H., Magee, J. W., & Jull, A. (1997). Low-latitude glacial cooling in the Southern Hemisphere from amino-acid racemization in emu eggshells. Nature, 385(6613), 241–244.

Miller, G. H., Mangan, J., Pollard, D., Thompson, S., Felzer, B., & Magee, J. (2005b). Sensitivity of the Australian Monsoon to insolation and vegetation: implications for human impact on continental moisture balance. Geology, 33(1), 65–68.

Minyuk, P., & Subbotnikova, T. (2021). Rock magnetic properties of Grand Lake sediments as evidence of environmental changes during the last 60 000 years in North-East Russia. Boreas, 50(4), 1027–1042.

Moffa-Sanchez, P., Rosenthal, Y., Babila, T. L., Mohtadi, M., & Zhang, X. (2019). Temperature evolution of the Indo-Pacific Warm Pool over the Holocene and the last deglaciation. Paleoceanography and Paleoclimatology, 34(7), 1107–1123.

Mohtadi, M., Oppo, D. W., Steinke, S., Stuut, J.-B. W., De Pol-Holz, R., Hebbeln, D., & Lückge, A. (2011). Glacial to Holocene swings of the Australian–Indonesian monsoon. Nature Geoscience, 4(8), 540–544.

Moreno, A., Cacho, I., Canals, M., Grimalt, J. O., Sánchez-Goñi, M. F., Shackleton, N., & Sierro, F. J. (2005). Links between marine and atmospheric processes oscillating on a millennial time-scale. A multi-proxy study of the last 50,000 yr from the Alboran Sea (Western Mediterranean Sea). Quaternary Science Reviews, 24(14–15), 1623–1636.

Moreno, A., Cacho, I., Canals, M., Prins, M. A., Sánchez-Goñi, M.-F., Grimalt, J. O., & Weltje, G. J. (2002). Saharan dust transport and high-latitude glacial climatic variability: the Alboran Sea record. Quaternary Research, 58(3), 318–328.

Morgan-Edel, K. D., Boston, P. J., Spilde, M. N., & Reynolds, R. E. (2015). Phytoliths (plant-derived mineral bodies) as geobiological and climatic indicators in arid environments. New Mexico Geology, 37(1), 3–20.

Moss, P. T., & Kershaw, P. A. (2000). The last glacial cycle from the humid tropics of northeastern Australia: comparison of a terrestrial and a marine record. Palaeogeography, Palaeoclimatology, Palaeoecology, 155(1–2), 155–176.

Mueller, N., Lewis, A., Roberts, D., Ring, S., Melrose, R., Sixsmith, J.,…Curnow, S. (2016). Water observations from space: Mapping surface water from 25 years of Landsat imagery across Australia. Remote Sensing of Environment, 174, 341–352.

Muller, J., Kylander, M., Wüst, R. A., Weiss, D., Martinez-Cortizas, A., LeGrande, A. N.,…Jacobson, G. (2008). Possible evidence for wet Heinrich phases in tropical NE Australia: the Lynch's Crater deposit. Quaternary Science Reviews, 27(5–6), 468–475.

Muller, J., McManus, J. F., Oppo, D. W., & Francois, R. (2012). Strengthening of the Northeast Monsoon over the Flores Sea, Indonesia, at the time of Heinrich event 1. Geology, 40(7), 635–638.

Munsell, C. (2009). Munsell soil color charts, new revised edition. Macbeth Division of Kollmorgen Instruments, New Windsor.

Murakoshi, N., & Masuda, F. (1991). A depositional model for a flood-tidal delta and washover sands in the late Pleistocene Paleo-Tokyo Bay, Japan. In Clastic Tidal Sedimentology, Canadian Society of Petroleum Geologists, Memoir, 16, 219–226.

Murakoshi, N., & Masuda, F. (1992). Estuarine, barrier-island to strand-plain sequence and related ravinement surface developed during the last interglacial in the Paleo-Tokyo Bay, Japan. Sedimentary Geology, 80(3–4), 167–184.

Murphy, B. P., & Bowman, D. M. (2007). Seasonal water availability predicts the relative abundance of C3 and C4 grasses in Australia. Global Ecology and Biogeography, 16(2), 160–169.

Murray, A. S., & Wintle, A. G. (2000). Luminescence dating of quartz using an improved single-aliquot regenerative-dose protocol. Radiation Measurements, 32(1), 57–73.

Naafs, B., Hefter, J., & Stein, R. (2013). Millennial-scale ice rafting events and Hudson Strait Heinrich(-like) Events during the late Pliocene and Pleistocene: a review. Quaternary Science Reviews, 80, 1–28.

Nanson, G. C., & Price, D. M. (1998). Quaternary change in the Lake Eyre basin of Australia: an introduction. Palaeogeography Palaeoclimatology Palaeoecology, 144(3–4), 235–237.

Nanson, G. C., Callen, R. A., & Price, D. M. (1998). Hydroclimatic interpretation of Quaternary shorelines on south Australian playas. Palaeogeography Palaeoclimatology Palaeoecology, 144(3–4), 281–305.

Nanson, G. C., Chen, X. Y., & Price, D. M. (1992a). Lateral Migration, Thermoluminescence Chronology and Color Variation of Longitudinal Dunes near Birdsville in the Simpson Desert, Central Australia. Earth Surface Processes and Landforms, 17(8), 807–819.

Nanson, G. C., Chen, X. Y., & Price, D. M. (1995). Aeolian and Fluvial Evidence of Changing Climate and Wind Patterns during the Past 100 Ka in the Western Simpson Desert, Australia. Palaeogeography Palaeoclimatology Palaeoecology, 113(1), 87–102.

Nanson, G. C., Jones, B. G., Price, D. M., & Pietsch, T. J. (2005). Rivers turned to rock: Late Quaternary alluvial induration influencing the behaviour and morphology of an anabranching river in the Australian monsoon tropics. Geomorphology, 70(3–4), 398–420.

Nanson, G. C., Jones, B. G., Price, D. M., Pietsch, T., Bristow, C., & Hollands, C. B. (2006). Aeolian-fluvial interaction: evidence for Late Quaternary channel change and wind-rift linear dune formation in the northwestern Simpson Desert, Australia. Quaternary Science Reviews, 25(1–2), 142–162.

Nanson, G. C., Price, D. M., Jones, B. G., Maroulis, J. C., Coleman, M., Bowman, H.,…Larsen, J. R. (2008). Alluvial evidence for major climate and flow regime changes during the middle and late Quaternary in eastern central Australia. Geomorphology, 101(1–2), 109–129.

Nanson, G. C., Price, D. M., & Short, S. A. (1992b). Wetting and drying of Australia over the past 300 ka. Geology, 20(9), 791–794.

Nanson, G. C., Young, R., Price, D., & Rust, B. (1988). Stratigraphy, sedimentology and late Quaternary chronology of the Channel Country of western Queensland. Fluvial geomorphology of Australia, 151–175.

NCoSA. (2009). Australian soil and land survey field handbook. CSIRO Publishing.

Neal, A., Richards, J., & Pye, K. (2003). Sedimentology of coarse-clastic beach-ridge deposits, Essex, southeast England. Sedimentary Geology, 162(3–4), 167–198.

Nesbitt, H., & Young, G. M. (1982). Early Proterozoic climates and plate motions inferred from major element chemistry of lutites. Nature, 299(5885), 715–717.

Neukom, R., Gergis, J., Karoly, D. J., Wanner, H., Curran, M., Elbert, J.,…Mundo, I. (2014). Inter-hemispheric temperature variability over the past millennium. Nature Climate Change, 4(5), 362–367.

Nigam, R., Khare, N., & Nair, R. (1995). Foraminiferal evidences for 77-year cycles of droughts in India and its possible modulation by the Gleissberg solar cycle. Journal of coastal research, 1099–1107.

Nordt, L., Orosz, M., Driese, S., & Tubbs, J. (2006). Vertisol carbonate properties in relation to mean annual precipitation: implications for paleoprecipitation estimates. The Journal of Geology, 114(4), 501–510.

Nott, J., & Price, D. (1994). Plunge pools and paleoprecipitation. Geology, 22(11), 1047–1050.

NTGS. (2006). Geological map of the Northern Territory [Territory-wide Map GIS Data]. Northern Territory Geological Survey. https://geoscience.nt.gov.au/gemis/ntgsjspui/handle/1/82057.

Nutz, A., Schuster, M., Ghienne, J.-F., Roquin, C., & Bouchette, F. (2018). Wind-driven waterbodies: a new category of lake within an alternative sedimentologically-based lake classification. Journal of Paleolimnology, 59(2), 189–199.

O'Connell, J. F., & Allen, J. (2004). Dating the colonization of Sahul (Pleistocene Australia–New Guinea): a review of recent research. Journal of Archaeological Science, 31(6), 835–853.

O'Connell, J. F., & Allen, J. (2015). The process, biotic impact, and global implications of the human colonization of Sahul about 47,000 years ago. Journal of Archaeological Science, 56, 73–84.

O'Connell, J. F., Allen, J., Williams, M. A., Williams, A. N., Turney, C. S., Spooner, N. A.,…Cooper, A. (2018). When did Homo sapiens first reach Southeast Asia and Sahul? Proceedings of the National Academy of Sciences, 115(34), 8482–8490.

O'Leary, M. H. (1988). Carbon isotopes in photosynthesis. Bioscience, 38(5), 328–336.

Orr, T. J., Wurster, C. M., Levchenko, V., Ascough, P. L., & Bird, M. I. (2021). Improved pretreatment method for the isolation and decontamination of pyrogenic carbon for radiocarbon dating using hydrogen pyrolysis. Quaternary Geochronology, 61, 101124.

Otsu, N. (1979). A threshold selection method from gray-level histograms. IEEE transactions on systems, man, and cybernetics, 9(1), 62–66.

Pack, S. M., Miller, G. H., Fogel, M. L., & Spooner, N. A. (2003). Carbon isotopic evidence for increased aridity in northwestern Australia through the Quaternary. Quaternary Science Reviews, 22(5–7), 629–643.

Page, K., Nanson, G., & Price, D. (1996). Chronology of Murrumbidgee river palaeochannels on the Riverine Plain, southeastern Australia. Journal of Quaternary Science: Published for the Quaternary Research Association, 11(4), 311–326.

Paillard, D., Labeyrie, L., & Yiou, P. (1996). Macintosh program performs time-series analysis. Eos, Transactions American Geophysical Union, 77(39), 379–379.

Painter, M. G., Golding, S. D., Hannan, K. W., & Neudert, M. K. (1999). Sedimentologic, petrographic, and sulfur isotope constraints on fine-grained pyrite formation at Mount Isa Mine and environs, Northwest Queensland, Australia. Economic Geology, 94(6), 883–912.

Palmer, J. G., Cook, E. R., Turney, C. S. M., Allen, K., Fenwick, P., Cook, B. I.,…Baker, P. (2015). Drought variability in the eastern Australia and New Zealand summer drought atlas (ANZDA, CE 1500–2012) modulated by the Interdecadal Pacific Oscillation. Environmental Research Letters, 10(12).

Parker, D., Folland, C., Scaife, A., Knight, J., Colman, A., Baines, P., & Dong, B. (2007). Decadal to multidecadal variability and the climate change background. Journal of Geophysical Research: Atmospheres, 112, D18115.

Parth, S., Russell, J., & Waldmann, N. (2021). Reconstructing 1200 years of Hydroclimate Variability in the Southern Margins of the Arabian Desert: Insights From a Paleo-Lake in Southern Yemen. Frontiers in Earth Science, 9, 712443.

Partin, J. W., Cobb, K. M., Adkins, J. F., Clark, B., & Fernandez, D. P. (2007). Millennial-scale trends in west Pacific warm pool hydrology since the Last Glacial Maximum. Nature, 449(7161), 452–455.

Pasquier, V., Sansjofre, P., Rabineau, M., Revillon, S., Houghton, J., & Fike, D. A. (2017). Pyrite sulfur isotopes reveal glacial−interglacial environmental changes. Proceedings of the National Academy of Sciences, 114(23), 5941–5945.

Pearson, M., & Lennon, J. (2010). Pastoral Australia: fortunes, failures and hard yakka: a historical overview 1788–1967. CSIRO Publishing.

Pécsi, M. (1995). The role of principles and methods in loess-paleosol investigations. GeoJournal, 36, 117–131.

Peinerud, E. K. (2000). Interpretation of Si concentrations in lake sediments: three case studies. Environmental geology (Berlin), 40(1–2), 64–72.

Peinerud, E. K., Ingri, J., & Pontér, C. (2001). Non-detrital Si concentrations as an estimate of diatom concentrations in lake sediments and suspended material. Chemical Geology, 177(3–4), 229–239.

Pell, S. D., Chivas, A. R., & Williams, I. S. (2000). The Simpson, Strzelecki and Tirari Deserts: development and sand provenance. Sedimentary Geology, 130(1–2), 107–130.

Peng, J., Dong, Z. B., Han, F. Q., Long, H. & Liu, X. J. R package numOSL: numeric routines for optically stimulated luminescence dating. Ancient TL, 31, 41–48 (2013).

Pestiaux, P., Van der Mersch, I., Berger, A., & Duplessy, J. C. (1988). Paleoclimatic variability at frequencies ranging from 1 cycle per 10 000 years to 1 cycle per 1000 years: Evidence for nonlinear behaviour of the climate system. Climatic Change, 12, 9–37.

Pitman, A., & Hesse, P. (2007). The significance of large-scale land cover change on the Australian palaeomonsoon. Quaternary Science Reviews, 26(1–2), 189–200.

Pourali, M., Sepehr, A., & Mahmudy Gharaie, M. H. (2020). Depositional pattern of sediments in a dry-lake Playa in NE Iran; Implication for geomorphologic characteristics. Desert Ecosystem Engineering Journal, 3(1), 11–24.

Power, S., Casey, T., Folland, C., Colman, A., & Mehta, V. (1999). Inter-decadal modulation of the impact of ENSO on Australia. Climate Dynamics, 15, 319–324.

Pranzini, E. (2001). Updrift river mouth migration on cuspate deltas: two examples from the coast of Tuscany (Italy). Geomorphology, 38(1–2), 125–132.

Price, G. J., Webb, G. E., Zhao, J. X., Feng, Y. X., Murray, A. S., Cooke, B. N., ... & Sobbe, I. H. (2011). Dating megafaunal extinction on the Pleistocene Darling Downs, eastern Australia: the promise and pitfalls of dating as a test of extinction hypotheses. Quaternary Science Reviews, 30(7–8), 899–914.

Psuty, N. P. (1992). Spatial variation in coastal foredune development. In Coastal Dunes: Geomorphology, Ecology and Management for Conservation. Balkema: Rotterdam, 3–13.

QGlobe. (2024a). Queensland Globe, Detailed Surface Geology 1:100,000 Map. Retrieved 03/04/2023 from https://qldglobe.information.qld.gov.au/

QGlobe. (2024b). Queensland Globe, Inland Waters, Watercourse Map. . Retrieved 11/07/2023 from https://qldglobe.information.qld.gov.au/

QImagery. (2023). Queensland Government, QImagery, Machattie 1970. https://qimagery.information.qld.gov.au/

Quigley, M. C., Horton, T., Hellstrom, J. C., Cupper, M. L., & Sandiford, M. (2010). Holocene climate change in arid Australia from speleothem and alluvial records. The Holocene, 20(7), 1093–1104.

Rabineau, M., Berné, S., Olivet, J.-L., Aslanian, D., Guillocheau, F., & Joseph, P. (2006). Paleo sea levels reconsidered from direct observation of paleoshoreline position during Glacial Maxima (for the last 500,000 yr). Earth and Planetary Science Letters, 252(1–2), 119–137.

Rashid, H., Hesse, R., & Piper, D. J. (2003). Evidence for an additional Heinrich event between H5 and H6 in the Labrador Sea. Paleoceanography, 18(4), 1077.

Rasmussen, M., Guo, X., Wang, Y., Lohmueller, K. E., Rasmussen, S., Albrechtsen, A.,…Jombart, T. (2011). An Aboriginal Australian genome reveals separate human dispersals into Asia. Science, 334(6052), 94–98.

Rasmussen, T. L., Oppo, D. W., Thomsen, E., & Lehman, S. J. (2003). Deep sea records from the southeast Labrador Sea: Ocean circulation changes and ice-rafting events during the last 160,000 years. Paleoceanography, 18(1), 1018.

Raspopov, O., Dergachev, V., Esper, J., Kozyreva, O., Frank, D., Ogurtsov, M.,…Shao, X. (2008). The influence of the de Vries (~200-year) solar cycle on climate variations: Results from the Central Asian Mountains and their global link. Palaeogeography, Palaeoclimatology, Palaeoecology, 259(1), 6–16.

Ratcliffe, F. (1937). Further observations on soil erosion and sand drift, with special reference to south-western Queensland. Council for Scientific and Industrial Research, Pamphlet 70, Government Printer, Canberra.

Raymo, M. E. (1997). The timing of major climate terminations. Paleoceanography, 12(4), 577–585.

Rees, C. E., Jenkins, W., & Monster, J. (1978). The sulphur isotopic composition of ocean water sulphate. Geochimica Et Cosmochimica Acta, 42(4), 377–381.

Reeves, J. M., Barrows, T. T., Cohen, T. J., Kiem, A. S., Bostock, H. C., Fitzsimmons, K. E.,…Petherick, L. (2013). Climate variability over the last 35,000 years recorded in marine and terrestrial archives in the Australian region: an OZ-INTIMATE compilation. Quaternary Science Reviews, 74, 21–34.

Rech, J. A., Currie, B. S., Jordan, T. E., Riquelme, R., Lehmann, S. B., Kirk-Lawlor, N. E.,…Gooley, J. T. (2019). Massive middle Miocene gypsic paleosols in the Atacama Desert and the formation of the Central Andean rain-shadow. Earth and Planetary Science Letters, 506, 184–194.

Reheis, M. C., Reynolds, R. L., Goldstein, H., Roberts, H. M., Yount, J. C., Axford, Y.,…Shearin, N. (2005). Late Quaternary eolian and alluvial response to paleoclimate, Canyonlands, southeastern Utah. Geological Society of America Bulletin, 117(7–8), 1051–1069.

Reimann, T., Tsukamoto, S., Harff, J., Osadczuk, K., & Frechen, M. (2011). Reconstruction of Holocene coastal foredune progradation using luminescence dating—An example from the Świna barrier (southern Baltic Sea, NW Poland). Geomorphology, 132(1–2), 1–16.

Reimer, P. J., Austin, W. E., Bard, E., Bayliss, A., Blackwell, P. G., Ramsey, C. B., ... & Talamo, S. (2020). The IntCal20 Northern Hemisphere radiocarbon age calibration curve (0–55 cal kBP). Radiocarbon, 62(4), 725–757.

Reineck, H.-E., & Singh, I. B. (2012). Depositional sedimentary environments: with reference to terrigenous clastics. Springer Science & Business Media.

Retallack, G. J. (1983). A paleopedological approach to the interpretation of terrestrial sedimentary rocks: The mid-Tertiary fossil soils of Badlands National Park, South Dakota. Geological Society of America Bulletin, 94(7), 823–840.

Retallack, G. J. (1999). Postapocalyptic greenhouse paleoclimate revealed by earliest Triassic paleosols in the Sydney Basin, Australia. Geological Society of America Bulletin, 111(1), 52–70.

Retallack, G. J. (2001). Soils of the Past: An Introduction to Paleopedology (2 ed.). John Wiley & Sons, Incorporated.

Retallack, G. J. (2003). Soils and global change in the carbon cycle over geological time. Treatise on geochemistry, 5, 605.

Retallack, G. J. (2008). Cambrian paleosols and landscapes of South Australia. Australian Journal of Earth Sciences, 55(8), 1083–1106.

Retallack, G. J. (2021a). Paleosols and weathering leading up to Snowball Earth in central Australia. Australian Journal of Earth Sciences, 68(8), 1122–1148.

Retallack, G. J. (2021b). Zebra rock and other Ediacaran paleosols from Western Australia. Australian Journal of Earth Sciences, 68(4), 532–556.

Retallack, G. J., Gose, B. N., & Osterhout, J. T. (2015). Periglacial paleosols and Cryogenian paleoclimate near Adelaide, South Australia. Precambrian Research, 263, 1–18.

Retallack, G. J., Reinhardt, J., & Sigleo, W. (1988). Field recognition of paleosols. Geological Society of America Special Paper, 216, 1–20.

Reuning, L., Reijmer, J. J., Betzler, C., Timmermann, A., & Steph, S. (2006). Sub-Milankovitch cycles in periplatform carbonates from the early Pliocene Great Bahama Bank. Paleoceanography, 21(1), PA1017.

Risbey, J. S., Pook, M. J., McIntosh, P. C., Wheeler, M. C., & Hendon, H. H. (2009). On the remote drivers of rainfall variability in Australia. Monthly Weather Review, 137(10), 3233–3253.

Roberts, R. G., & Jones, R. (1994). Luminescence dating of sediments: new light on the human colonisation of Australia. Australian Aboriginal Studies, 2, 2–17.

Roberts, R. G., Jacobs, Z., Li, B., Jankowski, N. R., Cunningham, A. C., & Rosenfeld, A. B. (2015). Optical dating in archaeology: thirty years in retrospect and grand challenges for the future. Journal of Archaeological Science, 56, 41–60.

Roberts, R. G., Jones, R., & Smith, M. A. (1990). Thermoluminescence dating of a 50,000-year-old human occupation site in northern Australia. Nature, 345(6271), 153–156.

Roberts, R. G., Jones, R., Spooner, N. A., Head, M. J., Murray, A. S., & Smith, M. A. (1994). The human colonisation of Australia: optical dates of 53,000 and 60,000 years bracket human arrival at Deaf Adder Gorge, Northern Territory. Quaternary Science Reviews, 13(5–7), 575–583.

Roberts, R. G., Flannery, T. F., Ayliffe, L. K., Yoshida, H., Olley, J. M., Prideaux, G. J.,…Jones, R. (2001). New ages for the last Australian megafauna: continent-wide extinction about 46,000 years ago. Science, 292(5523), 1888–1892.

Roberts, R. G., Galbraith, R., Yoshida, H., Laslett, G., & Olley, J. M. (2000). Distinguishing dose populations in sediment mixtures: a test of single-grain optical dating procedures using mixtures of laboratory-dosed quartz. Radiation Measurements, 32(5–6), 459–465.

Rodrigo-Gámiz, M., Martínez-Ruiz, F., Rodríguez-Tovar, F. J., Jiménez-Espejo, F. J., & Pardo-Igúzquiza, E. (2014). Millennial-to centennial-scale climate periodicities and forcing mechanisms in the westernmost Mediterranean for the past 20,000 yr. Quaternary Research, 81(1), 78–93.

Rohling, E. J., & Pälike, H. (2005). Centennial-scale climate cooling with a sudden cold event around 8,200 years ago. Nature, 434(7036), 975–979.

Rosen, M. R. (1994). The importance of groundwater in playas: a review of playa classifications and the sedimentology and hydrology of playas. Geological Society of America Special Papers, 289, 1–18.

Rosen, M. R., & Warren, J. K. (1990). The origin and significance of groundwater-seepage gypsum from Bristol Dry Lake, California, USA. Sedimentology, 37(6), 983–996.

Rozanski, K., Araguás-Araguás, L., & Gonfiantini, R. (1993). Isotopic patterns in modern global precipitation. Climate change in continental isotopic records, 78, 1–36.

Rule, S., Brook, B. W., Haberle, S. G., Turney, C. S., Kershaw, A. P., & Johnson, C. N. (2012). The aftermath of megafaunal extinction: ecosystem transformation in Pleistocene Australia. Science, 335(6075), 1483–1486.

Rust, B. R. (1981). Sedimentation in an arid-zone anastomosing fluvial system; Cooper's Creek, central Australia. Journal of Sedimentary Research, 51(3), 745–755.

Rust, B. R., & Nanson, G. C. (1986). Contemporary and palaeo channel patterns and the late Quaternary stratigraphy of Cooper Creek, southwest Queensland, Australia. Earth Surface Processes and Landforms, 11(6), 581–590.

Rust, B. R., & Nanson, G. C. (1989). Bedload transport of mud as pedogenic aggregates in modern and ancient rivers. Sedimentology, 36(2), 291–306.

Saji, N., Goswami, B. N., Vinayachandran, P., & Yamagata, T. (1999). A dipole mode in the tropical Indian Ocean. Nature, 401(6751), 360–363.

Sallenger Jr, A. H. (2000). Storm impact scale for barrier islands. Journal of coastal research, 16, 890–895.

Saltré, F., Rodríguez-Rey, M., Brook, B. W., Johnson, C. N., Turney, C. S., Alroy, J., ... & Bradshaw, C. J. (2016). Climate change not to blame for late Quaternary megafauna extinctions in Australia. Nature communications, 7(1), 10511.

Saltré, F., Chadoeuf, J., Peters, K. J., McDowell, M. C., Friedrich, T., Timmermann, A., ... & Bradshaw, C. J. (2019). Climate-human interaction associated with southeast Australian megafauna extinction patterns. Nature Communications, 10(1), 5311.

Sánchez Goñi, M., Cacho, I., Turon, J.-L., Guiot, J., Sierro, F., Peypouquet, J.,…Shackleton, N. (2002). Synchroneity between marine and terrestrial responses to millennial scale climatic variability during the last glacial period in the Mediterranean region. Climate Dynamics, 19, 95–105.

Sarjeant, W. A. S. (1975). Plant trace fossils. In The Study of Trace Fossils: a Synthesis of Principles, Problems, and Procedures in Ichnology. Springer, 163–179.

Scafetta, N. (2012). Multi-scale harmonic model for solar and climate cyclical variation throughout the Holocene based on Jupiter–Saturn tidal frequencies plus the 11-year solar dynamo cycle. Journal of Atmospheric and Solar-Terrestrial Physics, 80, 296–311.

Scafetta, N., Milani, F., Bianchini, A., & Ortolani, S. (2016). On the astronomical origin of the Hallstatt oscillation found in radiocarbon and climate records throughout the Holocene. Earth-Science Reviews, 162, 24–43.

Scanlon, T. M., Caylor, K. K., Levin, S. A., & Rodriguez-Iturbe, I. (2007). Positive feedbacks promote power-law clustering of Kalahari vegetation. Nature, 449(7159), 209–212.

Schefuß, E., Kuhlmann, H., Mollenhauer, G., Prange, M., & Pätzold, J. (2011). Forcing of wet phases in southeast Africa over the past 17,000 years. Nature, 480(7378), 509–512.

Schulz, M. (2002). On the 1470-year pacing of Dansgaard-Oeschger warm events. Paleoceanography, 17(2), 1014.

Schwartz, R. K. (1982). Bedform and stratification characteristics of some modern small-scale washover sand bodies. Sedimentology, 29(6), 835–849.

Shaw, J., You, Y., Mohrig, D., & Kocurek, G. (2015). Tracking hurricane-generated storm surge with washover fan stratigraphy. Geology, 43(2), 127–130.

Shen, C., Wang, W. C., Gong, W., & Hao, Z. (2006). A Pacific Decadal Oscillation record since 1470 AD reconstructed from proxy data of summer rainfall over eastern China. Geophysical Research Letters, 33(3), L03702.

Shen, L., Wang, L., Liu, C., & Zhao, Y. (2021). Sr, S, and O Isotope Compositions of Evaporites in the Lanping–Simao Basin, China. Minerals, 11(2), 96.

Sheldon, N. D., & Tabor, N. J. (2009). Quantitative paleoenvironmental and paleoclimatic reconstruction using paleosols. Earth-Science Reviews, 95(1–2), 1–52.

Sheldon, N. D., Retallack, G. J., & Tanaka, S. (2002). Geochemical climofunctions from North American soils and application to paleosols across the Eocene-Oligocene boundary in Oregon. The Journal of Geology, 110(6), 687–696.

Shiau, L. J., Chen, M. T., Huh, C. A., Yamamoto, M., & Yokoyama, Y. (2012). Insolation and cross-hemispheric controls on Australian monsoon variability over the past 180 ka: New evidence from offshore southeastern Papua New Guinea. Journal of Quaternary Science, 27(9), 911–920.

Shulmeister, J. (1992). A Holocene pollen record from lowland tropical Australia. The Holocene, 2(2), 107–116.

Shulmeister, J., & Lees, B. G. (1995). Pollen evidence from tropical Australia for the onset of an ENSO-dominated climate at c. 4000 BP. The Holocene, 5(1), 10–18.

Shulmeister, J., Goodwin, I., Renwick, J., Harle, K., Armand, L., McGlone, M.,…Mayewski, P. (2004). The Southern Hemisphere westerlies in the Australasian sector over the last glacial cycle: a synthesis. Quaternary International, 118, 23–53.

Shulmeister, J., Kemp, J., Fitzsimmons, K. E., & Gontz, A. (2016). Constant wind regimes during the Last Glacial Maximum and early Holocene: evidence from Little Llangothlin Lagoon, New England Tablelands, eastern Australia. Climate of the Past, 12(7), 1435–1444.

Singarayer, J. S., Valdes, P. J., & Roberts, W. H. (2017). Ocean dominated expansion and contraction of the late Quaternary tropical rainbelt. Scientific reports, 7(1), 9382.

Singh, G., & Luly, J. (1991). Changes in vegetation and seasonal climate since the last full glacial at Lake Frome, South Australia. Palaeogeography, Palaeoclimatology, Palaeoecology, 84(1–4), 75–86.

Singh, G., Opdyke, N., & Bowler, J. (1981). Late Cainozoic stratigraphy, palaeomagnetic chronology and vegetational history from Lake George, NSW. Journal of the Geological Society of Australia, 28(3–4), 435–452.

Singh, K. V., Setia, R., Sahoo, S., Prasad, A., & Pateriya, B. (2015). Evaluation of NDWI and MNDWI for assessment of waterlogging by integrating digital elevation model and groundwater level. Geocarto International, 30(6), 650–661.

Sinnesael, M., De Vleeschouwer, D., Zeeden, C., Batenburg, S. J., Da Silva, A.-C., de Winter, N. J.,…Hilgen, F. J. (2019). The Cyclostratigraphy Intercomparison Project (CIP): consistency, merits and pitfalls. Earth-Science Reviews, 199, 102965.

Sirocko, F., Garbe-Schönberg, D., McIntyre, A., & Molfino, B. (1996). Teleconnections between the subtropical monsoons and high-latitude climates during the last deglaciation. Science, 272(5261), 526–529.

Skilbeck, C. G., Rolph, T. C., Hill, N., Woods, J., & Wilkens, R. H. (2005). Holocene millennial/centennial-scale multiproxy cyclicity in temperate eastern Australian estuary sediments. Journal of Quaternary Science: Published for the Quaternary Research Association, 20(4), 327–347.

Snoeckx, H., Grousset, F., Revel, M., & Boelaert, A. (1999). European contribution of ice-rafted sand to Heinrich layers H3 and H4. Marine Geology, 158(1–4), 197–208.

Smith, B. N., & Epstein, S. (1971). Two categories of 13C/12C ratios for higher plants. Plant physiology, 47(3), 380–384.

Song, M. (2005). Sedimentary environment geochemistry in the Shasi section of southern ramp, Dongying depression. Journal of Mineralogy and Petrology, 25(1), 67–73.

Spinoni, J., Vogt, J., Naumann, G., Carrao, H., & Barbosa, P. (2015). Towards identifying areas at climatological risk of desertification using the Köppen-Geiger classification and FAO aridity index. International journal of climatology, 35(9), 2210–2222.

Stager, J. C., Ryves, D. B., Chase, B. M., & Pausata, F. S. (2011). Catastrophic drought in the Afro-Asian monsoon region during Heinrich event 1. Science, 331(6022), 1299–1302.

Stanistreet, I. G., Boyle, J. F., Stollhofen, H., Deocampo, D. M., Deino, A., McHenry, L. J.,…Njau, J. K. (2020). Palaeosalinity and palaeoclimatic geochemical proxies (elements Ti, Mg, Al) vary with Milankovitch cyclicity (1.3 to 2.0 Ma), OGCP cores, Palaeolake Olduvai, Tanzania. Palaeogeography, Palaeoclimatology, Palaeoecology, 546, 109656.

Stein, J. L., Hutchinson, M. F., & Stein, J. A. (2011). National Drainage Basins v1.1.3. Geoscience Australia, Canberra. http://pid.geoscience.gov.au/dataset/ga/73079.

Steinhilber, F., Abreu, J. A., Beer, J., Brunner, I., Christl, M., Fischer, H.,…McCracken, K. G. (2012). 9,400 years of cosmic radiation and solar activity from ice cores and tree rings. Proceedings of the National Academy of Sciences, 109(16), 5967–5971.

Stern, J. V., & Lisiecki, L. E. (2014). Termination 1 timing in radiocarbon-dated regional benthic δ18O stacks. Paleoceanography, 29(12), 1127–1142.

Stirling, C., Esat, T., Lambeck, K., & McCulloch, M. (1998). Timing and duration of the Last Interglacial: evidence for a restricted interval of widespread coral reef growth. Earth and Planetary Science Letters, 160(3–4), 745–762.

Stirling, C., Esat, T., McCulloch, M., & Lambeck, K. (1995). High-precision U-series dating of corals from Western Australia and implications for the timing and duration of the Last Interglacial. Earth and Planetary Science Letters, 135(1–4), 115–130.

Stoops, G., Marcelino, V., & Mees, F. (2018). Interpretation of micromorphological features of soils and regoliths. Elsevier.

Stuiver, M., & Polach, H. A. (1977). Discussion reporting of 14C data. Radiocarbon, 19(3), 355–363.

Stuut, J.-B. W., De Deckker, P., Saavedra-Pellitero, M., Bassinot, F., Drury, A. J., Walczak, M. H.,…Murayama, M. (2019). A 5.3-Million-Year History of Monsoonal Precipitation in Northwestern Australia. Geophysical Research Letters, 46(12), 6946–6954.

Stuut, J.-B. W., Temmesfeld, F., & De Deckker, P. (2014). A 550 ka record of aeolian activity near North West Cape, Australia: inferences from grain-size distributions and bulk chemistry of SE Indian Ocean deep-sea sediments. Quaternary Science Reviews, 83, 83–94.

Summons, R. E., Jahnke, L. L., & Roksandic, Z. (1994). Carbon isotopic fractionation in lipids from methanotrophic bacteria: relevance for interpretation of the geochemical record of biomarkers. Geochimica Et Cosmochimica Acta, 58(13), 2853–2863.

Suppiah, R., & Hennessy, K. J. (1998). Trends in total rainfall, heavy rain events and number of dry days in Australia, 1910–1990. International Journal of Climatology: A Journal of the Royal Meteorological Society, 18(10), 1141–1164.

Swan, A., Hartley, A. J., Owen, A., & Howell, J. (2018). Reconstruction of a sandy point-bar deposit: implications for fluvial facies analysis. Fluvial Meanders and Their Sedimentary Products in the Rock Record, 445–474.

Tabor, N. J., & Myers, T. S. (2015). Paleosols as indicators of paleoenvironment and paleoclimate. Annual Review of Earth and Planetary Sciences, 43, 333–361.

Tachikawa, K., Cartapanis, O., Vidal, L., Beaufort, L., Barlyaeva, T., & Bard, E. (2011). The precession phase of hydrological variability in the Western Pacific Warm Pool during the past 400 ka. Quaternary Science Reviews, 30(25–26), 3716–3727.

Takahashi, G. (2015). Sample preparation for X-ray fluorescence analysis. Rigaku Journal, 31(1), 26–30.

Tankard, A. J., & Hobday, D. K. (1977). Tide-dominated back-barrier sedimentation, early Ordovician Cape Basin, Cape Peninsula, South Africa. Sedimentary Geology, 18(1–3), 135–159.

Tanner, W. F. (1967). Ripple mark indices and their uses. Sedimentology, 9(2), 89–104.

Taschetto, A. S., & England, M. H. (2009). An analysis of late twentieth century trends in Australian rainfall. International Journal of Climatology: A Journal of the Royal Meteorological Society, 29(6), 791–807.

Tedford, R. H., & Wells, R. (1990). Pleistocene deposits and fossil vertebrates from the "Dead Heart of Australia". Memoirs of the Queensland Museum, 28(1), 263–284.

Telfer, M., Gholami, H., Hesse, P., Fisher, A., & Hartley, R. (2020). Testing models of linear dune formation by provenance analysis with composite sediment fingerprints. Geomorphology, 364, 107208.

Telfer, M. W. (2011). Growth by extension, and reworking, of a south-western Kalahari linear dune. Earth Surface Processes and Landforms, 36(8), 1125–1135.

Teranes, J. L., & Bernasconi, S. M. (2005). Factors controlling δ13C values of sedimentary carbon in hypertrophic Baldeggersee, Switzerland, and implications for interpreting isotope excursions in lake sedimentary records. Limnology and Oceanography, 50(3), 914–922.

Thode, H., & Monster, J. (1965). Sulfur-isotope geochemistry of petroleum, evaporites, and ancient seas.

Thompson, W. G., & Goldstein, S. L. (2005). Open-system coral ages reveal persistent suborbital sea-level cycles. Science, 308(5720), 401–404.

Tobler, R., Rohrlach, A., Soubrier, J., Bover, P., Llamas, B., Tuke, J.,…O'Donoghue, A. (2017). Aboriginal mitogenomes reveal 50,000 years of regionalism in Australia. Nature, 544(7649), 180–184.

Toggweiler, J. R., Russell, J. L., & Carson, S. R. (2006). Midlatitude westerlies, atmospheric $CO_2$, and climate change during the ice ages. Paleoceanography, 21(2), PA2005.

Treble, P., Baker, A., Ayliffe, L. K., Cohen, T. J., Hellstrom, J. C., Gagan, M. K.,…Borsato, A. (2017). Hydroclimate of the Last Glacial Maximum and deglaciation in southern Australia's arid margin interpreted from speleothem records (23–15 ka). Climate of the Past, 13(6), 667–687.

Tsai, W. Y.-H., Lu, M.-M., Sui, C.-H., & Cho, Y.-M. (2021). Subseasonal forecasts of the northern Queensland floods of February 2019: Causes and forecast evaluation. Atmosphere, 12(6), 758.

Tunbridge, I. P. (1981). Sandy high-energy flood sedimentation — some criteria for recognition, with an example from the Devonian of SW England. Sedimentary Geology, 28(2), 79–95.

Turney, C. S., Bird, M. I., Fifield, L. K., Roberts, R. G., Smith, M., Dortch, C. E.,…Miller, G. H. (2001). Early human occupation at Devil's Lair, southwestern Australia 50,000 years ago. Quaternary Research, 55(1), 3–13.

Turney, C. S., Flannery, T. F., Roberts, R. G., Reid, C., Fifield, L. K., Higham, T. F.,…Kalin, R. M. (2008). Late-surviving megafauna in Tasmania, Australia, implicate human involvement in their extinction. Proceedings of the National Academy of Sciences, 105(34), 12150–12153.

Turney, C. S., Kershaw, A. P., Clemens, S. C., Branch, N., Moss, P. T., & Fifield, L. K. (2004). Millennial and orbital variations of El Nino/Southern Oscillation and high-latitude climate in the last glacial period. Nature, 428(6980), 306.

Twidale, C., Prescott, J., Bourne, J., & Williams, F. (2001). Age of desert dunes near Birdsville, southwest Queensland. Quaternary Science Reviews, 20(12), 1355–1364.

Ummenhofer, C. C., England, M. H., McIntosh, P. C., Meyers, G. A., Pook, M. J., Risbey, J. S.,…Taschetto, A. S. (2009). What causes southeast Australia's worst droughts? Geophysical Research Letters, 36(4).

USEPA. (2007). Field portable X-ray fluorescence spectrometry for the determination of elemental concentrations in soil and sediment. United States Environmental Protection Agency: Washington, DC.

Usoskin, I., Gallet, Y., Lopes, F., Kovaltsov, G., & Hulot, G. (2016). Solar activity during the Holocene: the Hallstatt cycle and its consequence for grand minima and maxima. Astronomy & Astrophysics, 587, A150.

Usoskin, I. G., Solanki, S. K., Krivova, N. A., Hofer, B., Kovaltsov, G. A., Wacker, L.,…Kromer, B. (2021). Solar cyclic activity over the last millennium reconstructed from annual 14C data. Astronomy & Astrophysics, 649, A141.

Valero-Garces, B. L., Delgado-Huertas, A., Navas, A., MachÍn, J., GonzÁlez-SampÉriz, P., & Kelts, K. (2000). Quaternary palaeohydrological evolution of a playa lake: Salada Mediana, central Ebro Basin, Spain. Sedimentology, 47(6), 1135–1156.

Van der Kaars, S., De Deckker, P., & Gingele, F. X. (2006). A 100 000-year record of annual and seasonal rainfall and temperature for northwestern Australia based on a pollen record obtained offshore. Journal of Quaternary Science: Published for the Quaternary Research Association, 21(8), 879–889.

Van Kreveld, S. A., Knappertsbusch, M., Ottens, J., Ganssen, G. M., & van Hinte, J. E. (1996). Biogenic carbonate and ice-rafted debris (Heinrich layer) accumulation in deep-sea sediments from a Northeast Atlantic piston core. Marine Geology, 131(1–2), 21–46.

Van Kreveld, S. A., Sarnthein, M., Erlenkeuser, H., Grootes, P., Jung, S., Nadeau, M.,…Voelker, A. (2000). Potential links between surging ice sheets, circulation changes, and the Dansgaard-Oeschger cycles in the Irminger Sea, 60–18 kyr. Paleoceanography, 15(4), 425–442.

Vance, T., Roberts, J., Plummer, C., Kiem, A., & Van Ommen, T. (2015). Interdecadal Pacific variability and eastern Australian megadroughts over the last millennium. Geophysical Research Letters, 42(1), 129–137.

Vance, T. R., Kiem, A. S., Jong, L. M., Roberts, J. L., Plummer, C. T., Moy, A. D.,…van Ommen, T. D. (2022). Pacific decadal variability over the last 2000 years and implications for climatic risk. Communications Earth & Environment, 3(1), 1–9.

Veevers, J., & Rundle, A. (1979). Channel Country fluvial sands and associated facies of central-eastern Australia: modern analogues of Mesozoic desert sands of South America. Palaeogeography, Palaeoclimatology, Palaeoecology, 26, 1–16.

Verdon, D. C., Wyatt, A. M., Kiem, A. S., & Franks, S. W. (2004). Multidecadal variability of rainfall and streamflow: Eastern Australia. Water Resources Research, 40(10), W10201.

Verschuren, D., Sinninghe Damsté, J. S., Moernaut, J., Kristen, I., Blaauw, M., Fagot, M., & Haug, G. H. (2009). Half-precessional dynamics of monsoon rainfall near the East African Equator. Nature, 462(7273), 637–641.

Veth, P., Ditchfield, K., & Hook, F. (2014). Maritime deserts of the Australian northwest. Australian Archaeology, 79(1), 156–166.

Veth, P., Ward, I., Manne, T., Ulm, S., Ditchfield, K., Dortch, J.,…Questiaux, D. (2017). Early human occupation of a maritime desert, Barrow Island, North-West Australia. Quaternary Science Reviews, 168, 19–29.

Vieira, L., Norton, A., Dudok de Wit, T., Kretzschmar, M., Schmidt, G., & Cheung, M. (2012). How the inclination of Earth's orbit affects incoming solar irradiance. Geophysical Research Letters, 39(16), L16104.

Wakshal, E., & Nielsen, H. (1982). Variations of δ34S (SO4), δ18O (H2O) and Cl/SO4 ratio in rainwater over northern Israel, from the Mediterranean Coast to Jordan Rift Valley and Golan Heights. Earth and Planetary Science Letters, 61(2), 272–282.

Wang, H., Follmer, L. R., & Liu, J. C.-l. (2000). Isotope evidence of paleo–El Niño–Southern Oscillation cycles in loess-paleosol record in the central United States. Geology, 28(9), 771–774.

Wang, X., Auler, A. S., Edwards, R., Cheng, H., Ito, E., Wang, Y.,…Solheid, M. (2007). Millennial-scale precipitation changes in southern Brazil over the past 90,000 years. Geophysical Research Letters, 34(23), L23701.

Wang, Y.-J., Cheng, H., Edwards, R. L., An, Z., Wu, J., Shen, C.-C., & Dorale, J. A. (2001). A high-resolution absolute-dated late Pleistocene monsoon record from Hulu Cave, China. Science, 294(5550), 2345–2348.

Wang, Y., Cheng, H., Edwards, R. L., Kong, X., Shao, X., Chen, S.,…An, Z. (2008). Millennial-and orbital-scale changes in the East Asian monsoon over the past 224,000 years. Nature, 451(7182), 1090–1093.

Wardle, R., & Smith, I. (2004). Modeled response of the Australian monsoon to changes in land surface temperatures. Geophysical Research Letters, 31(16), L16205.

Wasson, R. J. (1983a). Dune sediment types, sand colour, sediment provenance and hydrology in the Strzelecki-Simpson dunefield, Australia. In Developments in Sedimentology (Vol. 38). Elsevier, 165–195.

Wasson, R. J. (1983b). The Cainozoic history of the Strzelecki and Simpson dunefields (Australia), and the origin of the desert dunes. Zeitschrift für Geomorphologie Supplementband, 45, 85–115.

Wasson, R. J. (1986). Geomorphology and Quaternary history of the Australian continental dunefields. Geographical review of Japan, Series B., 59(1), 55–67.

Wasson, R. J., Fitchett, K., Mackey, B., & Hyde, R. (1988). Large-Scale Patterns of Dune Type, Spacing and Orientation in the Australian Continental Dunefield. Australian Geographer, 19(1), 89–104.

Wende, R., Nanson, G., & Price, D. (1997). Aeolian and fluvial evidence for Late Quaternary environmental change in the east Kimberley of Western Australia. Australian Journal of Earth Sciences, 44(4), 519–526.

Westerhold, T., Bickert, T., & Röhl, U. (2005). Middle to late Miocene oxygen isotope stratigraphy of ODP site 1085 (SE Atlantic): new constrains on Miocene climate variability and sea-level fluctuations. Palaeogeography, Palaeoclimatology, Palaeoecology, 217(3–4), 205–222.

Whalley, W. R., Dumitru, E., & Dexter, A. (1995). Biological effects of soil compaction. Soil and Tillage research, 35(1–2), 53–68.

Wheeler, M. C., Hendon, H. H., Cleland, S., Meinke, H., & Donald, A. (2009). Impacts of the Madden–Julian oscillation on Australian rainfall and circulation. Journal of Climate, 22(6), 1482–1498.

Whiticar, M. J. (1999). Carbon and hydrogen isotope systematics of bacterial formation and oxidation of methane. Chemical Geology, 161(1–3), 291–314.

Williams, M. A., Spooner, N. A., McDonnell, K., & O'Connell, J. F. (2021). Identifying disturbance in archaeological sites in tropical northern Australia: Implications for previously proposed 65,000-year continental occupation date. Geoarchaeology, 36(1), 92–108.

Williams, A. N., Veth, P., Steffen, W., Ulm, S., Turney, C. S., Reeves, J. M., ... & Smith, M. (2015). A continental narrative: Human settlement patterns and Australian climate change over the last 35,000 years. Quaternary Science Reviews, 123, 91–112.

Wopfner, H., & Twidale, C. (2001). Australian desert dunes: wind rift or depositional origin? Australian Journal of Earth Sciences, 48(2), 239–244.

Wroe, S., & Field, J. (2006). A review of the evidence for a human role in the extinction of Australian megafauna and an alternative interpretation. Quaternary Science Reviews, 25(21–22), 2692–2703.

Wu, C. H., Lee, S. Y., Chiang, J. C., & Hsu, H. H. (2016). The influence of obliquity in the early Holocene Asian summer monsoon. Geophysical Research Letters, 43(9), 4524–4530.

Wyrwoll, K.-H., Liu, Z., Chen, G., Kutzbach, J. E., & Liu, X. (2007). Sensitivity of the Australian summer monsoon to tilt and precession forcing. Quaternary Science Reviews, 26(25–28), 3043–3057.

Wyrwoll, K. H., & Valdes, P. (2003). Insolation forcing of the Australian monsoon as controls of Pleistocene mega-lake events. Geophysical Research Letters, 30(24), 2279.

Xu, H. (2006). Modification of normalised difference water index (NDWI) to enhance open water features in remotely sensed imagery. International journal of remote sensing, 27(14), 3025–3033.

Yim, W.-S., Huang, G., Fontugne, M., Hale, R., Paterne, M., Pirazzoli, P., & Thomas, W. R. (2006). Postglacial sea-level changes in the northern South China Sea continental shelf: evidence for a post-8200 calendar yr BP meltwater pulse. Quaternary International, 145, 55–67.

Yizhaq, H., Ashkenazy, Y., & Tsoar, H. (2009). Sand dune dynamics and climate change: A modeling approach. Journal of Geophysical Research: Earth Surface, 114, F01023.

Yoo, S. H., Yang, S., & Ho, C. H. (2006). Variability of the Indian Ocean sea surface temperature and its impacts on Asian-Australian monsoon climate. Journal of Geophysical Research: Atmospheres, 111, D03108.

Yndestad, H. (2022). Jovian planets and lunar nodal cycles in the Earth's climate variability. Frontiers in Astronomy and Space Sciences, 9, 839794.

Zhang, R., Li, X., Xu, Y., Li, J., Sun, L., Yue, L.,…Cao, Y. (2022). The 173-kyr Obliquity Cycle Pacing the Asian Monsoon in the Eastern Chinese Loess Plateau From Late Miocene to Pliocene. Geophysical Research Letters, 49(2), e2021GL097008.

Zhao, L., Hong, H., Fang, Q., Hei, H., & Algeo, T. J. (2023). Hydrologic regulation of clay-mineral transformations in a redoximorphic soil of subtropical monsoonal China. American Mineralogist, 108(10), 1881–1896.

Zhiyao, S., Tingting, W., Fumin, X., & Ruijie, L. (2008). A simple formula for predicting settling velocity of sediment particles. Water Science and Engineering, 1(1), 37–43.

Zhou, Y., Retallack, G. J., & Huang, C. (2015). Early Eocene paleosol developed from basalt in southeastern Australia: implications for paleoclimate. Arabian Journal of Geosciences, 8, 1281–1290.

Zou, C., Mao, L., Tan, Z., Zhou, L., & Liu, L. (2021). Geochemistry of major and trace elements in sediments from the Lubei Plain, China: Constraints for paleoclimate, paleosalinity, and paleoredox environment. Journal of Asian Earth Sciences: X, 6(1), 100071.

Zuraida, R., Holbourn, A., Nürnberg, D., Kuhnt, W., Dürkop, A., & Erichsen, A. (2009). Evidence for Indonesian Throughflow slowdown during Heinrich events 3–5. Paleoceanography, 24(2), PA2205.

# Appendix A

## A1 Supplemental Figures

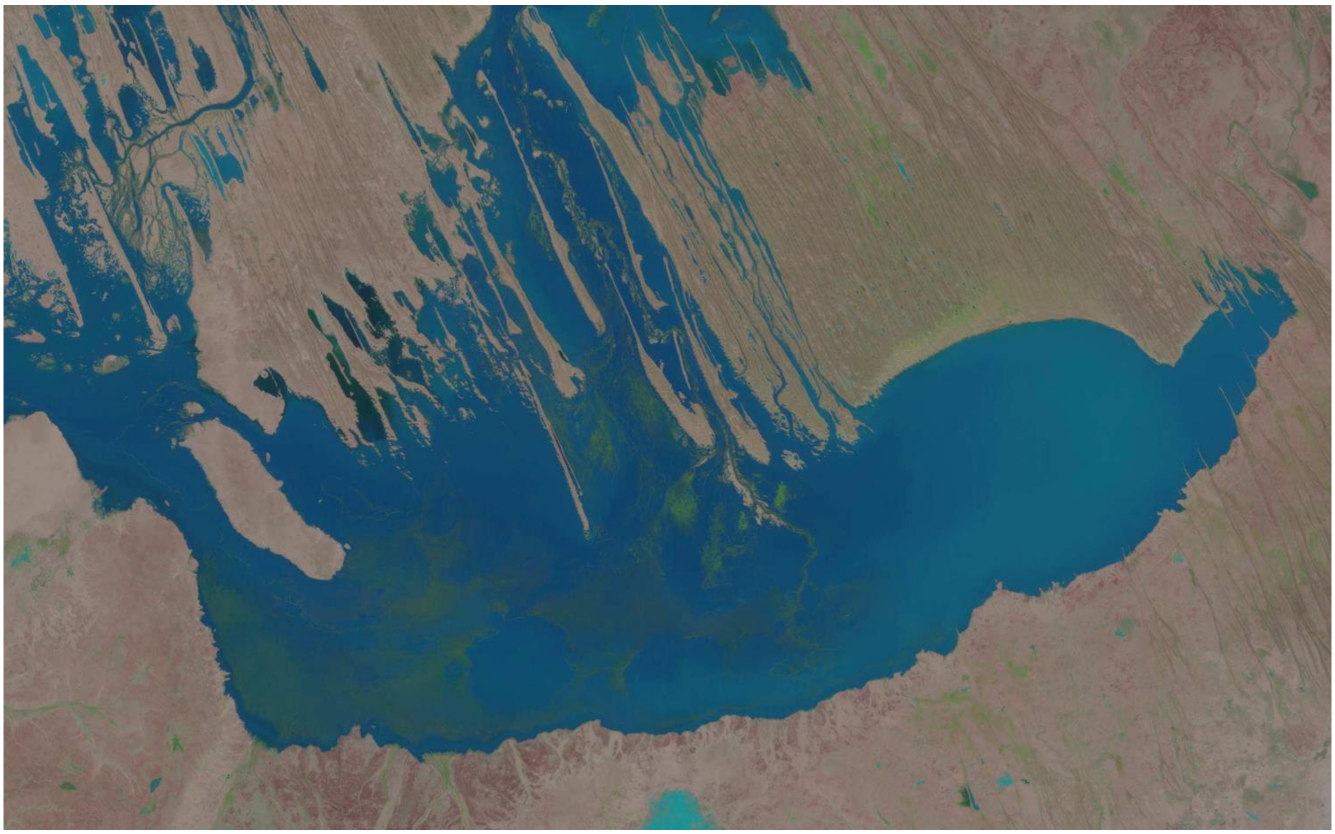

**Figure S1.** Lake Machattie Area in full flood. Landsat image 30/03/1997. Downloaded from the United States Geological Survey Global Visualization Viewer (GloVis, 2023).

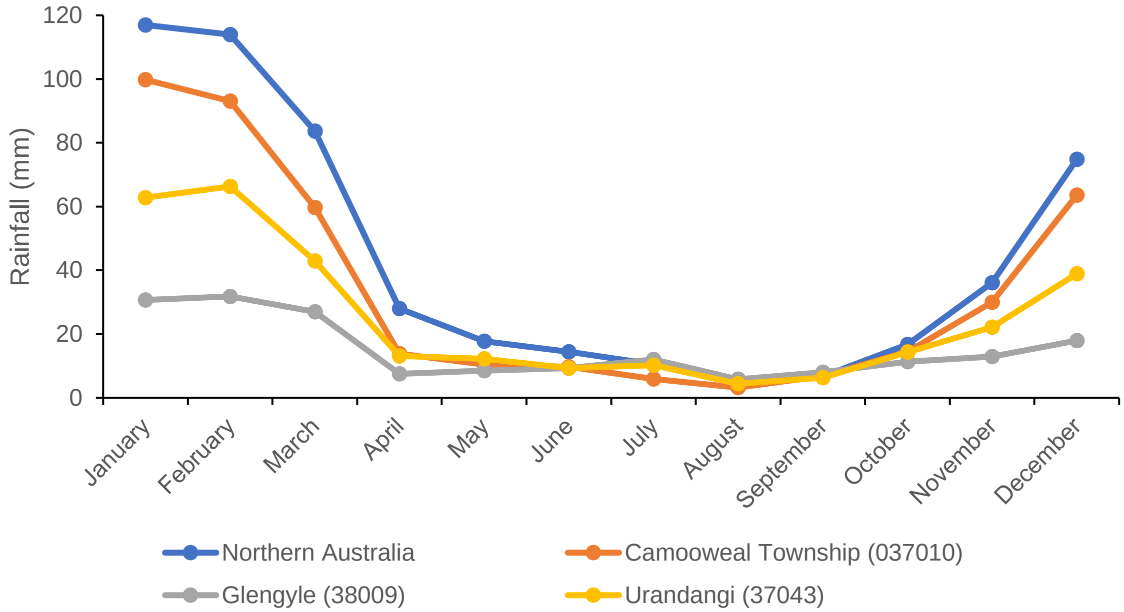


**Figure S2**. Mean monthly rainfall for northern Australia (1951 – 2024) and Georgina catchment weather stations in the northern (Camooweal Township; 19.92°S, 138.12°E; 1891-2024), central (Urandangi; 21.61°S, 138.31°E; 1891-2012) and southern (Glengyle; 24.79°S, 139.59°E; 1914-2024) regions (BOM, 2024a). Station ID numbers in parentheses. For map locations, refer to Chapter 2, Figure 2.1a.

**<u>Lake Machattie – Single grain OSL radial plots</u>**

**LMA50**

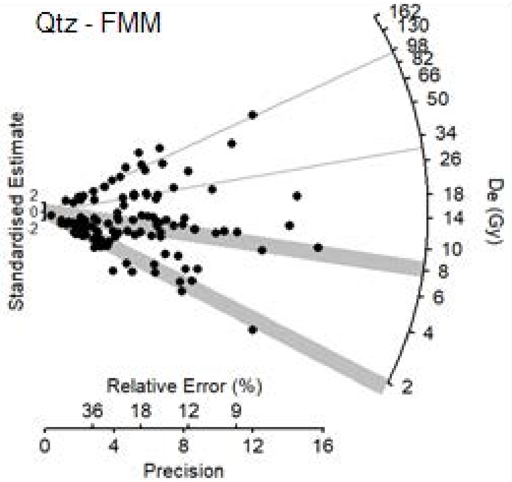


**LMB90**

KF – nMAD CAM

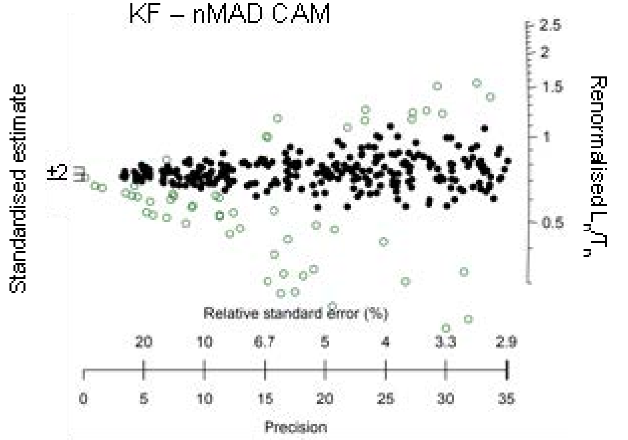


**LMB110**

KF – nMAD CAM

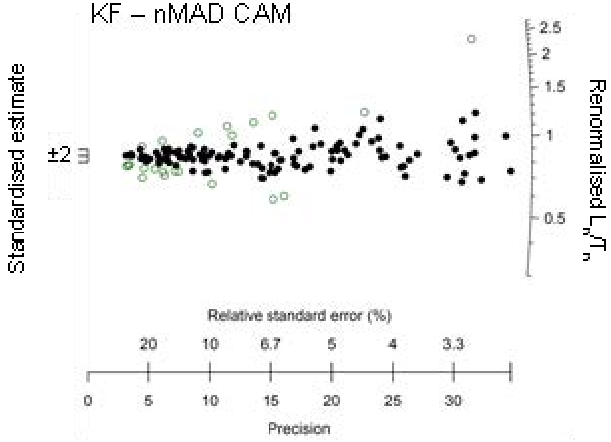


**LMB155**

KF – nMAD CAM

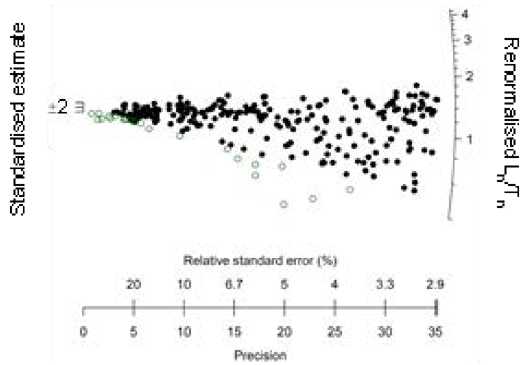


**LMC270**

KF – nMAD CAM

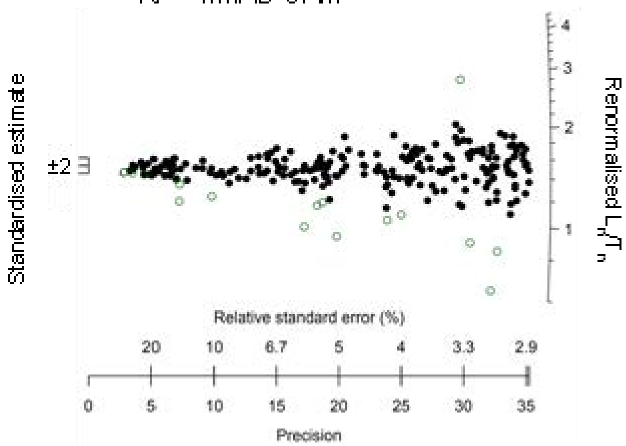

**Lake Koolivoo – Single grain OSL radial plots**

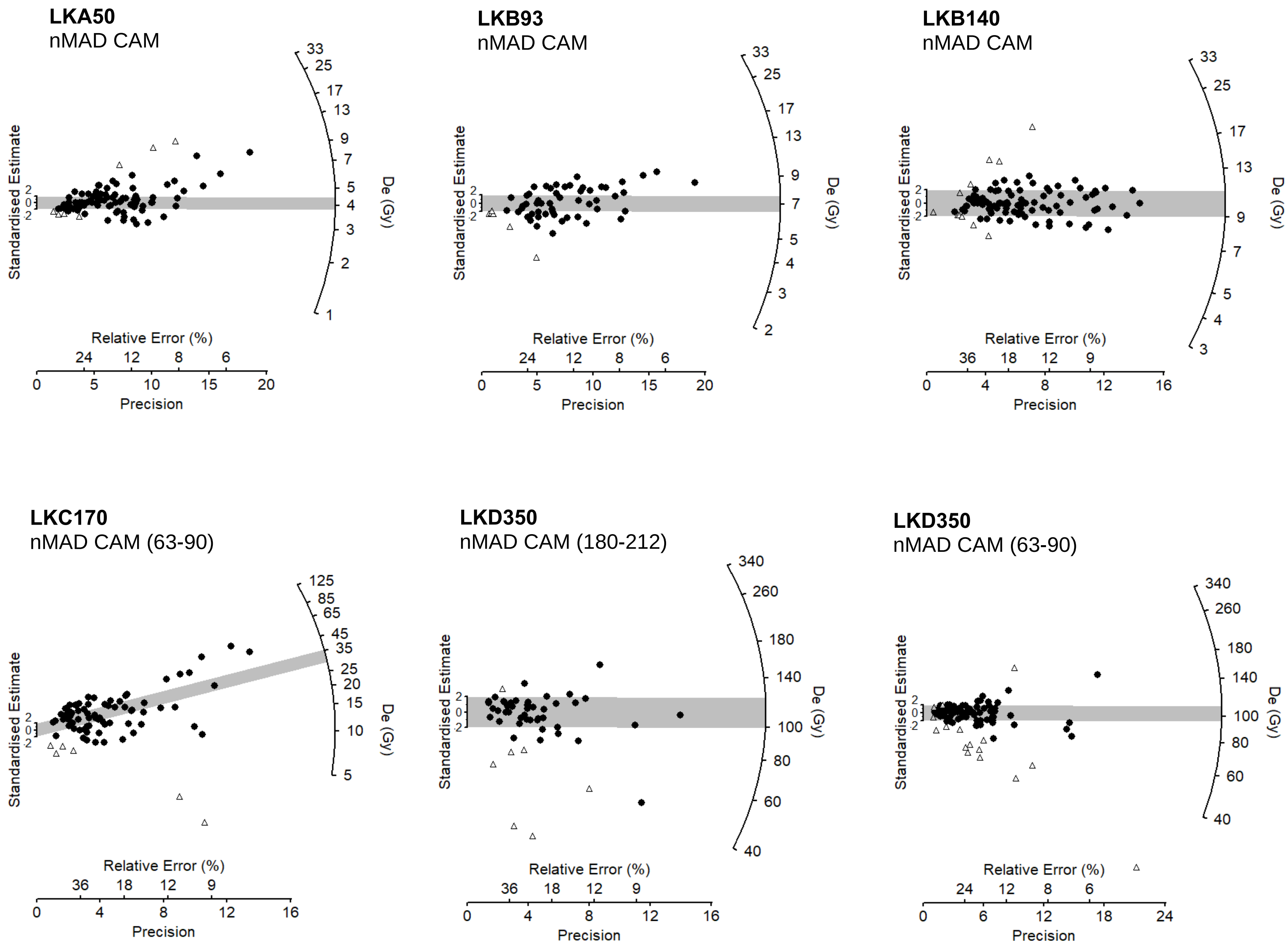

## Eyre Creek – Single grain OSL radial plots

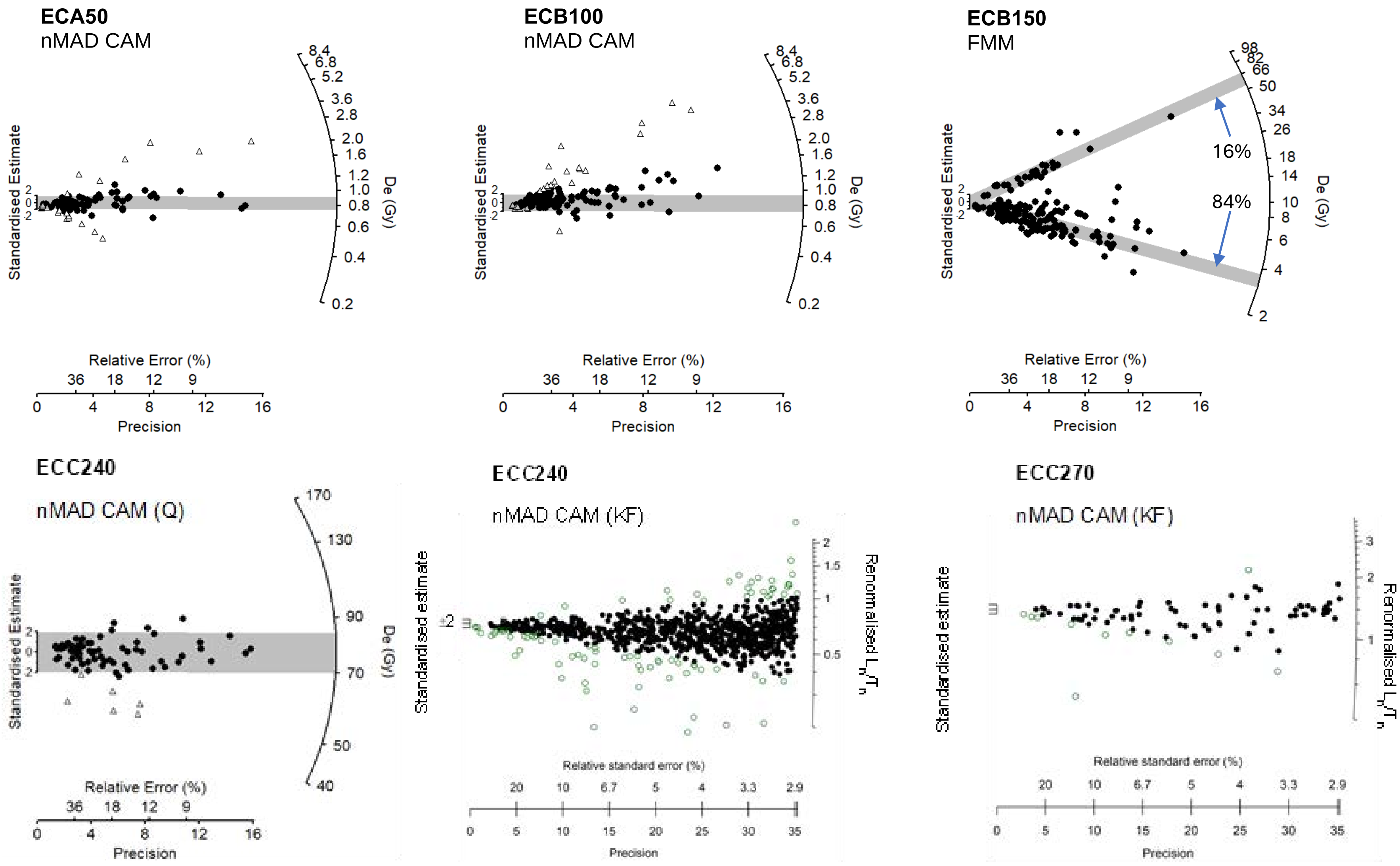

**Figure S3**. Radial plots of single-grain $D_e$ distributions for core samples collected from Lake Machattie, Lake Koolivoo and Eyre Creek. OSL ages for most samples were estimated using the central age model (CAM) after identifying statistical outliers (shown as open triangles or circles in the radial plots) using the normalised median absolute deviation (nMAD) method. The finite mixture model (FMM) was used for samples LMA50 and ECB150 that clearly contain discrete dose components. The grey bands are centred on the FMM or CAM weighted mean De values for each dose population. Quartz (Q) grains were tested using the conventional single-aliquot regenerative-dose (SAR) method and, where possible, sensitivity corrected natural signals (Ln/Tn) were used on quartz and K-feldspar (KF) grains to test whether distributions may be truncated.

## A2 Supplemental Tables

**Table S1.** Location of marine sediment cores and speleothem records (outside of Australia) referred to in text with GPS coordinates.

| Location | Marine core ID# | Lat | Long | Reference |
|---|---|---|---|---|
| Liang Luar Cave, Flores Indonesia | - | 8.5333°S | 120.4333°E | (Griffiths et al., 2009) |
| Indian Ocean, Aust | Fr10/95-17 | 22.0456°S | 113.5018°E | (Van der Kaars et al., 2006) |
| Southern Ocean, Aust | MD03-2607 | 36.9666°S | 137.4108°E | (De Deckker et al., 2019) |
| Coral Sea, Aust | ODP site 820 Leg 133 | 16.63°S | 146.3°E | (Moss and Kershaw, 2000) |
| Bismarck Sea, PNG | MD05-2920 | 2.8633°S | 144.5344°E | (Tachikawa et al., 2011) |
| Bismarck Sea, PNG | KX12-1 (KX08-973121) | 1.8135°S | 143.6683°E | (Liang and Liu, 2018) |
| Coral Sea, PNG | MD052928 | 11.2876°S | 148.86°E | (Shiau et al., 2012) |
| Alboran Sea, western Mediterranean | MD95-2043 | 36.1433°N | 2.6216°W | (Sánchez Goñi et al., 2002)<br>(Cacho et al., 1999)<br>(Moreno et al., 2002)<br>(Moreno et al., 2005) |
| Southern Indian Ocean | MD73025 | 43.8166°S | 51.2666°E | (Pestiaux et al., 1988) |
| Arabian Sea, northern Indian Ocean | 74KL | ~19.50°N | ~65.00°E | (Sirocko et al., 1996) |
| Sulu Sea, Borneo | MD972141 | 8.7833°N | 121.2833°E | (de Garidel-Thoron et al., 2001) |

**Table S2**. Results of single-grain OSL analysis for cores Lake Machattie (LM), Lake Koolivoo (LK) and Eyre Creek (EC).

| Sample | Grain size | Water (%)[a] | External dose rate (Gy/ka)[b] Beta | Gamma | Cosmic | Internal dose rate (Gy/ka)[c] | Total | Grains[d] | De (Gy)[e] | Method (mineral)[f] | Model | OD (%)[g] | Age (ka)[h] |
|---|---|---|---|---|---|---|---|---|---|---|---|---|---|
| Lake Machattie | | | | | | | | | | | | | |
| LMA50 | 180-212 | 25 ±6 (22) | 0.67 ±0.04 | 0.49 ±0.03 | 0.184 | | 1.37 ±0.06 | 115 | 1.87 ±0.17 | SAR (Q) | FMM-1(39%) | 141 ±10 (34) | **1.37 ±0.14** |
| | | | | | | | | | 8.1 ±0.7 | | FMM-2(35%) | | **5.9 ±0.6** |
| | | | | | | | | | 94.6 ±11.6 | | FMM-3(22%) | | **69.0 ±9.1** |
| | | | | | | | | | 29.8 ±4.4 | | FMM-3(22%) | | **21.7 ±3.4** |
| LMB90 | 180-212 | 25 ±6 (21) | 0.43 ±0.03 | 0.33 ±0.02 | 0.146 | | 0.94 ±0.04 | 326 | 81.1 ±2.9 | SAR (Q) | nMAD CAM | 85 ±6 (29) | 86.1 ±5.4 |
| | | | | | | | | | 89.0 ±7.0 | LnTn (Q) | nMAD CAM | | 94.4 ±8.8 |
| | | | | | | 0.85 ±0.07 | 1.76 ±0.08 | | 181.4 ±4.0 | LnTn (KF) | nMAD CAM | 54 ±2 (20) | **103.0 ±5.7** |
| LMB110 | 180-212 | 25 ±6 (24) | 0.41 ±0.03 | 0.31 ±0.02 | 0.143 | | 0.89 ±0.04 | 147 | 94.4 ±4.1 | SAR (Q) | nMAD CAM | 43 ±4 (33) | 106.7 ±7.2 |
| | | | | | | | | | 112.4 ±7.9 | LnTn (Q) | nMAD CAM | | 127.0 ±11.1 |
| | | | | | | 0.85 ±0.07 | 1.70 ±0.08 | | 209.3 ±7.4 | LnTn (KF) | nMAD CAM | 35 ±2 (20) | **122.8 ±7.7** |
| LMB155 | 180-212 | 35 ±9 (32) | 0.53 ±0.04 | 0.39 ±0.03 | 0.124 | | 1.08 ±0.06 | 257 | saturated | SAR (Q) | | | saturated |
| | | | | | | | | | saturated | LnTn (Q) | | | saturated |
| | | | | | | 0.85 ±0.07 | 1.94 ±0.09 | | 334 ±17 | LnTn (KF) | nMAD CAM | 44 ±2 (35) | **176.1 ±12.8** |

| | | | | | | | | | | | | |
|---|---|---|---|---|---|---|---|---|---|---|---|---|
| LMC270 | 180-212 | 30 ±8 (27) | 0.52 ±0.04 | 0.36 ±0.03 | 0.113 | 1.03 ±0.05 | 239 | saturated | SAR (Q) | | | saturated |
| | | | | | | | | saturated | LnTn (Q) | | | saturated |
| | | | | | | 1.85 ±0.09 | | 927 ±47 | LnTn (KF) | nMAD CAM | 23 ±1 (15) | **501 ±36** |
| Lake Koolivoo | | | | | | | | | | | | |
| LKA50 | 180-212 | 35 ±9 (34) | 0.77 ±0.06 | 0.53 ±0.04 | 0.146 | 1.48 ±0.08 | 97 | 4.4 ±0.2 | SAR (Q) | nMAD CAM | 59 ±5 (46) | **3.0 ±0.2** |
| LKB93 | 180-212 | 30 ±8 (28) | 0.78 ±0.06 | 0.55 ±0.04 | 0.148 | 1.51 ±0.08 | 60 | 7.0 ±0.5 | SAR (Q) | nMAD CAM | 64 ±7 (47) | **4.6 ±0.4** |
| LKB140 | 180-212 | 25 ±7 (24) | 0.65 ±0.04 | 0.48 ±0.03 | 0.15 | 1.31 ±0.06 | 106 | 10.0 ±0.03 | SAR (Q) | nMAD CAM | 36 ±3 (21) | **7.6 ±0.4** |
| LKC170 | 63-90 | 25 ±7 (26) | 0.31 ±0.02 | 0.23 ±0.02 | 0.147 | 0.71 ±0.04 | 78 | 32.1 ±3.9 | SAR (Q) | nMAD CAM | 144 ±12 (99) | **45.0 ±6.0** |
| LKC230 | none | | | | | | | no grains | | | | no grains |
| LKD350 | 180-212 | 35 ±9 (32) | 0.60 ±0.05 | 0.50 ±0.04 | 0.121 | 1.26 ±0.07 | 51 | 111 ±8 | SAR (Q) | nMAD CAM | 107 ±12 (39) | **89.0 ±8.0** |
| | 180-212 | | | | | | | 127 ±8 | LnTn (Q) | nMAD CAM | 19 ±3 | 101 ±9.0 |
| LKD350 | 63-90 | 35 ±9 (32) | 0.64 ±0.05 | 0.50 ±0.04 | 0.121 | 1.29 ±0.07 | 97 | 104 ±5 | SAR (Q) | nMAD CAM | 70 ±6 (34) | 81 ±6.0 |
| | 63-90 | | | | | | | 114 ±8 | LnTn (Q) | nMAD CAM | 19 ±3 | 88 ±8.0 |
| LKE400 | none | | | | | | | no grains | | | | no grains |
| LKF530 | 63-90 | 3 ±1 (1.4) | 0.43 ±0.02 | 0.29 ±0.01 | 0.263 | 1.02 ±0.05 | | saturated | SAR (Q) | | | saturated |
| LKG630 | 63-90 | 3 ±1 (1.4) | 0.43 ±0.02 | 0.29 ±0.01 | 0.263 | 1.02 ±0.05 | | saturated | SAR (Q) | | | saturated |
| Eyre Creek | | | | | | | | | | | | |
| ECA50 | 180-212 | 15 ±4 (13) | 0.97 ±0.05 | 0.73 ±0.04 | 0.177 | 1.91 ±0.07 | 91 | 0.84 ±0.05 | SAR (Q) | nMAD CAM | 86 ±8 (33) | **0.44 ±0.03** |

| | | | | | | | | | | | | | |
|---|---|---|---|---|---|---|---|---|---|---|---|---|---|
| ECB100 | 180-212 | 25 ±6 (24) | 1.04 ±0.07 | 0.78 ±0.05 | 0.156 | | 2.01 ±0.09 | 134 | 1.07 ±0.05 | SAR (Q) | nMAD CAM | 81 ±6 (32) | **0.53 ±0.04** |
| ECB150 | 180-212 | 25 ±6 (23) | 0.91 ±0.06 | 0.67 ±0.04 | 0.153 | | 1.76 ±0.08 | 176 | 3.4 ±0.2 | SAR (Q) | FMM-1 (84%) | 117 ±7 (47) | **1.9 ±0.1** |
| | | | | | | | | | 59.9 ±6.6 | | FMM-2 (16%) | | 34 ±4.0 |
| ECC240 | 180-212 | 20 ±5 (18) | 0.77 ±0.05 | 0.84 ±0.04 | 0.15 | | 1.79 ±0.07 | 176 | 77.1 ±2.1 | SAR (Q) | nMAD CAM | 51 ±5 (11) | 43.0 ±2.1 |
| | | | | | | | | | 89.7 ±3.0 | LnTn (Q) | nMAD CAM | 30 ±5 (11) | 49.4 ±2.6 |
| | | | | | | 0.85 ±0.07 | 2.61 ±0.10 | 893 | 127.8 ±1.7 | LnTn (KF) | nMAD CAM | 40 ±1 (23) | **48.9 ±2.1** |
| ECC270 | 180-212 | 25 ±6 (25) | 1.15 ±0.08 | 1.01 ±0.07 | 0.14 | | 2.33 ±0.10 | | saturated | SAR (Q) | | | saturated |
| | | | | | | 0.85 ±0.07 | 3.15 ±0.13 | 87 | 628 ±51 | LnTn (KF) | nMAD CAM | 63 ±6 (18) | **199 ±18** |

[a] Water content calculated as the % mass of water per unit of dried sediment measured in the laboratory. Dried dose rates were corrected to the weighted mean (±1σ) water content for age determination.
[b] Measured and calculated dose rates (±1σ). Cosmic-ray dose rate based on longitude, latitude and altitude of site as well as depth and density of current sediment overburden, sediment densities estimated at 1.8 g/cm$^3$.
[c] K-feldspar grains assumed to be K-rich – internal dose rate based on assumed 12.5 ±0.5 wt% K and 400 ±100 ppm Rb (standard values).
[d] Number of grains accepted for $D_e$ determinations.
[e] Mean ± total (1σ) uncertainty.
[f] OSL ages for most samples were estimated using the central age model (CAM) after identifying statistical outliers (shown as open triangles or circles in the radial plots; Figure S3) using the normalised median absolute deviation (nMAD) method. The finite mixture model (FMM) was used for samples LMA50 and ECB150 that clearly contain discrete dose components. Quartz (Q) grains were tested using the conventional single-aliquot regenerative-dose (SAR) method and, where possible, sensitivity corrected natural signals (Ln/Tn) were used on quartz and K-feldspar (KF) grains to test whether distributions may be truncated.
[g] Overdispersion (OD) in $D_e$ values.
[h] Age estimates thought to be most reliable are shown in bold in the table.

**Table S3**. Core sample $^{14}C$ AMS results.

| Sample ID | Depth | Waikato | Prep | $^{14}C$ (1σ) | Radiocarbon age | Calibrated age range (cal. yr BP) (95.4%) | |
|---|---|---|---|---|---|---|---|
| | (cm) | Code | | (pMC) | (years BP) | From | To |
| **ECB180** | 180 | Wk-53797 | ABA/HyPy | 23.4 ±0.7 | 11,675 ±248 | 14,140 | 13,090 |
| **ECC200** | 200 | Wk-53798 | ABA/HyPy | 12.5 ±0.8 | 16,688 ±499 | 21,480 | 18,940 |

PMC = percent modern carbon.
Calibration of samples following Stuiver and Polach (1977)**.**
Carbon-13 stable isotope value ($\delta^{13}C$) measured on prepared graphite using the AMS spectrometer. The radiocarbon date has therefore been corrected for isotopic fractionation. However**,** the AMS-measured $\delta^{13}C$ value can differ from the $\delta^{13}C$ of the original material and it is therefore not shown.

# Appendix B

## B1 Supplemental Figures

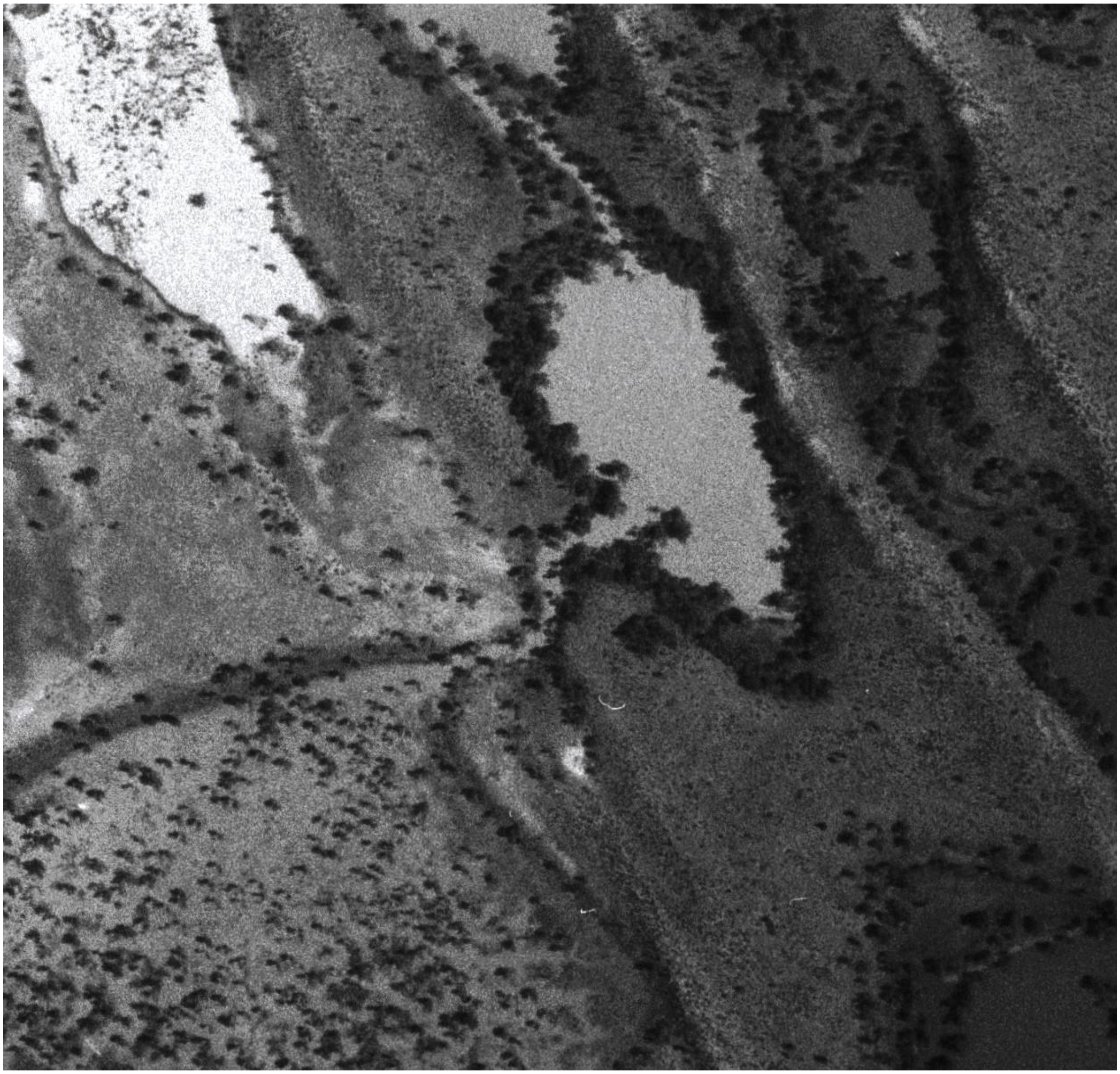

**Figure S1.** Aerial imagery of dune breach (Film CAB8774 Frame 110; Run 1; Flight date 04/11/1978).

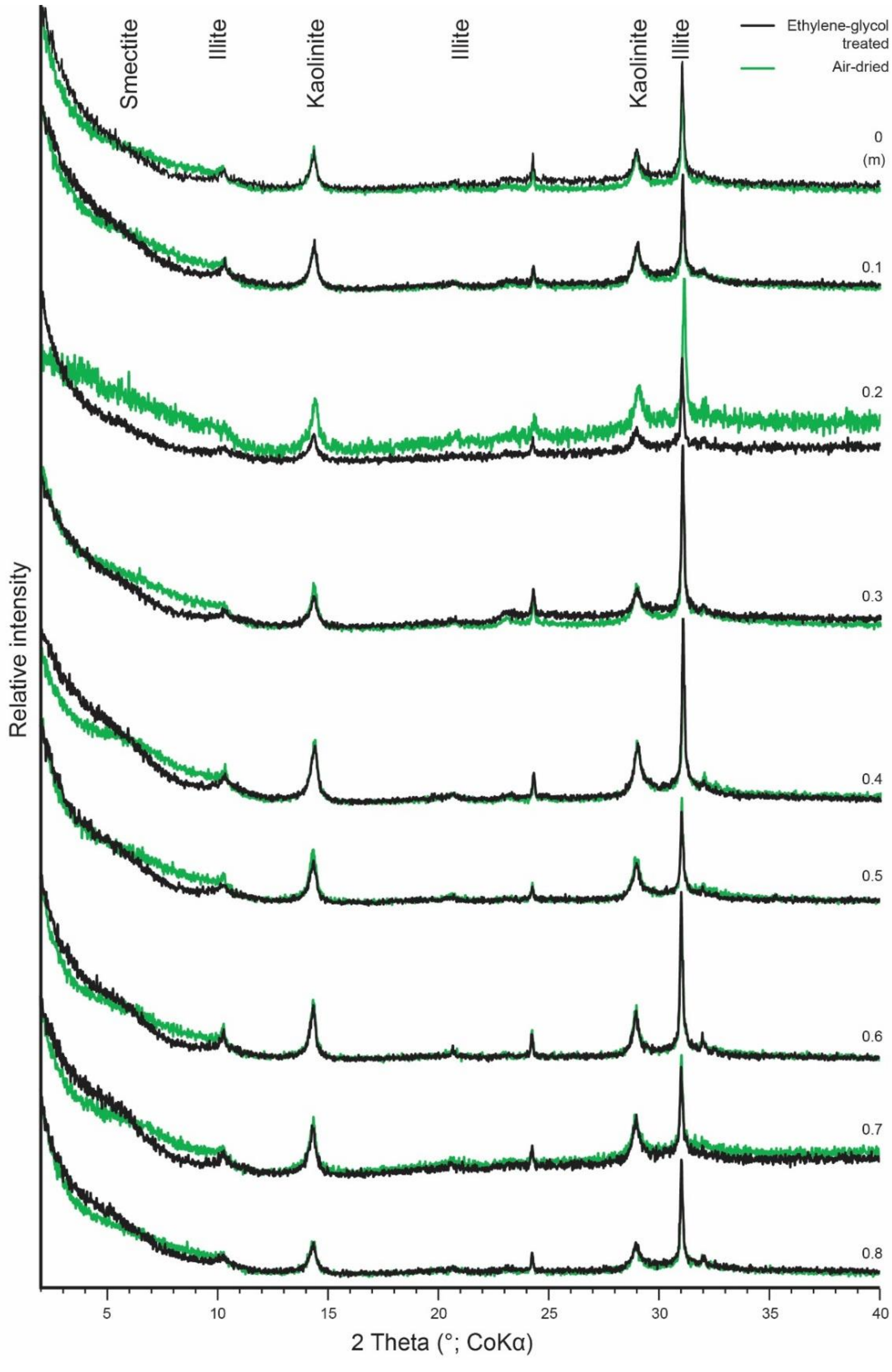


**Figure S2.** X-ray diffraction data for the Glenormiston palaeosol clay fraction.

## B2 Supplemental Table

**Table S1:** Major element weight % data of the Glenormiston palaeosol.

| SAMPLE DESCRIPTION | DEPTH (Note 1) DESCRIPTION | **$Al_2O_3$** % | **CaO** % | **$Fe_2O_3$** % | **$K_2O$** % | **MgO** % | **MnO** % | **$Na_2O$** % | **$P_2O_5$** % | **$SO_3$** % | **$SiO_2$** % | **SrO** % | **$TiO_2$** % | **Total** % | **LOI** % |
|---|---|---|---|---|---|---|---|---|---|---|---|---|---|---|---|
| Limit of Detection | | **0.01** | **0.01** | **0.01** | **0.01** | **0.01** | **0.01** | **0.01** | **0.01** | **0.01** | **0.01** | **0.01** | **0.01** | **0.01** | **0.01** |
| X22076-1 | 0 cm | 2.54 | 0.11 | 1.21 | 0.36 | 0.17 | 0.01 | 0.02 | 0.03 | 0.02 | 93.26 | <0.01 | 0.13 | 99.07 | 1.19 |
| X22076-2 | 10 cm | 3.57 | 0.14 | 1.75 | 0.51 | 0.26 | 0.01 | 0.04 | 0.02 | 0.01 | 91.96 | <0.01 | 0.19 | 100.05 | 1.56 |
| X22076-3 | 20 cm | 3.88 | 0.15 | 1.5 | 0.52 | 0.27 | 0.01 | 0.04 | 0.02 | 0.01 | 91.49 | <0.01 | 0.19 | 99.81 | 1.68 |
| X22076-4 | 30 cm | 3.94 | 0.16 | 1.74 | 0.55 | 0.29 | 0.01 | 0.05 | 0.02 | 0.01 | 90.55 | <0.01 | 0.21 | 99.3 | 1.72 |
| X22076-5 | 40 cm | 3.28 | 0.12 | 1.36 | 0.46 | 0.23 | 0.01 | 0.04 | 0.01 | 0.01 | 92.63 | <0.01 | 0.19 | 99.79 | 1.41 |
| X22076-6 | 50 cm | 3.43 | 0.13 | 1.4 | 0.47 | 0.25 | 0.01 | 0.05 | 0.01 | 0.02 | 93.33 | <0.01 | 0.19 | 100.7 | 1.37 |
| X22076-7 | 60 cm | 3.31 | 0.12 | 1.38 | 0.46 | 0.24 | 0.01 | 0.04 | 0.01 | 0.02 | 92.15 | <0.01 | 0.2 | 99.34 | 1.37 |
| X22076-8 | 70 cm | 3.28 | 0.12 | 1.38 | 0.47 | 0.24 | 0.01 | 0.05 | 0.01 | 0.01 | 92.57 | <0.01 | 0.18 | 99.66 | 1.28 |
| X22076-9 | 80 cm | 3.1 | 0.12 | 1.31 | 0.45 | 0.24 | 0.01 | 0.04 | 0.01 | 0.01 | 94.08 | <0.01 | 0.17 | 100.85 | 1.26 |
| QC | NCSDC73037 | 12.72 | 7.87 | 13.8 | 1.19 | 5.08 | 0.19 | 3.6 | 0.46 | 0.02 | 46.79 | <0.01 | 3.88 | 100.5 | |
| QC | SARM-3 | 13.53 | 3.16 | 9.97 | 5.51 | 0.27 | 0.76 | 8.44 | 0.05 | 0.16 | 52.41 | 0.55 | 0.48 | 100.2 | |
| QC | SARM-4 | 16.41 | 11.5 | 8.91 | 0.25 | 7.55 | 0.19 | 2.42 | 0.01 | 0.01 | 52.46 | 0.03 | 0.19 | 100.1 | |
| QC | SiO2 | 0.02 | <0.01 | 0.01 | <0.01 | <0.01 | <0.01 | <0.01 | <0.01 | 0.01 | 100.00 | <0.01 | 0.02 | 100.5 | |

*Note 1: Sample depth is palaeosol profile depth (not pit depth)*

*Note 2: Major element analysis conducted by X-ray fluorescence by Queensland University of Technology (QUT) X-Ray and Particle Laboratory.*

# Appendix C

## C1 Supplemental Table

**Table S1.** Gauging stations in Georgina catchment, with map reference numbers (Figure 4.1a), station names, ID numbers and GPS coordinates.

| Map Ref # | Station Name | ID# | Lat | Long |
|---|---|---|---|---|
| 1 | Soudan | 15040 | 20.05°S | 137.02°E |
| 2 | Avon Downs | 15005 | 20.03°S | 137.49°E |
| 3 | Rocklands | 37115 | 19.86°S | 138.10°E |
| 4 | Camooweal | 37010 | 19.92°S | 138.12°E |
| 5 | Barkley Downs | 37003 | 20.47°S | 138.47°E |
| 6 | Headingly Station | 37024 | 21.32°S | 138.29°E |
| 7 | Urandangi Aerodrome | 37058 | 21.60°S | 138.37°E |
| 8 | Urandangi | 37043 | 21.61°S | 138.31°E |
| 9 | Phosphate Hill | 37106 | 21.88°S | 139.97°E |
| 10 | Chatsworth | 37013 | 21.97°S | 140.30°E |
| 11 | Manners Creek | 15560 | 22.11°S | 137.98°E |
| 12 | Tobermorey | 15618 | 22.27°S | 137.97°E |
| 13 | Roxborough Downs | 38032 | 22.52°S | 138.84°E |
| 14 | Alderley Station | 37109 | 22.49°S | 139.66°E |
| 15 | Glenormiston | 38010 | 22.92°S | 138.80°E |
| 16 | Marion Downs | 38014 | 23.36°S | 139.66°E |
| 17 | Sandringham | 38025 | 24.05°S | 139.06°E |
| 18 | Kamaran Downs | 38048 | 24.34°S | 139.28°E |
| 19 | Bedourie | 38000 | 24.36°S | 139.47°E |
| 20 | Cluny | 38005 | 24.51°S | 139.59°E |
| 21 | Glengyle | 38009 | 24.79°S | 139.59°E |

## C2 Supplemental Figures

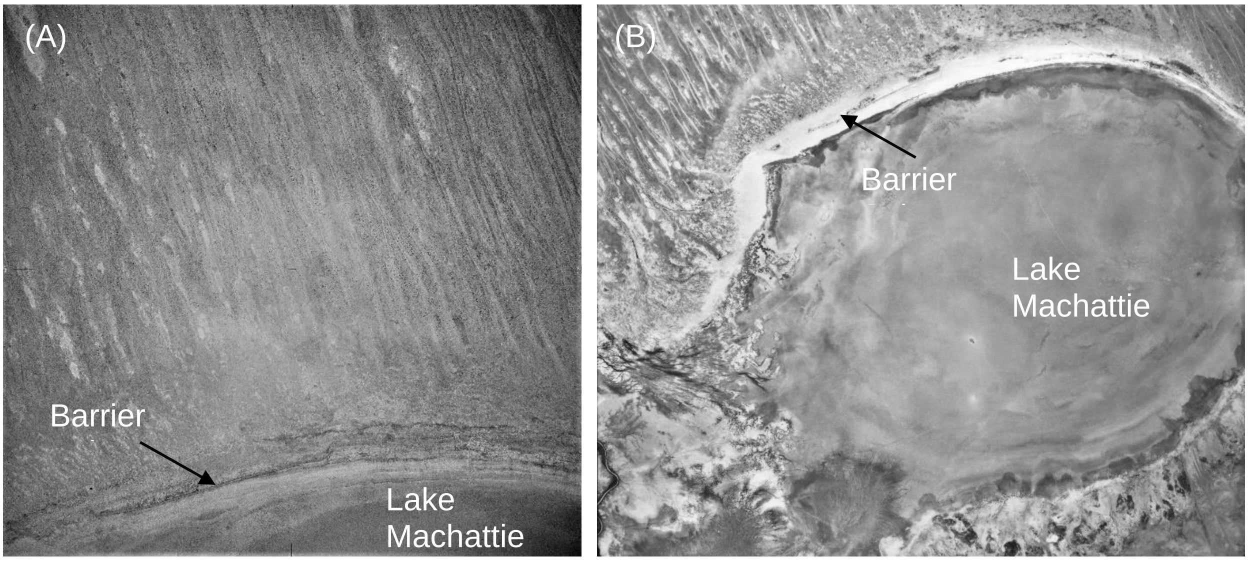


**Figure S1.** Historical Imagery. (**A**) Lake Machattie 1957: Film CABG9; Frame 5054; Run 12; Flight date: 11/10/1957. (**B**) Lake Machattie 1970: Film CAB7057; Frame 244; Run 7; Flight date: 01/09/1970.

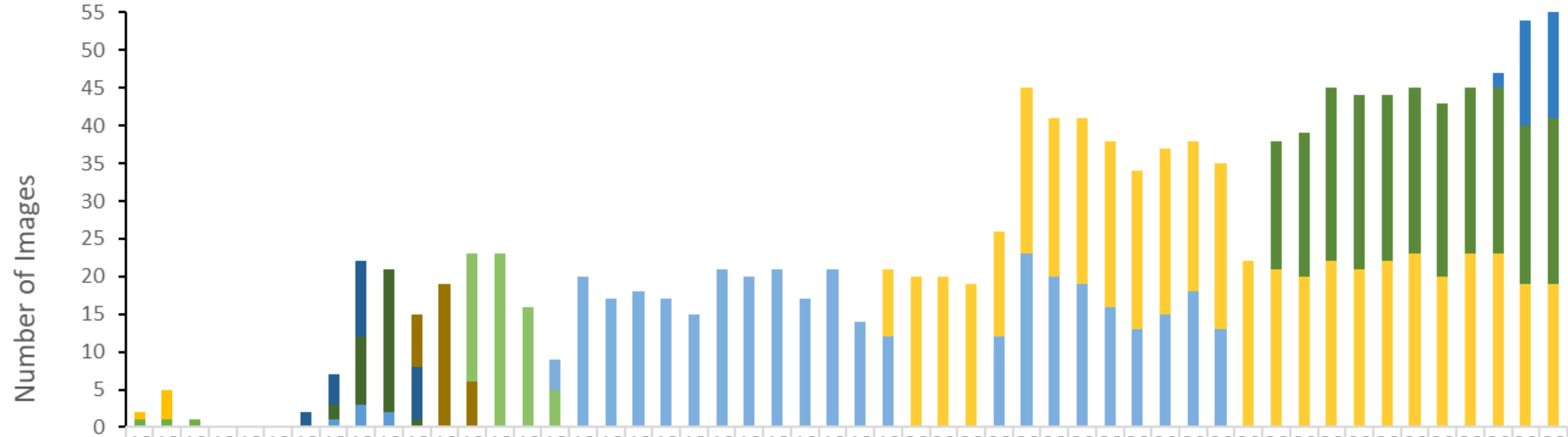


| | 1972 | 1973 | 1974 | 1975 | 1976 | 1977 | 1978 | 1979 | 1980 | 1981 | 1982 | 1983 | 1984 | 1985 | 1986 | 1987 | 1988 | 1989 | 1990 | 1991 | 1992 | 1993 | 1994 | 1995 | 1996 | 1997 |
|---|---|---|---|---|---|---|---|---|---|---|---|---|---|---|---|---|---|---|---|---|---|---|---|---|---|---|
| L9 \| p098r077 | | | | | | | | | | | | | | | | | | | | | | | | | | |
| L8 \| p098r077 | | | | | | | | | | | | | | | | | | | | | | | | | | |
| L7 \| p098r077 | | | | | | | | | | | | | | | | | | | | | | | | | | |
| L5 \| p098r077 | | | | | | | | | | | | | | | | 4 | 20 | 17 | 18 | 17 | 15 | 21 | 20 | 21 | 17 | 21 |
| L5 \| p098r077 | | | | | | | | | | | | | 17 | 23 | 16 | 5 | | | | | | | | | | |
| L4 \| p098r077 | | | | | | | | | | | 7 | 19 | 6 | | | | | | | | | | | | | |
| L3 \| p105r077 | | | | | | | 2 | 4 | 10 | | 7 | | | | | | | | | | | | | | | |
| L2 \| p105r077 | | | | | | | | 2 | 9 | 19 | 1 | | | | | | | | | | | | | | | |
| L1 \| p105r077 | 1 | 4 | | | | | | | | | | | | | | | | | | | | | | | | |
| L2 \| p104r077 | | | | | | | | 1 | 3 | 2 | | | | | | | | | | | | | | | | |
| L1 \| p104r077 | 1 | 1 | 1 | | | | | | | | | | | | | | | | | | | | | | | |

| | 1998 | 1999 | 2000 | 2001 | 2002 | 2003 | 2004 | 2005 | 2006 | 2007 | 2008 | 2009 | 2010 | 2011 | 2012 | 2013 | 2014 | 2015 | 2016 | 2017 | 2018 | 2019 | 2020 | 2021 | 2022 | 2023 |
|---|---|---|---|---|---|---|---|---|---|---|---|---|---|---|---|---|---|---|---|---|---|---|---|---|---|---|
| L9 \| p098r077 | | | | | | | | | | | | | | | | | | | | | | | | 2 | 14 | 19 |
| L8 \| p098r077 | | | | | | | | | | | | | | | | 17 | 19 | 23 | 23 | 22 | 22 | 23 | 22 | 22 | 21 | 22 |
| L7 \| p098r077 | | 9 | 20 | 20 | 19 | 14 | 22 | 21 | 22 | 22 | 21 | 22 | 20 | 22 | 22 | 21 | 20 | 22 | 21 | 22 | 23 | 20 | 23 | 23 | 19 | 19 |
| L5 \| p098r077 | 14 | 12 | | | | 12 | 23 | 20 | 19 | 16 | 13 | 15 | 18 | 13 | | | | | | | | | | | | |
| L5 \| p098r077 | | | | | | | | | | | | | | | | | | | | | | | | | | |
| L4 \| p098r077 | | | | | | | | | | | | | | | | | | | | | | | | | | |
| L3 \| p105r077 | | | | | | | | | | | | | | | | | | | | | | | | | | |
| L2 \| p105r077 | | | | | | | | | | | | | | | | | | | | | | | | | | |
| L1 \| p105r077 | | | | | | | | | | | | | | | | | | | | | | | | | | |
| L2 \| p104r077 | | | | | | | | | | | | | | | | | | | | | | | | | | |
| L1 \| p104r077 | | | | | | | | | | | | | | | | | | | | | | | | | | |

**Figure S2**. Landsat Imagery used in this study. Tier 2 MSS images viewed ranged between 1972 and 1986. Tier 1 TM, ETM+ and OLI images were used from 1987 onwards. Numbered Landsat (L) satellites are shown in data table with corresponding path/row numbers.

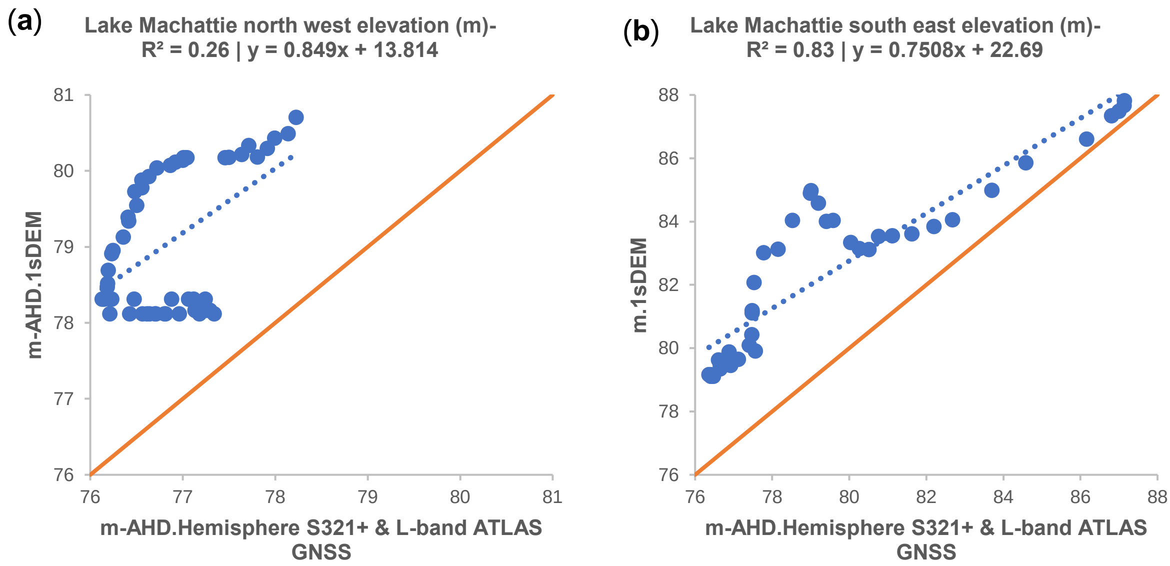


**Figure S3.** Comparison between in-field elevation measurements, using Hemisphere S321+ receiver with L-band ATLAS® GNSS system, and the equivalent point-extracted 1-sec Digital Elevation Model (DEM) (Gallant et al., 2011) data across transects at **(a)** Lake Machattie northwest (LMNW) and **(b)** Lake Machattie southeast (LMSE). Solid line (orange) bisecting each graph represents 1:1 relationship. Dotted blue line represents the straight-line regression and shows how well the 1-sec DEM values agree with in-field elevation measurements. Units are in meters Australian Height Datum (m-AHD).

**Notes for Figures S4–S14:**

**Flood Event Climate Data Information.** Climate data including rainfall, RMM MJO charts, and tropical cyclone track maps were sourced from the Australian Bureau of Meteorology (http://www.bom.gov.au/). Precipitable water content (kg/m$^2$) used NCEP/NCAR Reanalysis 1 (Kalnay et al., 1996) of 4x daily individual observations where the atmosphere is considered as a single layer. Back trajectory frequencies were calculated using the Hybrid Single-Particle Lagrangian Integrated Trajectory model (HYPLIT) (Draxler and Rolph, 2010) and NCEP/NCAR Global Reanalysis Data (1948 onwards) with air parcels arriving at 1500 mAGL in the Georgina catchment.

**1973 Flood**

**Rainfall**

Jan 73:

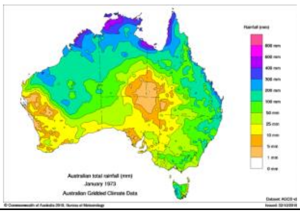

Feb 73:

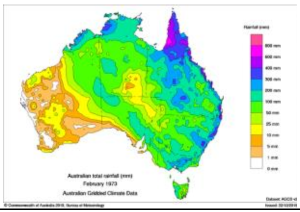

Mar 73:

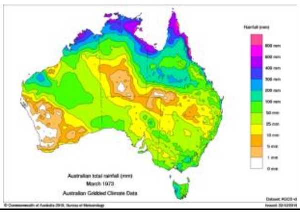

**MJO**

NA until June 1974

**March 25-28, 1973:**

**(a) Rainfall**
(March 21-28)

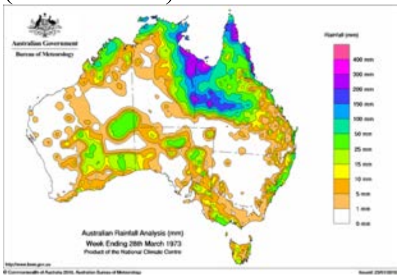

**(b) Precipitable Water Content (kg/m²)**

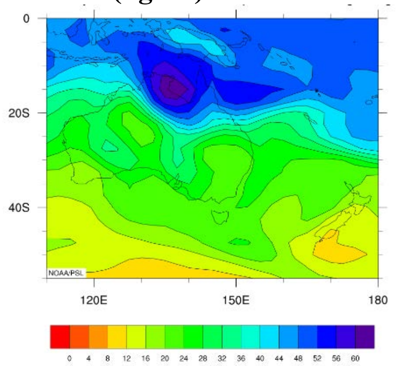


**(c) Back Trajectory Frequency**
(Camooweal)

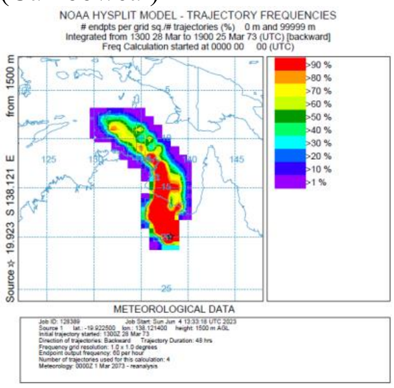


**(d) Tropical Cyclone**
(Bella)

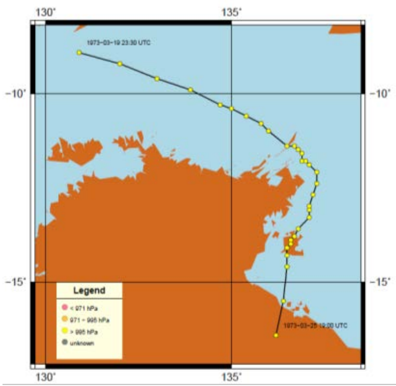


**(e) Back Trajectory Frequency**
(Glenormiston)

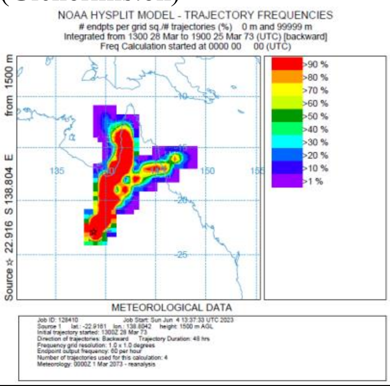


**Figure S4. 1973 Flood.** Top (left to right): Monthly rainfall totals January-March 1973, RMM MJO (NA). Sub-heading: **March 25–28, 1973**, **(a)** 1-week rainfall ending March 28 (left column); **(b)** Precipitable water content (25–28/03/1973); Back Trajectory Frequency (25–28/03/1973) ending at **(c)** Camooweal and **(e)** Glenormiston; **(d)** Tropical Cyclone track map (Bella).

**1974 Flood**

| **Rainfall** | | **MJO** |
|---|---|---|
| Jan 74: | Feb 74: | NA until June 1974 |

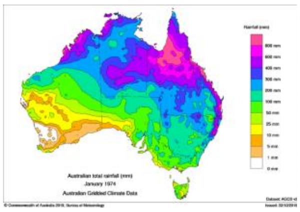

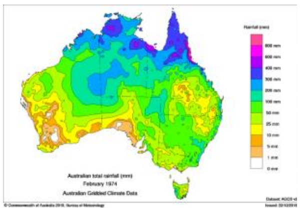

| **Rainfall** | **Precipitable Water Content** | **Back Trajectory Frequency** |
|---|---|---|
| See Figure 10C | See Figure 10A | See Figure 10B |

**Figure S5**. 1974 Flood. Top (left to right): Monthly rainfall totals January–February 1974, RMM MJO (NA). See Figure 10 for more details.

**1991 Flood**

**Rainfall**

Jan 91:

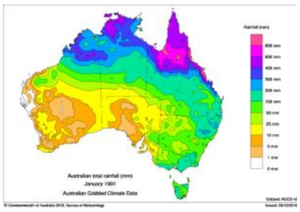

Feb 91:

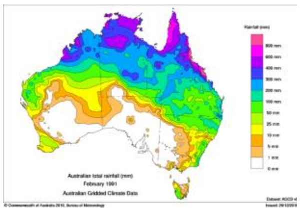

**(a) MJO**

(J-F-M)

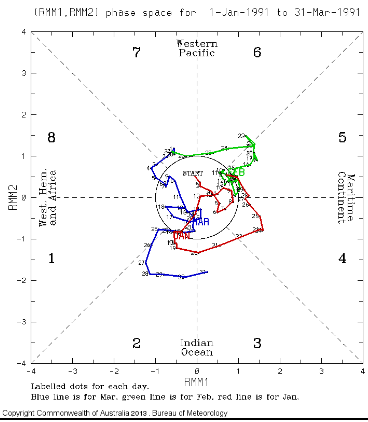


**February 5-12, 1991:**

**(b) Rainfall**

(February 5-12)

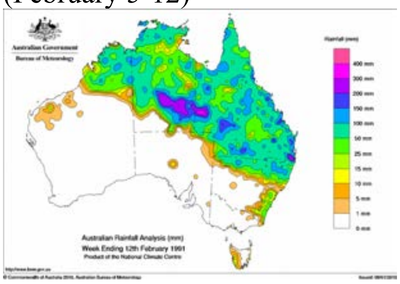

**(c) Precipitable Water Content (kg/m$^2$)**

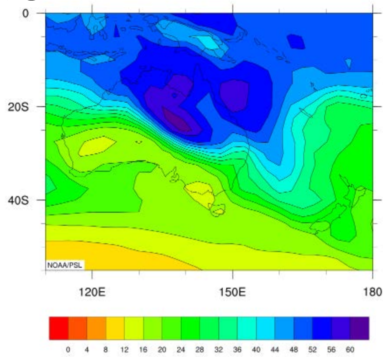


**(d) Back Trajectory Frequency**

(Glenormiston)

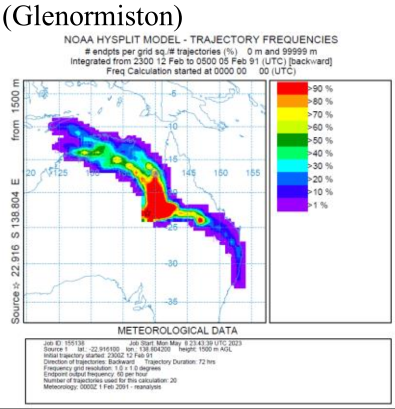

**Figure S6. 1991 Flood.** Top (left to right): Monthly rainfall totals January-February 1991, **(a)** RMM MJO (J-F-M). Sub-heading: **March 5–12, 1991**, **(b)** 1-week rainfall ending February 12; **(c)** Precipitable water content (5–12/02/1991); Back trajectory frequency (5–12/02/1991) ending at **(d)** Glenormiston.

**1997 Flood:**

**Rainfall**

Jan:

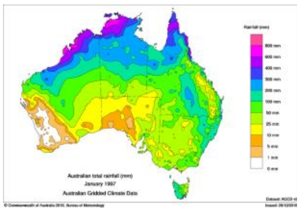

Feb:

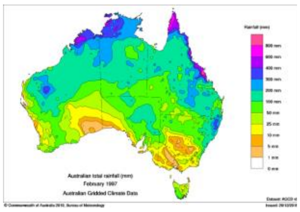

Mar:

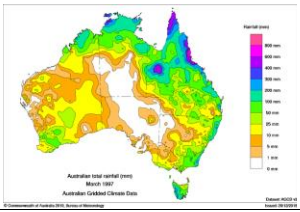

**(a) MJO**
(J-F-M)

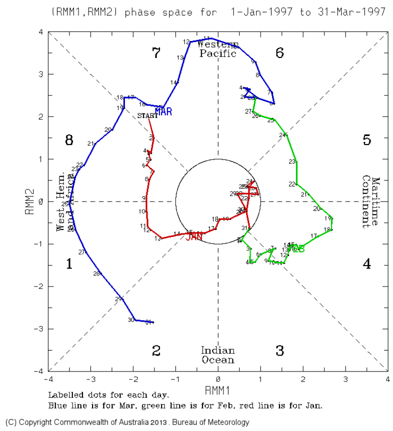


**March 1-7, 1997:**

**(b) Rainfall**
(March 1-7)

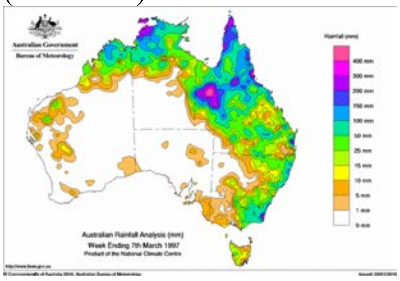

**(c) Precipitable Water Content (kg/m$^2$)**

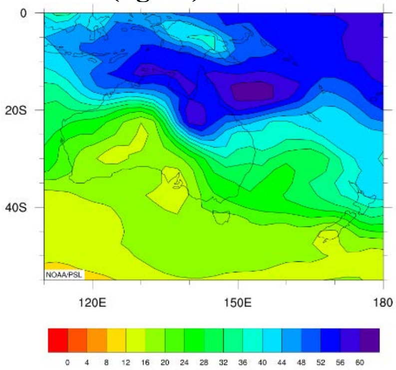


**(d) Back Trajectory Frequency**
(Headingly Station)

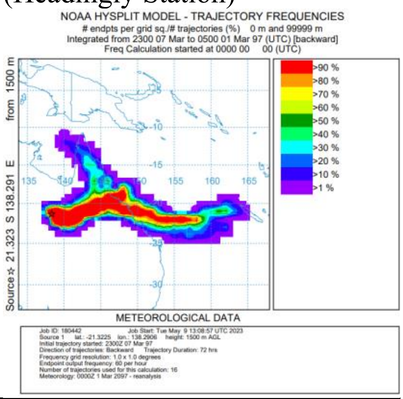


**Figure S7. 1997 Flood.** Top left: Monthly rainfall totals January-March 1997; Top right: **(a)** RMM MJO (J-F-M). Sub-heading: **March 1–7, 1997**, **(b)** 1-week rainfall ending March 7; **(c)** Precipitable water content (1–7/03/1997); **(d)** Back trajectory frequency (1–7/03/1997) ending at Headingly Station.

## 2001 Flood

**Rainfall**

Dec 2000:

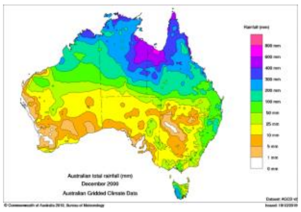

Jan 2001:

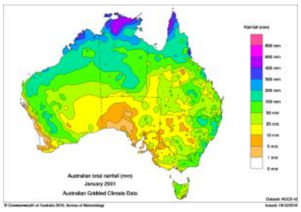

**(a) Tropical Cyclone**

Sam

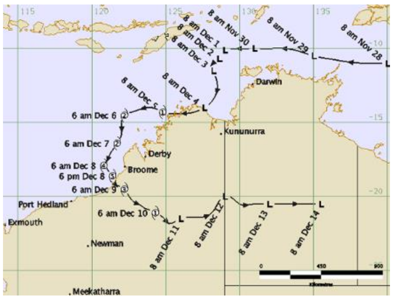


**(b) Back Trajectory Frequency**

(Camooweal) Dec 2000:

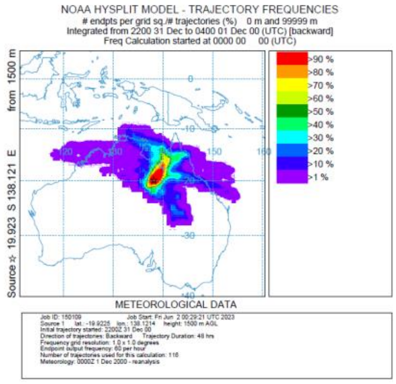


**(c) MJO**

(O-N-D 2000)

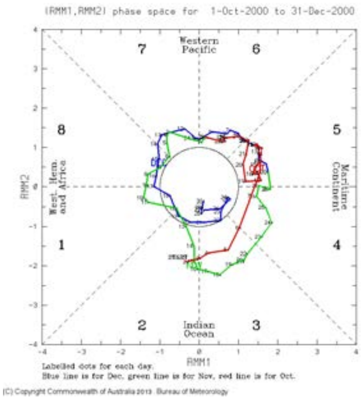


**(d) MJO**

(J-F-M 2001)

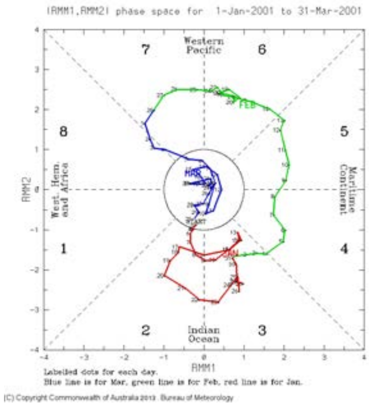


**(e) Back Trajectory Frequency**

(Camooweal) Jan 2001:

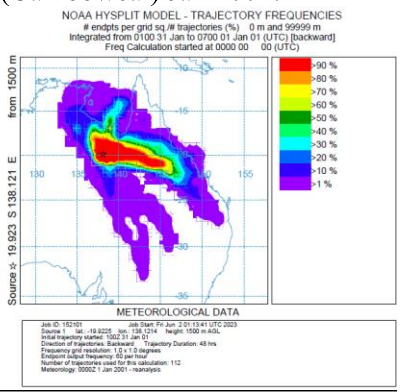


**December 7-29, 2000:**

**Rainfall**

See December rainfall total above.

**(f) Precipitable Water Content (kg/m$^2$)**

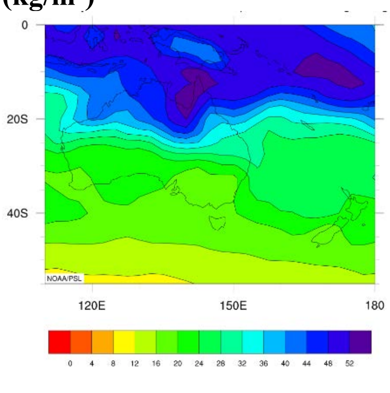


**(g) Back Trajectory Frequency**

(Camooweal)

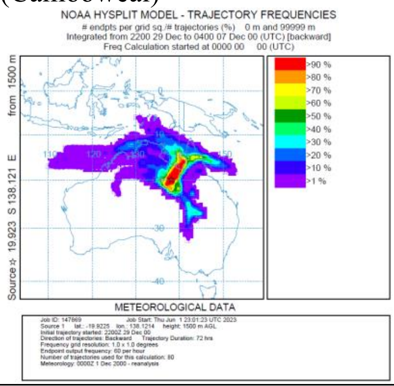

**Figure S8. 2001 Flood.** Top (left to right): Monthly rainfall totals December 2000 to January 2001, **(a)** Tropical Cyclone track map (Sam), Back trajectory frequency ending at **(b)** Camooweal (1–31/12/2000). Middle row (left to right): RMM MJO **(c)** O-N-D, 2000 and **(d)** J-F-M, 2001; Back trajectory frequency (1–31/12/2000) ending at **(e)** Camooweal. Sub-heading: **December 7-29, 2000, (f)** Precipitable water content (7–29/12/2000); **(g)** Back trajectory frequency (7–29/12/2000) ending at Camooweal.

**2007 Flood**

**Rainfall**

Jan 2007:

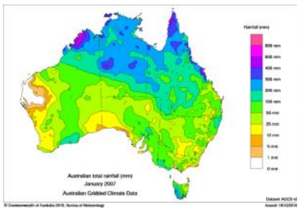

Feb 2007:

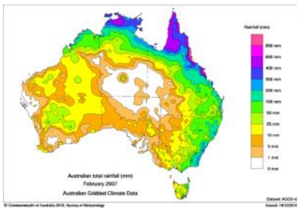

**(a) MJO**

(J-F-M)

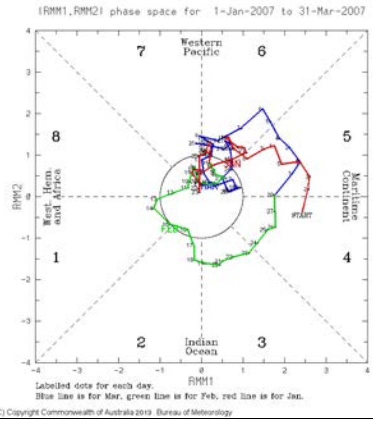


**January 20-21, 2007:**

**Rainfall**

Jan 20:

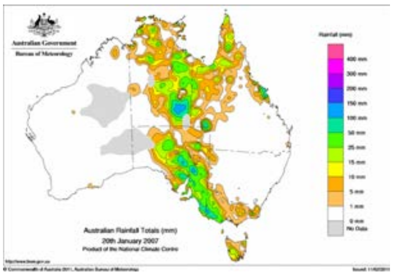

Jan 21:

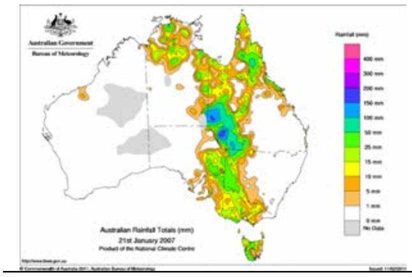

**(b) Precipitable Water Content (kg/m$^2$)**

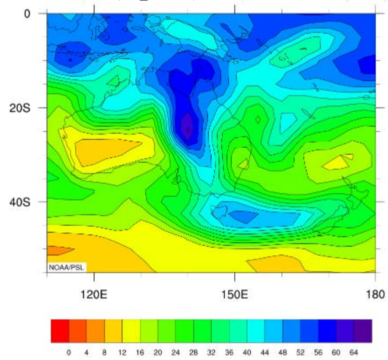


**(c) Back Trajectory Frequency**

(Glengyle)

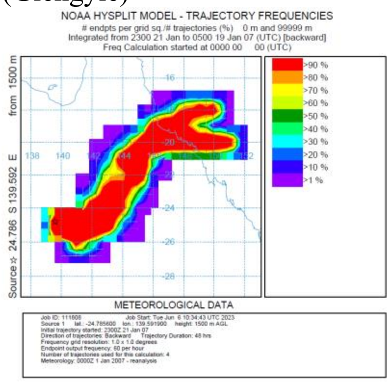


**Figure S9. 2007 Flood.** Top (left to right): Monthly rainfall totals January-February 2007, **(a)** RMM MJO (J-F-M; Sub-heading: **January 20–21, 2007,** Daily rainfall totals on January 20 and 21, 2007, **(b)** Precipitable water content (20–21/01/2007); **(c)** Back trajectory frequency (19–21/01/2007) ending at Glengyle.

## 2009 Flood

**Rainfall**

Dec 2008:

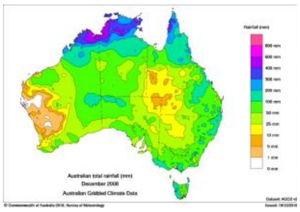

Jan 2009:

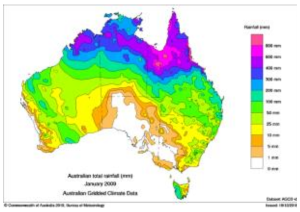

**(a) MJO**

(J-F-M 2009)

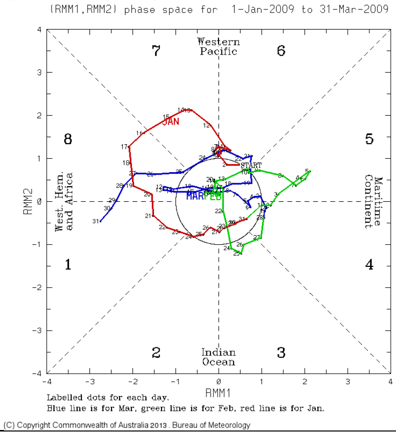


**January 1-7, 2009**

**Rainfall**

(January 1-7)

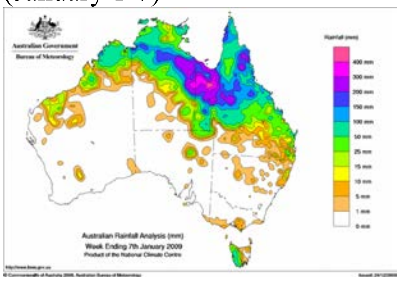

**(b) Precipitable Water Content (kg/m$^2$)**

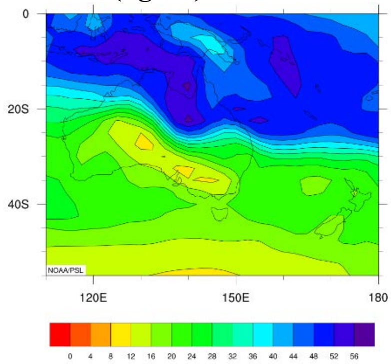


**(c) Back Trajectory Frequency**

(Camooweal)

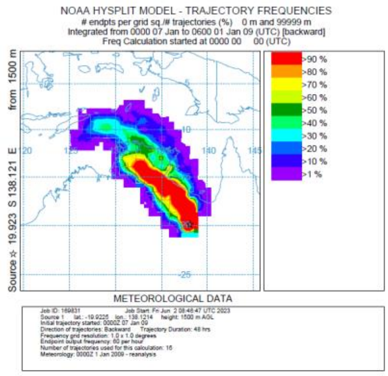


**(d) Back Trajectory Frequency**

(Glengyle)

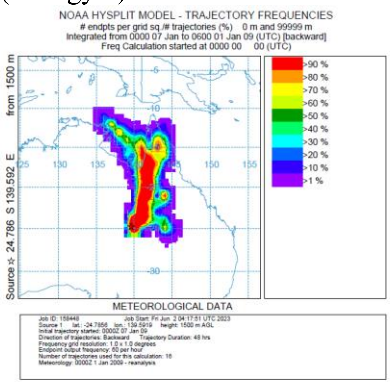


**Figure S10. 2009 Flood.** Top (left to right): Monthly rainfall totals December 2008 and January 2009, **(a)** RMM MJO (J-F-M). Sub-heading: **January 1–7, 2009,** 1-week rainfall ending January 7; **(b)** Precipitable water content (1–7/01/2009); Back trajectory frequency (1–7/01/2009) ending at **(c)** Camooweal and **(d)** Glengyle.

## 2010 Flood

### Rainfall

Dec 2009:

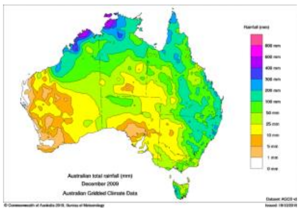

Jan 2010:

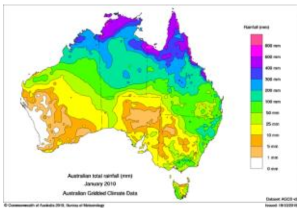

Feb 2010:

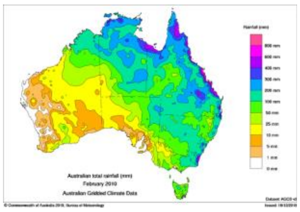

Mar 2010:

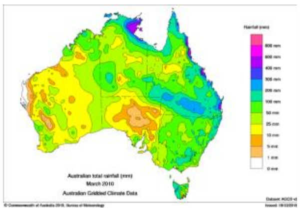

**(a) MJO**
(J-F-M)

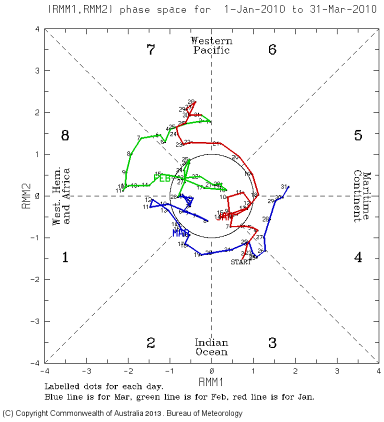


**(b) MJO**
(A-M-J)

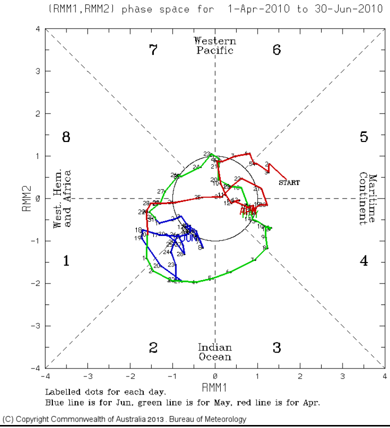


**Dec 29, 2009 – Jan 10, 2010:**

**Rainfall**

Dec 28, 2009 – Jan 03, 2010

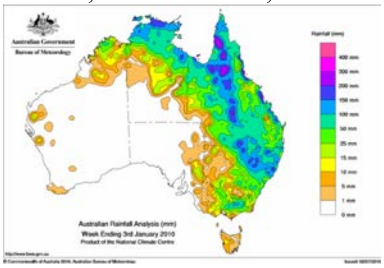

**(c) Precipitable Water Content (kg/m$^2$)**

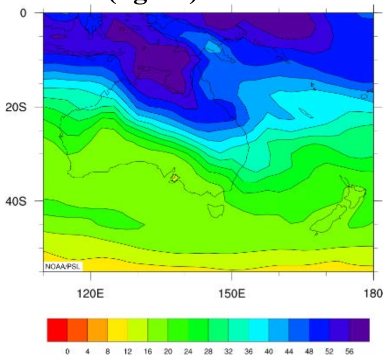


**(d) Back Trajectory Frequency**
(Camooweal)

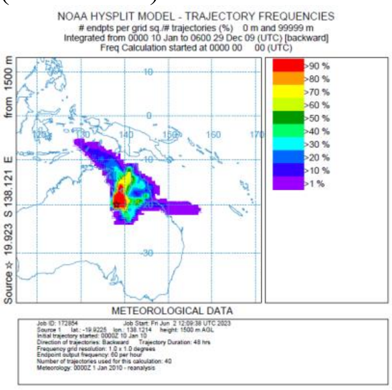


Jan 3-10, 2010

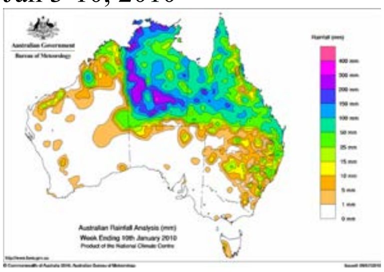

**(e) Back Trajectory Frequency**
(Roxborough Downs)

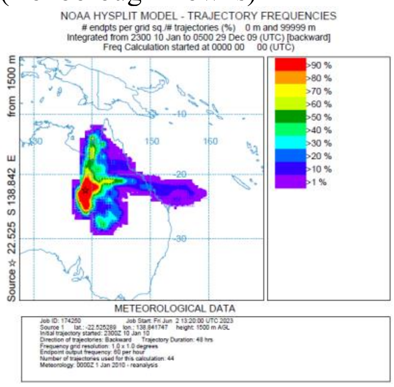

**February 22 – March 01**
**Rainfall**

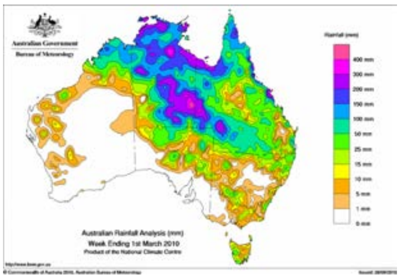

**(f) Precipitable Water Content ($kg/m^2$)**

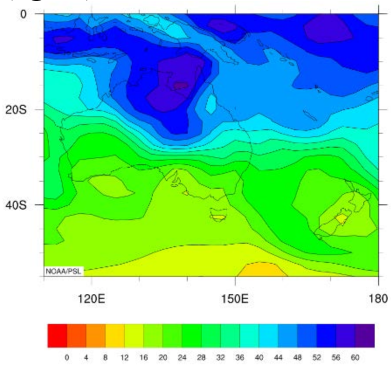


**(g) Back Trajectory Frequency**
(Camooweal)

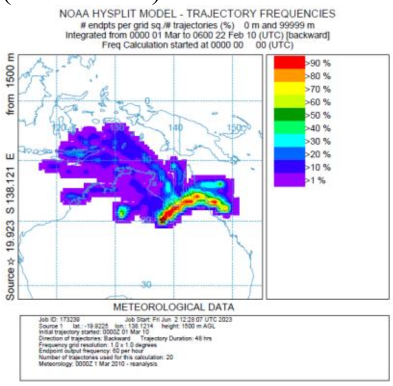


**(h) Back Trajectory Frequency**
(Roxborough Downs)

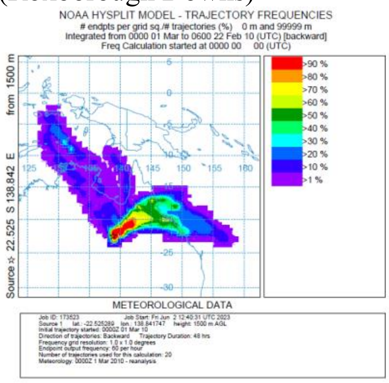


**(i) Back Trajectory Frequency**
(Glengyle)

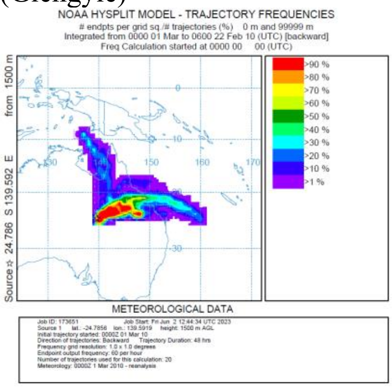


**Figure S11. 2010 Flood.** Top (left to right): Monthly rainfall totals December 2009 to March 2010. Middle row (left to right): RMM MJO **(a)** J-F-M, 2009 and **(b)** A-M-J, 2010. Sub-heading: **December 29, 2009, to January 10, 2010,** 1-week rainfall ending January 03 and January 10 (left column); **(c)** Precipitable water content (29/12/2009–10/01/2010); Back Trajectory Frequency (29/12/2009–10/01/2010) ending at **(d)** Camooweal and **(e)** Roxborough Downs. Sub-heading: **February 22 to March 1, 2010,** 1-week rainfall ending March 1 (left column); **(f)** Precipitable water content (22/02/2010–01/03/2010); Back Trajectory Frequency (22/02/2010–01/03/2010) ending at **(g)** Camooweal, **(h)** Roxborough Downs and **(i)** Glengyle.

**2011 Flood**

**Rainfall**

Dec 2010:

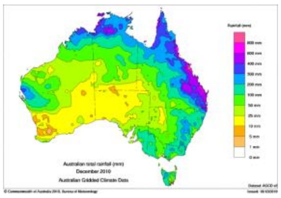

Jan 2011:

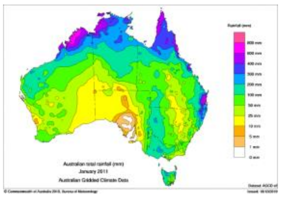

Feb 2011:

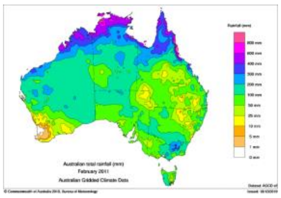

Mar 2011:

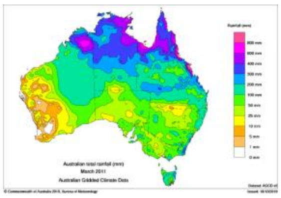

**(a) MJO**
(O-N-D 2010)

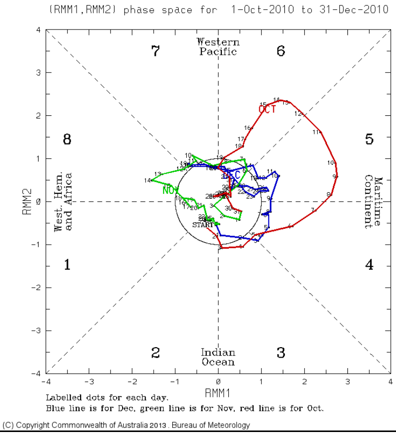


**(b) MJO**
(J-F-M 2011)

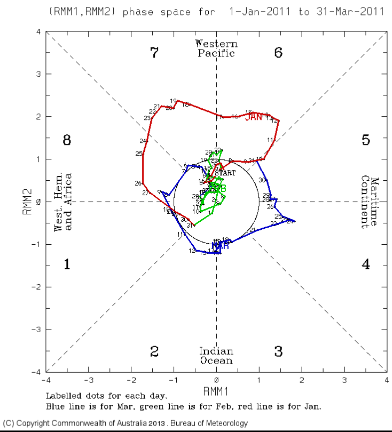


**(c) Tropical Cyclone**
Yasi

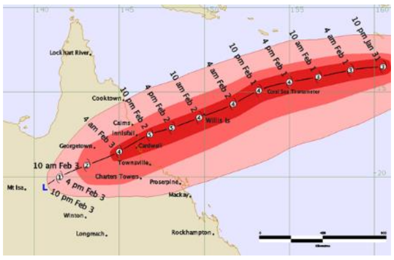

**March 1-20, 2011:**
**Rainfall**

See March rainfall total above.

**(d) Precipitable Water Content (kg/m$^2$)**

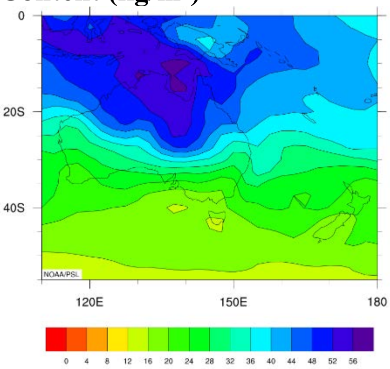


**(e) Back Trajectory Frequency**
(Glengyle)

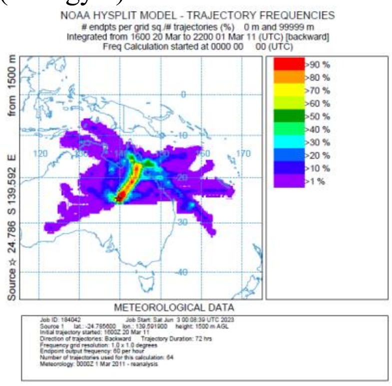


**Figure S12. 2011 Flood.** Top (left to right): Monthly rainfall totals December 2010 to March 2011. Middle row (left to right): RMM MJO **(a)** O-N-D, 2010 and **(b)** J-F-M, 2011; **(c)** Tropical Cyclone track map (Yasi). Sub-heading: **March 1–20, 2011, (d)** Precipitable water content (1–20/03/2011); **(e)** Back Trajectory Frequency (1–20/03/2011) ending at Glengyle.

## 2019 Flood

**Rainfall**

Jan:

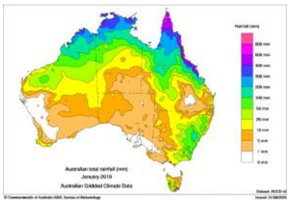

Feb:

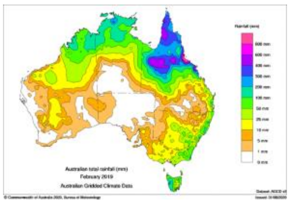

Mar:

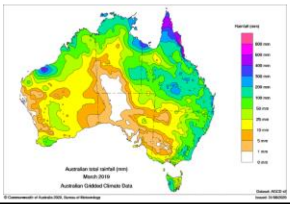

**(a) MJO**

(J-F-M)

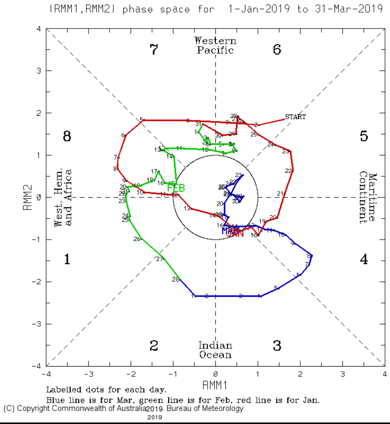


**February 1-8, 2019: Rainfall**

Feb 2-8:

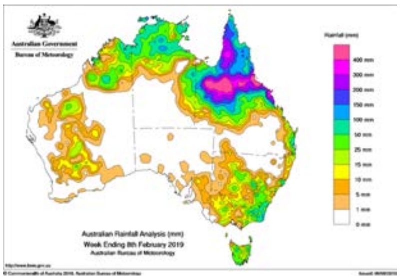

**(b) Precipitable Water Content (kg/m$^2$)**

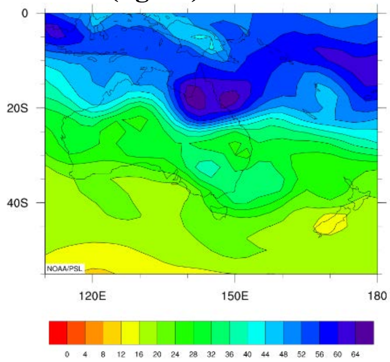


**(c) Back Trajectory Frequency**

(Camooweal)

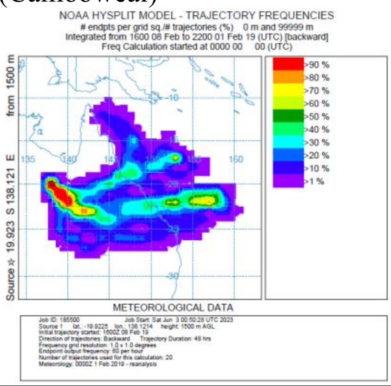


**March 24-31, 2019: Rainfall**

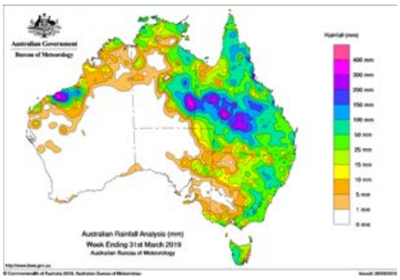

**(d) Precipitable Water Content (kg/m$^2$)**

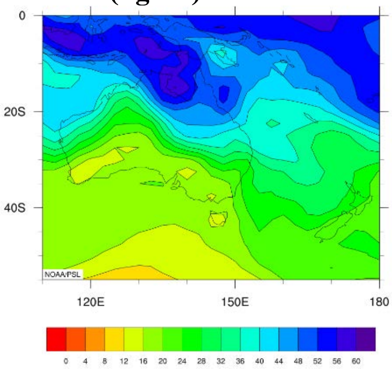


**(e) Back Trajectory Frequency**

(Glenormiston)

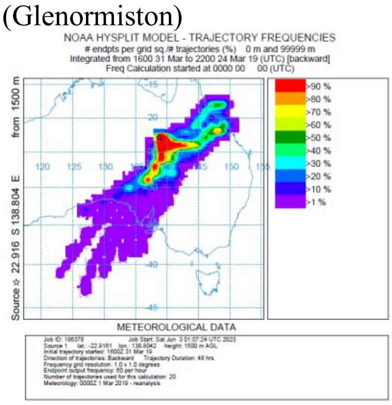

**(f) Tropical Cyclone**
Trevor


**Figure S13. 2019 Flood.** Top left: Monthly rainfall totals January-March 2019; Top right: RMM MJO **(a)** J-F-M, 2019. Sub-heading: **February 1–8, 2019,** 1-week rainfall ending February 8 (left column); **(b)** Precipitable water content (1–8/02/2019); **(c)** Back Trajectory Frequency (1–8/02/2019) ending at Camooweal. Sub-heading: **March 24–31, 2019,** 1-week rainfall ending March 31 (left column top); **(d)** Precipitable water content (24–31/03/2019); **(e)** Back Trajectory Frequency (24–31/03/2019) ending at Camooweal; **(f)** Tropical Cyclone track map (Trevor) (left column bottom).

## 2023 Flood

**Rainfall**

Dec 2022:

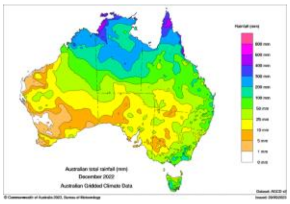

Jan 2023:

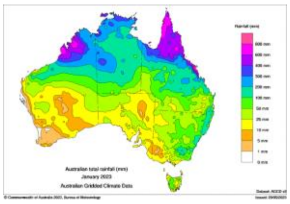

Feb 2023:

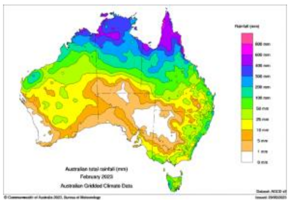

Mar 2023

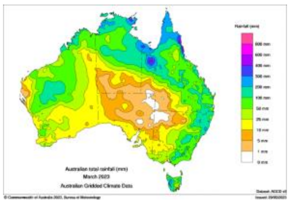

**(a) MJO**
(O-N-D)

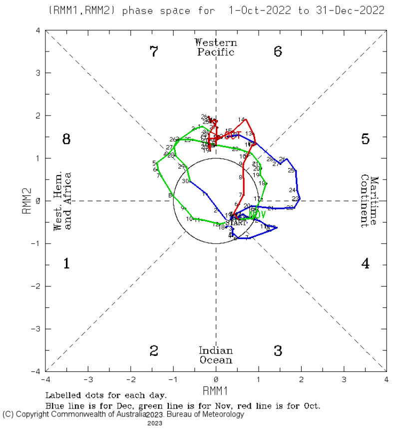


**(b) MJO**
(J-F-M)

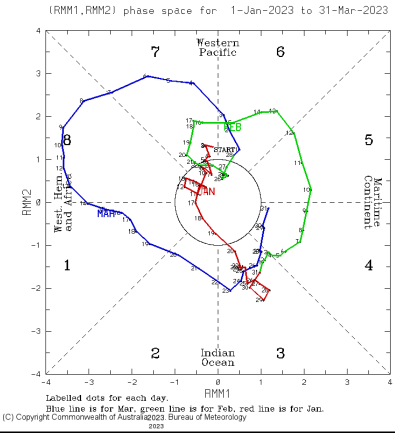


**Dec 22-27, 2022:**
**Rainfall**
(Dec 20-27)

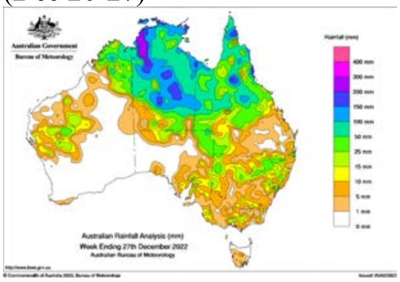

**(c) Precipitable Water Content (kg/m$^2$)**

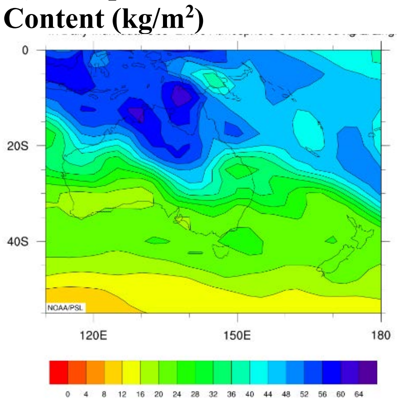


**(d) Back Trajectory Frequency**
(Camooweal)

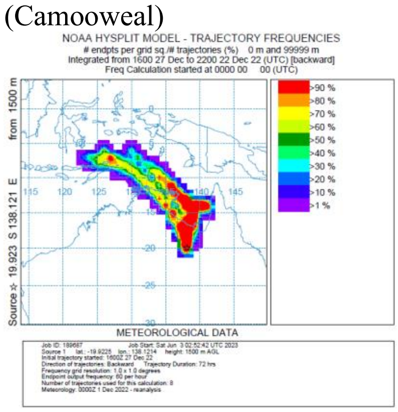

**(e) Tropical Cyclone**
Ellie

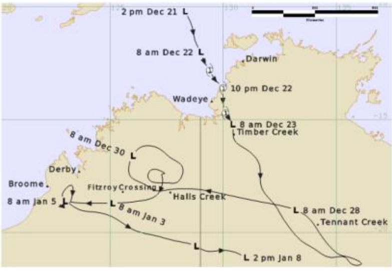


**(f) Back Trajectory Frequency**
(Glenormiston)

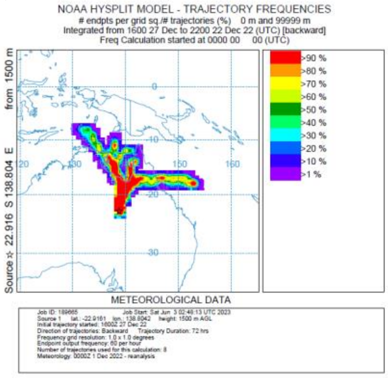


**March 1-11, 2023: Rainfall**
Mar 1-7:

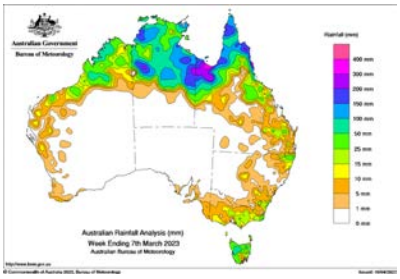

Mar 7-14:

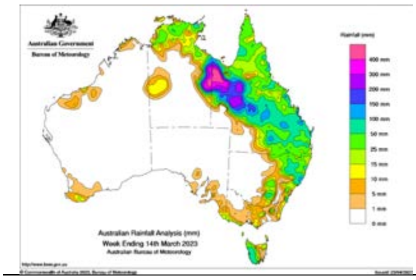

**(g) Precipitable Water Content (kg/m$^2$)**

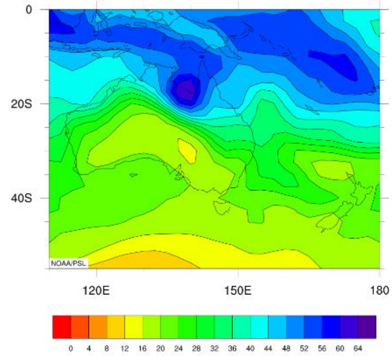


**(h) Back Trajectory Frequency**
(Camooweal)

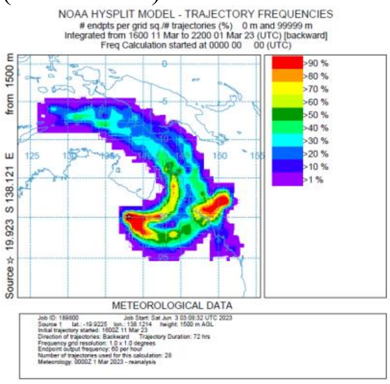


**Figure S14. 2023 Flood.** Top (left to right): Monthly rainfall totals December 2022 to March 2023. Middle row (left to right): RMM MJO **(a)** O-N-D, 2022 and **(b)** J-F-M, 2023. Sub-heading: **December 22–27, 2022,** Top left: 1-week rainfall ending December 27; **(c)** Precipitable water content (22–27/12/2022); Back Trajectory Frequency (22–27/12/2022) ending at **(d)** Camooweal and **(e)** Glenormiston; **(f)** Tropical Cyclone track map (Ellie). Sub-heading: **March 1–11, 2023,** 1-week rainfall ending March 7 and 14 (left column); **(g)** Precipitable water content (1–11/03/2023); **(h)** Back Trajectory Frequency (1–11/03/2023) ending at Camooweal.

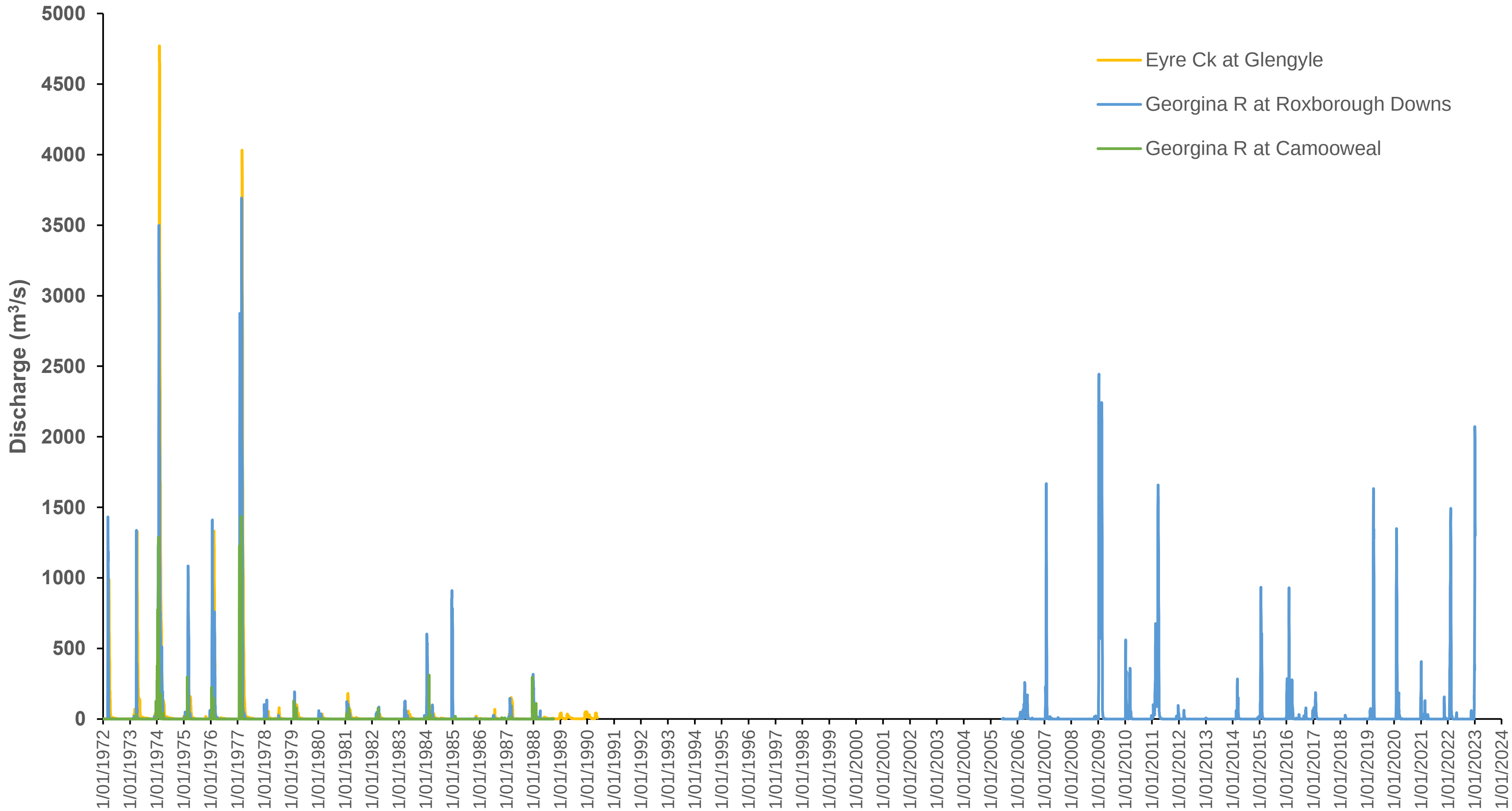


**Figure S15.** Daily river discharge ($m^3/s$) for gauging stations on the Georgina River at Camooweal (#001204A) and Roxborough Downs (#001203A) and on Eyre Creek at Glengyle (#001101A). No data is available for Camooweal after 29/09/1988 and for Glengyle after 21/05/1990 and for Roxborough Downs between 30/09/1988 and 5/06/2005.